

11-2-2020

Surface Enhanced Raman Spectroscopy (SERS) as a Nanoscale Adsorption Phenomenon: Development of Tailored Nanomaterials for Applications in Drug Detection

Chiara Deriu

Florida International University, cderi005@fiu.edu

Follow this and additional works at: <https://digitalcommons.fiu.edu/etd>

 Part of the [Analytical Chemistry Commons](#), [Materials Chemistry Commons](#), [Nanoscience and Nanotechnology Commons](#), and the [Physical Chemistry Commons](#)

Recommended Citation

Deriu, Chiara, "Surface Enhanced Raman Spectroscopy (SERS) as a Nanoscale Adsorption Phenomenon: Development of Tailored Nanomaterials for Applications in Drug Detection" (2020). *FIU Electronic Theses and Dissertations*. 4583.

<https://digitalcommons.fiu.edu/etd/4583>

This work is brought to you for free and open access by the University Graduate School at FIU Digital Commons. It has been accepted for inclusion in FIU Electronic Theses and Dissertations by an authorized administrator of FIU Digital Commons. For more information, please contact dcc@fiu.edu.

FLORIDA INTERNATIONAL UNIVERSITY

Miami, Florida

SURFACE ENHANCED RAMAN SPECTROSCOPY (SERS)
AS A NANOSCALE ADSORPTION PHENOMENON:
DEVELOPMENT OF TAILORED NANOMATERIALS
FOR APPLICATIONS IN DRUG DETECTION

A dissertation submitted in partial fulfillment of the

requirements for the degree of

DOCTOR OF PHILOSOPHY

in

CHEMISTRY

by

Chiara Deriu

2020

To: Dean Michael R. Heithaus
College of Arts, Sciences, and Education

This dissertation, written by Chiara Deriu, and entitled Surface Enhanced Raman Spectroscopy (SERS) as a Nanoscale Adsorption Phenomenon: Development of Tailored Nanomaterials for Applications in Drug Detection, having been approved in respect to style and intellectual content, is referred to you for judgment.

We have read this dissertation and recommend that it be approved.

Yesim Darici

Anthony P. DeCaprio

Alexander M. Mebel

Jaroslava Mikšovská

Stanislaw F. Wnuk

Bruce R. McCord, Major Professor

Date of Defense: November 2, 2020

The dissertation of Chiara Deriu is approved.

Dean Michael R. Heithaus
College of Arts, Sciences, and Education

Andrés G. Gil
Vice President for Research and Economic Development
and Dean of the University Graduate School

Florida International University, 2020

© Copyright 2020 by Chiara Deriu

ORCID 0000-0003-3077-5029

All rights reserved by the author with the exception of Figures 2.4, 2.5, 2.7, 2.8, 4.1, 5.6, 7.2, 7.3, 7.8 b, 8.1, and Sections 8.1, 8.2.1, 8.3.1. These figures and sections have been included with permission of their respective publishers.

CC BY-NC-ND 4.0 International Public License.

DEDICATION

A Maestra Rita e Maestra Gabriella

ACKNOWLEDGMENTS

I would like to acknowledge the National Institute of Justice (NIJ), Office of Justice Programs, U.S. Department of Justice (Award #2015-IJ-CX-K006) for funding the work on synthetic cannabinoids detection by SERS, and for the research assistantship support during the Fall 2016–Spring 2019 period. My acknowledgments also go to the NSF IUCRC for the award 1739805 to FIU - Center for Advanced Research in Forensic Science, which supported the research on fentanyl and fentalogs detection by SERS, to the International Forensic Research Institute (IFRI) for funding the transmission electron microscopy studies of the nanostars developed in this dissertation through their 2019 IFRI Student Development Award, and to the University Graduate School at FIU for the Dissertation Year Fellowship (Fall 2020).

I would like to thank my advisor, Dr. Bruce McCord, for trusting me and giving me the invaluable opportunity to shape my research according to my own interests. My most sincere gratitude goes also to Dr. Mebel and Dr. Morozov, who taught me all I know about Density Functional Theory and guided me in the development of the computational studies of this dissertation. Special thanks go also to Dr. Cai for letting me monopolize the zetasizer in his laboratory, and all of my committee members for providing feedback during these years as a PhD student. Thanks to the McCord group, in particular Dr. Ling Wang and the interns and visiting students whom I mentored and collaborated with: Irene Conticello, Majlinda Prifti, and Asier Bracho.

My final and biggest thanks go to my friends, here and overseas, who supported me every day during this journey, and to Maestro Tack-Fang and the people at the Miami fencing club, who welcomed me into their family and introduced me to the beautiful (and difficult!) art of fencing. I would like to especially thank the new very good friends I made here in Miami; Jenna, “my friend from Atlanta” who is not from Atlanta, Quentin, the

best pandemic companion (!) I could have ever wished for, and Fabiana, without whom I would had been even more puzzled about this place. Vi voglio un mondo di bene!

And I know I have just written that the preceding paragraph contained my final thanks, but I would also like to acknowledge my family, my grandparents, and the events of life who and which contributed to shaping the person (and scientist) I am — profoundly curious and perseverant.

ABSTRACT OF THE DISSERTATION
SURFACE ENHANCED RAMAN SPECTROSCOPY (SERS)
AS A NANOSCALE ADSORPTION PHENOMENON:
DEVELOPMENT OF TAILORED NANOMATERIALS
FOR APPLICATIONS IN DRUG DETECTION

by

Chiara Deriu

Florida International University, 2020

Miami, Florida

Professor Bruce R. McCord, Major Professor

Surface enhanced Raman spectroscopy (SERS) is an analytical technique in which nanostructured substrates amplify the inherently weak Raman signal of an adsorbed species by several orders of magnitude, enabling the detection of trace compounds, up to the single molecule level. While this may be an exceptional tool for any analytical scientist, SERS is at present relegated to the role of academic sensation, and is underutilized in everyday analytical practice. This setback could be attributed to a poor understanding of nanoscale surfaces and their chemical environment; since molecular adsorption at the nanostructured surface enables SERS detection, uncertainty about what happens at the surface makes SERS experiments convoluted and often inaccessible. Therefore, there is a pressing need to further nanoscale surface chemistry studies: they are the key to effect the transition of SERS from academic sensation to benchmark technique for routine diagnostics.

The present research takes this call by developing a library of SERS-active bimetallic nanostars, and utilizing them to systematically study the interplay between colloidal stability and SERS performance. Emphasis is given to elucidating the adsorption process of stabilizers to the nanoparticle surface, which was studied utilizing a multi-analytical approach. In addition, DFT calculations were performed in support of mechanistic and

structural hypotheses. A population of structures for a simplified all-gold cluster system were obtained at the B3LYP/LANL2DZ level of theory, using both explicit solvent molecules and the continuum solvent model SMD.

The experimental results suggest that stabilizers such as citrate are weakly chemisorbed to the bimetallic surface, and have K_{ad} values that make them easily displaceable by drug analytes. The DFT results provided a population of possible gold-citrate structures, which show significance of gold-ligated water in the adsorption of carboxylates. Preliminary results on a bimetallic system suggest a similar trend as well.

This multi-analytical, theory-assisted approach to colloid development allowed for the formulation of a set of well characterized SERS-active colloids, capable of providing a high level of surface control during SERS measurements. This ultimately allows for straightforward protocol development, as demonstrated by applications in drug detection, and sets foundations for the establishment of SERS as a routine analytical technique.

TABLE OF CONTENTS

CHAPTER	PAGE
1. Introduction	1
1.1 Statement of the problem	1
1.2 Objectives	3
1.3 Structure of the work	4
REFERENCES	5
2. Surface Enhanced Raman Spectroscopy (SERS) as a surface phenomenon	8
2.1 Theory of Surface Enhanced Raman Spectroscopy (SERS)	8
2.2 SERS substrates	15
2.2.1 Colloidal nanomaterials and colloidal stability	15
2.2.1.1 Stability of colloidal noble metal nanoparticles	18
2.2.1.2 Sample preparation for colloid-based SERS measurements	21
2.2.2 Extinction in colloids and shape effects on optical properties	23
2.2.2.1 Noble metal nanostars	28
2.3 Remarks on SERS and surface adsorption	35
REFERENCES	41
3. Materials and Methods	50
3.1 Materials	50
3.2 Methods	51
3.2.1 Synthesis of nanostars	51
3.2.2 Synthesis of reference AuAg nanospheres	51
3.2.3 Electrophoretic Light Scattering (ELS)	52
3.2.4 Extinction and UV/Vis absorption spectroscopy	55
3.2.5 X-ray Photoelectron Spectroscopy (XPS)	56
3.2.6 Transmission Electron Microscopy (TEM)	57
3.2.7 Normal Raman and Surface-Enhanced Raman Spectroscopy (SERS)	57
3.2.8 Statistical Analysis	58
3.2.9 Density Functional Theory (DFT) calculations	58
3.2.10 FTIR spectroscopy	59
REFERENCES	60
4. Going surfactant-free: challenges in anisotropic nanoparticle stabilization	63
4.1 A nanostars platform to probe the surface chemical environment	63
4.2 Selection of candidate non-surfactant stabilizers and working hypotheses	69
4.2.1 Optimization of model surfactant-free formulation NS/Ct	72
4.2.2 Screening of other candidate stabilizers by ELS	78
4.2.3 Screening of effective candidate stabilizers by extinction spectroscopy	81
4.2.4 Summary	84
4.3 Chemical state of gold and silver	84

4.3.1	Surface characterization of NS/Ct by XPS	85
4.3.2	Crystallographic analysis by HR-TEM	88
4.3.3	Summary	91
	REFERENCES	92
5.	SERS performance studies of the new colloidal nanostar formulations	96
5.1	Crystal Violet as model target analyte for SERS performance studies	96
5.2	Reproducibility of optical properties and effects on SERS intensity	102
5.2.1	Optical properties and relationship with SERS response	106
5.2.2	Morphological characterization: variability and yield	117
5.2.3	Recommendations	122
5.3	AEF as a function of capping species	123
5.4	Shelf life of the new NS formulations	131
5.5	Summary	138
	REFERENCES	139
6.	The stabilizer-metal interaction: strength and adsorption modes	142
6.1	Experimental estimates of the citrate-AuAg interaction	142
6.2	ζ potential titrations	142
6.3	FTIR spectroscopy: coordination modes	152
6.4	Summary	159
	REFERENCES	161
7.	DFT calculations for nanoscale adsorption modeling	165
7.1	Density Functional Theory (DFT): overview	165
7.1.1	DFT calculations of plasmonic nanoparticles and nanoalloys	169
7.1.2	Modeling ligand adsorption on coinage metal nanostructures	172
7.2	Modeling the adsorption of citrate on nanostars	180
7.2.1	DFT calculations of Citrate/Au ₂₀	183
7.2.2	Au ₁₉ Ag: homotops and citrate adsorption	196
7.2.3	Summary	198
	REFERENCES	201
8.	Applications	209
8.1	The application of SERS in forensic toxicology	209
8.2	Applications that make use of the new colloidal nanostar formulations	219
8.2.1	Surface-enhanced Raman spectroscopy, Raman, and density functional theoretical analyses of fentanyl and six analogs	222
8.2.2	Summary and Prospects	239
8.3	Applications that make use of traditional nanoparticles	240
8.3.1	Micro Solid Phase Extraction Surface-Enhanced Raman Spectroscopy (μ - SPE/SERS) Screening Test for the Detection of the Synthetic Cannabinoid JWH-018 in Oral Fluid	241

8.3.2	Other synthetic cannabinoids	263
8.3.2.1	Complete vibrational and adsorption study of JWH-081	264
8.3.2.2	Towards an <i>in silico</i> Raman library for synthetic cannabinoids	271
8.3.2.3	Summary and Prospects	281
	REFERENCES	283
9.	Conclusions	294
	REFERENCES	299
	APPENDICES	301
	VITA	346

LIST OF TABLES

TABLE	PAGE
3.1 Post-synthetic addition of candidate stabilizing agents.	52
3.2 Viscosity, dielectric permittivity, and refractive index ($\lambda = 633$ nm) at varying temperature.	54
3.3 Bjerrum length at varying temperature.	55
4.1 Summary of reagents concentrations and volumes for nanostars synthesis. . .	66
4.2 NS/Ct formulations. Observations on visual signs of coagulation at the 12 hour mark after synthesis.	76
4.3 Candidate NS formulations. Observations on visual signs of coagulation at the 2 hour mark after synthesis.	80
5.1 DFT, Normal Raman (λ_{exc} 785 nm), and SERS (λ_{exc} 785 nm, NS/Ct) of Crystal Violet	100
5.2 ANOVA F-test for the normalized SERS intensity of CV at 1170 cm^{-1} over time. 101	101
5.3 Redox potentials of metallic species relevant to the nanostars synthesis. . . .	105
5.4 λ_{LSPR} of 5 individual NS batches.	107
5.5 ANOVA F-test for the normalized SERS intensity of CV at 1170 cm^{-1} for each of the five individual NS batches.	107
5.6 Tukey's HSD test. Ordered differences of the normalized SERS intensity of CV at 1170 cm^{-1} for each pair of individual NS batches.	109
5.7 Lettered Tukey's HSD groupings for the normalized SERS intensity of CV at 1170 cm^{-1} for each of the five individual NS batches.	109
5.8 λ_{LSPR} of 5 NS_{pooled} samples.	111
5.9 Comparison of NS with NS_{pooled} . Descriptive statistics.	112
5.10 ANOVA F-test for the normalized SERS intensity of CV at 1170 cm^{-1} for each of the five NS_{pooled} samples.	114
5.11 Tukey's HSD test. Ordered differences of the normalized SERS intensity of CV at 1170 cm^{-1} for each pair of NS_{pooled} samples.	114
5.12 Lettered Tukey's HSD groupings for the normalized SERS intensity of CV at 1170 cm^{-1} for each of the five NS_{pooled} samples.	114

5.13	ANOVA F-test for the normalized SERS intensity of CV at 1170 cm ⁻¹ at different concentrations, and obtained with different NS _{pooled} samples.	116
5.14	Tukey's HSD test. Ordered differences of the normalized SERS intensity of CV at 1170 cm ⁻¹ at different concentrations, and obtained with different NS _{pooled} samples.	116
5.15	Lettered Tukey's HSD groupings for the normalized SERS intensity of CV at 1170 cm ⁻¹ at different concentrations, and obtained with different NS _{pooled} samples.	116
5.16	Normalized SERS and Raman intensities at CV's marker band 1170 cm ⁻¹ and AEF values for each of the CV-NS systems.	127
5.17	Normalized SERS and Raman intensities at CV's marker band 1170 cm ⁻¹ and AEF values for each of the CV-NS systems.	128
5.18	ANOVA F-test for the AEF values of the CV-NS systems under study.	128
5.19	Tukey's HSD test. Ordered differences of the AEF values of the CV-NS systems under study.	129
5.20	Lettered Tukey's HSD groupings for the AEF values of the CV-NS systems under study.	129
5.21	ANOVA F-test for the AEF values of the CV-NS systems under study, compared to CV-NS/OH.	129
5.22	Tukey's HSD test. Ordered differences of the AEF values of the CV-NS systems under study, compared to CV-NS/OH.	130
5.23	Lettered Tukey's HSD groupings for the AEF values of the CV-NS systems under study, compared to CV-NS/OH.	131
5.24	λ_{LSPR} and Extinction at λ_{LSPR} of the pooled NS formulations over time.	131
5.25	Observations on the visual state of coagulation of the NS formulations over time.	132
5.26	Mean and σ of the time zero reference SERS intensities of CV at 1170 cm ⁻¹ utilized for the shelf life study.	135
5.27	Shelf lives of the NS formulations: t-test results.	137
5.28	Shelf lives of the NS formulations.	137
6.1	Fitting and thermodynamic parameters for the NS/Ct system, at 10 and 20°C.	148
7.1	Interatomic distances of the Au ₂₀ cluster, optimized at the B3LYP/LANL2DZ level.	184

7.2	Interatomic distances and bond angles of the citrate/Au ₂₀ complex <i>S1</i> , optimized at the B3LYP/LANL2DZ level.	187
7.3	Interatomic distances and bond angles of the citrate/Au ₂₀ complex <i>S2</i> , optimized at the B3LYP/LANL2DZ level.	192
7.4	Interatomic distances and bond angles of the citrate/Au ₂₀ complex <i>S3</i> , optimized at the B3LYP/LANL2DZ level.	193
7.5	Interatomic distances and bond angles of the citrate/Au ₂₀ complex <i>VI</i> , optimized at the B3LYP/LANL2DZ level.	194
7.6	Theoretical thermodynamic quantities for the formation of the <i>S1</i> , <i>S2</i> , <i>S3</i> , and <i>VI</i> complexes in the gas phase, obtained at the B3LYP/LANL2DZ level.	196
7.7	Theoretical thermodynamic quantities for the formation of the <i>S1</i> , <i>S2</i> , <i>S3</i> , and <i>VI</i> complexes in solution, obtained at the B3LYP/LANL2DZ level, with the introduction of the continuum solvent model SMD. ⁷⁰	196
7.8	Interatomic distances for the three inequivalent Au ₁₉ Ag tetrahedral homotops, “ <i>c</i> ”, “ <i>e</i> ”, and “ <i>v</i> ”, compared to Au ₂₀ and Ag ₂₀ , optimized at the same level of theory (B3LYP/SRSC).	198
8.1	Common interfering bands in biological matrices.	213
8.2	DFT-calculated and experimental Raman and SERS frequencies of fentanyl, and assignment of normal modes.	227
8.3	DFT-calculated and experimental Raman and SERS frequencies of acetylfentanyl, and assignment of normal modes.	228
8.4	DFT-calculated and experimental Raman and SERS frequencies of acrylfentanyl, and assignment of normal modes.	228
8.5	DFT-calculated and experimental Raman and SERS frequencies of benzylfentanyl, and assignment of normal modes.	229
8.6	DFT-calculated and experimental Raman and SERS frequencies of butyrylfentanyl, and assignment of normal modes.	229
8.7	DFT-calculated and experimental Raman and SERS frequencies of furanylfentanyl, and assignment of normal modes.	230
8.8	DFT-calculated and experimental Raman and SERS frequencies of para-fluorofentanyl, and assignment of normal modes.	230
8.9	DFT, normal Raman, and SERS bands of JWH-018, vibrational assignments, and error metrics.	252
8.10	Langmuir adsorption and thermodynamic parameters (T = 294.15 K).	257

8.11	Analytical figures of merit.	258
8.12	Analytical figures of merit for fortified oral fluid samples.	260
8.13	DFT, Raman, and SERS frequencies of JWH-081, and assignment of vibrational modes.	268
8.14	Figures of Merit JWH-081.	271
8.15	Percent errors between experimental Raman and DFT-predicted frequencies.	273
8.16	DFT and Raman bands of JWH-175, and normal modes assignment.	275
8.17	DFT and Raman bands of JWH-250, and normal modes assignment.	276
8.18	DFT and Raman bands of RCS-4, and normal modes assignment.	278
8.19	DFT and Raman bands of XLR-11, and normal modes assignment.	279
8.20	DFT and Raman bands of ADB-PINACA, and normal modes assignment.	280

LIST OF FIGURES

FIGURE	PAGE	
1.1	Keyword frequencies (Web of Science database) within (a) SERS publications and (b) nanotechnology and nanofabrication publications for the year 2017. (c) The same proportions are found to be constant trends in the time window from 1997 to 2017.	3
2.1	Behavior of the change in free energy as a function of interparticle distance. The components associated with both (a) attractive forces and (b) electrostatic repulsions are reported. (c) A possible form of the total-interaction free energy of a colloidal system (DLVO curve) as a function of interparticle distance (r) (red profile). Maximum minimization of the free energy will occur at very short distances (primary minimum), where coagulation occurs. A shallower minimum at intermediate distances is often also present; no energy barrier is required (secondary minimum), and flocculation (reversible aggregation) occurs. .	17
2.2	Solid-solution interface phenomena at the basis of the development of surface charge and onset of Coulombic repulsions: (a) ionization of acid groups constituting the surface; (b) ionization of basic group constituting the surface; (c) and (d) differential dissolution of sparingly soluble compounds; (e) isomorphous substitution in a surface; (f) specific adsorption of an ionic compound. Figure inspired by D.H. Everett. ³⁶ . . .	18
2.3	(a) Schematic depiction of a colloidal nanoparticle with nomenclature: the electrical double layer, or electrical interfacial layer (shaded yellow area), ³⁹ is composed of a firmly held layer, often referred to as Stern layer, and a diffuse layer. The slipping plane identifies the boundary between the electrical interfacial layer, hydrodynamically immobile, and the rest of the solution, which is hydrodynamically mobile. The way(s) in which the electrical interfacial layer develops in colloidal noble metal nanoparticles is not fully elucidated yet, and it is closely related to the chemical state of the metallic surface. This is thought to exist as either (b) a double domain with outer partially positively charged region, (c) a double domain with outer region charged by integer positive charges, or (d) a monodomain of zero-valent noble metal.	20
2.4	High resolution XPS spectra of the Au $4f$ core peaks of citrate-capped monometallic gold nanospheres (left) and reference bulk gold specimen (right). Peak deconvolution profiles highlights the presence of Au ⁰ (blue) and Au ^{δ^+} (green). The latter is calculated to account for 4% of the total gold nanospheres surface. Adapted with permission of Springer Nature, from Al-Johani <i>et al.</i> , ⁴² Copyright 2017; permission conveyed through Copyright Clearance Center, Inc.	22

2.5	(a) Extinction spectra of gold nanorods of various aspect ratios: AR 2 (pink), AR 2.5 (purple), AR 2.75 (blue), AR 3 (green), AR 3.5 (brown), and AR 4.5 (orange). The excitation line used for SERS measurements is marked in red. (b) Normalized SERS spectra of 10^{-6} M methylene blue obtained using gold nanorods of various aspect ratios (color coded according to (a) panel) and an excitation line at 785 nm. The highest enhancements are observed for gold nanorods exhibiting their λ_{LSPR} 55 to 105 nm in pre-resonance with the excitation source. Modified with permission from Sivapalan, S.T. <i>et al.</i> ⁶² Copyright (2013) American Chemical Society.	27
2.6	Extinction spectra of different colloidal nanostructures showing the effect of size and shape on the λ_{LSPR} . Highly monodispersed gold nanospheres with hydrodynamic diameters of 16 nm (pink) and 68 nm (blue) were synthesized following Frens' and Bastús' procedures, respectively; ^{68,69} polydispersed prolate gold nanospheroids with average diameter of 161 nm (orange) were synthesized using Frens' method; ⁶⁸ gold/silver nanostars (green) were synthesized using a modified version of He's protocol. ⁶⁶ The largest red-shift of the plasmon band is observed when altering the shape. Intensities were scaled for ease of comparison.	29
2.7	Reproduced with permission from Masango, S.S. <i>et al.</i> ⁷⁹ Copyright (2016) American Chemical Society. Experimental data (red scatter plot) obtained in integrated ALD-SERS experiment are fitted to the adjusted expression for SERS signal decay as a function of distance from enhancing surface (black solid line). The top insets show a SEM micrograph side view of the Al_2O_3 film over Ag nanosphere substrate (AgFON) used for the study (left), and a false-color rendering of the near-field intensity distribution obtained using the finite-difference time-domain method in computational electrostatics (right).	31
2.8	SERS spectra of Crystal Violet dye obtained with CTAB-capped nanostars at various concentrations of surfactant (left), and relative analytical enhancement factors as a function of CTAB concentration (right). Modified from He, S. <i>et al.</i> , ⁶⁶ Copyright 2015; permission conveyed through Copyright Clearance Center, Inc.	33
2.9	Some common adsorption models: (a) Langmuir, also known as class L, sub-group 2 isotherm, according to the Giles classification system; (b) BET, also known as class L, sub-group 3, . . . , n isotherm, according to the Giles classification system; (c) Anti-Langmuir, also know as class S, sub-group 2 isotherm, according to the Giles classification system. ^{93,94}	36

2.10	Different adsorption scenarios that could happen during a SERS measurement, provided that the $K_{AS} > K_{AA}$. If $K_{AS} > K_{CS}$, direct adsorption can occur, (a) either involving the formation of chemical bonds (<i>e.g.</i> , thiols on Au or Ag), or (b) other strong physical interactions, such as π interactions (<i>e.g.</i> , aromatic hydrocarbons on Au). If $K_{AS} < K_{CS}$, and $K_{CS} \geq K_{CA}$, adsorption occurs without displacement of the capping species, (c) either by ion pairing if the capping species is charged, or (d) by physical (i) or chemical (ii) interactions if the capping species is neutral (sterically stabilized colloids).	38
4.1	Effect of varying molar ratios of reactants in the synthesis of colloidal AuAg bimetallic nanostars, as proposed by He <i>et al.</i> ² The effect of increasing excess of L-ascorbic acid while keeping the ratio of gold to silver constant at 18:1 is displayed horizontally, with the largest excess L-ascorbic acid on the left. The effect of having L-ascorbic acid as the limiting reagent is shown on the rightmost side. The effect of increasing the silver content while keeping the ratio of gold to L-ascorbic acid constant at 3:5 is instead displayed horizontally, with the lowest silver content at the bottom. Highlighted in red is a TEM image of the nanostars produced with the selected protocol for this research work, Au:Ag of 18:1 and Au:L-AA of 3:5, and stabilized with CTAB. All TEM images are reproduced with permission from He, S. <i>et al.</i> , ² Copyright 2015; permission conveyed through Copyright Clearance Center, Inc.	65
4.2	Oxidation of L-ascorbic acid, $H(L-AA)_{red}$. At neutral pH, ascorbic acid is present in solution as ascorbate, $(L-AA)^{-}_{red}$, an anion stabilized by resonance. Ascorbate exchanges one electron at a time, ⁵ yielding the radical $(L-AA)^{\cdot}$ first, and the neutral, oxidized species dehydroascorbate second, $(L-AA)_{ox}$	67
4.3	Temporal evolution of the extinction spectrum of a batch of the as-synthesized Au/Ag colloidal nanostars. Coagulation, thus instability, is reflected by the rapid decrease of the intensity at the λ_{LSPR}	68
4.4	Structure of cetyltrimethylammonium bromide (CTAB).	69
4.5	Structure of trisodium citrate with pK_a values for each dissociable group. Citrate is a common reducing agent for the synthesis of colloidal gold and silver monometallic nanoparticles. ¹² Excess of this reagent and charged oxidation products are thought to provide stability to these suspensions.	71
4.6	Structures of disodium L-tartrate (left) and sodium acetate (right) with pK_a values for each dissociable group.	72
4.7	Structures of 1,3-propanedisulfonic acid disodium salt.	72
4.8	ζ potential (red) and conductivity (blue) behavior of AuAg colloidal nanostars titrated with trisodium citrate. The error bars report the standard error for each measured point. The data trend is highlighted by polynomial fits (dotted lines).	74

4.9	(a) Absolute value of the ζ potential of AuAg colloidal nanostars titrated with trisodium citrate. A fourth degree polynomial fit was utilized to highlight the trend, which resembles a class L isotherm, according to the Giles classification system. ^{18,19} The inset shows the initial linear relationship between $ \zeta $ and citrate concentration (R^2 0.9975), while the yellow shaded area indicates the point at which the system likely approaches saturation. (b) Class L isotherm according to the Giles classification system. The solid line shows a pure Langmuir behavior (cartoon in panel (c)) while the dashed line describes a BET behavior (cartoon in panel (d)).	75
4.10	Variation of the total interaction potential curve for a colloidal system with fixed size (a , dimension of the smallest nanoparticle feature) and varying ionic strength, I , and Debye length, κ^{-1} . The potential barrier to be overcome for coagulation to occur is highest at lowest ionic strength ($V_1 > V_2$). The secondary minimum at which flocculation occurs is found at shorter separation distances for higher ionic strength dispersions. Figure inspired by Atkins, de Paula, and Keeler, 2018. ²⁰	77
4.11	Average ζ potential (yellow) and conductivity (red) values for a series of AuAg nanostars formulations, at (a) fixed concentration of the candidate stabilizer (0.96×10^{-3} M), and (b) fixed molar ionic strength of the formulation (3.4×10^{-3} M). The shaded area in green highlights the ζ potential values associated with formulation stability ($ \zeta \geq 25 $ mV), ⁶ while the shaded areas in blue highlight increase or decrease of conductivity compared to the as-synthesized nanostars (NS, top bar in both graphs). Results relative to the use of sodium hydroxide (NS/OH) are also reported.	79
4.12	Decay curves of AuAg nanostars formulations obtained with different candidate stabilizing agents. The top panels show a comparison among sodium carboxylates: trisodium citrate (NS/Ct, red), disodium tartrate (NS/Tt, yellow), and sodium acetate (NS/Ac, green), (a) at a constant concentration of 0.96×10^{-3} M, and (b) at a constant molar ionic strength of 3.4×10^{-3} M. (c) Comparison between model effectively stabilized formulation NS/Ct (positive control, red) model ineffectively stabilized formulation NS/PrSulf (1,3-propanedisulfonic acid disodium salt, negative control); both NS/PrSulf at constant concentration (light blue) and at constant molar ionic strength (indigo) are shown. (d) Comparison between model effectively stabilized formulation NS/Ct and NS/CO ₃ ²⁻ ; both formulations at constant concentration (light purple) and at constant molar ionic strength (purple) are shown. All grey profiles refer to the as-synthesized nanostars with no candidate stabilizer added. Dashed B-spline connectors are used to highlight data trends.	83
4.13	Survey XPS scan of NS/Ct. Blue asterisks mark the peaks produced by the bimetallic component of the colloidal nanostars. The other detected species can be attributed to the glass substrate utilized for drop-casting the sample (Mg, Na, O, Cl, Si), or to the presence of unwashed stabilizers (Na, O, Cl, C).	85

4.14	C 1s high resolution XPS raw data for NS/Ct. The carbon peak presents a multimodal distribution, suggesting convolution of at least three different bands. This is commonly observed in C 1s peaks, as well as expected for the analyzed sample, in that there are at least three types of carbon: C-OH (citrate's alcoholic functions), COO ⁻ (citrate's carboxylic functions), and aliphatic C=C (adventitious carbon). The latter is the one traditionally used for binding energy referencing, as it is ubiquitously detected in XPS. ²⁴	86
4.15	High resolution XPS spectra of NS/Ct: (a) Au 4f core peaks with peak deconvolution, and (b) Ag 3d core peaks. Both spectra are reported after standard Shirley background subtraction.	89
4.16	(a1–3) TEM micrographs of three nanostars, sampled from different batches of NS/Ct, and (b1–3) high resolution details of selected areas. (c1–3) Indexed SAED patterns relative to each of the three nanostars' selected areas.	90
4.17	HR-TEM micrographs of NS/Ct nanostars (left) and highlighted possible grain boundaries and twinning planes (right).	92
5.1	Structure of Crystal Violet, CV.	96
5.2	UV/Vis absorption spectrum of Crystal Violet (10 ⁻⁵ M in water). The red line marks the excitation wavelength used for Normal Raman and SERS experiments.	97
5.3	(a) Normal Raman spectrum of CV in aqueous solution, at a concentration of 10 ⁻³ M. (b) SERS spectrum of CV at a concentration of 10 ⁻⁷ M, obtained using NS/Ct as the colloidal substrate. Both spectra were baseline-corrected, and their intensities were normalized to the intensity of the band at 3200 cm ⁻¹ , assigned to ν(OH) of water (§ 3.2.7).	99
5.4	Time evolution of the average normalized SERS intensity of the CV band at 1170 cm ⁻¹ (bottom) with ANOVA plot (top). The off-color band around each spectrum represents the standard error. In the ANOVA plot (R ² 0.6761), the pink line represents the global mean (2.32 ± 0.05 a.u.), while the green rhomboids represent the quartiles relative to each time point: t ₀ , 8, 16, 26, and 35 minutes.	101
5.5	(a) Extinction spectrum of a 10% dilution of citrate-reduced silver nanospheres (Ag/Ct) in water, synthesized according to the procedure reported by Lee and Meisel. ¹⁷ The plasmon band is relatively narrow, with FWHM of 120 nm. (b) Representative extinction spectrum of colloidal AuAg nanostars (NS/CO ₃ ²⁻ formulation). The plasmon band is wider than traditional Ag/Ct nanoparticles, with FWHM of 234 nm.	104

5.6	Extinction spectrum of gold nanostars (Au NS, <i>blue</i>) and simulated extinction spectrum (red). The simulated extinction spectrum shows the distinct contributions from the spheroid core (centered at about 512 nm), and that of the branches (centered around 610 nm). Reproduced with permission from Minati, L. <i>et al.</i> , ⁸ Copyright (2014), with permission from Elsevier.	104
5.7	Kinetic (blue) versus thermodynamic (red) control of (a) two parallel reactions and (b) a series of sequential reactions. Figures inspired by Xia <i>et al.</i> , 2015. ¹¹	106
5.8	ANOVA plot (R^2 0.9304) for the normalized SERS intensity of CV at 1170 cm^{-1} obtained by utilizing five individual $\text{NS}/\text{CO}_3^{2-}(\text{c})$ batches as enhancing substrates. The samples have been ordered on the basis of the λ_{LSPR} of the NS batch. The pink line represents the global mean (2.2 ± 0.5 a.u.), while the green rhomboids represent the quartiles relative to each NS sample.	108
5.9	Scatter plot of the normalized SERS intensity of CV at 1170 cm^{-1} as a function of the NS's λ_{LSPR} . The data can be fitted to a regression line (dotted red line) of equation $y = (0.020 \pm 0.002)x - (12 \pm 1)$ and R^2 of 0.9024. The 95% confidence band is shown in dark red, while the 95% prediction band is shown in light red.	110
5.10	Box and whiskers plot of the λ_{LSPR} of the individual NS and $\text{NS}_{\text{pooled}}$. The blue dots represent the medians, while the red squares represent the means.	112
5.11	ANOVA plot (R^2 0.8831) for the normalized SERS intensity of CV at 1170 cm^{-1} obtained by utilizing five different $\text{NS}_{\text{pooled}}$ samples as enhancing substrates. The samples have been ordered on the basis of the λ_{LSPR} of the $\text{NS}_{\text{pooled}}$. The pink line represents the global mean (1.18 ± 0.05 a.u.), while the green rhomboids represent the quartiles relative to each NS sample.	113
5.12	ANOVA plot (R^2 0.8960) for the normalized SERS intensity of CV at 1170 cm^{-1} obtained by utilizing different $\text{NS}_{\text{pooled}}$ as enhancing substrates, and different concentrations of CV: 5×10^{-9} M ($\text{NS}_{\text{pooled}}$ #6), 10^{-8} M ($\text{NS}_{\text{pooled}}$ #7), and 10^{-7} M ($\text{NS}_{\text{pooled}}$ #1–5). The pink line represents the global mean (0.79 ± 0.08 a.u.), while the green rhomboids represent the quartiles relative to each sample group.	115
5.13	TEM micrographs of NS/Ct, obtained from different aliquots from different batches. Polydispersity in terms of size is observed, while the number of non-branched nanoparticles is negligible.	118
5.14	Pie chart illustrating the morphological distribution of the analyzed NS/Ct batches. Five subtypes are identified; from left to right, g, h I, h II, f I, and f II. The same subtypes are found in all other analyzed nanostars formulations (Appendix B).	119
5.15	Proposed mechanism for the formation of the nanostars utilized in this research.	121

5.16	Percent frequency histograms representing the size distribution of (a) the equivalent tip-to-tip diameter of the nanostars, and (b) the length of their branches.	122
5.17	Lognormal distribution probability plot for the equivalent tip-to-tip diameter (Anderson-Darling value = 0.283; p-value = 0.630; $\alpha = 0.05$).	123
5.18	(a) SERS spectra of CV at a concentration of 10^{-7} M, obtained using each of the developed alternatively stabilized NS formulations as the enhancing substrate: NS/Ct (red), NS/Tt (yellow), NS/Ac (green), NS/CO ₃ ²⁻ (c) (blue), and NS/CO ₃ ²⁻ (l) (purple). (b) Comparison between the CV spectrum obtained with NS/Ct as the enhancing substrate (green), and that of CV obtained with the original ⁴ NS/CTAB formulation (pink). All spectra were baseline-corrected, and their intensities were normalized to the intensity of the band at 3200 cm ⁻¹ , assigned to $\nu(\text{OH})$ of water. Spectra in (a) are stacked for ease of comparison.	125
5.19	Hydrolysis of Crystal Violet in basic conditions.	126
5.20	ANOVA plot (R^2 0.9110) for the AEF values of the CV-NS systems under study. The pink line represents the global mean ($1.2 \pm 0.5 \times 10^5$), while the green rhomboids represent the quartiles relative to each sample group.	128
5.21	ANOVA plot (R^2 0.7766) for the AEF values of the CV-NS systems under study, compared to CV-NS/OH and ordered as a function of pH of the formulation. The pink line represents the global mean ($1.2 \pm 0.5 \times 10^5$), while the green rhomboids represent the quartiles relative to each sample group.	130
5.22	Schematics of the method based on linear regression utilized by the pharmaceutical industry for the determination of the shelf life of a product. The line of best fit is shown in red, the upper and lower 95% confidence bands are shown as dashed blue lines, and the upper and lower specification limits of the acceptance criterion are shown as yellow dashed lines. The x-coordinate of the point corresponding to the intersection between the (upper) 95% confidence band and the (upper) specification limit of the acceptance criterion corresponds to the calculated shelf life of the product under study. The upper confidence band and specification limit were chosen because the slope of the regression line is positive; for linear regression models with a negative slope, the lower confidence band and specification limit are utilized instead.	133
5.23	Scatter plot comparison of the 1 month time point samples of (a) NS/Ac and (b) NS/CO ₃ ²⁻ (l), with their respective t_0 references, A and B. The pink lines represent the global means, which are 1.62 ± 0.06 for the A t_0 -NS/Ac $t_{1\text{month}}$ pair, and 0.81 ± 0.04 for the B t_0 -NS/CO ₃ ²⁻ (l) $t_{1\text{month}}$ pair.	136

6.1	Four drugs of forensic and public health interest whose K_{ad} with citrate-reduced Au nanospheres are known: (a) salbutamol (β agonist, K_{ad} $1.0 \pm 0.3 \times 10^5 \text{ M}^{-1}$); ² (b) terbutaline (β agonist, K_{ad} $4.4 \pm 0.5 \times 10^5 \text{ M}^{-1}$); ² (c) clenbuterol (β agonist, K_{ad} $9 \pm 2 \times 10^5 \text{ M}^{-1}$); ² (d) JWH-018 (synthetic cannabinoid, K_{ad} $93 \pm 12 \times 10^5 \text{ M}^{-1}$). ³	144
6.2	Plots of the change in the absolute value of the ζ potential, $\Delta \zeta $, as a function of increasing concentration of trisodium citrate, at 10°C (blue) and 20°C (red). The data points were fitted to the Hill expansion of the Langmuir adsorption model (Equation 6.4).	149
6.3	Schematic representation of the ATR configuration. The IR source, IR_0 , is introduced inside the IRE at an angle above the critical angle. The light is internally reflected and attenuated by the generation of an evanescent wave. The exiting IR light, IR_1 , is different from IR_0 and carries the vibrational information of the sample.	153
6.4	FT-IR ATR spectra of the free citrate ion (red), obtained by drop-casting a 1 M trisodium citrate solution on the IRE, and of the purified and dried NS/Ct residues (blue). Spectra are on the same scale but stacked for ease of comparison.	155
6.5	FT-IR ATR spectra of the free tartrate ion (red), obtained by drop-casting a 1 M disodium tartrate solution on the IRE, and of the purified and dried NS/Tt residues (blue).	157
6.6	FT-IR ATR spectra of the free acetate ion (red), obtained by drop-casting a 1 M sodium acetate solution on the IRE, and of the purified and dried NS/Ac residues (blue).	158
6.7	From left to right, proposed coordination modes of citrate, L-tartrate (I and II), and acetate on the surface of the nanostars.	159
7.1	Three of the $5!/(3!2!)$ possible homotops of an A_3B_2 bimetallic cluster of fixed geometry.	170
7.2	Full-DFT global optimization minima and some lowest-energy isomers of Au clusters of 2 to 20 atoms. Adapted from Assadollahzadeh and Schwerdtfeger, 2009, ¹⁶ with the permission of AIP Publishing.	173
7.3	Some global minima from the 34-atom Ag_mAu_n sequence obtained by Rossi <i>et al.</i> ²⁰ by semi-empirical method. Light colored spheres correspond to Ag atoms, while dark colored spheres correspond to Au. Low symmetry, disordered structures appear in Au-rich clusters as the Ag content increases. Adapted from Rossi <i>et al.</i> , 2005, ²⁰ with the permission of AIP Publishing.	174
7.4	Examples of citrate coordination modes reported in literature: ^{51,56} (a) unidentate (κ), (b) bidentate (μ_2), and (c) terminus-terminus bidentate bridging (μ_4).	179

7.5	Thermodynamic cycle for the computation of the free energy of adsorption in solution, illustrated for the citrate/Au ₂₀ system.	183
7.6	Structure of the Au ₂₀ cluster, optimized at the B3LYP/LANL2DZ level: (a) side view, (b) top view, (c) bottom view. Gold atoms are labeled and numbered: <i>c</i> , center (N = 4); <i>e</i> , edge (N = 12); <i>v</i> , vertex (N = 4).	184
7.7	Structure of the citrate/Au ₂₀ complex (<i>SI</i>) in the gas phase, optimized at the B3LYP/LANL2DZ level. Atoms and molecules of interest are labeled: the central Au atom <i>c</i> ₁ , the two opposite vertices <i>v</i> ₁ and <i>v</i> ₄ , the edge Au atom <i>e</i> ₆ , the two molecules of water, <i>w</i> ₁ and <i>w</i> ₂ , and the central carboxylate [O(1)C(<i>x</i>)O(2)] ⁻	186
7.8	(a) Configuration of the adsorbed water <i>w</i> ₁ and central carboxylate of citrate. (b) Structure of a water dimer on a Cu(110) surface, optimized at the DFT level; adapted with permission of Springer, from Kumagai, T., ⁷⁷ Copyright 2012; permission conveyed through Copyright Clearance Center, Inc.	188
7.9	Stable structures of <i>SI</i> , <i>S2</i> , <i>S3</i> , and <i>VI</i> citrate/Au ₂₀ complexes.	191
7.10	Schematic representation of the three inequivalent homotops for the Au ₁₉ Ag tetrahedral cluster: (a) Au ₁₉ Ag “ <i>c</i> ”; (b) Au ₁₉ Ag “ <i>v</i> ”; (c) Au ₁₉ Ag “ <i>e</i> ”. Silver atoms are represented in grey, while gold atoms are shown in yellow.	197
7.11	Converged structure after geometry optimization of the Au ₁₉ Ag/citrate complex in the gas phase.	199
8.1	Application of Principal Component Analysis (PCA) to the detection of cocaine in oral fluid. SERS spectrum of a recovered supernatant aliquot of an oral fluid sample containing cocaine at an initial concentration of 100 ng/mL (green), compared to that of a recovered supernatant aliquot of a neat oral fluid sample (red). Cocaine’s marker band is observed at 1003 cm ⁻¹ . Plot of first two Principal Components relative to the SERS spectra of cocaine-fortified (green cluster) and neat oral fluid (red cluster). Each cluster consists of 20 spectra, and ellipses indicate 95% confidence intervals. Reprinted from Dies, H. <i>et al.</i> , ³⁵ Copyright (2018), with permission from Elsevier.	218
8.2	Examples of opiates and opioids: (a) morphine (μ agonist, primarily); (b) heroin (μ agonist); (c) buprenorphine (mixed agonist-antagonist); (d) fentanyl (μ agonist); (e) naloxone (antagonist).	220
8.3	General structure of the fentanyl skeleton, and chemical structures of the seven analytes utilized in this study.	223
8.4	(a) Comparison of the simulated spectra obtained with the different DFT methods; (b) Experimental SERS (blue) and Raman (red) spectra of fentanyl, compared to the best DFT-simulated Raman spectrum (ω B97XD/cc-pVTZ, black).	225
8.5	Calculated (scaled) and experimental spectra of the six fentanyl analogs.	226

8.6	SERS spectra of benzylfentanyl and acrylfentanyl, at a concentration of 10 ng/mL, obtained with two different morphologies of carbonate-capped AuAg nanomaterials, nanostars (NS/CO ₃ ²⁻ _(c) , blue) and nanospheres (NSph/CO ₃ ²⁻ _(c) , pink), and with CTAB-capped nanostars (NS/CTAB, green).	232
8.7	TEM micrographs of the two different morphologies of carbonate-capped AuAg nanomaterials utilized in this study, (a) nanospheres (NSph/CO ₃ ²⁻ _(c)) and (b) nanostars (NS/CO ₃ ²⁻ _(c)).	233
8.8	Comparison of Raman (left) and SERS (right) spectra of fentanyl and six of its analogs.	234
8.9	2-D principal component analysis (PCA) plots showing the separation of SERS spectra into different classes of substances. The plot on the left has been obtained utilizing SERS spectra in the 3278–200 cm ⁻¹ range, while the plot on the right was obtained using SERS spectra in the 1700–400 cm ⁻¹ range.	238
8.10	(a) Structure of JWH-018 with highlighted synthetic cannabinoids nomenclature and (b) 3D ball-and-stick model of the optimized geometry. C atoms are shown in gray, H in white, O in red, and N in blue.	250
8.11	(left) DFT simulated Raman (bottom, blue) and solid state experimental normal Raman (top, red) spectra of JWH-018. Intensities have been scaled for ease of comparison. (right) Normal Raman spectrum of JWH-018 at a concentration of 5.0 mg/mL in methanol. Asterisks indicate bands assigned to the solvent. The intensities have been normalized to the solvent band at 3200 cm ⁻¹ assigned to H-bound ν(OH) of the alcohol.	251
8.12	Comparison of SERS spectrum of JWH-018 standard methanolic solution at a concentration of 1000 ng/mL (bottom, green) with normal Raman spectrum of JWH-018 in the solid state (top, red). Intensities are on the same scale, and spectra have been stacked for ease of comparison.	254
8.13	Adsorption isotherm of JWH-018 on traditional citrate-reduced Au nanospheres (left) and linear fit of low concentration data points (right), having equation $y = 0.14221 \pm 0.007x + 0.16 \pm 0.04$. The dotted lines in the linear fit graph represent the upper and lower 95% confidence limit.	255
8.14	SERS spectra obtained from fortified oral fluid extracts at different initial concentration of JWH-018. The SERS spectrum of the matrix blank is reported in gray. The vertical dotted line marks the drugs reference band at 1370 cm ⁻¹ assigned to the ν(C=C) of the naphthalene moiety.	260
8.15	Molecular structures of the selected synthetic cannabinoids.	263
8.16	Molecular structures of the selected synthetic cannabinoids.	265

8.17	(left) DFT (bottom) and Raman (top) spectra of JWH-081. (right) Normal Raman spectrum of JWH-081 in methanolic solution. The dotted grey line is the spectrum of the solvent, obtained in the same experimental conditions.	266
8.18	SERS (bottom, pink) and normal Raman (top, purple) spectra of JWH-081. .	267
8.19	(left) Adsorption isotherm of JWH-081 on citrate-capped gold nanospheres. The red line represents the Langmuir fitting (adjusted R^2 0.989). (right) Linear portion of the adsorption isotherm of JWH-081 on citrate-capped gold nanospheres. The linear fit is described by the following equation: $y = 0.0101 \pm 0.0007x + 0.019 \pm 0.004$ (adjusted R^2 0.986).	270
8.20	Hypothesized prevalent orientations to the surface for JWH-018 and JWH-081.	272
8.21	Normal Raman (top) and DFT-simulated (B3LYP/6-311G**, bottom) spectra of JWH-175.	274
8.22	Normal Raman (top) and DFT-simulated (B3LYP/6-311G**, bottom) spectra of JWH-250.	274
8.23	Normal Raman (top) and DFT-simulated (B3LYP/6-311G**, bottom) spectra of RCS-4.	277
8.24	Normal Raman (top) and DFT-simulated (B3LYP/6-311G**, bottom) spectra of XLR-11.	277
8.25	Normal Raman (top) and DFT-simulated (B3LYP/6-311G**, bottom) spectra of ADB-PINACA.	281

LIST OF SYMBOLS

◇ Latin

A	Nucleus
A_{eff}	Effective transverse area of a light beam
a	Particle size or dimension of field-enhancing feature of a substrate
$E(\lambda)$	Extinction
e	Euler's number
G	Magnitude of SERS enhancement
g	Average enhancement of the electric field at a plasmonic surface
H	Hamiltonian operator
\hbar	Reduced Planck's constant
I_0	Intensity of the Raman source
I_{SERS}	Intensity of the SERS signal
i	Imaginary part of a complex number
m	Mass
m_e	Mass of the electron
m_A	Mass of a generic nucleus A
N	Number of electrons
n	Refractive index
n_c	Number concentration
q_e	Elementary charge
$-1q_e$	Charge of the electron
r	distance
Z	Atomic number
z	Formal charge of a species

◇ Greek

α	Polarizability
γ	Conductivity
δ^+	Partial positive charge
ε	(relative) Electric permittivity
ε_0	Electric permittivity of vacuum
ζ	Zeta potential
η	Viscosity
κ^{-1}	Debye length
λ	Wavelength
λ_{exc}	Wavelength of excitation source
λ_{LSPR}	Wavelength of maximum localized surface plasmon resonance
λ_{max}	Wavelength of maximum absorption or extinction
μ	Electrophoretic mobility
ρ	Electron density
ρ_{cond}	Density of conduction electrons
σ	Standard deviation
σ_{abs}	Absorption cross section
σ_{ext}	Extinction cross section
σ_{sca}	Scattering cross section
χ	Nanoparticle shape factor
Ψ	Wavefunction
ψ_0	Surface potential
ψ_S	Stern potential
ω	Frequency
ω_p	Plasma frequency

◇ Miscellaneous

∇^2	Laplacian operator
------------	--------------------

ABBREVIATIONS AND ACRONYMS

Ac	Acetate
AEF	Analytical Enhancement Factor
ALD	Atomic Layer Deposition
ANOVA	Analysis of Variance
AR	Aspect Ratio
ATR	Attenuated Total Reflection
CT	Charge Transfer
Ct	Citrate
CTAB	Cetyltrimethylammonium bromide
CV	Crystal Violet
DFT	Density Functional Theory
DLVO	Derjaguin-Landau-Verwey-Overbeek (theory of colloid stability)
E	Electric (field)
ECP	Effective Core Potential
EF	Enhancement Factor
ELS	Electrophoretic Light Scattering
EM	Electromagnetic (field)
fcc	Face-centered cubic
FWHM	Full Width at Half Maximum
GA	Genetic Algorithm
HF	Hartree-Fock
HRTEM	High Resolution Transmission Electron Microscopy
HSD	(Tukey's) Honestly Significant Difference
IQR	Interquartile Range
IR	Infrared
L-AA	L-ascorbic acid
LSPR	Localized Surface Plasmon Resonance
LOD	Limit of Detection

LOQ	Limit of Quantitation
MO	Molecular Orbital
NMR	Nuclear Magnetic Resonance
NP	Nanoparticles
NPS	Novel Psychoactive Substances
NR	Normal (traditional) Raman
NS	Nanostars
PES	Potential Energy Surface
RGL	Rosato-Guillopé-Legrand (potential)
SCB	Synthetic Cannabinoid
SCF	Self Consistent Field
SERS	Surface Enhanced Raman Spectroscopy
SPR	Surface Plasmon Resonance
Std	Standard
TEM	Transmission Electron Microscopy
Tt	Tartrate
UV/Vis	Ultraviolet/Visible
XPS	X-Ray Photoelectron Spectroscopy

Introduction

1.1 Statement of the problem

Surface Enhanced Raman Spectroscopy (SERS) is a surface spectroscopic technique in which the excitation of the localized surface plasmon resonance (LSPR) of a nanostructured substrate amplifies the inherently weak¹ Raman signal of an adsorbed analyte by several orders of magnitude, up to the single molecule level.¹⁻⁴

SERS has gained increasing popularity, and has found applications in several different fields within ultratrace analysis,⁵ ranging from environmental and food safety⁶⁻⁸ to homeland security,^{9,10} art conservation,^{11,12} and clinical diagnostics.¹³⁻¹⁵ This growth in the application of SERS has been propelled by the significant advances that have been achieved in the field of nanotechnology over the last twenty years. Advances in nanofabrication have facilitated the production of new plasmonic materials, offering a plethora of colloidal nanoparticle morphologies to be used as SERS substrates, and an even larger number of synthetic pathways to obtain them. However, SERS is not an established technique yet, and, contrary to what should be expected, it is still relegated to the role of academic sensation.

SERS is a highly multidisciplinary technique, and thus, it relies heavily on input from a collection of different branches of science — from photonics to materials science, from analytical chemistry to spectroscopy.⁵ While this multidisciplinary nature makes SERS research fascinating and vibrant, it also lends the technique a certain *reliance* on these interconnected research fields; this means that, while progress in a related sub-discipline can propel SERS towards new improvements, road-blocks encountered in related sub-disciplines can halt its progress. For example, despite the large enthusiasm that SERS

¹In a Raman experiment, only $1/10^6$ to $1/10^8$ of scattered photons is Raman scattered.¹

sparked in the decade following its serendipitous discovery (Fleischmann, et al.,¹⁶ 1974), a significant halt was observed in the development of SERS as an analytical technique during the 1985–2000 period. This is widely attributed to a much underdeveloped field of nanoscience and nanotechnology at that time, which was too immature to support the needs of SERS.² From the early 2000s on, the exponential growth observed in the field of nanotechnology fueled great advances in SERS, contributing to a second wave of heightened interest in the subject.² By taking advantage of this historical pattern, attention can be posed on under-explored correlated sciences, with the aim of furthering SERS and contributing to its advancement, from niche specialty to benchmark analytical technique.

A possible factor contributing to the halt in progress of SERS is the relatively poor understanding and theoretical description of surface chemistry phenomena at the nanoscale. Surface chemistry effects directly enable SERS, and they are particularly important when colloidal suspensions are utilized as enhancing substrates. While to date a large number of publications exist in the fields of nanotechnology and nanofabrication, there is not an equivalent body of literature describing the *chemistry* of the fundamental processes occurring at the nanoscale (*Figure 1.1*). Most publications on SERS focus on the exceptionally low limits of detection of a given target analyte or class of molecules, with little elaboration on which particular surface environment makes those exceptional enhancements possible and why.

As reported in *Figure 1.1 a*, for the year 2017, slightly more than half of the total number of publications on SERS had sensitivity as the focus, while only 0.9% were centered on the fundamental aspects of surface chemistry enabling signal production. A similar trend can also be observed within the literature on nanotechnology and nanofabrication (*Figure 1.1 b*), where in 2017 only 6% of scholarly products focused on fundamental processes, such as surface chemistry and capping environment, thermodynamics, and kinetics. As it will be discussed more in depth throughout this dissertation, the signal enhancement in SERS

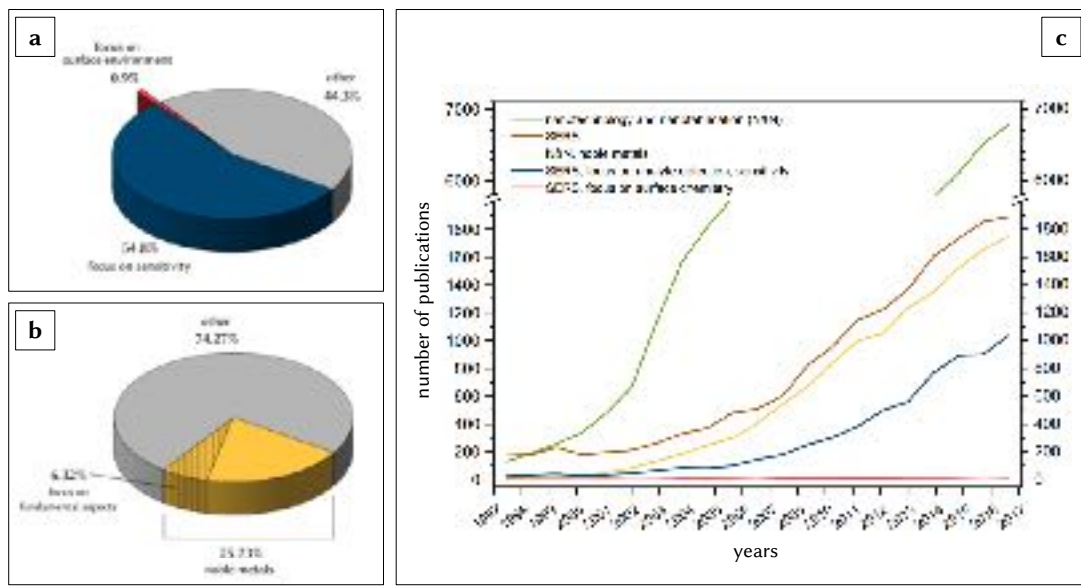


Figure 1.1: Keyword frequencies (Web of Science database) within (a) SERS publications and (b) nanotechnology and nanofabrication publications for the year 2017. (c) The same proportions are found to be constant trends in the time window from 1997 to 2017.

is a near field effect,^{18,19} and as such, nanoscale surface phenomena play a crucial role in enabling it. Consequently, it can be stated that a neglect of this aspect constitutes a setback and limiting factor for the progress of the technique.^{17,20} In fact, a more in-depth understanding of the phenomena at the solid-liquid interface can be a key step in moving SERS out of the research laboratory, and into routine applications.

1.2 Objectives

The present work puts surface chemistry and adsorption phenomena at the center of the strategy for the optimization of a state-of-the-art colloidal SERS substrate. This optimization has as ultimate objective the fabrication of (one or more) colloiddally stable bimetallic gold-silver nanostar formulations that are compatible with SERS requirements for ideal measurement conditions. To achieve this, a collection of organic and inorganic

anionic species were surveyed as possible substitutes of non-ideal surfactant stabilizer cetyltrimethylammonium bromide (CTAB), and they were tested for immediate and short-term stability (*Objective 1*). The resulting viable formulations were tested for longer-term stability, as well as for SERS activity and performance reproducibility (*Objective 2*). Reproducibility in terms of morphology was also addressed (*Objective 3*). The surface energetics and adsorption modes of the capping species were estimated experimentally and compared to computational models obtained via Density Functional Theory (DFT) calculations (*Objective 4*). Finally, proof of concept applications of the developed surfaces to the detection of drugs of forensic and public health interest were addressed (*Objective 5*).

1.3 Structure of the work

An overview of the principles necessary to understand the theoretical foundations of SERS and colloidal systems, as well as an overview on adsorption phenomena, is given in *Chapter 2*. *Chapter 3* presents the materials and methods utilized for the research, while *Chapter 4* illustrates the challenges inherent to nanoparticle stabilization for SERS substrates and the experiments that led to the obtainment of a library of colloidal nanostars (*Objective 1*). *Chapter 5* discusses optical and SERS reproducibility and performance, right after synthesis and over time (*Objective 2*); a morphological characterization is also presented in this chapter (*Objective 3*). *Chapter 6* deals instead with the experimental methods that were implemented to elucidate the adsorption modes of the stabilizers and to estimate the strength of the stabilizer-metal interaction. These results are accompanied and supported by the computational work discussed in *Chapter 7*; this chapter gives an overview of Density Functional Theory (DFT), and then presents the computational modeling of citrate adsorption in solution on a prototype monometallic Au₂₀ cluster; preliminary work towards

the modeling of an Au₁₉Ag bimetallic cluster system is also presented (*Objective 4*). Finally, *Chapter 8* gives some examples of how SERS can be utilized in applications of public health and forensic interest, such as the detection of opioids and synthetic cannabinoids (*Objective 5*); these applications made use of the developed nanostars, as well as of traditional nanoparticles. DFT calculations were also examined as a powerful tool for structural elucidation, demonstrating great potential for *in silico* spectral library building.

REFERENCES

- [1] Smith, E.; Dent, G. *Modern Raman Spectroscopy, a practical approach*, second edition, John Wiley & Sons Ltd: Chichester, 2019.
- [2] Le Ru, E.C.; Etchegoin, P.G. *Principles of surface enhanced Raman spectroscopy and related plasmonic effects*, Elsevier: Amsterdam, 2009.
- [3] Kneipp, K.; Wang, Y.; Kneipp, H.; Perelman, L.T.; Itzkan, I.; Dasari, R.R.; Feld, M.S. Single Molecule Detection Using Surface-Enhanced Raman Scattering (SERS). *Phys. Rev. Lett.*, **1997**, 78(9), 1667–1670.
- [4] Kneipp, K.; Kneipp, H.; Bohr, H.G. Single-Molecule SERS Spectroscopy. In *Surface-Enhanced Raman Scattering*, Kneipp, K., Moskovits, M., Kneipp, H., Eds.; Topics in Applied Physics Series, volume 103; Springer-Verlag: Berlin Heidelberg, Germany, 2006.
- [5] Fan, M.; Andrade, G.F.S.; Brolo, A.G. A review on recent advances in the applications of surface-enhanced Raman scattering in analytical chemistry. *Anal. Chim. Acta*, **2020**, 1097, 1–29.
- [6] Guo, H.; He, L.; Xing, B. Applications of surface-enhanced Raman spectroscopy in the analysis of nanoparticles in the environment. *Environ. Sci.: Nano*, **2017**, 4, 2093–2107.

- [7] Jiang, Y.; Sun, D-W.; Pu, H.; Wei, Q. Surface enhanced Raman spectroscopy (SERS): A novel reliable technique for rapid detection of common harmful chemical residues. *Trends Food Sci. Technol.*, **2018**, *75*, 10–12.
- [8] Tang, H.; Zhu, C.; Meng, G.; Wu, N. Surface-Enhanced Raman Scattering Sensors for Food Safety and Environmental Monitoring. *J. Electrochem. Soc.*, **2018**, *165*(8), B3098–B3118.
- [9] Muehlethaler, C.; Leona, M.; Lombardi, J.R. Review of Surface Enhanced Raman Scattering Applications in Forensic Science. *Anal. Chem.*, **2016**, *88*(1), 152–169.
- [10] Fikiet, M.A.; Khandasammy, S.R.; Mistel, E.; Ahmed, Y.; Halámková, L.; Bueno, J.; Lednev, I.K. Surface enhanced Raman spectroscopy: A review of recent applications in forensic science. *Spectrochim. Acta, Part A*, 2018, *197*, 255–260.
- [11] Analytical Methods Committee, Surface-enhanced Raman spectroscopy (SERS) in cultural heritage, *Anal. Methods*, **2017**, *9*, 4338–4340.
- [12] Zalaffi, M.S.; Karimian, N.; Ugo, P. Electrochemical and SERS Sensors for Cultural Heritage Diagnostics and Conservation: Recent Advances and Prospects. *J. Electrochem. Soc.*, **2020**, *167*(3), 037548.
- [13] Cialla-May, D.; Zheng, X-S.; Weber, K.; Popp, J. Recent progress in surface-enhanced Raman spectroscopy for biological and biomedical applications: from cells to clinics. *Chem. Soc. Rev.*, **2017**, *46*(13), 3945–3961.
- [14] Premasiri, W.R.; Chen, Y.; Fore, J.; Brodeur, A.; Ziegler, L.D. SERS Biomedical Applications: Diagnostics, Forensics, and Metabolomics. In *Frontiers and Advances in Molecular Spectroscopy*, Laane, J. Ed.; Elsevier Science: Amsterdam, The Netherlands, 2018.
- [15] Dardir, K.; Wang, H.; Martin, B.E.; Atzampou, M.; Brooke, C.B.; Fabris, L. SERS Nanoprobe for Intracellular Monitoring of Viral Mutations, *J. Phys. Chem. C*, **2020**; *124*(5), 3211–3217.
- [16] Fleischmann, M.; Hendra, P.J.; McQuillan, A.J. Raman spectra of pyridine adsorbed at a silver electrode, *Chem. Phys. Lett.*, **1974**, *26*(2), 163–166.
- [17] Álvarez-Puebla, R.A.; Liz-Marzán, L.M. Traps and cages for universal SERS detection, *Chem. Soc. Rev.*, **2012**, *41*, 43–51.

- [18] Moskovits, M. Surface-enhanced Raman spectroscopy: a brief retrospective. *J. Raman Spectrosc.*, **2005**, 36(6-7), 485–496.
- [19] Jain, P.K.; El-Sayed, M.A. Plasmonic coupling in noble metal nanostructures. *Chem. Phys. Lett.*, **2010**, 487, 153–164.
- [20] Shi, R.; Liu, X.; Ying, Y. Facing Challenges in Real-Life Application of Surface-Enhanced Raman Scattering: Design and Nanofabrication of Surface-Enhanced Raman Scattering Substrates for Rapid Field Test of Food Contaminants. *J. Agric. Food Chem.*, **2018**, 66(26), 6525–6543.

Surface Enhanced Raman Spectroscopy (SERS) as a surface phenomenon

2.1 Theory of Surface Enhanced Raman Spectroscopy (SERS)

In order to elucidate the mechanisms behind the SERS effect, a brief discussion on the optical properties of metals at their nanoscale is necessary.

When light impinges on a thin metallic surface, the conduction electrons of such a surface start to collectively oscillate in what is referred to as a *surface plasmon resonance* (SPR).^{1,2} This also happens with metallic *nanostructures*, that is, structures of much smaller dimensions than the wavelength of the impinging beam, where the ratio between the radius of the structure and the light's wavelength is less than 0.1.³ In this case, the collective oscillation of the surface conduction electrons assumes a confined character, therefore taking the name of *localized* surface plasmon resonance (LSPR).¹ The LSPR frequency is related to the metal's relative permittivity function, denoted by ϵ , which describes the electrical behavior of the metal compared to vacuum (ϵ_0), and is in turn strongly dependent on the frequency of the incident light (hence on its frequency, ω).³ Such a function can be expressed as a complex number:

$$\epsilon_{np}(\lambda) = \epsilon_{np}(\omega) = \epsilon' + i\epsilon'' \quad (2.1)$$

where ϵ' designates the real part of the function, and ϵ'' is the imaginary part. The former term is responsible for the polarizability and scattering properties of the metal,^{3,4} because it is directly related to the natural oscillation frequency of the conduction electrons. This is known as the plasma frequency ω_p (*Equation 2.2*, valid at room temperature), which is a

function of the material's density of conduction electrons (ρ_{cond}), as shown in *Equation 2.3*, where $-1q_e$ is the charge of the electron, and m_e is the electron mass.³

$$\epsilon' = 1 - \frac{\omega_p^2}{\omega^2} \quad (2.2)$$

$$\omega_p^2 = \frac{\rho_{cond}(-1q_e)^2}{m_e\epsilon_0} \quad (2.3)$$

This equation explains why metals with a negative real relative permittivity, such as coinage metals (silver and gold), are widely used as enhancing substrates for SERS. The negative value is ultimately caused by their high electron density, which results in an ω_p that is larger than the frequency of the incident light ω . This relationship results in a high degree of resonant scattering from the nanostructure, which is at the basis of the LSP excitation that produces the SERS phenomenon.

These basic relationships set the criteria for the resonance conditions that must be met in order to trigger the LSP excitation, and the LSPR can only occur if the following equation is satisfied:³

$$\epsilon_{np}(\lambda) = -\chi\epsilon_{env} \quad (2.4)$$

where ϵ_{np} is the relative permittivity of the nanoparticle, ϵ_{env} is the relative permittivity of the surrounding environment, and χ is the shape factor for the nanostructure, which is equal to 2 for a sphere, and becomes larger with increasing anisotropic morphology.^{3,5} For gold and silver, resonance conditions are met when excitation occurs in the visible spectrum,³ a fact that constitutes a very important aspect for the application of this phenomenon to Raman spectroscopy. A typical Raman spectrometer utilizes a laser source emitting in the visible range. It follows that when silver or gold nanostructures are irradiated with such a light source, the resonance expression above is satisfied, and the LSPR is induced.

A second crucial aspect of the LSPR is that it is able to couple with the electromagnetic field of the exciting radiation, generating the so-called *surface plasmon polaritons*.⁴ These are spatially confined quasiparticles at the interface between the metal and the dielectric medium surrounding it,⁴ which are capable of giving rise to a second electromagnetic field (EM_{np}) that is much stronger than the one initiating the the whole excitation process (EM_0).⁹ Thus, an analyte that is in close proximity to a nanoscale metal undergoing this physical process can interact with the strong EM_{np} , resulting in a scattered radiation from the nanoparticle that contains the Raman signal from the molecule — the surface-enhanced Raman signal.^{1,4,10–12} Plasmonic nanostructures behave like *nano-antennas*, and the radiative process *from* the nanostructure to the far-field is what ultimately enables SERS.⁸

Because the wavelength dependence of ϵ plays a crucial role in enabling the SERS phenomenon, it follows that excitation of the LSPR is a *conditio sine qua non* for this process to occur. In addition to laser source excitation and chemical identity of the metallic nanostructure, parameters that pertain to the *morphological* characteristics of the nanoparticle are also involved in the LSPR excitation. Size and shape represent very fine tools that can be exploited when optimizing a SERS-based analytical protocol. In general for silver and gold spherical or spheroidal nanoparticles, the LSPR will be excited in the visible range at *increasing wavelength* with *increasing size*,^{1,3,4} and the same will happen with increasing aspect ratio, defined as the ratio between the in-plane width and the out-of-plane height of the nanostructure ($AR_{sphere} = 1$).⁵

The process described so far is known as *electromagnetic* (or *plasmonic*)⁸ *theory of SERS*, and it is currently posited to account for the vast majority of the amplification of the Raman scattering observed in SERS experiments ($\sim 10^4$ – 10^8).^{33,12–14} The electromagnetic theory of SERS was first elaborated in 1977 by Jeanmaire and van Duyne,¹⁵ in an effort to better explain the very first reported observation of SERS, published by Fleischmann's

research group in 1974.¹⁶ This account reported the amplification ($\sim 10^6$)^{15,17} of the Raman signal of aqueous pyridine adsorbed on an electrochemically roughened silver electrode, and was justified by Fleischmann and co-workers in terms of an increase in the number of adsorbed pyridine molecules as a consequence of the larger surface area available in a roughened electrode when compared to a smooth surface¹⁶ — an argument that was proven to be quantitatively insufficient in order to reach such levels of magnification.^{1,15}

The magnitude of the enhancement produced by the EM mechanism is often reported to be proportional to the fourth power of the absolute value of the overall electric field surrounding the nanoparticle (E^4 enhancement), with the magnetic field component being decoupled from it and negligible.^{3,14} However, such a magnitude of scaling is only true for bands in the low wavenumbers region of a SERS spectrum, where the assumption can be made that factors g and g' (*vide infra*) are approximately equal can be made.^{3,12} In a more generic approximation, the electric and magnetic fields are still considered as decoupled, with the latter component being negligible.³ If g is the average enhancement of the electric field over the nanostructure supporting the LSPR, and E_0 the magnitude of the electric field of the excitation source, then the average magnitude of the resulting amplified electric field at the nanoparticle can be expressed as:¹²

$$E_{np} = gE_0 \quad (2.5)$$

which is the magnitude of the field with which a suitably close analyte of polarizability α could interact.

As previously mentioned, the Raman scattering signal from such an analyte, with electric field component designated here as E_R , will experience a field enhancement that results from the enhanced nature of the E_{np} field, as well as from the enhanced Raman-shifted light that is scattered by the LSPR-excited nanoparticle.¹² If g' is the average factor

by which the latter enhancement occurs, then the relationships described so far can be formalized as follows:¹²

$$E_R \propto \alpha E_{np} \propto \alpha g E_0 \quad (2.6)$$

$$E_{SERS} \propto g' E_R \propto \alpha g g' E_0 \quad (2.7)$$

$$I_{SERS} \propto |\alpha|^2 |g g'|^2 I_0 \quad (2.8)$$

where I_{SERS} is the intensity of the SERS signal, and I_0 that of the exciting source.

Compared to a normal Raman (*NR*) experiment, an enhancement factor *EF* can be intuitively and empirically defined as the ratio between I_{SERS} and I_{NR} , provided that the concentration of the analyte and other experimental parameters are kept constant.³

$$EF = \frac{I_{SERS}}{I_{NR}} \quad (2.9)$$

In analytical chemistry practice, where the concentration c_{NR} of the analyte in the normal Raman experiment might be significantly higher, and therefore different, than the concentration c_{SERS} measured in the SERS experiment, the *analytical* enhancement factor (AEF) is calculated instead.⁵⁵

$$AEF = \left(\frac{I_{SERS}}{c_{SERS}} \right) \left(\frac{I_{NR}}{c_{NR}} \right) \quad (2.10)$$

When this approach is used, EF values up to 10^{11} can be obtained. However, exact mathematical models¹⁸ that take into account the EM mechanism tend to yield EF values that are significantly smaller than the one mentioned above ($10^4 - 10^5$), and do not explain the full magnitude of the observed enhancements.³ Although a detailed discussion of

such models goes beyond the scope of this SERS overview, the discrepancy between the two orders of magnitude opens up to an important point in SERS theory that should be addressed. As discussed, the EM effect depends on the nature and morphology of the substrate and on the light source used to generate the phenomenon, therefore it is considered to be analyte-independent.^{10,12,19} However, it has been observed that some analytes produce higher SERS intensities than others, namely molecules bearing atoms with lone electron pairs.^{12,20} Thus, additional factors must be co-occurring or cooperating to yield the remainder of the SERS effect, and these must depend on the chemical nature of the analyte.^{11,17,19}

For example, when an analyte is in close vicinity with a metal surface *and* has a suitable structure, it may *chemically* interact with the surface, so that an electron can be transferred through vibronic coupling from the Fermi level of the metal to a frontier orbital of the analyte molecule, or vice versa.¹¹ Such a phenomenon, which is referred to as the *charge transfer* (CT) mechanism,¹⁷ has been shown to produce an additional magnification of the Raman signal,¹¹ thus explaining the higher EF values sometimes obtained in SERS experiments. At this point, another simplified formalization for the overall EF, as reported by Moskovits,¹² can be introduced:

$$EF = \left| \frac{\alpha}{\alpha_0} \right| |gg'|^2 \quad (2.11)$$

where α_0 is the polarizability of the isolated target molecule. In the case in which the target is *physisorbed* and no charge transfer occurs, α_0 will be equal or approximately equal to α ; this reduces the EF expression above to be a function of the absolute value of the $|gg'|^2$ term which, in a simplistic way, can be essentially attributed to the EM mechanism. On the other hand, in the case in which the molecule is *chemisorbed*, $\alpha \neq \alpha_0$ and the metal-analyte ensemble, as opposed to the analyte alone, must be considered for the polarizability.¹² Such

value changes are particularly significant when CT complexes are formed, and a variety of other factors (coordination complexes, presence of heteroatoms, . . .) are responsible for the extra enhancement that cannot be explained by the sole EM theory.¹²

Although historically treated in opposition to the EM mechanism,⁶⁻⁸ the “chemical effect”, or more specifically, the formation of metal-analyte adducts may rather be seen as a further proof of the validity of the plasmonic basis of SERS. Indeed, the surface complexes arising from chemisorption processes can be viewed as an “optimization factor” for the EM mechanism itself; by reducing the distance between the active metal substrate and the probing molecule, the latter can benefit from a greater electromagnetic field intensity, resulting in a greater overall enhancement of its Raman scattering signal.^{1,21} It must be recalled that the EM amplification is a *near field* effect,^{12,22} as the LSPR-resulting enhanced field displays the strongest intensity *at* the metal nanoparticle surface, and decays exponentially away from it.¹

While the formation of surface complexes is desirable in terms of overall signal enhancement, it is important to note that the resulting SERS spectrum may not resemble the one obtained in normal Raman experiments because $\alpha \neq \alpha_0$, consequently both intensity and band position may change. Moreover, the adduct formation may force the analyte to attain a specific orientation with respect to the metal surface.³ As a result, the signal from a defined range of vibrational modes may be preferentially amplified, compared to that produced by a randomly physisorbed population of the same molecules. This phenomenon as a result of the directional, spatial character of the EM enhancement.^{1,12} In this respect, the use of computational methods such as Density Functional Theory (DFT) calculations has been demonstrated to be of significant aid both in determining whether a surface complex has formed, and in elucidating its possible structure and band assignments.^{1,20,23}

The physisorption and chemisorption nature of the nanostructure-analyte interaction makes it possible to utilize a series of synthetic and post-synthetic strategies for the

fabrication of substrates with the highest possible affinity for the chosen probing molecule(s).

2.2 SERS substrates

While multiple options exist as for the substrate fabrication, ranging from the early electrochemical etching methods^{15,16} to the more recent nanosphere lithography,^{24,25} this research will focus on metal colloids, since they are, to date, the cheapest and most widely used nanoscale platforms for SERS analysis. Moreover, they offer exceptional versatility, in that they can be utilized as such (*sols*) for measurements in solution, they can be concentrated and drop-casted as a thick slurry (*paste*) for measurements on either wet or dried residue,^{26,27} or utilized as starting materials to produce planar substrates by nanoparticle immobilization (*nanofilms*).^{24,25} When utilized as sols, they provide what is referred to as *average SERS*, that is, an overall SERS enhancement arising from a multiplicity of localized surface plasmon polaritons and analyte molecules.¹ This results in a good level of reproducibility and linearity,¹ which are essential features for the implementation of new analytical protocols.

2.2.1 Colloidal nanomaterials and colloidal stability

Colloidal sols, and colloidal systems at large, have a higher free energy than that of the corresponding bulk material. This results in the fact that colloids exist in *metastable equilibrium* — they are stable under small perturbations, but they thermodynamically tend to minimize the free energy by reaching a *state of contact*, that is, irreversible particle aggregation (*coagulation*).^{4,36} This process leads to the disruption of the colloidal sol, which transitions away from its initial finely dispersed status as it reaches the bulk state. An energy barrier of sufficient magnitude is therefore necessary to prevent the system from

coagulating, and to maintain it in its metastable state for an indefinite amount of time — that is, to achieve *colloidal stability*.³⁶

The magnitude of the energy barrier between two approaching particles results from the attractive and repulsive forces that additively act on the system. Attractive forces (van der Waals and London forces) exist at all separation distances between two particle surfaces, both in vacuum and in any medium.³⁶ As shown in *Figure 2.1 a*, this causes the change in free energy to decrease as distance decreases. It must also be noted that an interposed medium, such as a liquid (solid line in *Figure 2.1 a*), between surfaces reduces the magnitude of the free energy change compared to the behavior in vacuum (dashed line in *Figure 2.1 a*). This implies that, at a given fixed interparticle distance, a colloidal system will possess a lower free energy, thus it will be less prone to coagulation, *if* there is a medium filling such a distance. However, the presence of such a medium does not suppress the attractive forces, as these act at all distances and in all media.

If the interparticle medium is a solution, the properties of this solution will play a crucial role in modulating the attractive forces. Indeed, Coulombic repulsive forces are established as a result of various solid-solution interfacial phenomena, ranging from ionization of surface groups, to presence of charged crystal surfaces, or specific ion adsorption (*Figure 2.2*).³⁶ Regardless of their nature, these Coulombic repulsions have an opposite effect on the free energy of the system compared to attractive forces. As illustrated in *Figure 2.1 b*, the change in free energy experienced by the system, as a function of interparticle distance, tends to infinity as the latter is reduced, implying that free energy minimization will occur at increasing separation distance.

Assuming additive action of the two forces, a net free energy curve of the type depicted in *Figure 2.1 c* is obtained. This is also commonly referred to as the *DLVO curve*, as it stems from the Derjaguin-Landau-Verwey-Overbeek (DLVO) theory of colloid stability.^{37,38}

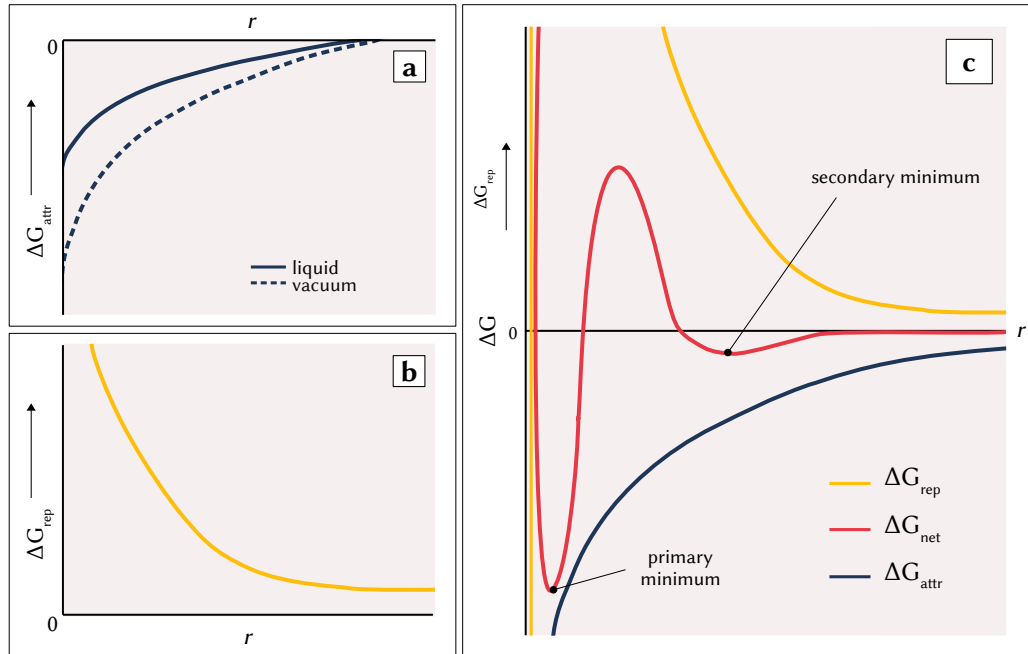


Figure 2.1: Behavior of the change in free energy as a function of interparticle distance. The components associated with both (a) attractive forces and (b) electrostatic repulsions are reported. (c) A possible form of the total-interaction free energy of a colloidal system (DLVO curve) as a function of interparticle distance (r) (red profile). Maximum minimization of the free energy will occur at very short distances (*primary minimum*), where coagulation occurs. A shallower minimum at intermediate distances is often also present; no energy barrier is required (*secondary minimum*), and flocculation (reversible aggregation) occurs.

$$\Delta G_{net} = \Delta G_{attr} + \Delta G_{rep} \quad (2.12)$$

From a qualitative point of view, DLVO theory states that for a dispersion to be colloidally stable, its repulsive forces must overpower its attractive forces. As shown in *Figure 2.1 c*, for two particles to coagulate, an energy barrier must be overcome. The height of this barrier is governed by the relative contribution of the repulsive forces to the total energy profile. It is clear now that to achieve colloidal stability, the Coulombic

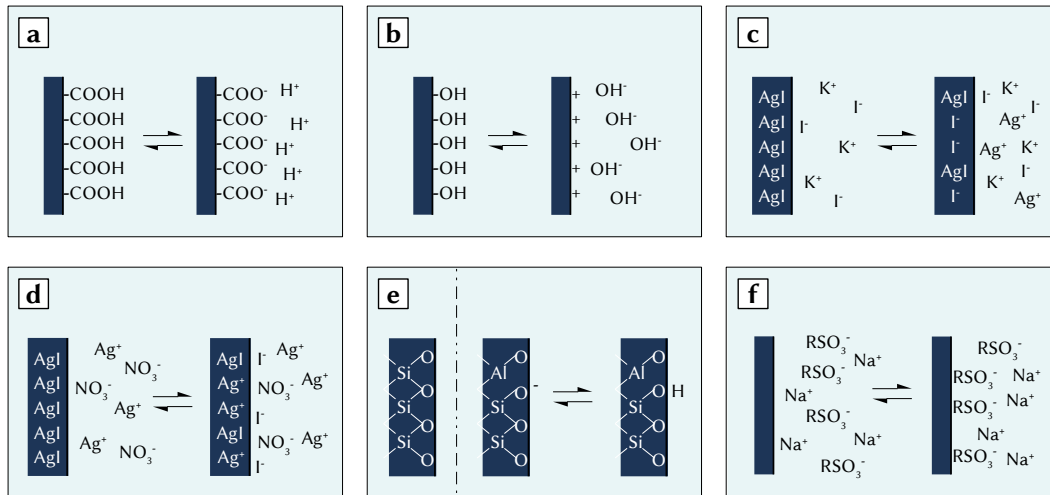


Figure 2.2: Solid-solution interface phenomena at the basis of the development of surface charge and onset of Coulombic repulsions: (a) ionization of acid groups constituting the surface; (b) ionization of basic group constituting the surface; (c) and (d) differential dissolution of sparingly soluble compounds; (e) isomorphous substitution in a surface; (f) specific adsorption of an ionic compound. Figure inspired by D.H. Everett.³⁶

repulsions within the system must be increased. The way in which this can be obtained, however, depends on the chemistry of the surface under study.

2.2.1.1 Stability of colloidal noble metal nanoparticles

As previously mentioned, the processes under which a surface develops electrostatic repulsive forces in solution are varied, and are summarized in *Figure 2.2*. The mechanism by which noble metal nanoparticles, which are the main focus of this research, acquire a charge in solution is not yet been fully elucidated.

The most widely encountered charging mechanism is depicted in *Figures 2.3 b* and *c*, which show two distinguishable domains within the nanoparticle — an inner region in which the metal is in its bulk state, and an outer, superficial layer in which the metal is positively charged, either by presence of partial positive charges or integer charges. This surface domain could be explained in terms of incomplete reduction of the metal precursor

during synthesis. The development of an electric double layer at the particle-solution interface, and the ensuing Coulombic repulsions, are therefore a result of the presence of a charged (poly)crystalline solid. This theory, presenting the traditional assumption on the oxidation state of noble metal nanoparticles, is deduced from generalizations on electrophoretic light scattering (ELS) experiments, in which the electrokinetic potential at the slipping plane^I is derived from the measured electrophoretic mobility of the colloidal nanoparticles. This potential, referred to as the ζ potential, reflects the magnitude and sign of the repulsive charges characterizing the colloid (*Figure 2.3 a*). For all traditional gold and silver colloidal sols (*i.e.*, citrate, borohydride, and hydroxylamine hydrochloride reductions), the ζ potential sign^{II} is negative.^{1,4,40}

Nanoparticle depictions of the type reported in *Figure 2.3 c* are common in the literature,^{1,41} and they seem to suggest that the negative charge is caused by a feature inherent to the charge state of the noble metal nanoparticle itself. For this to occur, the nanoparticle should be positively charged. In the typical case of monometallic (gold *or* silver) nanospheres obtained by citrate reduction, the final colloidal dispersion is therefore seen as stabilized by an *electrostatically retained* excess of unreacted citrate molecules, as well as negatively charged citrate oxidation products. Therefore, under this assumption, the magnitude of Coulombic repulsions is directly related to the number of *non-specifically* attracted ions of opposite charge (*negative*) to that of the nanoparticle outer domain (*positive*). According to this view, these species would act as capping agents, adsorbing to the nanoparticle surface by virtue of electrostatic attractions towards the residual positive charge present on the outermost layer of the noble metal nanoparticle.

^IThe slipping plane is defined as the “boundary between the hydrodynamically mobile and immobile fluid”.³⁹

^{II}On the other hand, the formation of positively charged colloidal systems are traditionally reported to be hardly achievable, unless micelle-forming cationic surfactants are used.¹

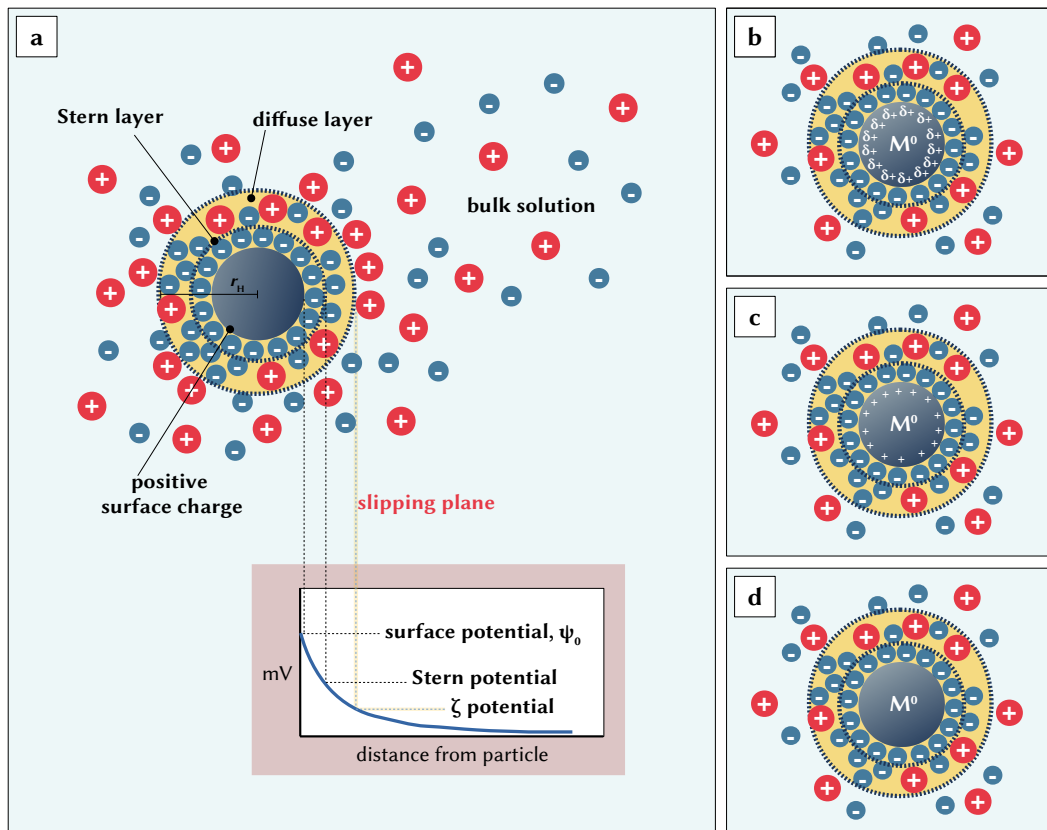


Figure 2.3: (a) Schematic depiction of a colloidal nanoparticle with nomenclature: the electrical double layer, or electrical interfacial layer (shaded yellow area),³⁹ is composed of a firmly held layer, often referred to as Stern layer, and a diffuse layer. The slipping plane identifies the boundary between the electrical interfacial layer, hydrodynamically immobile, and the rest of the solution, which is hydrodynamically mobile. The way(s) in which the electrical interfacial layer develops in colloidal noble metal nanoparticles is not fully elucidated yet, and it is closely related to the chemical state of the metallic surface. This is thought to exist as either (b) a double domain with outer partially positively charged region, (c) a double domain with outer region charged by integer positive charges, or (d) a monodomain of zero-valent noble metal.

Therefore, it must be stressed that the traditional assumption on the noble metal nanoparticle oxidation state should be regarded more as an axiom or principle, rather than a fully experimentally validated theory. In fact, in a recent (2017) publication, Al-Johani and co-workers systematically studied the interaction of citrate with monometallic gold nanospheres, and highlighted how the *surface* of the nanospheres is actually in its zero,

bulk, metallic state and not in its positively charged state.⁴² XPS data showed Au 4*f* peaks with binding energy centered at 84.0 eV (4*f*_{7/2}) and 3.7 eV spin-orbit coupling, which are characteristic of bulk gold (*Figure 2.4*). The two 4*f* core peaks show tailing at higher binding energies, which is a typical feature of XPS core peaks of metals.²⁶ The authors however used a conservative approach, and treated the exceeding tailing area as a contribution to a two-peak convoluted band. Peak integration of this secondary component was then used to calculate the percent of non-zero gold, which was accounted to be 4% of the total surface and assigned to Au^{δ+}. Further supporting evidence was given by NMR studies of the dried nanoparticle residues, which revealed the existence of *coordinate covalent bonds* between the capping citrate and gold. These findings are in contrast with the traditional assumption on noble metal nanoparticle oxidation state. *If* these data can be generalized to different noble metal nanosystems, then the capping process of colloidal nanoparticles at large, and the ensuing of Coulombic interparticle repulsions, are not driven by electrostatic interactions. As a consequence, the repulsive forces may not develop from the presence of *any* anionic species; on the contrary, only species which are able to *chemically interact* with the metal(s) will approach the surface and adsorb on it. By virtue of this *specific adsorption*, the capping species increase the ion density at the solid-liquid interface, and thus, they increase the interparticle Coulombic repulsions, ultimately imparting stability to the colloid. Experimental tests of this theory and comparisons with the traditional axiom are discussed in *Chapter 3*.

2.2.1.2 Sample preparation for colloid-based SERS measurements

A step that is routinely performed on colloids to improve the level of interaction with the analyte is the partial aggregation of the suspended metal nanoparticles through the addition of inorganic salts (KNO₃, MgCl₂, NaCl, ...). Using this technique, the electrostatic double layer that surrounds metal nanoparticles in the colloidal environment is compressed and

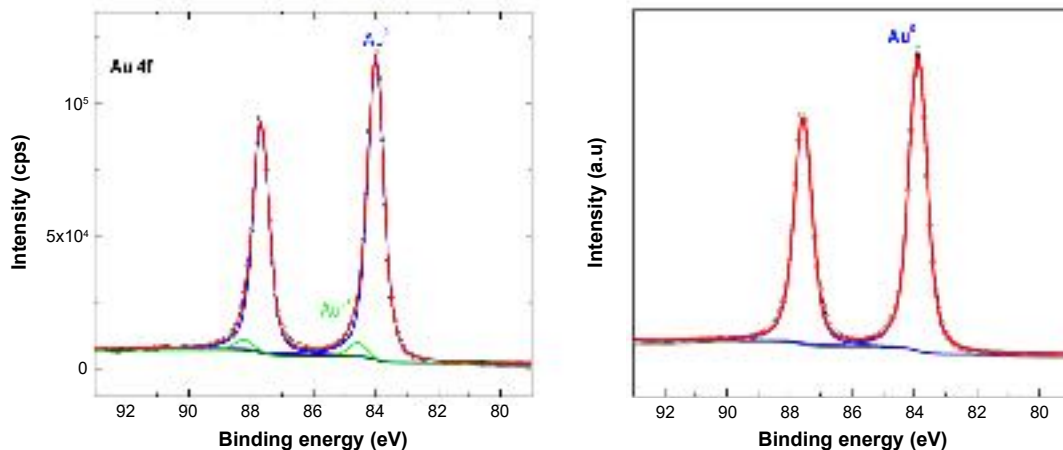


Figure 2.4: High resolution XPS spectra of the Au 4*f* core peaks of citrate-capped monometallic gold nanospheres (*left*) and reference bulk gold specimen (*right*). Peak deconvolution profiles highlights the presence of Au⁰ (blue) and Au^{δ+} (green). The latter is calculated to account for 4% of the total gold nanospheres surface. Adapted with permission of Springer Nature, from Al-Johani *et al.*,⁴² Copyright 2017; permission conveyed through Copyright Clearance Center, Inc.

minimized as a result of an increase in ionic strength, so that the net surface charge of the nanoparticle is decreased.^{21,28} Hence, improved interactions with the target molecule can occur.¹ Furthermore, this process leads to the formation of *hot spots*,^{1,4,8,12} localized interparticle regions in which the magnitude of the field enhancement can reach a factor of 10¹¹, as a consequence of near-field coupling between neighboring nanostructures.^{4,22,29–31}

Aggregation can also be achieved via linkers, generally α - ω thiolated or amino-moieties that are able to chemically react with the metal surface, producing hot spots that are controlled by the concentration, length, and conformation of the given linker.^{32,33} Such methodologies are usually characterized by a more uniform level and typology of aggregation, increasing the reproducibility among different batches.³²

In spite of the aggregation step, some analytes may still display a low affinity for the colloid substrate, such that a minimal SERS enhancement occurs. To target this problem, several strategies can be implemented, including pH adjustments to tune both surface and

analyte charges. In addition, colloidal sols can be concentrated into a paste and mixed with the analyte solution, with or without the addition of an inorganic salt as the aggregating agent. In this case, the interaction between the analyte and the plasmonic surface is improved by letting the residue dry, which “immobilizes” the analyte on the nanoscale features of the substrate, eliminating the complex and dynamic nature of molecular adsorption at the solid/liquid interface. While practical and straightforward, it must be highlighted that this strategy creates spatial heterogeneity within the sample, eliminating the advantages inherent to performing the measurements in solution (*average SERS*, § 2.2). The intensity of the signal will not only be a function of the analyte’s concentration and of the quality of the analyte–surface interaction, but also a function of the precise spot that will be illuminated by the laser, generating high variability from point to point. Alternatively and more elegantly, metal particle functionalization can be used to either impart a specific character to the surface (*e.g.*, polarity/apolarity) or to incorporate host-guest moieties with the scope of attracting the analyte closer to the metal.^{21,33–35} This approach, while more time consuming and complex, allows for the measurements to still be carried out in solution.

2.2.2 Extinction in colloids and shape effects on optical properties

The last few years have seen the emergence of exotic nanostructures with powerful optical properties that exceed the performance of traditional spheroidal nanoparticles. This has been shown in a plethora of fields, ranging from photocatalysis to theranostics, and from nanocircuits to surface-enhanced Raman spectroscopy (SERS).⁵⁶ With regard to SERS applications, great attention has been given to the development of anisotropic morphologies as enhancing substrates, because of the existing relationships between shape of nanostructures and their optical properties (§ 2.1). The excitation of the localized

surface plasmon resonance (LSPR) in metallic nanostructures is at the basis of the SERS effect (electromagnetic mechanism).^{2,4} Nanotechnology offers the possibility to tune the LSPR according to varying analytical needs, providing a platform for the development of rationally designed SERS substrates, able to yield optimal enhancements for set experimental conditions.^{3,5,57}

As seen in § 2.1, the resonance condition $\epsilon_{np}(\lambda) = -\chi\epsilon_{env}$ (Equation 2.4) must be met in order to trigger the LSPR.³ It must be noted that the relative permittivity, ϵ , is a function of wavelength. This implies that, as the wavelength is changed, the relative permittivity of a given metal also changes, as it does its plasmonic response upon interaction with light. It must also be recalled that the $\epsilon_{np}(\lambda)$ function can be described as a complex number (Equation 2.1), made up by a real part ϵ' that is responsible for the polarizability and scattering properties of the metal, and an imaginary part ϵ'' , which determines the ability of the metal to absorb radiation.^{3,4} The ensemble of absorption and scattering properties takes the name of *extinction*,³ $E(\lambda)$ — a property that can be conveniently assessed by means of traditional UV/Vis absorption spectroscopy measurements, which provide a graphical rendition of the extinction function itself. The $E(\lambda)$ function is mathematically defined as:^{3,5}

$$E(\lambda) = \frac{24\pi^2 N a^3 \epsilon_{env}^{3/2}}{\lambda \ln(10)} \left[\frac{\epsilon''_{np}(\lambda)}{(\epsilon'_{np}(\lambda) + \chi\epsilon_{env})^2 + \epsilon''_{np}(\lambda)^2} \right] \quad (2.13)$$

where N is the number of nanoparticles, and a is the size term, corresponding to the radius if a spherical nanostructure is assumed. If resonance conditions are met (Equation 2.4), and the metal's absorption ϵ''_{np} is small and positive, then $E(\lambda)$ reaches its maximum, which is conventionally designated as λ_{max} , or λ_{LSPR} .

As a practical consequence, UV/Vis absorption measurements of a candidate colloidal substrate can be used to determine the wavelength, thus the frequency, of the LSPR, so

that an appropriate, *pre-resonant* wavelength can be selected as the excitation source in the SERS experiment (*vide infra*). In the likely case where the Raman spectrometer used to perform SERS measurements is not equipped with a tunable laser source, the tuning process can be performed by altering the enhancing substrate at the nanofabrication level. Indeed, *Equation 2.13* shows that the LSPR frequency can be manipulated via the key parameters size (a) and shape (χ).

Empirically, perfect resonance conditions (*i.e.*, overlap) between the excitation source and the extinction maximum (λ_{LSPR}) are found to be counterproductive for SERS intensity.^{58–60} A paradigmatic example of this occurrence is the decrease of SERS intensity of non-resonant analytes when traditional gold colloidal nanospheres (λ_{LSPR} 520 nm) are irradiated at λ_{exc} 532 nm. This has been linked to gold's interband transition at 470 nm, which is also excited when irradiated at 532 nm, producing a dampening of the electromagnetic enhancement.^{58,61} However, significant lowering of the SERS intensity when $\lambda_{exc} \approx \lambda_{LSPR}$ has also been observed for gold nanoparticles of aspect ratios (AR) different from 1 ($AR_{sphere} = 1$), which exhibit LSPR maxima that are red-shifted from the metal's interband transition.⁶² This suggests the interband transition explanation is at least only partially representative of the actual underlying phenomenon. In fact, the nature of the transmission experiment and a competition between extinction and electromagnetic enhancement have been proposed as the origin of the significant decrease or absence of signal during in-resonance SERS experiments.^{60,62}

In a transmission measurement, the propagation of the excitation source into a colloidal dispersion follows the Lambert-Beer's law for a suspension of small particles:⁶³

$$I(h) = I(0)e^{-m[c]\sigma_{ext}} \quad (2.14)$$

where I is the intensity of the radiation after propagating through the medium for a distance r , n is the refractive index of the suspension medium, $[c]$ is the concentration of the colloidal nanostructures, and σ_{ext} is the extinction cross section, which is the sum of the absorption cross section (σ_{abs}) and the scattering cross section (σ_{sca}).⁶⁴ At perfect resonance between the λ_{LSPR} and the λ_{exc} , the extinction of the colloidal substrate is maximized, therefore the electromagnetic enhancement is also maximized (Equation 2.13). However, at these conditions the dampening of the radiation is maximized as well, as the attenuation experienced by the propagating light is proportional to the extinction cross section of the colloidal suspension (Equation 2.14). If the distribution of the nanostructures is considered homogeneous across the suspension, *i.e.*, if the concentration of the colloidal nanoparticles $[c]$ is independent of the direction of propagation of light into the suspension, then the SERS signal is:⁶⁰

$$SERS = \langle M \rangle A_{eff} R^0 G \frac{e^{-n\sigma_{ext}(\omega_0)r[c]} - e^{-n\sigma_{ext}(\omega)r[c]}}{n\sigma_{ext}(\omega) - n\sigma_{ext}(\omega_0)} \quad (2.15)$$

where $\langle M \rangle$ is the average number of molecules contributing to the enhanced SERS signal, A_{eff} is the effective transverse area of the excitation source, R^0 is the Raman signal for the analyte in the absence of the enhancing substrate, and G is the magnitude of the enhancement. The latter is adjusted by a factor that is regulated by the extinction cross section of the colloid and its concentration, which make the magnitude of the enhancement decay exponentially as they increase. The compromise to these competing processes is experimentally optimized by utilizing colloidal solutions^{III} in which the λ_{LSPR} is blue-shifted from the excitation source. The extent of this blue-shift is estimated from the literature to be in the order of 50 to 100 nm.^{62,65,66}

^{III}An interesting side note is that for solid substrates, peak signals are recorded when the λ_{LSPR} is close but *red*-shifted from λ_{exc} .^{58,59} This has been attributed to the negligible absorption component of the extinction experienced by solid enhancers (nano films, roughened electrodes, nanolithographed surfaces, ...).⁶²

Figure 2.5 illustrates the considerations made so far for colloidal suspensions of gold nanorods of varying aspect ratio. The extinction spectra are reported on the left panel, while the right panel shows the SERS spectra of methylene blue, obtained using each of the nanorod suspensions and an excitation line at 785 nm. Maximum enhancements are obtained for the two colloids displaying a λ_{LSPR} that is blue-shifted from the λ_{exc} by 55 and 105 nm.

Figure 2.5 also shows the effect of shape (χ parameter in Equation 2.13) on the shift of the plasmon band to the red with increasing aspect ratio. As observed in Figure 2.6, morphology changes have a more prominent effect on LSPR tuning than size changes (a parameter in Equation 2.13). Moreover, increasing the anisotropy, or increasing the presence of anisotropic features on an identifiable isotropic particle core-unit, has a positive effect on the magnitude of the enhancements.^{21,67}

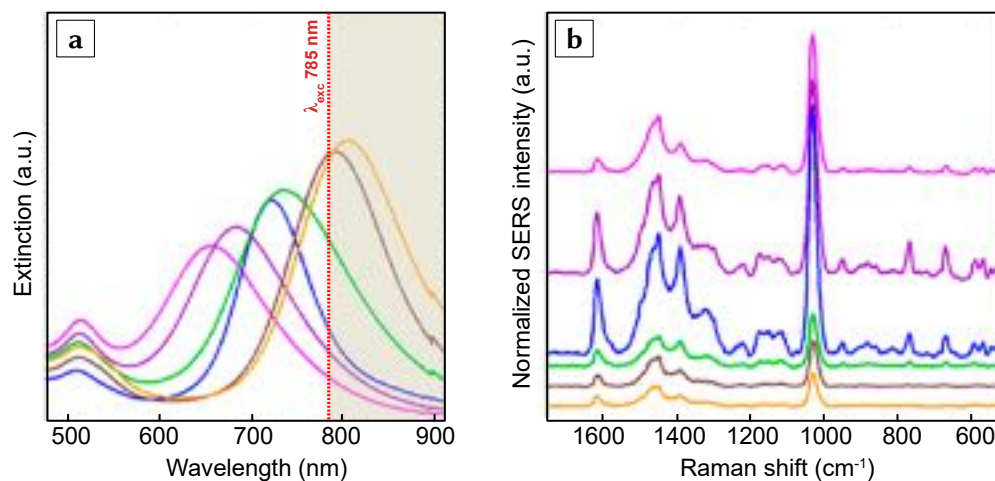


Figure 2.5: (a) Extinction spectra of gold nanorods of various aspect ratios: AR 2 (pink), AR 2.5 (purple), AR 2.75 (blue), AR 3 (green), AR 3.5 (brown), and AR 4.5 (orange). The excitation line used for SERS measurements is marked in red. (b) Normalized SERS spectra of 10^{-6} M methylene blue obtained using gold nanorods of various aspect ratios (color coded according to (a) panel) and an excitation line at 785 nm. The highest enhancements are observed for gold nanorods exhibiting their λ_{LSPR} 55 to 105 nm in pre-resonance with the excitation source. Modified with permission from Sivapalan, S.T. *et al.*⁶² Copyright (2013) American Chemical Society.

Nanostars are emblematic representatives of this category of nanostructures, and they are the state-of-the-art morphology for rationally designed SERS substrates.⁵⁶ Their reported superior optical properties derive from their branched shape, in that dipolar fields tend to concentrate at the tips of a prolate geometry, creating electric fields that are much more intense than those at flattened regions. Moreover, the more this prolate geometry is needle-like, the higher the concentration of dipolar fields.⁷⁰ This effect is known as the *lightning rod effect*, and it contributes to the formation of hot spots.^{4,56,67,71,72} For this reason, under suitable excitation conditions, nanostar-based colloidal suspensions may be used for SERS measurements without need for prior aggregation.⁶⁵

2.2.2.1 Noble metal nanostars: synthesis and impact of surface chemistry on SERS enhancement

Various synthetic protocols for branched nanostructures have been reported in recent years, with the main approaches involving the formation of gold nanostars via seed-mediated growth. These make use of preformed nanoparticles (twinned or single-crystalline) as the nucleation centers for the growth of anisotropic features (spikes or branches), and cationic surfactants as shape directors, most commonly cetyl-trimethylammonium bromide (CTAB).⁵⁶ Alternatively and increasingly more popularly, one-pot strategies can be employed instead, in which the nucleation and the growth of anisotropic features occur *in situ*, in the same reaction vessel.^{56,74} Also in this case, the key reactants are cationic surfactants, such as CTAB. Whether seed-mediated or one-pot synthetic approaches are chosen, surfactants are thought to direct the anisotropic growth by preferentially capping the nucleating crystal or growing seed on a specific crystal facet (the (110) for CTAB);^{73,56,75} this capping induces a facet-specific differentiation of the growth rates along the different crystallographic directions, ultimately causing the formation of anisotropic features.^{56,76}

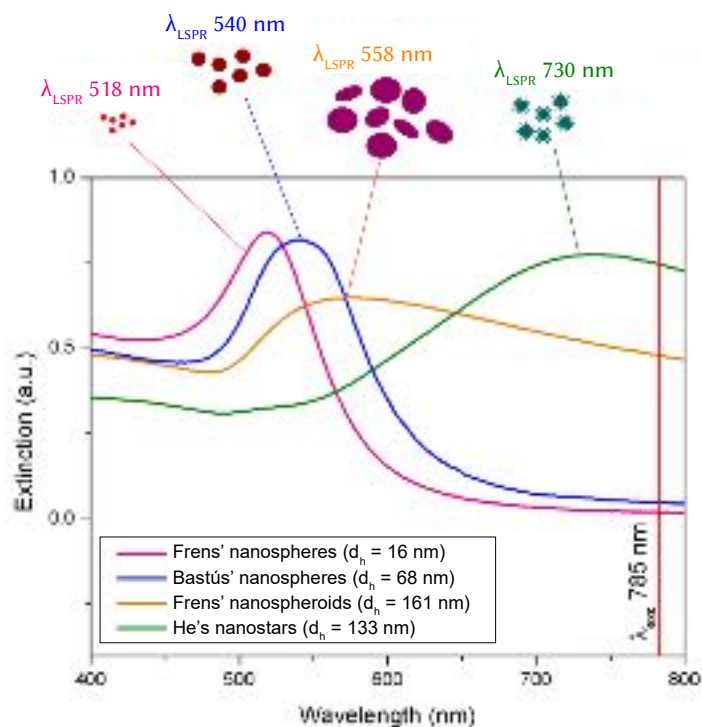


Figure 2.6: Extinction spectra of different colloidal nanostructures showing the effect of size and shape on the λ_{LSPR} . Highly monodispersed gold nanospheres with hydrodynamic diameters of 16 nm (pink) and 68 nm (blue) were synthesized following Frens' and Bastús' procedures, respectively;^{68,69} polydispersed prolate gold nanospheroids with average diameter of 161 nm (orange) were synthesized using Frens' method;⁶⁸ gold/silver nanostars (green) were synthesized using a modified version of He's protocol.⁶⁶ The largest red-shift of the plasmon band is observed when altering the shape. Intensities were scaled for ease of comparison.

While branched nanostructures represent the highest performing morphology in terms of signal enhancement in colloid-based SERS experiments, the presence of surfactants in their colloidal formulation is widely known to negatively impact their potential. Indeed, surfactant-capped SERS substrates show a decrease of the SERS intensity, compared to equivalent surfactant-free surfaces under same experimental conditions (*vide infra*). This forces the operator to carry out time-consuming washing treatments prior to their utilization, in order to reduce the surfactant content in the colloidal formulation.^{21,66,78}

This practice is necessary as SERS signal exhibits a strong distance dependence from the plasmon-sustaining surface (§ 2.1). Any species creating a barrier between the latter and the target analyte will increase the minimum distance at which the analyte can approach the surface, resulting in lower enhancements.

This happens because the electromagnetic enhancement in SERS is a near-field effect,⁴ and an exponential decay of the type reported in *Equation 2.16* is commonly used to describe the relationship between the intensity of the SERS signal and the distance an analyte is located from a plasmon-sustaining nanostructure:^{28,79}

$$I_{SERS} = \left(1 + \frac{r}{a}\right)^{-10} \quad (2.16)$$

where r is the distance between the metal surface and the analyte, and a is a term representing the average dimension of the field-enhancing features on the nanostructure. This generally coincides with the average *radius of curvature*,⁷⁹ that is, the radius of the best fitting arc of a circle for a given non-planar feature. Atomic layer deposition (ALD) experiments coupled with *in situ (operando)* SERS measurements have recently allowed for the refinement of *Equation 2.16*, accounting for the changes in the radius of curvature of the nanometric substrate with changing distance from the surface.⁷⁹

$$I_{SERS} = C_1 \left(1 + \frac{r}{a_1}\right)^{-10} + C_2 \left(1 + \frac{r}{a_2}\right)^{-10} \quad (2.17)$$

In *Equation 2.17*, the two different a terms are adjusting factors referring to the average radius of curvature of the enhancing substrate at the short- (a_1) and long-range (a_2), and the C terms are scaling constants that account for the different contributions of the two terms.

The short-range domain (gold portion of the graph in *Figure 2.7*) decays quickly within the first nanometer from the surface, but it is responsible for the highest electromagnetic

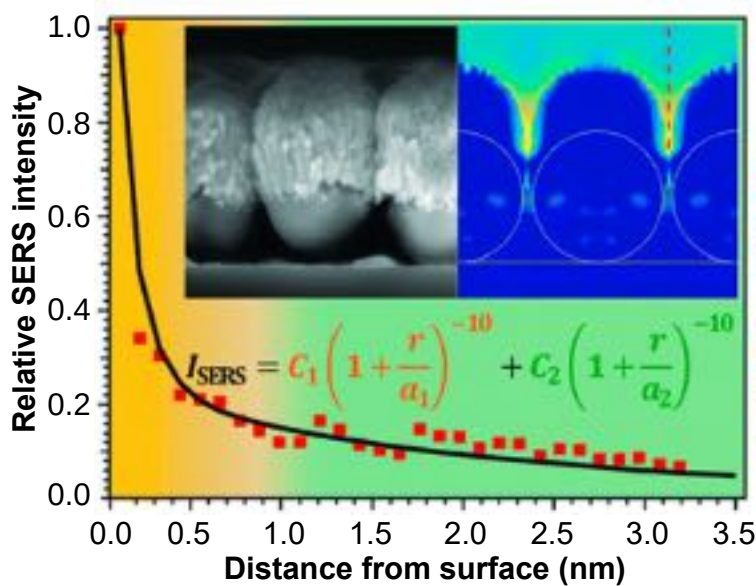


Figure 2.7: Reproduced with permission from Masango, S.S. *et al.*⁷⁹ Copyright (2016) American Chemical Society. Experimental data (red scatter plot) obtained in integrated ALD-SERS experiment are fitted to the adjusted expression for SERS signal decay as a function of distance from enhancing surface (black solid line). The top insets show a SEM micrograph side view of the Al₂O₃ film over Ag nanosphere substrate (AgFON) used for the study (*left*), and a false-color rendering of the near-field intensity distribution obtained using the finite-difference time-domain method in computational electrodynamics (*right*).

enhancements in a SERS measurement. On the other hand, the long-range domain decays in a less steep fashion (green portion of the graph in *Figure 2.7*), giving rise to significantly lower enhancements compared to the former field regime, yet still enabling the observation of SERS signal. This behavior further proves the physical basis of the plasmonic theory of SERS, § 2.1.⁷⁹ Although the values of the a and C factors in *Equation 2.17* are substrate-specific (the authors⁷⁹ utilized silver film over nanospheres, AgFONs), as are the distances r at which the short and long distance domains exist, this refined signal decay expression can be utilized as a conceptual cornerstone for the optimization of the surface environment of a colloidal formulation for SERS applications. In other words, the rational design of a colloidal SERS substrate must account for adsorbed species on the surface of the

nanostructure, and more specifically, for steric hindrance and how it may affect the distance of the analyte from the plasmonic surface.

Surfactants like CTAB are known to form interdigitated bilayers surrounding gold nanoparticles.^{21,80–82} Molecular dynamics simulations of CTAB in water estimate the average end-to-end length of the molecule to be 2.15 nm,⁸³ while Murphy's group estimated the bilayer thickness to range from 2.5 to approximately 6.0 nm in thickness, according to varying degrees of interdigitation.^{62,84} Assuming, for sake of simplicity, the same substrate utilized by Masango, S.S. *et al.* in the ALD operando experiments,⁷⁹ and postulating a fully interdigitated CTAB bilayer of 2.50 nm in thickness with no additional layers of surfactants, the barrier existing between the metallic surface and an analyte in a CTAB-capped substrate would be sufficient to make the system fall into the second regime of decay. The consequences of such a phenomenon are exemplified in *Figure 2.8*, where the effect of increasing concentration, thus capping, of CTAB on colloidal gold/silver nanostars is displayed in terms of both SERS profile intensity of model analyte Crystal Violet and analytical enhancement factor (AEF).⁶⁶ The authors report that treatment with double centrifugation of the CTAB-capped nanostars yields SERS enhancements comparable to 0.1 mM CTAB, with AEF values around 2×10^4 . This value is reported to be approximately 2.5 times smaller than the AEF for the same system in the absence of CTAB (*Figure 4*). Indeed, post-synthesis centrifugation treatments can remove the weaker associated adlayers of the capping agent, leaving the first adsorbed layer (*i.e.*, CTAB's first bilayer) intact.^{21,66}

Because the use of CTAB as a capping agent inhibits SERS enhancement, the use of alternative anisotropic growth directors should be considered. In fact, anisotropic growth may also be induced through the use of small inorganic ions, such as halogens and silver.⁵⁶ Silver ions are typically introduced as silver nitrate solutions, and there are both seed-mediated⁷⁷ and one pot studies⁶⁶ that demonstrates their ability to induce

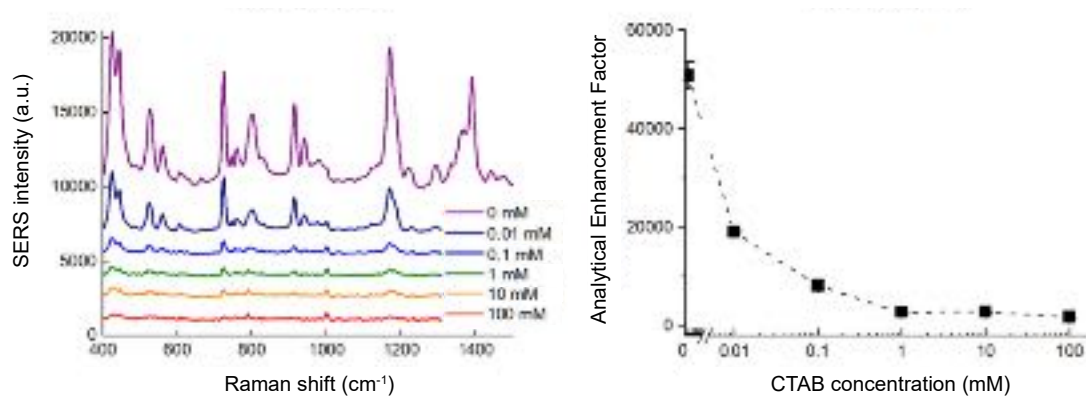


Figure 2.8: SERS spectra of Crystal Violet dye obtained with CTAB-capped nanostars at various concentrations of surfactant (*left*), and relative analytical enhancement factors as a function of CTAB concentration (*right*). Modified from He, S. *et al.*,⁶⁶ Copyright 2015; permission conveyed through Copyright Clearance Center, Inc.

anisotropic growth in gold in the absence of surfactants. The mechanism by which silver ions contribute to this growth is however not fully elucidated yet, as there are too few systematic studies on the subject.⁷⁷ Moreover, the mechanism might vary depending on the type of synthesis (seed-mediated *vs* one-pot), as well as on the choice and ratio of reactants. Important variables such as silver nitrate concentration, as well as the identity of the reducing agent and presence of other co-additives can affect the final product. The mechanistic explanations for this phenomenon vary and may include a combination of the following: selective adsorption (similar to what has been described for CTAB), symmetry breaking and twinning of the growing crystal during co-reduction, underpotential deposition, or kinetic entrapment.^{51,76}

At a practical level, however, the most important aspect of the use of silver as a shape director is not so much the mechanism by which it induces the anisotropic growth, but its *fate* during the nanoparticle synthesis instead, as this will determine the chemical identity of the final product. To the author's knowledge, there is at present only one study in the literature⁷⁷ that systematically examines the fate of silver in the synthesis of

gold nanostars. Atta *et al.*⁷⁷ studied the composition of their 6-branched gold nanostars, with particular attention to the spatial distribution of metallic, zero-valent gold and silver within the nanostar. By examining the effect of the concentration of silver nitrate utilized for the synthesis, they found that all concentrations of silver nitrate produced AuAg alloys. In more detail, the lowest investigated concentration (30 μM AgNO_3) yielded a gold-silver alloy with uniform silver distribution throughout the nanostar, while higher concentrations led to an uneven silver enrichment of the alloy. Indeed, this enrichment unfolded according to a concentration-dependent and directional pattern, starting at the side walls of the nanostar branches (100 μM AgNO_3) and progressing towards the core at higher concentrations (110 μM AgNO_3).⁷⁷

It may seem reasonable to just assume that nanostars obtained by processes in which silver (1) is the shape director and (2) is present in solution *at the same time* gold is reduced, will be made of AuAg nanoalloys, at least in part (*e.g.*, branches in core-preserving seed-mediated processes), because gold and silver are miscible at all⁸⁶ proportions. However, bimetallic nanoscale products of gold and silver may assemble as ordered phases as a result of a kinetically controlled process, especially when obtained by co-reduction and when forming an anisotropic crystal^{IV}. Therefore, the presence of an alloy as reported by Atta *et al.* is a non-trivial observation. At the higher silver nitrate concentrations, they also report the presence of both Ag^0 and Ag^+ , postulating a shape stabilization role of silver via the formation of a superficial $\text{Ag}-\text{Ag}_{\text{UDP}}-\text{Cl}$ monolayer obtained by underpotential deposition (UDP). This surface would inhibit atomic diffusion into thermodynamically more favored morphologies (*i.e.*, shorter and thicker spikes), preserving the branched shape.⁷⁷ The topics of kinetic vs thermodynamic control and morphological restructuring are discussed more in depth in *Chapter 5*.

^{IV} Anisotropic nanocrystals are not thermodynamically favored

2.3 Remarks on SERS and surface adsorption

The overview on the principles of SERS (§ 2.1) clarifies that the origin of the SERS phenomenon is plasmonic in nature, and consequently, an analyte's SERS signal is strongly dependent on its distance from the plasmonic surface. This “proximity requirement” raises the issue of dealing with surface interaction phenomena, and in particular with *adsorption*. The adsorption behavior that a molecule exhibits when approaching a surface is dependent on the interplay of the association constants existing between the analyte molecules themselves, and between the analyte molecules and the surface, which can be schematized in the following equilibria:



where A is the analyte or adsorbate, S is the surface, and K_{AA} and K_{AS} are the equilibrium constants towards the formation of complexes. In the ideal case, in which the adsorbate molecules have no interaction among each other ($K_{AA} = 0$), the adsorption process stops at the completion of the first monolayer. This assumption is the cornerstone of the *Langmuir model* (Figure 2.9 a).^{88,89} Even though the Langmuir model was originally theoreticized for systems of gases adsorbing on surfaces, it can also be applied to describe the adsorption of solutes on surfaces,⁹⁰ and thus, it can be utilized with good approximation to interpret SERS sensitivity studies and extrapolate limits of detection (LOD's) of target substances (§ 8.3.1).^{44,91,92}

If the interaction among analyte molecules is non-negligible ($K_{AA} \neq 0$), the adsorption process can take different routes; for instance, if $K_{AA} \ll K_{AS}$, adsorption can achieve monolayer coverage and then continue past it, with the formation of multiple adlayers (BET model, after Brunauer, Emmet, and Teller, Figure 2.9 b).^{90,95} On the other hand, if

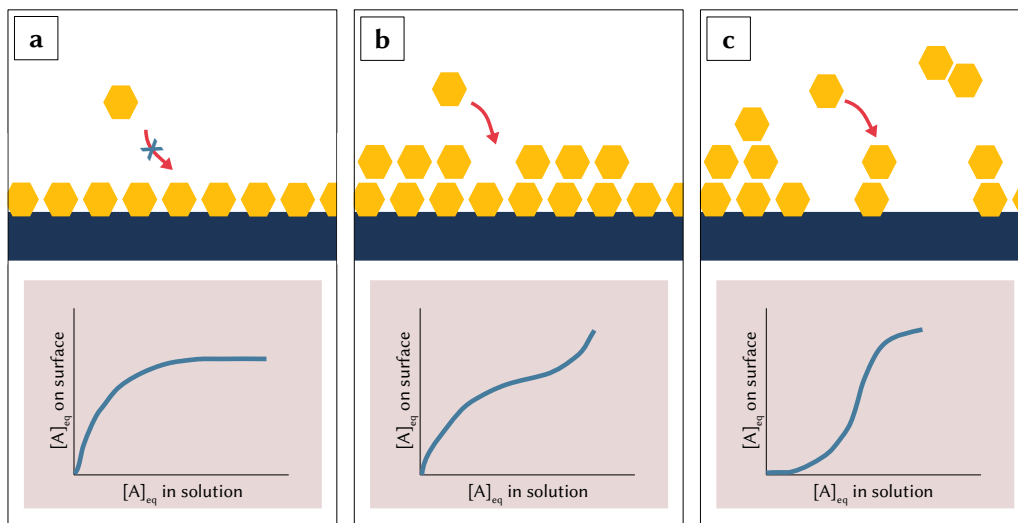


Figure 2.9: Some common adsorption models: (a) Langmuir, also known as *class L, sub-group 2* isotherm, according to the Giles classification system; (b) BET, also known as *class L, sub-group 3, . . . , n* isotherm, according to the Giles classification system; (c) Anti-Langmuir, also known as *class S, sub-group 2* isotherm, according to the Giles classification system.^{93,94}

$K_{AA} \gg K_{AS}$, the equilibrium will be shifted towards the formation of molecular aggregates, and the adsorption process, if favored, proceeds with the formation of islands of adlayers before a full monolayer coverage can be reached (Figure 2.9 c).⁹⁰

When considering colloidal surfaces, it must be recalled that these cannot exist as chemically bare entities,^{36,87} and will naturally have a population of already adsorbed species on their surfaces. Therefore, there are more than two association constants that need to be considered; several equilibria are established, not only between two analyte molecules and between analyte and surface (Equations 2.18–2.19), but also between capping species (C_1, C_2, \dots, C_i) and surface (K_{C_iS}), and between capping species and analyte (K_{C_iA}).



To simplify, it may be assumed that the association constant between individual molecules of an analyte is much lower than any other association constant of the system, such that the equilibrium will be shifted towards surface adsorption, rather than towards molecular aggregation.

$$K_{AA} \ll K_{AS} \quad (2.22)$$



What will exactly happen at the surface, will then depend on the magnitude of K_{AS} in relation to all of the K_{C_iA} and K_{C_iS} of the system. Assuming, for the sake of simplicity, only one chemical species C is capping the surface, and taking into account the two limiting cases $K_{AS} > K_{CS}$ and $K_{AS} < K_{CS}$, a number of scenarios are possible, as depicted in *Figure 2.10*. The implications of these relations are particularly important when the distances between the target analyte and the plasmonic surface are considered; when $K_{AS} > K_{CS}$, the adsorption process will be conducive to very short analyte-surface distances, while when $K_{AS} < K_{CS}$ the distances involved will be larger, as the capping layer will be acting as a spacer between the plasmonic surface and the analyte. As discussed in *Section 2.2.2.1*, this has important consequences on the magnitude of the achievable SERS enhancements (*vide infra*).

From an analytical standpoint, the surface phenomena discussed so far direct two fundamental aspects of SERS practice; the first is calibration curves are inherently never just linear and have a relatively narrow dynamic range (*Figure 2.9*), while the second is the limit of detection (LOD) of a substance is intimately related to how close of an interaction this substance has with the surface.^V The former is easily explained via the Langmuir

^VIn addition, of course, to the already discussed polarizability of the substance itself, or better, of the analyte-substrate complex. (§ 2.1)

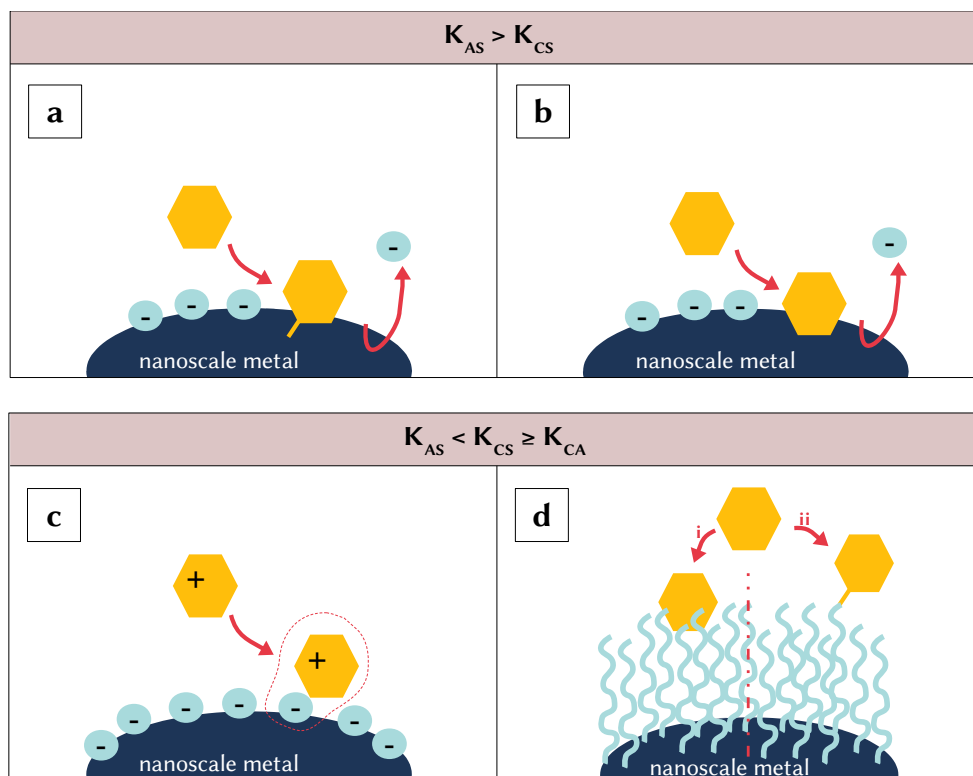


Figure 2.10: Different adsorption scenarios that could happen during a SERS measurement, provided that the $K_{AS} > K_{AA}$. If $K_{AS} > K_{CS}$, direct adsorption can occur, (a) either involving the formation of chemical bonds (e.g., thiols on Au or Ag), or (b) other strong physical interactions, such as π interactions (e.g., aromatic hydrocarbons on Au). If $K_{AS} < K_{CS}$, and $K_{CS} \geq K_{CA}$, adsorption occurs without displacement of the capping species, (c) either by ion pairing if the capping species is charged, or (d) by physical (i) or chemical (ii) interactions if the capping species is neutral (sterically stabilized colloids).

model, that is, in terms of availability of surface adsorption sites, which approaches saturation with increasing analyte concentration. The high substance-specificity of the LOD, on the other hand, may be seen as the very practical result of the near-field character of the SERS phenomenon, by which a well-interacting analyte A will be detectable at lower concentrations than a poorly-interacting analyte B , their polarizabilities being equal or comparable, and all experimental parameters being kept constant. It is self-evident that, for the rational design and optimization of a SERS colloidal substrate, not only the chemical identity and morphology metal nanoparticle must be taken into consideration, but

also the nature of the chemical environment at the solid/liquid interface and the energies governing it.

Finally, it must be recalled that adsorption is a dynamic process, and the associations that have been mentioned so far are not static in nature and represent instead instantaneous pictures of what might be happening on the surface of the nanomaterial during a given time interval. Molecules on a surface adsorb, desorb, diffuse,⁹⁰ and this dynamicity has a significant impact on the measurement of analytes at ultratrace concentrations (<1 nM, *single molecule*), where it is often said that SERS spectra are observed as “blinking” events.⁹⁶ This (spatial or temporal, *vide infra*) intermittence of the observation of SERS spectra in the ultratrace regime is caused not only by the dynamic nature of the equilibria established during adsorption, but also by the stochastic probability of a molecule adsorbing *on a hot spot*,⁹⁷ and the *kinetics* of the adsorption. At lower concentrations, the adsorption is not only a rare event, in that the flux (F) of analyte molecules (A) impinging on a surface is directly proportional to their concentration (*Equation 2.25*), but also a slower process, in that the rate of adsorption, r_{ad} , is proportional to the flux. This is shown by *Equation 2.26*, where s_0 is the initial *sticking probability* of A ($0 \leq s \leq 1$, defined as the probability that a molecule adsorbs after colliding with the surface at t_0 , when coverage Θ is 0), ΔE_{ad}^* is the adsorption energy barrier, and $f(\sigma_s)$ is a function that takes into account the decrease of available adsorption sites as the adsorption proceeds.⁹⁰

$$F = \frac{[A]}{\sqrt{2\pi mk_B T}} \quad (2.25)$$

$$r_{ad} = F s_0 \exp^{-\frac{\Delta E_{ad}^*}{k_B T}} f(\sigma_s) \quad (2.26)$$

For each rate of adsorption of any given analyte A there is a rate of *desorption*. For the principle of detailed balance, if the equilibrium expressed in *Equation 2.24* is considered, and if A is a species with high sticking probability, s , desorption will occur at a lower

rate, ultimately increasing the permanence time of the species *A* on the surface.^{90,97} This concept can be exploited in SERS by increasing the affinity of the surface for the analyte, in manners that were detailed in *Section 2.2.1.2*.

Departing momentarily from the strict use of colloidal substrates, an interesting and revolutionizing approach to deal with blinking in the single molecule regime has been developed by Brolo's group, who introduced the concept of *digital SERS* for the analysis of adsorbed species on planar SERS substrates (nanofilms).⁹⁷ Regardless of the type of substrate used, in a regular SERS sensitivity experiment, the intensity of either a marker band (single-variable approach) or of the full spectrum (multivariate approach) of a target analyte is plotted against concentration, enabling the determination of analytical figures of merit for that species and method. In a *digital SERS* experiment, the SERS intensity is substituted by the number of SERS (adsorption) events within an investigated region of space, and the *count* of these events is plotted against concentration, resulting in a linear relationship. The digital SERS approach provides the SERS community with a method that allows for the quantitative detection of species in the ultratrace regime *despite* the blinking nature of SERS observations in said regime. With this method, picomolar limits of quantification (LOQ) for non-resonant target analytes have been demonstrated.⁹⁷ This direction of research is a further demonstration of the pivotal role that surface chemistry has in fostering a third wave^{VI} of advancements in SERS research, finally enabling its establishment as a mature, benchmark analytical technique.

^{VI}Historically, there are two recognized waves of heightened interest in, and thus development of, SERS research; the first one came with the serendipitous uncovering of the SERS effect itself in the 1970's, and the second was driven by the flourishing of nanotechnology in the 2000's.⁴

REFERENCES

- [1] Aroca, R.F. *Surface-enhanced vibrational spectroscopy*, John Wiley & sons: Chichester, 2006.
- [2] Etchegoin, P.G.; Le Ru, E.C. Basic electromagnetic theory of SERS. In *Surface enhanced Raman spectroscopy*, Schlücker, S., Ed.; WILEY-VCH Verlag & Co. KGaA: Weinheim, 2011, pp 31–37.
- [3] Kosuda, K.M.; Bingham, J.M.; Wustholz, K.L.; van Duyne, R.P. Nanostructures and Surface-Enhanced Raman Spectroscopy. In *Comprehensive Nanoscience and Technology*, Andrews, D.L., Scholes, G.D., Wiederrecht, G.P., Eds.; Elsevier: Amsterdam, 2001; Vol. 3, pp 263–301.
- [4] Le Ru, E.C.; Etchegoin, P.G. *Principles of surface enhanced Raman spectroscopy and related plasmonic effects*, Elsevier: Amsterdam, 2009.
- [5] Haynes, C.L.; Haes, A.J.; McFarland, A.D.; van Duyne, R.P. Nanoparticles with tunable localized surface plasmon resonances, In *Topics in fluorescence spectroscopy*, Gedde, C.D., Lakowicz, J.R., Eds.; Springer Science+Business Media Inc.: New York, 2005; Vol. 8, pp 47–99.
- [6] Otto, A. What is observed in single molecule SERS, and why? *J. Raman Spectrosc.*, **2002**, *33*, 593–598.
- [7] Otto, A.; Lust, M.; Pucci, A.; Meyer, G. SERS active sites, facts, and open questions. *Can. J. Anal. Sci. Spectrosc.*, **2007**, *52*(3), 150–171.
- [8] Moskovits, M. Persistent misconceptions regarding SERS. *Phys. Chem. Chem. Phys.*, **2013**, *15*, 5301–5311.
- [9] Ferraro, J.R.; Nakamoto, K.; Brown, C.W. *Introductory Raman Spectroscopy*, 2 ed.; Academic Press (Elsevier Science): San Diego, 2003.
- [10] Smith, W.E.; Rodger, C. Surface-enhanced Raman scattering. In *Handbook of vibrational spectroscopy, vol. 1*; Chalmers, J.M.; Griffiths, P.R., Eds.; John Wiley & sons: Chichester, 2002.
- [11] Lombardi, J.R.; Birke, R.L.; Lu, T.; Xu, J. Charge-transfer theory of surface enhanced Raman spectroscopy: Herzberg-Teller contributions, *J. Chem. Phys.*, **1986**, *84*(8), 4174–4180.

- [12] Moskovits, M. Surface-enhanced Raman spectroscopy: a brief retrospective, *J. Raman Spectrosc.*, **2005**, 36(6-7), 485–496.
- [13] McQuillan, A.J. The discovery of surface-enhanced Raman scattering, *Notes & Records, The Royal Society Journal of the History of Science*, **2009**, 63, 105–109.
- [14] Pilot, R.; Signorini, R.; Durante, C.; Orian, L.; Bhamidipati, M.; Fabris, L. A Review on Surface-Enhanced Raman Scattering, *Biosensors*, **2019**, 9(2), 57.
- [15] Jeanmaire, D.L.; van Duyne, R.P. Surface raman spectroelectrochemistry: Part I. Heterocyclic, aromatic, and aliphatic amines adsorbed on the anodized silver electrode, *J. Electroanal. Chem. Interfacial Electrochem.*, **1977**, 84(1), 1–20.
- [16] Fleischmann, M.; Hendra, P.J.; McQuillan, A.J. Raman spectra of pyridine adsorbed at a silver electrode, *Chem. Phys. Lett.*, **1974**, 26(2), 163–166.
- [17] Albrecht, M.G.; Creighton, J.A. Anomalously intense Raman spectra of pyridine at a silver electrode, *J. Am. Chem. Soc.*, **1977**, 99(15), 5215–5217.
- [18] Wang, D.S.; Kerker, M. Enhanced Raman scattering by molecules adsorbed at the surface of colloidal spheroids, *Phys. Rev. B*, **1981**, 24(4), 1777–1790.
- [19] Cao, Y.; Zhang, J.; Yang, Y.; Huang, Z.; Viet Long, N.; Fu, C. Engineering of SERS Substrates Based on Noble Metal Nanomaterials for Chemical and Biomedical Applications, *Appl. Spectrosc. Rev.*, **2015**, 50(6), 499–525.
- [20] R.A. Davies, N.S. Chong, B.G. Ooi, Chemical Enhancement of the Surface Enhanced Raman Scattering Signals of Anilines via Their Ortho-Substituents, *Opt. Photonics J.*, **2013**, 3, 13–23.
- [21] Álvarez-Puebla, R.A.; Liz-Marzán, L.M. Traps and cages for universal SERS detection, *Chem. Soc. Rev.*, **2012**, 41, 43–51.
- [22] Jain, P.K.; El-Sayed, M.A. Plasmonic coupling in noble metal nanostructures, *Chem. Phys. Lett.*, **2010**, 487, 153–164.
- [23] Halls, M.D.; Velkovski, J.; Schlegel, H.B. Harmonic frequency scaling factors for Hartree–Fock, S–VWN, B–LYP, B3–LYP, B3–PW91 and MP2 with the Sadlej pVTZ electric property basis set, *Theor. Chem. Acc.*, **2001**, 105(6), 413–421.

- [24] Fana, M.; Andrade, G.F.S.; Brolo, A.G. A review on the fabrication of substrates for surface enhanced Raman spectroscopy and their applications in analytical chemistry, *Anal. Chim. Acta*, **2011**, 693(1–2), 7–25.
- [25] Mosier-Boss, P.A. Review of SERS Substrates for Chemical Sensing, *Nanomaterials*, **2017**, 7(6), 142.
- [26] Analytical Methods Committee, Surface-enhanced Raman spectroscopy (SERS) in cultural heritage, *Anal. Methods*, **2017**, 9, 4338–4340.
- [27] Saviello, D.; Alyami, A.; Trabace, M.; Giorgi, R.; Baglioni, P.; Mirabile, A.; Iacopino, D. Plasmonic colloidal pastes for surface-enhanced Raman spectroscopy (SERS) of historical felt-tip pens, *RSC Adv.*, **2018**, 8, 8365–8371.
- [28] Langer, J.; Jimenez de Aberasturi, D.; Aizpurua, J.; Alvarez-Puebla, R.A.; Auguie, B.; Baumberg, J.J.; Bazan, G.C.; Bell, S.E.J.; Boisen, A.; Brolo, A.G.; Choo, J.; Cialla-May, D.; Deckert, V.; Fabris, L.; Faulds, K.; García de Abajo, F.J.; Goodacre, R.; Graham, D.; Haes, A.J.; Haynes, C.L.; Huck, C.; Itoh, T.; Käll, M.; Kneipp, J.; Kotov, N.A.; Kuang, H.; Le Ru, E.C.; Lee, H.K.; Li, J-F.; Ling, X.Y.; Maier, S.A.; Mayerhöfer, T.; Moskovits, M.; Murakoshi, K.; Nam, J-M.; Nie, S.; Ozaki, Y.; Pastoriza-Santos, I.; Perez-Juste, J.; Popp, J.; Pucci, A.; Reich, S.; Ren, B.; Schatz, G.C.; Shegai, T.; Schlücker, S.; Tay, L-L.; Thomas, K.G.; Tian, Z-Q.; Van Duyne, R.P.; Vo-Dinh, T.; Wang, Y.; Willets, K.A.; Xu, C.; Xu, H.; Xu, Y.; Yamamoto, Y.S.; Zhao, B.; Liz-Marzán, L.M. Present and Future of Surface-Enhanced Raman Scattering. *ACS Nano*, **2020**, 14(1), 28–117.
- [29] P.K.Aravind, P.K.; Nitzan, A.; Metiu, H. The interaction between electromagnetic resonances and its role in spectroscopic studies of molecules adsorbed on colloidal particles or metal spheres. *Surf. Sci.*, 1981, 110(2), 189–204.
- [30] P.K.Aravind, P.K.; Metiu, H. The effects of the interaction between resonances in the electromagnetic response of a sphere-plane structure; applications to surface enhanced spectroscopy. *Surf. Sci.*, **1983**, 124(2–3), 506–528.
- [31] García-Vidal, F.J.; Pendry, J.B. Collective Theory for Surface Enhanced Raman Scattering. *Phys. Rev. Lett.*, **1996**, 77, 1163–1166.
- [32] Braun, G.B.; Joon Lee, S.; Laurence, T.; Fera, N.; Fabris, L.; Bazan, G.C.; Moskovits, M.; Reich, N.O. Generalized Approach to SERS-Active Nanomaterials via Controlled Nanoparticle Linking, Polymer Encapsulation, and Small-Molecule Infusion, *J. Phys. Chem. C*, **2009**, 113, 13622–13629.

- [33] Izquierdo-Lorenzo, I.; Kubackova, J.; Manchon, D.; Mosset, A.; Cottancin, E.; Sánchez-Cortés, S. Linking Ag Nanoparticles by Aliphatic α - ω Dithiols: A Study of the Aggregation and Formation of Interparticle Hot Spots, *J. Phys. Chem. C*, **2013**, *117*, 16203–16212.
- [34] Fang, C.; Bandaru, N.M.; Ellis, A.V.; Voelcker, N.H. Beta-cyclodextrin decorated nanostructured SERS substrates facilitate selective detection of endocrine disruptor chemicals, *Biosens. Bioelectron.*, **2013**, *42*, 632–639.
- [35] S. Sánchez-Cortés, J.V. García-Ramos, Influence of coverage in the surface enhanced Raman scattering of cytosine and its methyl derivatives on metal colloids: chloride and pH effects, *Surf. Sci.*, **2001**, *473*(1–2), 133–142.
- [36] Everett, D.H. *Basic Principles of Colloid Science*, Royal Society of Chemistry: London, 1988.
- [37] Derjaguin, B.; Landau, L. Theory of the stability of strongly charged lyophobic sols and of the adhesion of strongly charged particles in solution of electrolytes. *Acta Physicochim. URSS*, **1941**, *14*, 633–662.
- [38] Verwey, E.J.W.; Overbeek, J.T.G. *Theory of the Stability of Lyophobic Colloids*, Elsevier: New York, 1948.
- [39] Delgado, A.V.; González-Caballero, F; Hunter, R.J.; Koopal, L.K.; Lykelma, J. Measurement and Interpretation of Electrokinetic Phenomena. *Pure Appl. Chem.*, **2005**, *77*(10), 1753–1805.
- [40] Atkins, P.; de Paula, J.; Keeler, J. *Atkins' Physical Chemistry*, Eleventh edition, Oxford University Press: Oxford, 2018.
- [41] Milvaney, P. Metal Nanoparticles: Double Layers, Optical Properties, and Electrochemistry. In *Nanoscale Materials in Chemistry*; Klabunde, K.J., Ed.; Wiley-Interscience: New York, 2001.
- [42] Al-Johani, H.; Abou-Hamad, E.; Jedidi, A.; Widdifield, C.M.; Viger-Grave, J.; Sangaru, S.S.; Gajan, D.; Anjum, D.H.; Ould-Chikh, S.; Hedhili, M.N.; Gurinov, A.; Kelly, M.J.; El Eter, M.; Cavallo, L.; Emsley, L.; Basset, J-M. The structure and binding mode of citrate in the stabilization of gold nanoparticles. *Natur. Chem.*, **2017**, *9*, 890–895.
- [43] Hüfner, S.; Wertheim, G.K.; Wernick, J.H. XPS Core Line Asymmetries in metals. *Solid State Commun.*, **1975**, *17*, 417–422.

- [44] Izquierdo-Lorenzo, I.; Sanchez-Cortes, S.; Garcia-Ramos, J.V. Adsorption of Beta-Adrenergic Agonists Used in Sport Doping on Metal Nanoparticles: A Detection Study Based on Surface-Enhanced Raman Scattering. *Langmuir*, 2010, 26(18), 14663–14670.
- [45] Liu, S. Ishimoto, T.; Koyama, M. First-Principles calculations of OH⁻/OH Adsorption on Gold Nanoparticles. *Int. J. Quant. Chem.*, **2015**, 115, 1597–1605.
- [46] Santiago-Rodríguez, Y.; Herron, J.A.; Curet-Arana, M.; Mavrikakis, M. Atomic and molecular adsorption on Au(111). *Surf. Sci.*, **2014**, 627, 57–69.
- [47] Granqvist, C.G; Buhrman, R.A. Ultrafine metal particles. *J. Appl. Phys.*, **1976**, 47, 2220–2222.
- [48] Kiss, L.B.; Söderlund, J.; Niklasson, G.A.; Granqvist, C.G. New approach to the origin of lognormal size distributions of nanoparticles. *Nanotechnology*, **1999**, 10(1), 25–28.
- [49] Vegh, J. The Shirley background revised. *J. Electron Spectrosc. Relat. Phenom.*, **2006**, 151(3), 159–164.
- [50] Casaletto, M.P.; Longo, A.; Martorana, A. Prestianni, A.; Venezia, A.M. XPS study of supported gold catalysts: the role of Au⁰ and Au^{δ+} species as active sites. *Surf. Interface Anal.*, **2006**, 38, 215–218.
- [51] Gilroy, K.D.; Ruditskiy, A.; Peng, H-C.; Qin, D.; Xia, Y. Bimetallic Nanocrystals: Syntheses, Properties, and Applications. *Chem. Rev.*, **2016**, 116, 10414–10472.
- [52] Nakamoto, K. *Infrared and Raman Spectra of Inorganic and Coordination Compounds. Part B: Applications in Coordination, Organometallic, and Bioinorganic Chemistry*, Sixth edition, John Wiley & Sons: Hoboken, 2009.
- [53] Gomes de Mesquita, A.H.; MacGillavry, C.H.; Eriks, K. The structure of triphenylmethyl perchlorate at 85°C. *Acta Crystallogr.*, **1965**, 18, 437–443.
- [54] Cañamares, M.V.; Chenal, C.; Birke, R.L.; Lombardi, J.R. DFT, SERS, and Single-Molecule SERS of Crystal Violet. *J. Phys. Chem. C*, **2008**, 112, 20295–20300.
- [55] Le Ru, E.C.; Blackie, E.; Meyer, M.; Etchegoin, P.G. Surface Enhanced Raman Scattering Enhancement Factors: A Comprehensive Study. *J. Phys. Chem. C*, **2007**, 111, 13794–13803.

- [56] Guerrero-Martínez, A.; Barbosa, S.; Pastoriza-Santos, I.; Liz-Marzán, L.M. Nanostars shine bright for you. Colloidal synthesis, properties and applications of branched metallic nanoparticles, *Curr. Opin. Colloid Interface Sci.*, **2011**, *16*, 118–127.
- [57] Liz-Marzán, L.M. Tailoring surface plasmons through the morphology and assembly of metal nanoparticles, *Langmuir*, **2006**, *22*, 32–41.
- [58] Álvarez-Puebla, R.A. Effects of the excitation wavelength on the SERS spectrum. *J. Phys. Chem. Lett.* **2012**, *3*, 857–866.
- [59] McFarland, A.D.; Young, M.A.; Dieringer J.A.; Van Duyne, R.P. Wavelength-scanned surface-enhanced Raman spectroscopy. *J. Phys. Chem. B* **2005**, *109*, 11279–11285.
- [60] van Dijk, T.; Sivapalan, S.T.; Devetter, B.M.; Yang, T.K.; Schulmerich, M.V.; Murphy, C.J.; Bhargava, R.; Carney, P.S. Competition Between Extinction and Enhancement in Surface Enhanced Raman Spectroscopy. *J. Phys. Chem. Lett.* **2013**, *4*(7), 1193–1196.
- [61] Etchegoin, P.G.; Le Ru, E.C.; Meyer M. An analytic model for the optical properties of gold. *J. Chem. Phys.* **2006**, *125*, 164705–164707.
- [62] Sivapalan, S.T.; Devetter B.M.; Yang, T.K.; van Dijk, T.; Schulmerich, M.V.; Carney, P.S.; Bhargava, R.; Murphy, C.J. Off-Resonance Surface-Enhanced Raman Spectroscopy from Gold Nanorod Suspensions as a Function of Aspect Ratio: Not What We Thought. *ACS Nano* **2013**, *7*(3), 2099–2105.
- [63] van de Hulst, H.C. *Light scattering by small particles*; Dover Publications: Mineola, NY, 1982.
- [64] Bohren, C.F.; Huffmanm D.R. *Absorption and scattering of light by small particles*; John Wiley and Sons: New York, 1983.
- [65] Garcia-Leis, A.; Torreggiani, A.; García-Ramos, J.V.; Sánchez-Cortés, S. Hollow Au / Ag nanostars displaying broad plasmonic resonance and high surface-enhanced Raman sensitivity. *Nanoscale* **2015**, *7*, 13629–13637.
- [66] He, S.; Kang, M.W.C.; Khan, F.J.; Tan, E.K.M.; Reyes, M.A.; Kah, J.C.Y. Optimizing gold nanostars as a colloid-based surface-enhanced Raman scattering (SERS) substrate. *J. Opt.* **2015**, *17*, 1–13.

- [67] Rodríguez-Lorenzo, L.; Álvarez-Puebla, R. A.; Pastoriza Santos, I.; Mazzucco, S.; Odile, S.; Kociak, M.; Liz-Marzán, L. M.; García De Abajo, F. J. Zeptomol Detection Through Controlled Ultrasensitive Surface-Enhanced Raman Scattering. *J. Am. Chem. Soc.* **2009**, *131*, 4616–4618.
- [68] Frens, G. Controlled nucleation for the regulation of the particle size in monodisperse gold suspensions. *Nature* **1973**, *241*, 20–22.
- [69] Bastús, N.G.; Comenge, J.; Puentes, V. Kinetically Controlled Seeded Growth Synthesis of Citrate-Stabilized Gold Nanoparticles of up to 200 nm: Size Focusing versus Ostwald Ripening. *Langmuir* **2011**, *27*(17), 11098–11105.
- [70] Liao, P.F.; Wokaun, A. Lightning rod effect in surface enhanced Raman scattering. *J. Chem. Phys.* **1982**, *76*, 751–752.
- [71] Kelly, K.L.; Coronado, E.; Zhao, L.L.; Schatz, G.C. The Optical Properties of Metal Nanoparticles: The Influence of Size, Shape, and Dielectric Environment. *J. Phys. Chem. B* **2003**, *107*(3), 668–677.
- [72] Chung, T.; Lee, S-Y.; Song, E.Y.; Chun, H.; Lee, B. Plasmonic Nanostructures for Nano-scale Bio-sensing. *Sensors* **2011**, *11*, 10907–10929.
- [73] Sahoo, G.P.; Bar, H.; Bhui, D.K.; Sarkar, P.; Samanta, S.; Pyne, S.; Ash, S.; Misra, A. Synthesis and photo physical properties of star shaped gold nanoparticles. *Colloids and Surfaces A* **2011**, *375*, 30–34.
- [74] Xia, Y.; Xiong, Y.; Lim, B.; Skrabalak, S.E. Shape-Controlled Synthesis of Metal Nanocrystals: Simple Chemistry Meets Complex Physics? *Angew. Chem. Int. Ed.* **2009**, *48*, 60–103.
- [75] Tao, A.R.; Habas, S.; Yang, P. Shape Control of Colloidal Metal Nanocrystals. *Small*, **2008**, *4*(3), 310–325.
- [76] Sau, T.K.; Rogach, A.L. Nonspherical Noble Metal Nanoparticles: Colloid-Chemical Synthesis and Morphology Control. *Adv. Mater.*, **2010**, *22*, 1781–1804.
- [77] Atta, S.; Beetz, M.; Fabris, L. Understanding the role of AgNO₃ concentration and seed morphology in the achievement of tunable shape control in gold nanostars. *Nanoscale*, **2019**, *11*, 2946–2958.

- [78] Rodríguez-Lorenzo, L.; Álvarez-Puebla, R. A.; García De Abajo, F.J.; Liz-Marzán, L. M. Surface Enhanced Raman Scattering Using Star-Shaped Gold Colloidal Nanoparticles. *J. Phys. Chem. C* **2010**, *114*(16), 7336–7340.
- [79] Masango, S.S.; Hackler, R.A.; Large, N.; Henry, A-I.; McAnally, M.O.; Schatz, G.C.; Stair, P.C.; Van Duyne, R.P. High-Resolution Distance Dependence Study of Surface-Enhanced Raman Scattering Enabled by Atomic Layer Deposition. *Nano Lett.* **2016**, *16*, 4251–4259.
- [80] Nikoobakht, B.; El-Sayed, M. Evidence for Bilayer Assembly of Cationic Surfactants on the Surface of Gold Nanorods. *Langmuir* **2001**, *17*(20), 6368–6374.
- [81] Gao, J.; Bender, C.M.; Murphy, C.J. Dependence of the Gold Nanorod Aspect Ratio on the Nature of the Directing Surfactant in Aqueous Solution. *Langmuir* **2003**, *19*(21), 9065–9070.
- [82] da Silva, J.A.; Meneghetti, M.R. New Aspects of the Gold Nanorod Formation Mechanism via Seed-Mediated Methods Revealed by Molecular Dynamics Simulations. *Langmuir* **2018**, *34*(1), 366–375.
- [83] Fuglestad, B.; Gupta, K.; Wand, A.J.; Sharp, K.A. Characterization of Cetyltrimethylammonium Bromide/Hexanol Reverse Micelles by Experimentally Benchmarked Molecular Dynamics Simulations. *Langmuir*, **2016**, *32*, 1674–1684.
- [84] Murphy, C.J.; Sau, T.K.; Gole, A.M.; Orendorff, C.J.; Gao, J.; Gou, L.; Hunyadi, S.E.; Li, T. Anisotropic metal nanoparticles: Synthesis, assembly, and optical applications. *J. Phys. Chem. B*, **109**, 13857–13870.
- [85] Cheng, L-C.; Huang, J-H.; Chen, H.M.; Lai, T.C.; Yang, K.Y.; Liu, R.S.; Hsiao, M.; Chen, C-H.; Here, L-J.; Tsaid, D.P. Seedless, silver-induced synthesis of star-shaped gold/silver bimetallic nanoparticles as high efficiency photothermal therapy reagent. *J. Mater. Chem.*, **2012**, *22*, 2244–2253.
- [86] Ferrando, R.; Jellinek, J.; Johnston, R.L. Nanoalloys: From Theory to Applications of Alloy Clusters and Nanoparticles. *Chem. Rev.*, **2008**, *108*(3), 845–910.
- [87] Murphy, C.J.; Buriak, J.M. Best Practices for the Reporting of Colloidal Inorganic Nanomaterials. *Chem. Mater.*, **2015**, *27*(14), 4911–4913.
- [88] Langmuir, I. The Constitution and Fundamental Properties of Solids and Liquids. Part I. Solids. *J. Am. Chem. Soc.*, **1916**, *38*(11), 2221–2295.

- [89] Langmuir, I. The Constitution and Fundamental Properties of Solids and Liquids. II. Liquids. *J. Am. Chem. Soc.*, **1917**, 39(9), 1848–1906.
- [90] Christmann, K. *Introduction to Surface Physical Chemistry*, Topics in Physical Chemistry Vol. 1, Springer-Verlag: Berlin/Heidelberg, 1991.
- [91] Kubackova, J.; Fabriciova, G.; Miskovsky, P.; Jancura, D.; Sanchez-Cortes, S. Sensitive Surface-Enhanced Raman Spectroscopy (SERS) Detection of Organochlorine Pesticides by Alkyl Dithiol-Functionalized Metal Nanoparticles-Induced Plasmonic Hot Spots. *Anal. Chem.*, **2015**, 87(1), 663–669.
- [92] Deriu, C.; Conticello, I.; Mebel, A.M.; McCord, B. Micro Solid Phase Extraction Surface-Enhanced Raman Spectroscopy (-SPE/SERS) Screening Test for the Detection of the Synthetic Cannabinoid JWH-018 in Oral Fluid. *Anal. Chem.*, **2019**, 91(7), 4780–4789.
- [93] Giles, C.H.; MacEwan, T.H.; Nakhwa, S.N.; Smith, D. Studies in adsorption. Part XI. A system of classification of solution adsorption isotherms, and its use in diagnosis of adsorption mechanisms and in measurement of specific surface areas of solids. *J. Chem. Soc.*, **1960**, 3973–3993.
- [94] Giles, C.H.; Smith, D.; Huitson, A. A general treatment and classification of the solute adsorption isotherm. I. Theoretical. *J. Colloid Interface Sci.*, **1974**, 47(3), 755–765.
- [95] Brunauer, S.; Emmett, P.H.; Teller, E. Adsorption of Gases in Multimolecular Layers. *J. Am. Chem. Soc.*, **1938**, 60(2), 309–319.
- [96] dos Santos, D.P.; Temperini, M.L.A.; Brolo, A.G. Intensity Fluctuations in Single-Molecule Surface-Enhanced Raman Scattering *Acc. Chem. Res.*, **2019**, 52(2), 456–464.
- [97] de Albuquerque, C.D.L.; Sobral-Filho, R.G.; Poppi, R.J.; Brolo, A.G. Digital Protocol for Chemical Analysis at Ultralow Concentrations by Surface-Enhanced Raman Scattering, *Anal. Chem.*, **2018**, 90(2), 1248–1254.

CHAPTER 3

Materials and Methods

3.1 Materials

All solutions were made using ultra pure water and ACS grade reagents. Volumetric flasks were cleaned with aqua regia and rinsed with copious amounts of ultrapure water. The reagents used for the synthesis of nanostars were tetrachloroauric(III) acid trihydrate (Acros Organics, CAS 16961-25-4), silver nitrate (Fisher Chemical, CAS 7761-88-8), and L-ascorbic acid (Fisher Chemical, CAS 50-81-7). Stock solutions of candidate stabilizing agents were made using trisodium citrate dihydrate (Fisher Scientific, CAS 6132-04-3), disodium L-tartrate (Alfa Aesar, CAS 6106-24-7), sodium acetate (Fisher Scientific, CAS 127-09-3), sodium carbonate monohydrate (Spectrum, CAS 5968-11-6), sodium hydroxide (Fisher Scientific, CAS 1310-73-2), 1,3-propanedisulfonic acid disodium salt (Alfa Aesar, CAS 36589-58-9), sodium nitrate (Acros Organics, CAS 7631-99-4), disodium sulfite (Acros Organics, CAS 7757-83-7), disodium sulfate decahydrate (Aldrich, CAS 7727-73-3). The reference surfactant-stabilized formulation was prepared using cetyltrimethylammonium bromide, CTAB (Aldrich, CAS 57-09-0). SERS activity was probed using Crystal Violet as model analyte (Acros Organics, CAS 548-62-9, C.I. 42555, Basic Violet 3). The materials utilized for the application of the formulated nanomaterials to real case analytes are specified in *Chapter 8*.

3.2 Methods

3.2.1 Synthesis of nanostars

Nanostars were prepared in as-received glass vials wrapped in Al foil, following one of the protocols published by He *et al.*,¹ with a post-synthetic modification. Briefly, 36 μL of 10^{-2} M HAuCl_4 and 2 μL of 10^{-2} M AgNO_3 were added to 1 mL of ultrapure water and vortexed for 10 s. Subsequently, 6 μL of 10^{-1} M L-ascorbic acid were added all at once to the reactant mixture and vortexed for 20 s. An aliquot of candidate stabilizer, at an initial concentration of 1 M, was then added to the formed nanostars and vortexed for 5 s (*Table 3.1*). The resulting colloidal nanostars are teal in color and have a pH that varies between 5.5 and 9.5, depending on the formulation. Unless otherwise specified, the colloidal nanostars were incubated at room temperature for at least 12 hours before usage.

3.2.2 Synthesis of reference AuAg nanospheres

Reference AuAg nanospheres for shape effect studies were prepared in as-received glass vials wrapped in Al foil, following one of the protocols published by He *et al.*,¹ with a post-synthetic modification. Briefly, 36 μL of 10^{-2} M HAuCl_4 and 2 μL of 10^{-2} M AgNO_3 were added to 1 mL of ultrapure water and vortexed for 10 s. Subsequently, 4 μL of 10^{-1} M L-ascorbic acid were added all at once to the reactant mixture and vortexed for 20 s. Disodium carbonate monohydrate, at a final concentration of 0.96×10^{-3} M (*Table 3.1*), was then added to the formed nanostars and vortexed for 5 s. The resulting colloidal nanostars are bright pink in color and have a pH around 7. The colloidal nanostars were incubated at room temperature for at least 12 hours before usage.

Table 3.1: Post-synthetic addition of candidate stabilizing agents.

formulation	volume used (μL)	final concentration (M)	molar ionic strength increase ^a (M)
NS/Ct	1.00	0.96×10^{-3}	3.4×10^{-3}
NS/Tt (c)	1.00	0.96×10^{-3}	2.2×10^{-3}
NS/Tt (I)	1.50	1.4×10^{-3}	3.4×10^{-3}
NS/Ac (c)	4.32	4.1×10^{-3}	0.6×10^{-3}
NS/Ac (I)	4.32	4.1×10^{-3}	3.4×10^{-3}
NS/ CO_3^{2-} (c)	1.00	0.96×10^{-3}	2.4×10^{-3}
NS/ CO_3^{2-} (I)	3.30	3.2×10^{-3}	3.4×10^{-3}
NS/ OH^- (c)	1.00	0.96×10^{-3}	0.96×10^{-3}
NS/ OH^- (I)	3.52	3.4×10^{-3}	3.4×10^{-3}
NS/ NO_3^- (c)	1.00	0.96×10^{-3}	0.96×10^{-3}
NS/ NO_3^- (I)	3.52	3.4×10^{-3}	3.4×10^{-3}
NS/ SO_3^- (c)	1.00	0.96×10^{-3}	1.4×10^{-3}
NS/ SO_3^- (I)	2.20	2.1×10^{-3}	3.4×10^{-3}
NS/ SO_4^{2-} (c)	1.00	0.96×10^{-3}	2.9×10^{-3}
NS/ SO_4^{2-} (I)	1.18	1.1×10^{-3}	3.4×10^{-3}
NS/PrSulf (c)	1.00	0.96×10^{-3}	2.9×10^{-3}
NS/PrSulf (I)	1.17	1.1×10^{-3}	3.4×10^{-3}

Ct, trisodium citrate; *Tt*, disodium tartrate; *Ac*, sodium acetate; *PrSulf*, 1,3-propanedisulfonic acid disodium salt; *M*, constant final molarity of candidate stabilizer; *I*, constant molar ionic strength increase^a provided to the formulation.

^a Increase with respect to the baseline ionic strength of the as-synthesized nanostars.

3.2.3 Electrophoretic Light Scattering (ELS)

Electrophoretic mobility and conductivity measurements of the colloidal formulations were performed via electrophoretic light scattering (ELS) using a Malvern ZEN3600 Zetasizer and a disposable folded capillary DTS1070 Zeta cell. Standard operating procedures were created setting water as the dispersant, and assuming the sample viscosity, η_s , to be the same as the dispersant viscosity, $\eta_{\text{H}_2\text{O}}$. ELS studies were performed according to two different procedures, depending on their purpose. For the initial optimization of stabilizer's concentration (*Chapter 4*), NS formulations were prepared in triplicate and analyzed as 800 μL aliquots. Each measurement consisted of 20 sub-runs, and was subjected to a mean effective applied voltage of 148.4 V. Samples were equilibrated at 25 °C for 120 s prior to the start of the measurement (*vide infra*). For the estimate of the adsorption constant

of citrate onto the bimetallic nanostars (*Chapter 6*), three NS/Ct batches per each citrate concentration point were analyzed each in triplicate ($N = 9$), as 800 μL aliquots; the concentration of citrate in the final formulation ranged from a minimum of 1.9×10^{-4} M to a maximum of 5.2×10^{-3} M. Each measurement consisted of 25 sub-runs, and was subjected to a mean effective applied voltage of 148.4 V. Samples were equilibrated for 240 s at two different temperatures, 10 and 20 $^{\circ}\text{C}$. Temperature control was achieved by utilizing the built-in thermostated cell holder of the instrument.

The dispersant's viscosity, refractive index, and dielectric constant were set for each temperature as reported in *Table 3.2*. The viscosity and dielectric constant were obtained by published tabulated data,^{2,3} while the refractive index was calculated utilizing the method published by Bashkatov and Genina,⁴ as follows:

$$n_{(\lambda,T)} = A_{(T)} + \frac{B_{(T)}}{\lambda^2} + \frac{C_{(T)}}{\lambda^4} + \frac{D_{(T)}}{\lambda^6} \quad (3.1)$$

where A, B, C, and D are the Cauchy coefficients as a function of absolute temperature, obtained as follows:⁴

$$A_{(T)} = 1.3208 - 1.2325(10^{-5})T - 1.8674(10^{-6})T^2 + 5.0233(10^{-9})T^3 \quad (3.2)$$

$$B_{(T)} = 5208.2413 - 0.5179T - 2.284(10^{-2})T^2 + 6.9608(10^{-5})T^3 \quad (3.3)$$

$$C_{(T)} = 2.5551(10^8) - 18341.336T - 917.2319T^2 + 2.7729T^3 \quad (3.4)$$

$$D_{(T)} = 9.3495 - 1.7855(10^{-3})T + 3.6733(10^{-5})T^2 - 1.2932(10^{-7})T^3 \quad (3.5)$$

ζ potential values were obtained from the measured electrophoretic mobilities (μ) as calculated by the Zetasizer software:⁷

$$\mu = \frac{2\varepsilon_r}{3\eta} \zeta f(\kappa a) \quad (3.6)$$

Table 3.2: Viscosity, dielectric permittivity, and refractive index ($\lambda = 633 \text{ nm}$) at varying temperature.

T (°C)	T (K)	$\eta_{H_2O^2}$ (mPa·s)	$\epsilon_{H_2O^3}$	$n_{H_2O(633)}^4$
10	283.15	1.3059	83.83	1.332
20	293.15	1.0016	80.10	1.331
25	298.15	0.8900	78.30	1.331

η , viscosity; ϵ , dielectric permittivity; n , refractive index.

where ϵ_r is the dielectric permittivity of the dispersant, η is the viscosity of the dispersant, and $f(\kappa a)$ is the Henry's function, which can be approximated to 1.5 for colloidal suspensions in aqueous media (Smoluchowski approximation).⁷ The use of this simple model is justified by IUPAC's guidelines when the purpose of the electrokinetic study is the "identification of a plateau in the adsorption of an ionic species indicating optimum dosage for a dispersing agent".⁸ Therefore, this method was utilized for the work reported in Chapter 4.

For the estimate of the adsorption constants, a more quantitative method as published by Ohshima⁶ was utilized to derive the ζ potential values from the measured electrophoretic mobilities. The utilized equation is the following:⁶

$$\mu = \frac{\epsilon_r \epsilon_0}{\eta} \zeta f(\kappa a) \quad (3.7)$$

where ϵ_r and ϵ_0 are the dielectric permittivities of the dispersant and vacuum, respectively, η is the viscosity of the dispersant, and $f(\kappa a)$ is the Henry's function, which in this case can be approximated to the following expression:⁶

$$f(\kappa a) \approx \frac{2}{3} \left\{ 1 + \frac{1}{2 \left\{ 1 + \left[\frac{2.5}{\kappa a} \right] [1 + 2e(-\kappa a)] \right\}^3} \right\} \quad (3.8)$$

where a is the radius of curvature of the nanostructure [m], and κ is the Debye-Hückel parameter [m^{-1}], that is, the inverse of the Debye length (κ^{-1}). The Debye-Hückel parameter is calculated from:⁹

$$\kappa = 4\pi\lambda_B \sum (n_{c_i}z_i) \quad (3.9)$$

where λ_B is the Bjerrum length^I (Table 3.3), n_{c_i} is the number concentration of the i th charged species, and z_i is the corresponding formal charge. The Ohshima method is valid for all particle geometries,⁶ and was successfully utilized by Haes's group¹⁰ for quantitative studies on colloidal monometallic gold nanostars.

Table 3.3: Bjerrum length at varying temperature.

T (°C)	T (K)	λ_B (m)
10	283.15	7.04×10^{-10}
20	293.15	7.12×10^{-10}

3.2.4 Extinction and UV/Vis absorption spectroscopy

Extinction spectra of colloidal nanoparticles were obtained with a Varian Cary 100 Bio UV/Vis spectrophotometer fitted with a tungsten halogen lamp with quartz window as visible source, a deuterium arc lamps as ultraviolet source, a Czerny-Turner 0.28 M monochromator, and a high performance R928 photomultiplier detector. All measurements were performed in single beam arrangement in the 400 nm to 900 nm range with automatic baseline correction. The same instrument and instrumental specifications were utilized to collect UV/Vis absorption spectra of Crystal Violet, in the 200 nm to 900 nm range. Decay

^IThe Bjerrum length [m] is defined as $q_e^2/(4\pi\epsilon_r\epsilon_0k_B T)$, where q_e is the elementary charge and k_B is the Boltzmann constant

curves for each nanostar formulation were obtained by acquiring a series of extinction spectra, each at 10 minute intervals, for a total of 2 hours, immediately after synthesis. The mean and standard deviation of the intensity at the λ_{LSPR} for each time point were first converted to percent decrease from initial values at time zero, and then plotted against time. All measurements were performed in triplicate.

3.2.5 X-ray Photoelectron Spectroscopy (XPS)

Surface analysis of citrate-capped nanostars was performed at the Research Service Centers, Herbert Wertheim College of Engineering, University of Florida, Gainesville. An ultrahigh vacuum Phi VersaProbe III scanning X-ray photoelectron spectrometer was used for both survey scan and high resolution spectra acquisition. The survey scan was collected using a monochromatic Al $K\alpha$ source with 93.90 eV passing energy; high resolution spectra were acquired using a passing energy of 11.75 eV (Au, 4*f*) and 23.50 eV (Ag, 3*d*; C, 1*s*). A 5 mm² microscopy-grade glass substrate was sonicated once in acetone for 20 minutes, then twice in methanol for 20 minutes each time. The substrate was left to dry inside a clean, closed container. A 1 μ L aliquot of concentrated (*vide infra*) citrate-capped colloidal nanostars was then deposited onto the prepared glass substrate and left to dry at room temperature inside a clean, closed container. The concentrated formulation was obtained by centrifugation of a total volume of 1045 μ L citrate-capped colloidal nanostars for 1 minute at 5000 rpm, and subsequent removal of 990 μ L of supernatant. Peak deconvolution and integration of components were performed using CasaXPS software (v2.3.19PR1.0 demo, Casa Software Ltd, Teignmouth, UK).

3.2.6 Transmission Electron Microscopy (TEM)

Morphological studies were conducted via transmission electron microscopy at the Advanced Materials Engineering Research Institute (AMERI) at Florida International University. TEM micrographs were obtained using a Philips Philips CM200 transmission electron microscope with point and line resolution of 0.1 nm and 0.14 nm, respectively. 8 mL of each nanostar formulation were deposited on a copper grid and dried at room temperature for approximately 30 minutes before analysis. Micrographs processing was performed using Photoshop (v19.0 trial, Adobe Inc., San Jose, CA).

3.2.7 Normal Raman and Surface-Enhanced Raman Spectroscopy (SERS)

Normal Raman and SERS measurements were performed using a Perkin Elmer 400 F Raman benchtop spectrometer fitted with a 785 nm laser excitation source (350 mW power at the source, 100 mW power at the sample 0.05 nm FWHM) and a high sensitivity air-cooled (-50 °C) CCD detector. The resolution was 4 cm⁻¹ FWHM, and the exposure time was set to 10 s with 4 accumulations for all spectral acquisitions. All samples were analyzed in 250 μL solution aliquots and deposited in a 96-well quartz microplate (Hellma Analytics). SERS samples of model analyte Crystal Violet were prepared by mixing 247.5 μL of a colloidal nanostar formulation and 2.5 μL of Crystal Violet aqueous solution at a final concentration of 10⁻⁷ M. SERS samples of opioids were analyzed with prior aggregation instead, by mixing 245 μL of a colloidal nanostar formulation with 2.5 μL of 1.67 M MgCl₂, followed by addition of 2.5 μL of opioid methanolic solution at a final concentration of 10 μg/mL. All SERS samples were incubated for 20 minutes. All SERS and Normal Raman spectra were baseline-corrected, and the intensities were normalized to the intensity of the band at 3200 cm⁻¹, assigned to ν(OH) of water.

3.2.8 Statistical Analysis

Exploratory data analysis via box-and-whiskers plot, analysis of equal variances, and test for normality were performed with Minitab statistical software (v17.1.0, Minitab Inc., State College, PA). Analysis of Variance (ANOVA) F-test, Tukey's Honestly Significant Difference (HSD) test, and Student's t-test were performed with JMP statistical software (v15, SAS Institute, Cary, NC).

3.2.9 Density Functional Theory (DFT) calculations

Density Functional Theory (DFT) calculations were utilized to obtain putative structures of the stabilizer/metal cluster complex, and were performed with Q-Chem 5.0,¹¹ using the B3LYP hybrid exchange correlation functional;¹²⁻¹⁴ the LANL2DZ effective core potential (ECP) and basis set was utilized for Au and Na,¹⁵ while 6-31G was utilized for H, C, and O. All initial wavefunction guesses were obtained by the Hartree-Fock (HF) method. Molden was used to visualize the optimized geometries and measure interatomic distances.^{16,17} Bonds in structural representations were automatically drawn on the basis of a distance cutoff.

Citrate in its doubly deprotonated form (charge -2, multiplicity 1) was chosen as the model stabilizer, and optimized in the presence of one Na⁺ counterion and 12 molecules of water as explicit solvent (total charge -1, multiplicity 1). The starting guess for this geometry was obtained by manually positioning the water molecules to satisfy the first solvation shell of citrate. The bimetallic 18:1 Au:Ag metal cluster was initially approximated to a tetrahedral (111) Au₂₀ cluster (charge 0, multiplicity 1), with starting geometry modeled after Aikens and Schatz.¹⁸ The two systems were optimized individually and the resulting structures were utilized to obtain the initial geometry of the stabilizer/metal complex, by positioning the explicitly solvated citrate at about 7 Å from

the surface of the metal cluster (charge -1, multiplicity 1). All structures were checked for stability by calculating their frequencies.

Frequencies calculations were also utilized to obtain estimates of the free energy of adsorption in the gas phase, at T 298.15 K and p 1 atm. These estimates were adjusted for solvation effects by performing single point calculations of the optimized citrate and Au₂₀, both individually and as a complex. These calculations made use of the universal continuum model SMD and utilized water as a solvent.¹⁹

Preliminary work on the bimetallic cluster and citrate complex modeling was obtained following an analogous procedure. The bimetallic Au:Ag 18:1 system was approximated to an Au₁₉Ag cluster, which was obtained by manual substitution of 1 atom of gold with 1 of silver into the optimized Au₂₀ structure (charge 0, multiplicity 1). The resulting three homotops were optimized, and the structure with lowest energy was utilized for the optimization of the citrate complex structure, following the same procedure illustrated for the citrate/Au₂₀ complex. All calculations were performed using the B3LYP hybrid exchange correlation functional; the Stuttgart-Bonn Relativistic Small Core (SRSC) ECP and basis set were utilized for Au and Ag, while the 6-311G* basis set was utilized for H, C, O, and Na.

3.2.10 FTIR spectroscopy

Infrared spectroscopy measurements were performed in attenuated total reflection (ATR) mode using an Agilent Technologies Cary 670 FTIR spectrometer fitted with a PIKE MIRacle™ single reflection ATR accessory with diamond internal reflection element (IRE), and interfaced with Agilent Resolutions Pro software. Samples were obtained by pooling 35 mL of each colloidal nanostar formulation; an aliquot of 3 mL was kept for UV/Vis absorption spectroscopy, while the remaining volume was centrifuged at 5000

rpm for 15 minutes. Subsequently, 30 mL of supernatant were replaced with an equivalent amount of ultrapure water to ensure removal of unadsorbed capping species, and then centrifuged again at 5000 rpm for 15 minutes. 29 mL of supernatant were then removed, and the remaining volume was dried under vacuum centrifugation at room temperature for approximately 7 hours. The dried residues were then aliquoted in three sub-samples and placed on the IRE for analysis. Additionally, 1 M solutions of candidate stabilizing agents were analyzed by placing 2 μL of solution on the IRE. The acquisition method was the same for both solid and liquid samples, and consisted of 128 preliminary background scans and 128 sample scans, each at a resolution of 2 cm^{-1} .

REFERENCES

- [1] He, S.; Kang, M.W.C.; Khan, F.J.; Tan, E.K.M.; Reyes, M.A.; Kah, J.C.Y. Optimizing gold nanostars as a colloid-based surface-enhanced Raman scattering (SERS) substrate. *J. Opt.* **2015**, *17*, 1–13.
- [2] The International Association for the Properties of Water and Steam (IAPWS), *Release on the IAPWS Formulation 2008 for the Viscosity of Ordinary Water Substance*; Berlin, Germany, 2008.
- [3] Malmberg, C.G.; Maryott, A.A. Dielectric Constant of Water from 0° to 100°C. *J. Res. Natl. Bur. Stand.*, **1956**, *56*(1), 2641-1–2641-5.
- [4] Bashkatov, A.N.; Genina, E.A. Water refractive index in dependence on temperature and wavelength: a simple approximation. In *Proceedings of SPIE Vol. 5068, Laser Physics and Photonics, Spectroscopy, and Molecular Modeling III; Coherent Optics of Ordered and Random Media III*, Saratov, Russian Federation, Fall 2002; Tuchin, V.V., Ed.; Society of Photo-Optical Instrumentation Engineers (SPIE), 2003; 393–395.
- [5] Henry, D.C. The cataphoresis of suspended particles. Part I. The equation of cataphoresis. *Proc. R. Soc. London Ser. A*, **1931**, *133*(821), 106–129.

- [6] Ohshima, H. A Simple Expression for Henry's Function for the Retardation Effect in Electrophoresis of Spherical Colloidal Particles. *J. Colloid Interface Sci.*, **1994**, *168*(1), 269–271.
- [7] Malvern. *Zetasizer nano series, user manual*. Malvern Instruments Ltd., Worcestershire: UK, 2013.
- [8] Delgado, A.V.; González-Caballero, F; Hunter, R.J.; Koopal, L.K.; Lykelma, J. Measurement and Interpretation of Electrokinetic Phenomena. *Pure Appl. Chem.*, **2005**, *77*(10), 1753–1805.
- [9] Le Ru, E.C.; Etchegoin, P.G. *Principles of surface enhanced Raman spectroscopy and related plasmonic effects*, Elsevier: Amsterdam, 2009.
- [10] Xi, W.; Phan, H.T.; Haes, A.J. How to accurately predict solution-phase gold nanostar stability. *Anal. Bioanal. Chem.*, **2018**, *410*, 6113–6123.
- [11] Shao, Y.; Gan, Z.; Epifanovsky, E.; Gilbert, A.T.B; Wormit, M.; Kussmann, J.; Lange, A.W.; Behn, A.; Deng, J.; Feng, X.; Ghosh, D.; Goldey, M; Horn, P.R; Jacobson, L.D.; Kaliman, I.; Khaliullin, R.Z.; Ks, T.; Landau, A.; Liu, J.; Proynov, E.I.; Rhee, Y.M.; Richard, R.M.; Rohrdanz, M.A.; Steele, R.P.; Sundstrom, E.J.; Woodcock III, E.L.; Zimmerman, P.M.; Zuev, D.; Albrecht, B.; Alguire, E.; Austin, B.; Beran, G.J.O.; Bernard, Y.A.; Berquist, E.; Brandhorst, K.; Bravaya, K.B.; Brown, S.T.; Casanova, D.; Chang, C-M.; Chen, Y.; Chien, S.H.; Closser, K.D.; Crittenden, D.L.; Diedenhofen, M.; DiStasio Jr., R.A.; Dop, H.; Dutoi, A.D.; Edgar, R.G.; Fatehi, S.; Fusti-Molnar, L.; Ghysels, A.; Golubeva-Zadorozhnaya, A.; Gomes, J.; Hanson-Heine, M.W.D.; Harbach, P.H.P.; Hauser, A.W.; Hohenstein, E.G.; Holden, Z.C.; Jagau, T-C.; Ji, H.; Kaduk, B.; Khistyayev, K.; Kim, J.; Kim, J.; King, R.A.; Klunzinger, P.; Kosenkov, D.; Kowalczyk, T.; Krauter, C.M.; Lao, K.U.; Laurent, A.; Lawler, K.V.; Levchenko, S.V.; Lin, C.Y.; Liu, F.; Livshits, E.; Lochan, R.C.; Luenser, A.; Manohar, P.; Manzer, S.F.; Mao, S-P; Mardirossian, N.; Marenich, A.V.; Maurer, S.A.; Mayhall, N.J.; Oana, C.M.; Olivares-Amaya, R.; O'Neill, D.P.; Parkhill, J.A.; Perrine, T.M.; Peverati, R.; Pieniazek, P.A.; Prociuk, A.; Rehn, D.R.; Rosta, E.; Russ, N.J.; Sergueev, N.; Sharada, S.M.; Sharma, S.; Small, D.W.; Sodt, A.; Stein, T.; Stck, D.; Su, Y-C.; Thom, A.J.W.; Tsuchimochi, T.; Vogt, L.; Vydrov, O.; Wang, T.; Watson, M.A.; Wenzel, J.; White, A.; Williams, C.F.; Vanovschi, V.; Yeganeh, S.; Yost, S.R.; You, Z-Q.; Zhang, I.Y.; Zhang, X.; Zhou, Y.; Brooks, B.R.; Chan, G.K.L.; Chipman, D.M.; Cramer, C.J.; Goddard III, W.A.; Gordon, M.S.; Hehre, W.J.; Klamt, A.; Schaefer III, H.F.; Schmidt, M.W.; Sherrill, C.D.; Truhlar, D.G.; Warshel, A.; Xua, X.; Aspuru-Guzik, A.; Baer, R.; Bell, A.T.; Besley, N.A.; Chai, J-D.; Dreuw, A.; Dunietz, B.D.; Furlani, T.R.; Gwaltney, S.R.; Hsu, C-P; Jung, Y.; Kong, J.; Lambrecht, D.S.; Liang, W.; Ochsenfeld, C.; Rassolov, V.A.; Slipchenko, L.V.; Subotnik, J.E.; Van Voorhis, T.;

- Herbert, J.M.; Krylov, A.I.; Gill, P.M.W.; Head-Gordon, M. Advances in molecular quantum chemistry contained in the Q-Chem 4 program package. *Mol. Phys.*, **2015**, *113*, 184–215.
- [12] D. Becke, A.D. Density-functional thermochemistry. III. The role of exact exchange. *J. Chem. Phys.*, **1993**, *98*(7), 5648–5652.
- [13] Lee, C.; Yang, W.; Parr, R.G. Development of the Colle-Salvetti Correlation-Energy Formula into a Functional of the Electron Density. *Phys. Rev. B.*, **1988**, *37*, 785–789.
- [14] Stephens, P.J.; Devlin, F.J.; Chabalowski, C.F.; Frisch, M.J. Ab Initio Calculation of Vibrational Absorption and Circular Dichroism Spectra Using Density Functional Force Fields. *J. Phys. Chem.*, **1994**, *98*(45), 11623–11627.
- [15] Hay, P.J.; Wadt, W.R. Ab initio effective core potentials for molecular calculations. Potentials for K to Au including the outermost core orbitals. *J. Chem. Phys.*, **1985**, *82*, 299–310.
- [16] Schaftenaar, G.; Noordik, J. H. Molden: A Pre-and Post-Processing Program for Molecular and Electronic Structures. *J. Comput.-Aided Mol. Des.*, **2000**, *14*, 123–134.
- [17] Schaftenaar, G.; Vlieg, E.; Vriend, G. Molden 2.0: Quantum Chemistry Meets Proteins. *J. Comput.-Aided Mol. Des.*, **2017**, *31*(9), 789–800.
- [18] Aikens, C.M.; Schatz, G.C. TDDFT Studies of Absorption and SERS Spectra of Pyridine Interacting with Au₂₀. *J. Phys. Chem. A*, **2006**, *110*(49), 13317–13324.
- [19] Marenich, A.V.; Cramer, C.J.; Truhlar, D.G. J. Universal Solvation Model Based on Solute Electron Density and on a Continuum Model of the Solvent Defined by the Bulk Dielectric Constant and Atomic Surface Tensions. *Phys. Chem. B*, **2009**, *113*(18), 6378–6396.

CHAPTER 4

Going surfactant-free: challenges in anisotropic nanoparticle stabilization

4.1 A nanostars platform to probe the surface chemical environment:

He, S. *et al.*, *J. Opt.*, 2015

From *Chapter 2*, it can be deduced that a colloidal SERS substrate is conducive to high performance if it has morphological and compositional characteristics such that its LSPR wavelength is in pre-resonance with the excitation source (§ 2.2.2), and it has a surface chemical environment that provides sufficient stability without interfering with signal production (§ 2.2.2.1 and 2.3). Therefore, the nanoparticle capping species constituting the surface environment must (1) have a small SERS cross section, (2) adsorb less strongly to the surface than the target analyte does, and (3) have small dimensions, and thus, low steric hindrance. Indeed, since the exact adsorption mechanism of a target analyte might not be precisely identified *a priori*, an ideal stabilizing agent should accommodate for both scenarios. As a result, it should be sufficiently small to provide short surface-analyte distances *if* the adsorption of the target occurs indirectly, and it should be associated with the surface sufficiently loosely to be displaced *if* the adsorption of the target occurs directly (*Figures 2.10 a– c*).

With this in mind, a protocol for the synthesis of colloidal nanostars (NS) was chosen among those available in the literature. The reaction had to be such that no surfactant is required to achieve the desired branched morphology, and a relatively low (*vide infra*) nanoparticle surface coverage is present at reaction completion. Reactions of this type would provide on one hand a state of the art morphology that is inherently optically powerful (§ 2.2.2.1), and, on the other hand, a "blank canvas" for the intentional, post-

synthetic addition of capping species, providing an ideal platform for studying their adsorption mechanism and the effect they exert on the SERS signal. The selected synthetic protocol was originally developed by Cheng *et al.* for photothermal therapy applications,¹ and later refined by He *et al.* for use as SERS substrate.² The reaction makes use of L-ascorbic acid as the reducing agent, aurochloric acid as the precursor of the main metal constituent, and silver nitrate as the shape director.^{1,2} The latter metal ion is co-reduced and hypothesized to incorporate into the final, bimetallic nanostructure (Equation 4.1). Added practical advantages of this synthetic protocol are ambient temperature requirements, one-pot execution, and fast kinetics, going to completion in less than a minute.^{1,2}



Another advantage of this nanofabrication protocol is that a systematic optimization of synthetic parameters, as it relates to SERS performance, has already been conducted; indeed, He *et al.*² studied the relationship between the concentration of silver nitrate and the shape and length of the nanostars branches, as well as the role of molar ratios of metal precursors to reducing agent (*Figure 4.1*). They found that silver nitrate controlled the density of branches, but had negligible effects on the branches' length. This is in contrast with what has been observed by Atta *et al.*³ for their seed-mediated AuAg nanostars, in which the branches' length increased linearly with increasing silver nitrate concentration, until a threshold was reached (§ 2.2.2.1). This seems to suggest, as mentioned in § 2.2.2.1, that the mechanism of nanostar formation and the exact role of each reagent is likely dependent on reaction conditions, particularly when comparing seed-mediated protocols with one-pot procedures, and even when the identity of the reducing agent and precursor metals are kept constant.

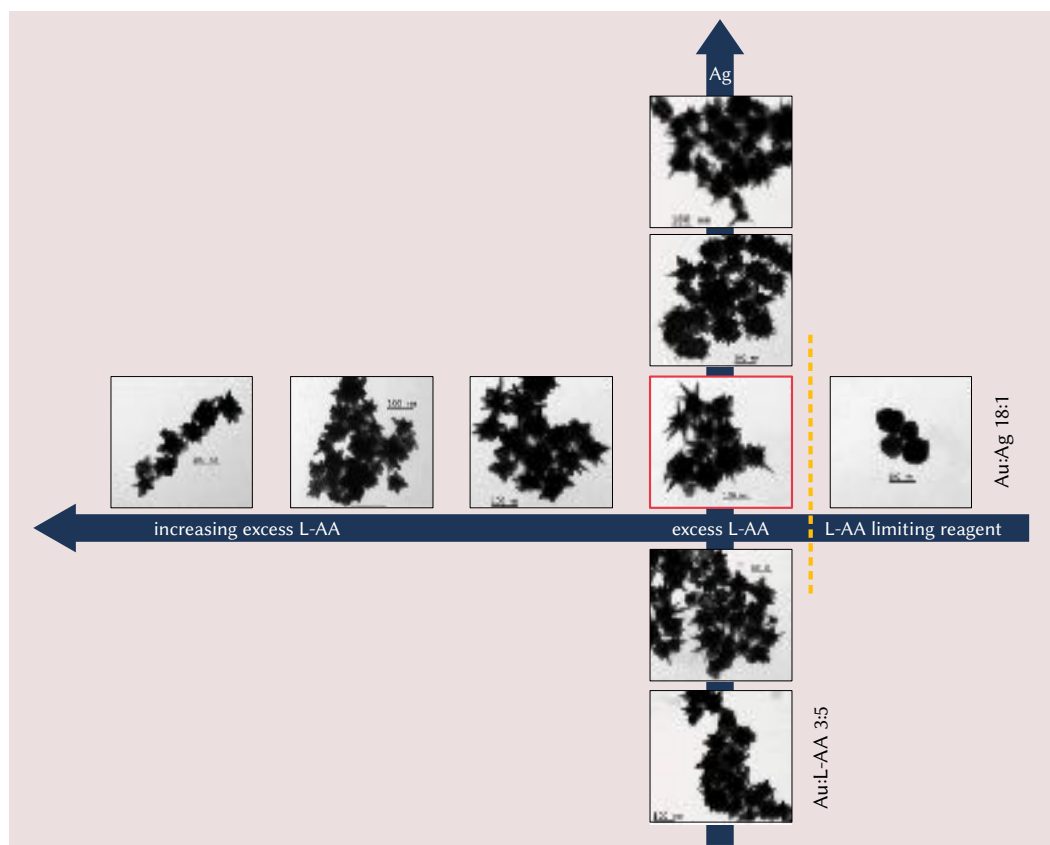


Figure 4.1: Effect of varying molar ratios of reactants in the synthesis of colloidal AuAg bimetallic nanostars, as proposed by He *et al.*² The effect of increasing excess of L-ascorbic acid while keeping the ratio of gold to silver constant at 18:1 is displayed horizontally, with the largest excess L-ascorbic acid on the left. The effect of having L-ascorbic acid as the limiting reagent is shown on the rightmost side. The effect of increasing the silver content while keeping the ratio of gold to L-ascorbic acid constant at 3:5 is instead displayed horizontally, with the lowest silver content at the bottom. Highlighted in red is a TEM image of the nanostars produced with the selected protocol for this research work, Au:Ag of 18:1 and Au:L-AA of 3:5, and stabilized with CTAB. All TEM images are reproduced with permission from He, S. *et al.*,² Copyright 2015; permission conveyed through Copyright Clearance Center, Inc.

The role of L-ascorbic acid was proven to have an effect on nanostar branch elongation, as well as anisotropy in general. The authors studied the effect of varying the molar ratio of gold to L-ascorbic acid (Au:L-AA) at a constant gold to silver ratio of 18:1, and reported an increase of branches elongation with increasing Au:L-AA, until a ratio of 3:3.3 was

Table 4.1: Summary of reagents concentrations and volumes for nanostars synthesis.

reagent	concentration (M)	volume (μL)
H _{Au} Cl ₄	10 ⁻²	36
AgNO ₃	10 ⁻²	2
L-AA	10 ⁻¹	6
H ₂ O	—	1000

reached. At these molar ratio conditions, no branching was observed at all, and isotropic particles were obtained. Therefore, it can be deduced that when the reducing agent is present in molar excess, anisotropic shapes can be obtained, while, when the reducing agent is the limiting reagent, isotropic shapes are obtained instead, so long as co-reduction of the two metal precursors occurs and the reaction proceeds stoichiometrically *Equation 4.1*. As a consequence, for this protocol, both the presence of silver and *excess* L-ascorbic acid are the necessary requisites for the fabrication of the branched morphology. The selected molar ratios for the present research were those reported by He *et al.*² to provide the highest SERS enhancements at an excitation wavelength of 785 nm, which also corresponded to the longest branches length (Au:L-AA of 3:5) and the most uniform spike density (Au:Ag of 18:1). This is consistent with the theoretical fundamentals outlined in *Chapter 1*. A detailed procedure for the synthesis of these nanostars is given in § 3.2.1 summarized in *Table 4.1*.

It has been mentioned in earlier paragraphs that these colloidal nanostars have relatively low surface coverage. The reason lies on the reduction conditions at which the reaction occurs. The chosen synthetic protocol makes use of the lowest amount of excess L-ascorbic acid among all variants presented by He *et al.* (*Figure 4.1*, red). At this concentration of ascorbic acid, assuming the reaction occurs stoichiometrically, only 5×10^8 moles are left unreacted at reaction completion. This corresponds to a final concentration of L-ascorbic acid, or better, ascorbate (pK_1 L-AA 4.1, $\text{pH NS} \sim 6$), of 4.8×10^5 M. As can be seen in *Figure 4.2*, the prevalent (5.3×10^4 M), oxidized form, dehydroascorbic acid, is

a neutral species. Even if dehydroascorbic acid adsorbs on the surface of the nanostars, it cannot participate in the ensuing of the Coulombic repulsive forces that are required for the colloid to achieve stability (DLVO theory). The other ionic species present in the colloidal suspension at reaction completion, namely, nitrate from the silver precursor, chloride from the gold precursor, and hydrogen ions from both the gold precursor and the dissociable proton in L-ascorbic acid, also have relatively low concentration. Together with ascorbate, these ions provide a total molar ionic strength of 4.2×10^4 M. Even assuming that all of these species adsorb on the surface and participate to the Coulombic repulsive component of the total interparticle interaction potential, they are not sufficient to achieve stability of the suspension,⁴ which in fact readily coagulates (*vide infra*).

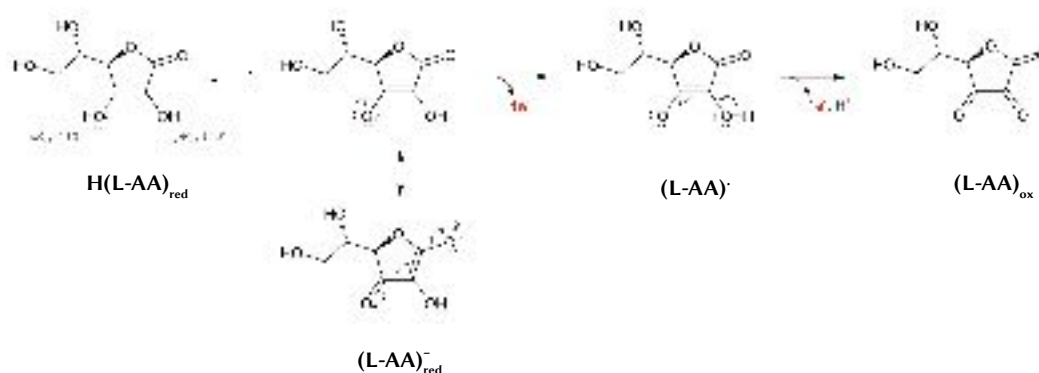


Figure 4.2: Oxidation of L-ascorbic acid, $\text{H(L-AA)}_{\text{red}}$. At neutral pH, ascorbic acid is present in solution as ascorbate, $(\text{L-AA})_{\text{red}}^-$, an anion stabilized by resonance. Ascorbate exchanges one electron at a time,⁵ yielding the radical $(\text{L-AA})\cdot$ first, and the neutral, oxidized species dehydroascorbate second, $(\text{L-AA})_{\text{ox}}$.

Further proof of this instability is given by measuring the ζ potential (§ 2.2.1); as a rule of thumb, systems having absolute values of ζ potential between 0 and $|25|$ mV are considered unstable,⁶ and the ζ potential value for these nanostars, as-synthesized, is -19.9 ± 3.2 mV. This indicates that the predominant charge giving raise to the electrostatic repulsion is negative, but not sufficient in magnitude to support stability. The as-synthesized

NS are observed to undergo rapid coagulation following synthesis, as shown in *Figure 4.3*, where the extinction behavior of a nanostar sol was observed during the first 30 minutes after synthesis (teal spectra), two hours after synthesis (green spectrum), and one week after synthesis (red spectrum). At the last time point, the extinction intensity is drastically reduced, and the λ_{max} is significantly red shifted (from 715 nm to 745 nm), indicating the formation of coagulated clusters.

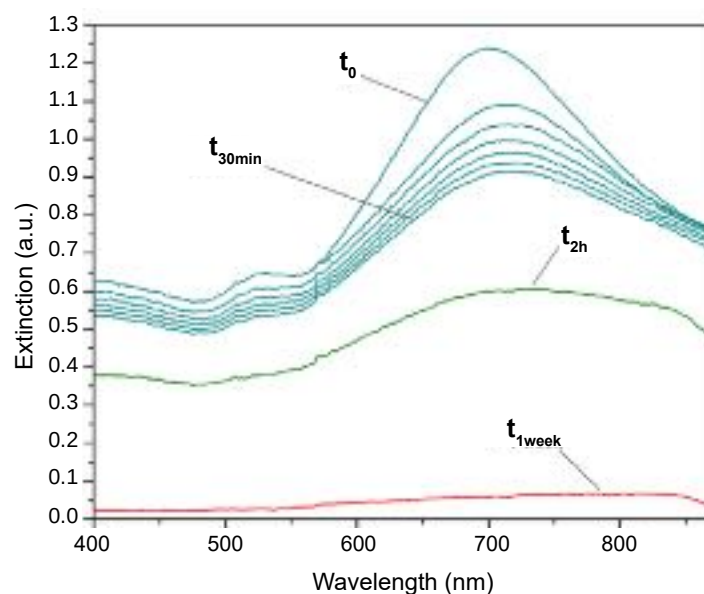


Figure 4.3: Temporal evolution of the extinction spectrum of a batch of the as-synthesized Au/Ag colloidal nanostars. Coagulation, thus instability, is reflected by the rapid decrease of the intensity at the λ_{LSPR} .

This instability was offset by Cheng *et al.*¹ via the post-synthetic addition of the polymer O-carboxymethylchitosan, while He *et al.*² substituted the polymer with the surfactant CTAB (*Figure 4.4*). As discussed in *Chapter 2*, and as addressed by the authors themselves,² bulky capping agents like CTAB gives rise to signal loss and higher limits of detection, and thus, they should be avoided. An ideal SERS-compatible stabilizer must increase the shelf-life of the colloidal formulation without interfering with the SERS signal production. This chapter presents the development of alternatively stabilized nanostars

formulations. The new stabilizers had to respond to the characteristics that were enunciated at the beginning: low SERS cross-section and small dimensions. The energies involved in the adsorption process are presented instead in *Chapter 7*. The selection of the initial array of candidate stabilizers was based on DLVO theory, and the selection and refinement of the colloidal formulations was achieved by using UV/Vis spectroscopy and electrophoretic light scattering (ELS). Surface characterization by XPS and a TEM-based crystallographic study was also performed.

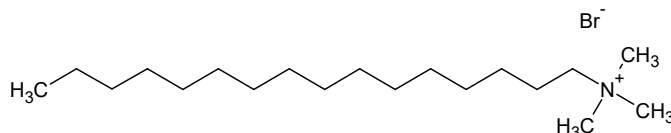


Figure 4.4: Structure of cetyltrimethylammonium bromide (CTAB).

4.2 Selection of candidate non-surfactant stabilizers and working hypotheses

In its simplest meaning, DLVO theory states that, to increase the stability of a colloidal suspension, the Coulombic repulsive forces at the particle-solution interface must be maximized (§ 2.2.1). To accomplish this, two variables must be determined; first, the *charge sign* of the stabilizing species, and second, the *identity* of this species. As reported in the previous section, the ζ potential sign of the as-synthesized nanostars is negative, indicating that the capping species population is predominantly negatively charged. Thus, *anionic* species should be added to the formulation to maximize the Coulombic repulsions.

Which anionic species should be selected, though? Can *any* anionic species adsorb on the surface of the nanoparticle and provide stability to the suspension?

Recalling the traditional assumption on the oxidation state of noble metal nanoparticles outlined in § 2.2.1.1, the outermost domain of the nanostructure should be at least partially positively charged. Thus, *any* negatively charged species would serve the purpose as a stabilizer, as it would be retained on the surface by virtue of electrostatic attractions. This process is known as *indifferent ion adsorption*.⁷ On the other hand, the alternative hypothesis developed by Al-Johani *et al.*,⁹ states that the adsorption process yielding the Coulombic repulsive forces among noble metal (gold) nanoparticles in aqueous suspensions is based on chemical affinity (*specific adsorption*)⁷ and the formation of coordination complexes between the metal and the ligand (gold-citrate complexes).⁹ Under this framework, not each and every negatively charged species would cap the surface.

At the beginning of this research study (2016-2017), the nanostars were initially hypothesized to follow the traditional assumption on the oxidation state of noble metal nanoparticles, according to which they would be capped *indifferently* by anionic species, as a result of ion pairing with the residual positive charge present on the surface of the nanostars. However, as outlined in § 2.2.1.1, this model is not experimentally verified. Moreover, it fails to explain why the addition of nitric acid, which is a common step to adjust the pH of colloidal systems to acidic values, is known to induce aggregation of negatively charged colloids, while the addition of NaOH to adjust to alkaline pH values is not known to destabilize such colloids.⁸ The hypothesis was then altered to propose that nanostar capping would occur as a result of *specific adsorption*. This hypothesis implies that the nanostar's surface is predominantly in its zero oxidation state, and finds support in the experimental findings reported by Al-Johani *et al.*⁹ for monometallic gold nanospheres.

Trisodium citrate (Ct, *Figure 4.5*) was selected as the prototypical, negatively charged, alternative stabilizing agent because of its well-known stabilizing properties in traditional colloidal sol formulations. Moreover, it has much smaller dimensions compared to CTAB, does not form micelles in solution, and has a pH-tunable charge that can be exploited to further optimize the interactions between the nanostructure and the analyte. Being a highly studied compound,^{9–11} trisodium citrate would also provide some basis for comparison with literature data.

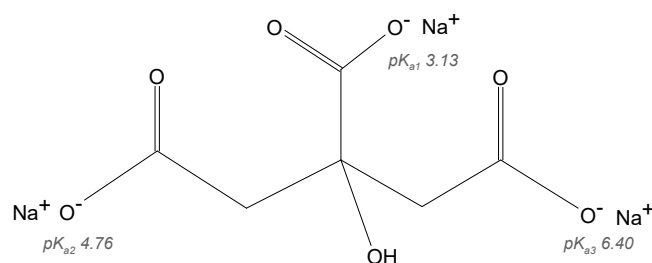


Figure 4.5: Structure of trisodium citrate with pK_a values for each dissociable group. Citrate is a common reducing agent for the synthesis of colloidal gold and silver monometallic nanoparticles.¹² Excess of this reagent and charged oxidation products are thought to provide stability to these suspensions.

The other candidate stabilizing agents were selected by reducing the carbon chain of the prototype trisodium citrate, as the thickness of the barrier separating the analyte from the surface should be as reduced as possible, in order for the system to yield the strongest enhancements (§ 1.2). Disodium L-tartrate (Tt) and sodium acetate (Ac) were selected for this purpose (*Figure 4.6*).

Initially, the candidate stabilizing agents selected as an alternative to CTAB had a common characteristic — the presence of one or more carboxylate functional group. This made it difficult to discern whether stabilization was occurring via an electrostatically driven ion pairing with the surface (indifferent ion adsorption), or rather, via a molecule-

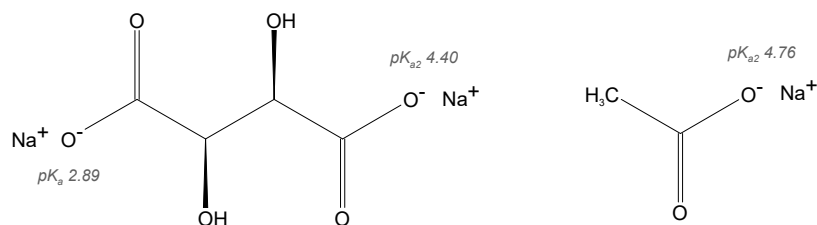


Figure 4.6: Structures of disodium L-tartrate (*left*) and sodium acetate (*right*) with pK_a values for each dissociable group.

specific adsorption process (specific ion adsorption and zero-valent state of nanoparticle surface). For this reason, 1,3-propanedisulfonic acid disodium salt (PrSulf) was added to the list of candidate stabilizers (*Figure 4.7*), together with an array of inorganic polyatomic ions, namely NaNO₃, NaSO₃, Na₂SO₄, and Na₂CO₃. For all selected species, the identity of the counterion was kept constant as Na⁺.

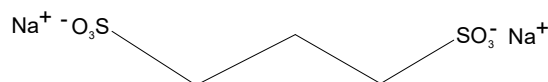


Figure 4.7: Structures of 1,3-propanedisulfonic acid disodium salt.

4.2.1 Optimization of model surfactant-free formulation NS/Ct

The concentration at which citrate best stabilizes the colloidal sol was determined via ζ potential and conductivity (γ) titrations of the as-synthesized bimetallic nanostars with increasing concentration of the anion (*Figure 4.8*). The ζ titration determined the concentration at which the maximum absolute value of ζ potential was observed,

corresponding to the point of maximum occurrence of Coulombic repulsions, hence maximum colloidal stability.

As expected, the ζ titration curve showed increasingly negative ζ potential values with increasing concentration of citrate (*Figure 4.8*). By definition, this indicates that citrate is adsorbed in a region comprised between the surface of the nanostructure and its slipping plane. While no deduction on whether citrate adsorbs indifferently or specifically can be made, it can be reasonably assumed that the change in ζ potential is caused by a change in surface charge density. For this reason, the change in ζ potential *reflects* surface adsorption, regardless of the specific mechanism. Indeed, for colloidal sols in which the surface charge density is proportional to the ion concentration, which is the case for these titrations, it has been demonstrated that the following equation is valid:^{4, 13–16}

$$\psi_0 = \zeta \left(1 + \frac{1}{\kappa a} \right) e \quad (4.2)$$

where ψ_0 is the *surface* potential, κ^{-1} is the Debye length, a is the radius of curvature of the smallest nanoparticle feature,¹⁷ and e is the Euler's number.

Another indication that surface adsorption is occurring is given by the trend described by the ζ titration curve, which resembles an upside-down Langmuir, or class L,^{18,19} adsorption isotherm (§ 2.3, *Figure 2.9 a*); the measured variable linearly increases in absolute value until a threshold is reached, which can be interpreted as an indication of monolayer saturation of the available adsorption sites (*Figure 4.9*). This could be followed by either no further adsorption, or the formation of ad-layers (*Figure 4.9 b–d*).

It is also interesting to observe the simultaneous behavior of conductivity (γ) and its relationship with the shape of the ζ titration curve. The conductivity is observed to initially decrease, as a result of the adsorption of citrate; this likely leads to the formation of a hybridized material, the capped nanoparticle, with different specific conductivity

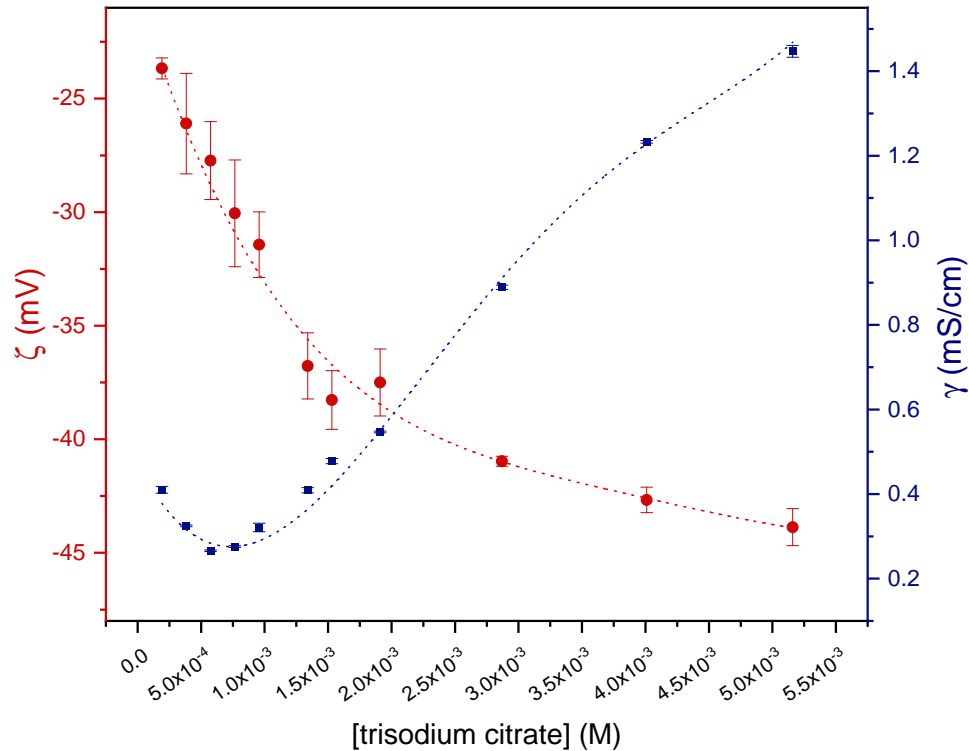


Figure 4.8: ζ potential (red) and conductivity (blue) behavior of AuAg colloidal nanostars titrated with trisodium citrate. The error bars report the standard error for each measured point. The data trend is highlighted by polynomial fits (dotted lines).

from the unmodified, sparingly capped nanoparticle. Alternatively or concomitantly, the conductivity decrease could be linked to the participation of solution counterions to the formation of the electric double layer, thus decreasing the population of free ions in solution. After this initial conductivity decrease, an inversion point is then observed at 0.77×10^{-3} M citrate, after which the conductivity increases linearly with citrate concentration. This can be explained by using the ζ titration curve and the Langmuir model as references. Indeed, there is a concentration, around 1.3×10^{-3} M (shaded yellow area in *Figure 4.9 a*), at which the system starts to approach its supposed maximum monolayer adsorption capacity. At saturation, the available adsorption sites are all occupied, and the addition of excess adsorbate molecules (*i.e.*, citrate), increases the ionic population of the solution

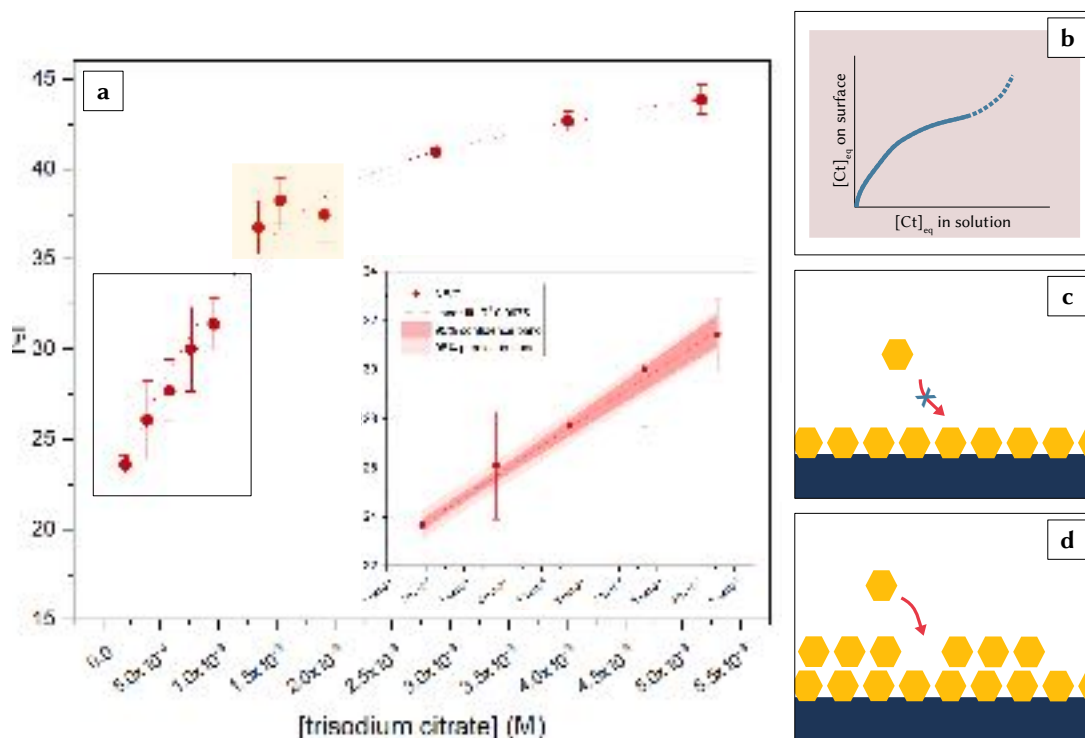


Figure 4.9: (a) Absolute value of the ζ potential of AuAg colloidal nanostars titrated with trisodium citrate. A fourth degree polynomial fit was utilized to highlight the trend, which resembles a class L isotherm, according to the Giles classification system.^{18,19} The inset shows the initial linear relationship between $|\zeta|$ and citrate concentration (R^2 0.9975), while the yellow shaded area indicates the point at which the system likely approaches saturation. (b) Class L isotherm according to the Giles classification system. The solid line shows a pure Langmuir behavior (cartoon in panel (c)) while the dashed line describes a BET behavior (cartoon in panel (d)).

environment, rather than that of the surface. This causes conductivity to rise. However, it must be noted that, at this level of information, it cannot be determined whether the adsorption strictly behaves in a Langmuir fashion, that is, with no further adsorption past the first monolayer, or if formation of ad-layers occurs instead. More on this topic is presented in Chapter 6.

Conductivity can also be utilized to explain the coagulation behavior of the various NS/Ct formulations. *Table 4.2* reports the visual observations on the formulations' state

of coagulation after a 12 hour incubation period. It can be seen that coagulation not only happens at the lower concentrations of citrate, but also at the highest, despite the ζ potential being still high in magnitude. The Debye length, which ultimately dictates the thickness of the nanoparticle's electrical interfacial layer, is inversely proportional to the ionic strength of the solution constituting the dispersing phase of the colloidal sol. Therefore, at higher ionic strengths the Debye length gets compressed, ultimately decreasing the distance at which flocculation, and eventually coagulation, occur (*Figure 4.10*). The concomitant high magnitude ζ potential of these higher ionic strength formulations can be explained by recalling that coagulation is a dynamic process, and the extent to which it occurs varies with time; at time 12 hours, two populations will be present in the solution — a coagulating population, and a still-dispersed population.

Table 4.2: NS/Ct formulations. Observations on visual signs of coagulation at the 12 hour mark after synthesis.

[Ct] (M)	molar ionic strength (M)	observations
0.19×10^{-3}	4.3×10^{-4}	complete coagulation
0.38×10^{-3}	8.5×10^{-4}	complete coagulation
0.57×10^{-3}	1.4×10^{-3}	little coagulation
0.77×10^{-3}	1.9×10^{-3}	no coagulation
0.96×10^{-3}	3.4×10^{-3}	no coagulation
1.3×10^{-3}	4.8×10^{-3}	no coagulation
1.5×10^{-3}	5.5×10^{-3}	no coagulation
1.9×10^{-3}	6.9×10^{-3}	no coagulation
2.9×10^{-3}	1.1×10^{-2}	little coagulation
4.0×10^{-3}	1.7×10^{-2}	complete coagulation
5.2×10^{-3}	2.2×10^{-2}	complete coagulation

Since coagulation can also be induced by the addition of analyte solution,²¹ it is wise to choose as optimum formulation one whose citrate concentration is not too close to the coagulation extremes, and has the lowest ionic strength and conductivity possible. This helps to avoid an overly rapid coagulation upon the addition of sample solutions when

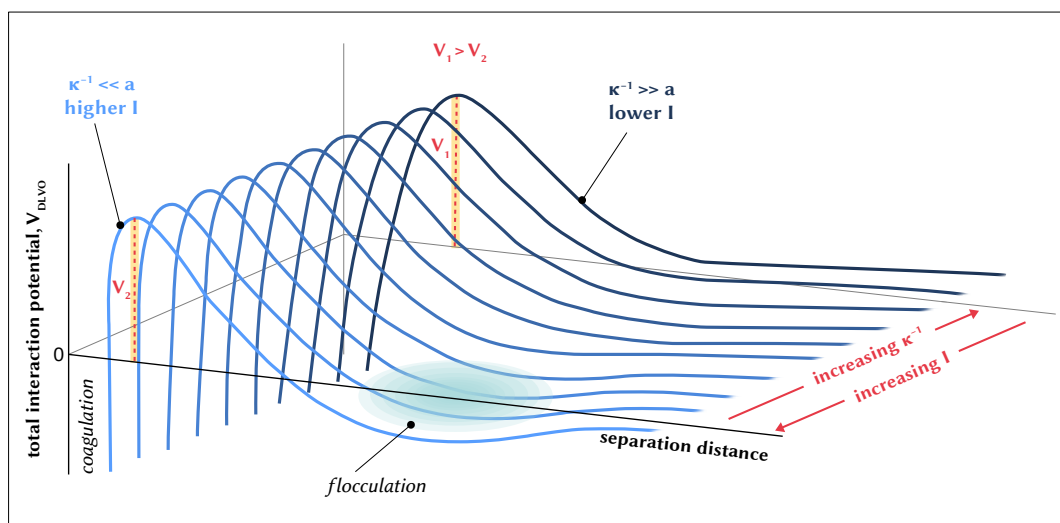


Figure 4.10: Variation of the total interaction potential curve for a colloidal system with fixed size (a , dimension of the smallest nanoparticle feature) and varying ionic strength, I , and Debye length, κ^{-1} . The potential barrier to be overcome for coagulation to occur is highest at lowest ionic strength ($V_1 > V_2$). The secondary minimum at which flocculation occurs is found at shorter separation distances for higher ionic strength dispersions. Figure inspired by Atkins, de Paula, and Keeler, 2018.²⁰

utilizing these colloidal nanoparticles as SERS substrates. As a result of these observations, the optimal concentration as per the ζ and σ values was found to be 0.96×10^{-3} M. This concentration of citrate causes an increase in molar ionic strength to 3.4×10^{-3} M, bringing the total molar ionic strength of the optimized NS/Ct formulation to 3.8×10^{-3} M.

The colloidal formulation with 0.96×10^{-3} M citrate showed no visual signs of coagulation for over four months (§ 5.4). On the other hand, the formation of flocs was observed after a period of approximately 48 hours. Flocs are *reversible* aggregates that are due to the presence of a secondary minimum in the free energy DLVO curve of the order of few $k_B T$ (Figure 2.1 c), where k_B is the Boltzmann's constant and T is the absolute temperature, such that regular Brownian motion provides the sufficient energy for collision and reversible formation of aggregates. The energy provided by manual shaking for approximately 2 s is sufficient to fully redisperse the colloidal sol.

4.2.2 Screening of other candidate stabilizers by ELS

ζ potential and conductivity measurements were also performed for the other candidate stabilizers listed in § 4.2, with the aim to explore whether the identity of the negatively charged functional group had a direct influence on the capping process. These species were screened at both the same concentration that was found optimal for citrate, 0.96×10^{-3} M, and at a second concentration, corresponding to the same molar ionic strength increase given by 0.96×10^{-3} M citrate, that is, 3.4×10^{-3} M.

As shown in *Figure 4.11*, both datasets, at constant concentration and at constant molar ionic strength, display a similar trend, although the formulations at constant ionic strength show a more pronounced division into two distinct groups: effective candidate stabilizers, and ineffective candidate stabilizers. Compounds bearing at least one carboxylate functional group, or even a carboxylate-like structure such as disodium carbonate, maximize the ζ potential past the threshold for nominal colloidal stability ($|\zeta| \geq |25|$ mV,⁶ shaded green area in *Figure 4.11*). This ζ potential increase is accompanied by a simultaneous decrease in conductivity, compared to the baseline levels of the as-synthesized nanostars (NS, top bar in *Figure 4.11*). These trends are not observed for the remainder of the surveyed anionic species, which either maintained the ζ potential around that of the as-synthesized nanostars, or decreased it, while a parallel increase of the conductivity was recorded. For these formulations a rapid onset of coagulation was observed (*Table 4.3*). All of the anionic species in this second group did not have any carboxylate function constituting their structure, nor did they possess a carboxylate-resembling group, such as carbonate.

These results suggest a connection between the molecular structure of a candidate stabilizer and its ability to effectively cap the bimetallic nanostructure and provide stability. This supports the hypothesis formulated at the beginning of this chapter, according to which capping, and thus stabilization, occurs on the basis of specific adsorption, rather

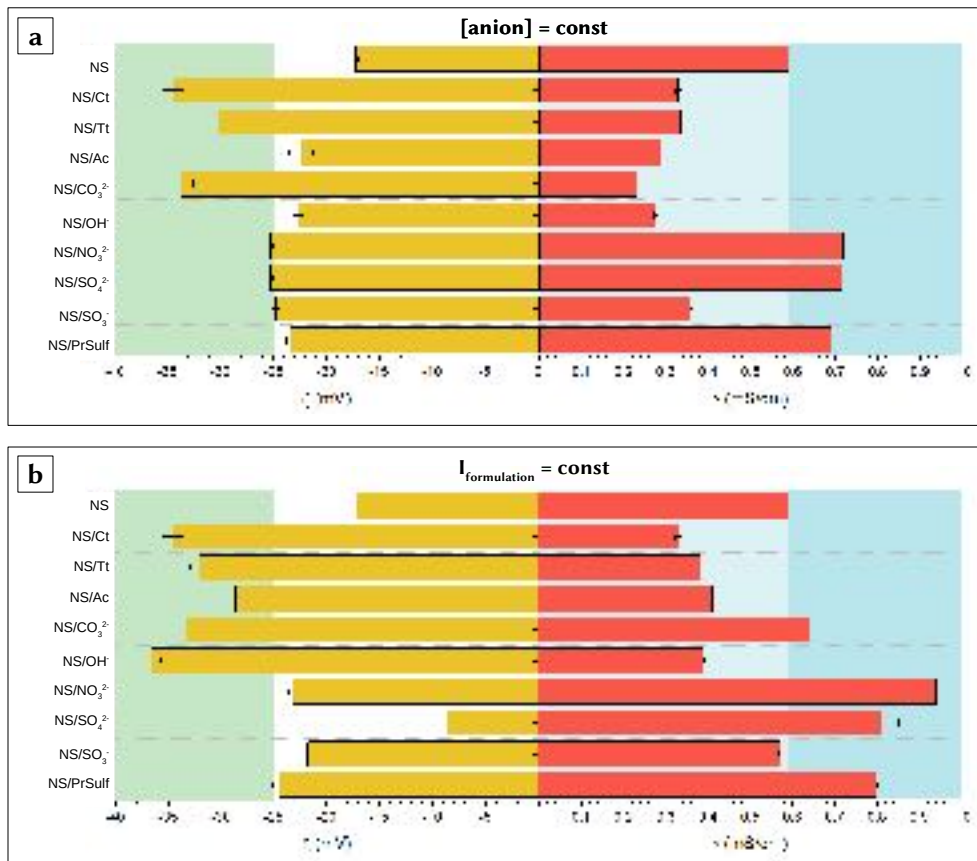


Figure 4.11: Average ζ potential (yellow) and conductivity (red) values for a series of AuAg nanostars formulations, at (a) fixed concentration of the candidate stabilizer (0.96×10^{-3} M), and (b) fixed molar ionic strength of the formulation (3.4×10^{-3} M). The shaded area in green highlights the ζ potential values associated with formulation stability ($|\zeta| \geq 25$ mV),⁶ while the shaded areas in blue highlight increase or decrease of conductivity compared to the as-synthesized nanostars (NS, top bar in both graphs). Results relative to the use of sodium hydroxide (NS/OH) are also reported.

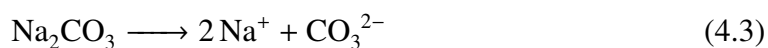
than via the retention of indifferently adsorbed anions. This also supports the hypothesis that the surface of the bimetallic nanoparticle is in its zero oxidation state.

Carbonate was the candidate stabilizer which brought the ζ potential to the most negative values, with maximum stability across the surveyed formulations, both at constant molar ionic strength and at constant concentration. This was an unexpected finding, in that inorganic salts are typically used to induce controlled aggregation and coagulation, and

Table 4.3: Candidate NS formulations. Observations on visual signs of coagulation at the 2 hour mark after synthesis.

formulation	observations
NS/Ct	no coagulation
NS/Tt _(c)	no coagulation
NS/Tt _(l)	no coagulation
NS/Ac _(c)	no coagulation
NS/Ac _(l)	no coagulation
NS/CO ₃ ²⁻ _(c)	no coagulation
NS/CO ₃ ²⁻ _(l)	no coagulation
NS/NO ₃ ⁻ _(c)	complete coagulation
NS/NO ₃ ⁻ _(l)	complete coagulation
NS/SO ₃ ⁻ _(c)	complete coagulation
NS/SO ₃ ⁻ _(l)	complete coagulation
NS/SO ₄ ²⁻ _(c)	complete coagulation
NS/SO ₄ ²⁻ _(l)	complete coagulation
NS/PrSulf _(c)	complete coagulation
NS/PrSulf _(l)	complete coagulation
NS/OH ⁻ _(c)	little coagulation
NS/OH ⁻ _(l)	no coagulation

thus, to cause *instability*. This unexpected stabilizing effect could be caused by either a structural similarity with the carboxylate functional group, which appears to be favoring an efficient capping of the bimetallic nanostructures, or by the fact that carbonate is an alkalinizing agent (*Equations 4.3–4.5*). There is evidence that hydroxyl ions, such as those normally produced in an aqueous solution of disodium carbonate, are able to adsorb to nanoscale gold.^{22,23} However, the presented results are not sufficient to conclude which of the two hypotheses (high capping efficiency or alkalinity) best describes the ensuing stability of AuAg nanostars by post-synthesis addition of disodium carbonate, or in which proportion the two factors are concomitantly occurring.





In light of what was observed for the two NS/CO₃²⁻ formulations, and of what was mentioned about hydroxyl ions adsorption on gold surfaces,^{22,23} additional experimental data at constant concentration and constant molar ionic strength were obtained by the post-synthetic addition of NaOH. Stability was observed for the constant molar ionic strength preparation only; the ζ potential of the constant concentration formulation was -22.7 ± 0.5 mV, a value that falls below the standard threshold for colloidal stability.⁶ The formulation indeed exhibited visual signs of aggregation after approximately 2 hours (Table 4.3). On the other hand, the constant molar ionic strength formulation, NS/OH⁻_(I), had a ζ potential of -36.5 ± 0.8 mV, and did not exhibit visual signs of coagulation. As far as the conductivity is concerned, the behavior of NS/OH⁻ followed the trend exhibited by the carboxylate-based and carbonate-based formulations, that is, conductivity decreased compared to the unmodified nanostars. This was observed for both constant concentration and constant molar ionic strength formulations. The behavior displayed by NS/OH⁻ is similar to that of NS/Ac. Given the demonstrated stabilizing effect of hydroxyl ions, it can be hypothesized that the mechanism by which disodium carbonate attains colloidal stability is likely caused by a combined action of both carbonate and hydroxyl ions.

4.2.3 Screening of effective candidate stabilizers by extinction spectroscopy

Decay studies based on extinction spectroscopy were performed on the formulations obtained with the effective candidate stabilizers (Ct, Tt, Ac, and CO₃²⁻), with the two-fold

aim of (1) spotting any early ensuing aggregation before they were visible to the naked eye, and (2) discerning which of the two formulations (constant concentration or constant molar ionic strength) had better stability. It was hypothesized that the constant molar ionic strength formulations would display superior stability, as ionic strength, rather than nominal concentration, plays an important role in determining the Debye length, and, ultimately, the interparticle distances at which aggregation occurs.

The decay curves of the NS formulations stabilized with carboxylates at fixed concentration (0.96×10^{-3} M, *Figure 4.12 a*) exhibited increasing stability with increasing nominal charge; on the other hand, at fixed molar ionic strength (3.4×10^{-3} M, *Figure 4.12 b*), all formulations showed analogous stability, with statistically constant extinction over the investigated two hour period. As expected, this indicates the total, effective charge density on the surface is the actual key factor for stability, rather than the nominal charge per molecule.

NS/PrSulf was chosen as model ineffectively stabilized formulation and thus, as negative control (*Figures 4.12 c*). As expected from the ζ potential and conductivity survey presented in the previous section, NS/PrSulf showed opposite behavior when compared to the carboxylate-stabilized formulations; the stability of both the constant concentration and the constant molar ionic strength formulations exhibited a steeper decay than the unmodified NS, suggesting that PrSulf not only does not improve the stability of the colloidal nanostars, but it also accelerates their coagulation.

Finally, as shown in *Figure 4.12 d*, CO_3^{2-} provided stability to the colloidal nanostars at both constant concentration and constant molar ionic strength formulation. Stability was also maintained past the two hour window selected for the decay study, with no visual signs of aggregation for up to four months (§ 5.4). This mirrors the behavior of NS/Ct, as earlier described. Also in this case, flocs are observed after 48 hours of incubation, and the colloidal sol is completely redispersed after approximately 2 s of manual shaking.

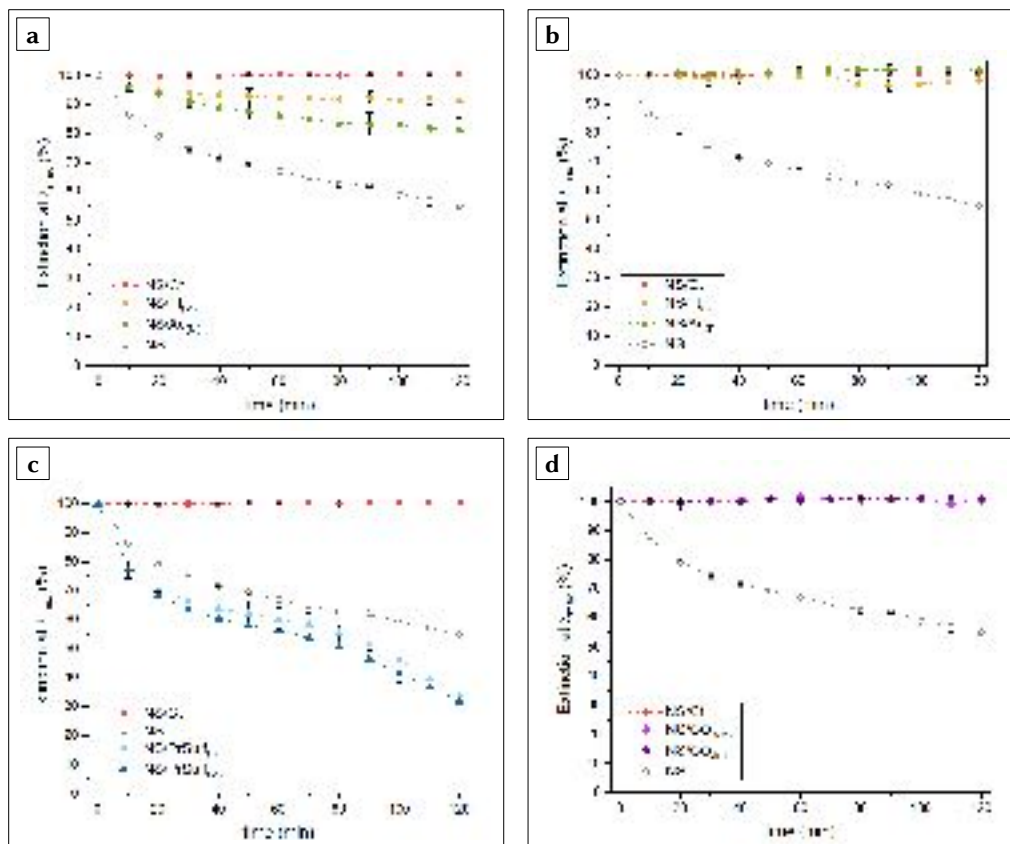


Figure 4.12: Decay curves of AuAg nanostars formulations obtained with different candidate stabilizing agents. The top panels show a comparison among sodium carboxylates: trisodium citrate (NS/Ct, red), disodium tartrate (NS/Tt, yellow), and sodium acetate (NS/Ac, green), (a) at a constant concentration of 0.96×10^{-3} M, and (b) at a constant molar ionic strength of 3.4×10^{-3} M. (c) Comparison between model effectively stabilized formulation NS/Ct (positive control, red) model ineffectively stabilized formulation NS/PrSulf (1,3-propanedisulfonic acid disodium salt, negative control); both NS/PrSulf at constant concentration (light blue) and at constant molar ionic strength (indigo) are shown. (d) Comparison between model effectively stabilized formulation NS/Ct and NS/CO₃²⁻; both formulations at constant concentration (light purple) and at constant molar ionic strength (purple) are shown. All grey profiles refer to the as-synthesized nanostars with no candidate stabilizer added. Dashed B-spline connectors are used to highlight data trends.

4.2.4 Summary

Four effective stabilizers were identified as alternatives to CTAB: trisodium citrate (Ct), disodium tartrate (Tt), sodium acetate (Ac), and $\text{Na}_2\text{CO}_3^{2-}$. These stabilizers respond to two of the qualities that were sought at the beginning of this chapter — they have (1) small SERS cross section, and (2) minimal steric hindrance. Their concentration in solution was optimized by ζ potential, conductivity, and extinction measurements, and the results showed optimal stability at a molar ionic strength of 3.4×10^{-3} M. $\text{Na}_2\text{CO}_3^{2-}$ was also found to impart sufficient stability at lower ionic strength. In more detail, this species was found to stabilize the nanostars at the same concentration that was found to be optimal for citrate, a species with a higher formal charge. This result was unexpected and was linked to the alkalinizing properties of carbonate in solution; hydroxyl ions are known to adsorb on gold surfaces and were shown to also adsorb on the bimetallic AuAg surface of the nanostars. This provides a potential fifth effective candidate stabilizer to be added to the list, NaOH. The remainder of the organic and inorganic anionic species that were surveyed did not demonstrate stabilization properties, thus supporting the hypothesis that the capping process is driven by *specific adsorption*.

4.3 Chemical state of gold and silver

The above results concern the solid-liquid interface, and specifically what happens at the slipping plane (ζ potential measurements) and in the bulk solution (conductivity measurements). Special attention was therefore given to the resulting macroscopic outcomes (*short-term stability*), as observed visually and via extinction spectroscopy. As previously discussed, the data acquired so far seem to suggest that there are reasons other than simple indifferent adsorption by electrostatic attraction that causes the stabilization of colloidal bimetallic nanostars when Ct, Tt, Ac, or CO_3^{2-} are added. In order to address this

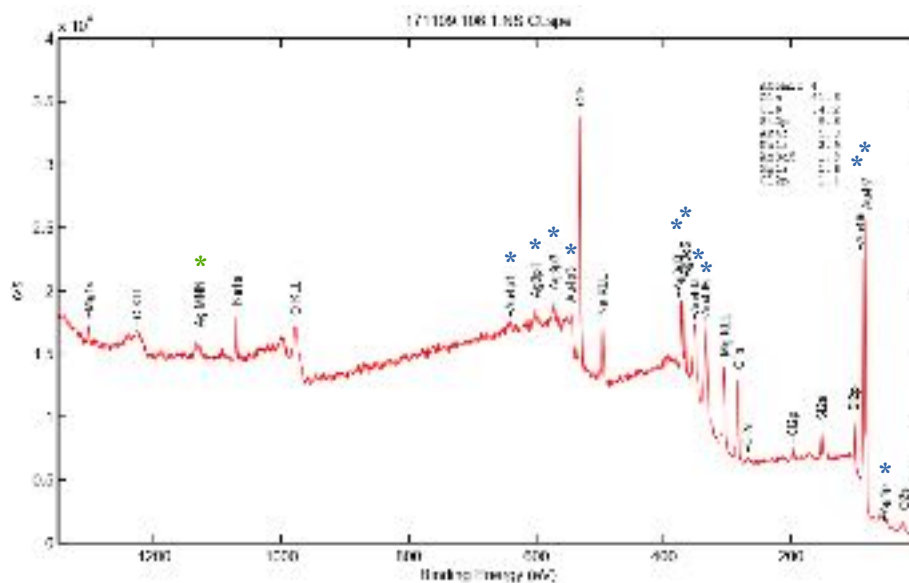


Figure 4.13: Survey XPS scan of NS/Ct. Blue asterisks mark the peaks produced by the bimetallic component of the colloidal nanostars. The other detected species can be attributed to the glass substrate utilized for drop-casting the sample (Mg, Na, O, Cl, Si), or to the presence of unwashed stabilizers (Na, O, Cl, C).

research question from a different perspective, XPS measurements were performed on model formulation NS/Ct. In this way, the oxidation state of the metallic surface can be examined, and the results can be utilized to infer whether electrostatic attraction or chemical binding drive the capping process.

4.3.1 Surface characterization of NS/Ct by XPS

Survey scan and high resolution scans of Au 4*f* and Ag 3*d* peaks are reported in *Figure 4.13*. The survey scan shows the presence of the expected constituting elements for the bimetallic nanostars, gold and silver; the other detected elements are mainly attributable to the glass substrate used for the deposition of the sample, as well as to the capping species that were not removed by the colloid rinsing procedure (§ 3.2.5).

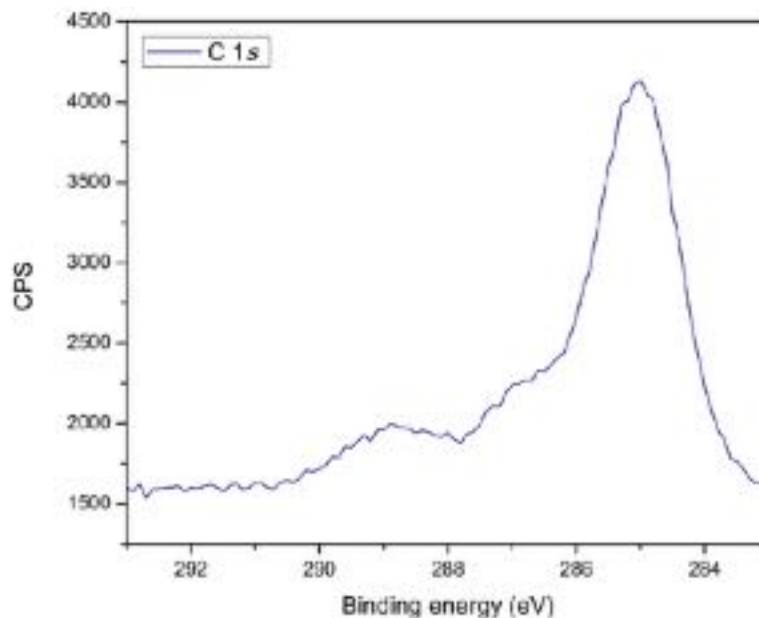


Figure 4.14: C 1s high resolution XPS raw data for NS/Ct. The carbon peak presents a multimodal distribution, suggesting convolution of at least three different bands. This is commonly observed in C 1s peaks, as well as expected for the analyzed sample, in that there are at least three types of carbon: C-OH (citrate's alcoholic functions), COO⁻ (citrate's carboxylic functions), and aliphatic C=C (adventitious carbon). The latter is the one traditionally used for binding energy referencing, as it is ubiquitously detected in XPS.²⁴

High resolution data were conventionally processed by applying a Shirley background correction,^{24,25} and referencing the binding energies to the C 1s peak at 284.8 eV (C=C, aliphatic, *Figure 4.14*).^{9,24} As shown in *Figure 4.15 a*, the binding energy for the Au 4f_{7/2} core peak was 84.0 eV, with spin coupling energy difference of 3.6 eV, which is consistent with bulk, elemental gold. A small degree of peak asymmetry was still present after background subtraction. This is typical of metals and conductive samples in general, and it is caused by conduction electrons taking part in *shake-up*-like phenomena, resulting in peak tailing on the higher energy side of the band.^{26,27} In a shake-up event, a photoemitted core electron interacts with a valence electron, resulting in the excitation (“shake up”) of the latter. This causes a reduction of the photoemitted core electron energy,

which is reflected in the spectrum as a satellite peak a few electronvolts apart from the original energy value (true core peak).²⁴ Au 4*f* peaks are known to be subjected to this phenomenon,²⁸ therefore, it can be assumed that the slight tailing observed in the high resolution spectra is not caused by the presence of multiple chemical states of gold, but instead, is a result of the conductive character of the sample. More evidence to adopt this assumption comes from considering a more conservative approach, and using peak deconvolution to reveal the possible simultaneous presence of multiple gold species. Under this approach, deconvolution of the band yields a second component that is not centered at an energy that is consistent with any oxidation state of Au. Indeed, the second component constituting the 4*f*_{7/2} core peak was found to be centered at 84.7 eV, which is higher than the binding energy for bulk gold, but significantly lower than the binding energy reported in the literature for nanoscale Au(I), 86.0 eV (purple dashed line in *Figure 4.15 a*).²⁹ For this reason, the second component could be tentatively assigned to the presence of Au^{δ+} instead.⁹ This partially charged component was then quantitated via peak integration utilizing a 0.81 Gaussian-Lorentzian curve shape, and found to account for 11.42% of the total surface gold. This implies that, even under this very conservative approach, the majority of the surface gold (88.58%) is in its bulk, elemental state, which is in strong agreement with what reported by Al-Johani *et al.*⁹ for monometallic gold nanospheres. This also strengthens the conclusions made following the ELS and extinction spectroscopy experiments discussed in the previous sections, *i.e.*, adsorption of the effective stabilizers occurs upon specific adsorption on a neutral surface.

Figure 4.15 b shows the high resolution data for silver. The peaks were symmetric both before and after background subtraction, and the binding energy was centered at 368.11 eV (Ag 3*d*_{5/2}), with a spin orbit coupling energy difference of 6.0 eV. The observed binding energy is slightly lower than values most commonly reported for elemental silver, 368.2 eV (50% citations on NIST database),³⁰ even though binding energies of 368.10

eV are also reported for the same chemical state (~ 23% citations on NIST database).³⁰ Typical values for Ag(I) in oxides exhibit a comparatively larger shift to lower energies (*i.e.*, 367.7–367.9 eV for Ag(I) in oxides).³⁰ If 368.2 eV is taken as the reference value, the small 0.1 eV difference could be interpreted as deriving from *alloyed* silver, which is reported to shift binding energies to lower values compared to the elemental state.³⁰ This interpretation would be in accordance with the hypothesis that co-reduction of metals with similar crystal lattice parameters such as Au and Ag can yield alloys (§ 4.1).³⁵ Further confirmation of this hypothesis could be obtained by acquiring high resolution data for the Ag-MNN Auger peak (marked in green in *Figure 4.13*). Auger peaks arise from the emission caused by external shell electrons filling the core vacancy left by the XPS ejected photoelectron, and typically show larger energy shifts among chemical states of the same species. For this, they can be utilized for more accurate speciation.^{24,32}

4.3.2 Crystallographic analysis by HR-TEM

Selected area electron diffraction (SAED) measurements were performed concomitantly with high resolution transmission electron microscopy (HR-TEM) analysis. SAED patterns are images in reciprocal space that result from the wave behavior of electrons when they interact with the crystal lattice of a solid; electrons are diffracted at specific angles based on the crystal structure of the sample, ultimately allowing for the identification of crystal facets, crystal plane distances, and defects.³³ Consequently, SAED patterns have a potential for qualitative analysis. The distance between parallel planes of atoms, the *d-spacing*, can be extrapolated from SAED patterns by taking the inverse of the distance between the center of the pattern and each illuminated dot composing the pattern. The d-spacings can then be compared to X-Ray Diffraction (XRD) libraries for crystal plane indexing

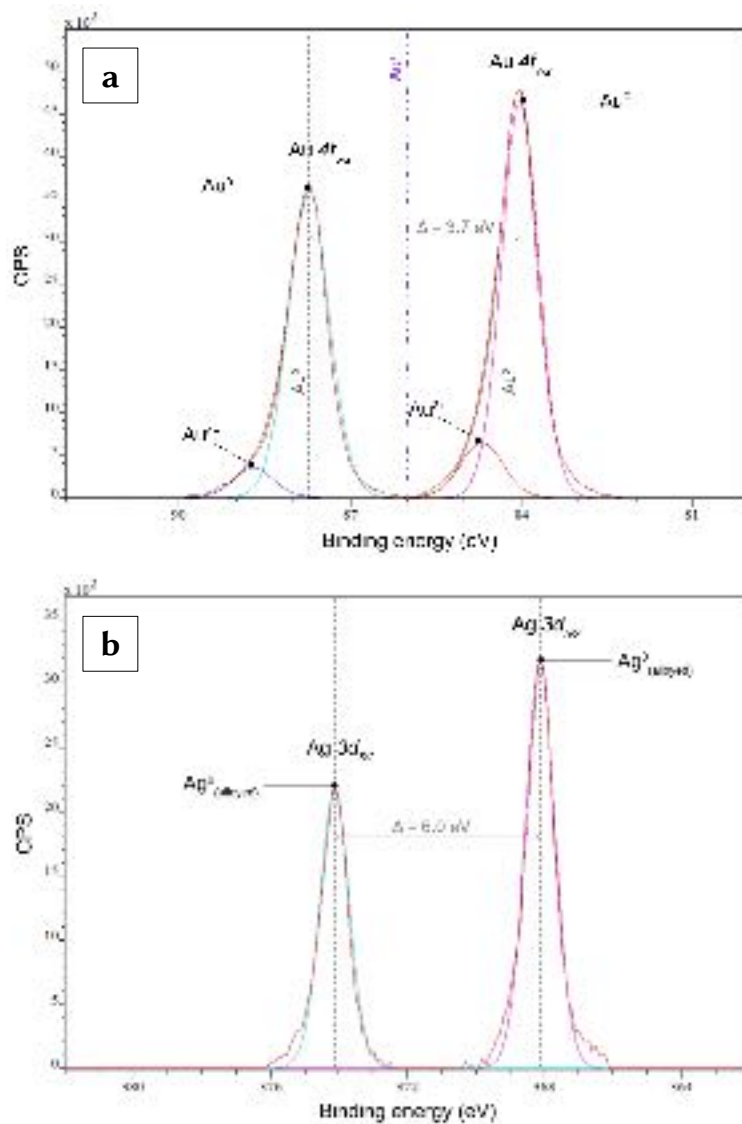


Figure 4.15: High resolution XPS spectra of NS/Ct: (a) Au 4f core peaks with peak deconvolution, and (b) Ag 3d core peaks. Both spectra are reported after standard Shirley background subtraction.

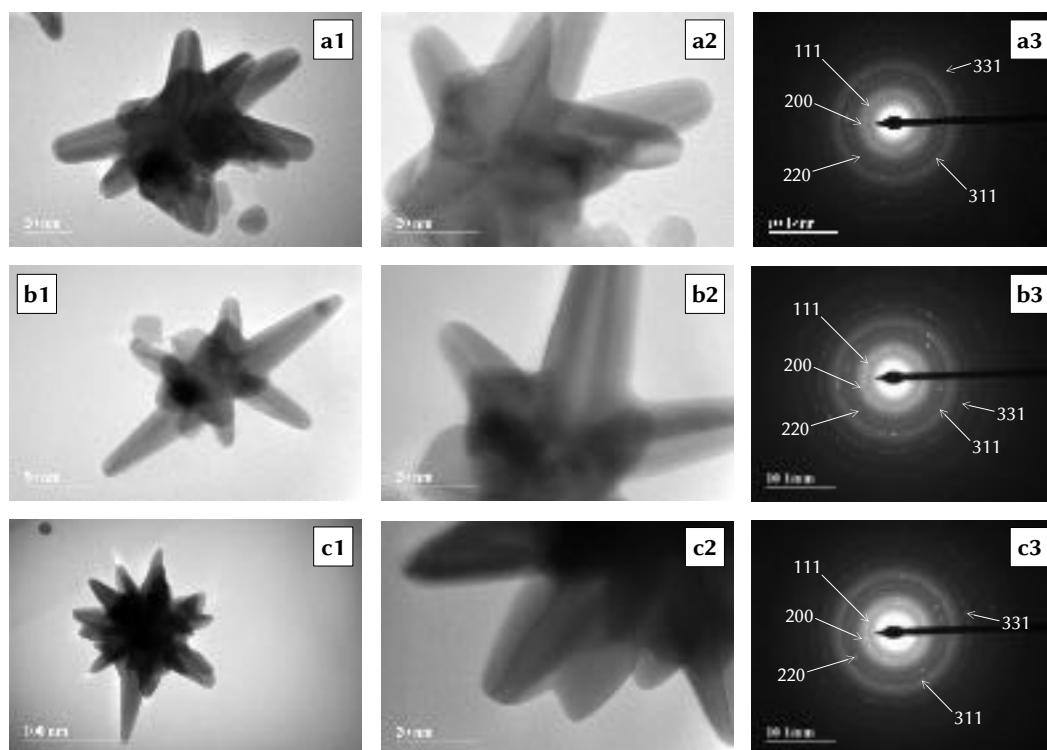


Figure 4.16: (a1–3) TEM micrographs of three nanostars, sampled from different batches of NS/Ct, and (b1–3) high resolution details of selected areas. (c1–3) Indexed SAED patterns relative to each of the three nanostars’ selected areas.

and compound matching. For this research, the International Center for Diffraction Data Powder Diffraction File 4+ database (ICDD PDF-4+ 2018 RDB) was utilized.

Figure 4.16 reports the SAED patterns relative to three nanostars sampled from the NS/Ct formulation. All of the SAED showed the typical dotted-rings pattern of polycrystalline samples, which is expected for anisotropic nanoparticles. The extrapolated d-spacings were used to index the SAED patterns, by comparison with ICDD PDF 4+ 2018 RDB database entries containing Au, Ag, and AuAg alloys. Common crystal planes for face-centered cubic (*fcc*) metals were observed, as marked in the right panels in Figure 4.16 — (111), (200), (220), (311), (331). The d-spacings were consistent with AuAg alloys entries in the database, which have crystallographic parameters that are

highly similar to pure gold and silver, as the two metals are miscible at all proportions and do not exhibit ionic radii mismatch. For this reason, no additional compositional interpretations could be made. However, on the basis of the XPS results discussed in the preceding section, and of previously published literature,³ it seems reasonable to assume that the two metals are uniformly distributed throughout the body of the nanostar. Further work could be done in the future, aimed at visualizing the distribution of the two metals by mapping the elemental composition.

4.3.3 Summary

In light of the XPS results, it was possible to affirm that the metals composing the nanostars, gold and silver, are alloyed and in their elemental oxidation state. The results here reported are consistent with what reported by Al-Johani *et al.*⁹ for monometallic gold nanospheres; this indicates that the traditional assumption on the oxidation state of noble metal nanoparticles (§ 2.2.1.1) may not be representative of the actual surface of these nanomaterials. According to the data here presented, the nanoparticle's surface is better described by a single-domain structure, in which *at least* the great majority (>88.58%) of the noble metals are in their bulk, elemental oxidation state (*Figure 2.3 d*).

Finally, HR-TEM imaging with *in situ* electron diffraction permitted to identify some of the crystal planes that are present in the nanostars: (111), (200), (220), (311), (331). The (111) facet is frequently observed in noble metal nanoparticles, and it is often associated with the presence of twinning planes, which can result in the formation of anisotropic structures.^{34,35} Indeed, HR-TEM micrographs show a number of possible twin boundaries along the elongation direction of the branches (*Figure 4.17*). A more in-depth analysis of the morphology of the nanostars is presented in the following chapter.

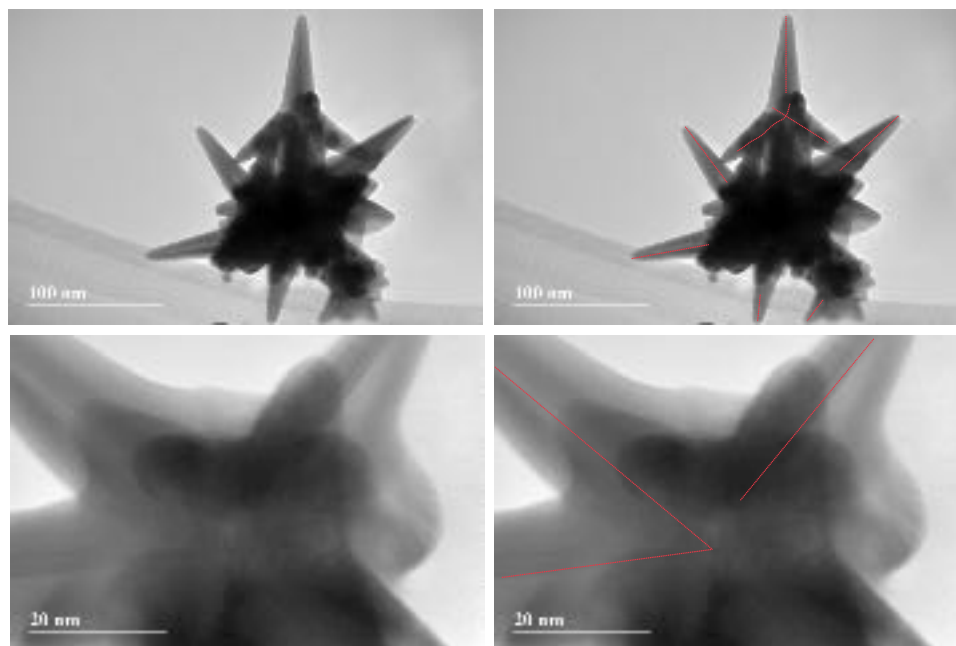


Figure 4.17: HR-TEM micrographs of NS/Ct nanostars (*left*) and highlighted possible grain boundaries and twinning planes (*right*).

REFERENCES

- [1] Cheng, L-C.; Huang, J-H.; Chen, H.M.; Lai, T.C.; Yang, K.Y.; Liu, R.S.; Hsiao, M.; Chen, C-H.; Here, L-J.; Tsaid, D.P. Seedless, silver-induced synthesis of star-shaped gold/silver bimetallic nanoparticles as high efficiency photothermal therapy reagent. *J. Mater. Chem.*, **2012**, *22*, 2244–2253.
- [2] He, S.; Kang, M.W.C.; Khan, F.J.; Tan, E.K.M.; Reyes, M.A.; Kah, J.C.Y. Optimizing gold nanostars as a colloid-based surface-enhanced Raman scattering (SERS) substrate. *J. Opt.* **2015**, *17*, 1–13.
- [3] Atta, S.; Beetz, M.; Fabris, L. Understanding the role of AgNO₃ concentration and seed morphology in the achievement of tunable shape control in gold nanostars. *Nanoscale*, **2019**, *11*, 2946–2958.

- [4] Wijenayaka, L. A.; Ivanov, M. R.; Cheatum, C. M.; Haes, A. J. Improved Parametrization for Extended Derjaguin, Landau, Verwey, and Overbeek Predictions of Functionalized Gold Nanosphere Stability. *J. Phys. Chem. C*, **2015**, *119*, 10064–10075.
- [5] Nelson, L.D.; Cox, M.M. *Lehninger Principles of Biochemistry*, Fifth edition. W. H. Freeman and Company: New York, 2008.
- [6] Shnoudeh, A.J.; Hamad, I.; Abdo, R.W.; Qadumii, L.; Jaber, A.Y.; Surchi, H.S.; Alkelany, S.Z. Synthesis, Characterization, and Applications of Metal Nanoparticles. In *Biomaterials and Bionanotechnology*, Advances in Pharmaceutical Product Development and Research series; Tekade, R.K., Ed.; Academic Press: London, 2019.
- [7] Delgado, A.V.; González-Caballero, F; Hunter, R.J.; Koopal, L.K.; Lykelma, J. Measurement and Interpretation of Electrokinetic Phenomena. *Pure Appl. Chem.*, **2005**, *77*(10), 1753–1805.
- [8] Alvarez-Puebla, R.A.; Arceo, E.; Goulet, P.J.G.; Garrido, J.J.; Aroca, R.F. Role of Nanoparticle Surface Charge in Surface-Enhanced Raman Scattering. *J. Phys. Chem. B*, **2005**, *109*(9), 3787–3792.
- [9] Al-Johani, H.; Abou-Hamad, E.; Jedidi, A.; Widdifield, C.M.; Viger-Grave, J.; Sangaru, S.S.; Gajan, D.; Anjum, D.H.; Ould-Chikh, S.; Hedhili, M.N.; Gurinov, A.; Kelly, M.J.; El Eter, M.; Cavallo, L.; Emsley, L.; Basset, J-M. The structure and binding mode of citrate in the stabilization of gold nanoparticles. *Natur. Chem.*, **2017**, *9*, 890–895.
- [10] Park, J. W.; Shumaker-Parry, J. S. Structural Study of Citrate Layers on Gold Nanoparticles: Role of Intermolecular Interactions in Stabilizing Nanoparticles. *J. Am. Chem. Soc.*, **2014**, *136*, 1907–1921.
- [11] Wulandari, P.; Nagahiro, T.; Michioka, K.; Tamada, K.; Ishibashi, K.; Kimura, Y.; Niwano, M. Coordination of Carboxylate on Metal Nanoparticles Characterized by Fourier Transform Infrared Spectroscopy. *Chem. Lett.*, **2008**, *37*, 888–889.
- [12] Aroca, R.F. *Surface-enhanced vibrational spectroscopy*, John Wiley & sons: Chichester, 2006.
- [13] Sonntag, H.; Strenge, K. *Coagulation Kinetics and Structure Formation*. Springer Science+Business Media: New York, 1987.

- [14] Sprycha, R.; Matijevic, E. Electrokinetics of uniform colloidal dispersions of chromium hydroxide. *Langmuir*, **1989**, *5*(2), 479–485.
- [15] Ohshima, H. Effective Surface Potential and Double-Layer Interaction of Colloidal Particles. *J. Colloid Interface Sci.*, **1995**, *174*(1), 45–52.
- [16] Liu, Y.; Yan, E.C.Y.; Zhao, X.; Eisenha, K.B. Surface Potential of Charged Liposomes Determined by Second Harmonic Generation. *Langmuir*, **2001**, *17*(7), 2063–2066.
- [17] Xi, W.; Phan, H.T.; Haes, A.J. How to accurately predict solution-phase gold nanostar stability. *Anal. Bioanal. Chem.*, **2018**, *410*, 6113–6123.
- [18] Giles, C.H.; MacEwan, T.H.; Nakhwa, S.N.; Smith, D. Studies in adsorption. Part XI. A system of classification of solution adsorption isotherms, and its use in diagnosis of adsorption mechanisms and in measurement of specific surface areas of solids. *J. Chem. Soc.*, **1960**, 3973–3993.
- [19] Giles, C.H.; Smith, D.; Huitson, A. A general treatment and classification of the solute adsorption isotherm. I. Theoretical. *J. Colloid Interface Sci.*, **1974**, *47*(3), 755–765.
- [20] Atkins, P.; de Paula, J.; Keeler, J. *Atkins' Physical Chemistry*, Eleventh edition, Oxford University Press: Oxford, 2018.
- [21] Goodacre, R.; Graham, D.; Faulds, K. Recent Developments in Quantitative SERS: Moving towards Absolute Quantification. *TrAC Trends Anal. Chem.*, **2018**, *102*, 359–368.
- [22] Liu, S.; Ishimoto, T.; Koyama, M. First-Principles calculations of OH⁻/OH Adsorption on Gold Nanoparticles. *Int. J. Quant. Chem.*, **2015**, *115*, 1597–1605.
- [23] Santiago-Rodríguez, Y.; Herron, J.A.; Curet-Arana, M.; Mavrikakis, M. Atomic and molecular adsorption on Au(111). *Surf. Sci.*, **2014**, *627*, 57–69.
- [24] van der Heide, P. *X-Ray Photoelectron Spectroscopy, An Introduction to Principles and Practices*. John Wiley & Sons, Inc.: Hoboken, 2012.
- [25] Vegh, J. The Shirley background revised. *J. Electron Spectrosc. Relat. Phenom.*, **2006**, *151*(3), 159–164.

- [26] Hüfner, S.; Wertheim, G.K.; Wernick, J.H. XPS Core Line Asymmetries in metals. *Solid State Commun.*, **1975**, *17*, 417–422.
- [27] Briggs, D. XPS: Basic Principles, Spectral Features and Qualitative Analysis. In *Surface Analysis by Auger and X-ray Photoelectron Spectroscopy*; Briggs, D., Grant, J.T., Eds.; IM Publications: Chichester, 2003.
- [28] XPS Interpretation of Gold <https://xpssimplified.com/elements/gold.php> (accessed Aug 11, 2020)
- [29] Casaletto, M.P.; Longo, A.; Martorana, A. Prestianni, A.; Venezia, A.M. XPS study of supported gold catalysts: the role of Au⁰ and Au^{δ+} species as active sites. *Surf. Interface Anal.*, **2006**, *38*, 215–218.
- [30] NIST X-ray Photoelectron Spectroscopy Database, NIST Standard Reference Database Number 20, Version 4.1, National Institute of Standards and Technology: Gaithersburg, 20899, 2000, <https://srdata.nist.gov/xps/Default.aspx> (accessed Aug 11, 2020).
- [31] Gilroy, K.D.; Ruditskiy, A.; Peng, H-C.; Qin, D.; Xia, Y. Bimetallic Nanocrystals: Syntheses, Properties, Applications. *Chem. Rev.*, **2016**, *116*, 10414–10472.
- [32] Wagner, C.D. Chemical shifts of Auger lines, and the Auger parameter. *Faraday Discuss. Chem. Soc.*, **1975**, *60*, 291–300.
- [33] Shindo, D.; Hiraga, K. *High-Resolution Electron Microscopy for Materials Science*. Springer-Verlag: Tokyo, 1998.
- [34] Sau, T.K.; Rogach, A.L. Nonspherical Noble Metal Nanoparticles: Colloid-Chemical Synthesis and Morphology Control. *Adv. Mater.*, **2010**, *22*, 1781–1804.
- [35] Gilroy, K.D.; Ruditskiy, A.; Peng, H-C.; Qin, D.; Xia, Y. Bimetallic Nanocrystals: Syntheses, Properties, Applications. *Chem. Rev.*, **2016**, *116*, 10414–10472.

SERS performance studies of the new colloidal nanostar formulations**5.1 Crystal Violet as model target analyte for SERS performance studies**

The SERS performance of the developed colloidal nanostar formulations was evaluated utilizing Crystal Violet (CV) as the model analyte (*Figure 5.1*). CV is a tri-*p*-dimethylaminophenyl carbonium ion dye with propeller-like shape given by the aryl units, which are equidistant from each other and tilted at 30° with respect to the carbonium ion plane.^{1,2} This dye was chosen as a model analyte because it has been extensively characterized by both FT-Raman (λ_{exc} 1064 nm) and SERS (λ_{exc} 633 nm, citrate-reduced Ag nanospheres), and the assignment of its vibrational modes has been made via DFT calculations.² Moreover, it is off-resonance with the excitation source (*Figure 5.2*), thus ensuring the observed enhancement arises from SERS only, and not from additional laser-dye resonance phenomena (*i.e.*, Resonance Raman, *RR*, or Surface Enhanced Resonance Raman, *SERRS*).

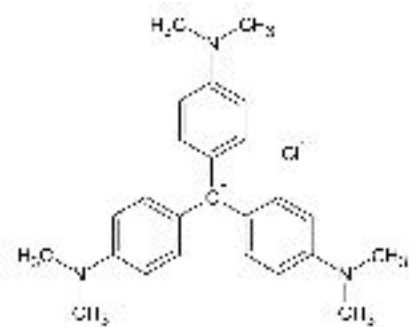


Figure 5.1: Structure of Crystal Violet, CV.

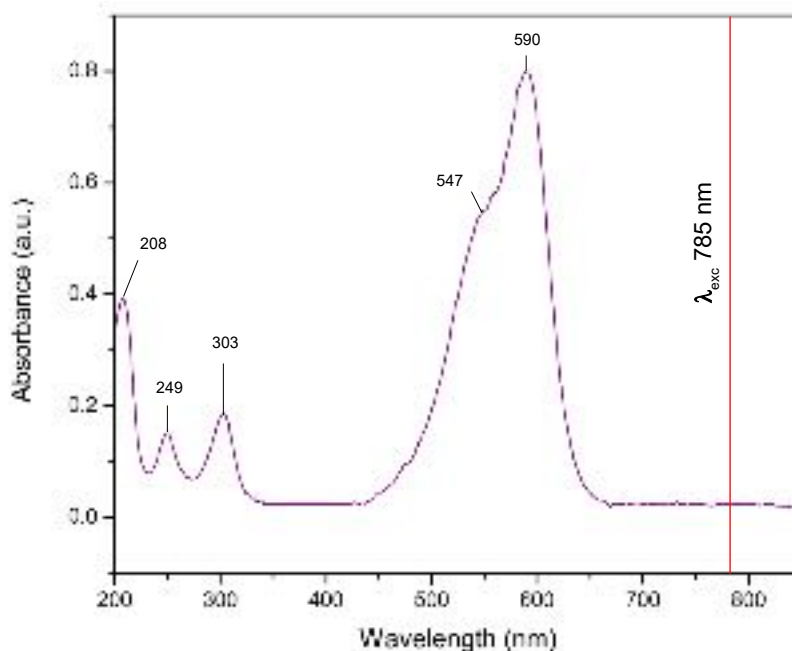


Figure 5.2: UV/Vis absorption spectrum of Crystal Violet (10^{-5} M in water). The red line marks the excitation wavelength used for Normal Raman and SERS experiments.

The normal Raman spectrum of CV in aqueous solution at a concentration of 10^{-3} M is reported in *Figure 5.3 a*, while *Figure 5.3 b* shows the SERS spectrum of the same dye at a concentration of 10^{-7} M. The SERS spectrum was obtained using the NS/Ct formulation with no aggregating agent added. The assignment of the vibrational modes is reported in *Table 5.1* and was performed by comparison with previously published DFT calculations data.² It must be noted that the differences in band position between the Normal Raman and the SERS spectra of CV are negligible, and no changes in the bands' relative intensity are observed. This suggests the dye is *physisorbing* onto the nanostars, rather than *chemisorbing*. The latter phenomenon would in fact produce changes in the spectral profile, especially in terms of band position, because the analyte would change its electronic environment upon complexation with the substrate. Physisorption of CV is also reported to occur on traditional citrate-reduced monometallic silver nanospheres.²

The band at 1170 cm^{-1} , assigned to the ensemble of $\nu_s(\text{CC}_{\text{center}}\text{C})$, $\delta(\text{CCC})_{\text{breathing}}$, and $\rho(\text{CH}_3)$ vibrational modes² was selected as the marker band for this performance study. This band is reported to originate from totally symmetric (a_1) modes,² therefore its intensity is directly and exclusively related to the effect of the electromagnetic enhancement.³ This is particularly important for the evaluation of the analytical enhancement factor (AEF) (§ 5.3). Because the intensity of a totally symmetric band is expected to be governed by the electromagnetic enhancement only, and because the electromagnetic enhancement directly depends on the analyte-substrate distance, the effect of the varying capping layer thicknesses among the different NS formulations on the magnitude of the AEF can be evaluated.

The incubation time of the analyte and NS mixture was determined by studying the evolution of the intensity profile over time. One batch of NS/ CO_3^{2-} (c) was utilized to this scope to avoid any variation that could possibly arise from inter-batch heterogeneity (*vide infra*, § 5.2). Measurements were obtained from duplicate samples at five consecutive time points: immediately after sample preparation (t_0), and then at 8, 16, 26, and 35 minutes. *Figure 5.4* shows the time evolution of the intensity of the CV marker band at 1170 cm^{-1} . Although there is an apparent difference between the intensity recorded at t_0 and the other four time points, it is not statistically significant (F value of $2.6096 < F_{4,9}$ critical of 3.633 , p-value of 0.1606 , $\alpha = 0.05$), as reported in *Table 5.2*. This notwithstanding, an incubation time of 20 minutes was chosen to maintain the same parameters as those utilized for samples containing an aggregating agent. Measurements in the presence of an aggregating agent are discussed in the *Applications* part of this dissertation, *Chapter 8*.

This chapter presents the studies relative to the performance of the nanostar formulations, where performance was evaluated in terms of both *SERS activity* and *long-term stability*. As for the SERS activity, the new formulations were compared to both each other and the original⁴ NS/CTAB formulation, in order to evaluate the effects of the

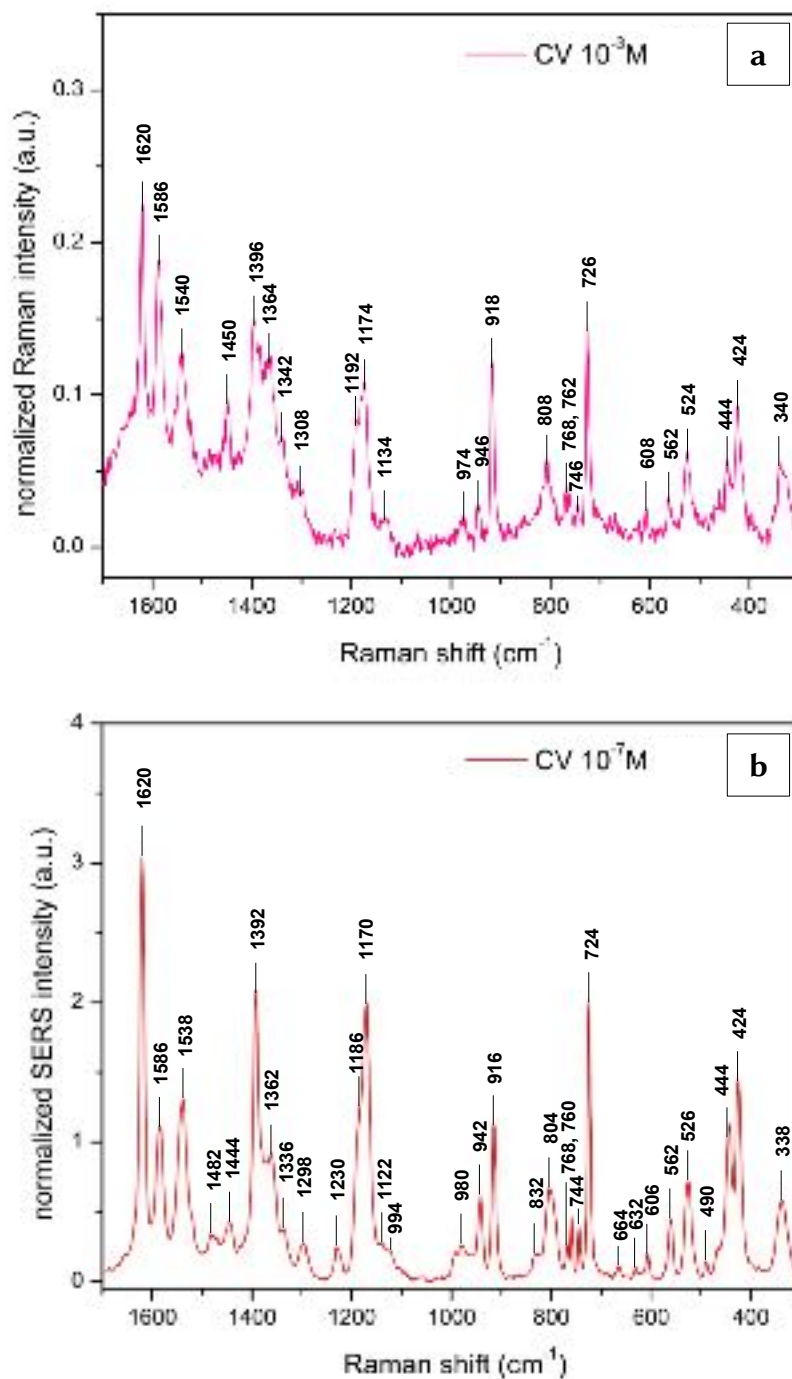


Figure 5.3: (a) Normal Raman spectrum of CV in aqueous solution, at a concentration of 10^{-3} M. (b) SERS spectrum of CV at a concentration of 10^{-7} M, obtained using NS/Ct as the colloidal substrate. Both spectra were baseline-corrected, and their intensities were normalized to the intensity of the band at 3200 cm^{-1} , assigned to $\nu(\text{OH})$ of water (§ 3.2.7).

Table 5.1: DFT, Normal Raman (λ_{exc} 785 nm), and SERS (λ_{exc} 785 nm, NS/Ct) of Crystal Violet

DFT (x 0.97) ²	assignments ²	Raman	SERS
1627 sh		1620 vs	1620 vs
1601 vs		1586 s	1586 vs
1532 s	$\nu_{C_{ring}N}$, $\delta_s(CH_3)$	1540 m	1538 s
1491 w	$\delta_{as}(CH_3)$		1482 sh
1462 w	$\delta_{as}(CH_3)$	1450 w	1444 m
1380 w	$\delta(CH)$, $\delta_s(CH_3)$, $\delta(CCC)_{ring}$	1396 s	1392 s
1360 s	$\nu_{as}(CC_{center}C)$, $\delta(CCC)_{ring}$, $\delta(CH)$	1364 m	1362 s
1335 w	$\delta(CCC)_{ring}$, $\nu_{as}(CC_{center}C)$, $\delta(CH)$	1342 sh	1336 sh
1295 vw	$\nu_{as}(CC_{center}C)$, $\delta(CCC)_{ring}$, $\delta(CH)$	1308 sh	1298 vw
1233 vw	$\nu(CN)$, $\rho(CH_3)$		1230 vw
1221 sh	$\nu_s(CC_{center}C)$, $\delta(CCC)_{breathing}$, $\delta(CH)$		
1187 w	$\nu_{as}(CC_{center}C)$	1192 sh	1186 sh
1165 vw	$\nu_s(CC_{center}C)$, $\delta(CCC)_{breathing}$, $\rho(CH_3)$	1174 m	1170 s
1137 vw	$\delta(CC_{center}C)$, $\nu(CN)$	1134 sh	1122 vw
984 vw	$\delta(CCC)$	974 vw	994 vw
952 vw		946	980 w
932 vw	$\rho(CH_3)$, $\nu(CN)$		942 w
902 vw	$\delta(CC_{center}C)$	918 m	916 s
844 vw			832 sh
792 vw		808 w	804 m
760 vw	$\nu_s(CC_{center}C)$, $\nu(CN)$	768 d, vw	768 d, w
		762 d, vw	760 d, w
		746 vw	744 w
715 w	$\nu(CN)$	726 s	724 s
			664 w
625 vw			632 vw
603 vw	$\delta(CCC)$, $\delta(CNC)$, $\nu_s(CC_{center}C)$	608 vw	606 w
560 vw	$\gamma(CCC)$, $\delta(CNC)$, $\delta(CC_{center}C)$	562 vw	562 w
522 vw	$\delta(CNC)$	524 w	526 m
			490 vw
435 vw	$\delta(CNC)$	444 w	444 w
430 vw	$\delta(CNC)$, $\delta(CC_{center}C)$	424 m	424 m
337 vw	$\gamma(CNC)$, $\rho(CH_3)$	340 w	338 w

vs, very strong; s, strong; m, medium; w, weak; vw, very weak; sh, shoulder; d, doublet. ν , stretching (*s*, symmetric; *as*, asymmetric); δ , bending; γ , out-of-plane deformation with respect to benzene ring; ρ , rocking.

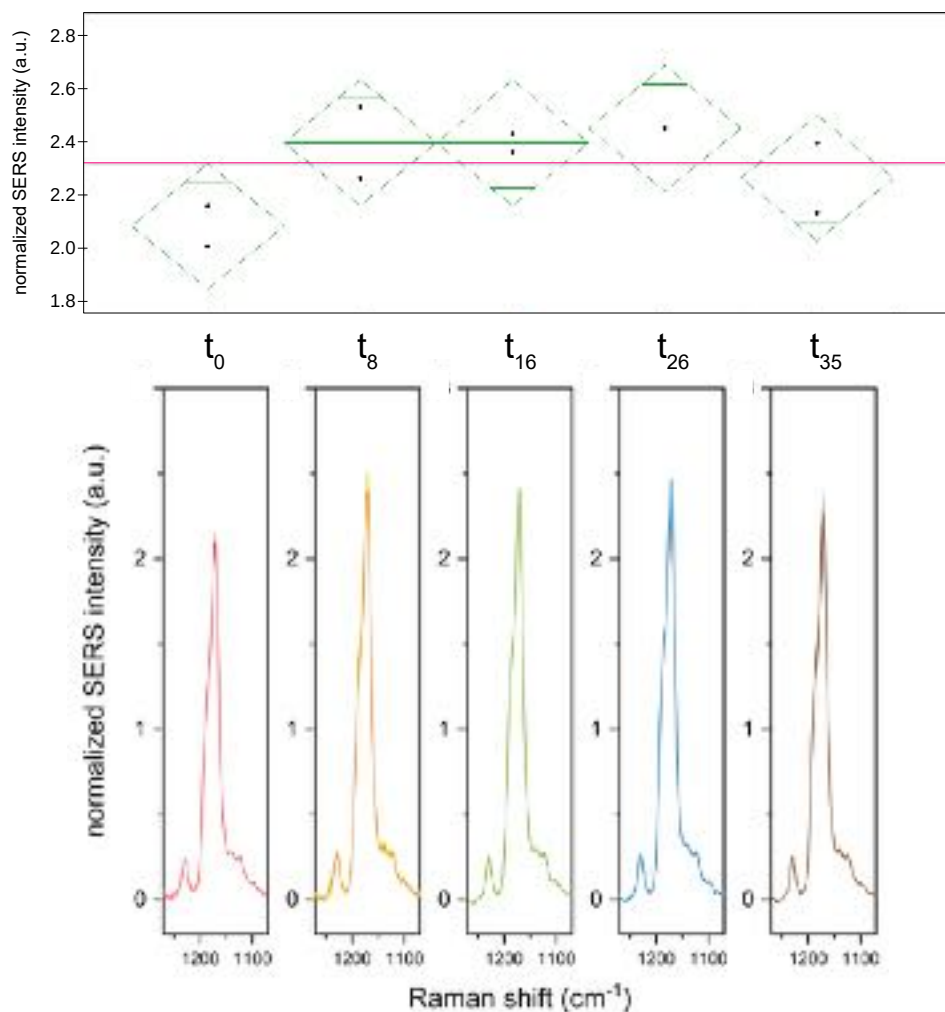


Figure 5.4: Time evolution of the average normalized SERS intensity of the CV band at 1170 cm^{-1} (*bottom*) with ANOVA plot (*top*). The off-color band around each spectrum represents the standard error. In the ANOVA plot (R^2 0.6761), the pink line represents the global mean (2.32 ± 0.05 a.u.), while the green rhomboids represent the quartiles relative to each time point: t_0 , 8, 16, 26, and 35 minutes.

Table 5.2: ANOVA F-test for the normalized SERS intensity of CV at 1170 cm^{-1} over time.

Source	Df	Sum of Squares	Mean Squares	F value	p-value
incubation time	4	0.17493836	0.043735	2.6096	0.1606
error	5	0.08379531	0.016759		
total	9	0.08379531			

Df, degrees of freedom; $\alpha = 0.05$; $F_{4,9}$ critical = 3.633.

different capping systems. To examine long-term stability, the shelf life of each new formulation was estimated in terms of magnitude of the SERS activity over time. Studies concerning the reproducibility of the nanostars substrates in terms of optical properties and morphology are also presented, and best practice recommendations for the use of the new NS formulations in analytical applications are discussed.

5.2 Reproducibility of optical properties and effects on SERS intensity

Before studying the performance of the NS formulations, it is important to determine the reproducibility of their optical properties. This ensures that any deviation in performance among different NS formulations is not linked to synthesis-related plasmon band variability. Repeatability and reproducibility of colloidal substrates is an important topic in SERS literature, and it has often been indicated as one of the main factors affecting signal reproducibility in SERS. However, this was recently disproved by Muehlethaler *et al.*, who demonstrated the largest source of variability in SERS data arises, in fact, at the interlaboratory level, when different Raman instruments, with different capabilities and specifications, are utilized.⁵ This notwithstanding, the optical and morphological properties (§ 2.2.2) of the bimetallic nanostars might diverge from the results reported by Muehlethaler *et al.*, in that their study entailed the use of traditional citrate-reduced silver nanoparticles (Ag/Ct).

Ag/Ct nanoparticles are spheroidal in shape and their plasmon band tends to have a relatively narrow full width at half maximum (FWHM). Branched shapes, on the other hand, tend to display wider FWHM's, as a result of plasmon hybridization between the core and the branches of the nanostructure (*Figures 5.5 and 5.6*).⁶⁻⁸ In addition, band broadening is associated with morphological polydispersity. For anisotropic nanoparticles,

this polydispersity is caused by the mechanism by which the nanoparticles themselves are obtained, that is, by *kinetic control* of their fabrication process.^{9,10} As shown in *Figure 5.7 a*, for a set of reactants, multiple products (*i.e.*, different nanoparticle morphologies) can be obtained, which are characterized by a given activation energy barrier, E_a , and a free energy, ΔG . The thermodynamic product will have higher E_a but lower ΔG (higher morphological stability), while the kinetic product will have lower E_a but higher ΔG (lower morphological stability);¹¹ the preferential formation of one (or more, *vide infra*) product over others can be induced by temperature control, as demonstrated by the Arrhenius equation:¹¹⁻¹³

$$k = Ae^{-\frac{E_a}{RT}} \quad (5.1)$$

where k is the rate constant of a reaction, A is the pre-exponential factor, and R is the ideal gas constant. This shows that thermodynamic control can be forced by working at relatively higher temperature, while kinetic control can be achieved by working at relatively lower temperature. Other factors that can be exploited to drive the reaction to kinetically controlled pathways are the choice of a weak reducing agent such as L-AA, as well as the slowing down of the decomposition or reduction rate of one or more precursors.¹⁵ In the case of the nanostars synthesis utilized for this project, the reducing agent was L-AA, and the slowing down of the reduction rate of the precursors was likely achieved by the presence of gold as AuCl_4^- in solution. This species has a reduction potential that is lower than free Au^{3+} (*Table 5.3*), thus decreasing the reduction potential gap with the coexisting precursor in solution Ag^+ , and ultimately slowing down the reduction rate of gold with respect to silver, effectively achieving co-reduction.^{10,16}

Since each potential product of a nanofabrication reaction has fixed composition and only differs in morphology, the reaction leading to them can be seen as a series of sequential reactions.¹¹ Because of this, more than one kinetic product will likely exist,

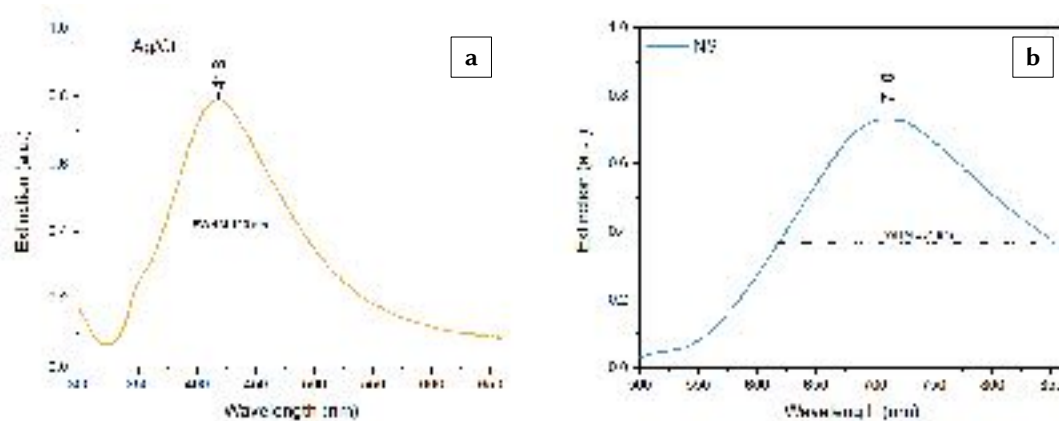


Figure 5.5: (a) Extinction spectrum of a 10% dilution of citrate-reduced silver nanospheres (Ag/Ct) in water, synthesized according to the procedure reported by Lee and Meisel.¹⁷ The plasmon band is relatively narrow, with FWHM of 120 nm. (b) Representative extinction spectrum of colloidal AuAg nanostars (NS/CO₃²⁻ formulation). The plasmon band is wider than traditional Ag/Ct nanoparticles, with FWHM of 234 nm.

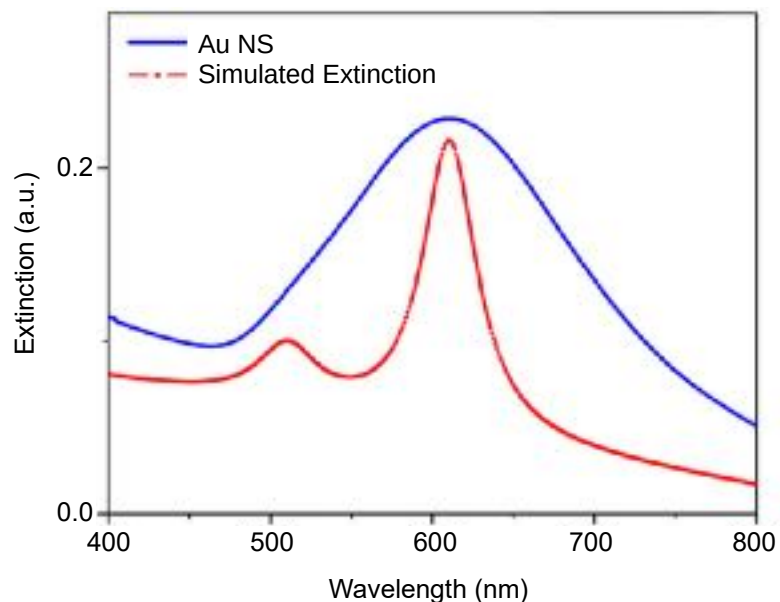


Figure 5.6: Extinction spectrum of gold nanostars (Au NS, *blue*) and simulated extinction spectrum (*red*). The simulated extinction spectrum shows the distinct contributions from the spheroid core (centered at about 512 nm), and that of the branches (centered around 610 nm). Reproduced with permission from Minati, L. *et al.*,⁸ Copyright (2014), with permission from Elsevier.

Table 5.3: Redox potentials of metallic species relevant to the nanostars synthesis.

reduction half-reaction	E_0 (V vs SHE)
$\text{Au}^{+3} + 3\text{e}^- \longrightarrow \text{Au}^0$	+1.40 ¹³
$\text{AuCl}_4^- + 3\text{e}^- \longrightarrow \text{Au}^0 + 4\text{Cl}^-$	+0.994 ¹⁴
$\text{Ag}^+ + \text{e}^- \longrightarrow \text{Ag}^0$	+0.80 ¹³

SHE, Standard Hydrogen Electrode; data at 298.15 K °C and 1 atm.

each of them corresponding to a *local* minimum on a free energy curve, as the one depicted in *Figure 5.6 b*. However, there will only be one thermodynamic product, as it is the one that sits at the *global* free energy minimum. Therefore, when comparing a population of nanostars (kinetic products) with a population of nanospheres (thermodynamic products), a higher morphological heterogeneity will be seen in the former (*e.g.*, different number of branches per nanostar, different branch orientations, ...) than in the latter. This heterogeneity will be particularly prominent when one-pot syntheses with high reaction kinetics are utilized, such as He *et al.*'s.⁴ Indeed, one-pot protocols inherently offer less reaction control, because they lack separation between nanofabrication steps (nucleation, seed formation, growth)¹⁵ — a level of control that can instead be achieved by adopting seed-mediated approaches. Since the shape is the factor that most influences the optical response of a plasmonic material (§ 2.2.2), this heterogeneity has potential to affect plasmon reproducibility.

Finally, it must be recalled that the NS reaction is optimized for approximately 1 mL volume (§ 3.2.1); SERS detection studies would inevitably require higher volumes of colloidal substrate to be completed, and several nanostars batches will be utilized for a single study (*e.g.*, for a single calibration curve). This issue is absent when utilizing traditional substrates, such as Ag/Ct, because their syntheses are optimized for higher volumes, typically 50 to 100 mL, and the reactions can be reproducibly scaled up.^{17–19}

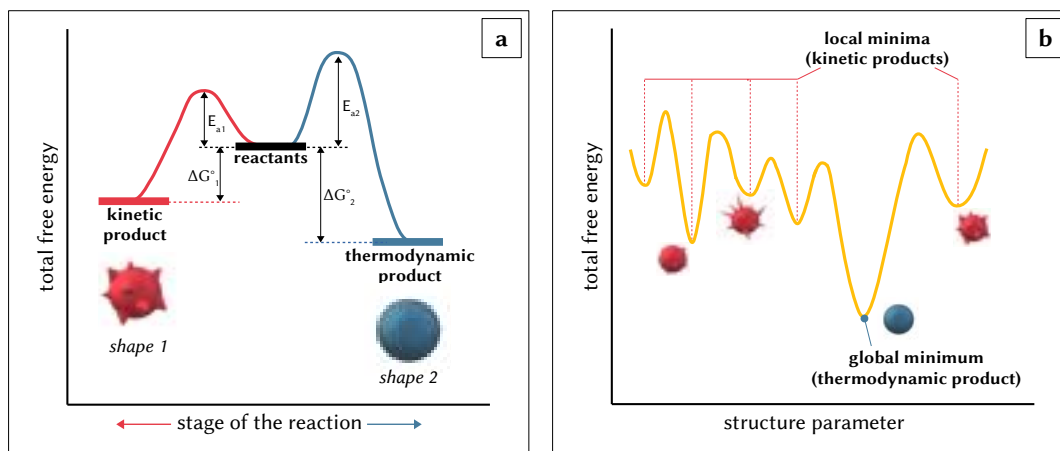


Figure 5.7: Kinetic (*blue*) versus thermodynamic (*red*) control of (a) two parallel reactions and (b) a series of sequential reactions. Figures inspired by Xia *et al.*, 2015.¹¹

Unfortunately, the nanostars reaction utilized for this research cannot be scaled up without the support of syringe pumps or microfluidic reactors. As reported in *Appendix A*, when scaling up the reaction, the plasmon band blue-shifts with increasing reagent volumes. Therefore, the optical and morphological batch-to-batch reproducibility of the substrate must be assessed, and the expected variation minimized. In addition, the plasmon shift tolerance should be identified, that is, how much variation can be considered to be acceptable in order to avoid statistically significant differences in the SERS response.

5.2.1 Optical properties and relationship with SERS response

The λ_{LSPR} of 5 individual batches of NS^I were determined in triplicate via extinction spectroscopy. As reported in *Table 5.4*, the NS showed an average λ_{LSPR} of 709 nm, with standard deviation (σ) of 25 nm. In order to determine whether this variation was such to cause significant differences in the SERS response, each NS batch was utilized

^IThe NS/ CO_3^{2-} (c) formulation was utilized for this section. The post-synthetic addition of the effective stabilizers Ct, Tt, Ac, and $\text{Na}_2\text{CO}_3^{2-}$ does not cause shifts in the λ_{LSPR} and thus, the specific identity of the formulation is irrelevant in this case.

as enhancing substrate for the SERS measurement of CV (10^{-7} M), and an ANOVA (Analysis of Variance) F-test was performed to determine if there were any differences in the intensities of the CV marker band at 1170 cm^{-1} .

Table 5.4: λ_{LSPR} of 5 individual NS batches.

NS	λ_{LSPR} (nm)				σ
	#1	#2	#3	Mean	
1	741	742	743	742	1
2	690	693	690	691	2
3	707	710	712	710	3
4	728	728	729	728	1
5	677	677	674	676	2
Mean				709 nm	
σ				25 nm	

ANOVA F-test results are shown in *Figure 5.8* and *Tables 5.5* and *C.4*. The F value was 33.4274, which is larger than the $F_{4,14}$ critical value for the dataset, 3.112; this, together with the calculated p-value of <0.0001 ($\alpha = 0.05$), is such to reject the null hypothesis^{II} and conclude that there is at least one significantly different mean in the dataset, and thus, there is at least one NS batch that performs significantly differently from the others.

Table 5.5: ANOVA F-test for the normalized SERS intensity of CV at 1170 cm^{-1} for each of the five individual NS batches.

Source	Df	Sum of Squares	Mean Squares	F value	p-value
individual NS batch	4	3.6269717	0.906743	33.4274	<0.0001
error	10	0.2712570	0.027126		
total	14	3.8982287			

Df, degrees of freedom; $\alpha = 0.05$; $F_{4,14}$ critical = 3.112.

^{II}The null hypothesis, H_0 , in an ANOVA F-test is always all means are equal; the alternative hypothesis, H_a , is at least one mean is not equal.²³

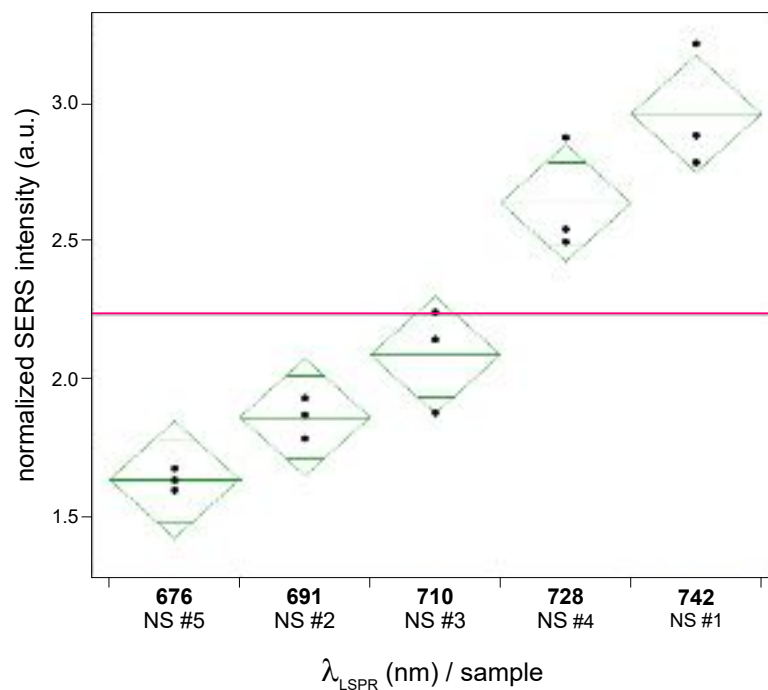


Figure 5.8: ANOVA plot (R^2 0.9304) for the normalized SERS intensity of CV at 1170 cm^{-1} obtained by utilizing five individual NS/ CO_3^{2-} (c) batches as enhancing substrates. The samples have been ordered on the basis of the λ_{LSPR} of the NS batch. The pink line represents the global mean (2.2 ± 0.5 a.u.), while the green rhomboids represent the quartiles relative to each NS sample.

To identify which NS batch was significantly different, a Tukey's honestly significant difference (HSD) test was performed ($\alpha = 0.05$). The graphical rendition of it is reported on the right side of Figure 5.8, while the summary of the statistics is reported in Tables 5.6. The pairs with the largest differences in λ_{LSPR} were found to be significantly different: 742 nm and 676 nm (p-value < 0.0001), 742 nm and 691 nm (p-value < 0.0001), 728 nm and 676 nm (p-value = 0.0002), 742 nm and 710 nm (p-value = 0.0005), 728 nm and 691 nm (p-value = 0.0013), 728 nm and 710 nm (p-value = 0.0145), and 710 nm and 676 nm (p-value = 0.0450). No significant difference was found for the pairs 742 nm and 728 nm (p-value = 0.1918), 691 nm and 676 nm (p-value = 0.4848), and 710 nm and 691 nm

Table 5.6: Tukey’s HSD test. Ordered differences of the normalized SERS intensity of CV at 1170 cm⁻¹ for each pair of individual NS batches.

Level	Level	Difference	Std Error	Lower CL	Upper CL	p-value
$\lambda_{LS\ PR}$ 742 nm	$\lambda_{LS\ PR}$ 676 nm	1.3	0.1	0.9	1.8	<i><0.0001</i>
$\lambda_{LS\ PR}$ 742 nm	$\lambda_{LS\ PR}$ 691 nm	1.1	0.1	0.6	1.5	<i><0.0001</i>
$\lambda_{LS\ PR}$ 728 nm	$\lambda_{LS\ PR}$ 676 nm	1.0	0.1	0.6	1.4	<i>0.0002</i>
$\lambda_{LS\ PR}$ 742 nm	$\lambda_{LS\ PR}$ 710 nm	0.9	0.1	0.4	1.3	<i>0.0005</i>
$\lambda_{LS\ PR}$ 728 nm	$\lambda_{LS\ PR}$ 691 nm	0.8	0.1	0.3	1.2	<i>0.0013</i>
$\lambda_{LS\ PR}$ 728 nm	$\lambda_{LS\ PR}$ 710 nm	0.6	0.1	0.1	1.0	<i>0.0145</i>
$\lambda_{LS\ PR}$ 710 nm	$\lambda_{LS\ PR}$ 676 nm	0.4	0.1	0.1 x 10 ⁻¹	1.9	<i>0.0450</i>
$\lambda_{LS\ PR}$ 742 nm	$\lambda_{LS\ PR}$ 728 nm	0.3	0.1	-0.1	1.8	0.1918
$\lambda_{LS\ PR}$ 691 nm	$\lambda_{LS\ PR}$ 676 nm	0.2	0.1	-0.2	1.7	0.4848
$\lambda_{LS\ PR}$ 710 nm	$\lambda_{LS\ PR}$ 691 nm	0.2	0.1	-0.2	1.7	0.4870

CL, confidence limit; the p-values reported in italics are significant ($\alpha = 0.05$). The standard error is aggregated (N = 15).

(p-value = 0.4870). These results indicate that a plasmon band variation within 20 nm does not cause statistically significant variations in the SERS intensity of an analyte at a fixed concentration. On the other hand, a variation larger than 20 nm does result in statistically significant SERS intensities. This can be best visualized in *Table 5.7*, which shows the lettered Tukey’s HSD groupings for the individual NS batches dataset, confirming the 20 nm plasmon band tolerance identified by analyzing the pair-wise p-values.

Table 5.7: Lettered Tukey’s HSD groupings for the normalized SERS intensity of CV at 1170 cm⁻¹ for each of the five individual NS batches.

Level	Letters	Mean (unrounded)
$\lambda_{LS\ PR}$ 742 nm (NS #1)	A	2.9591326
$\lambda_{LS\ PR}$ 728 nm (NS #4)	A	2.6361242
$\lambda_{LS\ PR}$ 710 nm (NS #2)	B	2.0858354
$\lambda_{LS\ PR}$ 691 nm (NS #2)	B C	1.8602600
$\lambda_{LS\ PR}$ 676 nm (NS #5)	C	1.6341324

The levels that are not connected by the same letter are significantly different ($\alpha = 0.05$).

Moreover, a strong linear trend of the SERS intensity as a function of the λ_{LSPR} was also identified, as reported in *Figure 5.9*. This was expected from the theory, as explained in § 2.2.2; indeed, for SERS measurements in transmission mode on colloidal substrates, the intensity of the SERS signal is expected to increase with increasing level of pre-resonance with the excitation source.^{20–22} NS batches with λ_{LSPR} closer to the λ_{exc} of 785 nm produced the largest SERS intensities. As mentioned, this behavior was found to be linear, according to $y = (0.020 \pm 0.002)x - (12 \pm 1)$, with a R^2 of 0.9024.

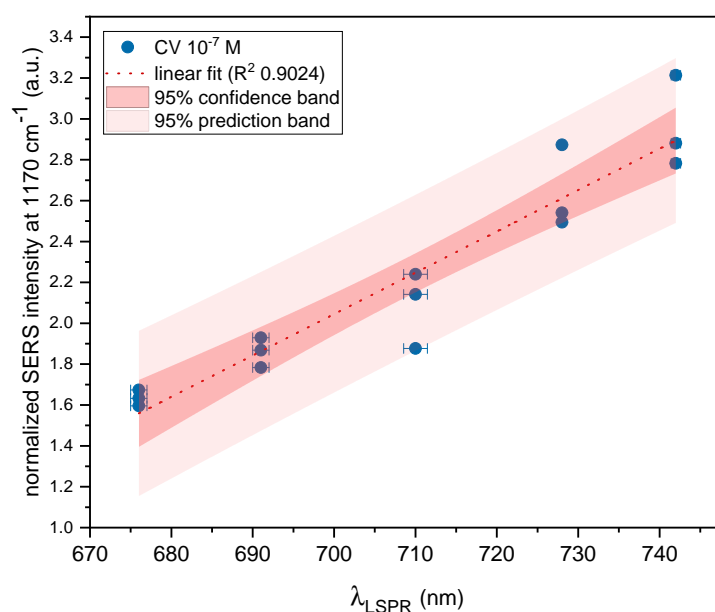


Figure 5.9: Scatter plot of the normalized SERS intensity of CV at 1170 cm^{-1} as a function of the NS's λ_{LSPR} . The data can be fitted to a regression line (dotted red line) of equation $y = (0.020 \pm 0.002)x - (12 \pm 1)$ and R^2 of 0.9024. The 95% confidence band is shown in dark red, while the 95% prediction band is shown in light red.

Because the variation observed among individual NS batches is such that irreproducibility could arise at the application level, a solution must be found in order for these substrates to be confidently utilized as SERS substrates. The easiest way to achieve this is by *pooling*: multiple individual NS samples are pooled together to obtain a larger volume of colloid to be utilized for SERS studies. To verify this, 5 NS samples ($\text{NS}_{\text{pooled}}$, 7

mL) were obtained by pooling 7 individual NS batches together, randomly selected from an array of 40 NS. A summary of their measured λ_{LSPR} is reported in *Table 5.8*. Since the variances between the individual samples discussed in the first part of this section and those of the pooled samples are heteroskedastic (*Appendix C*), no ANOVA F-test could be performed to compare the two groups.^{III} However, the box and whiskers plot reported in *Figure 5.10* shows that, although the mean λ_{LSPR} is similar between the two groups (NS 709 nm, NS_{pooled} 707 nm), the spread of the pooled NS samples (interquartile range, IQR, of 6 nm and $\sigma = 5$) is smaller than that of the individual NS batches (IQR = 39 nm, $\sigma = 25$), as expected (*Table 5.9*).

Table 5.8: λ_{LSPR} of 5 NS_{pooled} samples.

NS	λ_{LSPR} (nm)				
	#1	#2	#3	mean	σ
1	705	710	711	709	3
2	710	707	704	707	3
3	709	711	710	710	1
4	706	714	710	710	4
5	699	699	699	699	0
average	707 nm				
σ	5 nm				

In order to verify whether the NS_{pooled} also exhibit the same variation in SERS intensity as demonstrated by the individual NS, the same SERS study was performed, followed by ANOVA F-test and Tukey’s HSD test; no linear correlation between λ_{LSPR} and SERS intensity was found for this dataset (R^2 0.0392). As reported in *Figure 5.11* and *Tables 5.10* and *C.5*, the ANOVA F-test allowed the rejection of the null hypothesis (F

^{III}The assumptions upon which an ANOVA F-test is based are independence, linearity, within groups normality, and homoskedasticity (equality of variances).^{23,24}

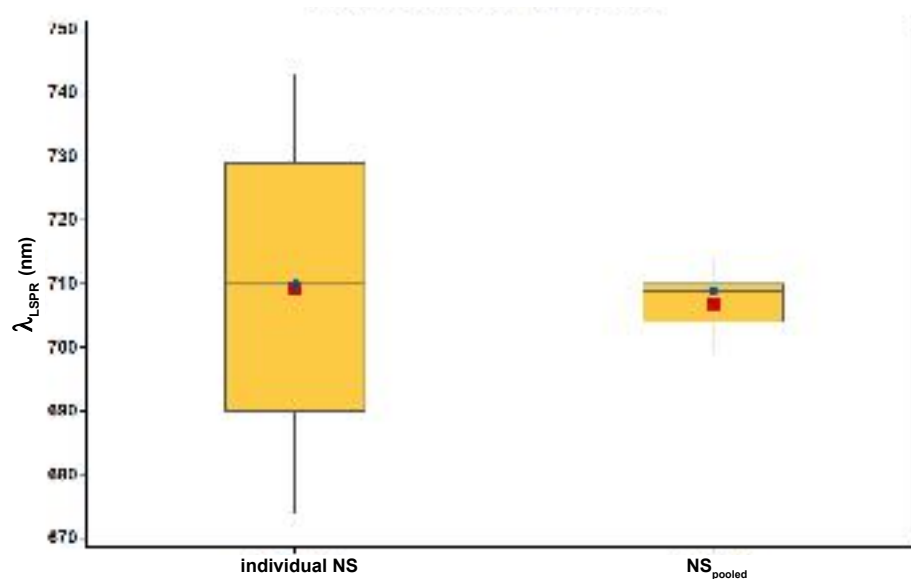


Figure 5.10: Box and whiskers plot of the λ_{LSPR} of the individual NS and NS_{pooled} . The blue dots represent the medians, while the red squares represent the means.

Table 5.9: Comparison of NS with NS_{pooled} . Descriptive statistics.

Statistic	NS	NS_{pooled}
mean	709 nm	707 nm
σ	25	5
Q1	690	704
median	710	709
Q3	729	710
IQR	39	6
whiskers to	674, 743	699, 714
N	15	14
removed outliers	0	1

Q1, first quartile; *Q3*, third quartile; *IQR*, interquartile range. The box and whiskers plot showing the detection of the outlier is reported in Appendix C, Figure C.1.

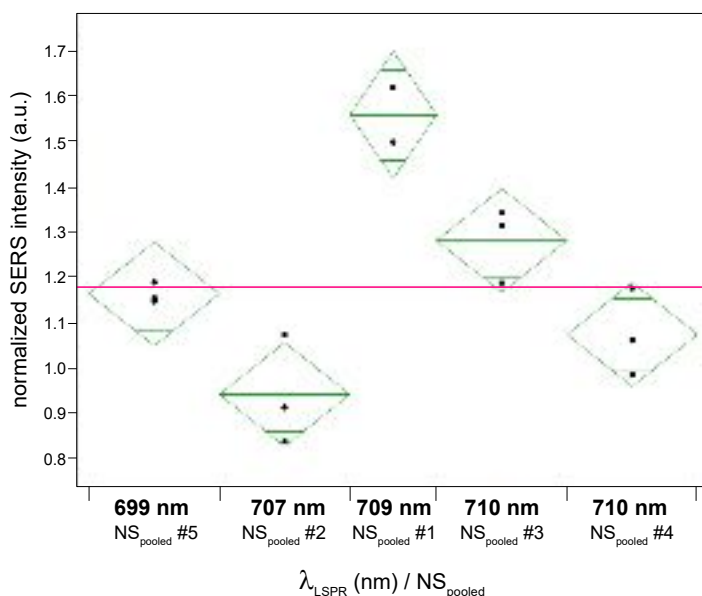


Figure 5.11: ANOVA plot (R^2 0.8831) for the normalized SERS intensity of CV at 1170 cm^{-1} obtained by utilizing five different $\text{NS}_{\text{pooled}}$ samples as enhancing substrates. The samples have been ordered on the basis of the λ_{LSPR} of the $\text{NS}_{\text{pooled}}$. The pink line represents the global mean (1.18 ± 0.05 a.u.), while the green rhomboids represent the quartiles relative to each NS sample.

value $17.0004 > F_{4,13}$ critical 3.411; p-value $0.0003 < \alpha$ 0.05). The Tukey-Kramer's test^{IV} further confirmed that the differences between each $\text{NS}_{\text{pooled}}$ pair are still statistically significant (Tables 5.11 and 5.12), although they are less spread out among samples than those calculated for the individual NS pairs. In more detail, the $\text{NS}_{\text{pooled}}$ #1 was the one yielding the most significant differences: between $\text{NS}_{\text{pooled}}$ #2 (p-value = 0.0002), $\text{NS}_{\text{pooled}}$ #4 (p-value = 0.0013), $\text{NS}_{\text{pooled}}$ #5 (p-value = 0.0054), and $\text{NS}_{\text{pooled}}$ #3 (p-value = 0.0429); the $\text{NS}_{\text{pooled}}$ pair #2–3 was also significantly different (p-value = 0.0070). A larger sample size study is suggested to further verify whether sample $\text{NS}_{\text{pooled}}$ 1 could be an outlier.

^{IV}Tukey-Kramer's test is applied in place of Tukey's HSD test when groups have unequal sample size; the N of 3 of $\text{NS}_{\text{pooled}}$ #1 was indeed reduced to 2 as a result of an outlier. This outlier was determined by exploratory data analysis via box-and-whiskers plot (Appendix C, Figure C.1).

Table 5.10: ANOVA F-test for the normalized SERS intensity of CV at 1170 cm⁻¹ for each of the five NS_{pooled} samples.

Source	Df	Sum of Squares	Mean Squares	F value	p-value
pooled NS batch	4	0.52451751	0.131129	17.0004	0.0003
error	9	0.06941977	0.007713		
total	13	0.59393728			

Df, degrees of freedom; $\alpha = 0.05$; $F_{4,13}$ critical = 3.411.

Table 5.11: Tukey's HSD test. Ordered differences of the normalized SERS intensity of CV at 1170 cm⁻¹ for each pair of NS_{pooled} samples.

Level	Level	Difference	Std Error	Lower CL	Upper CL	p-value
NS _{pooled} #1	NS _{pooled} #2	0.62	0.80	0.35	0.89	<i>0.0002</i>
NS _{pooled} #1	NS _{pooled} #4	0.48	0.80	0.22	0.76	<i>0.0013</i>
NS _{pooled} #1	NS _{pooled} #5	0.40	0.80	0.13	0.67	<i>0.0054</i>
NS _{pooled} #3	NS _{pooled} #2	0.34	0.80	0.10	0.58	<i>0.0070</i>
NS _{pooled} #1	NS _{pooled} #3	0.28	0.80	0.01	0.55	<i>0.0429</i>
NS _{pooled} #5	NS _{pooled} #2	0.22	0.80	-0.02	0.46	0.0734
NS _{pooled} #3	NS _{pooled} #4	0.21	0.80	-0.03	0.45	0.0990
NS _{pooled} #4	NS _{pooled} #2	0.13	0.80	-0.11	0.37	0.4046
NS _{pooled} #3	NS _{pooled} #5	0.12	0.80	-0.12	0.36	0.5079
NS _{pooled} #5	NS _{pooled} #4	0.09	0.80	-0.15	0.33	0.7250

CL, confidence limit; the p-values reported in italics are significant ($\alpha = 0.05$). The standard error is aggregated (N = 15).

Table 5.12: Lettered Tukey's HSD groupings for the normalized SERS intensity of CV at 1170 cm⁻¹ for each of the five NS_{pooled} samples.

Level	Letters	Mean (unrounded)
NS _{pooled} #1	A	1.5596068
NS _{pooled} #3	B	1.2815953
NS _{pooled} #5	B C	1.1636540
NS _{pooled} #4	B C	1.0739936
NS _{pooled} #2	C	0.9413495

The levels that are not connected by the same letter are significantly different ($\alpha = 0.05$).

Despite the results of the statistical analysis, the pooled NS were found to provide a SERS response that was indeed variable, but not such to prevent sensitivity studies. In other words, the variation observed within a single concentration level (CV 10^{-7} M) was not higher than the variation between different concentration levels in a simulated sensitivity study, as reported in *Figure 5.12*. This was demonstrated by comparing the CV intensity dataset obtained with the NS_{pooled} substrates (#1–#5), with those obtained by measuring CV at lower concentrations, namely 10^{-8} M and 5×10^{-9} M, each with a separate NS_{pooled} substrate. The comparison was achieved by performing an ANOVA F-Test and a Tukey-Kramer's test ($\alpha = 0.05$).

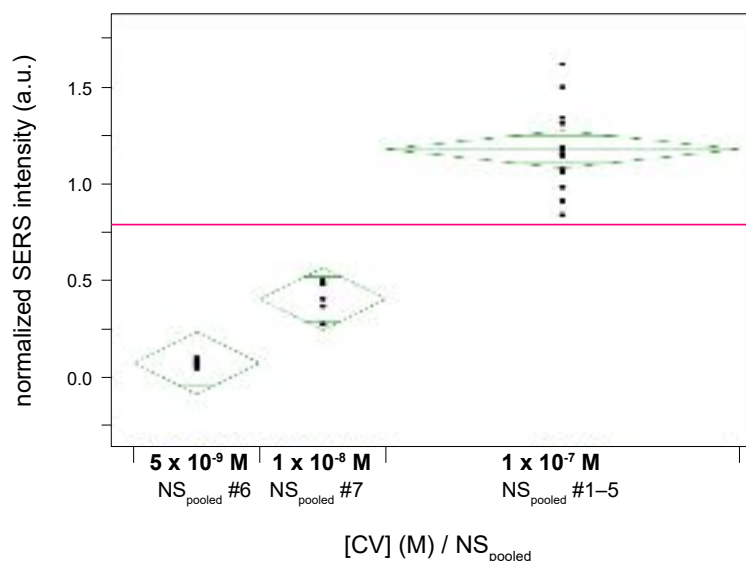


Figure 5.12: ANOVA plot (R^2 0.8960) for the normalized SERS intensity of CV at 1170 cm^{-1} obtained by utilizing different NS_{pooled} as enhancing substrates, and different concentrations of CV: 5×10^{-9} M (NS_{pooled} #6), 10^{-8} M (NS_{pooled} #7), and 10^{-7} M (NS_{pooled} #1–5). The pink line represents the global mean (0.79 ± 0.08 a.u.), while the green rhomboids represent the quartiles relative to each sample group.

The ANOVA F-test allowed for the detection of significant differences within the dataset, with a F value of 90.4931 that was higher than the $F_{2,23}$ critical, 3.422, and a

p-value of <0.0001, which was lower than the 0.05 α level (Tables 5.13 and C.6). The Tukey-Kramer's test revealed that all pairs were significantly different (Tables 5.14 and 5.15). This indicates that, despite the in-sample variability observed in the preceding SERS and statistical tests, the inter-sample variability was larger, allowing for the separation of variance resulting from different analyte concentrations. Therefore, these results support the use of the pooled NS for reliable analytical applications.

Table 5.13: ANOVA F-test for the normalized SERS intensity of CV at 1170 cm^{-1} at different concentrations, and obtained with different $\text{NS}_{\text{pooled}}$ samples.

Source	Df	Sum of Squares	Mean Squares	F value	p-value
[CV]/ $\text{NS}_{\text{pooled}}$ sample	2	5.4243218	2.71216	90.4931	<0.0001
error	21	0.6293892	0.02997		
total	23	6.0537110			

Df, degrees of freedom; $\alpha = 0.05$; $F_{2,23}$ critical = 3.422.

Table 5.14: Tukey's HSD test. Ordered differences of the normalized SERS intensity of CV at 1170 cm^{-1} at different concentrations, and obtained with different $\text{NS}_{\text{pooled}}$ samples.

Level	Level	Difference	Std Error	Lower CL	Upper CL	p-value
[CV] 10^{-7} M/ $\text{NS}_{\text{pooled}}$ #1-5	[CV] 5×10^{-9} M/ $\text{NS}_{\text{pooled}}$ #6	1.11	0.09	0.88	1.33	<0.0001
[CV] 10^{-7} M/ $\text{NS}_{\text{pooled}}$ #1-5	[CV] 10^{-9} M/ $\text{NS}_{\text{pooled}}$ #7	0.78	0.09	0.54	1.00	<0.0001
[CV] 10^{-9} M/ $\text{NS}_{\text{pooled}}$ #7	[CV] 5×10^{-9} M/ $\text{NS}_{\text{pooled}}$ #6	0.3	0.1	0.1	0.6	<i>0.0166</i>

CL, confidence limit; the p-values reported in italics are significant ($\alpha = 0.05$).

Table 5.15: Lettered Tukey's HSD groupings for the normalized SERS intensity of CV at 1170 cm^{-1} at different concentrations, and obtained with different $\text{NS}_{\text{pooled}}$ samples.

Level	Letters	Mean (unrounded)
[CV] 10^{-7} M/ $\text{NS}_{\text{pooled}}$ #1-5	A	1.1786422
[CV] 10^{-8} M/ $\text{NS}_{\text{pooled}}$ #7	B	0.4054540
[CV] 5×10^{-9} M/ $\text{NS}_{\text{pooled}}$ #6	C	0.0729880

The levels that are not connected by the same letter are significantly different ($\alpha = 0.05$).

5.2.2 Morphological characterization: variability and yield

Transmission Electron Microscopy (TEM) was utilized for the morphological characterization of the nanostar formulations, 24 hours after synthesis. No significant differences were observed across different formulations, as the stabilizer does not participate in the synthetic process (TEM micrographs reported in *Appendix B*). For this reason, an extensive morphological analysis is here restricted to the NS/Ct formulation.

A measure that might have some role in increasing the batch-to-batch variability of the optical performance of the nanostars is the morphological yield. As detailed in the introduction of this chapter, these nanostars are obtained via a one-pot, kinetically controlled process, which inherently causes morphological polydispersity of the colloidal product. Such polydispersity might either be the result of the presence of morphological variations within a single family of shapes (*e.g.*, nanostars with varying degree of branching), or be the result of the presence of multiple families of shapes (*e.g.*, nanostars, rods, spheroids, ...). Two different NS/Ct batches were each analyzed in triplicate by TEM, and the morphological yield was determined as the percent ratio of branched nanostructures over the total number of counted nanoparticles ($N = 905$):

$$yield_{morphology}(\%) = \frac{branched}{total} 100 = 79.2\% \quad (5.2)$$

While the micrographs showed a noticeable variability in terms of size (*Figure 5.13*), it was observed that even the smallest nanoparticles present a branched morphology. In more detail, five morphological subtypes were identified, four of which were branched. As illustrated in *Figure 5.14*, 61.3% of the branched nanoparticles exhibited a fully formed, multipodal morphology, which is typical of nanostars obtained by one-pot syntheses, and is in line with the TEM data reported for the same protocol by He *et al.*⁴ As part of this 61.3%, two morphological subtypes, *fI* and *fII*, were identified; the former has a smaller

number of branches, which are relatively elongated, while the latter has a larger number of branches, which appear to have a wider base, as for core enlargement. The remainder 17.9% of the branched nanoparticles are of smaller dimensions ($\approx 1/4$ or smaller) compared to the subtype *f* morphology, and have tripodal (*hI*) or tetrapodal and pentapodal (*hII*) shape. The presence of these two smaller subtypes could be interpreted as a result of halted nanoparticle growth, and might offer insight on the mechanism of nanostar formation.

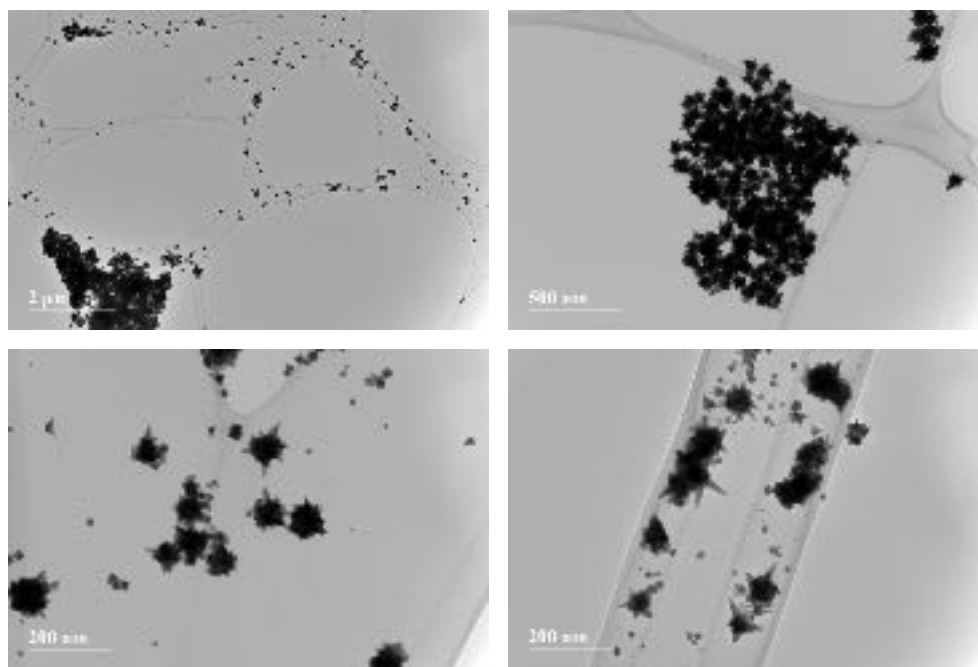


Figure 5.13: TEM micrographs of NS/Ct, obtained from different aliquots from different batches. Polydispersity in terms of size is observed, while the number of non-branched nanoparticles is negligible.

Because the subtype *h* nanoparticles have the smallest dimensions across all subtypes, even compared to the roughly globular subtype *g* morphology (Figure 5.14), it could be reinforced that the two metal precursors, tetrachloroauric acid and silver nitrate, are indeed *co-reduced*, thus allowing silver ions to act as symmetry-breaking shape directors from the early stages of nanoparticle formation. This is in contrast with the mechanism proposed

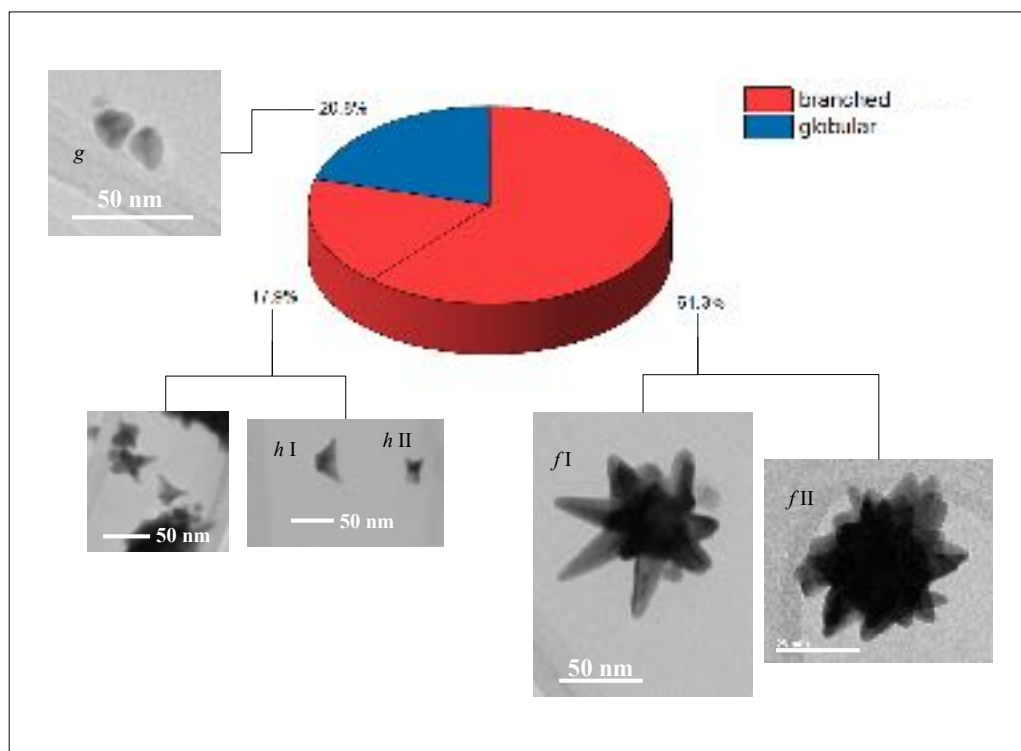


Figure 5.14: Pie chart illustrating the morphological distribution of the analyzed NS/Ct batches. Five subtypes are identified; from left to right, *g*, *hI*, *hII*, *fI*, and *fII*. The same subtypes are found in all other analyzed nanostars formulations (*Appendix B*).

by Cheng *et al.*,²⁵ who first reported this nanostars synthesis. Their proposed step-wise mechanism involves the formation of a gold core first, followed by the development of branches. These are thought to be the result of a delayed, underpotential deposition of silver islands on pre-formed gold cores, which would then elicit anisotropic growth of the remaining gold ions as they are reduced.²⁵ Alternatively, given the presence of very small tri-, tetra-, and pentapodal nanoparticles, as well as the presence of larger nanostar cores *only in concomitance* with shorter and wider branches, it seems more reasonable to propose a concerted mechanism, based on an effective co-reduction of Ag^+ and gold as AuCl_4^- (§ 5.2). Because the two metals are reduced at the same time, alloyed nucleation centers containing twinning defects are produced, thus allowing the anisotropic growth of the

nanocrystals. The anisotropic growth likely begins with the formation of higher-symmetry tri- and tetrapods (subtypes *hI* and *II*), which develop as asymmetric multipods with variable number of branches, as a result of the fabrication process being kinetically driven (subtype *fI*). Once a branching threshold is reached, the remaining precursors in solution are likely reduced and deposited on the formed branched structure, enriching its core portion and resulting in fuller structures with shorter and wider branches (subtype *fII*). The presence of small, globular nanoparticles (subtype *g*) could be explained as products that escaped true kinetic control, reaching energy minima close to the equilibrium shape (*Figure 5.7*). Alternatively or additionally, subtype *g* morphologies could be caused by the presence of reducing agent gradients in the solution during synthesis. As explained in § 4.1, spheroidal morphologies are obtained by lowering the reducing agent concentration, such that it becomes the limiting reagent. Localized volumes with an imbalance of the metal precursors to L-ascorbic acid ratio, combined with the fast reaction kinetics of this fabrication protocol, might generate globular nanostructures. A schematic representation the proposed mechanism is illustrated in *Figure 5.15*

Subtype *f* nanostars were further characterized and other measures were identified, such as the size distribution in terms of spike length, and the equivalent tip-to-tip diameter (*Figure 5.16 a and b*). The latter was obtained by measuring an average of 9 tip-to-tip distances per single nanostar ($N_{NS} = 20$; $N_d = 178$) and represents the diameter of an equivalent sphere inscribing the projected image of the nanostructure. The obtained percent frequency histogram of the equivalent tip-to-tip diameter shows a distribution centered at 139 nm, with mean of 144 nm, and 30 nm standard deviation. This fits a Gaussian distribution with an adjusted R^2 of 0.997 (orange outline in *Figure 5.17*). However, both reduced chi squared value and Anderson-Darling test statistics for the goodness of fit evaluation denote overfitting and departure from normality, respectively ($\chi^2_v = 1.4 \times 10^{-5}$; A-D = 1.16 with p-value <0.005; $\alpha = 0.05$). The departure from normality is also

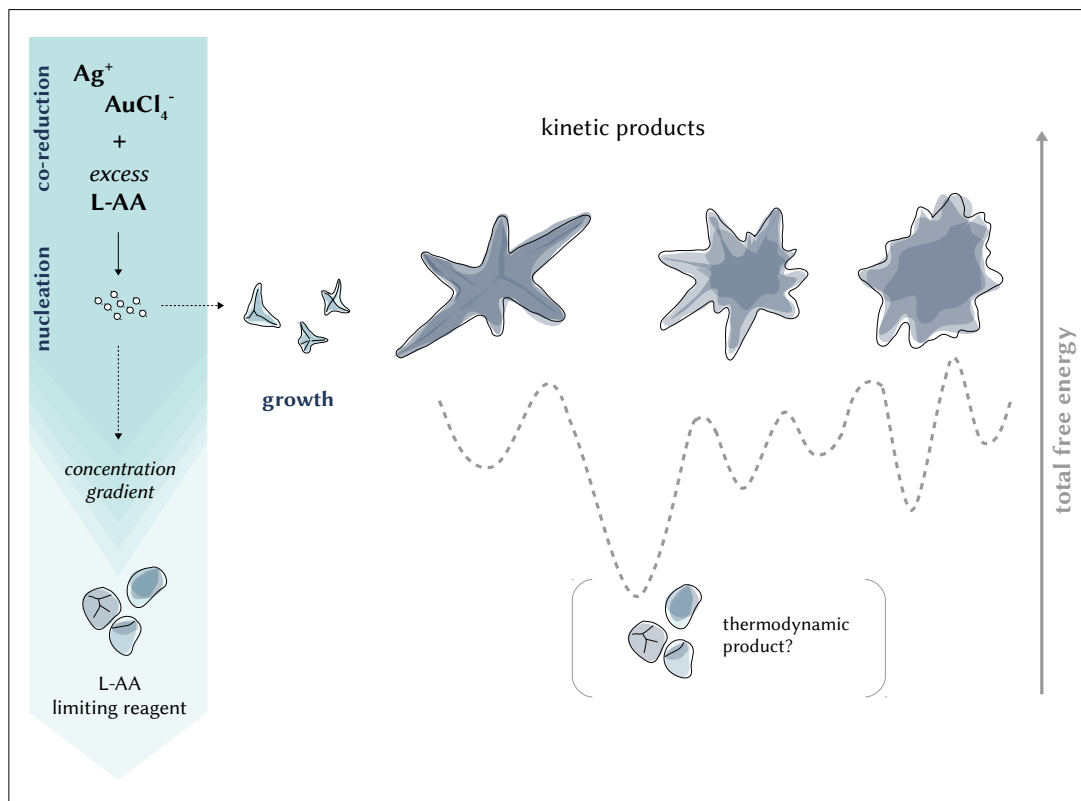


Figure 5.15: Proposed mechanism for the formation of the nanostars utilized in this research.

highlighted by the calculated skewness and excess kurtosis of 0.63 and 0.28, respectively. The equivalent size measurement dataset was found to be better described by a lognormal distribution. As shown in the probability plot at the 95% level of confidence in *Figure 5.17*, this exhibits a smaller Anderson-Darling value of 0.283 and a higher p-value of 0.630. The lognormal distribution describes a population whose logarithm is normally distributed, and it is typical of the size distribution of colloidal systems.^{26,27}

The size distribution of the branches (*Figure 5.16 b*, $N = 187$) is monomodal and polydisperse within a range from 12 to 100 nm, with a median of 35 nm, a mean of 40 nm, and a standard deviation of 18 nm. The calculated skewness is 1.37 and the excess kurtosis is 1.64. The distribution can be interpreted in terms of random branch growth

pattern, with preferential formation of branches of dimensions around the mean value, and occasional longer branches, as expected from previously published data.⁴ Because the number and length of branches are both linked to the number and performance of the colloidal suspension's hot spots (§ 2.2.2), it is hypothesized that they are the contributing factor to the residual variability that was observed after NS pooling.

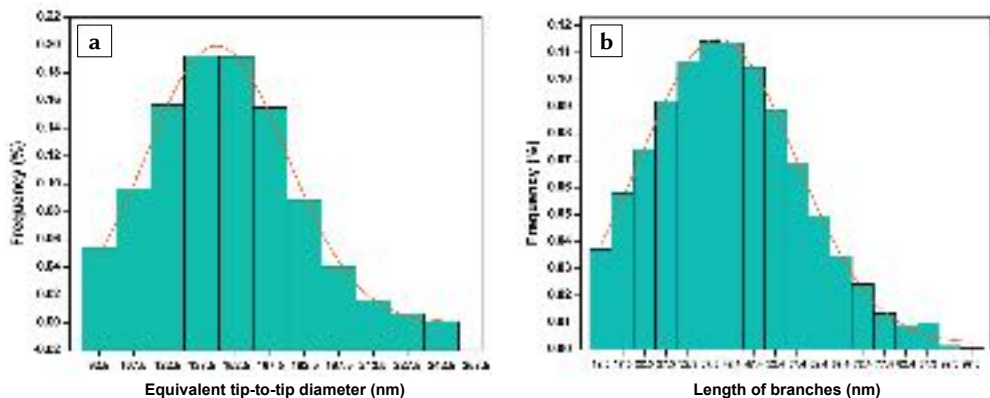


Figure 5.16: Percent frequency histograms representing the size distribution of (a) the equivalent tip-to-tip diameter of the nanostars, and (b) the length of their branches.

5.2.3 Recommendations

The measurements presented thus far demonstrated that, for best reproducibility of the SERS response, pooled NS samples should be utilized as enhancing substrates, as opposed to individual ≈ 1 mL batches. As expected, a narrower range of λ_{LSPR} was exhibited by this substrate preparation ($IQR_{NS} = 39$ nm, $\sigma_{NS} = 25$; $IQR_{NS_{pooled}} = 6$ nm, $\sigma_{NS_{pooled}} = 5$). The narrower range of λ_{LSPR} was mirrored by a reduction in the variability of the signal intensity among SERS spectra obtained by utilizing different pooled NS samples (ANOVA F-test p-values of <0.0001 for the NS, 0.0003 for the NS_{pooled} ; $\alpha = 0.05$). Despite not being removed, the inter-sample NS_{pooled} signal variability was found to have no effect on

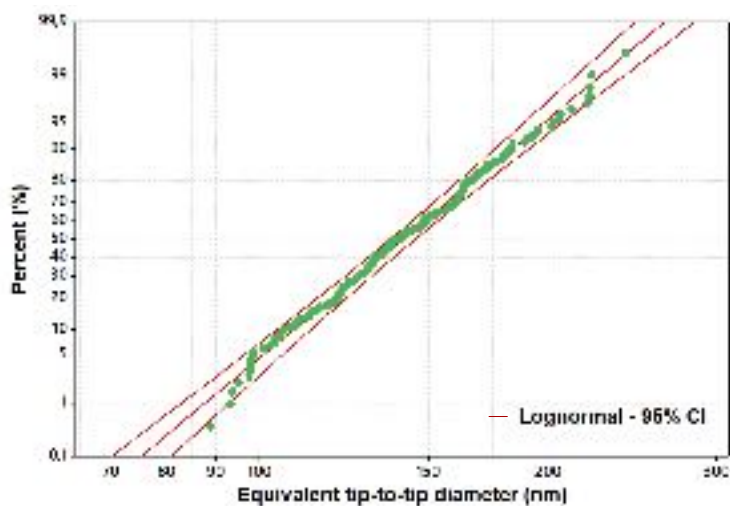


Figure 5.17: Lognormal distribution probability plot for the equivalent tip-to-tip diameter (Anderson-Darling value = 0.283; p-value = 0.630; $\alpha = 0.05$).

the feasibility of sensitivity studies. The intensities obtained from the model analyte CV at a given concentration were significantly different from other concentrations (ANOVA F-test p-value <0.0001, $\alpha = 0.05$). This implies that the developed NS formulations can be confidently utilized as pooled preparations for analytical applications involving sensitivity studies and quantification of species. If individual batches are to be utilized, measurement of the λ_{LSPR} should be strictly performed prior to the SERS measurement(s), and an inter-batch λ_{LSPR} tolerance of ± 20 nm should be adopted.

5.3 AEF as a function of capping species

An overview of the SERS spectra of CV obtained using each of the new effective formulations of nanostars, NS/Ct, NS/Tt, NS/Ac, NS/CO₃²⁻_(c), and NS/CO₃²⁻_(l), is given in *Figure 5.18 a*. When comparing these spectra with the reference Raman spectrum of CV, it can be observed that no foreign bands are present for any of the formulations, indicating

the capping species do not interfere with the analyte's signal. This lack of interference could be caused by the displacement of the capping species by the analyte, a small SERS cross section of the capping species itself, or a combination of the two. Both band intensity and band resolution of the spectra obtained with the new NS formulations is notably higher than that obtained by utilizing the original NS/CTAB formulation, as shown in *Figure 5.18 b*. A way to quantify these differences is by calculating the analytical enhancement factor, AEF.

To achieve this, the SERS profile of CV adsorbed on each of the new colloidal NS formulation, as well as on NS/CTAB, was measured at 24 hours after synthesis, at a fixed set of experimental conditions: analyte incubation time, analyte concentration in the Normal Raman experiment, excitation wavelength, laser power, exposure time, and number of accumulations (§ 3.2.7). The analytical enhancement factor (AEF) was calculated utilizing LeRu *et al.*'s definition:²⁸

$$AEF = \frac{\frac{I_{SERS}}{c_{SERS}}}{\frac{I_{NR}}{c_{NR}}} \quad (5.3)$$

where I_{SERS} is the intensity of the SERS signal at a given reference band, c_{SERS} is the concentration of CV in the SERS experiment, I_{NR} is the intensity of the normal Raman signal at the same reference band, and c_{NR} is the concentration of CV in the Raman experiment. This definition was chosen because it constitutes a reproducible way of accounting for signal magnification by colloidal sols.²⁸

Table 5.17 shows the mean (N = 5) intensities at the marker band for CV, 1170 cm^{-1} , for both Raman and SERS spectra obtained with the various NS formulations as enhancing substrates, together with the associated AEF values. The AEF values relative to CV adsorbed on the newly developed NS formulations are all in the same order of magnitude, ranging from a minimum of 0.8×10^5 to a maximum of 1.6×10^5 , while the CV

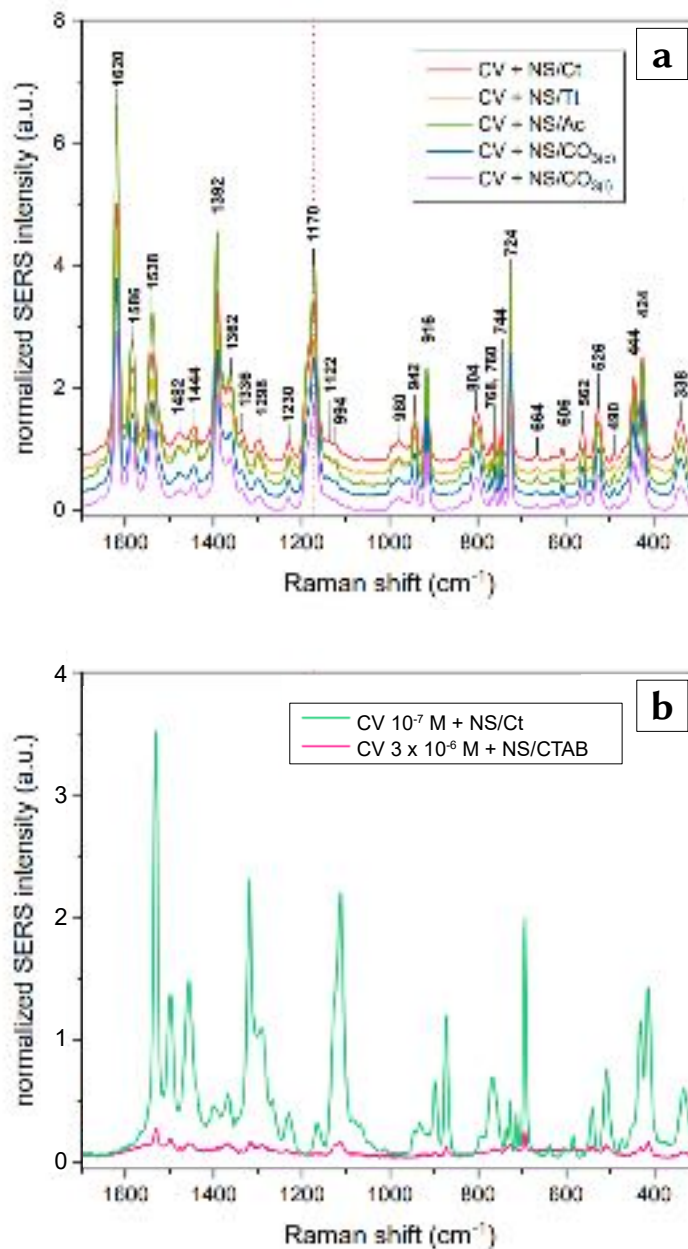


Figure 5.18: (a) SERS spectra of CV at a concentration of 10^{-7} M, obtained using each of the developed alternatively stabilized NS formulations as the enhancing substrate: NS/Ct (red), NS/Tt (yellow), NS/Ac (green), NS/CO₃²⁻(c) (blue), and NS/CO₃²⁻(l) (purple). (b) Comparison between the CV spectrum obtained with NS/Ct as the enhancing substrate (green), and that of CV obtained with the original⁴ NS/CTAB formulation (pink). All spectra were baseline-corrected, and their intensities were normalized to the intensity of the band at 3200 cm^{-1} , assigned to $\nu(\text{OH})$ of water. Spectra in (a) are stacked for ease of comparison.

+ NS/CTAB system ($N = 3$) had an AEF three orders of magnitude smaller (4.1×10^2). As reported in *Figure 5.20* and *Table 5.18*, the ANOVA F-test on the AEF values expectedly showed there is at least one significantly different group ($F_{5,27}$ critical 2.572 < F value 45.0495; p value < 0.0001 > α 0.05). These results were followed by a Tukey-Kramer's test, which confirmed the significant difference between the CV + NS/CTAB system and all other systems, with a p-value < 0.0001 for all pairs (*Table 5.19*). The CV + NS/CO₃²⁻_(l) system was also found to be significantly different than the other systems (*Table 5.20*), with a p-value < 0.0001 when paired with NS/Ct and NS/Ac, and a p-value of 0.0009 and 0.0012, when paired with NS/Tt and NS/CO₃²⁻_(c). This finding was unexpected, since the NS/CO₃²⁻_(l) formulation does not have any bulky capping agent, and has the most negative ζ potential, which, if anything, should increase the likelihood of ionic pairing between the capped surface of the nanoparticle and the positively charged CV. The only factor that could be negatively impacting the AEF is pH. The NS/CO₃²⁻_(l) formulation is the only one of the set to be characterized by an alkaline pH, 9.5, and triarylmethane dyes such as CV are known to undergo basic hydrolysis,²⁹ as depicted in *Figure 5.19*. The hydrolyzed bond participates in the normal modes associated with the 1170 cm⁻¹ band utilized as marker for CV, $\nu_s(\text{CC}_{\text{center}}\text{C})$, $\delta(\text{CCC})_{\text{breathing}}$, $\rho(\text{CH}_3)$, causing a decrease in its intensity.

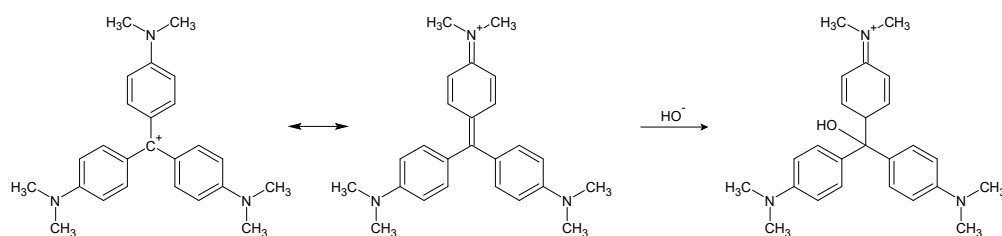


Figure 5.19: Hydrolysis of Crystal Violet in basic conditions.

In order to elucidate whether pH could be the possible cause of the significantly different AEF of the NS/CO₃²⁻_(l) when compared to the other new formulations, a second

Table 5.16: Normalized SERS and Raman intensities at CV's marker band 1170 cm^{-1} and AEF values for each of the CV-NS systems.

System	[CV] (M)	Mean I_{SERS} (a.u.)	I_{SERS} Std Error	Mean I_{NR} (a.u.)	I_{NR} Std Error
CV + NS/Ct	10^{-7}	1.6	0.8		
CV + NS/Tt	10^{-7}	1.46	0.6		
CV + NS/Ac	10^{-7}	1.55	0.3		
CV + NS/ $\text{CO}_3^{2-}(\text{c})$	10^{-7}	1.5	1		
CV + NS/ $\text{CO}_3^{2-}(\text{l})$	10^{-7}	0.93	0.3		
CV + NS/CTAB	3×10^{-6}	0.128	0.003		
CV only	10^{-3}			0.104	0.009

set of analogous SERS measurements were performed utilizing the NS/ $\text{OH}(\text{l})$ formulation. This formulation was previously utilized as a control in the initial stabilization studies discussed in *Chapter 4*, and because it has a pH of approximately 9.5, like NS/ $\text{CO}_3^{2-}(\text{l})$, it could be utilized as an additional point of comparison for measurements of CV in alkaline conditions. The results of the ANOVA F-test that was performed on this dataset are reported in *Figure 5.21* and *Table 5.21*, while *Tables 5.22* and show the results of the post-hoc Tukey's HSD test. The ANOVA F-test was significant ($F_{5,29}$ critical 2.545 < F value 16.6867; p value <0.0001 > α 0.05), as expected, and the Tukey's HSD test allowed two groups to be identified (5.23), the first one containing the NS formulations that have neutral or acidic pH, and the second containing the NS formulations having alkaline pH. This result supports the hypothesis that the lower AEF observed for the CV + NS/ $\text{CO}_3^{2-}(\text{l})$ system can be attributed to the basic hydrolysis of CV, which causes the band at 1170 cm^{-1} to decrease, resulting in a lower AEF.

Despite the difference between NS/ $\text{CO}_3^{2-}(\text{l})$ and the rest of the new formulations, and even though AEF values refer to the whole analyte-substrate system rather than to the substrate alone, this study validates the hypothesis that the alternatively stabilized formulations have superior SERS activity than the original⁴ surfactant-capped formulation. This is attributed to the decreased thickness of the capping agent when compared to the CTAB bilayer (§ 2.2.2.1).

Table 5.17: Normalized SERS and Raman intensities at CV's marker band 1170 cm⁻¹ and AEF values for each of the CV-NS systems.

System	Mean AEF (x 10 ⁵)	AEF Std Error (x 10 ⁵)
CV + NS/Ct	1.6	0.9
CV + NS/Tt	1.4	0.7
CV + NS/Ac	1.5	0.4
CV + NS/CO ₃ ²⁻ (c)	1	1
CV + NS/CO ₃ ²⁻ (l)	0.8	0.4
CV + NS/CTAB	0.0041	0.0001

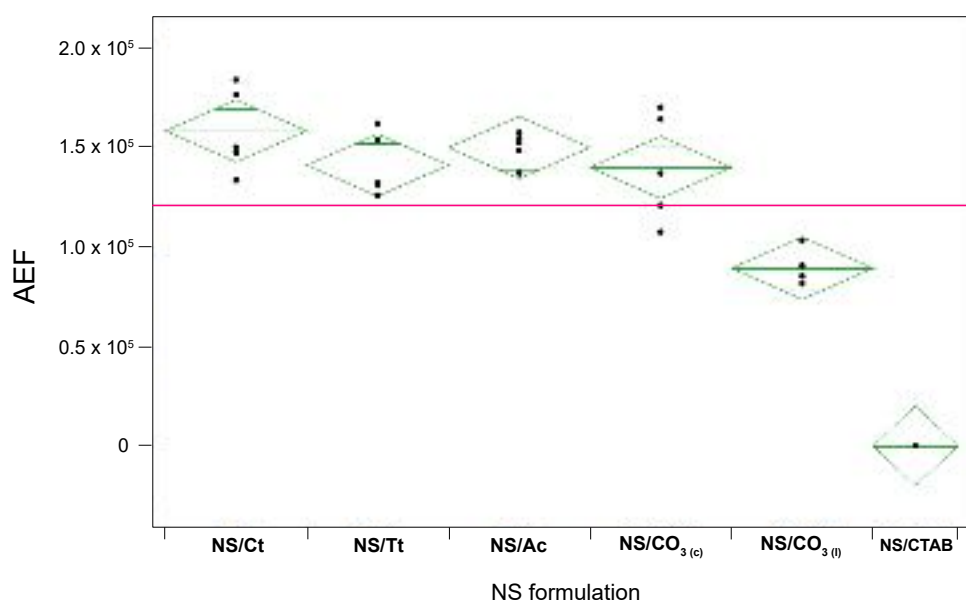


Figure 5.20: ANOVA plot (R^2 0.9110) for the AEF values of the CV-NS systems under study. The pink line represents the global mean ($1.2 \pm 0.5 \times 10^5$), while the green rhomboids represent the quartiles relative to each sample group.

Table 5.18: ANOVA F-test for the AEF values of the CV-NS systems under study.

Source	Df	Sum of Squares	Mean Squares	F value	p-value
CV + NS formulation	5	6.3453×10^{10}	1.269×10^{10}	45.0495	<0.0001
error	22	6197500949	281704589		
total	27	6.9651×10^{10}			

Df, degrees of freedom; $\alpha = 0.05$; $F_{5,27}$ critical = 2.572.

Table 5.19: Tukey's HSD test. Ordered differences of the AEF values of the CV-NS systems under study.

Level	Level	Difference	Std Error	Lower CL	Upper CL	p-value
CV + NS/Ct	CV + NS/CTAB	1.6×10^5	0.1×10^5	1.2×10^5	2.0×10^5	<i><0.0001</i>
CV + NS/Ac	CV + NS/CTAB	1.5×10^5	0.1×10^5	1.1×10^5	1.9×10^5	<i><0.0001</i>
CV + NS/Tt	CV + NS/CTAB	1.4×10^5	0.1×10^5	1.0×10^5	1.8×10^5	<i><0.0001</i>
CV + NS/CO ₃ ²⁻ (c)	CV + NS/CTAB	1.4×10^5	0.1×10^5	1.0×10^5	1.8×10^5	<i><0.0001</i>
CV + NS/CO ₃ ²⁻ (l)	CV + NS/CTAB	0.9×10^5	0.1×10^5	0.5×10^5	1.3×10^5	<i><0.0001</i>
CV + NS/Ct	CV + NS/CO ₃ ²⁻ (l)	0.7×10^5	0.1×10^5	0.4×10^5	1.0×10^5	<i><0.0001</i>
CV + NS/Ac	CV + NS/CO ₃ ²⁻ (l)	0.6×10^5	0.1×10^5	0.3×10^5	0.9×10^5	<i><0.0001</i>
CV + NS/Tt	CV + NS/CO ₃ ²⁻ (l)	0.5×10^5	0.1×10^5	0.2×10^5	0.8×10^5	<i>0.0009</i>
CV + NS/CO ₃ ²⁻ (c)	CV + NS/CO ₃ ²⁻ (l)	0.5×10^5	0.1×10^5	0.2×10^5	0.8×10^5	<i>0.0012</i>
CV + NS/Ct	CV + NS/CO ₃ ²⁻ (c)	0.2×10^5	0.1×10^5	-0.1×10^5	0.5×10^5	0.5329
CV + NS/Ct	CV + NS/Tt	0.2×10^5	0.1×10^5	-0.1×10^5	0.5×10^5	0.5973
CV + NS/Ac	CV + NS/CO ₃ ²⁻ (c)	0.1×10^5	0.1×10^5	-0.2×10^5	0.4×10^5	0.9327
CV + NS/Ac	CV + NS/Tt	0.09×10^5	0.1×10^5	-0.2×10^5	0.4×10^5	0.9585
CV + NS/Ct	CV + NS/Ac	0.09×10^5	0.1×10^5	-0.2×10^5	0.4×10^5	0.9671
CV + NS/Tt	CV + NS/CO ₃ ²⁻ (c)	0.01×10^5	0.1×10^5	-0.3×10^5	0.3×10^5	1.0000

CL, confidence limit; the p-values reported in italics are significant ($\alpha = 0.05$).

Table 5.20: Lettered Tukey's HSD groupings for the AEF values of the CV-NS systems under study.

Level	Letters	Mean (unrounded)
CV + NS/Ct	A	158160.93
CV + NS/Ac	A	149823.59
CV + NS/Tt	A	141007.13
CV + NS/CO ₃ ²⁻ (c)	A	139888.30
CV + NS/CO ₃ ²⁻ (l)	B	89426.80
CV + NS/CTAB	C	410.07

The levels that are not connected by the same letter are significantly different ($\alpha = 0.05$).

Table 5.21: ANOVA F-test for the AEF values of the CV-NS systems under study, compared to CV-NS/OH.

Source	Df	Sum of Squares	Mean Squares	F value	p-value
CV + NS formulation/pH	5	2.5982×10^{10}	5.1963×10^9	16.6867	<0.0001
error	24	7473691258	311403802		
total	29	3.3455×10^{10}			

Df, degrees of freedom; $\alpha = 0.05$; $F_{5,29}$ critical = 2.545.

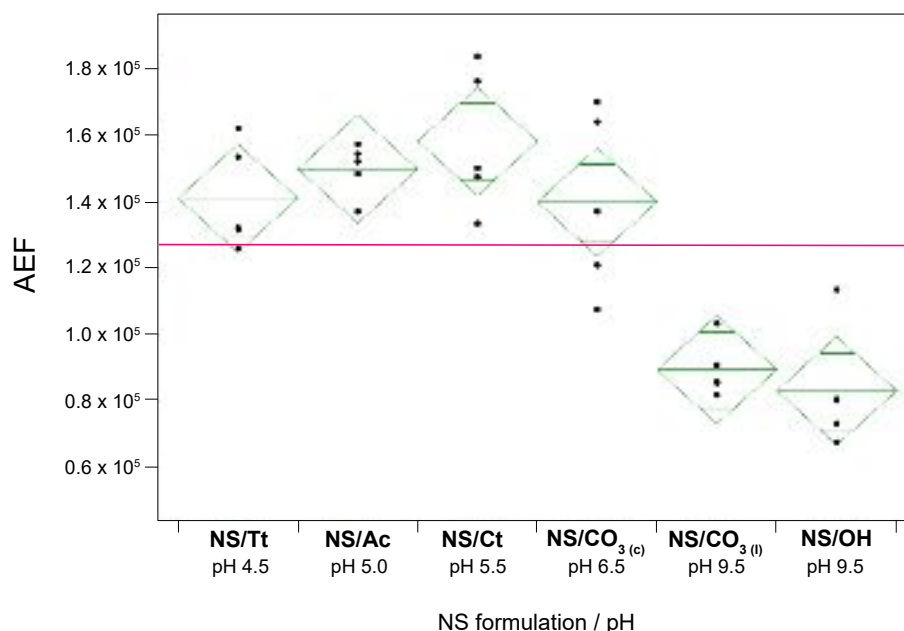


Figure 5.21: ANOVA plot (R^2 0.7766) for the AEF values of the CV-NS systems under study, compared to CV-NS/OH and ordered as a function of pH of the formulation. The pink line represents the global mean ($1.2 \pm 0.5 \times 10^5$), while the green rhomboids represent the quartiles relative to each sample group.

Table 5.22: Tukey's HSD test. Ordered differences of the AEF values of the CV-NS systems under study, compared to CV-NS/OH.

Level	Level	Difference	Std Error	Lower CL	Upper CL	p-value
CV + NS/Ct	CV + NS/OH	0.8×10^5	0.1×10^5	0.4×10^5	1.1×10^5	<i><0.0001</i>
CV + NS/Ct	CV + NS/CO ₃ ²⁻ (l)	0.7×10^5	0.1×10^5	0.3×10^5	1.0×10^5	<i><0.0001</i>
CV + NS/Ac	CV + NS/OH	0.7×10^5	0.1×10^5	0.3×10^5	1.0×10^5	<i><0.0001</i>
CV + NS/Ac	CV + NS/CO ₃ ²⁻ (l)	0.6×10^5	0.1×10^5	0.2×10^5	0.9×10^5	<i>0.0002</i>
CV + NS/Tt	CV + NS/OH	0.6×10^5	0.1×10^5	0.2×10^5	0.9×10^5	<i>0.0003</i>
CV + NS/CO ₃ ²⁻ (c)	CV + NS/OH	0.6×10^5	0.1×10^5	0.2×10^5	0.9×10^5	<i>0.0004</i>
CV + NS/Tt	CV + NS/CO ₃ ²⁻ (l)	0.5×10^5	0.1×10^5	0.2×10^5	0.9×10^5	<i>0.0014</i>
CV + NS/CO ₃ ²⁻ (c)	CV + NS/CO ₃ ²⁻ (l)	0.5×10^5	0.1×10^5	0.2×10^5	0.8×10^5	<i>0.0017</i>
CV + NS/Ct	CV + NS/CO ₃ ²⁻ (c)	0.2×10^5	0.1×10^5	-0.2×10^5	0.5×10^5	0.5834
CV + NS/Ct	CV + NS/Tt	0.2×10^5	0.1×10^5	-0.2×10^5	0.5×10^5	0.6450
CV + NS/Ac	CV + NS/CO ₃ ²⁻ (c)	0.1×10^5	0.1×10^5	-0.2×10^5	0.4×10^5	0.9452
CV + NS/Ac	CV + NS/Tt	0.09×10^5	0.1×10^5	-0.2×10^5	0.4×10^5	0.9666
CV + NS/Ct	CV + NS/Ac	0.09×10^5	0.1×10^5	-0.3×10^5	0.4×10^5	0.9737
CV + NS/CO ₃ ²⁻ (l)	CV + NS/OH	0.06×10^5	0.1×10^5	-0.3×10^5	0.4×10^5	<0.9921
CV + NS/Tt	CV + NS/CO ₃ ²⁻ (c)	0.01×10^5	0.1×10^5	-0.3×10^5	0.4×10^5	1.0000

CL, confidence limit; the p-values reported in italics are significant ($\alpha = 0.05$).

Table 5.23: Lettered Tukey’s HSD groupings for the AEF values of the CV-NS systems under study, compared to CV-NS/OH.

Level	Letters	Mean (unrounded)
CV + NS/Ct (pH 5.5)	A	158160.93
CV + NS/Ac (pH 5.0)	A	149823.59
CV + NS/Tt (pH 4.5)	A	141007.13
CV + NS/CO ₃ ²⁻ _(c) (pH 6.5)	A	139888.30
CV + NS/CO ₃ ²⁻ _(l) (pH 9.5)	B	89426.80
CV + NS/OH (pH 9.5)	B	83063.75

The levels that are not connected by the same letter are significantly different ($\alpha = 0.05$).

Table 5.24: λ_{LSPR} and Extinction at λ_{LSPR} of the pooled NS formulations over time.

Formulation	24 hours after synthesis				2 weeks after synthesis				1 month after synthesis			
	λ_{LSPR} (nm)		Extinction (a.u.)		λ_{LSPR} (nm)		Extinction (a.u.)		λ_{LSPR} (nm)		Extinction (a.u.)	
	Mean	σ	Mean	Std Error	Mean	σ	Mean	Std Error	Mean	σ	Mean	Std Error
NS/Ct	688	4	1.481	0.003	678	3	0.855	0.002	662	2	1.439	0.003
NS/Tt	675	2	1.483	0.001	630	6	0.216	0.004	623	2	0.439	0.002
NS/Ac	678	3	1.460	0.001	673	1	1.343	0.003	665	0	1.4304	0.0002
NS/CO ₃ ²⁻ _(c)	675	1	1.409	0.005	667	3	1.455	0.002	670	5	1.35	0.09
NS/CO ₃ ²⁻ _(l)	688	1	1.465	0.001	686	2	1.390	0.007	683	2	1.399	0.002

5.4 Shelf life of the new NS formulations

To characterize the shelf life of the developed NS formulations, a minimum of three time points were chosen for testing: 24 hours after synthesis (t_0), after 2 weeks, and after 1 month. In addition, the NS/Ct and NS/CO₃²⁻_(c) formulations were also evaluated after 4 months (*vide infra*). Each formulation was prepared as a set of 7 individual NS batches, stored at room temperature, and pooled at the moment of analysis, following the recommendations reported in § 5.2.3. All NS_{pooled} formulations were analyzed via extinction spectroscopy and their λ_{LSPR} was ensured to conform to the tolerance recommendations outlined in § 5.2.3; both λ_{LSPR} and extinction at λ_{LSPR} are reported in Table 5.24.

Table 5.25: Observations on the visual state of coagulation of the NS formulations over time.

Formulation	24 hours after synthesis	2 weeks after synthesis	1 month after synthesis
NS/Ct	no coagulation	no coagulation	no coagulation
NS/Tt	no coagulation	advanced coagulation	advanced coagulation
NS/Ac	no coagulation	no coagulation	some coagulation
NS/CO ₃ ²⁻ _(c)	no coagulation	no coagulation	no coagulation
NS/CO ₃ ²⁻ _(l)	no coagulation	no coagulation	some coagulation, discoloration

Observations on the visual state of coagulation are reported in *Table 5.25* for each of the selected time points. The NS/Tt formulation was the only one to display advanced signs of coagulation at the 2 weeks mark, while 2 out of the remaining 4 formulations, namely NS/Ac and NS/CO₃²⁻_(l), displayed signs of coagulation at the 1 month mark. Because of their observed visual stability at the 1 month mark, the NS/Ct and NS/CO₃²⁻_(c) formulations were also studied at a longer period mark, 4 months after synthesis. According to these observations, it was hypothesized that the formulations with the longest shelf life are NS/Ct and NS/CO₃²⁻_(c), followed by CO₃²⁻_(l) ≈ NS/Ac, and NS/Tt.

It is important to note that the shelf life of a SERS-active substrate is critical for establishing recommendations for use in analytical practice. However, no guideline for shelf life determination of colloidal nanoparticles has been issued yet.³⁰ As a result, the approach that has been adopted for the determination of the shelf life of the NS formulations has been in part borrowed by current practices in pharmaceutical quality control. These practices are typically based on three steps: (1) choosing an appropriate stability-limiting response, (2) determining the response's acceptance criteria, and (3) fitting the means of the response over time with a regression model, generally linear.³¹ The shelf life can then be determined as the x-coordinate of the intersection point between the 95% confidence interval band and the acceptance criterion value, in the direction of the slope of the regression function, as schematized in *Figure 5.22*.³¹

In the case of SERS-active formulations, a suitable stability-limiting response can be identified with the normalized SERS intensity of a given analyte band; as stability decreases

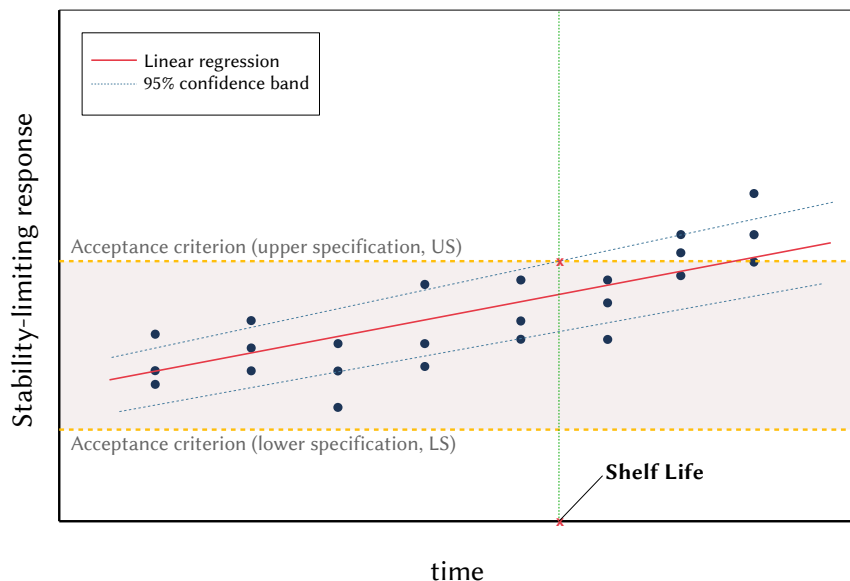


Figure 5.22: Schematics of the method based on linear regression utilized by the pharmaceutical industry for the determination of the shelf life of a product. The line of best fit is shown in red, the upper and lower 95% confidence bands are shown as dashed blue lines, and the upper and lower specification limits of the acceptance criterion are shown as yellow dashed lines. The x-coordinate of the point corresponding to the intersection between the (upper) 95% confidence band and the (upper) specification limit of the acceptance criterion corresponds to the calculated shelf life of the product under study. The upper confidence band and specification limit were chosen because the slope of the regression line is positive; for linear regression models with a negative slope, the lower confidence band and specification limit are utilized instead.

over time, the formulation coagulates, and thus, the SERS intensity is expected to increase because of the ongoing nanoparticle aggregation (§ 2.2.1.2). Therefore, measurements over time of the normalized SERS intensity can provide a platform for the characterization of the shelf life of the NS formulations.

This approach, while straightforward, poses a few inconveniences, such as the necessity of a sampling window that is long enough to allow for the observation of a clear (linear) trend over time, for which the change in slope is significant. This is only likely to be observed in relatively short terms (weeks to months) for formulations with poor stability,

in which the onset of the aggregation is early enough to observe full coagulation of the suspended phase over the observed period. A statistically significant linear trend was only observed for the NS/Tt formulation only (R^2 0.8207), in accordance with the visual observations that were made of the formulations reported in *Figure 5.25*.

For this reason, comparison of the SERS intensities at the different time points was chosen to be performed by two-tailed *and* right-tailed Student's t-tests (α 0.05). The two-tailed test was utilized to verify stability within acceptance values (*vide infra*), while the right-tailed test was utilized as an additional tool to identify the onset of aggregation within samples that were still within acceptable ranges. This type of test would indeed detect early increases in the mean SERS intensity, which, as discussed, are related to colloid aggregation, and thus, aid in making more informed decisions on whether to label a formulation at a given time point as stable or unstable. The Student's t-tests were implemented as pair-wise comparisons with a representative t_0 reference dataset, as a means to adopt the previously mentioned concept of *acceptance criteria* utilized in the pharmaceutical industry for shelf life determination. As the name suggests, and as depicted in *Figure 5.22*, the acceptance criteria are a set of upper and lower specification limits that determine the range of acceptability of a stability-limiting response. In pharmaceutical industry applications, these values must take into account aspects such as human safety as it relates to a drug's dose and degradation products; in the case of the NS formulations, these values must take into account the natural spread that data can have *independently* of time. As seen in § 5.2, the SERS intensity-based variation among different NS_{pooled} can be significant, and thus, the t_0 reference dataset must be representative of its spread.

The dataset that was chosen to build the t_0 reference with, was the same as that utilized for the study of the pH effect on the AEF in the preceding section (*Figure 5.21* and *Tables 5.21–5.23*). Since the statistical analysis of this dataset by Tukey's HSD test revealed the existence of two groups (A and B, *Table 5.23*), and since all sub-groups

Table 5.26: Mean and σ of the time zero reference SERS intensities of CV at 1170 cm^{-1} utilized for the shelf life study.

Reference group	Formulations to be referenced to	I_{SERS} mean	σ
A	NS/Ct, NS/Tt, NS/Ac, and $\text{NS/CO}_3^{2-}_{(c)}$	1.5	0.2
B	$\text{NS/CO}_3^{2-}_{(l)}$	0.9	0.1

Group A: NS/Ct, NS/Tt, NS/Ac, and $\text{NS/CO}_3^{2-}_{(c)}$; *Group B:* $\text{NS/CO}_3^{2-}_{(l)}$ and $\text{NS/OH}_{(l)}$.

(formulations) are homoskedastic, the intensities obtained with group A formulations (NS/Ct, NS/Tt, NS/Ac, and $\text{NS/CO}_3^{2-}_{(c)}$) were pooled together and utilized as t_0 reference for comparison at successive time points of group A NS formulations. A second t_0 reference for the evaluation of the $\text{NS/CO}_3^{2-}_{(l)}$ formulation was instead compiled by aggregating the intensities obtained with group B formulations ($\text{NS/CO}_3^{2-}_{(c)}$ and NS/OH). The mean and σ for each of the two t_0 references are reported in *Figure 5.26*.

The results of all Student's t-tests are shown in *Table 5.27*, and the shelf life estimates are summarized in *Table 5.28*. As expected, the formulation with the shortest shelf life was NS/Tt, whose time points were all significantly different from the reference data set at t_0 , with $\text{Prob} > |t|$ of 0.0407 and 0.0005 for the 2 weeks and 1 month time points, respectively. At the 2 weeks mark, no significant difference from the t_0 reference was detected for NS/Ac and $\text{NS/CO}_3^{2-}_{(c)}$, which is consistent with the visual observations of the colloids. As for the 1 month mark, NS/Ac had $\text{Prob} > |t|$ of 0.0879, thus not significantly different from the t_0 reference. However, the right-tailed test resulted in a $\text{Prob} > t$ of 0.0439, which reflects a shift of the data points towards higher intensity values (*Figure 5.23 a*). This can be attributed to the small level of aggregation that was observed visually. A mirrored behavior was observed at the 1 month mark for the $\text{NS/CO}_3^{2-}_{(l)}$ formulation (*Figure 5.23 b*), for which the two-tailed test yielded a $\text{Prob} > |t|$ of 0.0005, and the right-tailed test resulted in a $\text{Prob} > t$ of 0.9998. This indicates overall instability, and it is reflective of the the shift of the data points towards lower SERS intensity values. A faint color was observed for this

sample, which may be associated with a lower concentration of suspended nanoparticles, such as in the most advanced stages of aggregation. In this case, the enhancing effects of the aggregation-induced hotspots formation are superseded by the overall poor SERS enhancement given by the reduction in suspended nanoparticle concentration.

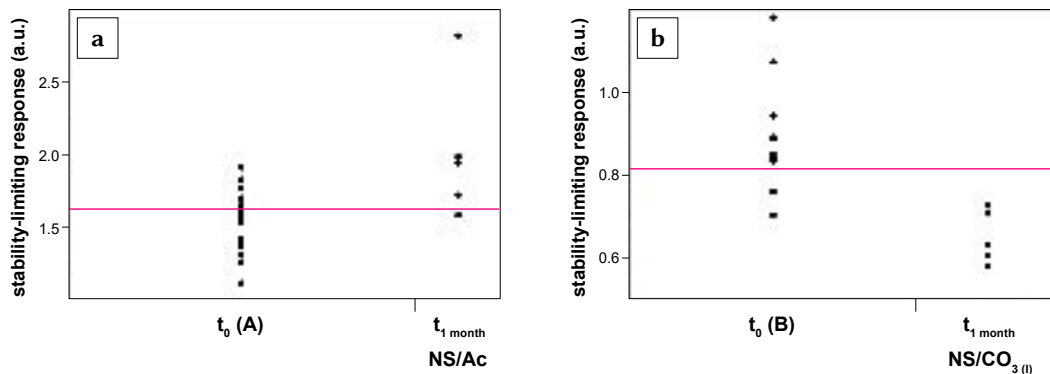


Figure 5.23: Scatter plot comparison of the 1 month time point samples of (a) NS/Ac and (b) NS/CO₃^{2-(I)}, with their respective t_0 references, A and B. The pink lines represent the global means, which are 1.62 ± 0.06 for the A t_0 -NS/Ac $t_{1\text{month}}$ pair, and 0.81 ± 0.04 for the B t_0 -NS/CO₃^{2-(I)} $t_{1\text{month}}$ pair.

The NS/Ct formulation exhibited no significant changes at the 2 weeks time point (Prob > |t| 0.2472), but had significant differences at the two successive time points of 1 and 4 months, with Prob > |t| of <0.0001 and 0.0266, respectively. Despite no signs of coagulation were visually observable, some level of aggregation had in fact occurred, as the Prob > t was <0.0001 for the 1 month mark, and 0.0133 for the 4 months mark. As for the NS/CO₃^{2-(c)} formulation at the second week mark, it produced SERS intensities that were flagged as significantly different from the t_0 reference, with a Prob > |t| of <0.0001. Since the right-tailed test yielded a Prob > t of 1.0000, which is not significant. Since no discoloration was observed as in the case of NS/CO₃^{2-(I)}, this point was treated as an anomaly. Indeed, the same formulation exhibited no statistically significant changes at

Table 5.27: Shelf lives of the NS formulations: t-test results.

Formulation	time point 1	time point 2	Prob > t	Prob >t
NS/Ct	24 hours (A)	2 weeks	0.2472	0.8764
	24 hours (A)	1 month	<0.0001	<0.0001
	24 hours (A)	4 months	0.0266	0.0133
NS/Tt	24 hours (A)	2 weeks	0.0407	0.0204
	24 hours (A)	1 month	0.0005	0.0002
NS/Ac	24 hours (A)	2 weeks	0.1543	0.0771
	24 hours (A)	1 month	0.0879	0.0439
NS/CO ₃ ²⁻ (c)	24 hours (A)	2 weeks	<0.0001	1.0000
	24 hours (A)	1 month	0.6583	0.3292
	24 hours (A)	4 months	0.2121	0.1060
NS/CO ₃ ²⁻ (l)	24 hours (B)	2 weeks	0.2040	0.1020
	24 hours (B)	1 month	0.0005	0.9998

both 1 and 4 months, compared to its t_0 reference. For this reason, it was identified as the formulation with longest shelf life among the studied array. A quantitative estimate of the formulations' shelf lives is summarized in Table 5.28.

Table 5.28: Shelf lives of the NS formulations.

Formulation	Estimated shelf life
NS/Ct	<1 month
NS/Tt	≪ 2 weeks
NS/Ac	<1 month
NS/CO ₃ ²⁻ (c)	≥ 4 months
NS/CO ₃ ²⁻ (l)	≈ 2 weeks

The final stability can be formalized as follows:

$$NS/Tt \ll NS/CO_3^{2-}(l) < NS/Ac < NS/Ct \ll NS/CO_3^{2-}(c) \quad (5.4)$$

5.5 Summary

The studies discussed in this chapter concerned the SERS activity, morphological variability, and shelf life of the new NS formulations, and allowed for the establishment of best practice recommendations for the use of the nanostars in analytical applications.

For best reproducibility of the SERS response, it is suggested that pooled NS samples be utilized as enhancing substrates, in place of individual ≈ 1 mL batches. Pooled NS samples exhibited a narrower range of λ_{LSPR} , which resulted in a reduction of the variability of the signal intensity in SERS experiments. Residual inter-sample variability in the SERS performance of NS_{pooled} substrates was attributed to morphological polydispersity at the nanostar's branches level (number of branches per nanostar and length of branches). However, the NS_{pooled} variability was not sufficient to impede sensitivity studies. In a mock sensitivity study, the intensities obtained from model analyte CV at three different concentration were statistically significant, implying that the developed NS formulations can be reliably utilized as pooled preparations for analytical applications involving sensitivity studies and quantification of species.

Finally, it was determined that the formulation with highest shelf life was the NS/CO₃²⁻_(c), which maintained a statistically constant SERS performance for a period of 4 months. The NS/CO₃²⁻_(c) formulation was utilized as the enhancing substrate in a number of applications involving the detection of opiates and opioids, which are outlined in *Chapter 9*.

REFERENCES

- [1] Gomes de Mesquita, A.H.; MacGillavry, C.H.; Eriks, K. The structure of triphenylmethyl perchlorate at 85°C. *Acta Crystallogr.*, **1965**, *18*, 437–443.
- [2] Cañamares, M.V.; Chenal, C.; Birke, R.L.; Lombardi, J.R. DFT, SERS, and Single-Molecule SERS of Crystal Violet. *J. Phys. Chem. C*, **2008**, *112*, 20295–20300.
- [3] Zhou, L.; Zhou, J.; Lai, W.; Yang, X.; Meng, J.; Su, L.; Gu, C.; Jiang, T.; Pun, E.Y-B.; Shao, L.; Petti, L.; Sun, X.W.; Jia, Z.; Li, Q.; Han, J.; Mormile, P. Irreversible accumulated SERS behavior of the molecule-linked silver and silver-doped titanium dioxide hybrid system. *Nat. Commun.*, **2020**, *11*, 1785-1–1785-10.
- [4] He, S.; Kang, M.W.C.; Khan, F.J.; Tan, E.K.M.; Reyes, M.A.; Kah, J.C.Y. Optimizing gold nanostars as a colloid-based surface-enhanced Raman scattering (SERS) substrate. *J. Opt.* **2015**, *17*, 1–13.
- [5] Muehlethaler, C.; Leona, M.; Lombardi, J.R. Towards a validation of surface-enhanced Raman scattering (SERS) for use in forensic science: repeatability and reproducibility experiments. *Forensic Sci Int.*, **2016**, *268*, 1–13.
- [6] Hao, F.; Nehl, C.L.; Hafner, J.H.; Norlander P. Plasmon Resonances of a Gold Nanostar. *Nano Lett.*, **2007**, *7*(3), 729–732.
- [7] Kumar, P.S.; Pastoriza-Santos, I.; Rodríguez-González, B.; García de Abajo, F.J.; Liz-Marzán, L.M. High-yield synthesis and optical response of gold nanostars. *Nanotechnology*, **2007**, *19*(1), 015606-1–015606-6.
- [8] Minati, L.; Benedetti, F.; Chiappini, A.; Speranza, G. One-step synthesis of star-shaped gold nanoparticles. *Colloids Surf., A*, **2014**, *441*, 623–628.
- [9] Sau, T.K.; Rogach, A.L. Nonspherical Noble Metal Nanoparticles: Colloid-Chemical Synthesis and Morphology Control. *Adv. Mater.*, **2010**, *22*, 1781–1804.
- [10] Gilroy, K.D.; Ruditskiy, A.; Peng, H-C.; Qin, D.; Xia, Y. Bimetallic Nanocrystals: Syntheses, Properties, Applications. *Chem. Rev.*, **2016**, *116*, 10414–10472.
- [11] Xia, Y. Xia, X.; Peng, H-C. Shape-Controlled Synthesis of Colloidal Metal Nanocrystals: Thermodynamic versus Kinetic Products. *J. Am. Chem. Soc.*, **2015**, *137*(25), 7947–7966.

- [12] Arrhenius, S.A. Über die Dissociationswärme und den Einfluß der Temperatur auf den Dissociationsgrad der Elektrolyt. *Z. Phys. Chem.*, **1889**, *4*, 96–116.
- [13] Atkins, P.; de Paula, J.; Keeler, J. *Atkins' Physical Chemistry*, Eleventh edition, Oxford University Press: Oxford, 2018.
- [14] Studies on the reactions of $[\text{AuCl}_4]^-$ with different nucleophiles in aqueous solution. *Dalton Trans.*, 2014, *43*, 8620–8632. Durović, M.D.; Puchta, R.; Bugarčić, Ž.D.; van Eldik, R.
- [15] Xia, Y.; Xiong, Y.; Lim, B.; Skrabalak, S.E. Shape-Controlled Synthesis of Metal Nanocrystals: Simple Chemistry Meets Complex Physics? *Angew. Chem. Int. Ed.* **2009**, *48*, 60–103.
- [16] Marcus, R.A. Electron Transfer Reactions in Chemistry: Theory and Experiment (Nobel Lecture). *Angew. Chem., Int. Ed.*, **1993**, *32*(8), 1111–1121.
- [17] Lee, P.C.; Meisel, D. Adsorption and Surface Enhanced Raman of Dyes on Silver and Gold Sols. *J. Phys. Chem.*, **1982**, *86*, 3391–3395.
- [18] John Turkevich, J.; Stevenson, P.C.; Hillier, J. A study of the nucleation and growth processes in the synthesis of colloidal gold. *Discuss. Faraday Soc.*, **1951**, *11*, 55–75.
- [19] Frens, G. Controlled nucleation for the regulation of the particle size in monodisperse gold suspensions. *Nature* **1973**, *241*, 20–22.
- [20] McFarland, A.D.; Young, M.A.; Dieringer, J.A.; Van Duyne, R.P. Wavelength-scanned surface-enhanced Raman spectroscopy. *J. Phys. Chem. B* **2005**, *109*, 11279–11285.
- [21] van Dijk, T.; Sivapalan, S.T.; Devetter, B.M.; Yang, T.K.; Schulmerich, M.V.; Murphy, C.J.; Bhargava, R.; Carney, P.S. Competition Between Extinction and Enhancement in Surface Enhanced Raman Spectroscopy. *J. Phys. Chem. Lett.* **2013**, *4*(7), 1193–1196.
- [22] Sivapalan, S.T.; Devetter, B.M.; Yang, T.K.; van Dijk, T.; Schulmerich, M.V.; Carney, P.S.; Bhargava, R.; Murphy, C.J. Off-Resonance Surface-Enhanced Raman Spectroscopy from Gold Nanorod Suspensions as a Function of Aspect Ratio: Not What We Thought. *ACS Nano* **2013**, *7*(3), 2099–2105.
- [23] Goos P.; Meintrup D. *Statistics with JMP: Hypothesis Tests, Anova and Regression*. Wiley: Hoboken, 2016.

- [24] Paolella, M.S. Linear Models and Time-Series Analysis: Regression, ANOVA, ARMA and GARCH. In *The Wiley Series in Probability and Statistics*; Balding, D.J., Cressie, N.A., Fitzmaurice, G., Goldstein, H., Givens, G., Molenberghs, G., Scott, D.W., Tsay, R.S., Smith, A.F.M., Eds.; John Wiley & Sons Ltd: Oxford, 2019.
- [25] Cheng, L-C.; Huang, J-H.; Chen, H.M.; Lai, T.C.; Yang, K.Y.; Liu, R.S.; Hsiao, M.; Chen, C-H.; Here, L-J.; Tsaid, D.P. Seedless, silver-induced synthesis of star-shaped gold/silver bimetallic nanoparticles as high efficiency photothermal therapy reagent. *J. Mater. Chem.*, **2012**, *22*, 2244–2253.
- [26] Granqvist, C.G; Buhrman, R.A. Ultrafine metal particles. *J. Appl. Phys.*, **1876**, *47*, 2220–2222.
- [27] Kiss, L.B.; Söderlund, J.; Niklasson, G.A.; Granqvist, C.G. New approach to the origin of lognormal size distributions of nanoparticles. *Nanotechnology*, **1999**, *10*(1), 25–28.
- [28] Le Ru, E.C.; Blackie, E.; Meyer, M.; Etchegoin, P.G. Surface Enhanced Raman Scattering Enhancement Factors: A Comprehensive Study. *J. Phys. Chem. C*, **2007**, *111*, 13794–13803.
- [29] Beach, S.F.; Hepworth, J.D.; Mason, D.; Swarbrick, E.A. A kinetic study of the hydrolysis of crystal violet and some terminal and bridged analogues. *Dyes Pigm.*, **1999**, *42*(1), 71–77.
- [30] Murphy, C.J.; Buriak, J.M. Best Practices for the Reporting of Colloidal Inorganic Nanomaterials. *Chem. Mater.*, **2015**, *27*(14), 4911–4913.
- [31] International Council on Harmonisation of Technical Requirements for Registration of Pharmaceuticals for Human Use (ICH), ICH Evaluation of Stability Data, Q1E, 2003.

The stabilizer-metal interaction: strength and adsorption modes

6.1 Experimental estimates of the citrate-AuAg interaction

As discussed in *Chapter 2*, a colloidal surface environment that is conducive to a high SERS performance has ideally three characteristics; it is composed of molecules that (1) have a small SERS cross section, (2) have low steric hindrance, and (3) adsorb less strongly to the surface than the target analyte does. The first two characteristics have already been addressed in *Chapters 4* and *5*. Small molecules with low SERS cross-section (citrate, tartrate, acetate, carbonate) were utilized to cap AuAg nanostars, substituting the original bulky stabilizer, CTAB. The obtained colloidal formulations demonstrated a higher SERS performance than the CTAB-capped nanostars (§ 5.3). The third and last aspect, the strength of the stabilizer-substrate interaction, is discussed in this chapter. An experimental method based on ζ potential titrations was developed as a means to obtain an estimate of the adsorption constant of model stabilizer trisodium citrate. In addition, infrared spectroscopy was utilized to characterize the adsorption mode of the stabilizer onto the surface of the bimetallic nanostars.

6.2 ζ potential titrations

While electrophoretic light scattering (ELS) measurements are typically utilized to assess the sign and extent of surface charging of a given system, they can also be utilized to extrapolate information regarding the strength of the interactions between a surface and associated charged species. Previously (§ 4, *Figure 4.9*), it was noted that the behavior of the ζ potential as a function of the concentration of model stabilizer trisodium citrate resembles an adsorption isotherm. By fitting the experimental data points with a suitable

adsorption model, the K_{ad} between the stabilizer and the AuAg surface can be estimated. Moreover, if the chosen adsorption model is thermodynamically derived,¹ it is possible to calculate the change in free energy upon adsorption, ΔG_{ad} . A similar strategy has been utilized in SERS studies to estimate the strength of the interaction between analyte and substrate,^{2,3} and an example³ of this is presented in *Chapter 8* of this dissertation. These SERS studies permitted the compilation of a set of reference K_{ad} values for the adsorption of drugs on citrate-reduced gold substrates. These values, ranging from $1.0 \pm 0.3 \times 10^5$ to $93 \pm 12 \times 10^5 \text{ M}^{-1}$, were then utilized as a term of comparison to evaluate the likelihood of citrate *being displaced* by analytes of comparable properties, when introduced in the NS/Ct formulation during SERS sample preparation.

Although drugs of forensic and public health concern are extremely varied in structure (*Figure 6.1*), they generally contain aromatic and lone-pair-bearing moieties, which are thought to be the functional groups that enable the adsorption of these substances on plasmonic surfaces.²⁻⁴ Provided that case-specific differences are accounted for (*e.g.*, the diversity of the colloidal substrate's chemical identity, the excitation wavelength, the presence of aggregating agents, ...), K_{ad} values obtained from the literature can be used as references to evaluate the potential ability of the colloidal nanostars to offer a tailored surface environment for the SERS detection of molecules of forensic and public health interest. Proof of concept data are illustrated in *Chapter 8*.

Ideal displacements of the stabilizer by the analyte are achieved when the former has an adsorption constant significantly smaller than the latter. To accommodate for accuracy differences in the K_{ad} values resulting from utilizing different analytical techniques (ELS for the metal-stabilizer K_{ad} , SERS for the metal-analyte K_{ad}), the two constants should differ by at least one order of magnitude for optimal prediction of displacement effects. Therefore, for applications in forensic and clinical toxicology, ideal SERS substrates

should have a metal-stabilizer K_{ad} around 10^4 M^{-1} or less, as the adsorption constants of common drugs of interest are $\approx 10^5 \text{ M}^{-1}$ (Figure 6.1).

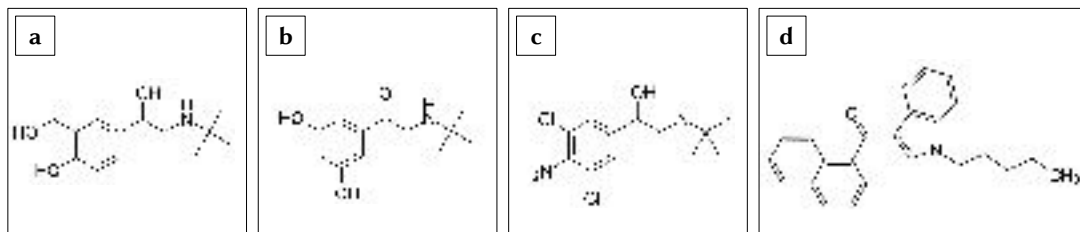


Figure 6.1: Four drugs of forensic and public health interest whose K_{ad} with citrate-reduced Au nanospheres are known: (a) salbutamol (β agonist, $K_{ad} 1.0 \pm 0.3 \times 10^5 \text{ M}^{-1}$);² (b) terbutaline (β agonist, $K_{ad} 4.4 \pm 0.5 \times 10^5 \text{ M}^{-1}$);² (c) clenbuterol (β agonist, $K_{ad} 9 \pm 2 \times 10^5 \text{ M}^{-1}$);² (d) JWH-018 (synthetic cannabinoid, $K_{ad} 93 \pm 12 \times 10^5 \text{ M}^{-1}$).³

As detailed in the Methods section (§ 3.2.3), two ζ potential datasets were obtained at two different temperatures: 10°C , as a mild refrigeration condition, and 20°C , as a room temperature condition. By using these two different conditions, recommendations regarding the most suitable storage conditions for the developed colloidal nanostars can be made; a significantly higher (*e.g.*, half an order of magnitude or higher) adsorption constant at a colder temperature would indicate the suitability of storing the nanostar formulations under refrigeration, possibly increasing their shelf life. The ζ potential values at each titration point were calculated from the directly measured electrophoretic mobilities, as described in § 3.2.3, utilizing *Equations 3.7* and *3.8*. Details on these calculations are reported in *Appendix E*.

When plotting the adsorption isotherms, possible contributions to the ζ potential from species other than citrate must be considered. As discussed in *Chapter 4*, the unmodified nanostars possess some surface charge. Even if this is not sufficient to stabilize the colloidal sol, it must be taken into consideration when studying the effects of an added species on the change in magnitude of the surface charge. Of the species that are present in solution,

the most likely to contribute to the surface charge is Cl^- , as they are known to interact with gold and silver. For example, the $\nu(\text{Ag}-\text{Cl})$ band at around 240 cm^{-1} is frequently observed in SERS spectra obtained by utilizing hydroxylamine chloride-reduced Ag nanospheres, which have a surface environment comprised of chloride ions.^{5,6} The same band is also observed when other Au or Ag colloidal systems are aggregated by the addition of inorganic chloride salts like NaCl or MgCl_2 .⁷ Chloride species, however, have been reported to have weaker interactions with bulk and nanoscale gold, compared to citrate.^{8,9} Recalling that the bimetallic nanostars utilized for this research are primarily composed of gold (Au:Ag 18:1), and that the surface charge of these (unmodified) nanostars is primarily caused by adsorbed chloride ions, the first addition of citrate to such a colloidal sol is expected to displace chloride ions. As a result, citrate is expected to cause an initial, *not purely additive* change in the magnitude of the ζ potential. This means that utilizing the ζ potential of the unmodified nanostars as the baseline, although informative when assessing the efficacy towards stabilization (*Chapter 3*), is not quantitatively adequate for the present scope. Because of the expected chloride ions displacement by citrate, the ζ potential value associated with the first addition of citrate would estimate *by defect* the actual change in the surface charge magnitude. Therefore, all ζ potential values were corrected by a factor corresponding to the lowest citrate titration point, and thus all ζ potential values were plotted as differences, $\Delta\zeta$. These differences represent the successive increases in surface charge upon addition of citrate, after initial displacement of chloride ions that are present in solution as a result of the synthetic process. Finally, the absolute value of these differences was taken, thus obtaining a set of positive responses, which allows the data to be fitted using common adsorption models. In these models, the response is always positive, as it corresponds to an increasing surface coverage, while the ζ potential caused by anionic species, such as trisodium citrate, is necessarily negative.

In earlier sections of this dissertation, such as 2.3 and 4.2.1, the Langmuir adsorption model was mentioned.^{10,11} This adsorption model can be mathematically expressed as:

$$\theta = \frac{y_i}{y_{sat}} = \frac{K_{ad} [adsorbate]_i}{1 + K_{ad} [adsorbate]_i} \quad (6.1)$$

where θ is the surface coverage, y_i and y_{sat} are the measured responses at the i th adsorbate concentration and at saturation, respectively, and K_{ad} is the adsorption constant expressed in M^{-1} . Notably, the Langmuir model is founded on a series of assumptions:¹²

1. there is a finite and fixed number of adsorption sites on a surface;
2. all adsorption sites are equivalent to each other;
3. only one molecule can adsorb per each adsorption site;
4. there is no cooperativity between adsorbate molecules;
5. the adsorption does not progress after the formation of a surface monolayer.

While the first three assumptions could be reasonably applied to the NS/Ct system, the last two might result in an unrealistic modeling of a *charged* adsorbate layer, which could in fact experience intramolecular attractions or repulsions, or organize in ad-layers. In order to avoid the *a priori* exclusion of cooperative adsorption and formation of ad-layers, the *Hill expansion* of the Langmuir model was chosen to fit the $\Delta|\zeta|$ data instead.¹³ The Hill-Langmuir model lies on the same assumptions of the pure Langmuir model, with the exception that *cooperativity* between adsorbate molecules is taken into account. As a matter of fact, this equation was initially established to model the allosteric behavior of hemoglobin binding of molecular oxygen.¹³ According to the Hill expansion of the Langmuir model, cooperativity is fixed, indicating it depends on the system and not on the adsorbate saturation conditions, and it can be modeled by an exponent, n , the *Hill coefficient*.¹⁹ In a system that obeys a pure Langmuir behavior, there is no cooperativity,

and n is equal to unity.¹⁹ Therefore, the adsorption can mathematically be described by the following expression:^{13,19}

$$\theta = \frac{y_i}{y_{sat}} = \frac{K_{ad}[adsorbate]_i^n}{1 + K_{ad}[adsorbate]_i^n} = \frac{[adsorbate]_i^n}{K_d[adsorbate]_i^n} \quad (6.2)$$

where K_d is the desorption constant expressed in M units, which is equal to $1/K_{ad}$, both in value and thermodynamic meaning. The Hill coefficient n is greater than unity in those cases in which the adsorption of a molecule favors the subsequent adsorption of other molecules (positive cooperativity), whether they are the same adsorbate species or not. On the other hand, when the adsorption of a molecule prevents or discourages further adsorption of species, the n coefficient is less than unity.¹⁹ This means that, if there is lateral cooperativity among citrate molecules, then $n \neq 1$; if, on the other hand, no lateral cooperativity takes place, $n = 1$, and a Langmuir model can be utilized to represent the adsorption of citrate onto the nanostars.

If *Equation 6.2* is adapted to ζ potential terms, the Hill expansion of the Langmuir adsorption model becomes:

$$\theta = \frac{\Delta|\zeta|_i}{\Delta|\zeta|_{sat}} = \frac{K_{ad}[Ct]_i^n}{1 + K_{ad}[Ct]_i^n} = \frac{[Ct]_i^n}{K_d[Ct]_i^n}; \quad (6.3)$$

$$\Delta|\zeta|_i = \Delta|\zeta|_{sat} \frac{[Ct]_i^n}{K_d[Ct]_i^n} \quad (6.4)$$

which is the form that was utilized to fit the experimental data, at the two different temperatures of 10 and 20°C, as shown in *Figure 6.2*. The Hill model demonstrated a good fit, with adjusted R^2 values of 0.9926 for the dataset at 10°C, and 0.9885 at 20°C, χ^2_v values of 1.0742 and 1.0644 at 10 and 20°C, respectively, and residual plots following a distribution close to normal at both temperatures (*Appendix C, Figure C.2*). The equations, whose parameters are summarized in *Table 8.1*, demonstrate the existence of a positive

cooperativity among the adsorbate molecules, with a Hill coefficient larger than 1 at both probed temperatures. An explanation of the positive cooperative binding of citrate onto the nanostars could be given by the establishment of hydrogen bonds among individual adsorbate molecules. This type of interaction has been reported to stabilize the multi-layer citrate crown of traditional gold nanoparticles in a series of publications.^{14–18} For example, Park *et al.*¹⁶ proposed a multi-layer citrate network model held by hydrogen bonds and van der Waals forces to describe the capping environment of citrate-reduced gold nanospheres, and Wall *et al.*¹⁴ proposed a similar hydrogen-bonded network with possible ad-layer formation. Although the nanostars are bimetallic, and thus, chemically different from pure gold nanoparticles, they are mostly composed of gold (§ 3.2.1). For this reason, an interpretation of the adsorption cooperativity of citrate on AuAg nanostars in terms of hydrogen bonding seems reasonably justified by the cited literature.

Table 6.1: Fitting and thermodynamic parameters for the NS/Ct system, at 10 and 20°C.

Parameter	10°C	20°C
Adjusted R ²	0.9926	0.9885
χ^2_v	1.0742	1.0644
$\Delta\zeta_{sat}$ (mV)	26 ± 1	20.6 ± 0.8
n	2.8 ± 0.3	3.4 ± 0.4
K_d (M)	4.9 ± 0.5 × 10 ⁻⁴	4.4 ± 0.4 × 10 ⁻⁴
K_{ad} (M ⁻¹)	2.0 ± 0.3 × 10 ³	2.3 ± 10 ³
K_{eq}	≈ 4.9 ± 0.5 × 10 ⁻⁴	≈ 2.3 ± 0.2 × 10 ³
ΔG_{ad} (kcal/mol)	-4.36 ± 0.08	-4.58 ± 0.05

The uncertainties of the $\Delta\zeta_{sat}$ and n parameters correspond to the respective standard error; the uncertainties on the K_d values are the 95% confidence interval; all uncertainties of derived parameters are calculated using error propagation rules.

The K_d values were directly extrapolated from the Hill fit, and were 4.9 ± 0.5 × 10⁻⁴ M at 10°C, and 4.4 ± 0.4 × 10⁻⁴ M at 20°C, where the associated uncertainties were calculated as the two-tailed 95% confidence intervals. These values were then utilized to calculate the

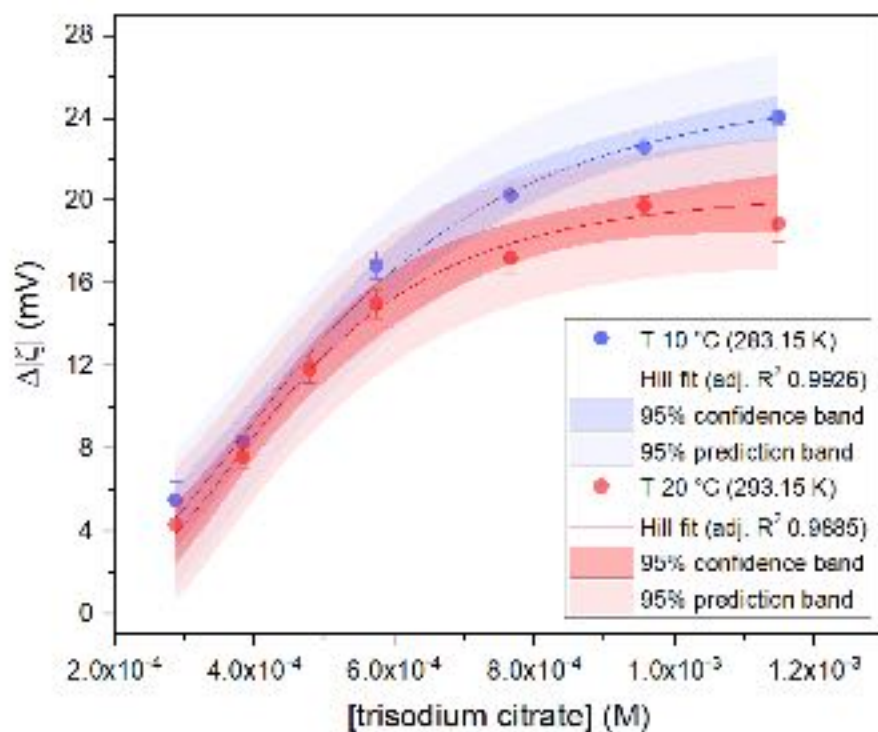


Figure 6.2: Plots of the change in the absolute value of the ζ potential, $\Delta|\zeta|$, as a function of increasing concentration of trisodium citrate, at 10°C (blue) and 20°C (red). The data points were fitted to the Hill expansion of the Langmuir adsorption model (Equation 6.4).

adsorption constants, K_{ad} , which were $2.0 \pm 0.3 \times 10^3 \text{ M}^{-1}$ at 10°C and $2.3 \pm 0.2 \times 10^3 \text{ M}^{-1}$ at 20°C. These constants indicate a strength that is two orders of magnitude lower than those reported for drugs of forensic and public health interest on plasmonic substrates, which are typically in the order of 10^5 M^{-1} , as reported earlier, in Figure 6.1. This is ideal for SERS applications involving drugs of similar structures, as it can be expected that they will be able to displace the citrate stabilizer and achieve a close contact with the enhancing substrate. As illustrated in § 2.3, assuming that the K_{ad} between individual analyte molecules (“ K_{AA} ”) is smaller than any other attraction at play, the SERS signal will likely be arising from adsorbed molecules lying at minimized distances from the

nanostar's surface, thus yielding maximized SERS intensities. Of course, while case-by-case specificities do play an important role in SERS experiments and the stabilizer might not be displaced as a result of these, a highly characterized surface such as that of the NS/Ct formulation does provide an ideal and advantageous starting point for the rational development of analytical protocols. As it has been discussed in the premise of this dissertation, knowing the nature and behavior of the components of a colloidal enhancing substrate is of paramount importance for the successful development of an optimized SERS-based analytical method.

Another thermodynamic parameter that can be derived from the Hill isotherm is the change in the free energy of adsorption, ΔG_{ad} . Earlier in this section, it was specified that this parameter can be directly derived from the constant of adsorption *only if* the model utilized to mathematically describe the isotherm is thermodynamically derived. Although it is common practice to utilize the adsorption constant obtained by *any* given adsorption model as numerically equivalent to the thermodynamic equilibrium constant K_{eq} and calculate the ΔG_{ad} , this approximation is only correct in *some* cases.^{1,20} In fact, not all adsorption models have a thermodynamic meaning, thus not all adsorption constants numerically represent the equilibrium constant between adsorbed and non-adsorbed ligand on a surface. It has been demonstrated^{1,20} that this numerical equivalence is only possible for K_{ad} obtained by the Langmuir model *and* expressed in M_{-1} , *provided that* the adsorbate is either a neutral or a diluted, weakly charged species such as an organic acid. As explained earlier, because the Hill model is an expansion of the Langmuir equation, the K_{ad} derived by it can be properly considered numerically equivalent to K_{eq} , such that:¹

$$\Delta G = -RT \ln(K_{eq}) \approx -RT \ln[K_{ad}(1M^{-1})] \quad (6.5)$$

where R is the ideal gas constant ($8.314 \text{ J} \times \text{K}^{-1} \times \text{mol}^{-1}$; $0.001987 \text{ kcal} \times \text{K}^{-1} \times \text{mol}^{-1}$) and T is the absolute temperature. This numerical equivalence allowed for the calculation of the ΔG_{ad} at the two temperatures of 10 and 20°C, which were $-4.3 \pm 0.1 \text{ kcal/mol}$ and $-4.58 \pm 0.05 \text{ kcal/mol}$, respectively. This indicates a spontaneous process.

When comparing the adsorption behavior at the two temperatures, the differences are not drastic, and a small increase in the magnitude of the adsorption is observed at the lower temperature. This trend might suggest two aspects, the shelf life might not improve by storing the NS/Ct under refrigerated conditions, and, more interestingly, the mechanism driving the adsorption of citrate to the nanostars surface might be *chemisorptive* in nature. Indeed, an increase of the apparent adsorption capacity with increasing temperature can be associated to chemisorption phenomena.²¹

In this case, the chemisorption of citrate to the nanostars is likely weak, because the order of magnitude of the K_{ad} at both probed temperatures is around 10^3 M^{-1} . This finding is consistent with what was reported by Al-Johani *et al.* for another type of citrate-capped colloidal nanoparticle.²² In their work, Al-Johani *et al.*²² studied the interaction modes of citrate on borohydride-reduced monometallic gold nanospheres, determining that citrate is chemisorbed to an essentially neutral gold surface, via coordinating covalent bonding. The results obtained thus far for the bimetallic nanostars seems to suggest a similar trend, where the gold-silver surface is both alloyed and in its elemental oxidation state (XPS results, § 4.3.1), and the carboxylate-based stabilizers interact with it by specific adsorption (Extinction spectroscopy and ζ potential vs conductivity studies, § 4.2). For citrate, this specific adsorption is likely the result of a weak chemisorption.

6.3 FTIR spectroscopy: coordination modes

The experimental determination of the adsorption mode of the model stabilizer trisodium citrate was performed by Fourier transform infrared (FTIR) spectroscopy, under attenuated total reflection (ATR) conditions. These conditions are achieved by placing the sample in tight contact with an optically denser medium, into which the IR source is shined at an angle greater than the critical angle¹. Because of the refractive index difference between the sample and the optically denser medium, part of the internally propagating wave enters the sample, in the form of an evanescent wave (*Figure 6.3*).²³ If the sample is IR active, the evanescent wave can be absorbed by it,²⁴ and this absorption can be recorded in terms of attenuation of the total internally reflected radiation.²⁵ The optically dense medium is called internal reflection element (IRE), and it is an IR-transparent, inorganic crystal, typically ZnSe or Ge.²³ This spectral acquisition mode is particularly convenient when studying thin films and capping systems on nanoparticles, as these samples can be directly drop-cast onto the IRE and analyzed *while* or *after* drying.²⁵⁻²⁷ Alternatively, dried residues of nanoparticles can be obtained separately, and pressed onto the IRE with no further sample preparation.²⁵

In addition to the convenient sample preparation offered by the ATR acquisition mode, some level of signal amplification can be achieved. Signal amplification is achieved via the IRE geometry, which controls the number of internal reflections that occur inside the crystal, before the propagating wave reaches the detector. When more than a single internal reflection is performed along the crystal-sample boundary, the spectral signal carried through the evanescent wave gets multiplied, and thus, amplified.^{23,24,28-30} When studying gold and silver nanoparticles, an additional contribution to signal amplification may derive from the presence of the nanoparticles themselves, as these can elicit a phenomenon

¹In optics, the critical angle is the incidence angle above which total internal reflection occurs.

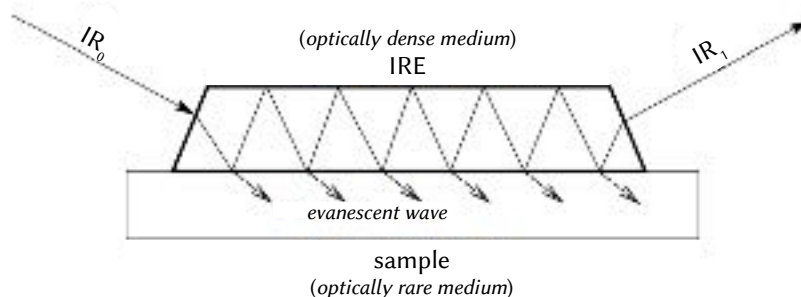


Figure 6.3: Schematic representation of the ATR configuration. The IR source, IR_0 , is introduced inside the IRE at an angle above the critical angle. The light is internally reflected *and* attenuated by the generation of an evanescent wave. The exiting IR light, IR_1 , is different from IR_0 and carries the vibrational information of the sample.

analogous to SERS, called Surface Enhanced Infrared Absorption (SEIRA).^{26,31} Both the number of internal reflections and the possibility of working under SEIRA conditions allow for the acquisition of spectra of adsorbates at nanoparticles' surfaces with a good signal-to-noise ratio, which would normally be unachievable as a result of the low concentration at which these species are present.

Besides providing evidence of the nature of an adsorbate on a nanoparticle surface, infrared spectroscopy is also able to provide information on the type of coordination that a ligand adopts with respect to a surface.^{32,33} In the specific case of carboxylates, it was noted by Deacon and Phillips³⁴ that the coordination chemistry of these compounds can be identified on the basis of the difference between the symmetric and asymmetric carbonyl stretching modes, $\Delta\nu(\text{COO}^-)$, as compared to that of the free, ionic carboxylate in solution. As a result of the observation of the IR spectra of a collection of formate and acetate complexes and correlation to their X-Ray crystallographic structures, Deacon and Phillips' were able to formulate the following guidelines for the assignment of the coordination modes of carboxylates:^{34,35}

- unidentate coordination — $\Delta\nu(\text{COO}^-)_{\text{sample}} \gg \Delta\nu(\text{COO}^-)_{\text{freeion}}$;
- bidentate coordination — $\Delta\nu(\text{COO}^-)_{\text{sample}} \ll \Delta\nu(\text{COO}^-)_{\text{freeion}}$;
- bridging coordination — $\Delta\nu(\text{COO}^-)_{\text{bidentate}} \ll \Delta\nu(\text{COO}^-)_{\text{sample}} \leq \Delta\nu(\text{COO}^-)_{\text{freeion}}$.

These $\Delta\nu(\text{COO}^-)$ trends have been demonstrated computationally to be the result of the changes in the COO^- bond length and angle, which are valid also for compounds in aqueous solution.³⁵ Free, ionic carboxylates in solution are approximately symmetrical and have equidistant carbon-oxygen pairs.^{33,35,36} However, upon unidentate coordination, the COO^- functional group experiences a shortening of the carbonyl bond and a lengthening of the carboxyl bond (C–O of C–O ··· M), while upon bidentate coordination, the COO^- angle becomes narrower.³⁵

In the present study, the NS/Ct formulation was studied after prior purification and drying under vacuum. The purification is a very important step in the analysis of adsorbates on colloidal nanoparticles, as it allows for the removal of unadsorbed species. Here, it allowed for the removal of unadsorbed citrate, and thus, for the characterization of the *actual* capping layer on the nanostars. As shown in *Figure 6.4*, the spectral profile of the purified and dried NS/Ct residue (blue line) shows two main bands at 1586 and 1396 cm^{-1} . These bands were assigned to the asymmetric and symmetric stretching modes of carboxylate, respectively, $\nu_{as}(\text{COO}^-)$ and $\nu_s(\text{COO}^-)$. Compared to the spectrum obtained from drop-casting aqueous trisodium citrate onto the IRE (red line in *Figure 6.4*), the $\nu_{as}(\text{COO}^-)$ band shows a shift of 18 cm^{-1} towards higher wavenumbers. This is typically observed in carboxylates that experience an *asymmetric* change in the bond length of the COO^- group. As detailed earlier, this can be caused by the formation of an unidentate complex with a metal.^{32,34} In an unidentate complex, the carboxylate group loses its symmetry and acquires a pseudo-ester configuration.³⁷ This new configuration is a reflection of the new electronic distribution within the carboxylate moiety, in such

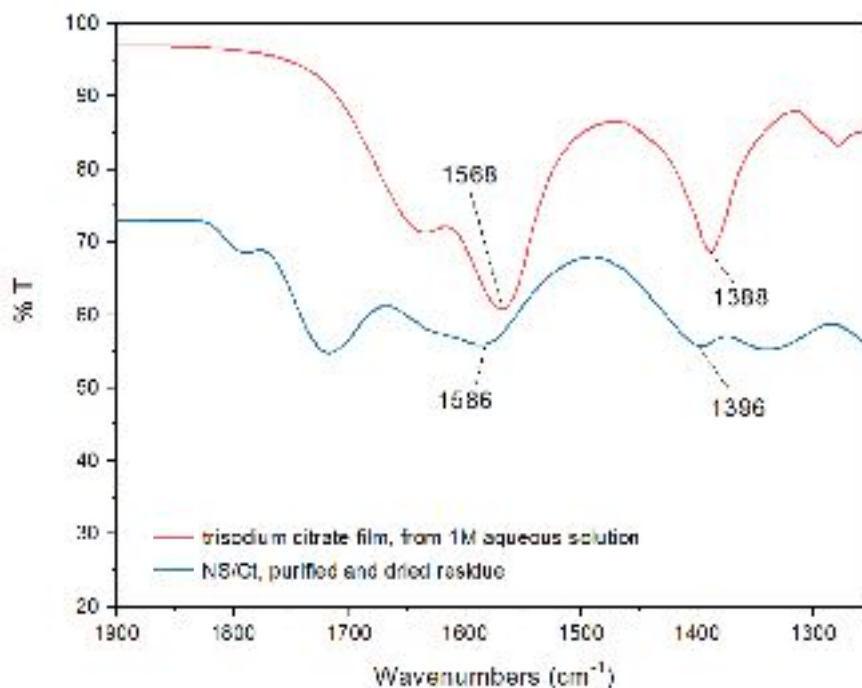


Figure 6.4: FT-IR ATR spectra of the free citrate ion (*red*), obtained by drop-casting a 1 M trisodium citrate solution on the IRE, and of the purified and dried NS/Ct residues (*blue*). Spectra are on the same scale but stacked for ease of comparison.

a way that the coordinated oxygen acquires more single bond character, thus resulting in C–O bond lengthening, and the uncoordinated oxygen acquires more double bond character, thus resulting in bond shortening.³⁷ This causes a shift of the $\nu_{as}(\text{COO}^-)$ band at higher wavenumbers ($\approx \nu_{as}(\text{C}=\text{O})$) and of the $\nu_s(\text{COO}^-)$ band at slightly lower wavenumbers ($\approx \nu_{as}(\text{C}-\text{O})$),³⁷ compared to the free, ionic citrate. These shifts ultimately result in the $\Delta\nu(\text{COO}^-)$ trends described by Deacon and Phillips for unidentate coordination complexes.^{32,34,35}

Since the calculated $\Delta\nu(\text{COO}^-)$ for the free ion is 180 cm^{-1} , while the $\Delta\nu(\text{COO}^-)$ for the NS/Ct residue is 190 cm^{-1} , the citrate can be inferred to be interacting with the bimetallic

surface by forming a *unidentate coordinate covalent bond* with it. This binding mode is in accordance to the concentration-coordination relationship trends highlighted by Al-Johani *et al.*²² in their study on citrate-capped gold monometallic nanospheres. Solid state NMR (SS-NMR) measurements of the citrate-capped nanospheres residues showed the ligand attained three different binding mode patterns as a function of surface coverage. At low concentrations, citrate interacted with the gold surface with a bridging coordination mode, then switched to a bidentate mode with increasing concentration, and finally to a unidentate mode when the surface coverage was near saturation. On the basis of the ζ titration results (§ 6.2), the concentration used to prepare the NS/Ct formulation was near the $[\text{Ct}]_{\text{sat}}$ for the system.

The $\Delta\nu(\text{COO}^-)$ value observed for NS/Ct is also in accordance with the hypothesis of hydrogen bonding among the different citrate units that was formulated as a result of the ζ titration experiments. Deacon and Phillips³⁴ report that unidentate coordination complexes of carboxylates with $\Delta\nu(\text{COO}^-)$ values lower than 200 cm^{-1} are associated with hydrogen bonding interactions between the non-coordinating C–O (\approx C=O) and other species that might be present in the system.

The same procedure was replicated for the NS/Tt and NS/Ac formulations. As reported in *Figure 6.5*, the $\nu_{as}(\text{COO}^-)$ band of the NS/Tt dried residue showed a 6 cm^{-1} shift towards higher wavenumbers, compared to free, ionic tartrate. As illustrated for citrate, this is typical of carboxylates that are coordinated to a metal by unidentate mode, in that this type of coordination alters the equivalent partial double bond character of the uncoordinated carboxylate functional group, causing the asymmetric stretching mode to move towards wavenumbers that are characteristic of a higher C=O double bond character. At the same time, a shift towards lower wavenumbers is expected for the $\nu_s(\text{COO}^-)$ band. However, this is not observed, and the $\nu_s(\text{COO}^-)$ band of tartrate in the nanoparticle residue is shifted upwards to 1403 cm^{-1} , compared to 1394 cm^{-1} of free tartrate. This unexpected shift could

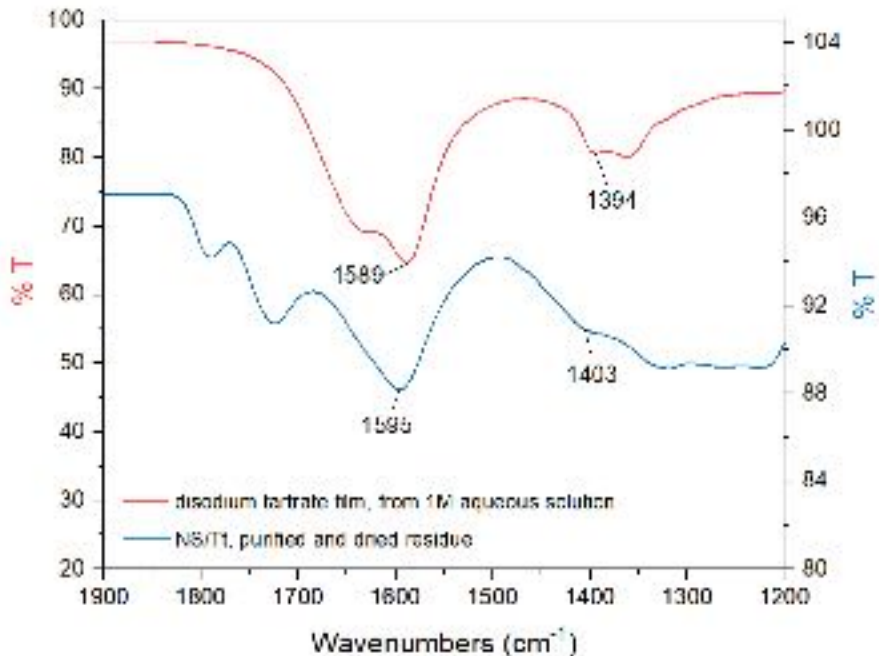


Figure 6.5: FT-IR ATR spectra of the free tartrate ion (*red*), obtained by drop-casting a 1 M disodium tartrate solution on the IRE, and of the purified and dried NS/Tt residues (*blue*).

be the result of the presence of a population of different coordination modes, as the band at 1403 cm^{-1} is characterized by significant broadening. If the $\Delta\nu(\text{COO}^-)$ value of the NS/Tt residue is compared to that of the free ligand, it can be observed that it is approximately unvaried, as the former is 192 cm^{-1} , while the latter is 195 cm^{-1} . As outlined earlier, $\Delta\nu(\text{COO}^-)$ values that stay close to those of the ionic ligand are associated with bridging coordination modes, in which each oxygen atoms of the carboxylate group coordinates a metal atom. A mixture of this surface configuration and a double unidentate bridging is therefore hypothesized for the NS/Tt formulation (*Figure 6.7*).

The NS/Ac residue, showed a small shift of the $\nu_{as}(\text{COO}^-)$ band, from 1551 cm^{-1} of the free reference acetate to 1559 cm^{-1} (*Figure 6.6*). The $\nu_s(\text{COO}^-)$ band also exhibited a

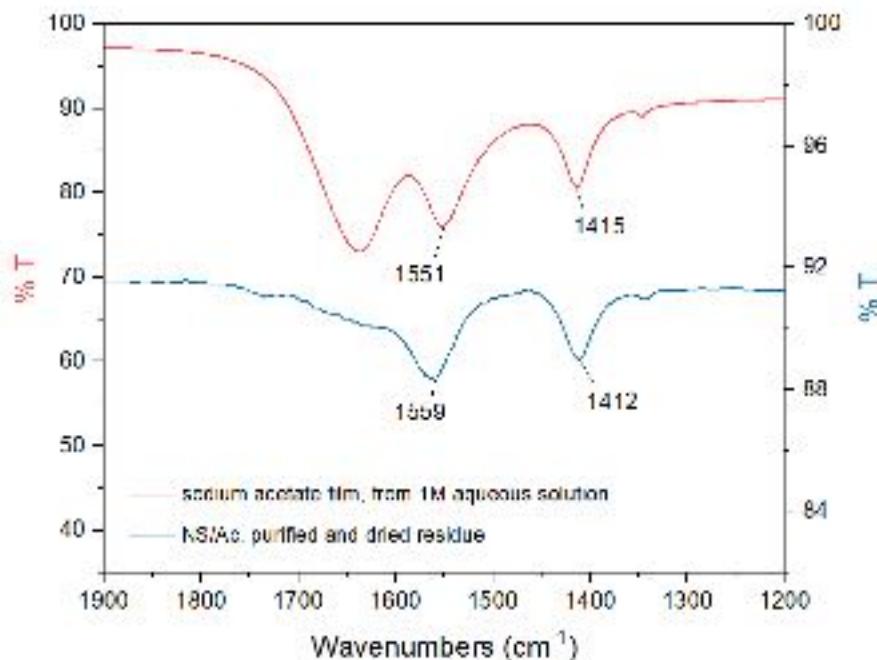


Figure 6.6: FT-IR ATR spectra of the free acetate ion (*red*), obtained by drop-casting a 1 M sodium acetate solution on the IRE, and of the purified and dried NS/Ac residues (*blue*).

very small shift, from 1415 cm^{-1} of the reference value to 1412 cm^{-1} . Even if these shifts are very small, they could be attributed to the formation of unidentate acetate complexes on the surface of the nanostars, as the $\Delta\nu(\text{COO}^-)$ of the NS/Ac residue is 147 cm^{-1} , while the $\Delta\nu(\text{COO}^-)$ of the free, ionic acetate is 136 cm^{-1} . As illustrated for citrate, low $\Delta\nu(\text{COO}^-)$ values in unidentate complexes could be the result of associated hydrogen bonding occurring between the uncoordinated C=O and other species in the system.

The NS/ CO_3^{2-} (₀) formulation was also analyzed by the same methodology, but it did not yield any significant spectral information. The absence of observable carbonate bands could be caused by an undetectable concentration of the species, such that $[\text{CO}_3^{2-}]_{\text{surface}} < \text{LOD}_{\text{CO}_3^{2-}}$, which would suggest that the main stabilizing species *on* the nanostars' surface are in fact hydroxyl ions, which are generated in solution by carbonate, as discussed in

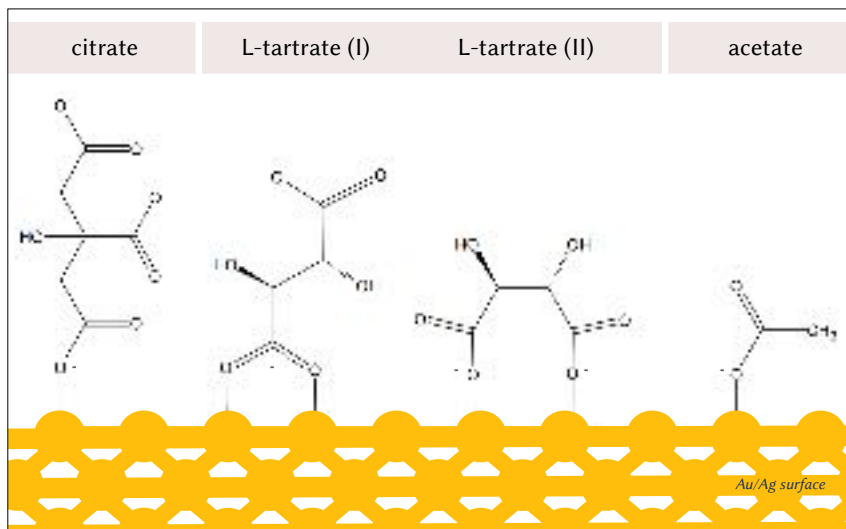


Figure 6.7: From left to right, proposed coordination modes of citrate, L-tartrate (I and II), and acetate on the surface of the nanostars.

§ 4.2.2. In this case, hydroxyl vibrations would be undistinguishable from the background signal, and thus, this hypothesis cannot be verified by the analytical protocol discussed here.

6.4 Summary

It has been demonstrated that measures of electrophoretic mobility of nanoparticles at increasing concentration of stabilizer can be utilized to extrapolate estimates of the adsorption constant between said stabilizer and the nanoparticle surface. This method was applied to the NS/Ct formulation, resulting in an estimate of the adsorption constant, K_{ad} , of citrate on the bimetallic nanostars in the order of 10^3 M^{-1} . This estimate was made possible by fitting the experimental data with a Hill-Langmuir adsorption function; this function made also possible to infer additional information about the NS/Ct system; for example, the adsorption process is spontaneous ($\Delta G_{ad} -4.36 \pm 0.08 \text{ kcal/mol}$ at 10°C ;

-4.58±0.05 kcal/mol at 20°C), is chemisorptive in nature, and it is characterized by positive cooperativity (Hill coefficient >1). The latter has been attributed to possible hydrogen bonding between citrate units, or other molecules in the system. The presence of hydrogen bonding in the citrate capping layer has also been demonstrated by the ATR-IR spectroscopic studies of the NS/Ct dried residues. In these samples, citrate was found to interact with the surface by unidentate coordination mode, in the presence of hydrogen bonding. The unidentate coordination mode is consistent with previous literature on the subject,²² which studied a similar system, citrate-capped borohydride-reduced gold nanoparticles, by SS-NMR.

ATR-IR spectroscopy was also utilized to characterize the binding modes of tartrate and acetate on NS/Tt and NS/Ac formulations, respectively. The spectral signatures of the dried nanoparticle residues were interpreted as the result of the simultaneous presence of unidentate and double-unidentate bridging complexes for tartrate, and unidentate complexes for acetate.

The information obtained at this stage of the research has been utilized to contextualize the theoretical results obtained by density functional theory (DFT) calculations, which are presented in the following chapter.

REFERENCES

- [1] Liu, Y. Is the Free Energy Change of Adsorption Correctly Calculated? *J. Chem. Eng. Data*, **2009**, *54*(7), 1981–1985.
- [2] Izquierdo-Lorenzo, I.; Sanchez-Cortes, S.; Garcia-Ramos, J.V. Adsorption of Beta-Adrenergic Agonists Used in Sport Doping on Metal Nanoparticles: A Detection Study Based on Surface-Enhanced Raman Scattering. *Langmuir*, 2010, *26*(18), 14663–14670.
- [3] Deriu, C.; Conticello, I.; Mebel, A.M.; McCord, B. Micro Solid Phase Extraction Surface-Enhanced Raman Spectroscopy (-SPE/SERS) Screening Test for the Detection of the Synthetic Cannabinoid JWH-018 in Oral Fluid. *Anal. Chem.*, **2019**, *91*(7), 4780–4789.
- [4] Nilsson, A.; Pettersson, L.G.M. Adsorbate Electronic Structure and Bonding on Metal Surfaces. In *Chemical Bonding at Surfaces and Interfaces*; Nilsson, A., Pettersson, L.G.M., Nørskov, J.K., Eds.; Elsevier: Amsterdam, 2008.
- [5] Leopold, N.; Lendl, B. A new method for fast preparation of highly surface-enhanced Raman scattering (SERS) active silver colloids at room temperature by reduction of silver nitrate with hydroxylamine hydrochloride. *J Phys Chem B.*, **2003**, *107*, 5723–5727.
- [6] Dong, X.; Gu, H.; Liu, F. Study of the surface-enhanced Raman spectroscopy of residual impurities in hydroxylamine-reduced silver colloid and the effects of anions on the colloid activity. *Spectrochim. Acta, Part A*, **2012**, *88*, 97–101.
- [7] Sánchez-Cortés, S.; García-Ramos, J.V. Influence of coverage in the surface-enhanced Raman scattering of cytosine and its methyl derivatives on metal colloids: chloride and pH effects. *Surf. Sci.*, **2001**, *473*, 133–142.
- [8] Thompson, D.W.; Collins, I.R. Electrical properties of the goldaqueous solution interface. *J. Colloid Interface Sci.*, **1992**, *152*(1), 197–204.
- [9] Biggs, S.; Mulvaney, P.; Zukoski, C.F.; Grieser, F. Study of the Anion Adsorption at the Gold-Aqueous Solution Interface by Atomic Force Microscopy. *J. Am. Chem. Soc.*, 1994, *116*, 9150–9157.
- [10] Langmuir, I. The Constitution and Fundamental Properties of Solids and Liquids. Part I. Solids. *J. Am. Chem. Soc.*, **1916**, *38*(11), 2221–2295.

- [11] Langmuir, I. The Constitution and Fundamental Properties of Solids and Liquids. II. Liquids. *J. Am. Chem. Soc.*, **1917**, 39(9), 1848–1906.
- [12] Foo, K.Y.; Hameed, B.H. Insights into the modeling of adsorption isotherm systems. *Chem. Eng. J. (Amsterdam, Neth.)*, **2010**, 156(1), 2–10.
- [13] Hill, A.V. The possible effects of the aggregation of the molecules of hmoglobin on its dissociation curves. *J. Physiol.*, **1910**, 40(Suppl), iv–vii.
- [14] Wall, J.F.; Grieser, F.; Zukoski, H.F. Monitoring chemical reactions at the gold/solution interface using atomic force microscopy. *J. Chem. Soc., Faraday Trans.*, **1997**, 93, 4017–4020.
- [15] Lee, Z.; Jeon, K-J.; Dato, A.; Erni, R.; Richardson, T.J.; Frenklach, M.; Radmilovic, V. Direct Imaging of Soft-Hard Interfaces Enabled by Graphene. *Nano Lett.*, **2009**, 9(9), 3365–3369.
- [16] Park, J. W.; Shumaker-Parry, J. S. Structural Study of Citrate Layers on Gold Nanoparticles: Role of Intermolecular Interactions in Stabilizing Nanoparticles. *J. Am. Chem. Soc.*, **2014**, 136, 1907–1921.
- [17] Wright, L.B.; Rodger, P.M.; Walsh, T.R. Structure and properties of citrate overlayers adsorbed at the aqueous Au(111) interface. *Langmuir*, **2014**, 30(50), 15171–15180.
- [18] Perfilieva, O.A.; Pyshnyi, D.V.; Lomzov, A.A. Molecular Dynamics Simulation of Polarizable Gold Nanoparticles Interacting with Sodium Citrate. *J. Chem. Theory Comput.*, **2019**, 15(2), 1278–1292.
- [19] Stefan, M.I. Le Novère, N. Cooperative Binding. *PLoS Comput Biol.*, **2013**, 9(6), e1003106-1–e1003106-6.
- [20] Ghosal, P.S.; Gupta, A.K. Determination of thermodynamic parameters from Langmuir isotherm constant - revisited. *J. Mol. Liq.*, **2017**, 225, 137–146.
- [21] IUPAC, Physical Chemistry Division, Commission on Colloid and Surface Chemistry including Catalysis. Chemisorption and Physisorption. In *Manual on Definitions, Terminology and Symbols in Colloid and Surface Chemistry, Internet Edition*, 2001. Originally Everett, D.H. Definitions, Terminology and Symbols in Colloid and Surface Chemistry - Part I, Appendix to Manual of Symbol and Terminology for Physicochemical Quantities and Units. *Pure Appl. Chem.*, **1972**, 31(4), 579–638.

- [22] Al-Johani, H.; Abou-Hamad, E.; Jedidi, A.; Widdifield, C.M.; Viger-Grave, J.; Sangaru, S.S.; Gajan, D.; Anjum, D.H.; Ould-Chikh, S.; Hedhili, M.N.; Gurinov, A.; Kelly, M.J.; El Eter, M.; Cavallo, L.; Emsley, L.; Basset, J-M. The structure and binding mode of citrate in the stabilization of gold nanoparticles. *Natur. Chem.*, **2017**, *9*, 890–895.
- [23] Griffiths, P.R.; de Haseth, J.A. *Fourier transform infrared spectrometry*; John Wiley & sons: Hoboken, 2007.
- [24] Derrick, M.; Stulik, D.; Landry, J.M. *Infrared spectroscopy in conservation science*; The Getty Conservation Institute: Los Angeles, 1999.
- [25] Fitzpatrick, J.; Reffner, J.A. Macro and micro internal reflection accessories. In *Handbook of vibrational spectroscopy, vol. 2*; Chalmers, J.M., Griffiths, P.R., Eds.; John Wiley & sons: Chichester, 2002.
- [26] López-Lorente, A.I.; Mizaikoff, B. Recent advances on the characterization of nanoparticles using infrared spectroscopy. *TrAC, Trends Anal. Chem.*, **2016**, *84(A)*, 97–106.
- [27] Mudunkotuwa, I.A.; Al Minshida, A.; Grassian, V.H. ATR-FTIR spectroscopy as a tool to probe surface adsorption on nanoparticles at the liquid-solid interface in environmentally and biologically relevant media. *Analyst*, **2014**, *139*, 870–881.
- [28] Harrick, N.J. Electric field strengths at totally reflecting interfaces. *J. Opt. Soc. Am.*, **1965**, *55(7)*, 851–857.
- [29] N. Sheppard, The historical development of experimental techniques in vibrational spectroscopy. In *Handbook of vibrational spectroscopy, vol. 2*; Chalmers, J.M., Griffiths, P.R., Eds.; John Wiley & sons: Chichester, 2002.
- [30] R.W. Hannah, Standard sampling techniques for infrared spectroscopy. In *Handbook of vibrational spectroscopy, vol. 2*; Chalmers, J.M., Griffiths, P.R., Eds.; John Wiley & sons: Chichester, 2002.
- [31] Aroca, R.F. *Surface-enhanced vibrational spectroscopy*, John Wiley & sons: Chichester, 2006.
- [32] Nakamoto, K. *Infrared and Raman Spectra of Inorganic and Coordination Compounds. Part B: Applications in Coordination, Organometallic, and Bioinorganic Chemistry, Sixth edition*, John Wiley & Sons: Hoboken, 2009.

- [33] Colthup, N.B.; Daly, L.H.; Wiberley, S.E. *Introduction to Infrared and Raman Spectroscopy, third edition*. Academic Press: Boston, 1990
- [34] Deacon, G.B; Phillips, R.J. Relationships between the carbon-oxygen stretching frequencies of carboxylato complexes and the type of carboxylate coordination. *Coord. Chem. Rev.*, **1980**, 33(3), 227–250.
- [35] Sutton, C.C.R.; da Silva, G.; Franks, G.V. Modeling the IR spectra of aqueous metal carboxylate complexes: correlation between bonding geometry and stretching mode wavenumber shifts. *Chem. - Eur. J.*, **2015**, 21(18), 6801–6805.
- [36] Palacios, E.G.; Juárez-López, G.; Monhemius, A.J. Infrared spectroscopy of metal carboxylates: II. Analysis of Fe(III), Ni and Zn carboxylate solutions. *Hydrometallurgy*, **2004**, 72(1–2), 139–148.
- [37] Dresseyn, H.O. Vibrational analysis of acid derivatives. In *The Chemistry of Acid Derivatives, The Chemistry of Functional Groups, Supplement B, vol. 2*; Patai, S., Ed.; Wiley: Chichester, 1992.

DFT calculations for nanoscale adsorption modeling

7.1 Density Functional Theory (DFT): overview

Within the Born-Oppenheimer approximation,¹ nuclear motion is decoupled from electronic motion, and nuclei are fixed in position. This is justified in terms of the great difference in mass existing between the two particles ($m_A \approx 1800 m_e$), which reflects on their vastly different motion speed, such that nuclei can be thought of as stationary.² As a result of the decoupling, the kinetic energy terms for the nuclei (*Equation 7.1*) can be omitted, and as a result of the fixed position, the repulsive term between nuclei can be treated as a constant, V_N , for a given system geometry (*Equation 7.2*).² Therefore:

$$H = - \sum_i \frac{\hbar^2}{2m_e} \nabla_i^2 - \sum_k \frac{\hbar^2}{2m_k} \nabla_k^2 - \sum_i \sum_k \frac{(-1q_e)^2 Z_k}{r_{ik}} + \sum_{i<j} \frac{(-1q_e)^2}{r_{ij}} + \sum_{k<l} \frac{(-1q_e)^2 Z_k Z_l}{r_{kl}} \quad (7.1)$$

$$H = - \sum_i \frac{\hbar^2}{2m_e} \nabla_i^2 - V_N - \sum_i \sum_k \frac{(-1q_e)^2 Z_k}{r_{ik}} + \sum_{i<j} \frac{(-1q_e)^2}{r_{ij}} \quad (7.2)$$

where i and j are used to denote electrons, k and l to denote nuclei, m is the mass, $-1q_e$ is the electronic charge, Z is the atomic number, r is the interparticle distance, \hbar is the reduced Planck's constant, and ∇^2 is the Laplacian operator, which is the sum of the second derivatives with respect to the three spatial Cartesian coordinates x, y, z .^{2,3}

Under this approximation, the wavefunction of a quantum system of fixed nuclear coordinates \mathbf{q}_k can be formalized as solely dependent on the individual electrons constituting it, and thus, on each electron's spin and spatial coordinates \mathbf{q}_i ; nuclear coordinates \mathbf{q}_k are present as fixed parameters.²

$$(H_{el} + V_N)\Psi_{el}(\mathbf{q}_i; \mathbf{q}_k) = E_{el}\Psi_{el}(\mathbf{q}_i; \mathbf{q}_k) \quad (7.3)$$

While it is known that the an *exact* solution to the Schroedinger equation cannot be achieved for systems larger than two electrons (*i.e.*, helium atom), the Variational Principle can be used to approximate solutions for larger systems.³ This is the approach used in Molecular Orbital (MO) theory to model chemical systems and calculate their properties. Briefly, according to the Variational Principle, an arbitrary trial wavefunction of any form can be expressed in terms of a set of basis functions, and utilized to obtain the approximate upper bound ground state energy of a chemical system by sole minimization of the energy eigenvalues associated with it.² If Φ is the arbitrary wavefunction and ϕ_i is the complete set of mathematically convenient functions constructing it (*basis set*), then

$$\Phi = \sum_i c_i \phi_i \quad (7.4)$$

where c_i is the set of coefficients that define how all ϕ_i combine orthonormally to form Φ , and Φ is related to its energy eigenvalues by the Schroedinger equation in the form of $H\Phi = E\Phi$. It can be demonstrated that the function to be minimized is

$$\int \Phi H \Phi d\mathbf{r} \quad (7.5)$$

and that the equation resulting from the minimization process is the Secular Equation.² The specific form of the determinant of the Secular Equation will depend on the mathematical method used to construct the trial wavefunction Φ — in its simplest example, Φ can be expressed as a set of linear combinations of hydrogenic atomic orbital wavefunctions (*i.e.*, LCAO approach). Regardless of the form, the analytical procedure needed to obtain the approximate solution of the Schroedinger equation for a many-body chemical system consists in solving a number of integrals that depends on a number N of basis functions, in which accuracy scales with N . Although allowing for the calculation of the energy of a many-body quantum system, the mathematical complexity of this approach clearly

becomes computationally challenging, when not unfeasible, the larger the system under study is.

The revolution brought about by Density Functional Theory (DFT) resides in simplifying this mathematical complexity by treating a many-body quantum system in terms of a “collective” *physical observable* that still allows for the *a priori* construction of the Hamiltonian operator. This physical observable is the electron density, ρ . Indeed, the Hamiltonian exclusively depends on the number of electrons, N , and on the position and atomic number Z of nuclei A_i , which can be derived from electron density as follows:

$$N = \int \rho(\mathbf{r}) d\mathbf{r} \quad (7.6)$$

$$\left. \frac{\partial \bar{\rho}(r_A)}{\partial r_A} \right|_{r_A=0} = -2Z_A \rho(\mathbf{r}_A) \quad (7.7)$$

where $d\mathbf{r}$ is a 3n-dimensional volume element (Equation 7.6), $\bar{\rho}$ is the spherically averaged electron density, r_A is the radial distance from A , and \mathbf{r}_A is the volume at which the electron density maximum is located (Equation 7.7).

By *reductio ad absurdum*, it can be demonstrated that, for every ground state electron density, there is exactly *one* external potential¹ (*Hohenberg-Kohn existence theorem*);⁴ this ultimately means that, for every ground state electron density, there is exactly *one* Hamiltonian operator. This Hamiltonian can be utilized to obtain a wavefunction which, by Variational Principle, yields an expected energy that is greater than, or equal to, the real ground state energy (*Hohenberg-Kohn variational theorem*).⁴ Energy is therefore a density *functional* (function of a function).

¹The external potential in DFT is the potential given by the electrons' attraction to nuclei.²

$$Energy = F[\rho(\mathbf{r})] \quad (7.8)$$

Since the electron density depends only on the spatial coordinates x , y , and z , DFT calculations scale as N^3 , where N is the number of basis functions. In terms of computational cost, this N^3 scaling represents a great advantage over other *ab initio* methods, which have all scaling of at least one factor higher; indeed, compared to Hartree-Fock (HF) theory, which is the simplest^{II} *ab initio* method and scales as N^4 , DFT has lower computational cost while also including electron correlation effects (*vide infra*), thus having higher accuracy.²

The method by which, in the framework of Density Functional Theory, the energy is calculated on the basis of electron density, *without* having to solve for the wavefunction, is called Kohn-Sham Self-Consistent Field (KS SCF) procedure.⁵ Briefly, this approach is based on the assumption that a real system can have identical ground state electron density as a simpler, fictitious system, in which the electrons do not interact with each other, such that the energy functional can be expressed as a simple sum of other density functionals, as follows:²

$$E[\rho(\mathbf{r})] = T_{ni}[\rho(\mathbf{r})] + V_{ne}[\rho(\mathbf{r})] + V_{ee}[\rho(\mathbf{r})] + \Delta T[\rho(\mathbf{r})] + \Delta V_{ee}[\rho(\mathbf{r})] \quad (7.9)$$

where the T_{ni} density functional describes the kinetic energy of the non-interacting (*ni*) electrons, the V_{ne} density functional describes the interaction between nuclei and electrons, V_{ee} the repulsion between electrons, and finally, ΔT and ΔV_{ee} correct for the electron interaction in the kinetic energy term and for all non-classical interactions in the electron repulsion energy term, respectively. These last two terms are frequently considered as a single correction term, which is known as the *exchange-correlation energy*, $E_{xc}[\rho(\mathbf{r})]$.

^{II}No electron correlation is considered in HF theory, while it is included in DFT, see following paragraph.

The way in which this term is computed defines a DFT method. For the present research, all DFT calculations were performed utilizing the hybrid exchange correlation functional B3LYP.⁶⁻⁸

7.1.1 DFT calculations of plasmonic nanoparticles and nanoalloys

DFT can be applied to the study of structural and electronic properties of molecules and materials, including plasmonic nanostructures. While structural modeling via geometry optimization can be quite straightforward for organic molecules (§ *Chapter 8*), in that the first guess can be made by simply drawing the molecular structure and utilizing standard bond angles, lengths, and dihedral angles, coming up with a valid initial guess for a plasmonic nanostructure can be a challenging task in and of itself. Plasmonic nanostructures are typically made of silver, gold, or a combination of these elements,⁹ and they are held together by metallic bonds; the poorly directional character of the metallic bond, together with the high and variable coordination number that metals can adopt, make metallic nanostructures *fluxional*, that is, they can be found in a multitude of atomic arrangements, all of which lying in a relatively narrow energy range.¹⁰ As a result, metallic nanostructures tend to have a highly “rough” energy landscape — their configuration energy as a function of atomic coordinates, the *potential energy surface* (PES), is rich in local minima, which differ from one another by relatively small energy values.¹⁰ As for multimetallic systems, such as nanoalloys, the multitude of atomic arrangements that a cluster can adopt is to be intended *both* in terms of geometrical isomers, that is, for a fixed stoichiometry, the stable overall “shapes” that a cluster can attain (*i.e.*, atomic packing), *and* in terms of permutations, within a fixed stoichiometry *and* geometry, of all unlike atoms (*Figure 7.1*). This type of isomeric clusters take the name of *homotops*.¹¹ For a bimetallic cluster A_mB_n , where $m + n = N$, the number of homotops is given by:¹⁰

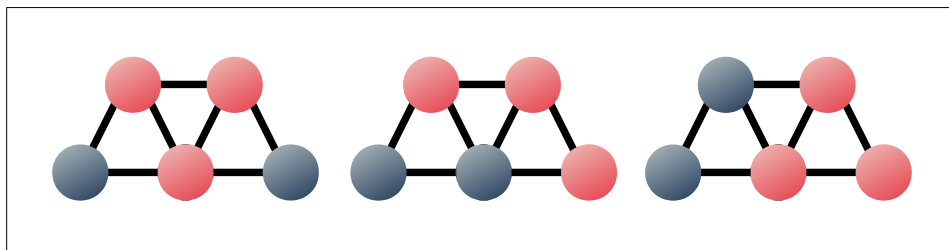


Figure 7.1: Three of the $5!/(3!2!)$ possible homotops of an A_3B_2 bimetallic cluster of fixed geometry.

$$\text{homotops} = \frac{N!}{(m!n!)} \quad (7.10)$$

This makes nanoalloys challenging systems within an already difficult-to-model category of species.

For these reasons, global optimizations with full-DFT methods can be extremely time consuming, and typically, only limited portions of the PES are explored in this way. Most commonly, a small group of stable structures within a selected cluster motif are obtained and compared.¹³ These cluster motifs, which mainly comprise atomic packing and overall shape of the cluster (tetrahedra, cuboctahedra, icosahedra, . . .), can be obtained by a full or more extensive exploration of the PES with more approximate computational methods, such as semi-empirical potential calculations (Lennard-Jones,¹⁴ Gupta,¹⁵ . . .).^{10,13} This step-wise approach is in some ways similar to those adopted for other systems with high degrees of freedom, such as biological macromolecules, when X-Ray data on which to base the structural first guess(es) are not available.

Full-DFT-obtained global minimum geometries of plasmonic nanostructures have primarily been reported for either monometallic clusters of relatively small size (*e.g.*, Au_2 to Au_{20}),¹⁶ or for even smaller size AuAg clusters (*e.g.*, $N = 8$;¹⁷ $N \leq 10^{19}$), with emphasis on Ag-rich stoichiometries.¹⁹ Selected AuAg cluster geometries of relatively larger size

(*e.g.*, face-centered cubic, *fcc*, truncated octahedron, $N = 38$; icosahedron, $N = 55$)¹⁸ or equiatomic and fixed stoichiometry AuAg clusters (*e.g.*, $\text{Au}_{10}\text{Ag}_{10}$, $\text{Au}_8\text{Ag}_{12}$)¹⁹ have also been studied by full-DFT methods. This type of studies focuses on chemical ordering and segregation effects within a fixed cluster geometry, and, even if they do not address the issue of finding the true global minimum, they offer insight on shape-related inter-species interactions at the nanoscale.

The general trends that can be found in the literature are that, for small Au_mAg_n systems, where $n + m \leq 10$,^{17,19} segregation of atomic species is not favorable at the DFT level, and Au atoms tend to attain peripheral positions (low coordination sites) within the structures. In larger Au_mAg_n systems ($m + n = 38; 55$),¹⁸ segregation phenomena do occur, and the extent and structural arrangement of the segregated phases depend on the nanoparticle shape, as well as on the ratio of Au to Ag. As an example, Ag-rich clusters of *fcc* truncated octahedron shape, in which Au is present as an impurity (*e.g.*, Au_mAg_n , with $1 \leq m \leq 6$), present minimum energy homotops with core-shell structures in which Au constitutes the core; analogous clusters of icosahedral shape, on the other hand, exhibit minimum energy homotops with Au atoms tendentially occupying surface sites.¹⁸ These results, obtained at the DFT level, are consistent with those of global optimizations performed with semi-empirical methods, such as those reported by Rossi *et al.*²⁰ In their work, Rossi *et al.*²⁰ modeled the atom-atom interactions by Rosato-Guillopé-Legrand (RGL) potential²¹ and explored the PES by genetic algorithm (GA),²² determining that the global minimum shape for clusters of 34 and 38 atoms, at all stoichiometries, are mostly truncated octahedron shapes, and that Ag-rich clusters tend to adopt core-shell configurations with Au as the core. Indeed, RGL potentials are reportedly in good agreement with both experimental and *ab initio* calculations of noble metal systems, especially silver or silver-rich clusters.²³

The study of Au-rich clusters, which have a composition that is more similar to that of the nanostars utilized for this research project, is less explored by DFT methods than by semi-empirical methods. This is probably a result of the larger number of electrons of Au ($Z = 79$) as compared to Ag ($Z = 47$), which necessarily^{III} increases the computational cost, and the need for a more complex treatment of the electronic structure, such to include relativistic effects^{IV}. According to the already mentioned study by Rossi *et al.*,²⁰ semi-empirical, GA-sampled, global optimizations based on RGL potentials suggest that Au-rich clusters of 34 atoms exhibit surface-segregation of Ag impurities and adopt configurations that are ascribable to fcc geometries, with varying degrees of distortion. Predilection of Au for fcc non-icosahedral geometries is in line with what obtained by full-DFT global optimization methods for monometallic Au clusters of $N \leq 20$ (*Figure 7.2*),¹⁶ and with experimental observations of Au nanoparticles.²⁵ Symmetry breaking and transition to disordered structures occur instead with increasing number of Ag atoms (*Figure 7.3*).²⁰ This is particularly interesting in terms of visualizing the possible mechanism by which Ag intervenes as a shape-director during the synthesis of nanostars.

Kumagai

7.1.2 Modeling ligand adsorption on coinage metal nanostructures

Ligand adsorption on coinage metal nanostructures has been modeled by DFT primarily for the purpose of studying fundamental processes and catalytic surfaces,^{26–32} and, to a lesser extent, analyte-substrate interactions in SERS systems.^{33–35} For SERS-related

^{III}DFT calculations scale as N^3 , where N is the number of basis functions, and the larger the number of electrons of a species, the larger the number of basis function that are necessary to describe them.²

^{IV}Relativistic effects come into play when the speed of a particle approaches the speed of light; this happens with very large elements, such as transition metals, and Au is an archetypal example of element that has significant relativistic effects.²⁴

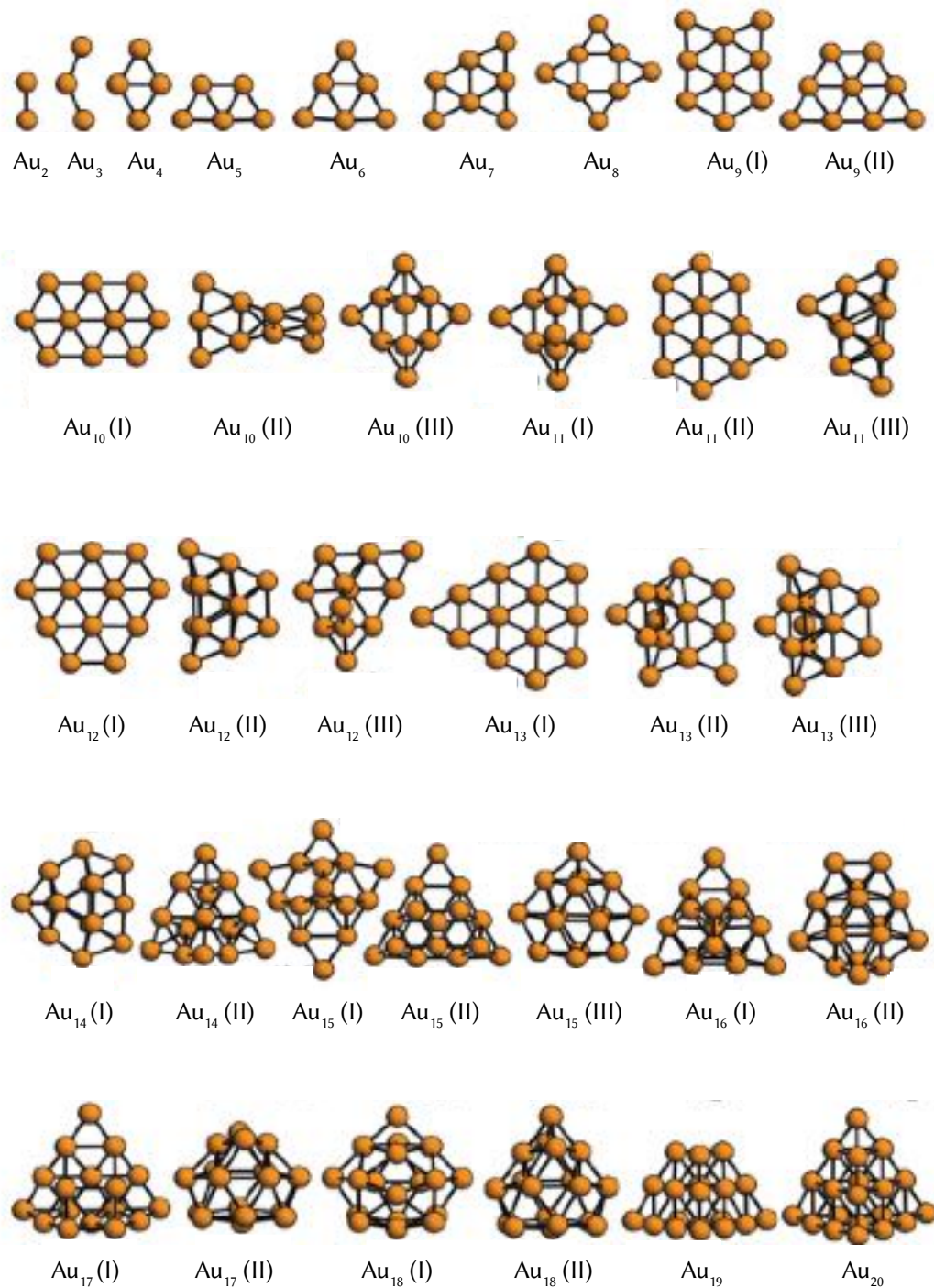


Figure 7.2: Full-DFT global optimization minima and some lowest-energy isomers of Au clusters of 2 to 20 atoms. Adapted from Assadollahzadeh and Schwerdtfeger, 2009,¹⁶ with the permission of AIP Publishing.

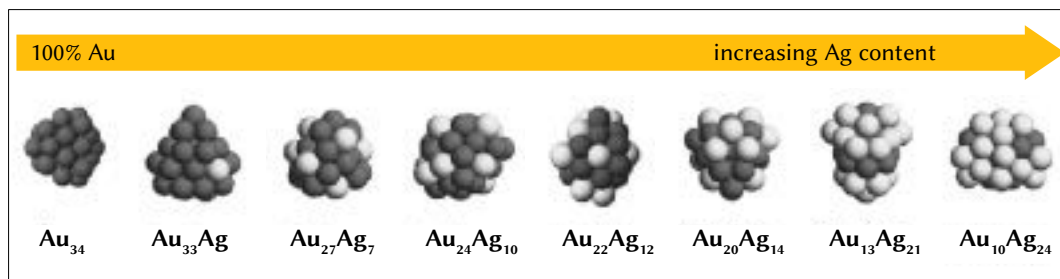


Figure 7.3: Some global minima from the 34-atom Ag_mAu_n sequence obtained by Rossi *et al.*²⁰ by semi-empirical method. Light colored spheres correspond to Ag atoms, while dark colored spheres correspond to Au. Low symmetry, disordered structures appear in Au-rich clusters as the Ag content increases. Adapted from Rossi *et al.*, 2005,²⁰ with the permission of AIP Publishing.

studies aiming at estimating the chemical and electromagnetic contributions to the total signal enhancement, time-dependent DFT (TD-DFT) calculations are employed.^{36–39} Alternatively, when an evaluation of the SERS enhancement is not the objective of the study, and the aim is to characterize the adsorption modes of a SERS probe and the frequency shifts observed upon its complexation, ground state DFT calculations are utilized instead. Because the focus of these studies is placed more on the analyte molecule than on the metal surface, and because a compromise with available computational resources is often necessary, the nanoparticle surface is frequently modeled as a very small cluster of one or a few atoms (*e.g.*, atomic Ag,⁴⁰ atomic Au and Au^+ ,⁴¹ Ag_2 ,³⁵ Ag_3 ,^{42,43} Au_4^+ ,³³ ...). As mentioned in the previous section, plasmonic nanomaterials of SERS interest are primarily composed of coinage metals Ag and Au, which have atomic numbers of 47 and 79, respectively, and thus, the explicit treatment of their electrons can require a high computational cost. Besides the triviality of reducing the size of the cluster, a common way to mediate between accuracy and cost is the use of the pseudopotential approximation.^{2,44}

In the pseudopotential approximation, atomic species are seen as composed of frozen core electrons, which do not take significant part in chemical reactions, and outer electrons

(*vide infra*), which, on the contrary, are responsible for essentially all chemical properties.⁴⁴ Therefore, the core electrons can be treated implicitly, by substituting them with a potential, the *effective core potential* (ECP), that represents an ensemble of their properties — Pauli principle, attraction to nucleus, electron-electron repulsions, and relativistic effects. The latter are particularly important for heavier elements, such as Au,²⁴ allowing not only for a higher computational efficiency, but also for a more accurate modeling of the behavior of these elements.^{2,44} Relativistic effects are included in ECPs by the use of experimental data, which makes ECPs semi-empirical in nature. As far as the outer electrons are concerned, they are treated explicitly, and this treatment can either be limited to the valence shell, and ECPs of this kind are termed *large core* ECPs, or include the second outermost shell, too, taking the name of *small core* ECPs.² The most commonly utilized ECPs in noble metal clusters optimization are those known as “LANL”, after Los Alamos National Laboratory, such as the LANL2DZ ECP.⁴⁵ In the LANL2DZ ECP, the electrons of atoms from H to Ne, included, are treated fully explicitly, utilizing the 6-31G basis,⁴⁶ while the electronic structure of atoms from Na onwards are modeled with a set ECP and valence basis function; Ag is modeled as [Ar] + 3*d* core and (3*s*, 3*p*, 2*d*) matching valence basis, while Au is modeled as [Kr] + 4*d* + 4*f* core and (3*s*, 3*p*, 2*d*) matching valence basis.

DFT calculations of nanoparticle systems have to deal with the issue of accurately representing, albeit in an abstracted or simplified way, the properties of matter in the condensed phase. One of the phenomena that cannot be neglected when modeling condensed phases, especially when the determination of the free energy of the system is required, is *solvation*. All of the DFT calculations mentioned so far, for example, achieve this by making use of implicit, or continuum, solvent models; solvation can in fact be accounted for in two different ways, either *explicitly* or *implicitly*. Explicit solvent models, as the name suggests, treat solvent molecules atomistically, either by representing them with molecular mechanics approaches (*e.g.*, water molecules as point charges),^{61,62} or

quantum mechanically, that is, by treating the solvent molecules in the same way as the solute is treated.² In the simplest-to-visualize approach, solvent molecules, such as water, can be included in the Cartesian representation of the system under study, by placing them around the molecule, cluster, or complex of interest, as to mimic the first, second, *n*th solvation shell. Of course, this approach is computationally demanding, as the size of a system grows very rapidly with each included explicit solvation shell. Moreover, this approach increases the degrees of freedom of a system, thus causing the same PES sampling problems already described when addressing the issue of homotops in nanoalloys (§ 7.1.1). However, an explicit treatment of the solvent allows for the evaluation of direct solvent participation in reactions which cannot be modeled by an implicit solvent model. In fact, implicit solvent models substitute the discrete molecules of solvent by a homogeneous (*continuum*) medium, with equivalent, statistically averaged properties as the solvent to be modeled (*e.g.*, polarizability, dielectric behavior, . . .); this continuum extends in space around a suitably shaped cavity, in which the solute is embedded.^{2,63} By eliminating the atomistic representation of the solvent, these solvation models obviously achieve a significant reduction in the computation time, compared to explicit models.² Mixed explicit/implicit models can also be utilized. These approaches are frequently adopted when dealing with highly charged systems, for which charge screening by the introduction of a first solvation shell is necessary to obtain physically reasonable structures and computed properties at the DFT-level.⁶⁴ In such systems, the solvent, for example water, is introduced both explicitly, as a coordination sphere around the solute of interest, and implicitly, as a dielectric continuum, which accounts for the bulk behavior of the rest of the solvent.²

In the present work, citrate was chosen as the model ligand for the DFT study of the adsorption of the effective stabilizers (*Chapters 4–5*) on monometallic and bimetallic clusters. As outlined in § 4.2, trisodium citrate is a very popular colloidal nanoparticle

reducing agent and stabilizer, and thus, it has been extensively studied in the literature, both experimentally and computationally.⁴⁷⁻⁵⁶ DFT literature on the interaction of this molecule with coinage metal clusters is however scarce, as a more common approach is to simplify the citrate structure by utilizing smaller ligands that retain functional groups and connectivity patterns found in citrate, namely, formate,²⁸ acetate, glutarate, and succinate.⁵¹ Explicit treatment of citrate was however reported this year (2020) by Gisbert-González *et al.*,⁵⁶ who modeled the citrate adsorption to gold, in an effort to elucidate the shape directing effect that this molecule has in traditional nanoparticle synthesis, such as the Turkevich⁵⁷ method^V. Gisbert-González *et al.*⁵⁶ modeled three different Au surfaces according to the bulk geometry of (111), (100), and (110) Au facets, respectively, utilizing periodic supercells composed of 48 atoms organized in four layers; for each supercell, the geometry of the two bottom layers was kept fixed, while the two top layers were allowed to relax upon interaction with citrate. Citrate was modeled as citric acid, and allowed to undergo deprotonation as proton-coupled electrons transfers, which were modeled via the computational hydrogen electrode formalism.⁵⁸ Solvation was then taken into account by implicit solvent model COSMO (Conductor-like Screening Model).^{56,59,60} The stable structures that were obtained resulted from direct binding of citrate, via bidentate coordination mode, with all three types of Au facets. This bidentate coordination involved the terminus and central carboxylate groups simultaneously, in both the stable structure of citrate on Au(100) and Au(110); on the other hand, the stable structure for citrate on Au(111) exhibited bidentate coordination involving all three carboxylate groups simultaneously. These structures were found to be consistent with the experimental findings that the group obtained by FT-IR spectroscopy, which indicated that

^VThe Turkevich method consists in the reduction of aurochloric acid by citrate, at a temperature around the boiling point of the solution, producing colloidal spherical nanoparticles. In this reaction, citrate is both the reducing agent and the capping species.⁵⁷

the citrate adopts a bidentate coordination mode when capping gold nanospheres obtained by Turkevich method.⁵⁶

As already discussed in § 2.2.1.1 and 4.3.1, Al-Johani *et al.*⁵¹ extensively characterized the surface of borohydride-reduced citrate-capped gold nanospheres, utilizing a wide range of analytical techniques, such as XPS and nuclear magnetic resonance, NMR. In the same publication, Al-Johani *et al.* also modeled the interaction between the gold nanospheres and citrate by DFT, utilizing a series of 15-to-20-atom, three-layered Au clusters modeled after bulk (111) and (100) facets, and simpler carboxylate ligands as proxies for citrate, namely, acetate (one carboxylate), succinate (two carboxylates, separated by a 2-carbon chain), and glutarate (two carboxylates, separated by a 3-carbon chain). Acetate was utilized to mimic low loadings of citrate and single-carboxylate interactions, succinate was utilized to model citrate adsorption via the central and terminus carboxylates, and glutarate was chosen to mimic citrate adsorption via the two terminal carboxylates. Because of computational constraints and the variety of research questions that can animate a given DFT study, citrate is often “deconstructed”; as previously mentioned, smaller or simpler (*i.e.*, linear *vs* branched, no alcoholic functions, . . .) carboxylates are often studied in its place. Al-Johani *et al.* performed DFT calculations utilizing both fixed and non-fixed geometries for the Au surfaces, and accounted for both dispersion forces and solvation. The latter was accounted for by utilizing the continuum solvent model COSMO, as previously outlined for Gisbert-González *et al.*⁵⁶ Their results show that all ligands were able to directly bind to the modeled Au surfaces, and that, while all computed energies were lower than the reported experimentally derived energy for the covalent Au-O bond (25–55 kcal/mol, compared to ≈ 70 kcal/mol),⁵¹ the interactions between the carboxylates and the Au surfaces were not insignificant. On both (111) and (100) facets, acetate was found to interact with Au in a bidentate fashion, while glutarate and succinate were found to interact with Au in a bidentate bridging mode, that is, with both carboxylate functional

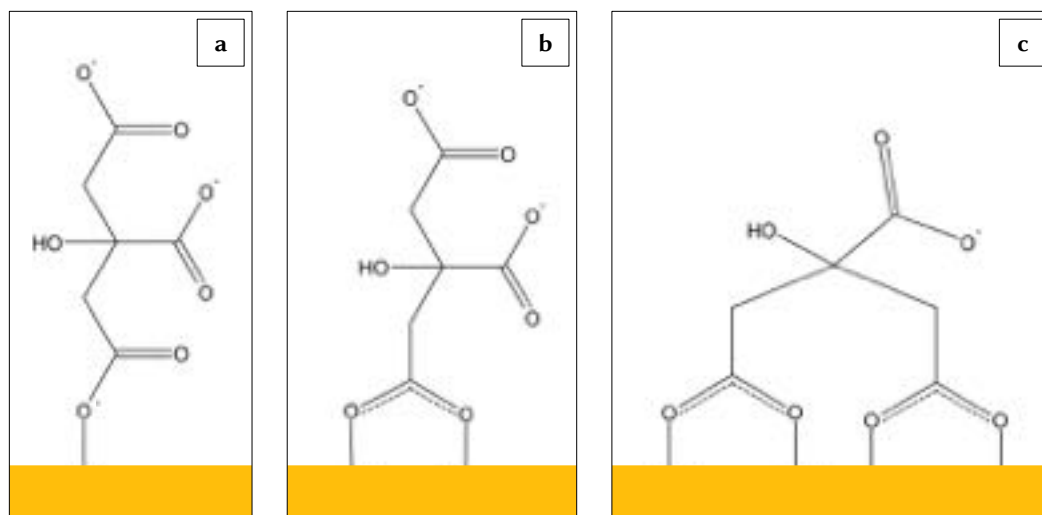


Figure 7.4: Examples of citrate coordination modes reported in literature:^{51,56} (a) unidentate (κ), (b) bidentate (μ_2), and (c) terminus-terminus bidentate bridging (μ_4).

groups adsorbing simultaneously on the surface (Figure 7.4). Since the computed strain energy was higher on succinate than on glutarate, Al-Johani *et al.* concluded that, by analogy, citrate likely binds directly with gold surfaces in a bridging mode involving the two terminal carboxylates. Solid State NMR (SS-NMR) studies of the borohydride-reduced citrate-capped gold nanospheres confirmed this preferred interaction mode at low temperature and low coverage.⁵¹

Another relevant study was published by Provorse and Aikens,²⁸ who evaluated the successive adsorption of formate molecules on various binding sites on Au₂₀. This cluster is derived from (111) bulk Au facets, has all gold atoms located on the surface, and a closed-shell electron configuration; moreover, it has been utilized as model surface for SERS enhancement studies at the TD-DFT level.^{28,37} DFT calculations were performed at the PB86/DZ and PB86/TDZ levels of theory, both in the gas phase and in water, which, also in this case, was accounted for implicitly, by application of the continuum solvent model COSMO.²⁸ From their results, Provorse and Aikens²⁸ were able to conclude that

carboxylates, such as formate, preferentially bind to low coordination sites within the Au cluster, such as the atoms at the vertex of the tetrahedron; these interactions appear stabilized by the introduction of water as an implicit solvent. Binding at higher coordination sites is not favored, and this led the authors to postulate that, for high carboxylate coverages to be possible on carboxylate-reduced gold nanoparticles, the involvement of other species in the adsorption process is likely. These species were hypothesized to be the redox by-products of nanoparticle synthesis. As far as the binding mode is concerned, a shift was noted with increasing formate loading on the surface, such that, when formate was present as a single molecule, it attained a bidentate coordination mode, while when more than one formate molecules were present, these interacted to the surface via unidentate coordination mode.²⁸

7.2 Modeling the adsorption of citrate on nanostars

As mentioned in the previous section, citrate was utilized as model carboxylate stabilizer for all calculations. It was modeled explicitly, in its doubly deprotonated form, which bears formal charge of -2; this protonation state was selected on the basis of the most prevalent form of citrate at the pH of the NS/Ct formulation, which was determined utilizing the Henderson-Hasselbalch equation. The geometry of citrate was then optimized in the gas phase, in the presence of 12 molecules of water as explicit solvent, and Na⁺ as counterion. The choice to include Na⁺ as a counterion stems from the necessity to reduce the formal charge of the whole supramolecular system, as well as from its physical relevance in the nanoparticle system to be represented. Indeed, citrate is typically introduced in nanoparticle formulations as trisodium citrate (*Chapter 4*) and, in the already cited work by Al-Johani *et al.*,⁵¹ both TEM/EDS (Energy Dispersive X-ray Spectroscopy) and ²³Na multiple-quantum magic-angle spinning (MQMAS) NMR studies highlighted the presence of Na⁺ in the

vicinity of the surface of citrate-capped borohydride-reduced gold nanospheres, suggesting a possible role of this counterion in maintaining the stability of the layer, especially at high citrate coverages, where electrostatic repulsions between citrate molecules might happen. The tendency of sodium ions to stay close to gold surfaces and participate in the stabilization of the citrate capping crown was also observed in molecular dynamics simulations.^{49,52,55} At the time of presentation of this work, no DFT study has been reported yet that includes sodium ions in the representation of a citrate/noble metal system.

In § 4.1, the environment of the as-synthesized nanostars was discussed, highlighting all possible species that could be surrounding the bimetallic surface — chloride from the gold precursor, nitrate from the silver precursor, hydrogen ions from both the gold precursor and the dissociable proton in L-ascorbic acid, and a negligible amount of unreacted L-ascorbic acid. Of these species, Cl^- is the only one that is both present in potentially significant amounts (≈ 0.3 mM) and known to interact with gold and silver surfaces.⁶⁵⁻⁶⁷ However, as detailed in *Chapter 5*, chloride ions adsorbed on gold surfaces are also known to be displaced by citrate.⁶⁸ Therefore, because the bimetallic nanostars utilized for this research are primarily composed of gold (Au:Ag 18:1), and because the introduction of chloride ions in the system would contribute to increasing the formal charge of the whole system, which, as discussed, is to be avoided when modeling systems for DFT studies, the presence of Cl^- was omitted from the model.

A cluster exclusively composed of gold atoms was utilized as the starting point for the development of a bimetallic cluster that could account for the presence of trace silver in the real nanostar system. This monometallic gold cluster was modeled after that of Aikens and Schatz,³⁷ and it is analogous to the one discussed in the previous section for the adsorption of formate.²⁸ This cluster was selected because of its previous use in DFT studies on carboxylate surface adsorption, its computationally affordable size, and its symmetry. Symmetry is indeed extremely helpful when modeling bimetallic clusters, as it

reduces the number of non-equivalent homotops. Other important characteristics of this cluster are that it corresponds to a stable, close shell structure, and it is neutral.²⁸ The latter is very important, since the gold composing the nanostars to be modeled was found to be essentially in its elemental state, Au⁰ (§ 4.3.1). The bimetallic cluster was then modeled by atomic substitution of silver on the Au₂₀ cluster, and only the most stable homotop was utilized to model the citrate/bimetallic cluster complex. The stoichiometry of the bimetallic system was restricted to Au₁₉Ag only, in order to reduce both the complexity of the geometry optimization problem, and the number of possible homotops. The chosen stoichiometry is close to that of the nanostars as predicted by their reaction protocol, that is, 1 atom of silver every each 18 atoms of gold (§ 4.1).

To model the adsorption of citrate on the metal cluster, and thus, the structure of the cluster-stabilized complex, a standard approach was used, consisting on performing geometry optimization of the supramolecular ligand, [HCitrate²⁻ + Na⁺ + 12 H₂O] in the presence of the substrate, the metal cluster, after prior geometry optimization of the individual components, as described in the Methods chapter of this dissertation (§ 3.2.9). This approach allows for the estimate of the free energy of adsorption in the gas phase, $\Delta G_{ad(g)}$, which can be computed as any state function, as follows:

$$\Delta G_{ad(g)} = G(\text{product}) - \sum G(\text{reactants}) \quad (7.11)$$

where the product is the citrate/cluster complex, the reactants are the [HCitrate²⁻ + Na⁺ + 12 H₂O] and the metal cluster, and the G is the electronic and thermal Gibbs free energy for each system, which are computed as

$$G = (E_{SCF} + E_{therm}) - TS \quad (7.12)$$

where E_{SCF} is the electronic energy as obtained from geometry optimization, E_{therm} is the thermal enthalpy correction from frequencies calculation, T is the absolute temperature in Kelvin (298.15 K), and S is the entropy as obtained from frequencies calculation. The same thermodynamic quantities were computed also in solution, with the introduction of the continuum solvent model SMD⁷⁰ in single point calculations for each component of the adsorption process. This allowed to determine the Gibbs free energy of adsorption of the system in solution, $\Delta G_{ad(aq)}$, and thus, the extent of the solvation effects, as illustrated by the thermodynamic cycle reported in *Figure 7.5*.

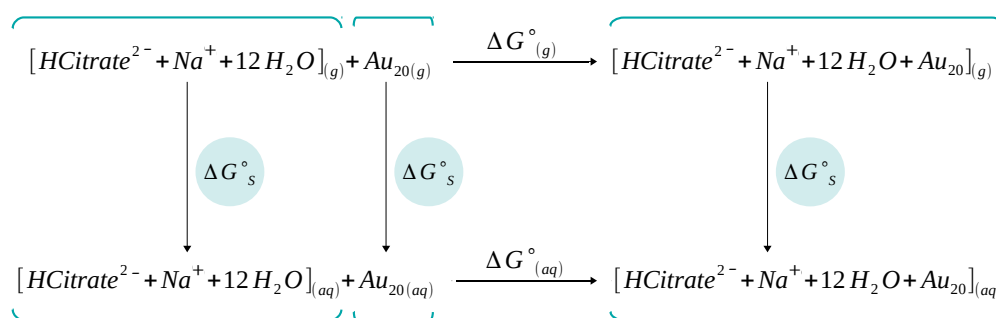


Figure 7.5: Thermodynamic cycle for the computation of the free energy of adsorption in solution, illustrated for the citrate/Au₂₀ system.

7.2.1 DFT calculations of Citrate/Au₂₀

Figure 7.6 and *Table 7.1* show the optimized geometry of the Au₂₀ cluster and the interatomic distances, respectively, while the full Cartesian coordinates are reported in *Appendix F*. This cluster presents Au in three different coordination modes — the highest coordination atom is located in the center of the surface, then coordination decreases for atoms on the edges, and becomes the lowest for the atoms at the vertices of the

tetrahedron. According to the work of Provorse and Aikens,²⁸ these lowest coordination sites are those predicted to be the binding sites for carboxylates.

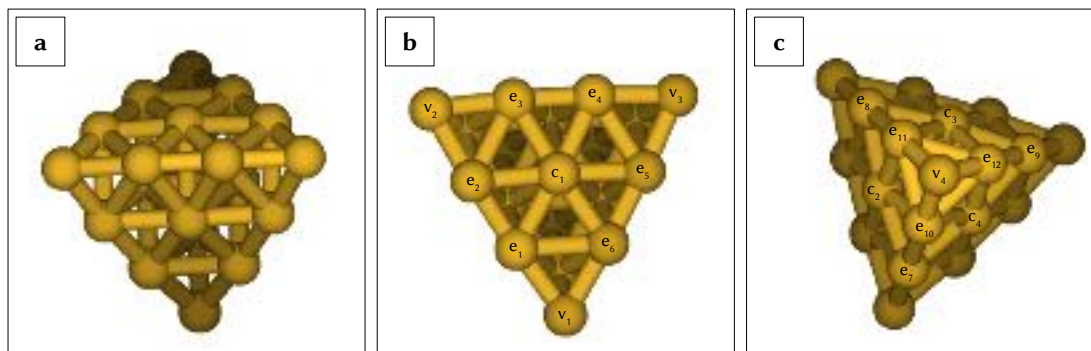


Figure 7.6: Structure of the Au₂₀ cluster, optimized at the B3LYP/LANL2DZ level: (a) side view, (b) top view, (c) bottom view. Gold atoms are labeled and numbered: *c*, center (N = 4); *e*, edge (N = 12); *v*, vertex (N = 4).

Table 7.1: Interatomic distances of the Au₂₀ cluster, optimized at the B3LYP/LANL2DZ level.

Au–Au bond	bond length (Å)
<i>c</i> _{<i>i</i>} – <i>c</i> _{<i>i</i>}	2.91
<i>e</i> _{<i>i</i>} – <i>e</i> _{<i>j</i>}	2.73
<i>v</i> _{<i>i</i>} – <i>e</i> _{nearest neighbor}	2.80

As labeled in *Figure 7.6*: *c*, center; *e*, edge; *v*, vertex. The cluster is symmetric.

As described in the *Methods* section (§ 3.2.9), the first optimized structure was obtained by manually placing the [HCitrate²⁻ + Na⁺ + 12 H₂O] supramolecular system on top of the Au₂₀ cluster, at a sufficient distance, ≈ 7 Å, in order to avoid biasing towards a pre-selected ligand-substrate interaction mode (*Appendix F, Figure F.1*). For the same reason, citrate was oriented with the two deprotonated groups horizontal with respect to the plane described by the Au₂₀ surface. The resulting optimized structure is reported in *Figure 7.7*

and shows a direct involvement of the explicit solvent in the interaction of citrate with Au₂₀. Indeed, two molecules of water, labeled w_1 and w_2 in *Figure 7.7*, are oriented with the oxygen towards the gold surface, at an Au–O distance of 2.43 Å and 2.20 Å, respectively; the Au atoms coordinating with these water oxygens are the lower coordination sites at the vertex and edge of the tetrahedron, which is consistent with the work of Provorse and Aikens, who noted preferential ligand binding at the Au₂₀ tetrahedron’s vertices.²⁸ As for the water hydrogens, these coordinate with the unprotonated central carboxylate of citrate, forming a hydrogen bond with relatively short distances of 1.51 Å (w_1) and 1.65 Å (w_2). All distances are summarized in *Table 7.2*.

Adsorption of water on noble metal surfaces, as well as other transition metals, is a known phenomenon, and it has been observed experimentally thanks to scanning electron tunneling microscopy (STM) imaging studies.^{71–76} As a result of intrinsic limitations of the application of STM to water systems,⁷⁸ the orientation of water with respect to the metal surface and other water molecules cannot be directly probed by STM, and DFT studies are typically utilized to elucidate these aspects. With this respect, Liu⁷⁹ studied the adsorption and reactivity of water on Au (111) surfaces and other transition metals, using a plane wave basis set and pseudopotentials, and the PW91⁸⁰ exchange correlation functional. Liu’s results indicated that water orients itself with its oxygen atom towards gold, in line with the structure here discussed for the citrate/Au₂₀ complex. Liu justified this interaction as a result of the hybridization of the p orbital of the water’s oxygen with the metal’s d orbital;⁷⁹ lone-pair-driven adsorption of species on metal surfaces is indeed a documented binding mechanism in surface chemistry.⁸¹ A similar interaction is therefore hypothesized for the water molecules w_1 and w_2 in the citrate/Au₂₀ here discussed. Some level of validation for this hypothesis could come from the change in the water’s O–H length and HOH angle; indeed, an increase in the former and a widening of the latter are associated with electron transfer from the oxygen atom to a surface.^{82,83} In the [HCitrate²⁻

+ Na⁺ + 12 H₂O] supramolecular system, the O–H bond length involving w_1 's coordination to the carboxylate group is 1.00 Å, the uncoordinated O–H bond is 0.97 Å, and the HOH angle is 109.6°; in the citrate/Au₂₀ complex, these measurements are 1.04 Å, 0.97 Å, and 112.3°, respectively, thus indicating charge transfer between the solvent molecule and the surface. A similar trend, but with minor changes in bond lengths, is observed for w_2 . As for the central carboxylate moiety, the bond lengths do not significantly change upon water-mediated coordination with the surface, but the OCO angle increases from 124.9° to 126.2°, possibly also indicating a charge transfer character in the interaction with w_1 . The bond lengths and bond angles of w_1 and w_2 waters and the central carboxylate, before and after surface adsorption, are reported in *Table 7.2*.

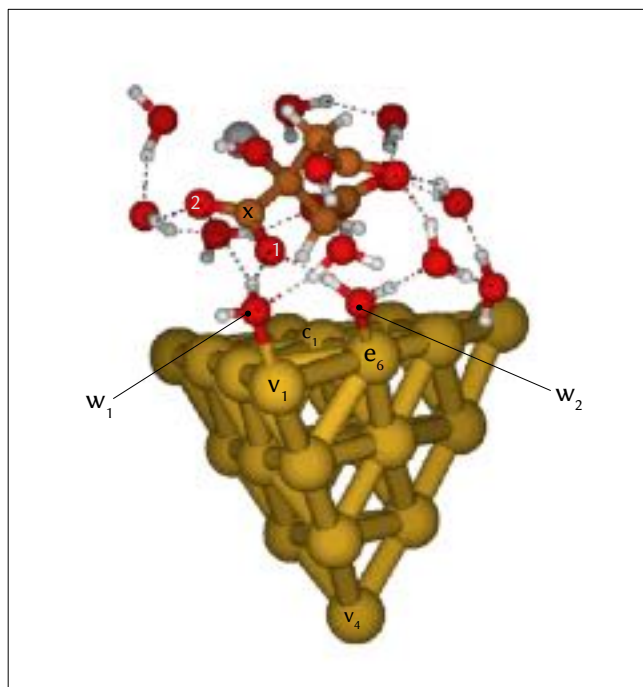


Figure 7.7: Structure of the citrate/Au₂₀ complex (*SI*) in the gas phase, optimized at the B3LYP/LANL2DZ level. Atoms and molecules of interest are labeled: the central Au atom c_1 , the two opposite vertices v_1 and v_4 , the edge Au atom e_6 , the two molecules of water, w_1 and w_2 , and the central carboxylate [O(1)C(x)O(2)]⁻.

Table 7.2: Interatomic distances and bond angles of the citrate/Au₂₀ complex *SI*, optimized at the B3LYP/LANL2DZ level.

groups of atoms	distance (Å)	angle
O _(w1) –Au _(v1)	2.43	
O _(w2) –Au _(e6)	2.20	
COO···H _(w1)	1.51	
COO···H _(w2)	1.65	
COO···Au _(v1)	3.51	
COO···Au _(e6)	4.02	
COO/O _(w1)	2.50	
COO/O _(w2)	4.12	
C _(x) –O ₍₂₎	1.28, <i>1.28</i>	
C _(x) –O ₍₁₎	1.30, <i>1.30</i>	
OCO _(central)		124.9°, <i>124.9</i>
O–H (<i>w</i> ₁ , COO-bonded)	1.04, <i>1.00</i>	
O–H (<i>w</i> ₁ , free)	0.974, <i>0.974</i>	
HOH (<i>w</i> ₁)		112.3°, <i>109.6</i> °
O–H _(w2) (<i>w</i> ₂ , COO-bonded)	0.998, <i>0.990</i>	
O–H _(w2) (<i>w</i> ₂ , H-bonded with H ₂ O)	1.01, <i>0.993</i>	
HOH _(w2)		115.6°, <i>106.9</i> °
Au _(v1) –Au _(e6)	3.28	
Au _(e6) –Au _(e5)	2.74	
Au _(v1) –Au _(e6) –Au _(e6)		166.6°, <i>175.9</i> °
Na ⁺ ···OH ₂ (I)	2.27	
Na ⁺ ···OH ₂ (II)	2.28	
Na ⁺ ···OH ₂ (III)	2.48	
Na ⁺ ···OOC _(terminal)	2.56	
Na ⁺ ···OH _(citrate)	2.34	
Na ⁺ ···Au _(e2,e3,c1 plane) (nearest neighbor)	5.52	

Distances and angles in italics refer to values prior to surface adsorption. Atoms labeling follows *Figure 7.7*.

The metal-water-carboxylate interaction exhibited by the citrate/Au₂₀ complex presents some similarities with the typical adsorption mode of a water dimer on a metallic surface.^{75,76} In these structures, the water molecule lying the closest to the surface binds with the metal substrate directly, *and* acts as the hydrogen bond donor within the dimer; the water molecule farther apart, on the other hand, acts as the hydrogen bond acceptor (*Figure 7.8 b*).^{76,77} In a similar way, in the citrate/Au₂₀ complex, water coordinates

directly to the Au₂₀ surface and, simultaneously, acts as a hydrogen bond donor towards the central carboxylic group of citrate, the hydrogen bond acceptor (Figure 7.8 a). The intermolecular distance between the hydrogen bond donor (water) and acceptor (citrate), estimated as the distance between the water and the carboxylate oxygens, is 2.50 Å for w_1 and 2.63 Å for w_2 . These distances are close to those reported for a water dimer on another coinage metal, Cu (2.72 Å),⁷⁶ and are associated with strong hydrogen bonding.⁸³

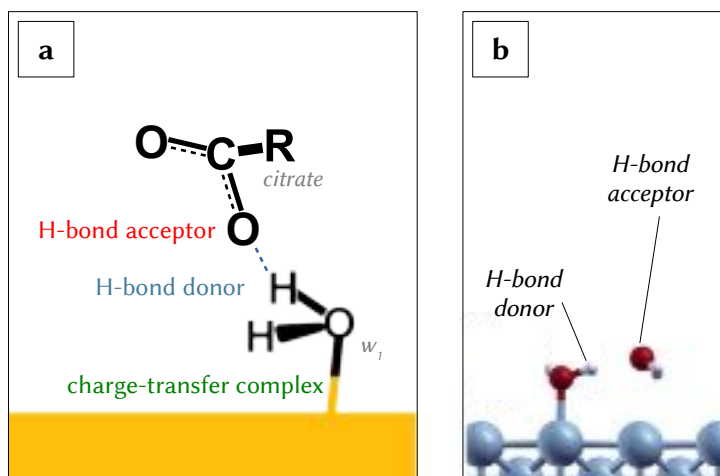


Figure 7.8: (a) Configuration of the adsorbed water w_1 and central carboxylate of citrate. (b) Structure of a water dimer on a Cu(110) surface, optimized at the DFT level; adapted with permission of Springer, from Kumagai, T.,⁷⁷ Copyright 2012; permission conveyed through Copyright Clearance Center, Inc.

Some distortion of the symmetric tetrahedron structure is observed on the Au₂₀ cluster as a result of the adsorption events. The distortion is localized at the sites of water adsorption, and it is of larger magnitude around the Au(v_1) atom, that is, the site in which water has the tightest coordination with citrate. The distance between the v_1 and the e_6 gold atoms increases from 2.80 Å to 3.28 Å, while the e_5 and e_6 gold atoms show a minimal increase, from 2.73 Å to 2.74 Å. Finally, the sodium ion was found to be highly coordinated by three molecules of water (H₂ Na⁺ of 2.28, 2.27, and 2.48 Å), and by citrate's alcoholic group (HO···Na⁺ of 2.34 Å) and deprotonated terminal carboxylate

(COO \cdots Na $^+$ of 2.56 Å). The vicinity of sodium ions to citrate's coordination sphere is in line with numerous experimental studies, such as that by Al-Johani *et al.*,⁵¹ which has been discussed in the preceding section.

To investigate the significance of the water-mediated adsorption of citrate on Au₂₀, three other stable putative surface complex structures were obtained. These structures were the result of successive geometry optimizations of initial guesses obtained by manual displacement of water molecule(s), and they are reported in *Figure 7.9*. Complex *S2* is the optimized structure of an initial geometry obtained by vertically displacing, by ≈ 4 Å, the w_1 water molecule on the first optimized complex, from now on referred to as *S1*. Complex *S3* was instead obtained by applying a translation vector to 5 molecules of water, including w_1 and w_2 (*Appendix F, Figure F.2*), to the stable structure of complex *S2*. The translation vector was calculated as reported in *Equation 7.13*. Finally, the last complex, *VI*, was obtained by taking the starting geometry utilized for complex *S1*, and rotating the Au₂₀ cluster by 180°, perpendicularly to the c_1-v_4 axis. This geometry was utilized to evaluate ad-atom sites, in an analogous way to what was reported by Aikens and Schatz³⁷ for the study of the adsorption of pyridine on the same type of cluster. All Cartesian coordinates of the optimized complexes are reported in *Appendix F*.

$$\vec{t} = 1.5[O_{(\text{COOH})}(x, y, z) - O_{(w_1)}(x, y, z)] \quad (7.13)$$

As reported in *Figure 7.9*, of the four complexes, two of them, *S1* and *S2*, show a water-mediated interaction between citrate and the surface, while the other two, *S3* and *VI*, show direct binding of the carboxylate via unidentate coordination with either the v_1 (complex *S3*) or the v_4 (complex *VI*) gold atom. This low-coordination site was hypothesized to be favored for direct adsorption on the basis of the results published by Provorse and Aikens²⁸ for the formate ion adsorbed on the same cluster. Bond lengths

and other distances of interest for each of the complexes are reported in *Tables 7.3 to 7.5*. It can be observed that the oxygen-gold distances between the ligated water and the metal surface, and between the central carboxylate of citrate and the metal surface, are of the same order of magnitude, ranging from 2.20 to 2.43 Å in the former, and from 2.27 to 2.32 Å in the latter. When the carboxylate is directly adsorbed on the gold surface (*S3* and *VI* complexes), the OCO bond angle slightly increases, from an initial value of 124.9° in the optimized, water-coordinated, unadsorbed ligand, to 126.1° and 126.7° of the adsorbed ligands on the *S3* and *VI* complexes, respectively. A similar level of increase is observed also for the water-ligated structures, possibly indicating the existence of some charge transfer character that extends past the first ligated water. As for the COO bond lengths, these remain substantially unvaried when comparing the two families of complexes (water-ligated *vs* direct adsorption).

Another feature shared across all complexes is the deformation of the gold cluster upon adsorption; besides the already mentioned Au–Au interatomic distance increase, a distortion of the vertex-edge-edge angle is observed. In the free Au₂₀ cluster, the $v_1-e_6-e_5$ angle ($\equiv v_4-e_{10}-e_7$) measures 175.9°, while, in all complexes, this decreases to 166.6° (*S1*), 165.1° (*S2* and *S3*), and 165.0° (*VI*). Surface reconstruction of a metal cluster upon adsorption is a known phenomenon,⁸⁴ and it is especially observed in Au, including in the more densely packed (111) planes.⁸⁵ This surface reconstruction typically occurs as a relaxation and contraction of the surface layer of the cluster,⁸⁶ which is consistent with the small decrease in the $v_1-e_6-e_5$ angle observed for the optimized complex structures.

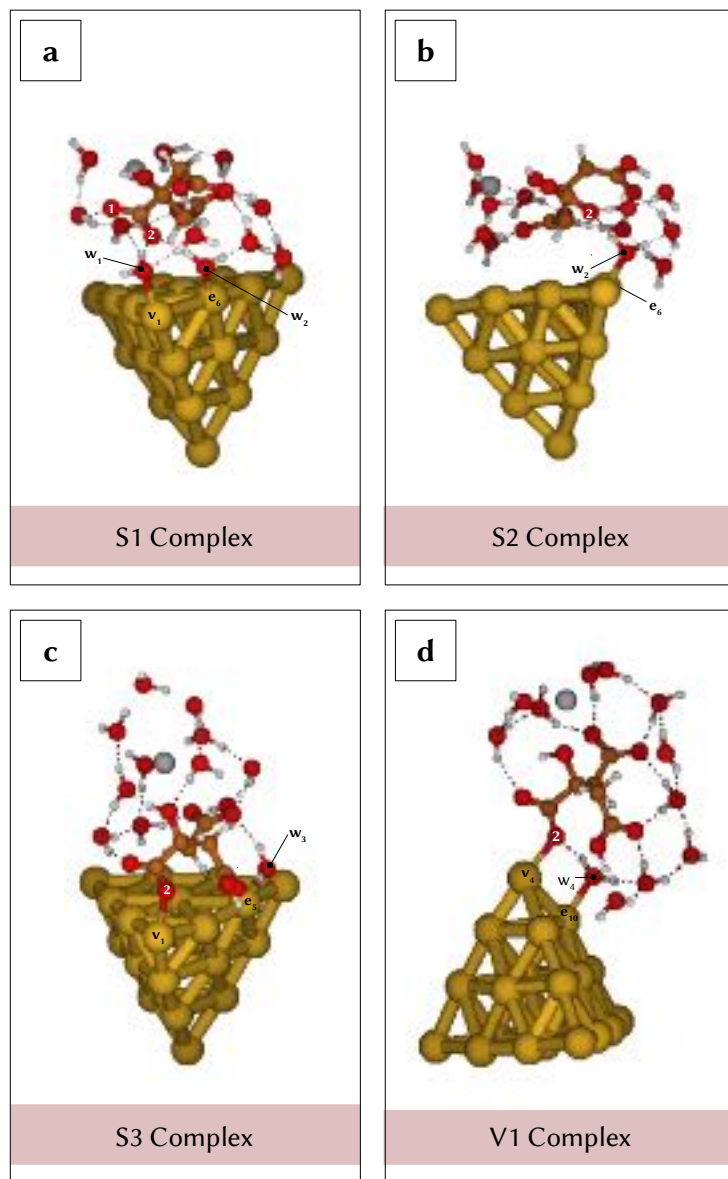


Figure 7.9: Stable structures of *S1*, *S2*, *S3*, and *V1* citrate/Au₂₀ complexes.

Table 7.3: Interatomic distances and bond angles of the citrate/Au₂₀ complex S2, optimized at the B3LYP/LANL2DZ level.

groups of atoms	distance (Å)	angle
O _(w2) -Au _(e6)	2.22	
COO···H _(w2)	1.65	
COO···Au _(e6)	4.09	
COO/O _(w2)	2.65	
C _(x) -O ₍₂₎	1.27, 1.28	
C _(x) -O ₍₁₎	1.29, 1.30	
OCO _(central)		126.3°, 124.9
O-H _(w2) (w2, COO-bonded)	1.00, 0.990	
O-H _(w2) (w2, H-bonded with H ₂ O)	1.02, 0.993	
HOH _(w2)		112.9°, 106.9°
Au _(v1) -Au _(e6)	3.19	
Au _(e6) -Au _(e5)	2.75	
Au _(v1) -Au _(e6) -Au _(e6)		165.1°, 175.9°
Na ⁺ ···OH ₂ (I)	2.26	
Na ⁺ ···OH ₂ (II)	2.27	
Na ⁺ ···OH ₂ (III)	2.48	
Na ⁺ ···OOC _(terminal)	2.67	
Na ⁺ ···OH _(citrate)	2.32	
Na ⁺ ···Au _(e3) (nearest neighbor)	5.61	

Distances and angles in italics refer to values prior to surface adsorption. Atoms labeling follows *Figure 7.7*.

Table 7.4: Interatomic distances and bond angles of the citrate/Au₂₀ complex *S3*, optimized at the B3LYP/LANL2DZ level.

groups of atoms	distance (Å)	angle
COO–Au _(v1)	2.32	
C _(x) –O ₍₂₎	1.27, <i>1.28</i>	
C _(x) –O ₍₁₎	1.31, <i>1.30</i>	
OCO _(central)		126.1°, <i>124.9</i>
O _(w3) –Au _(e5)	2.44	
HOCO···H _(w3)	1.84	
HOCO/O _(w3)	2.81	
HOCO···Au _(e5)	4.13	
COO _(terminal) ···H _(w3)	1.92	
COO _(terminal) /O _(w3)	2.84	
COO _(terminal) ···Au _(e5)	4.40	
O–H _(w3) (HOCO-bonded)	0.988, <i>0.988</i>	
O–H _(w3) (COO _(terminal) -bonded)	0.987, <i>0.992</i>	
HOH _(w3)		107.7°, <i>107.4</i> °
Au _(v1) –Au _(e6)	2.77	
Au _(e6) –Au _(e5)	2.76	
Au _(v1) –Au _(e6) –Au _(e6)		165.1°, <i>175.9</i> °
Na ⁺ ···OH ₂ (I)	2.38	
Na ⁺ ···OH ₂ (II)	2.38	
Na ⁺ ···OH ₂ (III)	2.39	
Na ⁺ ···OH ₂ (IV)	2.53	
Na ⁺ ···OOC _(terminal)	2.63	
Na ⁺ ···OH _(citrate)	3.57	
Na ⁺ ···Au _(c1) (nearest neighbor)	6.38	

Distances and angles in italics refer to values prior to surface adsorption. Atoms labeling follows *Figure 7.7*.

Table 7.5: Interatomic distances and bond angles of the citrate/Au₂₀ complex *VI*, optimized at the B3LYP/LANL2DZ level.

groups of atoms	distance (Å)	angle
COO–Au _(v1)	2.27	
C _(x) –O ₍₂₎	1.30, <i>1.28</i>	
C _(x) –O ₍₁₎	1.27, <i>1.30</i>	
OCO _(central)		126.7°, 124.9
O _(w4) –Au _(e10)	2.30	
O–H _(w4) (H-bonded with H ₂ O)	1.01	
O–H _(w4) (pointing towards COO–Au)	0.989	
HOH _(w4)		111.7°
Au _(v4) –Au _(e10)	3.11	
Au _(e10) –Au _(e7)	2.76	
Au _(v4) –Au _(e10) –Au _(e7)		165.0°, 175.9°
Na ⁺ ···OH ₂ (I)	2.23	
Na ⁺ ···OH ₂ (II)	2.24	
Na ⁺ ···OH ₂ (III)	2.45	
Na ⁺ ···OOC _(terminal)	3.38	
Na ⁺ ···OH _(citrate)	2.32	
Na ⁺ ···Au _(v1) (nearest neighbor)	7.89	

Distances and angles in italics refer to values prior to surface adsorption. Atoms labeling follows *Figure 7.7*.

The free energies of adsorption, ΔG_{ad} , were estimated in the gas phase and in solution, at 298.15 K, as detailed in the preceding section, § 7.2. As reported in *Tables 7.6* and *7.7*, the calculated thermodynamic parameters show that all adsorption configurations are the result of exothermic and exergonic adsorption processes, and that the change in entropy is negative, as expected for any order-increasing phenomena, such as surface adsorption. The theoretical values for ΔG_{ad} in the gas phase show that the complexes have increasing stability with increasing number of adsorbed molecules of water, such that the most favorable adsorption configurations are, in order, those adopted by complexes *S1* and *S2*. On the other hand, direct adsorption is less favored. Upon application of an implicit solvent model, SMD,⁷⁰ the ΔG_{ad} decreases for all complexes, as expected.² The estimated solvation effects ranged from -67.71 kcal/mol of complex *S2* to -73.01

kcal/mol of complex *S3*. The complexes in solution show a slightly different order of thermodynamic favorability, as follows: *S2* < *SI* < *VI* < *S3*; however, water-ligated complex structures are still thermodynamically favored over direct adsorption, even after application of a continuum solvent model. This trend is of particular interest if the work by Provorse and Aikens²⁸ is recalled; in their work, they observed higher thermodynamic favorability of structures in the presence of a continuum solvent, and postulated the cooperation of a species *other than* the carboxylate ligand (formate, in their case) or the gold surface, in the ligation and stabilization of the adsorbate layer on actual gold nanoparticles. Indeed, Provorse and Aikens²⁸ hypothesized that by-products of the nanofabrication process, for example, the citrate oxidation species in the case of citrate-reduced gold nanoparticles, contribute to the formation and stabilization of the capping layer. While the study here presented did not include any nanostars reaction species or by-products, the results do seem to suggest that the adsorption of citrate is most favorably mediated by another species besides the ligand and the cluster themselves — this species is water. Further studies could be performed to evaluate the role of other species in the adsorption of citrate to gold, for example, dehydroascorbic acid. As it can be deduced from the reaction protocol (§ 3.2.1), dehydroascorbic acid is the reaction product with the second highest concentration^{VI} in the as-synthesized nanostars, and it is an electron-rich but neutral species (*Figure 4.2*) that does not contribute to the surface charge of the nanoparticle (§ 4.1). Dehydroascorbic acid has been excluded from the NS/Ct modeling primarily, but not exclusively, because of limitations of computational resources; other reasons for its exclusion were that it has been assumed to have negligible interactions with the surface, and that, to the author's knowledge, it is not reported to have relevant interactions with citrate. However, should

^{VI}The species present in solution in the highest concentration after synthesis is Cl⁻. A justification for its exclusion from the adsorption modeling is given in § 7.2.

available resources allow, it would be interesting to include it in future DFT studies, and observe whether it demonstrates any role in the surface adsorption of citrate.

Table 7.6: Theoretical thermodynamic quantities for the formation of the *S1*, *S2*, *S3*, and *V1* complexes in the gas phase, obtained at the B3LYP/LANL2DZ level.

Formation of complex	$\Delta H_{\text{ads(g)}}$ (kcal/mol)	$\Delta S_{\text{ads(g)}}$ (kcal/mol)	$\Delta G_{\text{ads(g)}}$ (kcal/mol)
$[\text{Au}_{20}]_{\text{(g)}} + [\text{HCitrate}^{2-} + \text{Na}^+ + 12 \text{H}_2\text{O}]_{\text{(g)}} \rightarrow [\text{S1}]_{\text{(g)}}$	-50.9	-0.05	-35.6
$[\text{Au}_{20}]_{\text{(g)}} + [\text{HCitrate}^{2-} + \text{Na}^+ + 12 \text{H}_2\text{O}]_{\text{(g)}} \rightarrow [\text{S2}]_{\text{(g)}}$	-48.8	-0.05	-33.8
$[\text{Au}_{20}]_{\text{(g)}} + [\text{HCitrate}^{2-} + \text{Na}^+ + 12 \text{H}_2\text{O}]_{\text{(g)}} \rightarrow [\text{S3}]_{\text{(g)}}$	-41.4	-0.04	-28.3
$[\text{Au}_{20}]_{\text{(g)}} + [\text{HCitrate}^{2-} + \text{Na}^+ + 12 \text{H}_2\text{O}]_{\text{(g)}} \rightarrow [\text{V1}]_{\text{(g)}}$	-36.6	-0.04	-26.1

Table 7.7: Theoretical thermodynamic quantities for the formation of the *S1*, *S2*, *S3*, and *V1* complexes in solution, obtained at the B3LYP/LANL2DZ level, with the introduction of the continuum solvent model SMD.⁷⁰

Formation of complex	Free energy of solvation (kcal/mol)	$\Delta G_{\text{(aq)}}$ (kcal/mol)
$[\text{S1}]_{\text{(g)}} \rightarrow [\text{S1}]_{\text{(aq)}}$	-70.6	-13.0
$[\text{S2}]_{\text{(g)}} \rightarrow [\text{S2}]_{\text{(aq)}}$	-67.7	-15.9
$[\text{S3}]_{\text{(g)}} \rightarrow [\text{S3}]_{\text{(aq)}}$	-73.0	-10.9
$[\text{V1}]_{\text{(g)}} \rightarrow [\text{V1}]_{\text{(aq)}}$	-72.8	-10.8

7.2.2 Au₁₉Ag: homotops and citrate adsorption

As explained in § 7.2, the Au₁₉Ag bimetallic cluster was modeled starting from the Au₂₀ cluster, by atomic substitution of one atom of gold with one atom of silver. The resulting three inequivalent homotops are shown in *Figure 7.10*. If the same atom labeling system as that reported in *Figure 7.6* is utilized, the first (*Figure 7.10 a*) homotop has the silver atom in the c_1 position ($\equiv c_2, c_3, c_4$), the second in the v_1 position ($\equiv v_2, v_3, v_4$), and the third in the e_6 position ($\equiv e_1, \dots, e_{12}$). The geometry of all three homotops was optimized at the B3LYP/SRSC level; a different ECP and basis set, the Stuttgart-Bonn relativistic small core (SRSC),⁸⁷ was necessary in place of the original LANL2DZ utilized for the Au₂₀ cluster,

as the latter proved to be inadequate to obtain stable structures of the bimetallic system. As a means of comparison, the optimized structures of Au₂₀ and Ag₂₀ were obtained at the same level of theory. The Cartesian coordinates of all stable structures are reported in *Appendix F*.

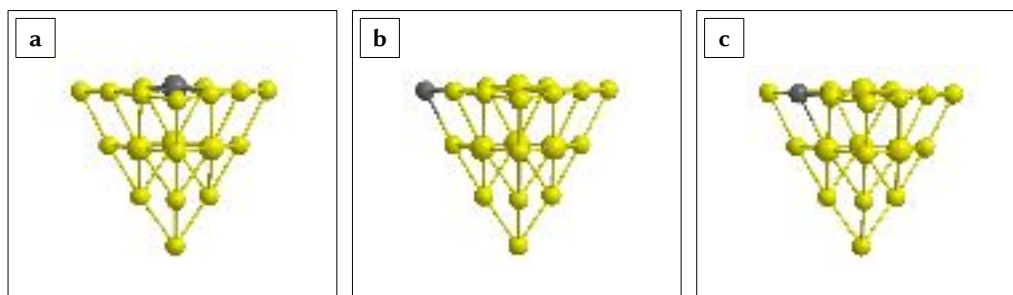


Figure 7.10: Schematic representation of the three inequivalent homotops for the Au₁₉Ag tetrahedral cluster: (a) Au₁₉Ag “c”; (b) Au₁₉Ag “v”; (c) Au₁₉Ag “e”. Silver atoms are represented in grey, while gold atoms are shown in yellow.

The minimum energy homotop was the Au₁₉Ag “c” cluster, followed, in order, by the “e” and the “v” homotops. This is consistent with what has been reported for smaller bimetallic Au_mAg_n ($m + n \leq 10$) clusters,^{17,19} for which species segregation is not thermodynamically favorable, and thus, the less abundant phase tends to form as many hetero-bonds as possible. The *c* position in this tetrahedral cluster is indeed the one with the highest coordination. Simultaneously, gold atoms are in the most peripheral positions, v_i and e_i , which is also reported to be thermodynamically favored for Au_mAg_n ($m + n \leq 10$) clusters.^{17,19}

The introduction of a silver atom did not cause major distortions of the original tetrahedral geometry in any of the homotops. The structure of the “c” homotop was essentially unchanged compared to the Au₂₀ cluster, while some minor distortions were observed in the “e” and “v” homotops, in proximity of the silver atom. The interatomic distances for each homotop are reported in *Table 7.8*, and compared to those measured for

the Au₂₀ cluster, re-optimized at the B3LYP/SRSC level of theory. Interatomic distances for an analogous tetrahedral Ag₂₀ cluster are also reported. As expected, the overall geometry of the Au₁₉Ag system is closer to the pure gold cluster than it is to the silver counterpart.

Table 7.8: Interatomic distances for the three inequivalent Au₁₉Ag tetrahedral homotops, “c”, “e”, and “v”, compared to Au₂₀ and Ag₂₀, optimized at the same level of theory (B3LYP/SRSC).

Group of atoms	Homotop “c”	Homotop “e”	Homotop “v”	Au ₂₀	Ag ₂₀
<i>v</i> ₁ - <i>e</i> ₆ - <i>e</i> ₅	175.8°	174.1°	178.5°	175.9°	177.3°
<i>v</i> ₁ - <i>e</i> ₁ - <i>e</i> ₂	175.8°	176.6°	178.5°	175.9°	177.4°
<i>e</i> ₁ - <i>v</i> ₁ - <i>e</i> ₆	67.0°	65.8°	63.8°	67.1°	64.1°
<i>v</i> ₁ - <i>e</i> ₆	2.79 Å	2.80 Å	2.81 Å	2.79 Å	2.81 Å
<i>v</i> ₁ - <i>e</i> ₁	2.79 Å	2.78 Å	2.81 Å	2.79 Å	2.81 Å
<i>e</i> ₆ - <i>e</i> ₅	2.72 Å	2.78 Å	2.75 Å	2.73 Å	2.79 Å
<i>c</i> ₁ - <i>e</i> ₆	2.91 Å	2.91 Å	2.92 Å	2.91 Å	2.89 Å
<i>c</i> ₁ - <i>e</i> ₅	2.91 Å	2.85 Å	2.90 Å	2.91 Å	2.89 Å
<i>c</i> ₁ - <i>e</i> ₁	2.91 Å	2.91 Å	2.92 Å	2.91 Å	2.89 Å
<i>c</i> ₁ - <i>e</i> ₂	2.91 Å	2.90 Å	2.90 Å	2.91 Å	2.89 Å
<i>c</i> ₁ - <i>e</i> ₃	2.91 Å	2.94 Å	2.90 Å	2.91 Å	2.89 Å
<i>c</i> ₁ - <i>e</i> ₄	2.91 Å	2.94 Å	2.90 Å	2.91 Å	2.89 Å

Preliminary results from the converged optimized structure of the Au₁₉Ag/citrate complex show a water-ligated adsorbate, similar to what has been observed for the monometallic gold cluster (*Figure 7.11*). Ongoing stability check and frequencies calculations will be utilized to ensure the converged structure corresponds to a true energy minimum, as done for all previous structures.

7.2.3 Summary

DFT calculations allowed for the modeling of a simplified gold-citrate system, which yielded a population of four possible adsorbate structures. Frequency calculations permitted the obtainment of thermodynamic trends within the optimized set of putative structures, indicating a possible significance of water-mediated adsorption processes in the formation

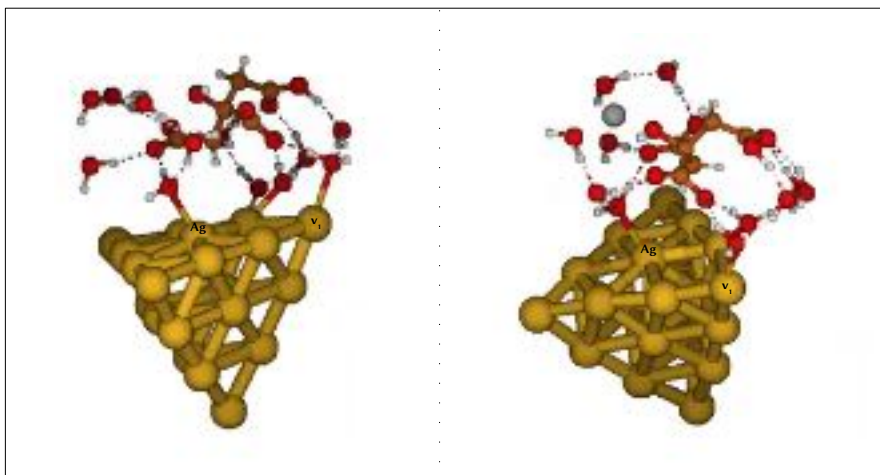


Figure 7.11: Converged structure after geometry optimization of the Au₁₉Ag/citrate complex in the gas phase.

of a citrate capping layer on colloidal gold nanoparticles. This type of interaction seems to be possible for Au₁₉Ag-citrate systems, too, although ongoing studies still have to confirm the obtained structure is a true energy minimum.

To the author's knowledge, the results here presented constitute the first reported case of water-mediated citrate adsorption on noble metal clusters. This novelty point could be attributed to the fact that prior literature on the subject did not include the presence of explicit solvent molecules in the representation of this type of system, which demonstrates one of the possible advantages of utilizing a mixed explicit/implicit solvent when modeling adsorption phenomena; processes that involve the direct participation of solvent molecules cannot be possibly modeled by an implicit solvent alone. However, the significance of these structures in terms of global minimum search should be carefully investigated, in that, as discussed in the earlier sections of this chapter, DFT studies with limited computational

resources are only capable of accessing a small portion of the potential energy landscape of systems of high complexity, such as solvated adsorbates on nanoalloys.

In retrospect, the results obtained from the ζ titration experiments discussed in *Chapter 6*, seem to offer new validation points for the actual presence of water in the adsorbate layer. The Hill-Langmuir model does not pose restrictions on the identity of the molecules participating to the cooperative binding — cooperativity could ensue among different molecules of the stabilizer itself, as well as among different chemical species that might be present in the system. Therefore, the positive cooperative binding that was deduced from the Hill-Langmuir fit of the ζ titration data might be interpreted not only as a result of hydrogen bonding among individual citrate molecules, but also as a result of the water-citrate charge transfer complex formation.

Even though DFT-calculated thermodynamic parameters do not have the necessary accuracy to be considered as absolute values,² the free energies of adsorption that were obtained for each putative citrate-gold complex seem physically realistic, if compared to the experimental values obtained by ζ potential titrations (*Chapter 6*). Indeed, the calculated ΔG_{ad} in solution ranged from -10.6 to -15.9 kcal/mol, which, net of temperature differences, silver doping, and of an accuracy around 10 kcal/mol, are in line with those determined experimentally, which were -4.36 ± 0.08 and -4.58 ± 0.05 kcal/mol, at 10 and 20°C, respectively. Free energies of adsorption of this order of magnitude are typically attributed to weak chemisorption. Lone-pair-driven interactions, such as that of water with transition metal surfaces, or carboxylate-involving charge transfer complexes, are generally reported to be stronger than physisorption, albeit of longer-range, and thus weaker, compared to other interactions, such as π -interactions with transition metal surfaces.⁸¹ Again, this is consistent with the interpretation of the ζ potential titration results, which indicated a strengthening of the adsorption constant of citrate to the

nanostars with increasing temperature, which, albeit relatively low in magnitude, is indicative of chemisorption phenomena.

REFERENCES

- [1] Blinder, S.M.; Sutcliffe, B.; Geppert, W. On the Quantum Theory of Molecules, **2002** (Engl. Transl.) Born, M.; Oppenheimer, J.R. Zur Quantentheorie der Molekeln, *Ann. Phys.*, **1927**, 389, 457-484.
- [2] Cramer, C.J. *Essentials of Computational Chemistry, Theories and Models*; Wiley: Chichester, 2002.
- [3] Atkins, P.; Friedman, R. *Molecular Quantum Mechanics*, Fifth Edition; Oxford University Press USA: New York, 2011.
- [4] Hohenberg, P.; Kohn, W. Inhomogeneous Electron Gas. *Phys. Rev.*, **1964**, 136(3B), B864–B871.
- [5] Kohn, W.; Sham, L.J. Self-Consistent Equations Including Exchange and Correlation Effects. *Phys. Rev.*, **1965**, 140(4A), A1133–A1138.
- [6] D. Becke, A.D. Density-functional thermochemistry. III. The role of exact exchange. *J. Chem. Phys.*, **1993**, 98(7), 5648–5652.
- [7] Lee, C.; Yang, W.; Parr, R.G. Development of the Colle-Salvetti Correlation-Energy Formula into a Functional of the Electron Density. *Phys. Rev. B.*, **1988**, 37, 785–789.
- [8] Stephens, P.J.; Devlin, F.J.; Chabalowski, C.F.; Frisch, M.J. Ab Initio Calculation of Vibrational Absorption and Circular Dichroism Spectra Using Density Functional Force Fields. *J. Phys. Chem.*, **1994**, 98(45), 11623–11627.
- [9] Le Ru, E.C.; Etchegoin, P.G. *Principles of surface enhanced Raman spectroscopy and related plasmonic effects*, Elsevier: Amsterdam, 2009.
- [10] Fortunelli, A.; Barcaro, G. Density-Functional Theory of Free and Supported Metal Nanoclusters and Nanoalloys. In *Metal Clusters and Nanoalloys From Modeling*

to Applications; Mariscal, M.M., Oviedo, O.A., Leiva, E.P.M., Eds.; Nanostructure Science and Technology Series; Lockwood, D.J., Ed.; Springer: New York, 2013.

- [11] Jellinek, J.; Krissinel, E.B. Ni_nAl_m alloy clusters: analysis of structural forms and their energy ordering. *Chem. Phys. Lett.*, **1996**, 258(12), 283–292.
- [12] Johnston, R.L. Metal Nanoparticles and Nanoalloys. In *Metal Nanoparticles and Nanoalloys*; Johnston, R.L., Wilcoxon, J.P., Eds.; Frontiers of Nanoscience Series; Palmer, R.E., Ed.; Elsevier: Oxford, 2012.
- [13] Ferrando, R.; Jellinek, J.; Johnston, R.L. Nanoalloys: From Theory to Applications of Alloy Clusters and Nanoparticles. *Chem. Rev.*, **2008**, 108(3), 845–910.
- [14] Wales, D.J.; Doye, J.P.K. Global optimization by basin-hopping and the lowest energy structures of Lennard-Jones clusters containing up to 110 atoms. *J. Phys. Chem. A*, **1997**, 101(28), 5111–5116.
- [15] Gupta, R.P. Lattice relaxation at a metal surface. *Phys. Rev. B*, **1981**, 23(12), 6265–6270.
- [16] Assadollahzadeh, B.; Schwerdtfeger, P. A systematic search for minimum structures of small gold clusters Au_n (n = 2–20) and their electronic properties. *J. Chem. Phys.*, **2009**, 131, 064306-1–064306-11.
- [17] Heiles, S.; Logsdail, A.J.; Schäfer, R.; Johnston, R.L. Dopant-induced 2D-3D transition in small Au-containing clusters: DFT-global optimisation of 8-atom Au-Ag nanoalloys. *Nanoscale*, **2012**, 4(4), 1109–1115.
- [18] Rapetti, D.; Ferrando, R. Density functional theory global optimization of chemical ordering in AgAu nanoalloys. *J. Alloys Compd.*, **2019**, 779, 582–589.
- [19] Bonačić-Koutecký, V.; Burda, J.; Mitrić, R.; Maofa, G.; Zampella, G.; Fantucci, P. Density functional study of structural and electronic properties of bimetallic silvergold clusters: Comparison with pure gold and silver clusters. *J. Chem. Phys.*, **2002**, 117(7), 3120–3131.
- [20] Rossi, G.; Ferrando, R.; Rapallo, A.; Fortunelli, A.; Curley, B.C.; Lloyd, L.D.; Johnston, R.J. Global optimization of bimetallic cluster structures. II. Size-matched Ag-Pd, Ag-Au, and Pd-Pt systems. *J. Chem. Phys.*, **2005**, 122, 194309

- [21] Rosato, V.; Guillopé, M.; Legrand, B. Thermodynamical and structural properties of f.c.c transition metals using a simple tight-binding model. *Phil. Mag. A*, **1989**, *59*(2), 321–336.
- [22] Johnston, R.L. Evolving better nanoparticles: Genetic algorithms for optimising cluster geometries. *Dalton Trans.*, **2003**, *22*, 4193–4207.
- [23] Baletto, F.; Ferrando, R.; Fortunelli, A.; Montalenti, F.; Mottet, C. Crossover among structural motifs in transition and noble-metal clusters. *J. Chem. Phys.*, **2002**, *116*(9), 3856–3863.
- [24] Bartlett, N. Relativistic effects and the chemistry of gold. *Gold Bull.*, **1998**, *31*, 22–25.
- [25] Tao, A.R.; Habas, S.; Yang, P. Shape Control of Colloidal Metal Nanocrystals. *Small*, **2008**, *4*(3), 310–325.
- [26] Wells Jr., D.H.; Delgass, W.N.; Thomson, K.T. Density functional theory investigation of gold cluster geometry and gas-phase reactivity with O₂. *J. Chem. Phys.*, **2002**, *117*(23), 10597–10603.
- [27] Goel, S.; Velizhanin, K.A.; Piryatinski, A.; Tretiak, S.; Ivanov, S.A. DFT Study of Ligand Binding to Small Gold Clusters. *J. Phys. Chem. Lett.*, **2010**, *1*, 927–931.
- [28] Provorse, M.R.; Aikens, C.M. Binding of carboxylates to gold nanoparticles: A theoretical study of the adsorption of formate on Au₂₀. *Comput. Theor. Chem.*, **2012**, *987*, 16–21.
- [29] Hull, J.M.; Provorse, M.R.; Aikens, C.M. Formylxyl Radical Gold Nanoparticle Binding: A Theoretical Study. *J. Phys. Chem. A*, **2012**, *116*(22), 5445–5452.
- [30] Santiago-Rodríguez, Y.; Herron, J.A.; Curet-Arana, M.; Mavrikakis, M. Atomic and molecular adsorption on Au (111). *Surf. Sci.*, **2014**, *627*, 57–69.
- [31] Liu, S.; Ishimoto, T.; Koyama, M. First-Principles Calculations of OH⁻/OH Adsorption on Gold Nanoparticles. *Int. J. Quantum Chem.*, **2015**, *115*, 1597–1605.
- [32] Chang, L.; Fisher, A.; Liu, Z.; Cheng, D. A density functional theory study of sulfur adsorption on AgAu nanoalloys. *Comput. Theor. Chem.*, **2016**, *1085*, 66–74.

- [33] Yao, G.; Zhai, Z.; Zhong, J.; Huang, Q. DFT and SERS Study of ^{15}N Full-labeled Adenine Adsorption on Silver and Gold Surfaces. *J. Phys. Chem. C*, **2017**, *121*, 9869–9878.
- [34] You, T.; Lang, X.; Huang, A.; Yin, P. A DFT study on surface-enhanced Raman spectroscopy of aromatic dithiol derivatives adsorbed on gold nanojunctions. *Spectrochim. Acta, Part A*, **2018**, *188*, 222–229.
- [35] Lopez-Tocn, I.; Valdivia, S.; Soto, J.; Otero, J.C.; Muniz-Miranda, F.; Menziani, M.C.; Muniz-Miranda, M. A DFT Approach to the Surface-Enhanced Raman Scattering of 4-Cyanopyridine Adsorbed on Silver Nanoparticles. *Nanomaterials*, **2019**, *9*(9), 1211-1–1211-12.
- [36] Zhao, L.; Jensen, L.; Schatz, G.C. Pyridine- Ag_{20} Cluster: A Model System Studying Surface-Enhanced Raman Scattering. *J. Am. Chem. Soc.*, **2006**, *128*, 2911–2919.
- [37] Aikens, M.C.; Schatz, G.C. TDDFT Studies of Adsorption and SERS Spectra of Pyridine Interacting with Au_{20} . *J. Phys. Chem. A*, **2006**, *110*, 13317–13324.
- [38] Jensen, L.; Zhao, L.L.; Schatz, G.C. Size-Dependence of the Enhanced Raman Scattering of Pyridine Adsorbed on Ag_n ($n = 2-8, 20$) Clusters. *J. Phys. Chem. C*, **2007**, *111*, 4756–4764.
- [39] Lofrumento, C.; Platania, E.; Ricci, M.; Becucci, M.; Castellucci, E.M. SERS Spectra of Alizarin Anion Ag_n ($n = 2, 4, 14$) Systems: TDDFT Calculation and Comparison with Experiment. *J. Phys. Chem. C*, **2016**, *120*(22), 12234–12241.
- [40] Biswas, N.; Thomas, S.; Sarkar, A.; Mukherjee, T.; Kapoor, S. Adsorption of Methimazole on Silver Nanoparticles: FTIR, Raman, and Surface-Enhanced Raman Scattering Study Aided by Density Functional Theory. *J. Phys. Chem. C*, **2009**, *113*(17), 7091–7100.
- [41] Caporali, S.; Muniz-Miranda, F.; Pedone, A.; Muniz-Miranda, M. SERS, XPS and DFT Study of Xanthine Adsorbed on Citrate-Stabilized Gold Nanoparticles. *Sensors*, **2019**, *19*(12), 2700-1–2700-10.
- [42] Rekha, T.N.; Umadevi, B.; Rajkumar, J.M. Structural and spectroscopic study of adsorption of naphthalene on silver. *J. Mol. Struct.*, **2015**, *1079*, 155–162.
- [43] Rekha, T.N.; Umadevi, B.; Rajkumar, J.M. Structural and spectroscopic study of adsorption of anthracene on silver. *Mol. Phys.*, **2015**, *113*(23), 3673–3682.

- [44] Schwerdtfeger, P. The Pseudopotential Approximation in Electronic Structure Theory. *Chem. Phys. Chem.*, **2011**, *12*, 3143–3155.
- [45] Hay, P.J.; Wadt, W.R. Ab initio effective core potentials for molecular calculations. Potentials for K to Au including the outermost core orbitals. *J. Chem. Phys.*, **1985**, *82*, 299–310.
- [46] Hehre, W.J.; Ditchfield, R.; Pople, J.A. Self-Consistent Molecular Orbital Methods. XII. Further extensions of Gaussian-type basis sets for use in molecular-orbital studies of organic-molecules. *J. Chem. Phys.*, **1972**, *56*, 2257–2261.
- [47] Wulandari, P.; Nagahiro, T.; Michioka, K.; Tamada, K.; Ishibashi, K.; Kimura, Y.; Niwano, M. Coordination of Carboxylate on Metal Nanoparticles Characterized by Fourier Transform Infrared Spectroscopy. *Chem. Lett.*, **2008**, *37*, 888–889.
- [48] Park, J. W.; Shumaker-Parry, J. S. Structural Study of Citrate Layers on Gold Nanoparticles: Role of Intermolecular Interactions in Stabilizing Nanoparticles. *J. Am. Chem. Soc.*, **2014**, *136*, 1907–1921.
- [49] Wright, L.B.; Rodger, P.M.; Walsh, T.R. Structure and properties of citrate overlayers adsorbed at the aqueous Au(111) interface. *Langmuir*, **2014**, *30*(50), 15171–15180.
- [50] Wulandari, P.; Nagahiro, T.; Fukada, N.; Kimura, Y.; Niwano, M.; Tamada, K. Characterization of citrated on gold and silver nanoparticles. *J. Colloid Interface Sci.*, **2015**, *438*, 244–248.
- [51] Al-Johani, H.; Abou-Hamad, E.; Jedidi, A.; Widdifield, C.M.; Viger-Grave, J.; Sangaru, S.S.; Gajan, D.; Anjum, D.H.; Ould-Chikh, S.; Hedhili, M.N.; Gurinov, A.; Kelly, M.J.; El Eter, M.; Cavallo, L.; Emsley, L.; Basset, J-M. The structure and binding mode of citrate in the stabilization of gold nanoparticles. *Natur. Chem.*, **2017**, *9*, 890–895.
- [52] Monti, S.; Barcaro, G.; Sementa, L.; Carravetta, V.; Ågren, H. Characterization of the adsorption dynamics of trisodium citrate on gold in water solution. *RSC Adv.*, **2017**, *7*, 49655–49663.
- [53] Shi, L.; Buhler, E.; Boué, F.; Carn, F. How does the size of gold nanoparticles depend on citrate to gold ratio in Turkevich synthesis? Final answer to a debated question. *J. Colloid Interface Sci.*, **2017**, *492*, 191–198.

- [54] Chong, G.; Laudadio, E.D.; Wu, M.; Murphy, C.J.; Hamers, R.J.; Hernandez, R. Density, Structure, and Stability of Citrate³⁻ and H₂citrate⁻ on Bare and Coated Gold Nanoparticles. *J. Phys. Chem. C*, **2018**, *122*, 28393–28404.
- [55] Perfilieva, O.A.; Pyshnyi, D.V.; Lomzov, A.A. Molecular Dynamics Simulation of Polarizable Gold Nanoparticles Interacting with Sodium Citrate. *J. Chem. Theory Comput.*, **2019**, *15*(2), 1278–1292.
- [56] Gisbert-González, J.M.; Cheuquepn, W.; Ferre-Vilaplana, A.; Herrero, H.; Feliu, J.M. Citrate adsorption on gold: Understanding the shaping mechanism of nanoparticles. *J. Electroanal. Chem.*, **2020**, <https://doi.org/10.1016/j.jelechem.2020.114015>
- [57] Turkevich, J.; Stevenson, P.C.; Hillier J. A study of the nucleation and growth processes in the synthesis of colloidal gold. *Discuss. Faraday Soc.*, **1951**, *11*, 55–75.
- [58] Nørskov, J.K.; Rossmeisl, J.; Logadottir, A.; Lindqvist, L.; Kitchin, J.R.; Bligaard, T.; Jónsson, H. Origin of the overpotential for oxygen reduction at a fuel-cell cathode. *J. Phys. Chem. B*, **2004**, *108*, pp. 17886–17892.
- [59] Klamt, A. Conductor-like Screening Model for Real Solvents: A New Approach to the Quantitative Calculation of Solvation Phenomena. *J. Phys. Chem.*, **1995**, *99*(7), 2224–2235.
- [60] Delley, B. The conductor-like screening model for polymers and surfaces. *Mol. Simulat.*, **2006**, *32*, 117–123.
- [61] Berendsen, H.J.C.; Postma, J.P.M.; van Gunsteren, W.F.; Hermans, J. Interaction Models for Water in Relation to Protein Hydration. In *Intermolecular Forces*; Pullman, B., Ed.; Springer: Berlin, 1981.
- [62] Jorgensen, W.L.; Chandrasekhar, J.; Madura, J.D.; Impey, R.W.; Klein, M.L. Comparison of simple potential functions for simulating liquid water. *J. Chem. Phys.*, **1983**, *79*(2), 926–935.
- [63] Tomasi, J.; Mennucci, B.; Cammi, R. Quantum Mechanical Continuum Solvation Models. *Chem. Rev.*, **2005**, *105*(8), 2999–3094.
- [64] Bryantsev, V.S.; Diallo, M.S.; Goddard III, W.A. Calculation of Solvation Free Energies of Charged Solutes Using Mixed Cluster/Continuum Models. *J. Phys. Chem. B*, **2008**, *112*, 9709–9719.

- [65] Leopold, N.; Lendl, B. A new method for fast preparation of highly surface-enhanced Raman scattering (SERS) active silver colloids at room temperature by reduction of silver nitrate with hydroxylamine hydrochloride. *J Phys Chem B.*, **2003**, *107*, 5723–5727.
- [66] Dong, X.; Gu, H.; Liu, F. Study of the surface-enhanced Raman spectroscopy of residual impurities in hydroxylamine-reduced silver colloid and the effects of anions on the colloid activity. *Spectrochim. Acta, Part A*, **2012**, *88*, 97–101.
- [67] Sánchez-Cortés, S.; García-Ramos, J.V. Influence of coverage in the surface-enhanced Raman scattering of cytosine and its methyl derivatives on metal colloids: chloride and pH effects. *Surf. Sci.*, **2001**, *473*, 133–142.
- [68] Thompson, D.W.; Collins, I.R. Electrical properties of the goldaqueous solution interface. *J. Colloid Interface Sci.*, **1992**, *152*(1), 197–204.
- [69] Biggs, S.; Mulvaney, P.; Zukoski, C.F.; Grieser, F. Study of the Anion Adsorption at the Gold-Aqueous Solution Interface by Atomic Force Microscopy. *J. Am. Chem. Soc.*, 1994, *116*, 9150–9157.
- [70] Marenich, A.V.; Cramer, C.J.; Truhlar, D.G. J. Universal Solvation Model Based on Solute Electron Density and on a Continuum Model of the Solvent Defined by the Bulk Dielectric Constant and Atomic Surface Tensions. *Phys. Chem. B*, **2009**, *113*(18), 6378–6396.
- [71] Morgenstern, K. Scanning tunnelling microscopy investigation of water in submonolayer coverage on Ag(111). *Surf. Sci.*, **2002**, *504*, 293–300.
- [72] Henderson, A. The interaction of water with solid surfaces: fundamental aspects revisited. *Surf. Sci. Rep.*, **2002**, *46*(1–8), 1–308.
- [73] Morgenstern, K.; Nieminen, J. Imaging water on Ag(111): Field induced reorientation and contrast inversion. *J. Chem. Phys.*, **2004**, *120*(22), 10786–10791.
- [74] Gawronski, H.; Morgenstern, K.; Rieder, K. Electronic excitation of ice monomers on Au(111) by scanning tunneling microscopy. *Eur. Phys. J. D*, **2005**, *35*, 349–353.
- [75] Angelos Michaelides, A.; Morgenstern, K. Ice nanoclusters at hydrophobic metal surfaces. *Nat. Mater.*, **2007**, *6*, 597–601.

- [76] T. Kumagai, T.; Kaizu, M.; Hatta, S.; Okuyama, H.; Aruga, T.; Hamada, I.; Morikawa, Y. Direct Observation of Hydrogen-Bond Exchange within a Single Water Dimer. *Phys. Rev. Lett.*, **2008**, *100*, 166101–
- [77] Kumagai, T. *Visualization of Hydrogen-Bond Dynamics, Water-Based Model Systems on a Cu(110) Surface*; Springer Theses; Springer: Tokyo, 2012.
- [78] Guo, J.; Bian, K.; Lin, Z.; Jiang, Y. Perspective: Structure and dynamics of water at surfaces probed by scanning tunneling microscopy and spectroscopy. *J. Chem. Phys.*, **2016**, *145*, 160901-1–160901-12.
- [79] Liu, R. Adsorption and dissociation of H₂O on Au(111) surface: A DFT study. *Comput. Theor. Chem.*, 2013, 1019, 141–145.
- [80] Perdew, J.P.; Burke, K. Generalized gradient approximation made simple. *Phys. Rev. Lett.*, **1996**, *77*, 3865–3868.
- [81] Nilsson, A.; Pettersson, L.G.M. Adsorbate Electronic Structure and Bonding on Metal Surfaces. In *Chemical Bonding at Surfaces and Interfaces*; Nilsson, A., Pettersson, L.G.M., Nørskov, J.K., Eds.; Elsevier: Amsterdam, 2008.
- [82] Meng, S.; Wang, E.G.; Gao, S. Water adsorption on metal surfaces: A general picture from density functional theory studies. *Phys. Rev. B*, **2004**, *69*(19), 195404-1–195404-13.
- [83] Maréchal, Y. *The hydrogen bond and the water molecule: the physics and chemistry of water, aqueous and bio media*. Elsevier: Amsterdam, 2007.
- [84] Germer, L.H.; Macrae, A.U. Surface Reconstruction Caused By Adsorption. *Proc. Natl. Acad. Sci. U.S.A.*, **1962**, *48*(6), 997–1000.
- [85] Tosatti, E.; Ercolessi, F. Surface Reconstruction of Noble Metals: Models and Consequences. *Mod. Phys. Lett. B*, **1991**, *5*(6), 413–425.
- [86] Woodruff, D.P.; Surface Structure. In *Chemical Bonding at Surfaces and Interfaces*; Nilsson, A., Pettersson, L.G.M., Nørskov, J.K., Eds.; Elsevier: Amsterdam, 2008.
- [87] Andrae, D.; Häußermann, U.; Dolg, M.; Stoll, H.; Preuß, H. Energy-adjusted *ab initio* pseudopotentials for the second and third row transition elements. *Theor. Chim. Acta*, **1990**, *77*, 123–141.

CHAPTER 8

Applications

8.1 The application of SERS in forensic toxicology

This section has been reprinted with modifications from: Deriu, C.; Paudyal, J.; Bhardwaj, V.; McCord, B. SERS for the Forensic Toxicological Screening of Drugs. In Surface-Enhanced Raman Spectroscopy: Methods, Analysis and Research; Bhardwaj, V., McGoron, A. J., Eds.; Nova Science Publishers: Hauppauge, NY, 2019, with permission from Nova Science Publishers, Inc.

Surface-enhanced Raman spectroscopy (SERS) has been demonstrated to have great potential as an analytical tool in forensic trace analysis, thanks to its high sensitivity and specificity. Several publications report on its application in all areas of forensic analysis, from questioned documents to explosive residues.¹ Among these applications, the SERS determination of controlled substances has gained particular interest in the last ten years, thanks to the ability of SERS to detect analytes in the trace and ultratrace regimes,² such as lacing agents in seized drugs or metabolites in toxicological samples.

In forensic practice, it is important to use analytical methods that provide the highest achievable discrimination power for drug identification. For this reason, the Scientific Working Group for the Analysis of Seized Drugs (SWGDRUG) has classified common analytical techniques used in forensic laboratories into three different categories, from A to C, according to decreasing discriminating ability.⁴ Even though SWGDRUG recommendations are tailored to provide guidelines for the analysis of seized drugs as opposed to drugs in toxicological samples, this categorization can be useful in determining the forensic value of the analytical determination. Traditional Raman spectroscopy is classified as a category A analytical method, and thus, it is considered of highest

discrimination ability, along with Mass Spectrometry (MS), Nuclear Magnetic Resonance (NMR) Spectroscopy, and Infrared (IR) Spectroscopy.⁴ Consequently, SERS can also be considered a category A analytical method, as it is a more sensitive extension of traditional Raman spectroscopy.

Analytical protocols for the detection of drugs in biological specimens typically involve presumptive testing (*screening*) via immunoassay, followed by confirmation using a gas or liquid chromatographic technique coupled to mass spectrometry.³ This two-tier analysis system provides assurance, to the courts and justice system, that samples are correctly characterized. Moreover, it minimizes the possibility of incurring contamination of the evidence and detecting false positives. Screening methods have typically high sensitivity and provide quick, on-the-spot, qualitative answers as to the presence or absence of target drugs in a sample. Therefore, they should exhibit a low false negative rate, but may lack specificity. On the other hand, confirmatory methods typically provide quantitative answers and should exhibit a low false positive rate with high discrimination power. SERS has shown great potential as both a screening and a confirmatory method, as it is a sensitive technique that yields molecular fingerprints with high discrimination capability. However, the technique suffers from interferences when confronted with the complexity of toxicological matrices, and thus, upstream sample extraction and cleanup procedures are key to its applicability in this field.

The use of SERS presents several advantages when compared to other analytical techniques aimed at detecting drugs in biological matrices.⁵ As an example, the vibrational information contained in SERS spectra permits structural determination of compounds and library searching. Moreover, SERS can in principle be applied to any molecule that exhibits a change in polarizability upon interaction with the localized surface plasmon resonance (LSPR) of an irradiated SERS substrate. Therefore, it can be used for virtually any analyte and it can be regarded as a nearly universal detection tool.⁶

On the other hand, immunoassays require the development of specific antibodies as *lock-and-key* recognition elements, while MS-based techniques often need drug-specific ionization methods. Although sample cleanup is challenging, SERS analysis shows high sensitivity, with typical detection limits in the nanogram to sub-nanogram per milliliter range. Most importantly, SERS can be performed on aqueous samples, which is crucial for the detection of xenobiotics in biological fluids. Unlike infrared spectroscopy, water is not a significant interference in SERS, as it has a very small Raman cross section.⁶ Another advantage that is particularly relevant to applications in forensic toxicology is that spectral libraries can be built with relative ease, and can facilitate the identification of unknown or suspect compounds. When experimental data are not available, and a given molecular structure is suspected for an unknown, theoretical calculations based on Density Functional Theory (DFT) can be used at a relatively low computational cost to predict vibrational frequencies, aid in the characterization of the sample, and ultimately expand spectral libraries.⁷

As discussed in the main core of this dissertation, a key factor in developing any efficient SERS analytical protocol is maximizing the interaction between the analyte and the enhancing substrate. While it is true that virtually any molecule can be detected by SERS, for high sensitivity detection, target analytes must be in close contact with the enhancing surface; the local environment at the surface of the enhancing nanomaterial is of crucial importance, and thus, it must be controlled and optimized. In addition to this general requirement, analytes in biological matrices pose an additional challenge, that is, the complex nature of the biological fluids themselves. Multiple chemical species may compete for the finite number of available adsorption sites on the SERS substrate, and the direct detection of a drug in a biological matrix will occur only if it exhibits a higher affinity for the substrate, when compared to other competing species present in the matrix:

$$K_{ad(\text{analyte-metal})} \gg [K_{ad(\text{stabilizer-metal})}, K_{ad(\text{matrix-metal})}, K_{ad(\text{matrix-stabilizer})}] \quad (8.1)$$

Common matrices in forensic toxicology — blood, urine, and oral fluid — all contain interfering species that hinder the signal of target analytes.^{8–10} Examples of such interfering matrix compounds are proteins, aminoacids such as L-tyrosine, adenine, thiocyanate, cellular debris, urea, and uric acid (*Table 8.1*).^{8–12} In addition to interfering bands, a broad background signal and uneven, rising baselines across the acquisition range can also be observed.² This is often attributed to background fluorescence, mirroring what is observed in traditional Raman spectroscopy, where the higher efficiency of fluorescence, compared to Raman scattering, often prohibits the analysis of organic, conjugated systems.² However, under SERS experimental conditions, fluorescence is often quenched.⁶ Whichever the actual source of this spectrally broadened background might be,¹ in the toxicological practice it is frequently observed at higher concentrations of biological matrices, and it affects the sensitivity and quality of the spectral signature of the target analyte. This drawback can be minimized in the same way as in traditional Raman spectroscopy, by utilizing low energy excitation sources, such as those emitting in the near infrared.¹⁵ Alternatively, extensive sample cleanup may be used to reduce interfering matrix components. Problems arising from adsorption competition phenomena are also observed when analyzing *mixtures* of xenobiotics, because, as in any label-free technique, the ensemble nature of the signal might make it difficult to distinguish the individual components.

While the use of multivariate statistical analysis can reduce, when not eliminate, the difficulties in interpreting SERS spectra from multi-analyte systems (*vide infra*), the effects of interfering matrix components make the use of upstream separation techniques

¹Some authors hypothesize the existence of a SERS-specific *continuum* effect, whose physical origin is still controversial.^{2,13,14}

imperative for a sensitive and straightforward SERS assay. In this regard, microfluidic-SERS approaches have been developed and optimized for the monitoring of various therapeutic drugs in biological fluids, such as the antibiotics levofloxacin and nitroxoline in urine.¹⁶ As far as drugs of abuse are concerned, microfluidic-SERS platforms have mostly been applied to standard solutions,^{17,18} with the exception of a lab-on-a-chip design for the detection of methamphetamine in oral fluid developed by Andreou and collaborators.¹⁹

Table 8.1: Common interfering bands in biological matrices.

Matrix	Band (cm ⁻¹)	Possible Assignment	Reference
oral fluid	2095, broad	$\nu(\text{CN})$ thiocyanate	9
	735	$\nu(\text{CS})$ thiocyanate	9
	445	$\delta(\text{NCS})$ thiocyanate	9
plasma	634	L-tyrosine	12
serum	(1132)		12
	(1096)		12
	(959)		12
	(810)		12
	723	$\delta(\text{CH})$ adenine	12
	(632)		12
	1650/1550	$\nu(\text{C=O}), \delta(\text{NH}), \nu(\text{NC})$ amides I and II	12
urine	1133	uric acid	12
	658	uric acid	12

Bands that are observed less frequently and with lower intensity are reported in parentheses.

As a general note, and as mentioned in *Chapter 2*, the SERS signal may vary with experimental conditions such as the composition of the enhancing substrate and the intensity and wavelength of the laser. Such changes can be the result of the formation of specific metal-analyte surface complexes,²⁰ the occurrence of metal-induced photochemical processes,²¹ or the excitation of electronic transitions within the analyte (Surface Enhanced Resonance Raman Spectroscopy, SERRS),² respectively. Although these phenomena contribute to signal variation, at fixed experimental conditions the repeatability of SERS measurements is typically good.²² In a recent study by Muehlethaler *et al.*,²² which was already mentioned in § 5.2, the repeatability of a SERS-based method utilizing aggregated

silver colloidal nanoparticles as substrates was studied, at various analytical levels, on three forensically relevant analytes. The level of repeatability was demonstrated to be analyte-sensitive. Molecules with higher affinity for the substrate (*i.e.*, Crystal Violet and TNT) showed low relative standard deviation (RSD) values (2-6% for crystal violet, and 5-16% for TNT), while analytes exhibiting weaker interactions had greater signal fluctuation (*i.e.*, methamphetamine, 5-29% RSD). While it is often believed the variability of the SERS signal is the result of a random distribution of hot spots produced by salt-induced aggregation, the study by Muehlethaler *et al.* demonstrated that these effects are actually negligible when compared to stochastic phenomena such as the Brownian motion of the colloidal nanoparticles and changes in concentration due to the evaporation of the dispersion medium, or the use of different instruments across different laboratories. In spite of these issues, qualitative analysis was demonstrated to be possible in each of the studied scenarios.

As opposed to qualitative analysis, reliable quantitation is currently a more challenging task.^{22,23} For this reason, SERS is often considered a semi-quantitative technique. While peak intensity and area are proportional to the concentration of the analyte, as in traditional Raman spectrometry, the strict dependence of the SERS signal on the metal-analyte distance and surface selection rules^{2,24} makes quantitation a function of analyte adsorption, surface coverage, and orientation to the surface.²³ A direct outcome of this is represented by the typical non-linear calibration curves observed in analytical practice.²³ As discussed in other sections of this dissertation, calibration curves may follow either a Langmuir²⁵ or an anti-Langmuir (*i.e.*, sigmoidal)²⁷ behavior, depending on the interplay among the affinity constants of the species that are present in the SERS sample. Additionally, when colloidal substrates are used, unintentional aggregation may occur as a result of high concentrations of analyte, causing the signal to counterintuitively decrease in intensity as the concentration of the target molecule increases.²³ Techniques commonly used to correct

for these issues, such as the use of internal standards, may fail as a result of problems with competitive adsorption and inhibition of signal. Competitive adsorption phenomena have been minimized by the use of isotopically labeled internal standards. Subaihi *et al.*²⁶ were able to identify and quantify codeine in human plasma extracts by utilizing codeine-*d*₆ as an internal standard. Since these analytes differ only in isotopic composition, their affinity for the SERS-active surface is assumed to be identical. Using this approach, wavelength shifts and band ratios of CH/CD stretching bands can be used for the purpose of quantitation.²³ A more typical strategy for the normalization of signals obtained by colloid-based SERS measurements entails referencing band intensities to the $\nu(\text{OH})$ band of water. This is the method utilized for the normalization of SERS spectra in the present research work, and it relies on the fact that water is always present in colloidal enhancing substrates.²⁷⁻²⁹ Alternatively, bands arising from the interaction between substrate and polyatomic aggregating agent can be used for this purpose.²⁵

As discussed so far, the detection of drugs in biological fluids is a challenging analytical task as a consequence of the complex nature of the matrix. The concentration of xenobiotics is usually very low (ng/mL) as compared to proteins or other biomolecules, which, on the other hand, account for the remainder of a toxicological sample. Therefore, the direct detection of drugs in such complex samples by bulk techniques like SERS may be severely compromised in repeatability, reproducibility, and accuracy, if not totally prevented. For this reason, research efforts are trending towards the development of either hyphenated chromatographic/SERS systems, or quick extraction procedures that minimize sample preparation. Traditional separation methods such as liquid-liquid extraction,³⁰ supported-liquid extraction,⁸ solid phase extraction,¹⁰ and liquid chromatography³¹ may all be used in laboratory settings for sample cleanup prior to SERS analysis.

While liquid-liquid extraction is the most common method for drug isolation from biological samples, it may exhibit drawbacks when combined with SERS, as a result of

the interaction of the solvent with the SERS substrate. Solvent molecules may negatively affect the chemical environment at the surface of the enhancing nanomaterial through specific adsorption or through alteration of the solvation shells of the dispersed species. This prevents the target analyte from obtaining close contact with the metal surface. For example, the common chromatographic eluent acetonitrile is known to readily adsorb on silver surfaces, causing the sensitivity of SERS-based analytical methods to decrease, as a consequence of both occupation of adsorption sites and collapse of the colloidal system. To avoid this, Trachta *et al.*³¹ used binary solutions of methanol and phosphate buffer as HPLC eluents. This allowed them to separate and detect multiple drugs in post-mortem urine and blood specimens, including codeine, methadone, and carbamazepine. As opposed to acetonitrile, methanol is not as readily adsorbed on the silver surface, and provides minimal interference bands. For this reason, it is often used in standard SERS practice for the preparation of reference solutions with no significant drawbacks at the spectral profile level.

An interesting approach concerning extraction solvents for downstream SERS analysis is presented by Ma *et al.*,³² who exploited the immiscibility of cyclohexane and water to form a self-assembled platform for the detection of amphetamines. In their extraction-to-SERS experimental design, the target analyte was first extracted from urine into the cyclohexane organic layer by traditional liquid/liquid extraction. Subsequently, it was induced to self-assemble onto colloidal gold nanoparticles at the cyclohexane-water interface by slow addition of the liquid/liquid extraction organic layer into the aqueous dispersion of the colloidal sol. After ethanol-induced evaporation of the solvent, the self-assembled gold-amphetamine system could be used to obtain SERS spectra from the extracted analyte. Yang *et al.*³³ used gold nanoparticle dotted magnetic nanocomposites (AMN) for coupled extraction and SERS detection of drugs in oral fluid, including cocaine's metabolite benzoylecgonine. The drugs were extracted from the matrix on the basis of their adsorption onto the AMN substrates, and analyzed by SERS after

magnetic-aided separation of the AMN from the biological fluid. Similarly, Subaihi *et al.*²⁶ used ultra-centrifugal filters (3 kDa) for selective removal of protein residues from human plasma samples before analyzing the remaining fraction containing the drug.

As anticipated earlier, multivariate analysis can be of great aid in treating SERS spectra, especially when multiple species are simultaneously investigated. The goal of statistical multivariate analysis is to simplify high dimensionality data such that underlying discriminating factors can be more easily observed and interpreted.³⁴ Multivariate analysis has been applied to several branches of analytical chemistry, and in recent years it has seen some applications to the SERS analysis of xenobiotics in biological fluids. While it is outside the scope of this chapter to detail the specific methodologies within multivariate analysis, it is important to highlight the advantages they offer in increasing the reliability of both identification and quantification of analytes by SERS. This is of utmost importance in the development of SERS as a widely recognized forensic standard.

Multivariate statistical approaches can be categorized into unsupervised and supervised learning methods.²³ The former, like Principal Component Analysis (PCA), require human interpretation, while the latter, like Partial Least Squares Regression (PLSR) or Artificial Neural Networks (ANNs), allow for the elimination of this step, once a method is trained and calibrated.²³ The power of PCA applied to SERS data has been demonstrated in several instances, for example in the detection of cocaine in oral fluid.³⁵ While the SERS spectrum of protein-crashed oral fluid containing cocaine was not readily discernible from that of neat oral fluid (*Figure 8.1, left*), PCA allowed for the conclusive discrimination of the two samples (*Figure 8.1, right*). Another example of statistical multivariate approaches that has been comprehensively used to support the SERS identification and quantification of drugs in biological fluids is given by Subaihi *et al.*¹² In their study, the highly substrate-interacting drug propranolol, a β -blocker and sports doping agent, was analyzed by SERS, directly from human urine and serum, without upstream purification steps.¹²

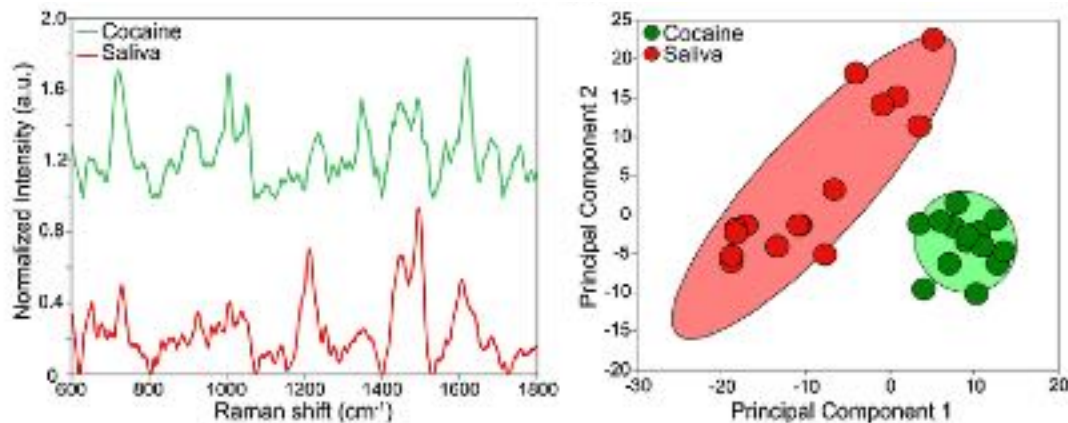


Figure 8.1: Application of Principal Component Analysis (PCA) to the detection of cocaine in oral fluid. SERS spectrum of a recovered supernatant aliquot of an oral fluid sample containing cocaine at an initial concentration of 100 ng/mL (green), compared to that of a recovered supernatant aliquot of a neat oral fluid sample (red). Cocaine's marker band is observed at 1003 cm^{-1} . Plot of first two Principal Components relative to the SERS spectra of cocaine-fortified (green cluster) and neat oral fluid (red cluster). Each cluster consists of 20 spectra, and ellipses indicate 95% confidence intervals. Reprinted from Dies, H. *et al.*,³⁵ Copyright (2018), with permission from Elsevier.

Propranolol in human plasma was also investigated, but samples needed to be submitted to centrifugal ultrafiltration to remove the protein component prior to SERS analysis.¹² Both unsupervised and supervised learning methods were used. PCA and Principal Component-Discriminant Function Analysis (PC-DFA) allowed discrimination between neat biological fluids and those containing propranolol. On the other hand, PLSR was used as a quantitation tool, permitting accurate prediction of concentrations, with RMS error values of 1.69 for urine, 0.58 for serum, and 9.68 for plasma.¹² The higher RMS error value reported for plasma samples has been linked to analyte loss caused by adduct formation between the drug and plasma proteins, which reduces the free drug content in the sample.¹² Proteins and peptides in biological fluids such as blood can act like trapping agents and cause covalent adduct formation with drugs of abuse.^{36,37} This phenomenon needs to be taken into account when designing any analytical method in toxicology, as low

extraction recoveries and discrepancies in quantitation may be directly connected. It must be noted that, for propranolol in biological fluids, LOD values are two orders of magnitude higher than those calculated for standard aqueous solutions.¹² As previously outlined, this is a well-known phenomenon, which is tied to the increase of the background signal from the biological fluid and to competitive adsorption of matrix components.¹²

In this chapter, examples of the application of the developed nanostars to the detection of analytes of forensic and public health importance are presented and discussed.³⁸ Finally, to contextualize and demonstrate the potential of SERS in the field of forensic toxicology and point-of-care clinical testing, a study of the synthetic cannabinoid JWH-018 is presented.¹⁰⁹ This study also illustrates the usefulness of DFT calculations for the obtainment of *in silico* spectral references. This aspect is more extensively explored in the last section of this chapter, in which a proof of concept demonstration of this capability is illustrated by the DFT study of 6 additional synthetic cannabinoids.

8.2 Applications that make use of the new colloidal nanostar formulations

As concluded in *Chapter 5*, the nanostars formulation with the highest stability was NS/CO₃²⁻(c). Therefore, this formulation was utilized for subsequent application studies that involved the detection of *opiates* and *opioids*. The former term refers to the naturally occurring analgesics produced by *Papaver somniferum* (“opium poppy”), while the latter term refers to semi-synthetic derivatives (*e.g.*, heroin), as well as synthetic compounds with analogous pharmacological properties (*e.g.*, fentanyl).³⁹ This notwithstanding, the word *opioid* is frequently used as an umbrella term, with no origin connotation.

Opiates and opioids (*Figure 8.2*) act as central nervous system (CNS) depressants by binding to the μ , κ , and δ receptors, as well as, to a certain extent, σ receptors.³⁹

Agonist activity at the μ receptors level is associated with the most notable pharmacologic effects caused by this family of substances, namely, analgesia, respiratory depression, bradycardia, euphoria, low gastrointestinal motility, tolerance build-up, and addiction; agonist activity at the level of the other receptors, κ and δ , causes different effects, such as sedation for the former, and respiratory stimulation for the second.³⁹ Antagonist or mixed agonist-antagonist behavior, on the other hand, has been taken advantage of in the formulation of antidote preparations to be administered in case of overdosing (*e.g.*, naloxone, antagonist), or in the management of detoxing treatments (*e.g.*, buprenorphine, mixed agonist-antagonist).³⁹

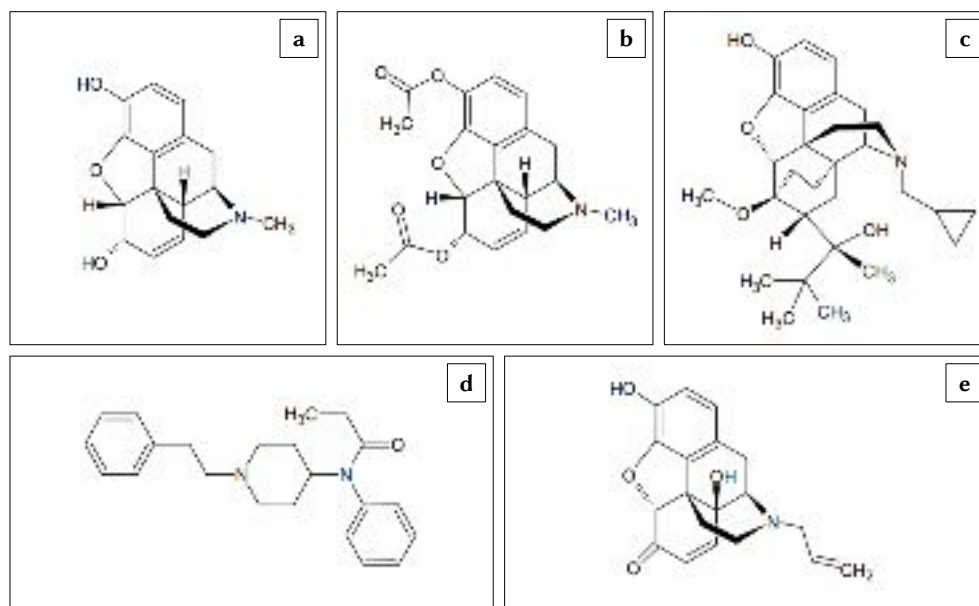


Figure 8.2: Examples of opiates and opioids: (a) morphine (μ agonist, primarily); (b) heroin (μ agonist); (c) buprenorphine (mixed agonist-antagonist); (d) fentanyl (μ agonist); (e) naloxone (antagonist).

Opioids have maintained nation-wide attention during the last thirty years, as a result of the progressive increases in correlated hospitalizations and deaths by overdose. Indeed, the opioid crisis in the United States is a decades-long issue which has caused approximately 450,000 overdose deaths in the last twenty years,⁴⁰ around 46,000 of which occurred

annually in the years 2017 and 2018.⁴¹⁻⁴³ Currently, this epidemic affects not only users of prescription opioids, but also users of other classes of substances, such as cocaine and methamphetamines. The main reason is that opioids, such as fentanyl and its analogs, are being used as lacing agents in common street drugs, and as cheaper alternatives in the manufacture of counterfeit pills.⁴⁴

Especially when unintentional, the use of fentanyl and related substances pose severe risks to the life of the person consuming it, as a result of the much higher potency characterizing these compounds. Fentanyl is estimated to be 50 to 100 times more potent than morphine,⁴⁵ and some of its analogs, such as carfentanil, have an estimated potency that is 100 times higher than fentanyl itself.⁴⁶ Because of this, even trace quantities can drastically increase the chances of overdosing, especially in unsuspecting and naïve users.⁴⁷⁻⁴⁹ In the case of fentanyl-laced cocaine or methamphetamines, the overdose risk is further heightened by the inherent health hazards of the concomitant use of stimulants and opioids.⁵⁰ As a consequence, the availability of analytical methods for the highly sensitive detection of opioids, and specifically, fentanyl and its analogs, is currently greatly valuable in both forensic and emergency room settings. This practical necessity was an excellent platform to demonstrate the usefulness of the developed nanostars formulations as SERS substrates that are tailored to drug detection.

The following section will present the work performed in collaboration with Dr. Ling Wang, which entailed the characterization and the demonstration of the selective detection of fentanyl and six of its analogs by SERS, utilizing the developed NS/CO₃²⁻_(c) formulation as enhancing substrate.

8.2.1 Surface-enhanced Raman spectroscopy, Raman, and density functional theoretical analyses of fentanyl and six analogs

This work focuses on fentanyl, benzylfentanyl (reference standard), and five popular fentanyl analogs (*fentalogs*) reported in forensic casework: acetylfentanyl, acrylfentanyl, butyrylfentanyl, furanylfentanyl, and para-fluorofentanyl (*Figure 8.3*). These substances were examined using Raman spectroscopy and SERS. DFT calculations were performed at the ω B97XD/cc-pVTZ level to provide the vibrational frequencies, Raman activities, and normal mode assignments for each analog. As expected, traditional Raman spectroscopy was only able to detect the substances in the crystalline phase, while SERS allowed for the detection of the samples in solution. Carbonate-capped gold/silver nanospheres (AuAg NSph/ CO_3^{2-} _(c)) and gold/silver nanostars (NS/ CO_3^{2-} _(c)) were utilized to perform the SERS experiments; as expected, the branched nanoparticles provided stronger SERS signal compared to the spheroidal counterpart. The SERS spectra thus obtained were able to be easily distinguished from those of non-fentanyl opioids and other common drugs of abuse with the aid of Principal Component Analysis (PCA). Overall, these results demonstrate that SERS shows great potential to distinguish fentanyl analogs and detect trace quantities of these compounds in mixtures of seized drugs.

This section is adapted with permission of John Wiley & Sons - Books from Wang, L.; Deriu, C.; Wu, W.; Mebel, A.M.; McCord, B. Surface-enhanced Raman spectroscopy, Raman, and density functional theoretical analyses of fentanyl and six analogs, *J. Raman Spectrosc*, **2019**, *50*, 1405–1415; permission conveyed through Copyright Clearance Center, Inc. Major support for this research was provided by award NIJ 2015-IJ-CX-K006 and NSF IUCRC award 1739805 to FIU - Center for Advanced Research in Forensic Science. Points of view in the section are those of the authors and do not necessarily represent the official view of the U.S. Department of Justice.

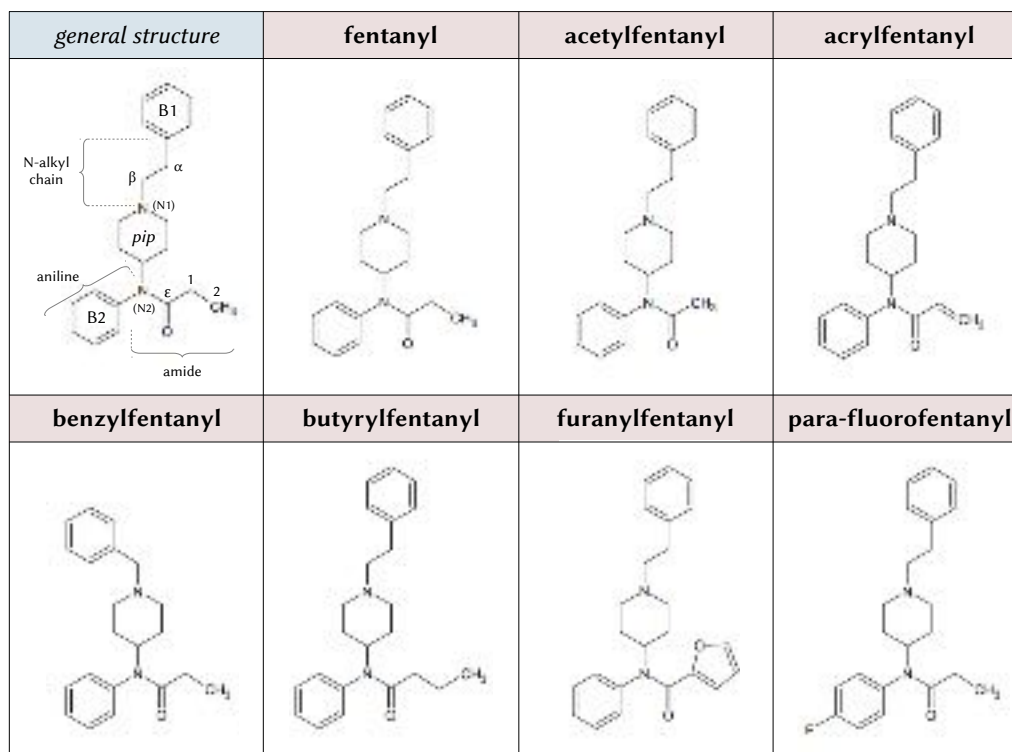


Figure 8.3: General structure of the fentanyl skeleton, and chemical structures of the seven analytes utilized in this study.

Methods

Fentanyl and the analogs acetylfentanyl, acrylfentanyl, benzylfentanyl, butyrylfentanyl, para-fluorofentanyl, and furanylfentanyl were purchased from Cayman Chemical (Ann Arbor, MI). Amphetamine, methamphetamine, morphine, hydrocodone, hydromorphone, oxycodone, heroin, codeine, and thebaine were purchased from RBI (Natick, MA).

The colloidal nanoparticles were prepared as described in the *Methods* section of this dissertation (§ 3.2.1 and 3.2.2). Fentanyl and its analogs were dissolved in methanol as 1 mg/mL standard solutions. Benzylfentanyl is not pharmacologically active, and because of its safety, it was utilized as prototype fentanyl analog in the initial optimization of parameters. To acquire the traditional Raman (NR) spectra of drugs in the solid state,

a total of 6 μL per each standard solution was deposited onto aluminum foil as three successive aliquots and allowed to dry. The NR measurements of the drugs in solution, on the other hand, utilized a mixture of 2.5 μL of methanolic standard solution and 247.5 μL of water. For the SERS measurements, 2.5 μL of 1.67 M magnesium chloride were added to 245 μL of colloidal nanoparticles, which were allowed to aggregate for 5 minutes. Subsequently, a 2.5 μL aliquot of each drug sample was added to the aggregated colloidal sol. This mixture was incubated for another 5 minutes and then transferred to a 96 wells quartz microtiter plate; instrumental details are reported in § 3.2.7. SERS measurements were performed at the 15th, 20th, 25th, and 30th minute time points to establish the most suitable incubation time, in a similar fashion to what described in § 5.1 of this dissertation; the selected incubation time was 20 minutes. The final concentration of drug used in this study was 10 $\mu\text{g}/\text{mL}$ for all measurements, except those related to the evaluation of the nanomaterial shape effects; in these experiments, the final concentration of the drug was 10 ng/mL .

The Gaussian 09 package was used for all DFT calculations.⁵¹ Raman frequency calculations were performed after prior optimization of molecular geometries. This was done by utilizing the hybrid exchange correlation functionals of B3LYP^{52,53} and ωB97XD ⁵⁴ coupled with the basis sets of 6-311G** and cc-pVTZ,⁵⁵ The obtained Raman frequencies and activities were converted to simulated spectra by utilizing MultiWFN⁵⁶ (λ_{exc} 12738.85 cm^{-1} , T 294.15 K, standard broadening Lorentzian function), whereas the optimized geometries were visualized by Molden 5.0.^{57,58}

Results and Discussion

DFT calculations

The fentanyl analogs shown in *Figure 8.3* illustrate the characteristic structures and the labeling of the fentanyl skeleton. For simplicity, the phenyl ring was designated as *B1*, the

aniline ring as *B2*, and the piperidine ring as *pip*. The optimal geometry and vibrational frequencies of benzylfentanyl were computed using B3LYP/6-311G**, which provided a set of Raman frequencies with a simulated spectrum closely resembling the experimental one (data not shown). When reproducing the same procedure for fentanyl, it was observed that the simulated spectrum appeared to be shifted relative to the experimental one in multiple regions, and exhibited a quadruple peak in the 1100–900 cm^{-1} range (*Figure 8.4 a*). In contrast, the experimental spectrum featured a double band in this range, and the intensities of the corresponding constituent bands at 1066 cm^{-1} and 1031 cm^{-1} were reversed. A similarly inadequate spectral profile was also noticed for the DFT results obtained at the B3LYP/cc-pVTZ level. As a result, ω B97XD/cc-pVTZ was examined as an alternative method for the geometry optimization and the calculation of frequencies. Using this approach, the simulated spectrum of fentanyl with a scaling factor (*vide infra*) of 0.966029 provided good agreement with experimental data. Therefore, the ω B97XD/cc-pVTZ computational method was also utilized to calculate the remaining fentanyl analogs (*Figure 8.5*).

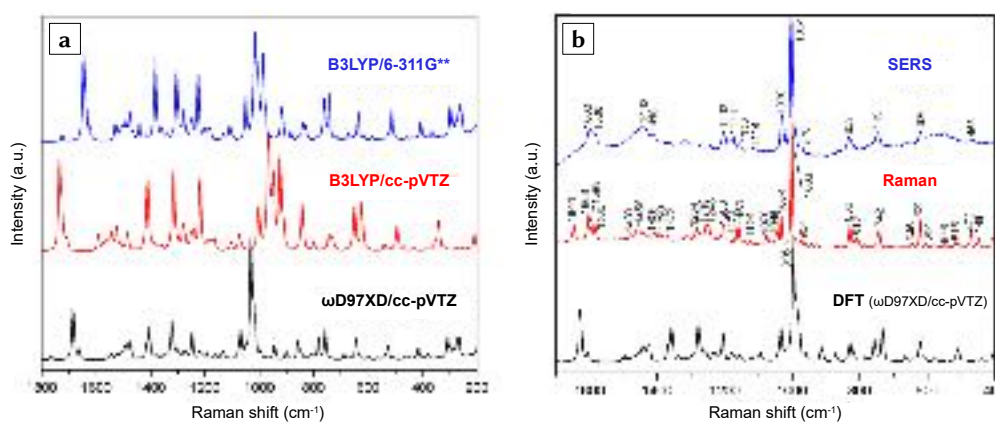


Figure 8.4: (a) Comparison of the simulated spectra obtained with the different DFT methods; (b) Experimental SERS (blue) and Raman (red) spectra of fentanyl, compared to the best DFT-simulated Raman spectrum (ω B97XD/cc-pVTZ, black).

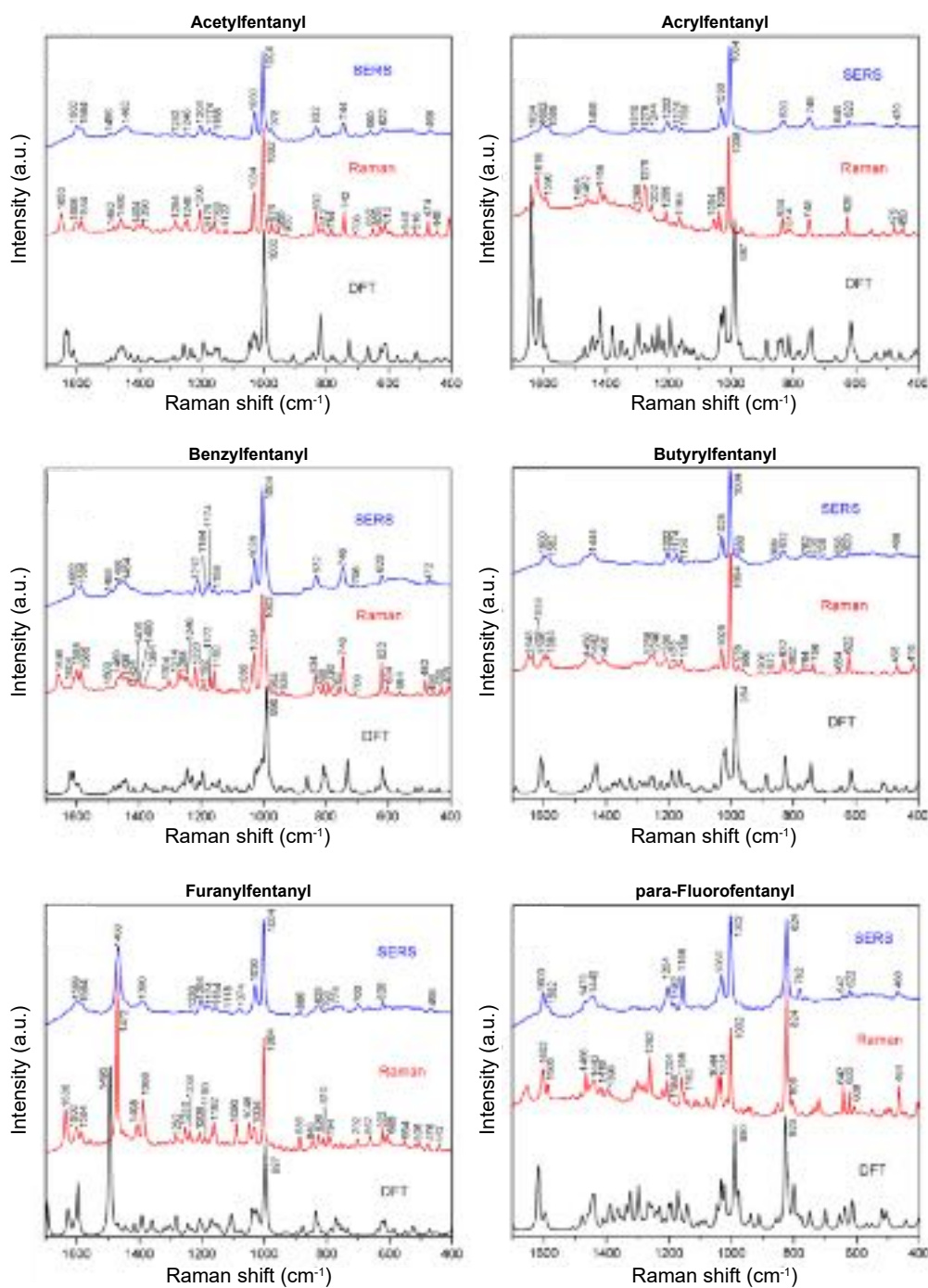


Figure 8.5: Calculated (scaled) and experimental spectra of the six fentanyl analogs.

Evaluation of scaling factors

DFT-calculated Raman frequencies are systematically higher than the experimental values, as a result of the theoretical treatment assumption that molecules behave as perfect harmonic oscillators.⁶⁰ Simulated spectra are therefore corrected for this overestimate by multiplying the calculated frequencies for a scaling factor, λ , obtained by a standard least-square minimization procedure between calculated and experimental frequencies.⁶⁰

Tables 8.2 to 8.8 present the bands that were used to calculate the scaling factors between the DFT-simulated spectra and the NR spectra. In a previous study on fentanyl and carfentanil by Leonard *et al.*,⁵⁹ such scaling factors were calculated separately for the high and low frequency regions of the spectrum; in this study, the scaling factors were not split to high and low frequency regions because the errors in the calculated frequencies were lower than 7.6% and a homogeneous direction of the shift was observed.

Table 8.2: DFT-calculated and experimental Raman and SERS frequencies of fentanyl, and assignment of normal modes.

DFT x 0.9573	Mode	Assignment	Raman (cm ⁻¹)	SERS (cm ⁻¹)
1629 s	124	$\nu(\text{C}=\text{C})_{\text{B1}}$	1606 w	1600 w
1605 w	122	$\nu(\text{C}=\text{C})_{\text{B1}}$	1586 w	1588 w
1425 m	108	$\delta(\text{H}-\text{C}-\text{N}_2)$	1456 w	1442 w
1206 m	85	$\nu(\text{N1}-\text{C}-\text{C}-\text{C}_{\text{B1}}); \gamma_t(\text{CH}_2)_a$	1206 w	1202 w
1154 w	80	$\delta(\text{CH})_{\text{B1},\text{B2}}$	1160 m	1158 vw
1034 m	70	$\nu(\text{C}=\text{C})_{\text{B1},\text{B2}}; \delta(\text{CH})_{\text{B1},\text{B2}}$	1034 m	1030 m
996 s	62	$\delta(\text{C}=\text{C})_{\text{B2}}; \nu(\text{C}_\epsilon-\text{C1}-\text{C2})$	1002 s	1004 s
961 w	57	$\delta_r(\text{CH}_2)_{\text{pip}}; \nu(\text{C}_\epsilon-\text{C1}-\text{C2})$	964 vw	970 w
830 m	49	$\nu(\text{C}_{\text{B1}}-\text{C}_\alpha-\text{C}_\beta-\text{N}_1); \beta(\text{ring})_{\text{B1}}$	830 m	832 w
732 m	42	$\gamma_t(\text{CH}_3); \delta_r(\text{CH}_2)_{\text{pip}}; \delta(\text{C}_\epsilon-\text{C1}-\text{C2})$	742 m	746 w
622 m	37	$\delta(\text{ring})_{\text{B1},\text{B2}}; \delta_r(\text{CH}_2)_{\text{alkyl}}; \delta_r(\text{CH}_3)$	622 m	620 w

ν , stretching; δ , in-plane bending (*s*, scissoring; *r*, rocking); γ , out-of-plane bending (*t*, twisting; *w*, wagging); β , ring breathing. Functional groups nomenclature and abbreviations follow Figure 8.3.

When envisioning the potential of DFT as a tool for *in silico* library building, scaling factors should be such that they are applicable to *family* of compounds, rather than be

Table 8.3: DFT-calculated and experimental Raman and SERS frequencies of acetylfentanyl, and assignment of normal modes.

DFT x 0.9696	Mode	Assignment	Raman (cm ⁻¹)	SERS (cm ⁻¹)
1636 m	117	$\nu(\text{C}=\text{C})_{\text{B1}}$	1598 w	1600 w
1611 w	115	$\nu(\text{C}=\text{C})_{\text{B2}}$	1584 w	1582 w
1460 m	106	$\delta(\text{CH}_2)_\beta$; $\delta_s(\text{CH}_3)$; $\delta_s(\text{CH}_2)_{\text{pip}}$	1460 w	1442 vw
1259 m	85	$\gamma_t(\text{CH}_2)_{\text{pip}}$; $\nu(\text{C}-\text{N}_2-\text{C})$; $\delta(\text{CH})_{\text{B2}}$	1284 w	1282 vw
1235 w	83	$\gamma_t(\text{CH}_2)_{\text{pip}}$; $\gamma_w(\text{CH}_2)_\beta$	1248 w	1248 vw
1195 m	81	$\nu(\text{B1}-\text{C})$; $\delta(\text{C}-\text{H})_{\text{B1}}$; $\gamma_w(\text{CH}_2)_\alpha$	1206 m	1204 w
1169 w	77	$\nu(\text{C}-\text{N}_1-\text{C})$; $\gamma_t(\text{CH}_2)_{\text{pip}}$; $\delta(\text{C}-\text{H})_{\text{B1,B2}}$	1176 vw	1174 vw
1153 w	74	$\delta(\text{CH})_{\text{B2}}$	1160 vw	1158 vw
1024 m	63	$\nu(\text{CC})_{\text{pip}}$	1034 s	1030 m
1000 s	59	$\delta(\text{C}=\text{C})_{\text{B2}}$	1002 s	1004 s
818 s	45	$\nu(\text{B1}-\text{C}-\text{C})$; $\delta_r(\text{CH}_2)_{\text{pip}}$; $\beta(\text{ring})_{\text{B1}}$	832 m	832 m
726 m	40	$\gamma(\text{CH})_{\text{B1}}$; $\gamma(\text{C}-\text{H})_{\text{B2}}$; $\delta_r(\text{CH}_2)_{\text{pip}}$; $\nu(\text{C}-\text{C}-\text{N}_2)$; $\delta_r(\text{CH}_3)$	742 m	744 m
666 m	37	$\nu(\text{C}-\text{N}_2-\text{C})$; $\nu(\text{C}=\text{C}-\text{N}_2)$; $\delta(\text{ring})_{\text{B2}}$	652 w	660 vw
624 m	35	$\delta(\text{ring})_{\text{B1}}$	628 w	622 vw

ν , stretching; δ , in-plane bending (*s*, scissoring; *r*, rocking); γ , out-of-plane bending (*t*, twisting; *w*, wagging); β , ring breathing. Functional groups nomenclature and abbreviations follow *Figure 8.3*.

Table 8.4: DFT-calculated and experimental Raman and SERS frequencies of acrylfentanyl, and assignment of normal modes.

DFT x 0.9573	Mode	Assignment	Raman (cm-1)	SERS (cm-1)
1610 s	118	$\nu(\text{C}=\text{C})_{\text{B2}}$	1618 m	1602 w
1445 m	110	$\delta_s(\text{CH}_2)_{\text{pip}}$; $\delta(\text{CH})_{\text{B1}}$	1462vw	
1297 m	94, 95	$\nu(\text{HC}=\text{CH}_2)$; $\gamma_t(\text{CH}_2)_{\text{pip}}$; $\gamma_t(\text{CH}_2)_\beta$; $\gamma_t(\text{CH}_2)_{\text{acryl}}$; $\gamma_t(\text{CH})_{\text{acryl}}$	1276 s	1278 vw
1232 m	88	$\gamma_t(\text{CH}_2)_{\text{pip}}$; $\gamma_t(\text{CH}_2)_\alpha$; $\nu(\text{C}-\text{N}_2-\text{C}-\text{C})$; $\gamma_t(\text{CH}_2)_\beta$; $\delta(\text{CH})_{\text{B2}}$	1208 w	1202 w
1194 m	85	$\gamma_t(\text{CH}_2)_{\text{pip}}$; $\gamma_t(\text{CH}_2)_{\alpha,\beta}$; $\nu(\text{N}_1-\text{C}-\text{C}-\text{C})$	1164 w	1158 vw
1020 s	69	$\nu(\text{C}=\text{C})_{\text{B1}}$; $\delta(\text{C}-\text{H})_{\text{B1}}$	1038 w	1030 m
987 s	61, 62	$\delta(\text{C}=\text{C})_{\text{B1}}$; $\gamma(\text{CH})_{\text{B2}}$	1008 s	1004 s
814 m	47	$\delta(\text{CCC})_{\text{pip}}$; $\delta_r(\text{CH}_2)_{\text{pip}}$	834 m	830 w
742 w	41	$\delta_r(\text{CH}_2)_{\text{pip}}$; $\delta_r(\text{CH}_2)_{\text{acryl}}$	748 m	748 w
664 w	38	$\delta(\text{C}=\text{C})_{\text{B2}}$; $\delta_r(\text{CH}_2)_{\text{acryl}}$; $\delta_r(\text{CH}_2)_{\text{pip}}$	646 vw	646 vw
614 s	35	$\delta_r(\text{ring})_{\text{B1,B2}}$	626 m	620 w

ν , stretching; δ , in-plane bending (*s*, scissoring; *r*, rocking); γ , out-of-plane bending (*t*, twisting; *w*, wagging); β , ring breathing. Functional groups nomenclature and abbreviations follow *Figure 8.3*.

substance-specific. In this way, in principle, a family-specific scaling factor, such as a *fentalog* scaling factor, can be reliably applied to a simulated spectrum of a putative new analog, and utilized to identify or assign an unknown spectrum, without the stringent need of prior comparison to an analytical reference standard, which might be expensive

Table 8.5: DFT-calculated and experimental Raman and SERS frequencies of benzylfentanyl, and assignment of normal modes.

DFT x 0.9592	Mode	Assignment	Raman (cm-1)	SERS (cm-1)
1610 m	116	$\nu(\text{C}=\text{C})_{\text{B}2}$	1598 m	1602 w
1597 w	115	$\nu(\text{C}=\text{C})_{\text{B}1}$	1586 m	1586 m
1144 w	76	$\gamma_t(\text{CH}_2)_{\text{pip}}$; $\gamma_t(\text{CH}_2)_{\alpha}$	1160 m	1158 w
1017 m	65	$\delta(\text{CH})_{\text{B}2}$; $\nu(\text{C}=\text{C})_{\text{B}2}$	1030 s	1028 s
990 s	58, 59	$\delta(\text{C}=\text{C})_{\text{B}2, \text{B}1}$; $\delta_r(\text{CH}_2)_{\alpha}$	1004 s	1004 s
860 m	49	$\delta_r(\text{CH}_2)_{\text{pip}}$	834 w	832 w
731 s	40	$\gamma_w(\text{CH}_3)$; $\delta_r(\text{CH}_2)_{\text{pip}}$; $\nu(\text{C}-\text{N}_2-\text{C})$; $\delta(\text{C}-\text{C}_1-\text{C}_2)$	746 s	746 m
619 m	35	$\delta(\text{ring})_{\text{B}1}$	622 m	620 w

ν , stretching; δ , in-plane bending (*s*, scissoring; *r*, rocking); γ , out-of-plane bending (*t*, twisting; *w*, wagging); β , ring breathing. Functional groups nomenclature and abbreviations follow Figure 8.3.

Table 8.6: DFT-calculated and experimental Raman and SERS frequencies of butyrylfentanyl, and assignment of normal modes.

DFT x 0.9536	Mode	Assignment	Raman (cm-1)	SERS (cm-1)
1610 s	131	$\nu(\text{C}=\text{C})_{\text{B}1}$	1596 m	1600 w
1587 w	129	$\gamma_t(\text{CH}_2)_{\alpha}$, $\nu(\text{CC})_{\text{B}1}$	1584 w	1582 vw
1432 s	117	$\delta_s(\text{CH}_2)_{\text{pip}}$, $\delta_s(\text{CH}_2)_{\beta}$	1442 w	1444 w
1223 w	93	$\gamma_t(\text{CH}_2)_{\text{pip}}$, $\gamma_t(\text{CH}_2)_{\alpha, \beta}$	1206 w	1202 w
1190 m	90	$\nu(\text{B}1-\text{C}-\text{C})$, $\delta_s(\text{CH})_{\text{B}1}$, $\gamma_t(\text{CH}_2)_{\text{pip}}$, $\gamma_t(\text{CH}_2)_{\alpha, \beta}$	1172 vw	1174 w
1164 m	87	$\gamma_t(\text{CH}_2)_{\text{pip}}$, $\gamma_t(\text{CH}_2)_{\alpha, \beta}$	1158 w	1158 vw
1017 s	72	$\nu(\text{CCC})_{\text{alkyl}}$	1028 m	1028 m
984 s	65	$\delta(\text{C}=\text{C})_{\text{B}1}$	1004 s	1004 s
958 w	61	$\gamma_t(\text{CH}_2)_{\text{pip}}$, $\nu(\text{CH}_2)_{\text{pip}}$, $\nu(\text{C}_1-\text{C}_\epsilon-\text{N}_2)$,	978 vw	980 vw
826 m	51	$\nu(\text{C}_{\text{B}1}-\text{C}_\alpha-\text{C}_\beta)$, $\nu(\text{CH}_2)_{\text{pip}}$	832 m	832 w
647 w	40	$\delta(\text{C}_{\text{B}2}-\text{N}_1-\text{C})$, $\delta(\text{ring})_{\text{pip}}$, $\beta(\text{ring})_{\text{B}2}$, $\delta(\text{CCC})_{\text{alkyl}}$	654 vw	656 vw
614 m	38	$\delta(\text{ring})_{\text{B}2}$	622 m	622 vw

ν , stretching; δ , in-plane bending (*s*, scissoring; *r*, rocking); γ , out-of-plane bending (*t*, twisting; *w*, wagging); β , ring breathing. Functional groups nomenclature and abbreviations follow Figure 8.3.

or unavailable. In order to obtain a fentanyl-specific scaling factor, fentanyl and four of its analogs (benzylfentanyl, parafluorofentanyl, acrylfentanyl, and butyrylfentanyl) were collectively utilized as a training set, and the scaling factor was calculated as the average of the ratios between their experimental and computed frequencies, $\lambda = \nu_{\text{exp}}/\nu_{\text{cal}}$.⁶⁰ The factor thus obtained, 0.9606, was then applied to the simulated spectra of acetylfentanyl (an analog without any special functional groups) and furanylfentanyl (an analog with a

Table 8.7: DFT-calculated and experimental Raman and SERS frequencies of furanylfentanyl, and assignment of normal modes.

DFT x 0.9536	Mode	Assignment	Raman (cm-1)	SERS (cm-1)
1596 s	125	$\nu(\text{C}=\text{C})_{\text{furan}}$	1602 m	1599 w
1496 s	122	$\nu(\text{C}=\text{C})_{\text{furan}}$	1472 s	1468 s
1393 m	112	$\gamma_w(\text{CH}_2)_{\text{pip}}; \gamma_w(\text{CH}_2)_\beta$	1388 m	1390 w
1205 w	92	$\gamma_t(\text{CH}_2)_{\text{pip}}; \delta(\text{CH})_{\text{furan}}; \delta(\text{C}_{\text{furan}}-\text{C}_\epsilon-\text{N}_2-\text{C}_{\text{pip}})$	1208 w	1204 w
1025 m	74	$\delta(\text{CH})_{\text{B2}}$	1034 w	1030 m
996 s	67	$\delta(\text{C}-\text{C})_{\text{B1}}$	1004 s	1004 s
877 w	56	$\delta(\text{ring})_{\text{furan}}; \delta(\text{ring})_{\text{pip}}$	886 w	886 w
826 m	51	$\delta(\text{C}_{\text{B2}}-\text{N}_2-\text{C}_\epsilon-\text{C}_{\text{furan}}); \delta(\text{C}_{\text{B2}}-\text{N}_2-\text{C}_{\text{pip}}); \gamma(\text{CH})_{\text{B2}}$	826 w	828 w
788 w	49	$\delta_r(\text{CH}_2)_{\alpha,\beta}; \delta_r(\text{CH}_2)_{\text{pip}}$	794 w	790 vw
622 vw	39	$\delta_r(\text{ring})_{\text{B1}}$	622 w	620 w

ν , stretching; δ , in-plane bending (*s*, scissoring; *r*, rocking); γ , out-of-plane bending (*t*, twisting; *w*, wagging); β , ring breathing. Functional groups nomenclature and abbreviations follow *Figure 8.3*.

Table 8.8: DFT-calculated and experimental Raman and SERS frequencies of para-fluorofentanyl, and assignment of normal modes.

DFT x 0.9593	Mode	Assignment	Raman (cm-1)	SERS (cm-1)
1616 s	124	$\nu(\text{C}=\text{C})_{\text{B1}}$	1602 m	1600 m
1598 m	123	$\nu(\text{C}=\text{C})_{\text{B2}}$	1586 w	1582 vw
1443 s	114	$\delta_s(\text{CH}_2)_\beta; \delta_s(\text{CH}_2)_{\text{pip}}; \delta(\text{CH})_{\text{B1}}$	1466 m	1470 w
1192 m	85	$\nu(\text{C}_\alpha-\text{B1}); \gamma_w(\text{CH}_2)_\alpha; \delta_r(\text{CH})_{\text{B1}}$	1204 m	1204 m
1172 m	84	$\gamma_t(\text{CH}_2)_{\text{pip}}; \gamma_t(\text{CH}_2)_{\alpha,\beta}$	1158 m	1158 m
1143 m	81	$\delta_s(\text{CH})_{\text{B2}}; \gamma_t(\text{CH}_2)_{\text{pip}}; \gamma_t(\text{CH}_2)_{\alpha,\beta}$	1152 w	
1023 m	70	$\nu(\text{C}=\text{C})_{\text{B1}}$	1034 m	1030 m
990 s	65	$\delta(\text{C}=\text{C})_{\text{B1}}$	1002 s	1002 s
828 s	52	$\nu(\text{N}_1-\text{C}_\alpha-\text{C}_\beta); \delta_r(\text{CH}_2)_{\text{pip}}; \gamma(\text{C}-\text{H})_{\text{B2}}; \delta(\text{C}-\text{C}_1-\text{C}_2)$	824 s	824 s
655 w	41	$\delta_r(\text{CH}_2)_{\text{pip}}; \nu(\text{C}-\text{N}_2-\text{C}); \nu(\text{C}_\epsilon-\text{C}_1-\text{C}_2); \delta_r(\text{CH}_3)$	642 m	622 w
637 w	40	$\delta(\text{ring})_{\text{B2}}$	622 m	621 m

ν , stretching; δ , in-plane bending (*s*, scissoring; *r*, rocking); γ , out-of-plane bending (*t*, twisting; *w*, wagging); β , ring breathing. Functional groups nomenclature and abbreviations follow *Figure 8.3*.

special functional group), resulting in band position prediction errors lower than 3%. On the basis of these results, it can be stated that the $\omega\text{B97XD/cc-pVTZ}$ method can be used to predict the Raman spectra of fentanyl analogs, if the required accuracy is not high, as the errors in the predicted frequencies should be lower than 4%.⁶¹

Effects of the nanomaterial's morphology and capping environment on the SERS intensity

It is known that the morphology of nanoparticles and their aggregation state affects the SERS response,⁶⁴ as extensively discussed in § 2.2.2 of this dissertation. This relationship was verified by studying the SERS spectra of acrylfentanyl and benzylfentanyl at a concentration of 10 ng/mL, utilizing both AuAg nanospheres (NSph/CO₃²⁻_(c)) and AuAg nanostars (NS/CO₃²⁻_(c)). The spectra presented in *Figure 8.7* demonstrate the superiority of the branched morphology in producing a SERS enhancement under λ_{exc} 785 nm conditions. For both analogs, this is reflected in an improved spectral quality and a higher signal-to-noise ratio. Moreover, the intensity of the characteristic band at 1004 cm⁻¹ was 4.36 times (benzylfentanyl) and 1.73 times (acrylfentanyl) higher when using NS/CO₃²⁻_(c) than that obtained with NSph/CO₃²⁻_(c). In the case of benzylfentanyl, the use of nanostars facilitated the observation of bands at 1158 and 832 cm⁻¹, which were otherwise undetectable. Hence, the NS/CO₃²⁻_(c) formulation was used exclusively to detect the rest of fentanyl analogs in this study.

The effect of the capping environment on the SERS intensity was even more pronounced than that caused by the nanoparticle morphology. *Figure 8.7* also reports the spectra of benzylfentanyl and acrylfentanyl obtained with the original NS formulation as proposed by He *et al.*,⁶² which contains the bulky surfactant CTAB as the stabilizing component. As it can be easily observed, the near field nature of the SERS signal is verified; CTAB is not displaced by the analytes, and because of its steric hindrance, it increases the distance at which the target molecules are able to interact with the surface. As a result, the intensity of the signal, as well as the overall spectral quality, are significantly lowered. In this case, the characteristic band at 1004 cm⁻¹ was 96.4% (benzylfentanyl) and 95.9% (acrylfentanyl) lower than that obtained using NS/CO₃²⁻_(c).

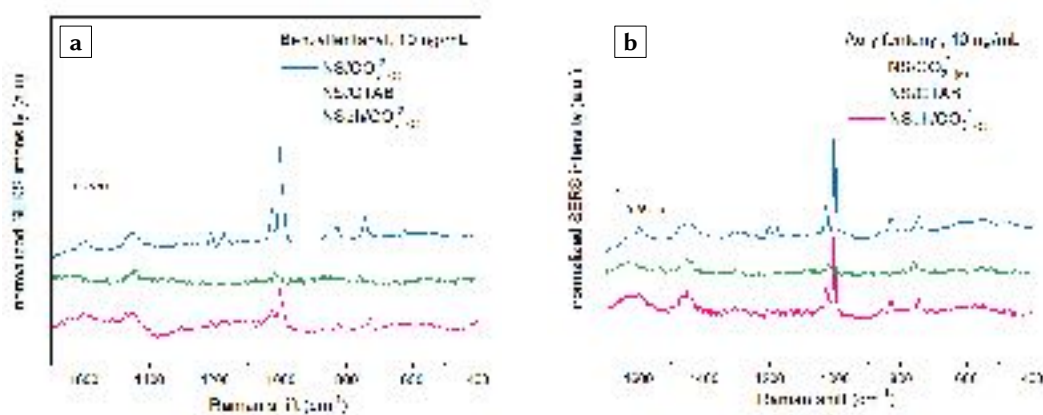


Figure 8.6: SERS spectra of benzylfentanyl and acrylfentanyl, at a concentration of 10 ng/mL, obtained with two different morphologies of carbonate-capped AuAg nanomaterials, nanostars (NS/CO₃²⁻_(c), *blue*) and nanospheres (NSph/CO₃²⁻_(c), *pink*), and with CTAB-capped nanostars (NS/CTAB, *green*).

Raman and SERS spectra of fentanyl analogs

Figures 8.4 b, 8.5, and 8.8, as well as Tables 8.2 to 8.8, show the characteristic bands of the Raman, SERS, and DFT-simulated spectra, and illustrate the differences between them in terms of shifts in band position and relative intensities. The main differences between the NR and the SERS spectra consisted of changes in intensities, rather than shifts in wavenumbers. NR measurements of the drugs in solution were not possible, as a result of the well-known sensitivity limitations of this type of spectroscopy.⁶³

Fentanyl and its six analogs were characterized by an ensemble of bands at 1620–1580 cm⁻¹. In the Raman spectra, butyrylfentanyl, para-fluorofentanyl, and furanylfentanyl exhibited two bands, whereas fentanyl, benzylfentanyl, acetylfentanyl, and acrylfentanyl exhibited three bands. However, in the SERS spectra of these compounds, the band at the highest frequency (~1650 cm⁻¹) was absent, and the two remaining bands appeared at ~1600 and 1580 cm⁻¹. This spectral pattern was shown by all analogs, except for acrylfentanyl, which retained a higher frequency shoulder at 1634 cm⁻¹.

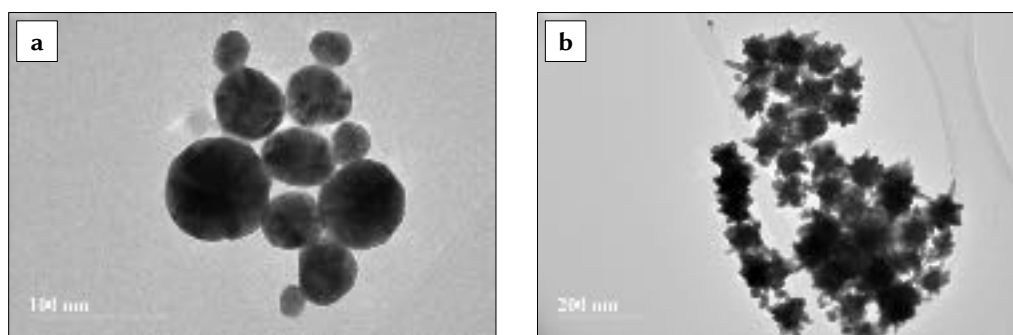


Figure 8.7: TEM micrographs of the two different morphologies of carbonate-capped AuAg nanomaterials utilized in this study, (a) nanospheres (NSph/CO₃²⁻_(c)) and (b) nanostars (NS/CO₃²⁻_(c)).

In the region from 1550 to 1350 cm⁻¹, all tested compounds, except furanylfentanyl, showed multiple weak bands in their NR spectra; furanylfentanyl had instead its most intense band in this region (1472 cm⁻¹), along with a weak band at 1388 cm⁻¹. This spectral signature was also observed in the SERS spectrum of furanylfentanyl. In this spectral region, the remaining analogs exhibited a SERS profile that was not characterized by resolved bands. Instead, a broad and weak band centered at ~1444 cm⁻¹ was observed. This broad band showed a shoulder at 1470 cm⁻¹ in the para-fluorofentanyl SERS spectrum, whereas two overlapping bands at 1454 and 1466 cm⁻¹ appeared in the benzylfentanyl SERS spectrum.

In the range between 1350 and 1050 cm⁻¹, medium and weak Raman bands were observed, the intensities of which were much weaker in the respective SERS profiles. All fentanyl analogs displayed bands at 1184 and 1158 cm⁻¹, whereas benzylfentanyl had an additional weak band at 1212 cm⁻¹. Fentanyl and the other five fentanyl analogs were characterized by an additional band at 1204 cm⁻¹. Acrylfentanyl had a triple band at 1310, 1278, and 1244 cm⁻¹.

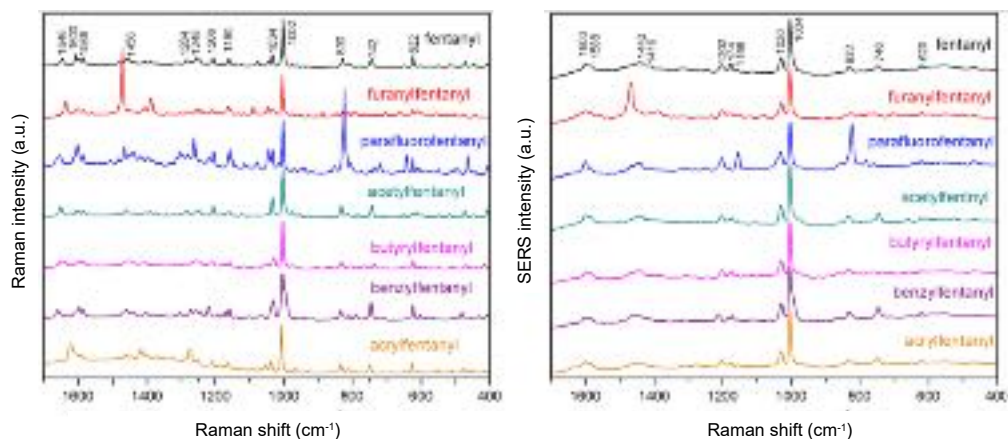


Figure 8.8: Comparison of Raman (*left*) and SERS (*right*) spectra of fentanyl and six of its analogs.

In all Raman and SERS spectra, two characteristic bands of fentanyl-related compounds were observed at ~ 1004 and 1030 cm^{-1} . In the fentanyl, acrylylfentanyl, and butyrylfentanyl spectra, the first characteristic band exhibited a shoulder at 970 cm^{-1} , 978 cm^{-1} , and at 980 cm^{-1} , respectively.

From 950 to 400 cm^{-1} , the fentanyl analogs showed many weak and very weak bands in both SERS and Raman spectra. Weak bands appeared at ~ 832 and $\sim 620\text{ cm}^{-1}$. Only para-fluorofentanyl had a very strong band in this region, which was centered at 824 cm^{-1} . Furanyl/fentanyl showed weak bands at 866 and 700 cm^{-1} ; acrylylfentanyl, acetylfentanyl, fentanyl, and benzylfentanyl had a band at 746 cm^{-1} . Very weak bands at 660 cm^{-1} and 646 cm^{-1} were observed for acetylfentanyl and acrylylfentanyl, respectively.

Vibrational characterization

Fentanyl analogs have two monosubstituted benzene rings, *B1* and *B2*. These are located at the two ends of the molecules and therefore do not interact with each other.⁵⁹ The *B1* aromatic ring connects to C_{α} , acting as a benzyl group. The *N2* atom is connected to a piperidine ring (*pip*), another benzyl ring (*B2*) with which it forms an aniline group,

and to a carbonyl functional group, with which it forms an amide. The selected fentanyl analogs had similar chemical structures, so their Raman and SERS spectra exhibited many similarities. Each of the NR spectra were compared to the respective DFT-simulated and SERS spectra; particular attention was given to the bands at ~ 622 , ~ 832 , ~ 1004 , ~ 1034 , ~ 1160 , ~ 1174 , ~ 1206 , ~ 1440 – 1460 , ~ 1582 – 1602 cm^{-1} .

First, the results of the NR spectra of the analytes in the solid phase were compared to the DFT-simulated spectra (Tables 8.2–8.8). The ring C=C stretches from two monosubstituted aromatic rings, *B1* and *B2*, contributed to the strongest band at ~ 1004 cm^{-1} in both NR and SERS spectra, for all seven analytes. Therefore, this band can be used to distinguish the fentanyl analogs from common opiates, for example, morphine, hydrocodone, hydromorphone, oxycodone, heroin, codeine, and thebaine, which, on the other hand, do not have any overlapping characteristic band at this wavenumber. The other characteristic band, ~ 1034 cm^{-1} in NR spectra and ~ 1030 cm^{-1} in SERS spectra, was also observed in all seven analytes. This band was the result of different vibration modes for each fentanyl analog. For fentanyl, benzylfentanyl, acrylfentanyl, para-fluorofentanyl, and furanylfentanyl, this band was the result of C=C stretches and C–H bends in the aromatic rings. As for butyrylfentanyl, the band was assigned to the C–C–C stretch of the side chain in the amide group. In the NR spectrum, this band was shifted to a slightly lower wavenumber and had medium intensity. Acetylfentanyl has only one carbon in the side chain of the amide group, and the strong band at ~ 1030 cm^{-1} is the result of a C–C stretch in the piperidine ring.

At high wavenumbers, all seven species had a double band at ~ 1586 and 1602 cm^{-1} , assigned to a C–C stretch of the aromatic rings. In addition to this double band, butyrylfentanyl had a CH₂ twist at the *C*_α and *C*_β atoms, while furanylfentanyl had extra in-plane bending of C–H groups for both the furane and piperidine rings. Theoretically, the C–C stretch of the aromatic rings can also produce a moderate band at ~ 1450 cm^{-1} .

The investigated compounds had other bands in the higher wavenumber region, which were found to be related to the C–H in-plane bend in *B1* (para-fluorofentanyl), the CH₂ scissoring in *pip* (fentanyl, acetylfentanyl, para-fluorofentanyl, and acrylfentanyl), the CH₂ twist at *C_α* (benzylfentanyl), the CH₂ scissoring at *C_α* (acrylfentanyl), the CH₂ scissoring at *C_β* (para-fluorofentanyl), and the CH₃ in-plane bend from the amide group (acetylfentanyl, para-fluorofentanyl, and butyrylfentanyl). In the NR spectra, furanylfentanyl had a very strong band at 1472 cm⁻¹ caused by the C–C stretch in the furane ring, while the other six compounds had a weak to moderate band at ~1460 cm⁻¹, assigned to the CH₂ scissoring in the piperidine ring.

Fentanyl analogs had three bands in the region of 1220–1170 cm⁻¹. These three bands were mainly caused by the CH₂ out-of-plane bend in the *pip* ring, *C_α* and *C_β*, as well as the stretch of N-alkyl chain (butyrylfentanyl, fentanyl, and para-fluorofentanyl), the stretch of amide side chain (acrylfentanyl), and the bend of piperidine-amide-furane group (furanylfentanyl). At low wavenumbers, the band at ~832 cm⁻¹ was related to the stretch of the N-alkyl chain (fentanyl, acrylfentanyl, and butyrylfentanyl), the rocking of CH₂ in piperidine (benzylfentanyl, acetylfentanyl, and acrylfentanyl), the in-plane bend of C–C–C in piperidine (acrylfentanyl), and the ring breathing of *B1* (acetylfentanyl). This strong band was shifted at ~824 cm⁻¹ for para-fluorofentanyl, and was assigned to the out-of-plane bending of CH in *B2* and the in-plane bending of the amide side chain. This band was absent in furanylfentanyl, which showed instead a weak band at 886 cm⁻¹, assigned to the complex in-plane bending of C_{B2}–N₂–C_ε–C_{furane} and C_{B2}–N₂–C_{piperidine}, as well as to the out-of-plane bending of CH in *B2*. The band at ~620 cm⁻¹ appeared in all fentanyl analogs and was related to the in-plane ring bending of either *B1* or *B2*, or both.

After the study of the NR bands as compared to the DFT-simulated spectra, the SERS profiles of fentanyl and the six analogs were compared to their respective NR signatures (Figure 8.8). The SERS spectra exhibited a smaller number of bands than the NR spectra.

The previously designated fentanyl marker band at $\sim 1004\text{ cm}^{-1}$ was observed for all analogs. Butyrylfentanyl was the only analog that did not have a weak band at $\sim 746\text{ cm}^{-1}$, whereas para-fluorofentanyl had it shifted at 824 cm^{-1} and was higher in intensity because of the presence of a fluorine on *B2*. Furanylfentanyl had an additional strong band at 1468 cm^{-1} caused by the presence of the furane ring. Interestingly, the double band at 1602 and 1586 cm^{-1} was observed to have a higher intensity on the component at 1602 cm^{-1} , except for benzylfentanyl, in which the intensities of the two components were much closer to one another. This analog also had a wide band, which shifted from 1442 cm^{-1} to 1454 cm^{-1} . Acrylfentanyl had a C–C bond in the amide group, and its in-plane bending contributed to a moderate band at 1357 cm^{-1} in the DFT spectra. The same group also gave a weak triple band at 1310 , 1278 , and 1224 cm^{-1} in the SERS spectrum, with a medium intensity band at 1276 cm^{-1} . Acetylfentanyl has only one methyl group in the amide side chain; the stretching of $\text{N}_2\text{--C}_\epsilon\text{--C}_1$ and the rocking of CH_3 yielded a band at 652 cm^{-1} in the NR spectrum and at 660 cm^{-1} in the SERS spectrum.

Statistical analysis

Thirteen SERS spectra from standard solutions were measured over two wavenumber ranges, from 3278 to 200 cm^{-1} , and from 1700 to 400 cm^{-1} . Data processing was performed using SPSS version 20. The PCA results are shown in *Figure 8.9*. To study the distinguishability of PC1 and PC2, descriptive statistics, independent-sample t-tests, and nonparametric Mann–Whitney U test were used. Thirteen samples were separated into two groups of fentanyl analogs (*FA*) and non-fentanyl drugs (*NF*, amphetamine, methamphetamine, morphine, hydrocodone, hydromorphone, oxycodone, heroin, codeine, and thebaine).

In the range between 3278 and 200 cm^{-1} , the PC1 of both groups displayed normal distributions (Shapiro–Wilk test, *FA* significance value = 0.089 , *NF* significance value =

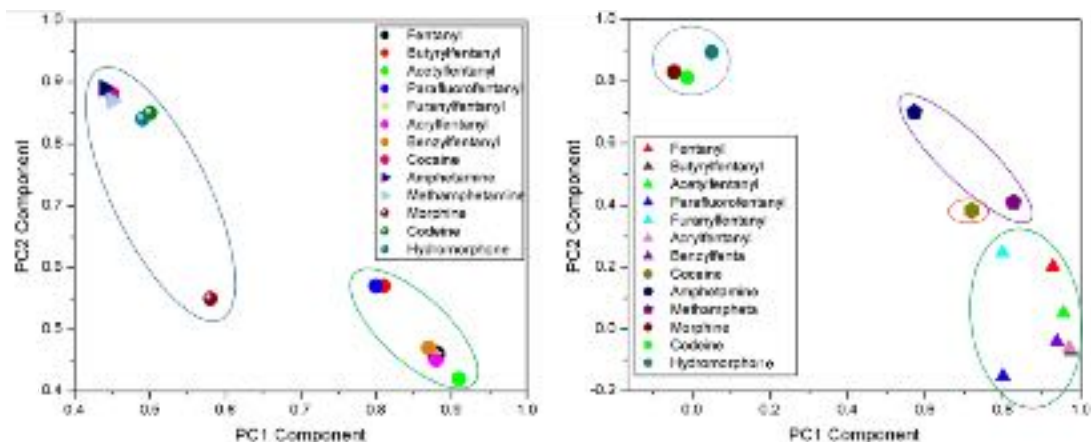


Figure 8.9: 2-D principal component analysis (PCA) plots showing the separation of SERS spectra into different classes of substances. The plot on the left has been obtained utilizing SERS spectra in the 3278–200 cm^{-1} range, while the plot on the right was obtained using SERS spectra in the 1700–400 cm^{-1} range.

0.089), and did not have unequal variance (Levene's test, $F = 0.224$, significance value = 0.645). Therefore, the PC1 of the fentanyl analogs (0.86 ± 0.04) was higher than that of the non-fentanyl drugs (0.48 ± 0.05); the difference value was 0.38 (95% CI [0.32, 0.43]). According to the t-test ($t = 16.60$, Prob < 0.0005), PC1 can distinguish the groups of fentanyl analogs from the non-fentanyl substances. As for PC2, the fentanyl analogs group displayed a non-normal distribution (Shapiro–Wilk test, significance value = 0.001), whereas the non-fentanyl drugs showed some outliers related to morphine (Shapiro–Wilk test, significance value = 0.057). A Mann–Whitney U test was applied to determine if there were differences in PC2 between fentanyls and non-fentanyls. The results showed that the median PC2 values for fentanyls (0.46) and non-fentanyl drugs (0.86) were statistically significantly different ($U = 2$, $Z = -2.714$, 0.005).

In the 1700–400 cm^{-1} range, PC1 displayed a non-normal distribution in the fentanyl analogs group (Shapiro–Wilk test, significance value = 0.018), while in the non-fentanyl drugs group it showed a normal distribution. A Mann–Whitney U test was applied to confirm that PC1 expressed differences between fentanyls and non-fentanyls. The median

PC2 values for fentanyl (0.94) and non-fentanyl drugs (0.31) were statistically significantly different — $U = 2$, $Z = -2.714$, 0.005 , using an exact sampling distribution for U . The PC2 of both groups displayed normal distributions (Shapiro–Wilk test, FA significance value = 0.357 , NF significance value = 0.138), with unequal variance (Levene’s test, $F = 1.836$, significance value = 0.203). Indeed, the PC2 of the fentanyl analogs (0.03 ± 0.15) was lower than that of nonfentanyl drugs (0.67 ± 0.22), and the difference value was -0.64 (95% CI [-0.87 , -0.42]). According to the t-test ($t = -6.235$, Prob < 0.0005), PC2 can distinguish between fentanyl analogs and non-fentanyl drugs. Therefore, the PC1 and PC2 loadings revealed that fentanyl analogs and nonfentanyl drugs can be distinguished by SERS spectra.

8.2.2 Summary and Prospects

Fentanyl and six of its analogs were examined by theoretical calculations, traditional Raman spectroscopy (samples in the solid phase), and SERS (samples in solution). Geometry optimization and calculation of vibrational frequencies and Raman activities were performed within DFT at the $\omega B97XD/cc-pVTZ$ level, and allowed for the assignment of normal modes to the experimental Raman and SERS bands. SERS spectra were obtained by utilizing the $NS/CO_3^{2-}_{(c)}$ formulation as the enhancing substrate, demonstrating their usefulness in the detection of compounds of forensic interest. These nanoparticles allowed for the obtainment of intense SERS spectra of fentanyl-related compounds at a concentration of 10 ng/mL , thus demonstrating their potential for applications in the trace and ultratrace domains. Moreover, the PCA results demonstrate the capability of SERS to distinguish between a variety of fentanyl analogs and non-fentanyl substances, both opiates and opioids *and* stimulants, indicating great

potential for multivariate analysis assisted SERS (MVA-SERS) to offer an analytical platform to discriminate between mixtures.

Indeed, NS/CO₃²⁻_(c)-enabled SERS measurements were recently utilized by the McCord group to detect trace fentanyl in binary mixtures of cocaine and heroin^{II}, utilizing a handheld Raman spectrometer and super partial least square discriminant analysis (sPLS-DA).⁶⁵ This method had a sensitivity of 0.20 ± 0.06 ng/mL towards fentanyl, demonstrating a fit-to-purpose of the developed colloidal formulation for the detection of compounds of forensic and public health interest, such as fentanyl and its analogs. The low limit of detection also indicates suitability of the analytical method for the detection of these opioids in toxicological samples.

8.3 Applications that make use of traditional nanoparticles

To illustrate the potential of SERS in forensic toxicology, an example involving the detection of synthetic cannabinoid JWH-018 in oral fluid is presented. In this work, traditional citrate-reduced gold nanospheres are utilized, and new method for upstream sample extraction is proposed.

^{II}Wang, L.; Vendrell-Dones, M.O.; Deriu, C.; Doğruer, S.; Harrington, P.; McCord, B. *Multivariate Analysis Assisted Surface Enhanced Raman Spectroscopy (MVA-SERS) Determination of Fentanyl in Cocaine and Heroin Mixtures Using a Handheld Raman Spectrometer*, manuscript in preparation.

8.3.1 Micro Solid Phase Extraction Surface-Enhanced Raman Spectroscopy (μ -SPE/SERS) Screening Test for the Detection of the Synthetic Cannabinoid JWH-018 in Oral Fluid

The following section is reprinted with minor modifications from Deriu, C.; Conticello, I.; Mebel, A. M.; McCord, B. Micro Solid Phase Extraction Surface-Enhanced Raman Spectroscopy (SPE/SERS) Screening Test for the Detection of the Synthetic Cannabinoid JWH-018 in Oral Fluid. Analytical Chemistry, 2019, 91(7), 4780–4789. Copyright (2019) American Chemical Society. This work was supported by Award #2015-IJ-CX-K006 of the National Institute of Justice, Office of Justice Programs, U.S. Department of Justice. Points of view in the document are those of the authors and do not necessarily represent the official view of the U.S. Department of Justice.

Abstract

An analytical protocol based on SERS and aimed at the detection of toxicologically relevant concentrations of JWH-018 in oral fluid is presented for the first time. A DFT-supported in-depth vibrational characterization of the drug in the solid state and in solution was also performed, providing a body of literature for future spectroscopic work on the compound. A Langmuir adsorption model was used to derive quantitative parameters such as the affinity of JWH-018 for citrate-capped gold nanospheres as well as the LOD. The application of the implemented method to the analysis of extracts from fortified oral fluid samples demonstrates the feasibility of SERS as an alternative to current immunoassays as a screening tool for use in emergency room settings.

Introduction

Synthetic cannabinoids (SCBs), also referred to as *Spice*,⁶⁶ are novel psychoactive substances (NPS) that represent a worldwide public health issue due to lack of knowledge on *in vivo* toxicological effects,⁶⁷ associated emergency room visits, and fatalities.^{68–70}

A major challenge for health professionals and law enforcement is the rapidity at which these compounds are modified and introduced into the market, making it difficult to detect them using standard screening tests.⁷¹ These are commonly based on enzyme-linked immunosorbent assay (ELISA) methods, which exploit the binding action of antibodies toward specific targets, in the presence of enzymatic colorimetric reactions used as a means of detection.^{72–76} The specificity of antibodies toward a given antigen depends on both structure and geometry. Because of the the ever-changing nature of SCBs and other NPSs molecular structures, and depending on the degree of structural modification imparted to drug analogs when compared to the drug used to produce the antibody, poor cross reactivity among drugs belonging to the same class can occur. This, as well as the presence of heterophile antibodies and autoantibodies, leads to reduced sensitivity and false negative results, severely limiting this approach.^{75,77}

Surface-enhanced Raman spectroscopy (SERS) has been shown to have great potential to solve these problems, by providing a sensitive, selective, label-free, and immuno-free screening approach that yields molecular fingerprint signals from xenobiotics at toxicological concentrations.^{8,78,79} SERS is a surface spectroscopic technique which achieves amplification of the inherently weak Raman scattering via the use of plasmonic nanostructures, thus, enabling the detection of trace analytes.² This was achieved by the McCord group with benzodiazepines and SCBs, both as standard solutions and in fortified urine samples.^{8,78,79} Furthermore, the work on SCBs demonstrated that SERS is a selective technique, which is able to discriminate between highly similar structures, such as JWH-018, JWH-073, JWH-081, and JWH-122.⁷⁹ Selectivity can also be achieved by

other screening approaches, such as molecularly imprinted polymer based quartz crystal microbalance sensors (MIP-QCM).⁸⁰ While selective and sensitive, MIP-QCM sensors incur the same problems as immunoassays. This is due to the fact that the selectivity of this type of sensor relies on the presence of a recognition element, the molecularly imprinted polymer, which mimics the lock-and-key interaction mechanism typical of antibodies or other biological receptors.⁸¹ In contrast, SERS is a detection platform which is not based on a recognition element, but instead yields a spectral signal that is unique to its structure.² This makes SERS a more flexible analytical technique, in that it is capable of identifying new drug analogs as they are introduced into the market. As far as toxicological samples are concerned, while traditional biological matrices such as blood and urine continue to be used for drug testing, oral fluid is becoming increasingly popular. This biological matrix is difficult to adulterate, can be collected under the supervision of nonspecialized personnel without privacy violation, and presents low risk of infection for analysts when compared to blood.^{76,82,83} Collection is generally achieved using devices such as adsorption pads or by direct collection into glass or plastic tubes.^{76,82-84} Oral fluid is mainly composed of water, and proteins such as mucinous and nonmucinous glycoproteins make up only 0.3% of its mass.⁸²⁻⁸⁴ This low protein content implies protein binding in oral fluid is negligible compared to blood, and target compounds, if present, can be assumed to mainly exist as free drugs.⁸² Moreover, the oral cavity is not a typical site of xenobiotic metabolism, leading to a higher concentration of the parent compound over possible metabolites. These are usually present at lower concentrations and result from passive diffusion across a concentration gradient from the bloodstream to the oral fluid.⁷⁶ These facts enable screening tests based on oral fluid analysis to be targeted at the sole parent drug, constituting an advantage when analyzing NPS, as their metabolic species are often unknown or not fully elucidated. Moreover, smoked substances such as SCBs tend to be present in oral fluid at higher concentrations, due to contamination of the oral cavity by direct contact with the drug.⁸⁵

While this might cause overestimation of concentration in quantitative studies aimed at relating drug levels in oral fluid to those in blood, this type of contamination represents an advantage for qualitative screening aimed at assessing recent drug exposure, as it mitigates potential false negatives due to sensitivity limitations.⁸⁶

To the authors knowledge, no SERS method for the analysis of synthetic cannabinoids in oral fluid has yet been developed. Moreover, the application of SERS for drug testing in oral fluid is at present limited, and only few research groups have published on the matter. The first SERS-based screening test for drugs of abuse in oral fluid was developed by Farquharson's group and was tailored at the development of a commercial lab-on-a-chip device for the detection of cocaine, benzoylecgonine, and a number of barbiturates in fortified oral fluid (FOF).⁸⁷ Sample cleanup is of fundamental importance when detecting analytes in complex matrices such as biological fluids, as the multitude of species constituting them competes for adsorption on the nanoparticle surface, ultimately preventing direct analysis of target drugs.^{8,88,89} Farquharson's group utilized dilution in sulfuric acid or acetic acid and sonication as an off-line pretreatment, followed by metal-doped solgels incorporated into capillaries as both enhancing substrates and in-line separation columns.⁸⁷ The same group later modified the lab-on-a-chip device by adding an octyl- and benzyl sulfone-functionalized SPE column for in-line analyte separation and preconcentration.⁸⁸ This method was optimized for the detection of cocaine for concentrations as low as 50 ng/mL. A number of unscheduled and scheduled drugs and metabolites in fortified oral fluid were tested with the same approach, including other stimulants, opiates and opioids, hallucinogens, Z-drugs, benzodiazepines, and antidepressants. Detection thresholds ranged from 1 g/mL for PCP and diazepam to 10 g/mL for acetaminophen.^{88,90,91}

Moskovits' group developed a microfluidic-SERS device based on salt-aggregated colloidal silver nanoparticles as the enhancing substrate, for the rapid detection of

methamphetamine.⁹² The microfluidic device combined the separation of the target analyte from the complex fluid, its adsorption on citrate-capped silver nanoparticles, and a LiCl-induced aggregation of the analyte–nanoparticle system in the interrogation region. Signal enhancements were found to be maximized in areas where formation of dimers and low order nanoparticle aggregates occurred. Although methamphetamine could be detected at concentrations as low as 10 nM (1.9 ng/mL), each device had a limited lifetime of 10 min, due to the accumulation of nanoparticle aggregates in the microfluidic channels and resultant clogging. Reversible aggregation was instead implemented by Yang et al.⁹³ by utilizing gold nanoparticle-dotted magnetic nanocomposites as enhancing substrates and exploiting their behavior in a magnetic field to control the level of nanoparticle aggregation for optimal SERS enhancement. These gold-decorated magnetic nanocomposites were also used as analyte capturing agents for sample pretreatment, and the protocol was applied to the detection of benzoylecgonine (LOD 29 ng/mL) and a nicotine metabolite, cotinine (LOD of 8.8 ng/mL), in fortified oral fluid.

The present work addresses a void in the literature, presenting the development of a rapid SERS-based screening test for the detection of synthetic cannabinoid JWH-018 in fortified oral fluid. JWH-018 is a naphthoylindole SCB, and it has been chosen as the model analyte for the present study because it is among the first to be designated as a Schedule I substance by the DEA,⁹⁴ as well as one of the most studied SCBs in terms of toxicological concentrations in humans and metabolic behavior.^{95–98}

As previously discussed, common screening tests for JWH-018 in oral fluid are based on ELISA, such as the one designed by Rodrigues and co-workers.⁷⁴ The approach here proposed is configured as a qualitative screening that is (1) complementary or alternative to immunoassays, (2) designed to be performed in shorter times, and (3) yet maintaining its sensitivity capabilities to a fit-to-purpose level. This level was set based on the median values reported for JWH-018 in oral fluid after controlled administration of the drug.⁹⁷

Because of the nature of the compound and the lack of in-depth spectroscopic studies on it, DFT calculations were used as a tool to identify the most stable molecular geometry and interpret vibrational modes. An in-depth study of the adsorption behavior on citrate-capped gold nanospheres was addressed, as well as a study of the drug as standard solution and in fortified oral fluid. A proof of concept translation of the method for use with portable Raman spectrometers is also discussed.

Experimental

Reference Materials

DEA scheduled naphthalen-1-yl-(1-pentylindol-3-yl)methanone (JWH-018) in powder form was purchased from Lipomed AG (CAS 209414-07-3, lot #1294.1B3.2). The powder was used to prepare a 20,000 ng/mL stock solution using UHPLC-UV grade methanol (Fisher Chemical, CAS 67-56-1, lot #173273). UHPLC-UV grade methanol was also used to prepare dilutions from the initial stock. Neat, unstimulated oral fluid was collected into polypropylene tubes from consenting volunteers (IRB-15-0203-AM02) and stored at 4 C until further use.

Methods

Fortified oral fluid samples were prepared by adding known volumes of JWH-018 methanolic solution to the collected neat oral fluid, as reported in *Appendix G, Table G.1*. The percentage of methanol was kept constant at 37.5% v/v across all samples, and it was implemented to mimic the preliminary step of methanol addition that would be required when preparing real samples for protein crash.

Sample cleanup was performed via μ -SPE after prior protein crashing. This was achieved by centrifuging a 400 μ L fortified oral fluid aliquot at 9.3 rcf for 10 min in the presence of 37.5% v/v methanol. Methanol is known to induce protein crashing, and

the volume was optimized to ensure the process while simultaneously avoiding large dilutions of the fortified oral fluid. After protein crashing, the supernatant was recovered, and 49.5 μL were aliquoted for subsequent $\mu\text{-SPE}$. This was performed using ZipTip 10 μL pipet tips (Millipore, lot #R7EA90580), fitted with a 0.6 μL reversed phase C_{18} chromatographic bed with no dead volume. The designed $\mu\text{-SPE}$ protocol (*Appendix G, Table G.2*) involves five steps: (1) wetting, (2) equilibrating, (3) binding, (4) washing, and (5) eluting. Each step is carried out by aspirating and releasing the various solvents and solutions using a common micropipettor that fits the 10 μL $\mu\text{-SPE}$ pipet tips, and it can be performed in only 4 minutes. The first step is performed in 100% acetonitrile (UHPLC/UV grade, Fisher Chemical, CAS 75-05-8, lot #181464) according to manufacturers directions, while the second step is performed in ultrapure water acidified to pH 2.5 via addition of formic acid (99% purity, Acros Organics, CAS 64-18-6, lot #A0022334000) at a final concentration of 1% v/v. The same extent of acidification is applied to the aliquot of fortified oral fluid supernatant recovered after protein crash, for a total volume of 50 μL . Washing is carried out using the same acidified solution used for the equilibration step, while the desorption-elution step is carried out in 100% methanol, due to the cannabinoids solubility in small carbon chain alcohols. Preconcentration of the extract is achieved by reducing the elution volume to 4 μL from the initial 10 μL used for steps 1 to 4.

Standard citrate-capped gold nanospheres (AuNPs) were chosen as plasmonic substrates because of their ease of preparation, broad use within the SERS community, and previous successful application to JWH-018 and other SCBs detection by the McCord group.^{6,79} These colloidal nanoparticles were prepared according to a modified Turkevich-Frens method, as reported by Cyrankiewicz.⁹⁹ Briefly, 100 mL of 0.5×10^3 M tetrachloroauric(III) acid trihydrate (Acros Organics, CAS 16961-25-4, lot #A0354619) were heated in a beaker to approximately 98°C under vigorous stirring. Once boiling had started, 4 mL of 1% w/w aqueous solution of trisodium citrate dihydrate (Fisher Scientific,

CAS 6132-04-3, lot #091236) were added all at once. The reaction mixture was kept at the same temperature and under vigorous stirring for another 30 minutes. The resulting colloidal suspension was allowed to cool, reconstituted to 100 mL, and allowed to equilibrate for a minimum of 24 h prior to use as a SERS substrate. Characterization data is provided in *Appendix G*.

Reference normal Raman spectra of JWH-018 in solution and SERS spectra were acquired using a PerkinElmer 400F benchtop Raman spectrometer fitted with an excitation laser line at 785 nm, as described in the Methods section of this dissertation (§ 3.2.7). All samples in solution were analyzed in 250 μL aliquots and deposited in a 96-well quartz microplate (Hellma Analytics). SERS samples were prepared by mixing 240 μL of AuNPs with 2.5 μL of MgCl_2 as aggregating agent at a final concentration of 1.67×10^2 M. Subsequently, 2.5 μL of JWH-018 standard solution or fortified oral fluid extract were added to the aggregated AuNPs, vortexed for a few seconds, and left to incubate for 20 min.

The normal Raman spectrum of solid JWH-018 is a library standard provided by Thermo Scientific and obtained using a portable Thermo Scientific First Defender RM Raman spectrometer in autoaccumulation and autoexposure operating mode. As described in other parts of this dissertation, all SERS spectra were baseline-corrected, and the intensities were normalized to the intensity of the solvent band at 3200 cm^{-1} , assigned to $\nu(\text{OH})$ of water.

SERS spectra of JWH-018 fortified oral fluid extracts were also acquired with a portable Thermo Scientific First Defender RM Raman spectrometer as a proof of concept. This instrument was fitted with a 785 nm laser source (250 mW power at the source) and run in autoexposure and autoaccumulation mode, with a resolution of 7 to 10.5 cm^{-1} FWHM across its range ($2875\text{--}250\text{ cm}^{-1}$). Samples were analyzed in a 1 mL quartz cuvette placed in contact with the spectrometer laser nose attachment and inside a custom chamber

designed to minimize environmental light exposure during spectral acquisitions. As a result of the limitations inherent to the upper spectral range of this instrument, the normalization of the intensities of these spectra was performed against the intensity of the JWH-018 band at 1370 cm^{-1} , assigned to $\nu(\text{C}=\text{C})$ of the naphthalene moiety.

DFT calculations involved geometry optimization and calculation of Raman frequencies and were performed using Gaussian 09 with the B3LYP hybrid exchange correlation functional and 6-311G** basis set.⁵¹ MultiWFN was used to convert Raman activities ($\lambda_{exc} = 12738.85\text{ cm}^{-1}$; $T = 294.15\text{ K}$) and to model the calculated frequencies into a simulated spectrum.⁵⁶ This was achieved by using a standard broadening Lorentzian function and 8.0 cm^{-1} FWHM. Molden was used to visualize the optimized geometry and assign the vibrational modes.^{57,58}

Results and Discussion

Geometry of JWH-018

The geometry of JWH-018 was optimized prior to the calculation of the Raman frequencies. The lack of negative predicted vibrational frequencies shows the geometry corresponds to a true energy minimum. The general structure of JWH-018 is given in the left panel of *Figure 8.10*, along with the standard nomenclature for SCBs moieties. The energy-minimized structure is displayed in the right panel of *Figure 8.10*. JWH-018 is of C_1 point group symmetry, with the core group, linker and linked group laying in three different planes. The optimized Cartesian coordinates are reported in *Appendix G*.

DFT, Normal Raman, and SERS Spectra of JWH-018

DFT Raman frequencies of JWH-018 were scaled by a factor of 0.9779, which was obtained according to standard least-squares minimization procedure over the $1800\text{--}200\text{ cm}^{-1}$ range of interest.⁶⁰ The simulated Raman spectrum is reported in the left panel of

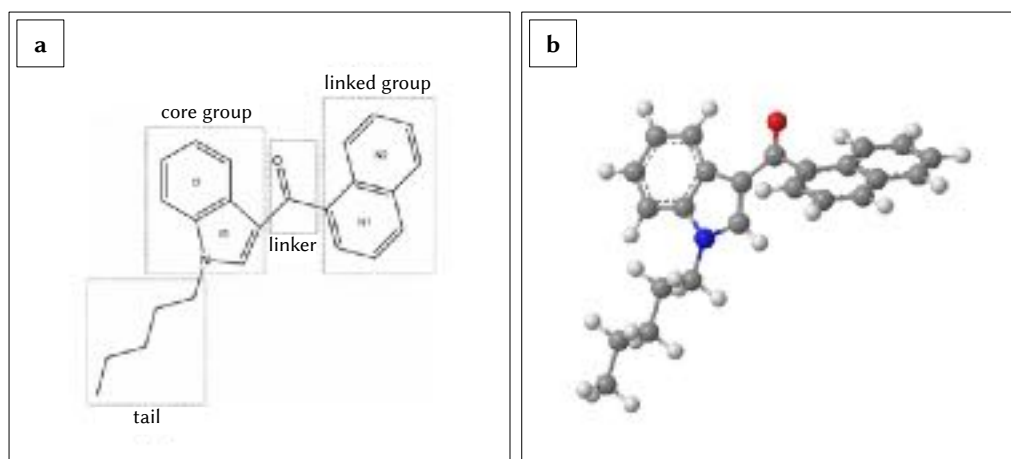


Figure 8.10: (a) Structure of JWH-018 with highlighted synthetic cannabinoids nomenclature and (b) 3D ball-and-stick model of the optimized geometry. C atoms are shown in gray, H in white, O in red, and N in blue.

Figure 8.11, together with the experimental normal Raman spectrum of solid state JWH-018. The former was obtained by modeling the calculated frequencies with a standard broadening Lorentzian function and 8.0 cm^{-1} FWHM.

To assess the level of agreement between the theoretical and experimental frequencies obtained in normal Raman setting, the absolute and percent error for each scaled theoretical-experimental frequency pair have been calculated (Table 8.9). The former is generally in the order of few wavenumbers, except for two bands at 1371 and 1238 cm^{-1} , and the shoulder at 613 cm^{-1} , which show absolute errors of 15, 15, and 10 cm^{-1} , respectively. In the case of the band at 1371 cm^{-1} , this larger discrepancy between experimental and calculated frequency is due to the convolution of more than one calculated transition into a single simulated Raman band. Overall, the low number of notable absolute error values, together with a percent error of predicted-experimental pairs that never exceeds 1.6% within the selected spectral range, denotes an excellent agreement of the predicted frequencies with the experimental data.

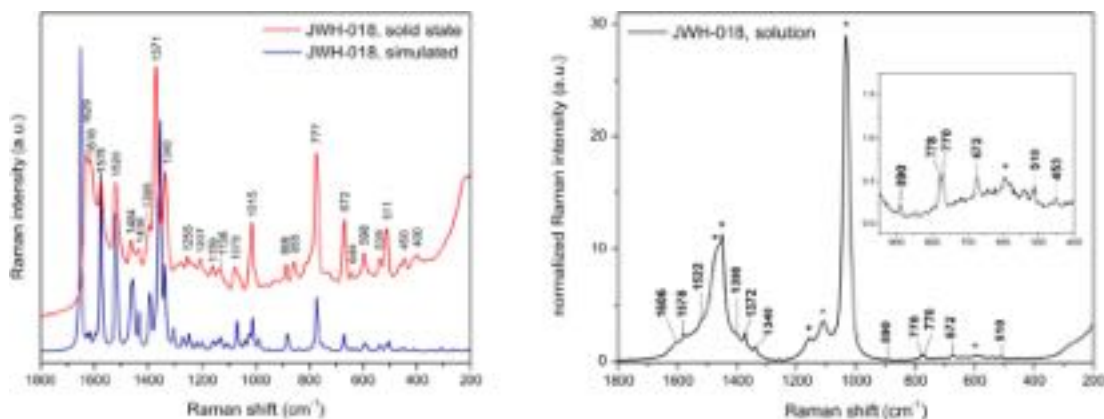


Figure 8.11: (left) DFT simulated Raman (bottom, blue) and solid state experimental normal Raman (top, red) spectra of JWH-018. Intensities have been scaled for ease of comparison. (right) Normal Raman spectrum of JWH-018 at a concentration of 5.0 mg/mL in methanol. Asterisks indicate bands assigned to the solvent. The intensities have been normalized to the solvent band at 3200 cm^{-1} assigned to H-bound $\nu(\text{OH})$ of the alcohol.

The correlation between the relative intensities of bands in the experimental and calculated Raman spectra is good, with few exceptions being in the region between 1700 and 1600 cm^{-1} . In particular, the band at 1653 cm^{-1} in the simulated spectrum is the one with the highest intensity, while it is absent in the experimental spectrum. On the other hand, the experimental spectrum exhibits the bands at 1629 and 1616 cm^{-1} as the most intense bands, which are very weak in the calculated spectrum. This could be caused by a slight discrepancy between the real and the optimized geometries of JWH-018 on which the calculated frequencies and intensities are based, or to an effect of molecular stacking in the real solid sample compared to the calculated values, which refer to a single, isolated molecule.

The assignment of vibrational modes to the bands observed in the experimental results was performed on the basis of the calculated frequencies, with the aid of the intensity data where needed (Table 8.9). The bands with highest intensity in the normal Raman spectrum of JWH-018 in the solid phase are those assigned to the naphthalene ring, and to

Table 8.9: DFT, normal Raman, and SERS bands of JWH-018, vibrational assignments, and error metrics.

DFT (x0.9779)	mode	assignment	normal Raman			SERS	
			solid state		solution		
			(cm ⁻¹)	%error	error	(cm ⁻¹)	(cm ⁻¹)
1653 vs	118	$\nu(\text{C}=\text{O})$					
1624 vw	117	$\nu(\text{C}=\text{C})$ Nph	1629 s	0.31	5		
1614 vw	116	$\nu(\text{C}=\text{C})$ I2	1616 s	0.12	2	1610 m	
1597 sh	115	$\nu(\text{C}=\text{C})$ N1				1606 w	
1577 s	114, 113	$\nu(\text{C}=\text{C})$ Nph, I2	1578 s	0.06	1	1578 w	1572 s
1521 s	112	$\nu(\text{C}-\text{C})$ CCN; $\delta(\text{CH})$ NCH ₂	1520 s	0.07	1	1522 w	1510 s
1460 m	105, 104, 103	$\delta_s(\text{CH}_2)$; $\delta_s(\text{CH}_3)$; $\delta_s(\text{CH}_2)$ I2; $\delta_s(\text{CH})$ Nph	1464 m	0.27	4		1462 m
1435 w	101	$\delta_r(\text{CH})$ Nph	1436 w	0.07	1		1432 m
1393 m	100	$\delta_r(\text{CH})$ Nph	1395 m	0.14	2	1398 sh	1392 m
1356 vs	94	$\nu(\text{C}=\text{C})$ Nph	1371 vs	1.1	15	1372 w	1370 vs
1340 m	93, 92	$\nu(\text{C}=\text{C})$ Ind; $\delta_r(\text{CH})$ I2, Nph	1340 s	0	0	1340 w	1338 s
1306 w	89	$\gamma_r(\text{CH}_2)$					
1272 vw	87	$\gamma_r(\text{CH}_2)$; $\delta_s(\text{CH})$ I2, N2	1277 vw	0.39	5		1272 w
1250 vw	85	$\gamma_w(\text{HCH})_{\text{trans}}$ tail; $\delta_s(\text{CH})$ I2, N2	1255 vw	0.4	5		1250 w
1223 vw	83	$\delta_s(\text{CH})$ N1	1238 vw	1.2	15		
1203 vw	81	$\delta_s(\text{CH})$ Nph; $\gamma_r(\text{CH}_2)$, $\gamma_r(\text{CH}_3)$ tail	1207 w	0.3	4		1204 w
1189 vw	80	$\delta_s(\text{CH})$ I2; $\delta_r(\text{CH})$ I2, N1					1182 vw
1157 vw	77	$\delta_s(\text{HCCH})$ I2, N1	1159 w	0.17	2		1156 w
1143 vw	76	$\delta_s(\text{HCCH})$ Nph					
1132 vw	75, 74	$\delta_s(\text{HCCH})$ I2; $\delta_s(\text{CH})$ NCH	1136 w	0.35	4		1132 w
1110 vw	73	$\gamma_w(\text{CH}_2)$, $\gamma_w(\text{CH}_3)$ tail; $\delta_s(\text{CH})$ N2	1108 sh	0.18	2		
1099 vw	72	$\delta_s(\text{HCCH})$ N2; $\gamma_r(\text{CH}_2)$, $\gamma_w(\text{CH}_3)$ tail					1100 vw
1068 w	71	$\delta_s(\text{HCCCH})$ N1	1075 w	0.66	7		1074 w
1041 vw	69	$\nu(\text{CC})$ tail					1054 sh
1024 vw	68	$\delta(\text{ring})$ N1					
1013 w	67, 66	$\beta(\text{ring})$ I2; $\nu(\text{CC})$ tail	1015 m	0.2	2		1014 w
			1003 sh				998 w
990 vw	64	$\nu(\text{CC})$ tail; $\delta(\text{ring})$ Ind, Nph					
950 vw	59	$\gamma_w(\text{CH})$ Nph					962 vw
			928 vw				928 w
884 vw	56, 55	$\nu(\text{CCH}_3)$; $\delta(\text{ring})$ I2, Nph	888 w	0.45	4	890 vw	884 w
			855 w				862 w
			817 sh				
837 vw	51	$\delta_r(\text{CH}_2)$; $\delta_r(\text{CH}_3)$; $\gamma_w(\text{CH})$ NCH					796 w
775 m	46	$\beta(\text{ring})$ Ind; $\gamma_w(\text{CH})$ Nph	777 s	0.26	2	778 vw	774 m
						770 vw	
754 vw	44	$\delta_r(\text{CH}_2)$; $\delta_r(\text{CH}_3)$					
726 vw	40	$\gamma_w(\text{CH})$ I2, Nph	727 vw	0.14	1		730 sh
673 vw	38	$\delta(\text{ring})$ Nph	672 m	0.15	1	672 vw	670 w
644 vw	37	$\delta(\text{ring})$ I1, Nph	644 vw	0	0		640 vw
623 vw	36	$\delta(\text{ring})$ Ind	613 sh	1.6	10		618 vw
597 vw	35	$\delta(\text{ring})$ Ind; $\gamma(\text{ring})$ Nph	598 w	0.17	1		586 w
575 vw	33	$\gamma(\text{ring})$ Ind	571 sh	0.7	4		
539 vw	31	$\delta(\text{ring})$ Ind, Nph	539 vw	0	0	542 vw	540 w
514 vw	30	$\delta(\text{ring})$ Nph				510 vw	510 w
504 vw	29	$\delta(\text{ring})$ Nph	511 m	1.4	7		
470 vw	28	$\gamma(\text{ring})$ Nph	466 sh	0.85	4		
447	26	$\gamma_w(\text{CH})$ Nph; $\delta(\text{ring})$ Ind	450 vw	0.67	3	453 vw	
410	24	$\delta(\text{ring})$ I2, Nph	415 sh	1.2	5		424 w
395	23	$\delta(\text{ring})$ Nph	400 vw	1.3	5		

vs, very strong; s, strong; m, medium; w, weak; vw, very weak; ν , stretching; δ , in plane deformation (s, scissoring; r, rocking); γ , out of plane deformation (w, wagging; t, twisting); β , breathing. Structural nomenclature and abbreviation is reported in Figure 8.10.

a lesser extent to the indole ring. The initial doublet at 1629 and 1616 cm^{-1} is assigned to the stretching modes of aromatic carbon in naphthalene and in the benzene ring of indole, respectively. The strongest signal is given by the triplet at 1395, 1371, and 1340 cm^{-1} , assigned to the rocking mode of CH in naphthalene, an ensemble of vibrations that include the aromatic carboncarbon stretching in naphthalene, and ensemble of stretching of aromatic carboncarbon bonds of indole and the CH scissoring of the naphthalene and benzene rings of indole. Other major characteristic bands are observed at 1015 (ring breathing of indoles benzene), 777 (ring breathing of indole), 672 (ring deformation of naphthalene), and 511 cm^{-1} (ring deformation of naphthalene).

The normal Raman spectrum of the drug in methanolic solution (5.0 mg/mL) was also acquired (*Figure 8.11*, right panel). In the range between 1700 and 900 cm^{-1} , the spectrum is dominated by the solvent, thus, the few observable JWH-018 bands correspond to the highest intensity bands in the spectrum of the drug in the solid state. At lower wavenumbers, weaker JWH-018 bands can be observed due to the absence of interferences from methanol. No significant differences in terms of band position are present in the calculated spectrum when compared to the spectrum of the drug in the solid state.

The SERS spectrum is reported in *Figure 8.12*. Also, in this case, the only two differences visible when the SERS spectrum is compared to the normal Raman spectrum at higher wavenumbers, where the intensity of the band at 1610 cm^{-1} (1616 cm^{-1} in the normal Raman spectrum) is lower, and the naphthalene $\nu(\text{C}=\text{C})$ band at 1629 cm^{-1} is not observed. This absence can be explained in terms of the low intensity of the band, in that it is hindered by the higher intensity and broadening of the adjacent band at 1610 cm^{-1} . Since the SERS spectrum shows a profile that is generally analogous to the one obtained in normal Raman setting, with comparable position and relative intensity of bands, no particular chemisorption event such as the formation of a chemical complex between the enhancing substrate and the analyte is hypothesized.

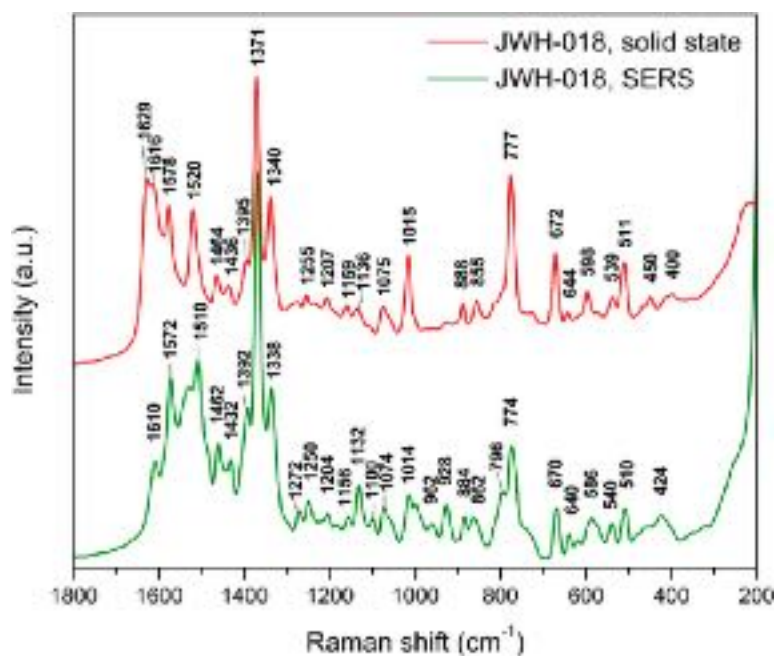


Figure 8.12: Comparison of SERS spectrum of JWH-018 standard methanolic solution at a concentration of 1000 ng/mL (bottom, green) with normal Raman spectrum of JWH-018 in the solid state (top, red). Intensities are on the same scale, and spectra have been stacked for ease of comparison.

Surface-Analyte Interaction and Thermodynamic Parameters

SERS is a surface spectroscopic technique which requires close proximity of the target analyte to the enhancing substrate. It can therefore be assumed that the observable signal is essentially the result of analyte molecules that are adsorbed onto the colloidal nanoparticles surface, either physically or chemically. Under this assumption, the normalized intensity (I_i) of a reference band can be used as a measure of the fractional surface coverage (θ), and plotted against the bulk concentration of the adsorbate ($[A]_i$) to obtain an adsorption isotherm:

$$\theta = \frac{N_i}{N_{sat}} = \frac{K_{ad}[A]_i}{1 + K_{ad}[A]_i} \quad (8.2)$$

where N_i is the number of adsorbed molecules at the i th concentration point, N_{sat} is the number adsorbed molecules at saturation, K_{ad} is the constant of adsorption, and $[A]_i$ is the i th molar concentration of the adsorbate.

The adsorption isotherm of JWH-018 on traditional citrate-reduced colloidal gold nanospheres is reported in the left panel of *Figure 8.13*. It was obtained using the normalized intensity of the band at 1370 cm^{-1} ($\nu(\text{C}=\text{C})$ of naphthalene moiety) as the marker band and shows a monotonic increase followed by a plateau. This is characteristic of Langmuir behavior, in which the dynamic equilibrium between the drug in the bulk of the solution and the drug adsorbed onto the nanoparticles surface is shifted toward the latter. Adsorption proceeds in the absence of lateral cooperativity with previously adsorbed drug molecules, until saturation conditions are achieved and the formation of a complete monolayer occurs.

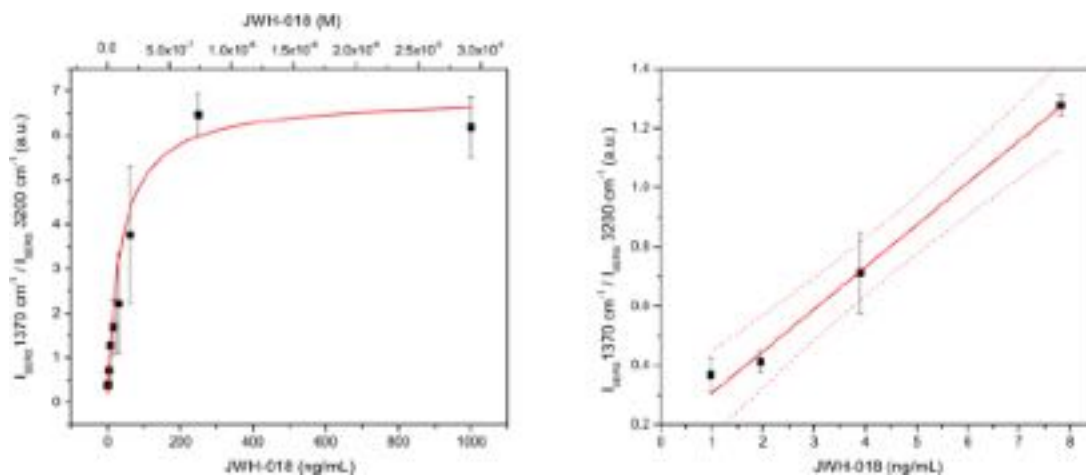


Figure 8.13: Adsorption isotherm of JWH-018 on traditional citrate-reduced Au nanospheres (*left*) and linear fit of low concentration data points (*right*), having equation $y = 0.14221 \pm 0.007x + 0.16 \pm 0.04$. The dotted lines in the linear fit graph represent the upper and lower 95% confidence limit.

A quantitative measure of the affinity between the target analyte and the substrate is given by the adsorption constant K_{ad} , which can be extrapolated from the mathematical description of the Langmuir adsorption model, here adapted to SERS parameters:¹⁰⁰

$$I_i = \frac{I_{sat}K_{ad}[A]_i}{1 + K_{ad}[A]_i} \quad (8.3)$$

where I_i is the SERS intensity at the i th concentration point, I_{sat} is the SERS intensity at saturation, and $[A]_i$ is the i th molar concentration of the adsorbate. This expression was used to fit the plotted adsorption isotherm data, with an adjusted R^2 value of 0.974. The extrapolated K_{ad} is $9.3 \times 10^6 \pm 1.2 \text{ M}^{-1}$ and represents a dynamic equilibrium constant that can be kinetically derived from the ratio k_{ad}/k_d between the adsorption and desorption kinetic constants of the analyte onto the metallic surface.¹⁰¹ From a qualitative point of view, the observed Langmuir behavior in conjunction with the obtained value of K_{ad} demonstrate a high affinity of JWH-018 for the colloidal gold substrate. More specifically, the affinity is higher than the strength of the intermolecular forces existing among individual drug molecules. This has positive consequences on the sensitivity of the analytical method, as the stronger the interaction between the analyte and the substrate, the greater the enhancement of the scattered Raman signal, and the lower the detection limit.

In thermodynamic terms, K_{ad} can be seen as the ratio between the activity of occupied sites over the product between the activity of vacant sites and the activity of the drug in solution.¹⁰² For neutral compounds such as JWH-018, K_{ad} expressed in M^{-1} units has been demonstrated to be numerically equivalent to the thermodynamic equilibrium constant K_{eq} ,¹⁰² such that it could be used to determine the free energy for the adsorption of JWH-018 on the citrate-reduced colloidal gold nanospheres (§ 6.2, Equation 6.5). The value of ΔG ($T = 294.15 \text{ K}$) for the adsorption process was calculated to be $-39.2 \pm 2.9 \text{ kJ/mol}$, indicating a spontaneous process. Both ΔG and K_{ad} are the same order of magnitude as

what was reported in the literature for thiol- and thione-containing analytes,¹⁰³ which are SERS reporters that strongly adsorb on gold,^{2,104} strengthening the argument for high affinity to the gold nanoparticles. Aromatic compounds are indeed found to strongly interact with gold nanoparticles, included citrate-capped nanospheres, on which they are thought to adsorb by either citrate displacement or reorientation.^{105, 106}

Finally, the concentration of JWH-018 at saturation, $[JWH-018]_{sat}$, was obtained iteratively from the Langmuir fitting, and it was used to estimate the number of adsorbed molecules at saturation, N_{sat} , which was found to be 1013 molecules/mL. All Langmuir adsorption and thermodynamic parameters are summarized in *Table 8.10*.

Table 8.10: Langmuir adsorption and thermodynamic parameters (T = 294.15 K).

K_{ad}	$9.3 \times 10^6 \pm 1.2 \text{ M}^{-1}$
I_{sat}	$6.9 \pm 0.7 \text{ a.u.}$
$[JWH-018]_{sat}$	$5928 \text{ ng/mL} (1.7 \times 10^5 \text{ M})$
N_{sat}	$10^{13} \text{ molecules/mL}$
ΔG	$39.2 \pm 2.9 \text{ kJ/mol}$

Sensitivity of SERS Protocol Using Standard Solutions and Analytical Enhancement Factor

For SERS systems following a Langmuir adsorption pattern, sensitivity can be studied using the low surface coverage limit of *Equation 8.3*, which can be applied when the analyte concentration is sufficiently low, such that:¹⁰⁰

$$K_{ad}[A]_i \ll 1; \quad (8.4)$$

$$1 + K_{ad}[A]_i \approx 1 \quad (8.5)$$

This results in a linearized expression:¹⁰⁰

$$I_i = K_{ad}I_{sat}[A]_i \quad (8.6)$$

that is applicable to the low concentration segment of the adsorption isotherm (7.81–0.977 ng/mL), and that was used to extrapolate the $[A]_{LOD}$ by setting I_i equal to three times the standard deviation, σ , of a sample blank.^{100,107} The latter was calculated using the spectral range from 1368 to 1374 cm^{-1} of three different method blank measurements, and the resulting LOD was 0.8 ng/mL (2×10^{-9} M). This indicates high sensitivity, reflecting what was deduced by the high adsorption constant K_{ad} . This LOD is of the same order of magnitude as that found in current immunoassay methods utilized for SCBs in oral fluid.⁷⁴ This level of sensitivity is also compatible with typically encountered toxicological levels of SCBs when effects of the drug are present (for JWH-018, 2.22–2036 ng/mL, with a median of 25.7 ng/mL),⁹⁷ thus, this procedure should be useful for drug detection in emergency room settings. Other analytical figures of merit such as the LOQ ($10\sigma_{noise}$ method blank) are reported in *Table 8.11*. The low concentration segment of the adsorption isotherm was also fitted by linear regression (adjusted R^2 0.992, left panel of *Figure 8.13*) to obtain a calibration curve for subsequent estimation of the JWH-018 recovered from fortified oral fluid extracts.

Table 8.11: Analytical figures of merit.

LOD	0.8 ng/mL (2×10^9 M)
LOQ	2 ng/mL (7×10^9 M)
dynamic range	2.0–7.8 ng/mL (7.0 – 2.5×10^9 M)
limit of linearity	16 ng/mL (5.0×10^8 M)
σ_{noise} method blank (1368–1374 cm^{-1})	0.04 a.u.
sensitivity (slope of calibration curve)	0.142 ± 0.007
std error of calibration curve	1 ng/mL

The information obtained from the adsorption isotherm was also used to choose an appropriate submonolayer concentration for the determination of the analytical

enhancement factor (AEF). This was calculated according to LeRu and Etchegoins definition (Equation 5.3), as it constitutes a reproducible way of accounting for signal magnification by colloidal sols.¹⁰⁸ Due to the overlap of the marker band at 1370 cm⁻¹ with solvent bands in the normal Raman spectrum (Figure 8.11, right panel), this calculation was performed by utilizing the band at 674 cm⁻¹ assigned to the naphthalene ring deformation as the reference. The resulting AEF for the optimized analytical method is 1.3 x 10⁵.

μ -SPE-SERS on JWH-018 in Fortified Oral Fluid

Although oral fluid is mainly composed of water, the small fraction of non-water components is sufficient to interfere with SERS analysis. This has been previously reported in the literature, and attributed to the presence of salivary mucins and thiocyanate.^{88,89} In order to desalt and minimize the protein fraction of fortified oral fluid samples, a two-step cleanup procedure has been implemented. This was constituted by a preliminary protein crashing produced in the presence of methanol, followed by a microsolid phase extraction (μ -SPE) using commercially available miniaturized C₁₈ cartridges mounted inside 10 μ L pipet tips, as described in the *Experimental* part of this section and in *Appendix G*. It is worth highlighting that this μ -SPE procedure is performed in only 4 minutes, making it a quick and easy-to-use cleanup method. The extracts of fortified oral fluid samples prepared with increasingly lower JWH-018 content (*Appendix G*) were then used to assess the sensitivity of the method on simulated samples. A summary of the spectral profiles obtained from these extracts is reported in the left panel of *Figure 8.14*, where the SERS profile of the matrix blank is also shown.

The SERS intensity of the marker band at 1370 cm⁻¹ versus the concentration of JWH-018 in the fortified oral fluid was fitted to a regression line having equation $y = 0.0029 \pm 0.0005x + 0.03 \pm 0.02$ and adjusted R² of 0.918 (*Appendix G*). This was used

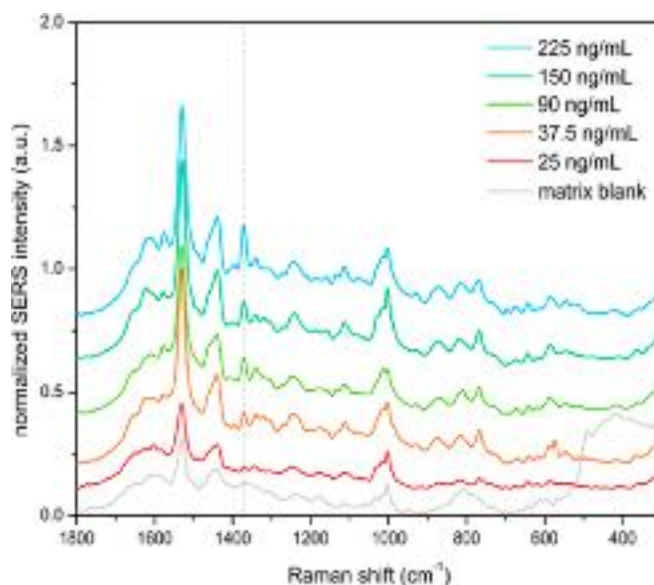


Figure 8.14: SERS spectra obtained from fortified oral fluid extracts at different initial concentration of JWH-018. The SERS spectrum of the matrix blank is reported in gray. The vertical dotted line marks the drugs reference band at 1370 cm^{-1} assigned to the $\nu(\text{C}=\text{C})$ of the naphthalene moiety.

to compute the LOD for JWH-018 in fortified oral fluid extracts, by setting the y value to three times the standard deviation of the matrix blank. This parameter was calculated analogously to the 3σ for the method blank, that is, by using the SERS intensity in the spectral range from 1368 to 1374 cm^{-1} of three different matrix blank measurements (Table 8.12). The resulting LOD for the target drug in oral fluid is 31 ng/mL .

Table 8.12: Analytical figures of merit for fortified oral fluid samples.

LOD in fortified oral fluid	31 ng/mL ($7.7 \times 10^8\text{ M}$)
σ_{noise} matrix blank ($1368\text{--}1374\text{ cm}^{-1}$)	0.04 a.u.
recovery	64.4%

As a proof of concept, fortified oral fluid extracts were also analyzed using portable instrumentation. An overview of the obtained spectral profile is reported in *Appendix*

G. The marker band at 1370 cm^{-1} was observed in all extracts above a concentration of 37.5 ng/mL , and it was used as an internal normalizing band. The secondary marker band at 674 cm^{-1} was clearly visible at concentrations above 180 ng/mL , while it appeared convoluted into a shoulder as the drug concentration decreased. This was caused by the presence of spurious bands in the regions $1700\text{--}1400\text{ cm}^{-1}$ and $1000\text{--}700\text{ cm}^{-1}$, which heavily affected the spectral profile at lower drug concentrations. This effect was attributed to the fully automated focus and exposure time of the portable instrument. We anticipate that manual control of the focus, exposure time, and number of accumulations would yield spectral profiles that are comparable to those obtained with the benchtop instrumentation.

The recovery of the extraction procedure was estimated at 64.4% using the calibration curve in the right panel of *Figure 8.13*. The loss of the remaining 35.6% of the drug could be attributed to one or more factors, namely, breakthrough of μ -SPE cartridge, partial solubility of the drug in the washing solution, or matrix effects that alter the SERS response. The investigation of these factors is outside the scope of the present paper and will be the object of future work by the McCord group.

Summary

This work demonstrates for the first time the detection of synthetic cannabinoid JWH-018 in oral fluid using surface-enhanced Raman spectroscopy. Unlike standard current immuno-based procedures, SERS allows for the acquisition of a molecular fingerprint of the detected compound. As such, it is better suited to address the analytical challenges associated with the detection of emerging psychoactive substances, as well as to complement molecular confirmatory techniques such as mass spectrometry. Moreover, when compared to immunoassay-based protocols, the discussed SERS approach is significantly faster, accounting for 36 min of total analysis time (from sample preparation to spectral acquisition) as opposed to the 120 min reported for ELISA methods designed

for the same analyte.⁷⁴ For a detailed breakdown of the temporal requirements of each μ -SPE/SERS protocol step, the reader is referred to *Appendix G*.

An in-depth vibrational study of the analyte in the solid state and in solution was performed using traditional Raman spectroscopy supported by theoretical data obtained using density functional theory. These results fill a void in the literature, as no such study had been published on this compound.

The adsorption of the drug on the citrate-capped gold nanospheres used as SERS substrate was also investigated, and it was found to follow a Langmuir behavior. This adsorption model was used to derive quantitative thermodynamic parameters that describe the affinity of the drug for the gold nanoparticle substrate (K_{ad} , $9.3 \times 10^6 \pm 1.2 \text{ M}^{-1}$; ΔG , $-39.2 \pm 2.9 \text{ kJ/mol}$), which were found to be of the same order of magnitude of known strong gold adsorbers, such as thiol- and thione-containing molecules.¹⁰³ The LOD for JWH-018 as a standard solution was calculated using the low concentration limit of the Langmuir equation and was 0.8 ng/mL, which is equivalent to $2 \times 10^{-9} \text{ M}$. This LOD is of the same order of magnitude as those found in current immunoassays for synthetic cannabinoids in oral fluid, including JWH-018.⁷⁴

The implemented analytical protocol was applied to JWH-018 fortified oral fluid extracts, after prior protein crashing and cleanup via commercially available miniaturized C_{18} SPE cartridges. This allowed for the detection of the drug at concentrations commonly found in oral fluid when the effects of the substance are present,⁹⁷ with an LOD of 31 ng/mL. For this reason, we believe the presented protocol could be useful in emergency room settings that require quick detection of JWH-018 and other synthetic cannabinoids. Indeed, the detection of a variety of synthetic cannabinoids, both as standard solutions and as fortified urine samples, has been already demonstrated by the McCord group using the same type of SERS enhancing substrate and aggregation approach.⁷⁹

The application of the developed extraction and SERS detection protocol was also replicated using a portable Raman instrumentation. Despite the presence of spectral interferences due to the presence of spurious bands, the drug was detectable in fortified oral fluid samples at a concentration of 37.5 ng/mL.

8.3.2 Other synthetic cannabinoids

This section presents the extension of the characterization method developed for JWH-018 to other synthetic cannabinoids: JWH-081, JWH-175, JWH-250, RCS-4, XLR-11, and ADB-PINACA (Figure 8.15).

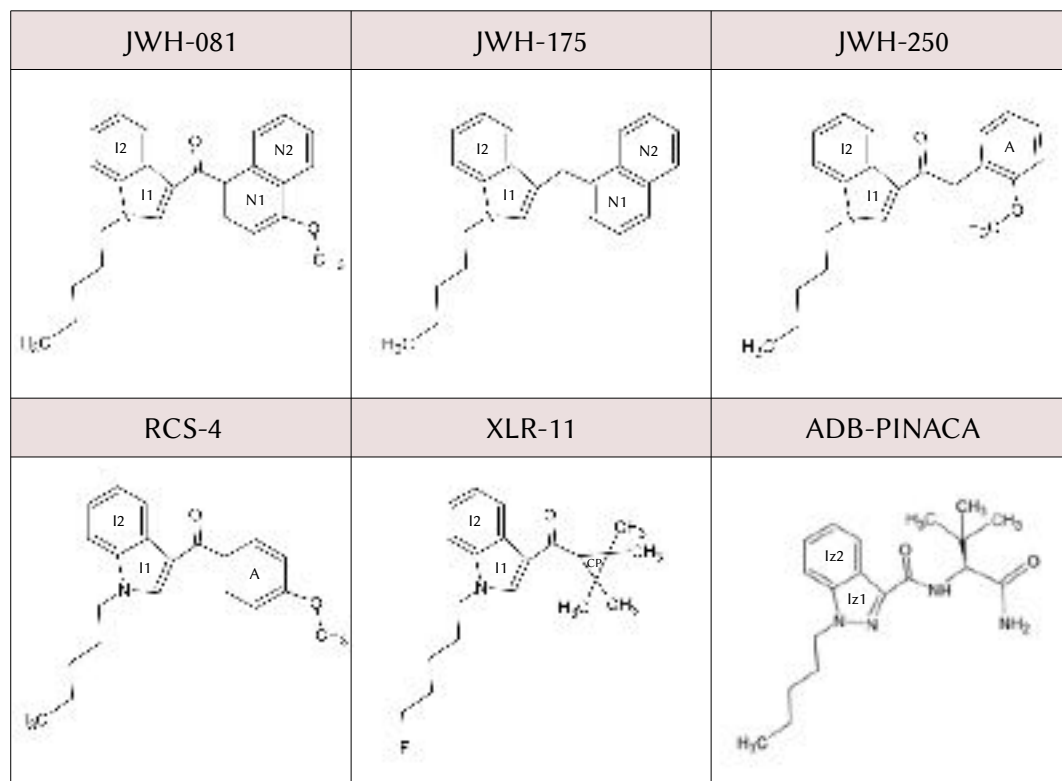


Figure 8.15: Molecular structures of the selected synthetic cannabinoids.

First, the complete vibrational and adsorption study of JWH-081 is discussed; this SCB is highly similar to JWH-018, as it only differs by a methoxy group on the naphthalene ring. This small structural difference offered a platform on which to evaluate the impact of the molecular structure on the SERS intensity, and thus, on the sensitivity of the analytical method across this class of NPS.

Besides JWH-081, the other selected SCBs were also vibrationally characterized, and their experimental spectra were compared to those obtained by DFT calculations, utilizing the same method applied for JWH-018. As mentioned in earlier parts of this chapter, DFT calculations offer a valuable tool to obtain Raman spectra when traditional reference standards are not available; this situation can be particularly common when studying NPS, as new analogs are introduced into the market at a faster pace than the ability of laboratories and companies to make these compounds available for purchase as standards. The potential for the use of the method developed for JWH-018 in the generation of an *in silico* library of SCB Raman spectra was therefore investigated.

This work was supported by Award #2015-IJ-CX-K006 of the National Institute of Justice, Office of Justice Programs, U.S. Department of Justice. Points of view in the document are those of the authors and do not necessarily represent the official view of the U.S. Department of Justice.

8.3.2.1 Complete vibrational and adsorption study of JWH-081

Geometry

The geometry of JWH-081 was optimized prior to the calculation of the Raman frequencies. The lack of negative predicted Raman frequencies shows the geometry corresponds to a true energy minimum. The general structure of JWH-081 is given in *Figure 8.15*, along with other SCBs, while the energy minimized structure is shown in *Figure 8.16*. Like JWH-018 (reported in *Figure 8.10*), JWH-081 is of C_1 point group symmetry, with the

core group, linker, and linked group laying on three different planes. Comparing JWH-018 and JWH-081's optimized geometries, it is possible to observe that the naphthalene group is oriented in opposite ways. In the first, the naphthalene ring is projecting out and down the plane described by the indole, while in the latter it is projecting out and up the plane described by the indole. Finally, the methoxy group in JWH-081 lies with both the oxygen and carbon atoms on the plane described by the naphthalene group.

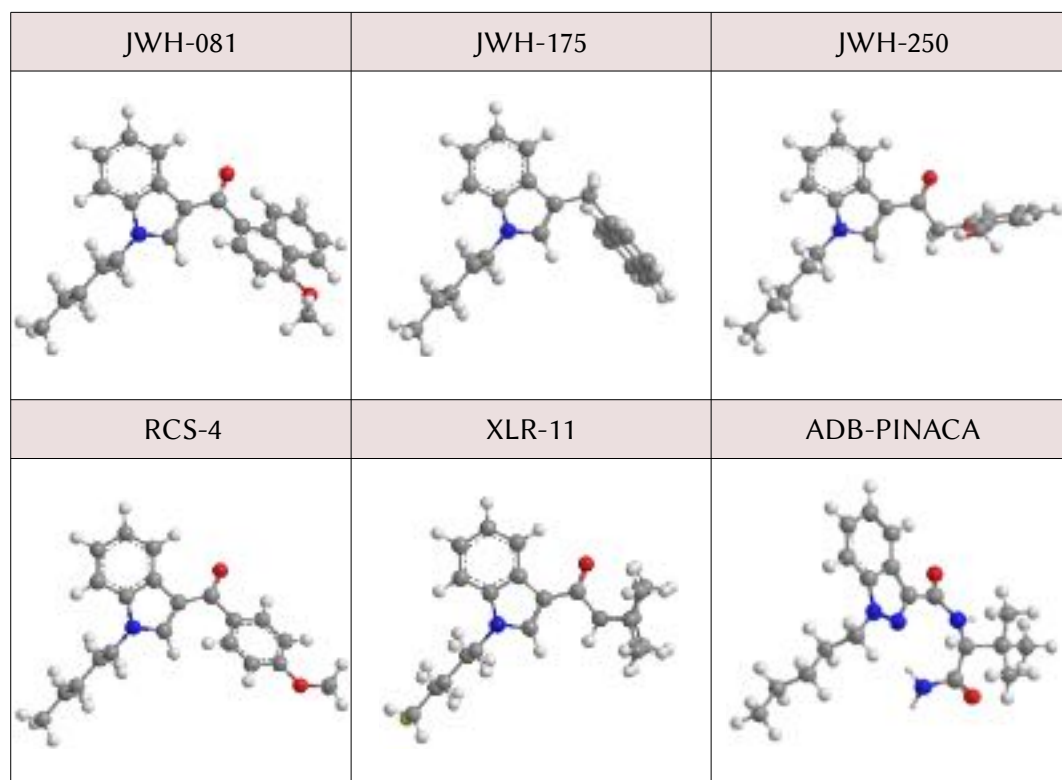


Figure 8.16: Molecular structures of the selected synthetic cannabinoids.

DFT-simulated Raman spectrum: quality of the prediction

Since the structural differences between JWH-018 and JWH-081 are minimal, the scaling factor calculated for JWH-018 in § 8.3.1 ($\lambda 0.9779$)¹⁰⁹ was hypothesized to be adequate for the scaling of JWH-081's simulated spectrum, as well as for the scaling of the spectra of

other molecules from the same class (*vide infra*, § 8.3.2.2). The DFT Raman frequencies of JWH-081 were therefore scaled by a factor λ of 0.9779. The resulting scaled DFT-simulated Raman spectrum of JWH-081 is in the left panel of *Figure 8.17*, together with the experimental normal Raman spectrum of solid state JWH-081.

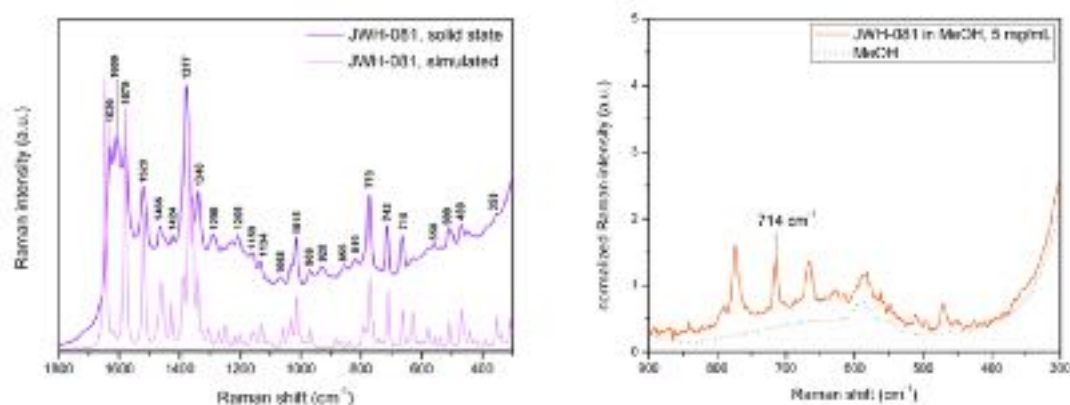


Figure 8.17: (*left*) DFT (*bottom*) and Raman (*top*) spectra of JWH-081. (*right*) Normal Raman spectrum of JWH-081 in methanolic solution. The dotted grey line is the spectrum of the solvent, obtained in the same experimental conditions.

The level of agreement with the experimental frequencies obtained in a normal Raman setting was quantified via the absolute and percent error for each scaled theoretical-experimental frequency pair (*Table 8.13*). The latter never exceeds 3.1%, and the former is generally in the order of few wavenumbers. Exceptions are a small number of bands at 1290, 896, 855, and 819 cm^{-1} , which have absolute errors of 16, 14, 15, and 25 cm^{-1} , respectively. This notwithstanding, the predicted frequencies are in very good agreement with the experimental ones, confirming the theoretical model used to obtain them, as well as the scaling factor used for anharmonicity adjustments, apply very well not only to the model compound JWH-018, but also to its analog JWH-081. The validity of this statement for other SCB analogs are discussed in § 8.3.2.2.

Normal Raman vs SERS spectra: comparison and assignment of vibrational modes

As done with JWH-018, the assignment of vibrational modes to the bands observed in the experimental spectra was performed on the basis of the calculated frequencies, with the aid of the intensity data where needed (*Table 8.13*). As observed for JWH-018, the most intense bands are those due to the naphthalene and indole rings. The major characteristic band for JWH-081 can be observed at 714 cm^{-1} , and it has been assigned to the ring breathing of the methoxynaphthalene group. This band has been chosen as the marker band for the compound, and its intensity has been utilized for both the calculation of the analytical enhancement factor and the study of the adsorption behavior (*vide infra*). As for the comparison between the Raman and the SERS experimental data, the band positions are essentially the same (*Figure 8.18*) and thus, physisorption of the drug to the citrate-capped gold nanoparticles is hypothesized as the substrate-analyte interaction mode.

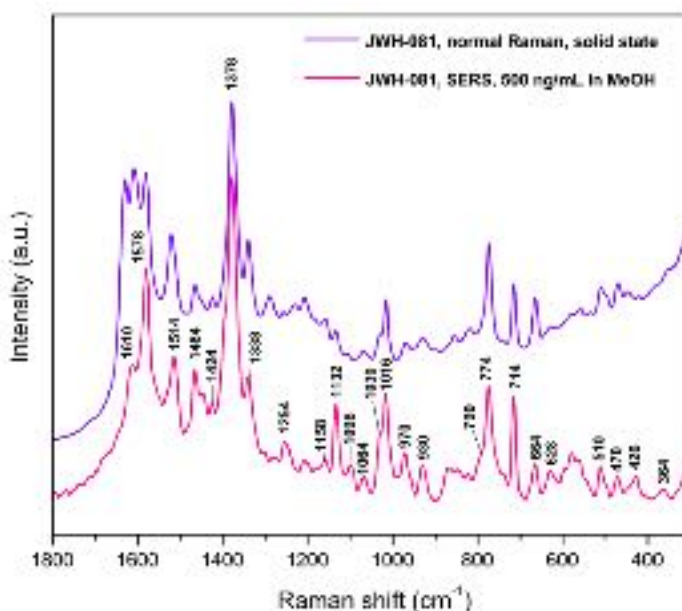


Figure 8.18: SERS (*bottom, pink*) and normal Raman (*top, purple*) spectra of JWH-081.

Table 8.13: DFT, Raman, and SERS frequencies of JWH-081, and assignment of vibrational modes.

DFT (x0.9779)	mode	assignment	normal Raman			SERS
			solid state		solution	
			(cm ⁻¹)	%error	error	(cm ⁻¹)
1647	128	$\nu(\text{C}=\text{O})$				
1621	127	$\nu(\text{C}=\text{C})$ Nph	1629	0.49	8	
1615	126	$\nu(\text{C}=\text{C})$ I2	1609	0.37	6	1610
1581	124	$\nu(\text{C}=\text{C})$ Nph	1579	0.13	2	1578
1521	122	$\nu(\text{C}=\text{C})$ CCN	1520	0.07	1	1514
1460	114, 113	$\delta_s(\text{CH}_2), \delta_s(\text{CH}_3)$ tail; $\delta_s(\text{CH}_3)$ OCH ₃	1466	0.41	6	1464 1444
1427	108	$\delta_s(\text{CH})$ Nph	1424	0.21	3	1424
1387	106	$\nu(\text{CN})$ tail; $\gamma_t(\text{CH}_2)$ NCH ₂				
1368	102	$\gamma_w(\text{CH}_2)$	1377	0.65	9	1378
1356	101	$\nu(\text{C}=\text{C})$ Ind; $\delta(\text{CH})$ Ind				
1340	100	$\nu(\text{C}=\text{C})$ Ind; $\delta(\text{CH})$ Ind	1340	0.00	0	1338
1324	98	$\nu(\text{C}=\text{C})$ Nph				
1306	96	$\gamma_t(\text{CH}_2); \gamma_t(\text{CH}_3)$ tail	1290	1.2	16	
1270	93	$\gamma_t(\text{CH}_2); \gamma_t(\text{CH}_3)$ tail				
1248	92	$\delta(\text{CH})$ I2, N2	1257	0.72	9	1254
1219	89	$\delta(\text{CH})$ I1; $\gamma_t(\text{CH}_2), \gamma_t(\text{CH}_3)$ tail	1229	0.81	10	
1201	88	$\delta(\text{CH})$ I1, Nph; $\gamma_t(\text{CH}_2), \gamma_t(\text{CH}_3)$ tail	1205	0.33	4	
1184	86	$\gamma_t(\text{CH}_3)$ OCH ₃ ; $\delta(\text{CH})$ I1, Nph				
1162	84	$\gamma_w(\text{CH}_3)$ OCH ₃ ; $\delta(\text{CH})$ Nph	1159	0.26	3	1158
1152	82	$\delta(\text{CH})$ Nph, I2; $\gamma_t(\text{CH}_3)$ OCH ₃				
1128	79	$\delta(\text{CH})$ I2	1134	0.53	6	1132
1110	78	$\delta_s(\text{CCC})$ tail; $\gamma_w(\text{CH}_2), \gamma_w(\text{CH}_3)$ tail	1106	0.36	4	1098
1059	75	$\delta(\text{ring})$ Ind	1068	0.84	9	1064
1042	74	$\nu(\text{CC})$ tail				
1031	73	$\beta(\text{ring})$ N2	1030	0.10	1	1030 sh
1012	71	$\beta(\text{ring})$ I2; $\nu(\text{CC})$ tail	1015	0.30	3	1016
968	66	$\beta(\text{ring})$ N1; $\nu(\text{COC})$ N1-OCH ₃	969	0.10	1	970
930	63	$\gamma(\text{CH})$ N1	928	0.22	2	930
882	61	$\gamma_w(\text{CH}_3)$ tail	896	1.6	14	
870	60	$\gamma(\text{CH})$ N2				
840	58	$\gamma(\text{CH})$ Ind	855	1.8	15	
794	54	$\delta(\text{ring})$ Nph	819	3.1	25	790 sh
774	52	$\gamma(\text{CH})$ Ind, Nph	773	0.13	1	774
762	49	$\delta_r(\text{CH}_2) \delta_r(\text{CH}_3)$ tail; $\delta(\text{ring})$ Ind				
743	47	$\delta_r(\text{CH}_2) \delta_r(\text{CH}_3)$ tail; $\gamma(\text{CH})$ I2	743	0	0	
711	44	$\beta(\text{ring})$ Nph	715	0.56	4	714
663	43	$\gamma(\text{CH})$ Nph	664	0.15	1	664
628	41	$\gamma(\text{CH})$ Ind, Nph	629	0.16	1	628
580	38	$\delta(\text{ring})$ Nph	581	0.17	1	
559	36	$\delta(\text{ring})$ Nph	558	0.18	1	
540	35	$\delta(\text{ring})$ Ind	535	0.93	5	
508	34	$\delta(\text{ring})$ Ind, Nph	509	0.20	1	510
468	32	$\delta(\text{ring})$ Nph	469	0.21	1	470
440	30	skeletal vibrations	448	1.8	8	
420	28	$\gamma(\text{ring})$ Nph	419	0.24	1	426
389	27	skeletal vibrations	388	0.26	1	
352	26	skeletal vibrations	353	0.28	1	364

vs, very strong; *s*, strong; *m*, medium; *w*, weak; *vw*, very weak; ν , stretching; δ , in plane deformation (*s*, scissoring; *r*, rocking); γ , out of plane deformation (*w*, wagging; *t*, twisting); β , breathing. Structural nomenclature and abbreviation is reported in Figure 8.15.

Analytical Enhancement Factor (AEF) calculation

The normal Raman spectrum of the drug in methanolic solution (5.0 mg/mL) was also acquired (*Figure 8.17, right*). As observed for JWH-018, in the range between 1700 and 900 cm^{-1} the spectrum is dominated by the solvent.¹⁰⁹ At lower wavenumbers, weak JWH-081 bands can be observed due to the absence of interferences from methanol. No significant differences in terms of band position are present, compared to the spectrum of the drug in the solid state.

The intensity of the marker band at 714 cm^{-1} in the Raman and SERS experiments was used to calculate the analytical enhancement factor (AEF), according to the definition given by LeRu and Etchegoin, as discussed in previous sections of this dissertation.¹⁰⁸ The calculated AEF for JWH-081 is 5.2×10^4 . This value is half an order of magnitude lower than the one calculated for JWH-018 in the same experimental conditions (1.3×10^4).¹⁰⁹ As a consequence, the LOD for this compound is expected to be higher than that calculated for JWH-018 in the same conditions.

Adsorption isotherm study and analytical figures of merit

Following the same approach adopted for the study of JWH-018, an adsorption isotherm at room temperature was obtained for JWH-081, by plotting the intensity of the marker band (714 cm^{-1} , ring breathing of the methoxynaphthalene group) against lowering concentration. The resulting curve (*Figure 8.19*) was fitted to the Langmuir equation, as reported for JWH-018 (§ 8.3.1) The extrapolated K_{ad} is $1.9 \times 10^7 \pm 1.4 \text{ M}^{-1}$ (*Table 8.14*), which is comparable to the K_{ad} obtained for JWH-018, $9.3 \times 10^6 \pm 1.2 \text{ M}^{-1}$.

The analytical figures of merit were studied by taking advantage of the low surface coverage limit of the Langmuir equation, as done for JWH-018.¹⁰⁹ Therefore, the $[\text{JWH-081}]_{\text{LOD}}$ was calculated by utilizing *Equation 8.6* and setting I_i equal to three times the standard deviation of a blank.¹⁰⁹ The latter was calculated using the spectral range from 710

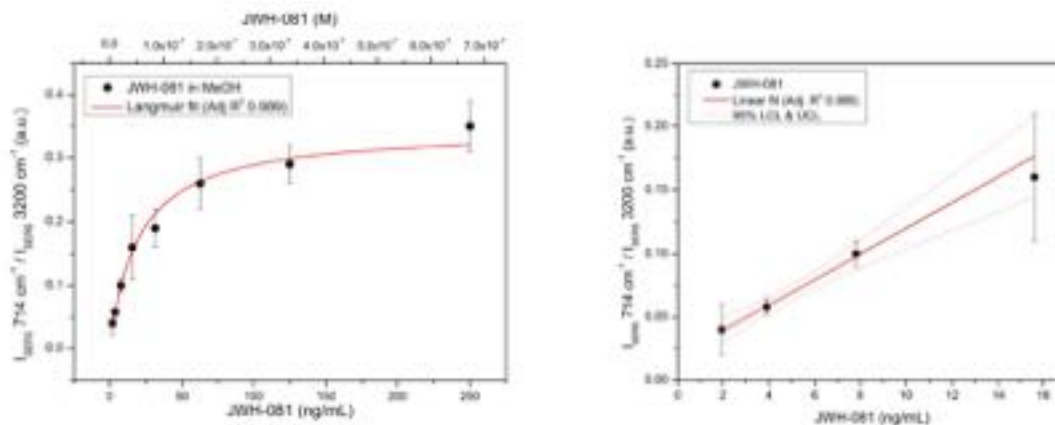


Figure 8.19: (*left*) Adsorption isotherm of JWH-081 on citrate-capped gold nanospheres. The red line represents the Langmuir fitting (adjusted R^2 0.989). (*right*) Linear portion of the adsorption isotherm of JWH-081 on citrate-capped gold nanospheres. The linear fit is described by the following equation: $y = 0.0101 \pm 0.0007x + 0.019 \pm 0.004$ (adjusted R^2 0.986).

to 718 cm^{-1} of three different method blank measurements, and the resulting LOD was 12 ng/mL ($3.16 \times 10^{-8} \text{ M}$). This value, although still fit-to-purpose for toxicological analyses, is about an order of magnitude higher than the one calculated for JWH-018 (0.8 ng/mL, $2 \times 10^{-8} \text{ M}$). This could be related to a difference in orientation to the surface between the two analytes, which would result in a closer contact for JWH-018. As discussed in multiple chapters of this dissertation, a closer contact between the analyte and the surface in SERS translates to higher enhancements,² and thus, ultimately, to lower LOD values.

Because in this case the analyte-surface complex is probably just the result of a physisorption, as no significant shift in band position was observed for either of the two SCBs, then, there must be a population of differently oriented molecules at the surface, rather than a fixed orientation; indeed, physisorptive interactions have a non-directional character, compared to chemisorption, and less ordered adsorbate layers are formed on the surface. This notwithstanding, it could be hypothesized that the prevalent surface orientation involves adsorption via the naphthalene ring in both compounds, JWH-018

and JWH-081, as aromatic moieties of this type are known to have affinity for gold.^{105,106} Among all possible random orientations that the two molecules can attain while having their naphthalene ring in contact with the surface, there are some that result in different analyte-surface distances depending on the compound. In particular, in a number of these random, naphthalene-involving orientations to the surface of JWH-081, the methoxy group on the naphthalene ring would act as a spacer, thus increasing the distance between the whole molecule and the surface. This was hypothesized as the cause of the higher LOD of JWH-081, compared to JWH-018. A summary of all analytical figures of merit calculated for JWH-081 is given in *Table 8.14*.

Table 8.14: Figures of Merit JWH-081.

LOD	12 ng/mL (3.16×10^{-8} M)
LOQ	39 ng/mL (1.1×10^{-7} M)
dynamic range	2.0–16 ng/mL
limit of linearity	16 ng/mL (5.0×10^{-8} M)
σ_{noise} method blank (710–718 cm ⁻¹)	0.07 a.u.
sensitivity (slope of calibration curve)	0.0101 ± 0.0007
standard error of calibration curve	0.2 ng/mL

8.3.2.2 Towards an *in silico* Raman library for synthetic cannabinoids

As previously explained, DFT-calculated Raman frequencies are systematically higher than the experimental values as a result of the assumption that molecules behave as perfect harmonic oscillators. Scaling factors (λ) can be therefore calculated to adjust for this overestimate.⁶⁰ It would be time consuming if this procedure had to be repeated for each studied compound belonging to the same chemical class; rather, it can be more convenient to explore whether the scaling factor calculated on the basis of a model compound (*i.e.*, JWH-018) could be successfully applied to correct the simulated spectra of other molecules belonging to the same class (*i.e.*, SCBs).

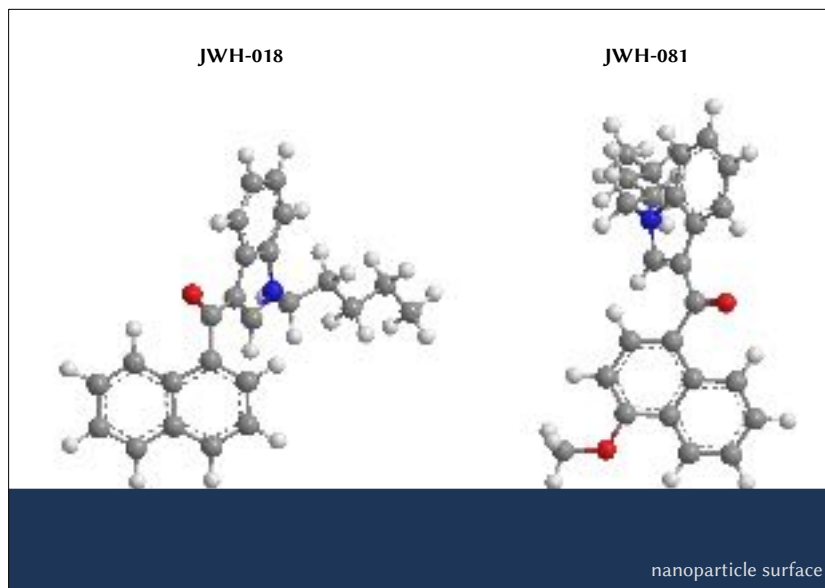


Figure 8.20: Hypothesized prevalent orientations to the surface for JWH-018 and JWH-081.

The simulated spectra of JWH-175, JWH-250, RCS-4, and XLR-11, and ADB-PINACA were obtained as already described for JWH-081, and are reported together with their respective experimental Raman spectra in *Figures 8.21 to 8.25*. These compounds were chosen on the basis of their structural differences (*Figure 8.15*), so that they could also be used in the future to investigate the relationship between structure, orientation to the surface, and LOD (§ 8.3.2.1).

The DFT Raman frequencies of all SCBs under study were scaled by the same factor λ of 0.9779, which was obtained on the basis of JWH-018's experimental-theoretical pairs (§ 8.3.1). As with the previously studied SCBs JWH-018 and JWH-081, the level of agreement between the predicted and experimental frequencies was assessed via the absolute and percent error metrics (*Table 8.15* and *Tables 8.16 to 8.20*). The compound which exhibited the largest maximum percent error was JWH-175 (6.5%, band at 1580 cm^{-1} assigned to the aromatic stretching of the naphthalene group), followed by XLR-11 (5.1%,

band at 996 cm⁻¹ assigned to the $\gamma_r(\text{CH}_3)$ of the cyclopropyl ring), ADB-PINACA (4.8%, band at 372 cm⁻¹ assigned to the $\delta(\text{C}_I\text{C}_{IV}\text{C}_I)$ of the t-But group and $\delta(\text{ring})$ of indazole), JWH-250 (2.4%, band at 650 cm⁻¹ assigned to the $\gamma_r(\text{CH}_2)$ of the CH₂ linked to the anisole ring and to the $\gamma(\text{CH})$ of the indole ring), and RCS-4 (1.6%, band at 434 cm⁻¹). However, the average percent error was 0.70% for JWH-175, 1.0% for XLR-11, 1.1% for ADB-PINACA, 2.4% for JWH-250, and 0.46% for RCS-4, highlighting excellent agreement between predicted and experimental data (Table 8.15), independently of how much the compounds depart from the prototypical JWH-018 structure. This makes the computational method and the scaling factor appropriate for these compounds, and possibly appropriate for the class of synthetic cannabinoids at large.

Table 8.15: Percent errors between experimental Raman and DFT-predicted frequencies.

compound	class	subclass	maximum %error	average %error
JWH-018	indole	naphthoylindole	1.6%	0.47%
JWH-081	indole	naphthoylindole	3.1%	0.53%
JWH-175	indole	naphthylmethylindole	6.5%	0.70%
JWH-250	indole	phenylacetylindole	2.4%	2.4%
RCS-4	indole	benzoylindole	1.6%	0.46%
XLR-11	indole	tetramethylcyclopropylindole	5.1%	1.0%
ADB-PINACA	indazole	indazolamide	4.8%	1.1%

Vibrational modes assignments of the experimental Raman bands of SCBs JWH-175, JWH-250, RCS-4, XLR-11, and ADB-PINACA were obtained as described for JWH-018 and JWH-081, and are reported in Tables 8.16 to 8.20.

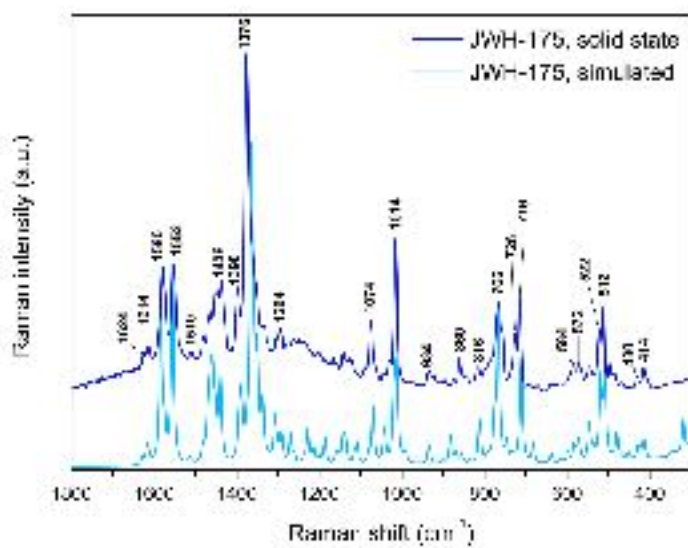


Figure 8.21: Normal Raman (*top*) and DFT-simulated (B3LYP/6-311G**, *bottom*) spectra of JWH-175.

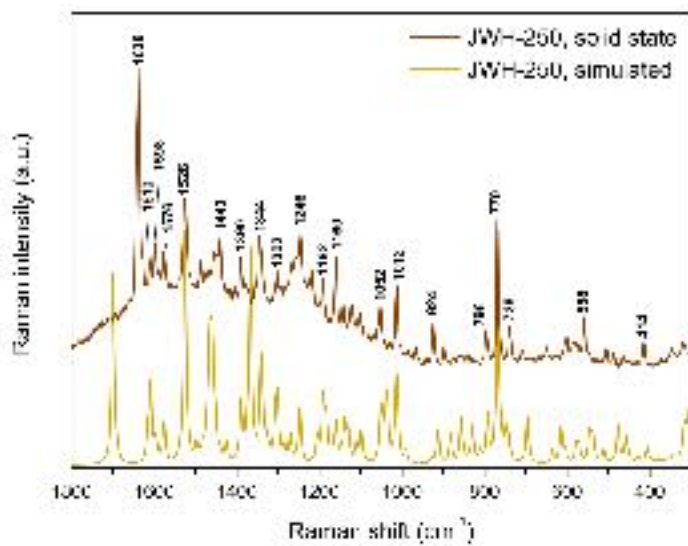


Figure 8.22: Normal Raman (*top*) and DFT-simulated (B3LYP/6-311G**, *bottom*) spectra of JWH-250.

Table 8.16: DFT and Raman bands of JWH-175, and normal modes assignment.

DFT (x 0.9779)	Mode	Assignment	Normal Raman		
			solid state		
			cm ⁻¹	%error	error (cm ⁻¹)
1625	119	$\nu(\text{C}=\text{C})$ Nph	1624	0.06	1
1616	118	$\nu(\text{C}=\text{C})$ I2	1614	0.12	2
1483	116	$\nu(\text{C}=\text{C})$ Nph	1580	6.5	97
1552	114	$\nu(\text{C}=\text{C})$ I1	1552	0	0
1514	113	$\nu(\text{C}=\text{C})$ Nph	1510	0.26	4
1482	112, 111	$\delta_s(\text{CH}_2)$, $\delta_s(\text{CH}_3)$ tail; $\delta(\text{CH})$ I2	1480	0.13	2
1460	106	$\delta(\text{CH})$ Nph; $\delta_s(\text{CH}_2)$ linker; $\delta_s(\text{CH}_2)$, $\delta_s(\text{CH}_3)$ tail	1464	0.27	4
			1452		
1440	102	$\delta(\text{CH})$ Nph; $\delta_s(\text{CH}_2)$ linker	1436	0.28	4
1389	100	$\nu(\text{CCNC})$ Ind-tail; $\gamma_t(\text{CH}_2)$ NCH ₂	1398	0.65	9
1364	96	$\nu(\text{C}=\text{C})$ Nph; $\gamma_t(\text{CH}_2)$ linker	1376	0.88	12
1349	93	$\nu(\text{C}=\text{C})$ Nph	1352	0.22	3
1337	92	$\nu(\text{C}=\text{C})$ Nph; $\gamma_t(\text{CH}_2)$ NCH ₂	1336	0.07	1
1304	90	$\gamma_t(\text{CH}_2)$ tail	1306	0.15	2
1294	88	$\delta_r(\text{CH})$ Nph; $\gamma_t(\text{CH}_2)$ linker	1294	0	0
1269	87	$\gamma_t(\text{CH}_2)$ tail	1260	0.71	9
1228	83	$\gamma_t(\text{CH}_2)$ tail; $\delta(\text{CH})$ I2	1202	2.1	26
1185	79	$\gamma_t(\text{CH}_2)$ linker; $\delta(\text{CH})$ Nph	1168	1.4	17
1156	76, 77	$\delta(\text{CH})$ I2, Nph	1156	0	0
1141	75	$\delta(\text{CH})$ Nph	1142	0.09	1
1081	71	$\delta(\text{CH})$ I2, N1; $\gamma_t(\text{CH}_2)$ tail; $\gamma_w(\text{CH}_2)$ linker	1088	0.65	7
1070	70	$\delta(\text{CH})$ Nph; $\gamma_t(\text{CH}_2)$ tail; $\delta(\text{ring})$ Ind	1074	0.37	4
1043	69	$\nu(\text{CC})$ tail	1046	0.29	3
1013	65	$\delta(\text{ring})$ I2	1014	0.10	1
933	57	$\delta_r(\text{CH}_2)$ linker	934	0.11	1
903	55	$\gamma(\text{CH})$ N2	898		
870	53	$\gamma(\text{CH})$ Nph	874	0.46	4
856	52	$\gamma(\text{CH})$ Nph	860	0.47	4
837	51	$\gamma_t(\text{CH}_2)$, $\gamma_t(\text{CH}_3)$ tail	842	0.60	5
811	49	$\gamma(\text{CH})$ Nph, I1	816	0.62	5
767	44	$\beta(\text{ring})$ Ind; $\gamma_t(\text{CH}_2)$ NCH ₂ tail; $\delta_r(\text{CH}_2)$, $\delta_r(\text{CH}_3)$ tail	766	0.13	1
746	42	$\delta_r(\text{CH}_2)$, $\delta_r(\text{CH}_3)$ tail	756	1.3	10
730	40	$\gamma(\text{CH})$ Nph	726	0.55	4
711	38	$\beta(\text{ring})$ N2	716	0.70	5
682	37	$\nu(\text{CN})$ NCH ₂ tail; $\gamma(\text{CH})$ Nph; $\gamma(\text{CCC})$ Nph-CH ₂ linker	672	1.5	10
639	36	$\nu(\text{CN})$ NCH ₂ tail; $\gamma(\text{CH})$ Nph; $\delta(\text{ring})$ Ind	640	0.16	1
613	35				
597	34				
582	33	$\gamma(\text{ring})$ Ind; $\delta(\text{ring})$ N2	584	0.34	2
571	32	$\gamma(\text{ring})$ Ind	572	0.18	1
545	31	$\delta(\text{ring})$ I2	544	0.18	1
518	29	$\delta(\text{ring})$ Ind	522	0.77	4
509	28	$\delta(\text{ring})$ Ind, Nph; $\delta_r(\text{CH}_2)$ linker	512	0.59	3
479	27	$\delta(\text{ring})$ Ind, Nph	484	1.0	5
451	25	$\delta_s(\text{CCC})$ tail;	468	3.8	17
427	24	$\delta_r(\text{CH}_2)$ linker; $\delta(\text{ring})$ Nph	430	0.70	3
412	22	$\gamma(\text{ring})$ Nph	414	0.49	2

ν s, very strong; s , strong; m , medium; w , weak; νw , very weak; ν , stretching; δ , in plane deformation (s , scissoring; r , rocking); γ , out of plane deformation (w , wagging; t , twisting); β , breathing; *Nph*, naphthalene ring; *Ind*, indole ring. Structural nomenclature and abbreviation is reported in Figure 8.15.

Table 8.17: DFT and Raman bands of JWH-250, and normal modes assignment.

DFT (x 0.9779)	Mode	Assignment	Normal Raman		
			solid state		
			cm ⁻¹	%error	error (cm ⁻¹)
1700	119	$\nu(\text{C}=\text{O})$	1638		
1610	117	$\nu(\text{C}=\text{C})$ A	1610	0	0
1596	116	$\nu(\text{C}=\text{C})$ A	1598	0.13	2
			1588		
1576	115	$\nu(\text{C}=\text{C})$ I2	1576	0	0
1525	114	$\nu(\text{C}=\text{C})$ I1	1526	0.07	1
1496	113	$\delta_r(\text{CH})$ A; $\delta_s(\text{CH}_3)$ OCH ₃	1486	0.67	10
1464	107	$\delta_s(\text{CH}_2)$, $\delta_s(\text{CH}_3)$ tail	1454	0.68	10
1460	106	$\delta(\text{CH})$ A; $\gamma_w(\text{CH}_3)$ OCH ₃	1440	1.4	20
1424	100	$\delta_s(\text{CH}_2)$ A-CH ₂	1406	1.3	18
1389	99	$\nu(\text{CCNC})$ Ind-tail; $\gamma_t(\text{CH}_2)$ NCH ₂	1390	0.07	1
1367					
1340	94	$\nu(\text{C}=\text{C})$ I1; $\delta(\text{CH})$ I2	1344	0.30	4
1301	89	$\gamma_t(\text{CH}_2)$ tail	1302	0.08	1
1286					
1270					
1246	85	$\gamma_w(\text{CH})$ A; $\delta(\text{CH})$ I2; $\nu(\text{CO})$ OCH ₃	1246	0	0
1205					
			1218		
1191	81	$\gamma_t(\text{CH}_2)$, $\gamma_t(\text{CH}_3)$ tail; $\nu(\text{CC})$ A-CH ₂ ; $\delta(\text{CH})$ A	1192	0.08	1
1160	77, 76	$\delta(\text{CH})$ Ind, A	1160	0	0
1137	74	$\delta(\text{CH})$ Ind	1142	0.44	5
1122	72	$\delta(\text{CH})$ A	1122	0.00	0
1097					
1050	69	$\delta(\text{CH})$ A	1052	0.19	2
1037					
1012	65	$\beta(\text{ring})$ Ind; $\delta(\text{CH})$ A	1012	0	0
990					
960	61	$\gamma_t(\text{CH}_2)$, $\gamma_t(\text{CH}_3)$ tail	966	0.63	6
911	56	$\delta(\text{ring})$ Ind; $\nu(\text{CC})$ O=C-CH ₂	924	1.43	13
882	55	$\gamma_t(\text{CH}_3)$ tail; $\nu(\text{CC})$ tail	898	1.81	16
			872		
856	54	$\gamma(\text{CH})$ A	858	0.23	2
828	51	$\gamma(\text{CH})$ A	840	1.4	12
810	50	$\gamma(\text{CH})$ NCH	822	1.5	12
792	49	$\gamma(\text{CH})$ A; $\delta(\text{ring})$ I2	796	0.51	4
768	48	$\beta(\text{ring})$ Ind	770	0.26	2
749	45	$\beta(\text{ring})$ A; $\delta_r(\text{CH}_2)$; $\gamma(\text{CH})$ A	738	1.5	11
695	40	$\gamma(\text{ring})$ A	708	1.9	13
635	39	$\gamma_t(\text{CH}_2)$ A-CH ₂ ; $\gamma(\text{CH})$ Ind	650	2.4	15
614	38	$\delta(\text{ring})$ A, Ind	600	2.3	14
573	35	$\delta(\text{ring})$ A, Ind	584	1.9	11
545	34	$\gamma(\text{ring})$ A	558	2.4	13
511	31	skeletal vibrations	504	1.4	7
476	30	$\delta_r(\text{CH}_2)$ A-CH ₂	486	2.1	10
457	29	skeletal vibrations	464	1.5	7
427	27	$\gamma(\text{ring})$ Ind	432	1.2	5
406	26	$\delta_s(\text{CCC})$ tail	414	2.0	8

ν , very strong; s , strong; m , medium; w , weak; vw , very weak; ν , stretching; δ , in plane deformation (s , scissoring; r , rocking); γ , out of plane deformation (w , wagging; t , twisting); β , breathing; Nph , naphthalene ring; Ind , indole ring. Structural nomenclature and abbreviation is reported in Figure 8.15.

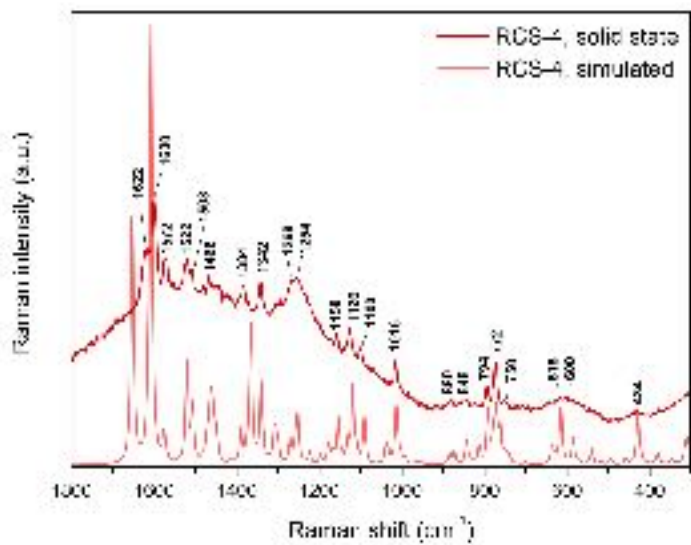


Figure 8.23: Normal Raman (*top*) and DFT-simulated (B3LYP/6-311G**, *bottom*) spectra of RCS-4.

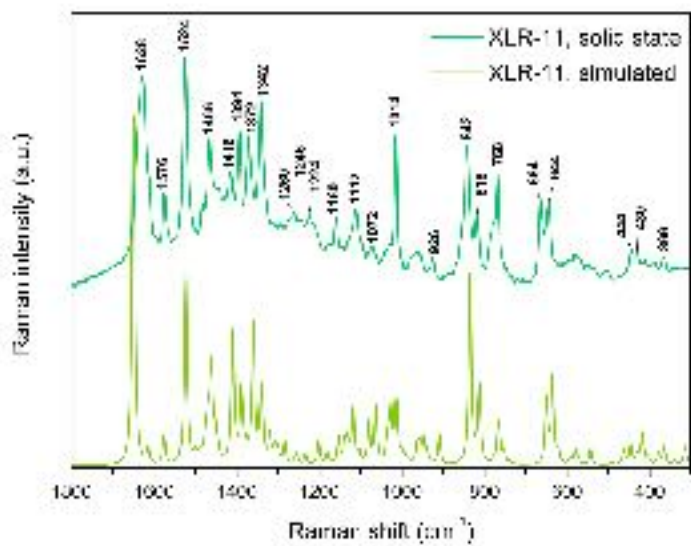


Figure 8.24: Normal Raman (*top*) and DFT-simulated (B3LYP/6-311G**, *bottom*) spectra of XLR-11.

Table 8.18: DFT and Raman bands of RCS-4, and normal modes assignment.

DFT (x 0.9779)	Mode	Assignment	Normal Raman		
			solid state		
			cm ⁻¹	%error	error (cm ⁻¹)
1653	112	$\nu(\text{C}=\text{O})$	1622		
1608	110	$\nu(\text{C}=\text{C})$ A	1600	0.50	8
1576	109	$\nu(\text{C}=\text{C})$ I2	1572	0.25	4
1521	107	$\nu(\text{C}=\text{C})$ I1	1522	0.07	1
1506	106	$\delta(\text{CH})$ A	1508	0.13	2
1460	99	$\delta_s(\text{CH}_3)$ OCH ₃	1466	0.41	6
1389	93	$\gamma_t(\text{CH})\text{textsubscript2}$ NCH ₂ ; $\delta(\text{CH})$ A, Ind	1384	0.36	5
1366					
1340	88	$\delta(\text{CH})$ Ind; $\nu(\text{C}=\text{C})$ Ind	1342	0.15	2
1308	85	$\nu(\text{C}=\text{C})$ A	1296	0.92	12
1270	81	$\gamma_t(\text{CH}_2)$, $\gamma_t(\text{CH}_3)$ tail; $\delta(\text{CH})$ I2	1268	0.16	2
1252	79	$\gamma_t(\text{CH}_2)$, $\gamma_t(\text{CH}_3)$ tail; $\delta(\text{CH})$ I2	1254	0.16	2
1223					
1197					
1178					
1154	72	$\delta(\text{CH})$ A, I2	1158	0.35	4
1119	69	$\delta(\text{CH})$ I2	1126	0.63	7
1090	66	$\gamma_t(\text{CH}_2)$, $\gamma_t(\text{CH}_3)$ tail	1100	0.92	10
1038					
1013	62	$\delta(\text{ring})$ I2	1016	0.30	3
993					
884	53	$\gamma_w(\text{CH}_2)$, $\gamma_w(\text{CH}_3)$ tail	880	0.45	4
872					
848	51	$\gamma(\text{CH})$ I2	848	0	0
813					
791	46	$\delta(\text{ring})$ A	794	0.38	3
772	44	$\beta(\text{ring})$ Ind	772	0	0
761	43	$\beta(\text{ring})$ Ind; $\delta_r(\text{CH}_2)$, $\delta_r(\text{CH}_3)$ tail	750	1.4	11
743					
699					
636	37		640	0.63	4
614	35		616	0.33	2
			600		
584					
540					
517					
494					
458					
427	26		434	1.6	7
380					
346					
308					

vs, very strong; *s*, strong; *m*, medium; *w*, weak; *vw*, very weak; ν , stretching; δ , in plane deformation (*s*, scissoring; *r*, rocking); γ , out of plane deformation (*w*, wagging; *t*, twisting); β , breathing; *Nph*, naphthalene ring; *Ind*, indole ring. Structural nomenclature and abbreviation is reported in Figure 8.15.

Table 8.19: DFT and Raman bands of XLR-11, and normal modes assignment.

DFT (x 0.9779)	Mode	Assignment	Normal Raman		
			solid state		
			cm ⁻¹	%error	error (cm ⁻¹)
1650	122	$\nu(\text{C}=\text{O})$	1628	1.3	22
1615	121	$\nu(\text{C}=\text{C})$ I2	1594	1.3	21
1576	120	$\nu(\text{C}=\text{C})$ I2	1576	0	0
1523	119	$\nu(\text{C}=\text{C})$ I1	1524	0.07	1
1499	118	$\delta_s(\text{CH}_3)$ cP	1482	1.1	17
1461	110	$\gamma_r(\text{CH}_3)$ cP	1466	0.34	5
1450	105	$\delta_s(\text{CH}_2)$ tail; $\delta(\text{CH})$ I2	1442	0.55	8
1410	103	$\delta(\text{CH})$ cP	1416	0.43	6
1388	100	$\gamma_t(\text{CH}_2)$ NCH ₂ ; $\nu(\text{CCNC})$ Ind-tail	1394	0.43	6
1359	94	$\nu(\text{C}=\text{C})$ I1; $\gamma_t(\text{CH}_2)$ NCH ₂	1372	0.96	13
1340	92	$\nu(\text{C}=\text{C})$ Ind; $\gamma_t(\text{CH}_2)$ NCH ₂ ; $\delta(\text{CH})$ cP	1342	0.15	2
1319					
1307					
1283	87	$\gamma_t(\text{CH}_2)$ tail; $\delta(\text{CH})$ I2	1260	1.8	23
1254	85	$\gamma_t(\text{CH}_2)$ tail; $\delta(\text{CH})$ I2	1246	0.64	8
1234	84	$\gamma_t(\text{CH}_2)$ tail	1224	0.81	10
1201					
1180	81	$\delta(\text{ring})$ cP; $\gamma_w(\text{CH}_3)$ cP	1160	1.7	20
1153					
1132	76	$\delta(\text{CH})$ I2; $\delta_r(\text{CH}_2)$ tail	1126	0.53	6
1118	75	$\delta_r(\text{CH}_3)$ cP	1112	0.54	6
1102	73	$\gamma_t(\text{CH}_2)$ NCH ₂ ; $\delta(\text{CH})$ I2	1094	0.73	8
1080	72	$\nu(\text{CC})$ tail	1072	0.74	8
1063					
1025	67	$\gamma_t(\text{CH}_3)$ cP; $\nu(\text{CF})$	1030	0.49	5
1013	66	$\delta(\text{ring})$ I2	1014	0.10	1
964	61	$\gamma_t(\text{CH}_3)$ cP	980	1.7	16
948	58	$\gamma_t(\text{CH}_3)$ cP	996	5.1	48
939	57	$\gamma_t(\text{CH}_3)$ cP	954	1.6	15
909	55	$\delta(\text{ring})$ cP	926	1.9	17
834	52	$\nu(\text{CC})$ O=C-cP; $\delta(\text{ring})$ cP; $\delta_r(\text{CH}_2)$ tail	842	0.96	8
813	50	$\delta(\text{ring})$ Ind; $\delta_r(\text{CH}_2)$ tail	818	0.62	5
766	48	$\beta(\text{ring})$ Ind; $\delta_r(\text{CH}_2)$ tail	768	0.26	2
650	42	$\delta(\text{ring})$ cP	664	2.2	14
635	41	$\delta(\text{ring})$ cP	644	1.4	9
593	39	$\beta(\text{ring})$ Ind; $\gamma_w(\text{CH})$ Nph	596	0.51	3
580	38	$\delta(\text{ring})$ Ind	582	0.34	2
543					
463					
446	33	$\delta_s(\text{CCC})$ tail; $\delta_s(\text{CCN})$ I1-tail;	444	0.45	2
430	32	$\gamma(\text{ring})$ cP	430	0	0
417	30	$\gamma_w(\text{CCC})$ cP-CH ₃	412	1.2	5
404					
378	28	$\delta_s(\text{CCC})$ H ₃ C-C-CH ₃ cP	390	3.2	12
363	27	$\delta_s(\text{CCCC})$ H ₃ C-C-C-CH ₃ cP	366	0.83	3

ν s, very strong; s , strong; m , medium; w , weak; νw , very weak; ν , stretching; δ , in plane deformation (s , scissoring; r , rocking); γ , out of plane deformation (w , wagging; t , twisting); β , breathing; Nph , naphthalene ring; Ind , indole ring. Structural nomenclature and abbreviation is reported in Figure 8.15.

Table 8.20: DFT and Raman bands of ADB-PINACA, and normal modes assignment.

DFT (x 0.9779)	Mode	Assignment	Normal Raman		
			solid state		
			cm ⁻¹	%error	error (cm ⁻¹)
1734	125	$\nu(\text{C=O})_{\text{linker}}$	1698	2.1	36
1680	124	$\nu(\text{C=O})_{\text{linker}}$	1646	2.0	34
1619	123	$\nu(\text{C=C})$ Iz2	1618	0.05	1
1603	122	$\delta_s(\text{NH}_2)_{\text{linker}}$	1574	1.9	29
1576	121	$\nu(\text{C=C})$ Iz2	1532	2.9	44
1494	119	$\delta_s(\text{CH}_3)$ <i>t</i> -But	1490	0.27	4
1479	116	$\nu(\text{C=C})$ Iz	1470	0.60	9
1458	109	$\delta_s(\text{CH}_2)$ tail	1442	1.1	16
1420	105	$\delta_s(\text{CH})$ Iz2; $\nu(\text{C-C=O})_{\text{linker}}$	1422	0.12	2
1404	104	$\nu(\text{CNNC})$ Iz1	1408	0.26	4
1373	100	$\gamma_w(\text{CH}_2)$ tail	1378	0.34	5
1355	95	$\nu(\text{C=C})$ Iz	1358	0.19	3
1319	93	$\gamma_t(\text{CH}_2)$ tail	1324	0.39	5
1308	91	$\gamma_t(\text{CH}_2)$ tail	1306	0.12	2
1290	89	$\delta_s(\text{CH})$ Iz2; $\gamma_t(\text{CH}_2)$ tail; $\nu(\text{CN})_{\text{linker}}$	1278	1.0	12
1264	87	$\delta_s(\text{CH})$ Iz2; $\gamma_t(\text{CH}_2)$ tail; $\delta(\text{CH})$ <i>t</i> -But			
1238	85	$\nu(\text{C}_{\text{III}}-\text{C}_{\text{IV}})$ <i>t</i> -But	1234	0.33	4
1230	84	$\gamma_t(\text{CH}_2)$ tail; $\gamma_t(\text{CH}_3)$ tail			
1214	83	$\nu(\text{C}_{\text{IV}}\text{C}_1)$ <i>t</i> -But	1218	0.35	4
1188	81	$\delta_r(\text{NH}_2)_{\text{linker}}$; $\delta_r(\text{CH})$ <i>t</i> -But; $\delta_r(\text{CH}_3)$ <i>t</i> -But; $\delta_r(\text{CH}_2)$ tail; $\delta_r(\text{CH}_3)$ tail	1188	0	0
1164	80	$\delta(\text{HCCH})$ Iz2	1164	0	0
1124	78	$\delta(\text{HCCH})$ Iz2; $\nu(\text{C}_{\text{linker}}-\text{N}_{\text{linker}})$	1128	0.31	4
1108	76	$\delta_r(\text{CH}_3)$ tail; $\nu_s(\text{CCC})$ tail	1104	0.33	4
1097	75	$\gamma_t(\text{CH}_3)$ <i>t</i> -But; $\gamma_t(\text{CH}_3)$ tail; $\delta(\text{HCCH})$ Iz2	1080	1.6	17
1074	74	$\gamma_t(\text{CH}_2)$ tail; $\gamma_t(\text{CH}_3)$ tail; $\nu(\text{NN})$ Iz1	1072	0.17	2
1043	73	$\nu_{\text{as}}(\text{CCC})$ tail	1034	0.84	9
1023	71	$\gamma_t(\text{CH}_3)$ <i>t</i> -But	1026	0.29	3
1006	69	$\nu(\text{C=C})$ Iz2	1006	0	0
953	64	$\nu(\text{C}_{\text{III}}\text{C}_{\text{IV}})$ <i>t</i> -But; $\gamma_t(\text{CH}_3)$ <i>t</i> -But	972	1.9	19
912	60	$\nu(\text{C}_{\text{IV}}\text{C}_1)$ <i>t</i> -But; $\gamma_t(\text{CH}_3)$ <i>t</i> -But	936	2.5	24
884	59	$\nu_{\text{as}}(\text{CCC})$ tail; $\gamma_t(\text{CH}_3)$ tail	912	3.1	28
858	58	$\nu(\text{C}_{\text{III}}\text{C}_{\text{IV}}\text{C}_1)$ <i>t</i> -But; $\delta_r(\text{NH}_2)_{\text{linker}}$	866	1.0	8
836	56	$\delta_r(\text{CH}_2)$ tail; $\delta_r(\text{CH}_3)$ tail	848	1.4	12
			824		
			810		
784	53	$\gamma(\text{CH})$ Iz2; $\delta(\text{ring})$ Iz1	788	0.46	4
767	51	$\delta(\text{ring})$ Iz; $\delta_r(\text{CH}_2)$ tail; $\gamma_t(\text{CH}_3)$ tail; $\nu(\text{C}_{\text{III}}\text{C}_{\text{IV}}\text{C}_1)$ <i>t</i> -But; $\gamma_t(\text{NH}_2)_{\text{linker}}$	776	1.1	9
639	44	$\gamma(\text{NH})_{\text{linker}}$; $\gamma_t(\text{NH}_2)_{\text{linker}}$	664	3.8	25
627	43	$\gamma_t(\text{NH}_2)_{\text{linker}}$; $\delta(\text{NC=O})_{\text{linker}}$; $\delta(\text{ring})$ Iz	630	0.44	3
614	42	$\gamma(\text{NH})_{\text{linker}}$; $\gamma_t(\text{NH}_2)_{\text{linker}}$; $\delta(\text{CCC})$ Iz2	610	0.62	4
598	41	$\gamma(\text{NH})_{\text{linker}}$; $\gamma_t(\text{NH}_2)_{\text{linker}}$; $\delta(\text{CCC})$ Iz2	596	0.34	2
580	40	$\gamma(\text{NH})_{\text{linker}}$; $\gamma_t(\text{NH}_2)_{\text{linker}}$; $\delta(\text{CCC})$ Iz	572	1.3	8
542	38	$\delta(\text{ring})$ Iz; $\delta_r(\text{CH}_2)$ NCH ₂ tail	542	0	0
488	36	$\gamma_w(\text{NH}_2)_{\text{linker}}$; $\delta(\text{CCCC})$ <i>t</i> -But	478	2.0	10
420	32	$\delta(\text{C}_1\text{C}_{\text{IV}}\text{C}_1)$ <i>t</i> -But; $\delta(\text{ring})$ Iz	406	3.4	14
390	30	$\delta(\text{C}_1\text{C}_{\text{IV}}\text{C}_1)$ <i>t</i> -But; $\delta(\text{ring})$ Iz	372	4.8	18
333	28	$\gamma(\text{C}_1\text{C}_{\text{IV}}\text{C}_1)$ <i>t</i> -But; $\delta(\text{C}_{\text{sp}2}\text{C}_{\text{III}}\text{C}_{\text{IV}})$	334	0.28	1

ν_s , very strong; s , strong; m , medium; w , weak; ν_w , very weak; ν , stretching; δ , in plane deformation (s , scissoring; r , rocking); γ , out of plane deformation (w , wagging; t , twisting); β , breathing; Iz , indazole ring. Roman numerals are used to indicate the primary, tertiary, and quaternary carbons in HC-*t*-But substituent within the linked group. Structural nomenclature and abbreviation is reported in Figure 8.15.

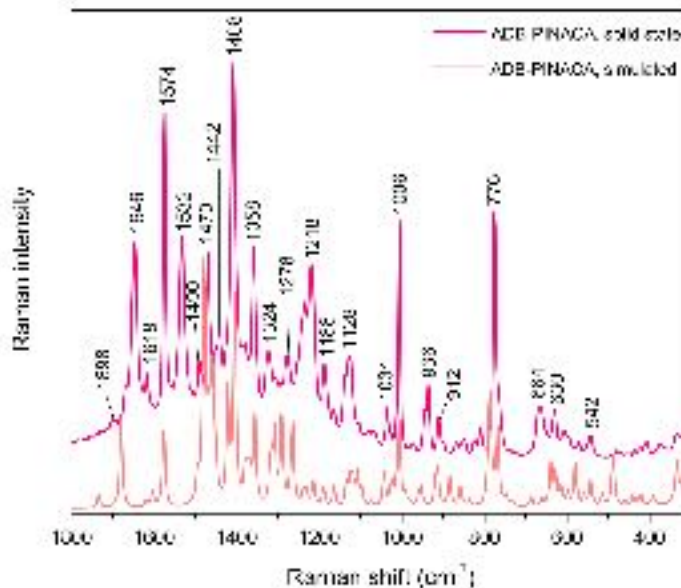


Figure 8.25: Normal Raman (*top*) and DFT-simulated (B3LYP/6-311G**, *bottom*) spectra of ADB-PINACA.

8.3.2.3 Summary and Prospects

In-depth vibrational studies of synthetic cannabinoids JWH-081, JWH-175, JWH-250, RCS-4, XLR-11, and ADB-PINACA in the solid state were performed using traditional Raman spectroscopy supported by theoretical data obtained by DFT, following the protocol established for JWH-018 (§ 8.3.1). The chosen computational method (B3LYP/6-311G**) proved to be excellent at predicting the Raman spectra of these compounds, with a percent error on the predicted frequencies consistently and significantly below 10%. This holds true not only for indole-bearing synthetic cannabinoids, which are the same sub-class as JWH-018, but also for indazole-based ones (*i.e.*, ADB-PINACA). This is particularly important when considering the trends in usage reported by the DEA for the present year

(2020), as indazole-bearing synthetic cannabinoids, with structures close to ADB-PINACA (e.g., 5F-MDMB-PINACA), are consistently identified.¹¹⁰

The results obtained thus far utilizing the proposed computational approach show high potential for the *in silico* building of a Raman database for synthetic cannabinoids. This is extremely important for the identification of novel psychoactive substances, both in the solid state and in toxicological samples. As a result of the rapidity at which new analogs are developed and introduced into the market, research on NPS is often dependent on, and thus slowed down by, the lengthy processes that are necessary to produce commercially available analytical standards. *In silico*-generated data can aid in the expansion of existing traditional spectral databases, when reference materials are not available for purchase, and thus, assist in the process of keeping analytical laboratories and spectral libraries up to date with current drug usage trends. In addition, *in silico*-generated libraries are inherently less expensive, and thus, ultimately more accessible. This implies that the benefits of considering DFT as an alternative to traditional spectral library building can not only assist analytical laboratories in a prompt identification of unknown substances, but also aid harm reduction and local emergency response organizations that offer drug testing services. These organizations are typically less funded, and the low costs and rapid turnaround of *in silico* libraries can make their work more impactful.

REFERENCES

- [1] Fikiel, M.A.; Khandasammy, S.R.; Mistek, E.; Ahmed, Y.; Halmkov, L.; Bueno, J.; Lednev, I.K. Surface Enhanced Raman Spectroscopy: A Review of Recent Applications in Forensic Science. *Spectrochim. Acta - Part A Mol. Biomol. Spectrosc.*, **2018**, *197*, 255–260.
- [2] Le Ru, E.C.; Etchegoin, P.G. *Principles of surface enhanced Raman spectroscopy and related plasmonic effects*, Elsevier: Amsterdam, 2009.
- [3] Society of Forensic Toxicologists Inc.; American Academy of Forensic Sciences. *Forensic Toxicology Laboratory Guidelines*. 2006.
- [4] Scientific Working Group for the Analysis of Seized Drugs (SWGDRUG). *Recommendations*. 2016.
- [5] Lad, A.N.; Pandya, A.; Agrawal, Y.K. Overview of Nano-Enabled Screening of Drug-Facilitated Crime: A Promising Tool in Forensic Investigation. *TrAC Trends Anal. Chem.*, **2016**, *80*, 458–470.
- [6] Aroca, R. *Surface-Enhanced Vibrational Spectroscopy*, John Wiley & Sons, Ltd: Chichester, UK, 2006.
- [7] Fairchild, S.Z.; Bradshaw, C.F.; Su, W.; Guharay, S.K. Predicting Raman Spectra Using Density Functional Theory. *Appl. Spectrosc.*, **2009**, *63*(7), 733–741.
- [8] Doctor, E.L.; McCord, B. The Application of Supported Liquid Extraction in the Analysis of Benzodiazepines Using Surface Enhanced Raman Spectroscopy. *Talanta*, **2015**, *144*, 938–943.
- [9] Farquharson, S.; Shende, C.; Inscore, F.E.; Maksymiuk, P.; Gift, A. Analysis of 5-Fluorouracil in Saliva Using Surface-Enhanced Raman Spectroscopy. *J. Raman Spectrosc.*, **2005**, *36*(3), 208–212.
- [10] Inscore, F.; Shende, C.; Sengupta, A.; Huang, H.; Farquharson, S. Detection of Drugs of Abuse in Saliva by Surface-Enhanced Raman Spectroscopy (SERS). *Appl. Spectrosc.*, **2011**, *65*(9), 1004–1008.
- [11] Nuntawong, N.; Eiamchai, P.; Somrang, W.; Denchitcharoen, S.; Limwichean, S.; Horprathum, M.; Patthanasettakul, V.; Chaiya, S.; Leelapojanaporn, A.; Saiseng, S.; Pongsethasant, P.; Chindaudom, P. Detection of Methamphetamine/Amphetamine

in Human Urine Based on Surface-Enhanced Raman Spectroscopy and Acidulation Treatments. *Sens. Actuators, B*, **2017**, *239*, 139–146.

- [12] Subaihi, A.; Almanqur, L.; Muhamadali, H.; AlMasoud, N.; Ellis, D.I.; Trivedi, D.K.; Hollywood, K.A.; Xu, Y.; Goodacre, R. Rapid, Accurate, and Quantitative Detection of Propranolol in Multiple Human Biofluids via Surface-Enhanced Raman Scattering. *Anal. Chem.*, **2016**, *88*(22), 10884–10892.
- [13] Itoh, T.; Biju, V.; Ishikawa, M. Surface-enhanced resonance Raman scattering and background light emission coupled with plasmon of single Ag nanoaggregates. *J. Chem. Phys.*, **2006**, *124*, 134708-1–134708-6.
- [14] Barnett, S.M.; Harris, N.; Baumberg, J.J. Molecules in the mirror: how SERS backgrounds arise from the quantum method of images. *Phys. Chem. Chem. Phys.*, **2014**, *16*, 6544–6549.
- [15] Ali, E.M.A.; Edwards, H.G.M.; Cox, R. Forensic and Security Applications of a Long-Wavelength Dispersive Raman System. *J. Raman Spectrosc.*, **2015**, *46*(3), 322–326.
- [16] Hidi, I.J.; Jahn, M.; Weber, K.; Bocklitz, T.; Pletz, M.W.; Cialla-May, D.; Popp, J. Lab-on-a-Chip-Surface Enhanced Raman Scattering Combined with the Standard Addition Method: Toward the Quantification of Nitroxoline in Spiked Human Urine Samples. *Anal. Chem.*, **2016**, *88*(18), 9173–9180.
- [17] Yüksel, S.; Schwenke, A.M.; Soliveri, G.; Ardizzone, S.; Weber, K.; Cialla-May, D.; Hoepfner, S.; Schubert, U.S.; Popp, J. Trace Detection of Tetrahydrocannabinol (THC) with a SERS-Based Capillary Platform Prepared by the in Situ Microwave Synthesis of AgNPs. *Anal. Chim. Acta*, **2016**, *939*, 93–100.
- [18] Kline, N.D.; Tripathi, A.; Mirsafavi, R.; Pardoe, I.; Moskovits, M.; Meinhart, C.; Guicheteau, J.A.; Christesen, S.D.; Fountain, A.W. Optimization of Surface-Enhanced Raman Spectroscopy Conditions for Implementation into a Microfluidic Device for Drug Detection. *Anal. Chem.*, **2016**, *88*(21), 10513–10522.
- [19] Andreou, C.; Hoonejani, M.R.; Barmi, M.R.; Moskovits, M.; Meinhart, C.D. Rapid Detection of Drugs of Abuse in Saliva Using Surface Enhanced Raman Spectroscopy and Microfluidics. *ACS Nano*, **2013**, *7*(8), 7157–7164.
- [20] Moody, A. S.; Sharma, B. Multi-Metal, Multi-Wavelength Surface-Enhanced Raman Spectroscopy Detection of Neurotransmitters. *ACS Chem. Neurosci.*, **2018**, *9*(6), 1380–1387.

- [21] Jurasekova, Z.; García-Ramos, J.V.; Domingo, C.; Sánchez-Cortés, S. Surface-Enhanced Raman Scattering of Flavonoids. *J. Raman Spectrosc.*, **2006**, *37*(11), 1239–1241.
- [22] Muehlethaler, C.; Leona, M.; Lombardi, J.R. Towards a Validation of Surface-Enhanced Raman Scattering (SERS) for Use in Forensic Science: Repeatability and Reproducibility Experiments. *Forensic Sci. Int.*, **2016**, *268*, 1–13.
- [23] Goodacre, R.; Graham, D.; Faulds, K. Recent Developments in Quantitative SERS: Moving towards Absolute Quantification. *TrAC Trends Anal. Chem.*, **2018**, *102*, 359–368.
- [24] Moskovits, M.; Suh, J. S. Surface Selection Rules for Surface-Enhanced Raman Spectroscopy: Calculations and Application to the Surface-Enhanced Raman Spectrum of Phthalazine on Silver. *J. Phys. Chem.*, **1984**, *88*(23), 5526–5530.
- [25] Izquierdo-Lorenzo, I.; Sánchez-Cortés, S.; García-Ramos, J. V. Adsorption of Beta-Adrenergic Agonists Used in Sport Doping on Metal Nanoparticles: A Detection Study Based on Surface-Enhanced Raman Scattering. *Langmuir* 2010, *26* (18), 14663-14670.
- [26] Subaihi, A.; Muhamadali, H.; Mutter, S.T.; Blanch, E.; Ellis, D.I.; Goodacre, R. Quantitative Detection of Codeine in Human Plasma Using Surface-Enhanced Raman Scattering via Adaptation of the Isotopic Labelling Principle. *Analyst*, **2017**, *142*(7), 1099–1105.
- [27] Izquierdo-Lorenzo, I.; García-Ramos, J.V.; Sánchez-Cortés, S. Vibrational Characterization and Surface-Enhanced Raman Scattering Detection of Probenecid Doping Drug. *J. Raman Spectrosc.*, **2013**, *44*(10), 1422–1427.
- [28] Procházka, M.; Mojzeš, P.; Vlčková, B.; Turpin, P-Y. Surface-Enhanced Resonance Raman Scattering from Copper(II) 5,10,15,20-Tetrakis(1-Methyl-4-Pyridyl)Porphyrin Adsorbed on Aggregated and Nonaggregated Silver Colloids. *J. Phys. Chem. B*, **1997**, *101*(16), 3161–3167.
- [29] Teng, Y.J.; Liu, W.H.; Liu, J.M.; Nie, Y.H.; Li, P.; He, C.J. Surface-Enhanced Raman Scattering Sensing of Trace Fenthion Coupled with Stable Silver Colloids and OH Stretching Band of Water as an Internal Standard. *J. Anal. Chem.*, **2016**, *71*(9), 891–895.
- [30] Triplett, J.S.; Hatfield, J. .; Kaeff, T.L.; Ramsey, C.R.; Robinson, S.D.; Standifer, A.F. Raman Spectroscopy as a Simple, Rapid, Nondestructive Screening Test for

- Methamphetamine in Clandestine Laboratory Liquids. *J. Forensic Sci.*, **2013**, 58(6), 1607–1614.
- [31] Trachta, G.; Schwarze, B.; Sägmüller, B.; Brehm, G.; Schneider, S. Combination of High-Performance Liquid Chromatography and SERS Detection Applied to the Analysis of Drugs in Human Blood and Urine. *J. Mol. Struct.*, **2004**, 693(1–3), 175–185.
- [32] Ma, Y.; Liu, H.; Mao, M.; Meng, J.; Yang, L.; Liu, J. Surface-Enhanced Raman Spectroscopy on Liquid Interfacial Nanoparticle Arrays for Multiplex Detecting Drugs in Urine. *Anal. Chem.*, **2016**, 88(16), 8145–8151.
- [33] Yang, T.; Guo, X.; Wang, H.; Fu, S.; wen, Y.; Yang, H. Magnetically Optimized SERS Assay for Rapid Detection of Trace Drug-Related Biomarkers in Saliva and Fingerprints. *Biosens. Bioelectron.*, **2015**, 68, 350–357.
- [34] Miller, J. N.; Miller, J. C. *Statistics and Chemometrics for Analytical Chemistry*, fifth edition; Pearson/Prentice Hall, 2005.
- [35] Dies, H.; Raveendran, J.; Escobedo, C.; Docoslis, A. Rapid Identification and Quantification of Illicit Drugs on Nanodendritic Surface-Enhanced Raman Scattering Substrates. *Sens. Actuators B*, **2018**, 257, 382–388.
- [36] Schneider, K. J.; DeCaprio, A. P. Covalent Thiol Adducts Arising from Reactive Intermediates of Cocaine Biotransformation. *Chem. Res. Toxicol.*, **2013**, 26(11), 1755–1764.
- [37] Gilliland, R. A.; Möller, C.; DeCaprio, A. P. LC-MS/MS Based Detection and Characterization of Covalent Glutathione Modifications Formed by Reactive Drug of Abuse Metabolites. *Xenobiotica*, **2018**, 1–13.
- [38] Wang, L.; Deriu, C.; Wu, W.; Mebel, A.M.; McCord, B. Surface-enhanced Raman spectroscopy, Raman, and density functional theoretical analyses of fentanyl and six analogs. *J. Raman Spectrosc.*, **2019**, 50, 1405–1415.
- [39] Kerrigan, S.; Goldberger, B.A. Opioids. In *Principles of Forensic Toxicology*; Levine, B., Ed.; AACCC Press: Washington DC, 2010.
- [40] Centers for Disease Control and Prevention (CDC). *Understanding the Epidemic*; <https://www.cdc.gov/drugoverdose/epidemic/index.html> (accessed April 16, 2020).

- [41] Drug Enforcement Administration (DEA). *DEA Issues Nationwide Alert On Fentanyl As Threat To Health And Public Safety*; <https://www.dea.gov/press-releases/2015/03/18/dea-issues-nationwide-alert-fentanyl-threat-health-and-public-safety> (accessed February 11, 2020).
- [42] Scholl, L.; Seth, P.; Kariisa, M.; Wilson, N.; Baldwin, G. Drug and Opioid-Involved Overdose Deaths United States, 2013-2017. *MMWR. Morb. Mortal. Wkly. Rep.*, **2018**, *67*(5152), 1419–1427.
- [43] Wilson, N.; Kariisa, M.; Seth, P.; Smith, H.; Davis, N.L. Drug and Opioid-Involved Overdose Deaths United States, 2017-2018. *MMWR. Morb. Mortal. Wkly. Rep.*, **2020**, *69*(11), 290–297.
- [44] United Nations Office on Drugs and Crime. *Global Synthetic Drugs Assessment*, Vienna, Austria, 2017.
- [45] National Institute on Drug Abuse (NIDA). *Fentanyl*; <https://www.drugabuse.gov/drugs-abuse/fentanyl> (accessed November 2, 2020)
- [46] Lipsman, Z. *A High Potency Opioid: Carfentanil, Lethal and on the Rise*; American College of Emergency Physicians (ACEP); <https://www.acep.org/how-we-serve/sections/toxicology/news/april-2017/a-high-potency-opioid-carfentanil-lethal-and-on-the-rise/> (accessed September 20, 2020)
- [47] Tamburro, L.P.; Al-Hadidi, J.H.; Dragovic, L.J. Resurgence of Fentanyl as a Drug of Abuse. *Forensic Sci. Med.*, **2016**, *2*(2), 111–114.
- [48] A. Poklis, Fentanyl: a review for clinical and analytical toxicologists. *J. Toxicol., Clin. Toxicol.*, **1995**, *33*, 439–447.
- [49] Lovrecic, B.; Lovrecic, M.; Gabrovec, B.; Carli, M.; Pacini, M.; Maremmani, A.G.I.; Maremmani, I. Non-medical use of novel synthetic opioids: A new challenge to public health. *Int. J. Environ. Res. Public Health*, **2019**, *16*, 177–198.
- [50] LaRue, L.; Twillman, R.K.; Dawson, E.; Whitley, P.; Frasco, M.A.; Huskey, A.; Guevara, M.G. Rate of Fentanyl Positivity Among Urine Drug Test Results Positive for Cocaine or Methamphetamine. *JAMA Netw. Open*, **2019**, *2*, e192851–192857.
- [51] Frisch, M. J.; Trucks, G. W.; Schlegel, H. B.; Scuseria, G. E.; Robb, M. A.; Cheeseman, J. R.; Scalmani, G.; Barone, V.; Mennucci, B.; Petersson, G. A.; Nakatsuji, H.; Caricato, M.; Li, X.; Hratchian, H. P.; Izmaylov, A. F.; Bloino,

J.; Zheng, G.; Sonnenberg, J. L.; Hada, M.; Ehara, M.; Toyota, K.; Fukuda, R.; Hasegawa, J.; Ishida, M.; Nakajima, T.; Honda, Y.; Kitao, O.; Nakai, H.; Vreven, T.; Montgomery, J. A. Jr.; Peralta, J. E.; Ogliaro, F.; Bearpark, M.; Heyd, J. J.; Brothers, E.; Kudin, K. N.; Staroverov, V.N.; Keith, T.; Kobayashi, R.; Normand, J.; Raghavachari, K.; Rendell, A.; Burant, J. C.; Iyengar, S. S.; Tomasi, J.; Cossi, M.; Rega, N.; Millam, J.M.; Klene, M.; Knox, J. E.; Cross, J. B.; Bakken, V.; Adamo, C.; Jaramillo, J.; Gomperts, R.; Stratmann, R. E.; Yazyev, O.; Austin, A. ; J.Cammi, R.; Pomelli, C.; Ochterski, J. W.; Martin, R. L.; Morokuma, K.; Zakrzewski, V. G.; Voth, G. A.; Salvador, P.; Dannenberg, J. J.; Dapprich, S.; Daniels, A. D.; Farkas, O.; Foresman, J. B.; Ortiz, J. V.; Cioslowski, J.; Fox, D. J. *Gaussian 09*, Revision B.01; Gaussian, Inc.: Wallingford, CT, 2010.

- [52] Becke, A.D. Density-functional thermochemistry. III. The role of exact exchange. *J. Chem. Phys.*, **1993**, *98*(7), 5648–5652.
- [53] Lee, C.; Yang, W.;Parr, R.G. Development of the Colle-Salvetti Correlation-Energy Formula into a Functional of the Electron Density. *Phys. Rev. B.*, **1988**, *37*, 785–789.
- [54] Chai, J-D.; Head-Gordon, M. Systematic optimization of long-range corrected hybrid density functionals. *J. Chem. Phys.*, **2008**, *128*(8), 084106-1–084106-15.
- [55] Dunning, T.H. Gaussian basis sets for use in correlated molecular calculations. I. The atoms boron through neon and hydrogen. *J. Chem. Phys.*, **1989**, *90*(2), 1007–1023.
- [56] Lu, T.; Chen, F. Multiwfn: A Multifunctional Wavefunction Analyzer. *J. Comput. Chem.*, **2012**, *33*(5), 580–592.
- [57] Schaftenaar, G.; Noordik, J. H. Molden: A Pre-and Post-Processing Program for Molecular and Electronic Structures. *J. Comput.-Aided Mol. Des.*, **2000**, *14*, 123–134.
- [58] Schaftenaar, G.; Vlieg, E.; Vriend, G. Molden 2.0: Quantum Chemistry Meets Proteins. *J. Comput.-Aided Mol. Des.*, **2017**, *31*(9), 789–800.
- [59] Leonard, J.; Haddad, A.; Green, O.; Birke, R.L.; Kubic, T.; Kocak, A.; Lombardi, J.R. SERS, Raman, and DFT analyses of fentanyl and carfentanil: Toward detection of trace samples. *J. Raman Spectrosc.*, **2017**, *48*(5), 1323–1329.
- [60] Scott, A.P.; Radom, L. Harmonic Vibrational Frequencies: An Evaluation of Hartree-Fock, Miller-Plesset, Quadratic Configuration Interaction, Density Functional Theory, and Semiempirical Scale Factors. *J. Phys. Chem.*, **1996**, *100*(41), 16502–16513.

- [61] Palafox, M.A. Scaling Factors for the Prediction of the Frequencies of the Ring Modes in Benzene Derivatives. *J. Phys. Chem. A*, **1999**, *103*(51), 11366–11377.
- [62] He, S.; Kang, M.W.C.; Khan, F.J.; Tan, E.K.M.; Reyes, M.A.; Kah, J.C.Y. Optimizing gold nanostars as a colloid-based surface-enhanced Raman scattering (SERS) substrate. *J. Opt.* **2015**, *17*, 1–13.
- [63] Smith, E.; Dent, G. *Modern Raman Spectroscopy, a practical approach*, second edition, John Wiley & Sons Ltd: Chichester, 2019.
- [64] Cañamares, M.V.; García-Ramos, J.V.; Gomez-Varga, J.D.; Domingo, C.; Sánchez-Cortés, S. Comparative study of the morphology, aggregation, adherence to glass, and surface-enhanced Raman scattering activity of silver nanoparticles prepared by chemical reduction of Ag⁺ using citrate and hydroxylamine. *Langmuir*, **2005**, *21*(18),
- [65] Harrington, P.D.B.; Kister, J.; Artaud, J.; Dupuy, N. Automated Principal Component-Based Orthogonal Signal Correction Applied to Fused Near Infrared-Mid-Infrared Spectra of French Olive Oils. *Anal. Chem.*, **2009**, *81*(17), 7160–7169.
- [66] Schneir, A. B.; Cullen, J.; Ly, B. T. “Spice” Girls: Synthetic Cannabinoid Intoxication. *J. Emerg. Med.*, **2011**, *40*(3), 296–299.
- [67] Wiley, J. L.; Marusich, J. A.; Huffman, J. W. Moving around the Molecule: Relationship between Chemical Structure and in Vivo Activity of Synthetic Cannabinoids. *Life Sci.*, **2014**, *97*(1), 55–63.
- [68] Paul, A. B. M.; Simms, L.; Amini, S.; Paul, A. E. Teens and Spice: A Review of Adolescent Fatalities Associated with Synthetic Cannabinoid Use. *J. Forensic Sci.*, **2017**, *63*(4), 1321–1324.
- [69] Trecki, J.; Gerona, R. R.; Schwartz, M. D. Synthetic Cannabinoid-Related Illnesses and Deaths. *N. Engl. J. Med.*, **2015**, *373*(2), 103–107.
- [70] Labay, L.M.; Caruso, J.L.; Gilson, T.P.; Phipps, R.J.; Knight, L.D.; Lemos, N.P.; McIntyre, I.M.; Stoppacher, R.; Tormos, L.M.; Weins, A.L.; Williams, E.; Logan, B.K. Synthetic Cannabinoid Drug Use as a Cause or Contributory Cause of Death. *Forensic Sci. Int.*, **2016**, *260*, 31–39.
- [71] Kemp, A.M.; Clark, M.S.; Dobbs, T.; Galli, R.; Sherman, J.; Cox, R. Top 10 Facts You Need to Know about Synthetic Cannabinoids: Not so Nice Spice. *Am. J. Med.*, **2016**, *129*(3), 240–244.

- [72] Arntson, A.; Ofsa, B.; Lancaster, D.; Simon, J.R.; McMullin, M.; Logan, B. Validation of a Novel Immunoassay for the Detection of Synthetic Cannabinoids and Metabolites in Urine Specimens. *J. Anal. Toxicol.*, **2013**, *37*(5), 284–290.
- [73] Namera, A.; Kawamura, M.; Nakamoto, A.; Saito, T.; Nagao, M. Comprehensive Review of the Detection Methods for Synthetic Cannabinoids and Cathinones. *Forensic Toxicol.*, **2015**, *33*(2), 175–194.
- [74] Rodrigues, W.C.; Catbagan, P.; Rana, S.; Wang, G.; Moore, C. Detection of Synthetic Cannabinoids in Oral Fluid Using ELISA and LC-MS-MS. *J. Anal. Toxicol.*, **2013**, *37*(8), 526–533.
- [75] Smith, M.L. Immunoassay. In *Principles of Forensic Toxicology*; Levine, B., Ed.; AACC Press: Washington DC, 2010.
- [76] D’Elia, V.; García, G.M.; Ruiz, C.G. Spectroscopic Trends for the Determination of Illicit Drugs in Oral Fluid. *Appl. Spectrosc. Rev.*, **2015**, *50*(9), 775–796.
- [77] Ward, G.; Simpson, A.; Boscato, L.; Hickman, P.E. The Investigation of Interferences in Immunoassay. *Clin. Biochem.*, **2017**, *50*(18), 1306–1311.
- [78] Doctor, E.L.; McCord, B. Comparison of Aggregating Agents for the Surface-Enhanced Raman Analysis of Benzodiazepines. *Analyst*, *2013*, *138*(20), 5926–5932.
- [79] Mostowtt, T.; McCord, B. Surface Enhanced Raman Spectroscopy (SERS) as a Method for the Toxicological Analysis of Synthetic Cannabinoids. *Talanta*, **2017**, *164*, 396–402.
- [80] Battal, D.; Akgönüllü, S.; Yalcin, M. S.; Yavuz, H.; Denizli, A. Biosensors and Bioelectronics Molecularly Imprinted Polymer Based Quartz Crystal Microbalance Sensor System for Sensitive and Label-Free Detection of Synthetic Cannabinoids in Urine. *Biosens. Bioelectron.*, **2018**, *111*, 10–17.
- [81] Cieplak, M.; Kutner, W. Artificial Biosensors: How Can Molecular Imprinting Mimic Biorecognition? *Trends Biotechnol.*, **2016**, *34*(11), 922–941.
- [82] Drummer, O. H. Drug Testing in Oral Fluid. *Clin. Biochem. Rev.*, **2006**, *27*(3), 147–159.
- [83] Elmongy, H.; Abdel-Rehim, M. Saliva as an Alternative Specimen to Plasma for Drug Bioanalysis. A Review. *TrAC Trends Anal. Chem.*, **2016**, *83*, 70–79.

- [84] Chojnowska, S.; Baran, T.; Wilińska, I.; Sienicka, P.; Cabaj-Wiater, I.; Knaś, M. Human Saliva as a Diagnostic Material. *Adv. Med. Sci.*, **2018**, *63*(1), 185–191.
- [85] Crouch, D.J. Oral Fluid Collection: The Neglected Variable in Oral Fluid Testing. *Forensic Sci. Int.*, **2005**, *150*(2–3), 165–173.
- [86] Drummer, O.H.; Odell, M. *The Forensic Pharmacology of Drugs of Abuse*; Arnold: London, 2001.
- [87] Shende, C.; Inscore, F.; Maksymiuk, P.; Farquharson, S. Ten-Minute Analysis of Drugs and Metabolites in Saliva by Surface-Enhanced Raman Spectroscopy. In *Smart Medical and Biomedical Sensor Technology III*; Cullum, B.M., Carter, J.C., Eds.; Boston, MA, 2005; 60070S.
- [88] Inscore, F.; Shende, C.; Sengupta, A.; Huang, H.; Farquharson, S. Detection of Drugs of Abuse in Saliva by Surface-Enhanced Raman Spectroscopy (SERS). *Appl. Spectrosc.*, **2011**, *65*(9), 1004–1008.
- [89] Farquharson, S.; Shende, C.; Inscore, F.E.; Maksymiuk, P.; Gift, A. Analysis of 5-Fluorouracil in Saliva Using Surface-Enhanced Raman Spectroscopy. *J. Raman Spectrosc.*, **2005**, *36*(3), 208–212.
- [90] Farquharson, S.; Shende, C.; Sengupta, A.; Huang, H.; Inscore, F. Rapid Detection and Identification of Overdose Drugs in Saliva by Surface-Enhanced Raman Scattering Using Fused Gold Colloids. *Pharmaceutics*, **2011**, *3*(3), 425–439.
- [91] Dana, K.; Shende, C.; Huang, H.; Farquharson, S. Rapid Analysis of Cocaine in Saliva by Surface-Enhanced Raman Spectroscopy. *J. Anal. Bioanal. Tech.*, **2015**, *6*(6), 1–5.
- [92] Andreou, C.; Hoonejani, M.R.; Barmi, M.R.; Moskovits, M.; Meinhart, C.D. Rapid Detection of Drugs of Abuse in Saliva Using Surface Enhanced Raman Spectroscopy and Microfluidics. *ACS Nano*, **2013**, *7*(8), 7157–7164.
- [93] Yang, T.; Guo, X.; Wang, H.; Fu, S.; wen, Y.; Yang, H. Magnetically Optimized SERS Assay for Rapid Detection of Trace Drug-Related Biomarkers in Saliva and Fingerprints. *Biosens. Bioelectron.*, **2015**, *68*, 350–357.
- [94] Drug Enforcement Administration (DEA). *DEA Moves to Emergency Control Synthetic Marijuana*; <https://www.dea.gov/pubs/pressrel/pr112410.html> (accessed June 18, 2018).

- [95] Coulter, C.; Garnier, M.; Moore, C. Synthetic Cannabinoids in Oral Fluid. *J. Anal. Toxicol.*, **2011**, *35*(7), 424–430.
- [96] Su, M.K.; Seely, K.A.; Moran, J.H.; Hoffman, R.S. Metabolism of Classical Cannabinoids and the Synthetic Cannabinoid JWH-018. *Clin. Pharmacol. Ther.*, **2015**, *97*(6), 562–564.
- [97] Toennes, S.W.; Geraths, A.; Pogoda, W.; Paulke, A.; Wunder, C.; Theunissen, E.L.; Ramaekers, J. =G. Pharmacokinetic Properties of the Synthetic Cannabinoid JWH-018 in Oral Fluid after Inhalation. *Drug Test. Anal.*, *10*(4), **2017**, 644–650.
- [98] Cooper, Z.D.; Poklis, J.L.; Liu, F. Methodology for Controlled Administration of Smoked Synthetic Cannabinoids JWH-018 and JWH-073. *Neuropharmacology*, **2018**, *134*, 92–100.
- [99] Cyrankiewicz, M.; Wybranowski, T.; Kruszewski, S. Study of SERS Efficiency of Metallic Colloidal Systems. *J. Phys. Conf. Ser.*, **2007**, *79*(1), 1–6.
- [100] Izquierdo-Lorenzo, I.; Sánchez-Cortés, S.; García-Ramos, J.V. Adsorption of Beta-Adrenergic Agonists Used in Sport Doping on Metal Nanoparticles: A Detection Study Based on Surface-Enhanced Raman Scattering. *Langmuir*, **2010**, *26*(18), 14663–14670.
- [101] Tien, C. *Adsorption Calculations and Modeling*; Butterworth-Heinemann: Newton, MA, 1994.
- [102] Liu, Y. Is the Free Energy Change of Adsorption Correctly Calculated? *J. Chem. Eng. Data*, **2009**, *54*(7), 1981–1985.
- [103] Ansar, S.M.; Haputhanthri, R.; Edmonds, B.; Liu, D.; Yu, L.; Sygula, A.; Zhang, D. Determination of the Binding Affinity, Packing, and Conformation of Thiolate and Thione Ligands on Gold Nanoparticles. *J. Phys. Chem. C*, **2011**, *115*(3), 653–660.
- [104] Pakiari, A.H.; Jamshidi, Z. Nature and Strength of MS Bonds (M = Au, Ag, and Cu) in Binary Alloy Gold Clusters. *J. Phys. Chem. A*, **2010**, *114*(34), 9212–9221.
- [105] Farkas, J.; Nizzetto, L.; Thomas, K.V. Science of the Total Environment The Binding of Phenanthrene to Engineered Silver and Gold Nanoparticles. *Sci. Total Environ.*, **2012**, *425*, 283–288.

- [106] Wang, H.; Campiglia, A.D. Determination of Polycyclic Aromatic Hydrocarbons in Drinking Water Samples by Solid-Phase Nanoextraction and High-Performance Liquid Chromatography. *Anal. Chem.*, **2008**, *80*(21), 8202–8209.
- [107] Kubackova, J.; Fabriciova, G.; Miskovsky, P.; Jancura, D.; Sánchez-Cortés, S. Sensitive Surface-Enhanced Raman Spectroscopy (SERS) Detection of Organochlorine Pesticides by Alkyl Dithiol-Functionalized Metal Nanoparticles-Induced Plasmonic Hot Spots. *Anal. Chem.*, **2015**, *87*(1), 663–669.
- [108] Le Ru, E.C.; Blackie, E.; Meyer, M.; Etchegoin, P.G. Surface Enhanced Raman Scattering Enhancement Factors: A Comprehensive Study. *J. Phys. Chem. C*, **2007**, *111*(37), 13794–13803.
- [109] Deriu, C.; Conticello, I.; Mebel, A.M.; McCord, B. Micro Solid Phase Extraction Surface-Enhanced Raman Spectroscopy (μ -SPE/SERS) Screening Test for the Detection of the Synthetic Cannabinoid JWH-018 in Oral Fluid. *Anal. Chem.*, **2019**, *91*(7), 4780–4789.
- [110] Drug Enforcement Administration (DEA). *Emerging Threat Report, Mid Year report 2020*; <https://cesar.umd.edu/sites/cesar.umd.edu/files/dea-emerging-threat-report-2020-mid-year.pdf> (accessed September 20, 2020)

CHAPTER 9

Conclusions

The goal of this dissertation was to develop a better understanding of how surface chemistry can be utilized as a platform to advance SERS and promote the adoption of this technique in routine analytical settings. As detailed in the introductory chapters of this dissertation, SERS is a surface spectroscopic technique that relies on the adsorption of analytes to nanoscale plasmonic substrates to enable trace and ultratrace detection. When colloidal substrates are utilized, knowledge of the adsorption phenomena at the nanoscale is an essential tool for the rational design of substrates and the development of detection protocols tailored to specific class of molecules.

Therefore, the present work utilized surface chemistry to develop colloidally stable bimetallic gold-silver nanostar formulations that are compatible with SERS requirements for ideal measurement. One way of achieving these conditions is to control the identity of the nanoparticle capping species and ensure that they (1) have a small SERS cross section, (2) have minimal steric hindrance, and (3) adsorb less strongly to the surface than the target analyte. Indeed, capping species must impart stability to the colloidal formulation without interfering with the SERS detection process.

To do this, a protocol for the synthesis of sparingly capped colloidal nanostars¹ was utilized as a platform to investigate the stabilizing properties of a selection of small anionic molecules, and to examine their behavior with respect to SERS performance. Among the surveyed species, the small anions that were found to achieve colloidal stability were citrate, L-tartrate, acetate, and carbonate sodium salts. Their concentration in solution was optimized via ζ potential, conductivity, and extinction measurements, and they were found to impart stability at a molar ionic strength of 3.4×10^{-3} M (*Objective 1*). Sodium carbonate was also found to impart sufficient stability at lower ionic strength, which was attributed to the alkalizing properties of carbonate in solution; hydroxyl ions are known

to adsorb on gold surfaces and were shown to also adsorb on the bimetallic surface of the nanostars. This provides a potential fifth effective candidate stabilizer to be added to the list, NaOH. The remaining organic and inorganic anionic species that were surveyed did not demonstrate stabilization properties, thus supporting the hypothesis that the capping process is driven by *specific adsorption*.

Surface characterization by XPS also supported the specific adsorption hypothesis, as it showed the two metals constituting the nanostars, gold and silver, are alloyed and in their elemental oxidation state. Chemically driven adsorption of species at the solid-liquid interface is therefore the reasonable explanation for the capping process and the ensuing surface charge on the nanostars. While the traditional assumption on nanoparticle capping states that noble metal nanoparticles contain a residual positive charge in their outermost layer that results in the electrostatic attraction of anionic species, the results in this dissertation indicate that surface adsorption involves *neutral* metallic surfaces being capped by chemically adsorbed negatively charged species. These findings are consistent with recent studies, such as that published by Al-Johani *et al.*,² who determined a similar oxidation state for monometallic gold nanospheres. Therefore, the results here presented can be thought of as an extension of their conclusions to bimetallic systems, and contribute to the reshaping of the knowledge around the surface of noble metal nanoparticles.

The shelf life (*Objective 2a*) of the formulations were dependent on the nature of the stabilizer, and the following stability series was determined:



where *Tt* stands for L-tartrate, *Ac* for acetate, and *Ct* for citrate.

The above mentioned formulations were demonstrated to achieve superior SERS performance compared to the original formulation in which the stabilizer was CTAB. Indeed, all new nanostars formulations exhibited AEF values in the order of 10^5 , compared to the AEF of NS/CTAB, which was $\approx 10^3$ AEF (*Objective 2b*). Although these

foundational experiments were all conducted utilizing Crystal Violet as an ideal SERS probe, the superiority in performance was also verified later with non-ideal probes, such as the opioids acrylfentanyl and benzylfentanyl (*Objective 5*).

Reproducibility in terms of optical properties and morphology was also discussed. The latter was investigated by TEM analysis, which assisted in the identification of the crystal facets of the nanoparticles, the characterization of morphological features, and the formulation of a hypothesis on the nanostar formation and growth. The nanostars were thought to be the product of the co-reduction of Ag^+ and AuCl_4^- under kinetic control conditions, which generated bimetallic nucleation centers with twinning defects, from which anisotropic growth developed. Branching is stochastic once the initial tri-, tetra-, and pentapodal nanocrystals are formed, and the growth was hypothesized to occur first in the form of branch elongation, and then core enlargement after a branch length threshold was reached. Effective co-reduction and alloying were in line with recent studies on the distribution of silver across the body of gold-silver nanostars obtained by other synthetic protocols.³

Citrate was taken as model stabilizer, and the energetics of its adsorption on the nanostars were studied via ζ titrations. These measurements were performed to evaluate the third capping environment requirement, which states that the stabilizer should adsorb less strongly to the surface than the target analyte (*Objective 3a*). Citrate was found to have an adsorption constant K_{ad} with the substrate in the order of 10^3 M^{-1} , which corresponds to an affinity that is two orders of magnitude lower than those reported for drugs of forensic and public health interest (typically, $\approx 10^5 \text{ M}^{-1}$).^{4,5} This is ideal for SERS applications, as it can be expected that drug analytes are able to displace the citrate stabilizer and achieve a close contact with the enhancing substrate, thus yielding high intensity SERS spectra. This statement should be taken with reasonable caution, as SERS is highly dependent on specific surface interactions and such interactions can not be *a priori* guaranteed.

Nevertheless, a highly characterized surface such as that of the NS/Ct formulation provides many advantages when implementing SERS-based analytical procedures. Knowledge of the surface environment necessarily facilitates troubleshooting during the optimization of experimental conditions, leading to robust analytical protocols.

The ζ titration experiments also allowed for the characterization of the interaction between the metal and citrate, and demonstrated that the nanoparticles are capped by weak *chemisorption*, in line with previous publications on monometallic gold nanoparticles.² In addition, this weak chemisorption was found to be characterized by *positive cooperativity*. An insight on the possible nature of the positive cooperativity was obtained via DFT calculations studies (*Objective 4*). These allowed for the modeling of a simplified gold-citrate system, which yielded a population of four possible adsorbate structures. The evaluation of the thermodynamic trends associated with these structures suggested the importance of water-mediated adsorption processes in the formation of the citrate capping layer. Consequently, the cooperative binding that was deduced from the ζ titration results could be interpreted as a result of water-citrate charge transfer complex formation, as well as the establishment of a hydrogen bonding network among adjacent citrate molecules.

The set of putative structures that were obtained by DFT indicated that citrate adsorbs via unidentate coordination with either water or gold; this coincided with the coordination mode that was deduced from the experimental examination of dried residues of the NS/Ct formulation by FTIR spectroscopy (*Objective 3b*). This adsorption mode was also consistent with previously published experimental findings that highlight a correlation between surface coverage and coordination of citrate.² Indeed, at concentrations close to monolayer coverage, which were utilized to obtain the NS/Ct residues, citrate adopts a unidentate coordination mode. The NS/Tt and NS/Ac formulations were also studied by this method; a bridging configuration at the surface was determined for L-tartrate, while acetate was found to coordinate in a unidentate fashion.

As already mentioned, the newly developed formulations were found to be suitable for applications in drug detection (*Objective 5*). The most stable formulation, NS/CO₃²⁻_(c), was successfully utilized to detect fentanyl and six of its analogs by SERS.⁶ These detection studies demonstrated the selectivity of SERS as an analytical technique, because they showed fentanyl analogs were able to be discerned from other opioids, as well as other abused substances, such as cocaine and amphetamines. Moreover, ongoing work in the McCord lab demonstrates that the use of NS/CO₃²⁻_(c) as an enhancing substrate results in high sensitivity, with sub-nanogram LODs achieved for fentanyl substances.⁷ Sub-nanogram detection limits coupled with robust statistical analysis of the spectral profile is essential in order to detect these compounds in both mixtures of seized samples and in toxicological matrices.⁷

Finally, a more generic example of the application of SERS to forensic toxicology was given. Synthetic cannabinoids were presented as examples of novel psychoactive substances and the analytical challenges associated with them. In the presented protocol, emphasis was put on the extraction of model synthetic cannabinoid JWH-018 from oral fluid, and on the use of DFT calculations to aid in structural elucidation and spectroscopic interpretation.⁵ These calculations allowed for the simulation of a Raman spectrum of the compound with prediction errors below 2%. These results suggested that the same method could be applied to a number of other synthetic cannabinoids, with the aim of testing the potential of DFT for use in developing an *in silico* library to define the spectra of unidentified substances. This was demonstrated with five other synthetic cannabinoids, which had average percent errors below 2.5%.

Overall, this dissertation work offers an example of how surface chemistry exploration can be of great aid in understanding SERS and in formulating tailored nanomaterials for rational protocol design. This approach has the potential of providing highly characterized surfaces that can be straightforwardly applied in subsequent protocol development, and

establishing SERS as a routine analytical technique. Future directions of this work may involve a more extended application of the developed colloidal nanostars. For example, they could be utilized to further lower the detection limits of synthetic cannabinoids, or to implement an analytical protocol for the SERS detection of fentanyl and other opioids in toxicological samples. Moreover, the general scheme utilized for the characterization and engineering of the surface environment of the nanostars could be adopted as a basis for further development and functionalization of these nanoparticles, as well as a methodological guide for the development and formulation of different colloidal nanomaterials.

REFERENCES

- [1] He, S.; Kang, M.W.C.; Khan, F.J.; Tan, E.K.M.; Reyes, M.A.; Kah, J.C.Y. Optimizing gold nanostars as a colloid-based surface-enhanced Raman scattering (SERS) substrate. *J. Opt.* **2015**, *17*, 1–13.
- [2] Al-Johani, H.; Abou-Hamad, E.; Jedidi, A.; Widdifield, C.M.; Viger-Grave, J.; Sangaru, S.S.; Gajan, D.; Anjum, D.H.; Ould-Chikh, S.; Hedhili, M.N.; Gurinov, A.; Kelly, M.J.; El Eter, M.; Cavallo, L.; Emsley, L.; Basset, J-M. The structure and binding mode of citrate in the stabilization of gold nanoparticles. *Natur. Chem.*, **2017**, *9*, 890–895.
- [3] Atta, S.; Beetz, M.; Fabris, L. Understanding the role of AgNO₃ concentration and seed morphology in the achievement of tunable shape control in gold nanostars. *Nanoscale*, **2019**, *11*, 2946–2958
- [4] Izquierdo-Lorenzo, I.; Sanchez-Cortes, S.; Garcia-Ramos, J.V. Adsorption of Beta-Adrenergic Agonists Used in Sport Doping on Metal Nanoparticles: A Detection Study Based on Surface-Enhanced Raman Scattering. *Langmuir*, 2010, *26*(18), 14663–14670.

- [5] Deriu, C.; Conticello, I.; Mebel, A.M.; McCord, B. Micro Solid Phase Extraction Surface-Enhanced Raman Spectroscopy (μ -SPE/SERS) Screening Test for the Detection of the Synthetic Cannabinoid JWH-018 in Oral Fluid. *Anal. Chem.*, **2019**, *91*(7), 4780–4789.
- [6] Wang, L.; Deriu, C.; Wu, W.; Mebel, A.M.; McCord, B. Surface-enhanced Raman spectroscopy, Raman, and density functional theoretical analyses of fentanyl and six analogs. *J. Raman Spectrosc.*, **2019**, *50*, 1405–1415.
- [7] Wang, L.; Vendrell-Dones, M.O.; Deriu, C.; Doğruer, S.; Harrington, P.; McCord, B. Multivariate Analysis Assisted Surface Enhanced Raman Spectroscopy (MVA-SERS) Determination of Fentanyl in Cocaine and Heroin Mixtures Using a Handheld Raman Spectrometer, *manuscript in preparation*.

APPENDICES

APPENDIX A

Reaction scaling-up

As reported in the *Methods* section, the nanostars synthesis utilized for this research is optimized for ≈ 1 mL volumes.^{1,2} Scaling-up by increasing reagent volumes resulted in blue-shifts of the product's plasmon band, as shown in *Figure A.1*.

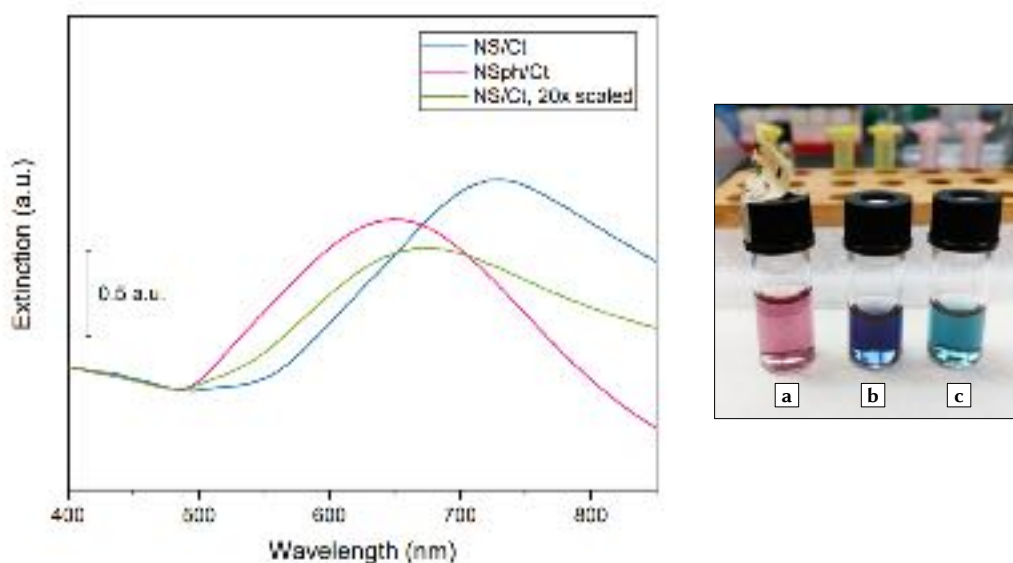


Figure A.1: (*left*) Extinction spectra of citrate capped AuAg nanostars (NS/Ct, *blue*), nanospheres (NSph/Ct, *pink*), and scaled nanostars (NS/Ct scaled 20x, *green*). The scaled nanostars were obtained by multiplying by 20 all volumes involved in the reaction. (*right*) Color of the analyzed colloidal sols: (a) nanospheres are pink, (b) scaled nanostars are purplish-blue, (c) nanostars are teal.

The observed shift was attributed to the creation of different kinetic conditions under the two different volume regimes. Effective kinetic control of a nanoparticle synthesis is achieved not only by acting on the temperature (§ 5.2), but also by acting on the

ratio between the rate of deposition and the rate of diffusion of the reduced metal(s).³ If the deposition rate (V_{dep}) is larger than the diffusion rate (V_{diff}), true kinetic control is achieved, and anisotropic morphologies are obtained; on the other hand, if the reduced metal has time to diffuse on the surface of the nucleating crystal or preformed seed, $V_{dep} < V_{diff}$, and thermodynamically controlled products are obtained instead (*Figure A.2*).⁴ In other words, under kinetic control, reduced atoms are incorporated at the sites of highest surface energy and are *trapped* in those positions as a result of the high rate at which other reduced atoms are deposited on top of them; this causes anisotropic growth along the direction perpendicular to the surface of highest energy (*e.g.*, $\langle 111 \rangle$).⁴ On the contrary, slow deposition rates allow reduced atoms to diffuse to more thermodynamically favored facets after first depositing on the highest energy surfaces, thus resulting in *isotropic* growth of nanocrystals.^{3,4}

When scaling-up a kinetically controlled reaction by simple proportional increase of reagent volumes, and performing the addition of the reducing agent manually via the use of traditional micropipettors, the fine relationship between the original deposition and diffusion rates is unavoidably altered. In the scaled-up conditions, the reducing agent is introduced at roughly the same velocity as in the original protocol, but has to diffuse through a larger volume of metal precursors solution; because of this, it can be hypothesized that under the scaled-up conditions the rate of atomic diffusion is allowed to increase in relation to the rate of deposition, thus shifting the product towards either a mixture of the expected kinetic product and a thermodynamic product (*e.g.*, spheroidal shape), or a morphology that lays in between the two extremes (*e.g.*, oblong or “popcorn” shape). Typically, for reliable scaling-up of kinetically controlled reactions and reproducible yield of products, syringe-pump systems are utilized, as they allow control of the velocity of deposition and ensure uniformity of the local concentration environment.

REFERENCES

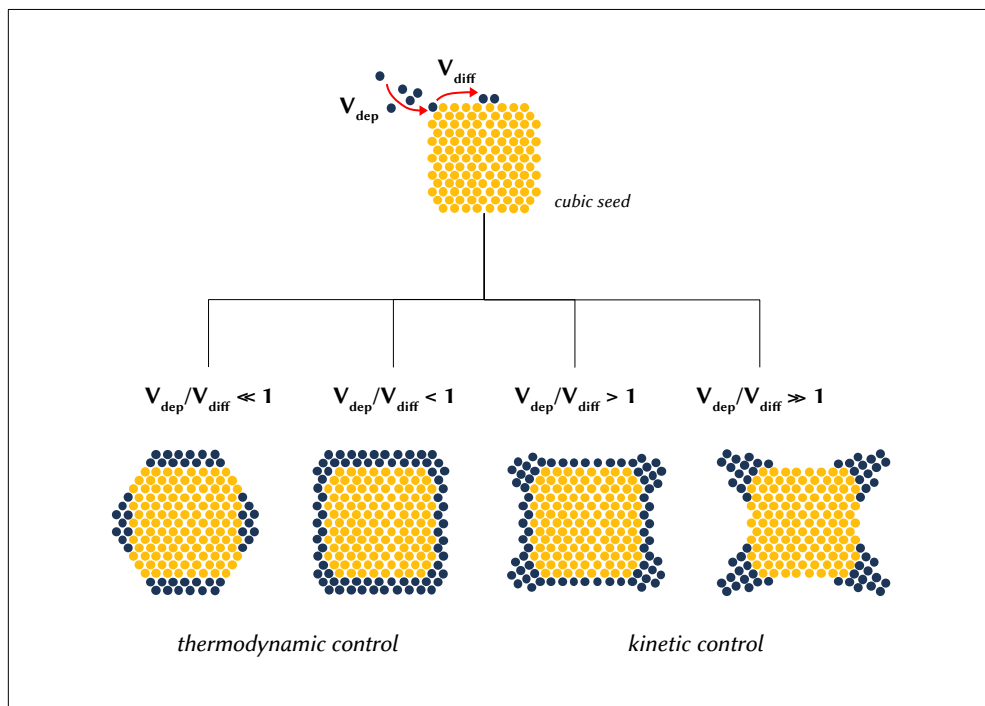


Figure A.2: Schematic representation of the morphology effects of four different kinetic conditions. Illustration inspired by Xia *et al.*,⁴ 2015.

[1] Cheng, L-C.; Huang, J-H.; Chen, H.M.; Lai, T.C.; Yang, K.Y.; Liu, R.S.; Hsiao, M.; Chen, C-H.; Here, L-J.; Tsaid, D.P. Seedless, silver-induced synthesis of star-shaped gold/silver bimetallic nanoparticles as high efficiency photothermal therapy reagent. *J. Mater. Chem.*, **2012**, *22*, 2244–2253.

[2] He, S.; Kang, M.W.C.; Khan, F.J.; Tan, E.K.M.; Reyes, M.A.; Kah, J.C.Y. Optimizing gold nanostars as a colloid-based surface-enhanced Raman scattering (SERS) substrate. *J. Opt.* **2015**, *17*, 1–13.

[3] Gilroy, K.D.; Ruditskiy, A.; Peng, H-C.; Qin, D.; Xia, Y. Bimetallic Nanocrystals: Syntheses, Properties, Applications. *Chem. Rev.*, **2016**, *116*, 10414–10472.

[4] Xia, Y. Xia, X.; Peng, H-C. Shape-Controlled Synthesis of Colloidal Metal Nanocrystals: Thermodynamic versus Kinetic Products. *J. Am. Chem. Soc.*, **2015**, *137*(25), 7947–7966.

APPENDIX B

TEM micrographs of the NS formulations

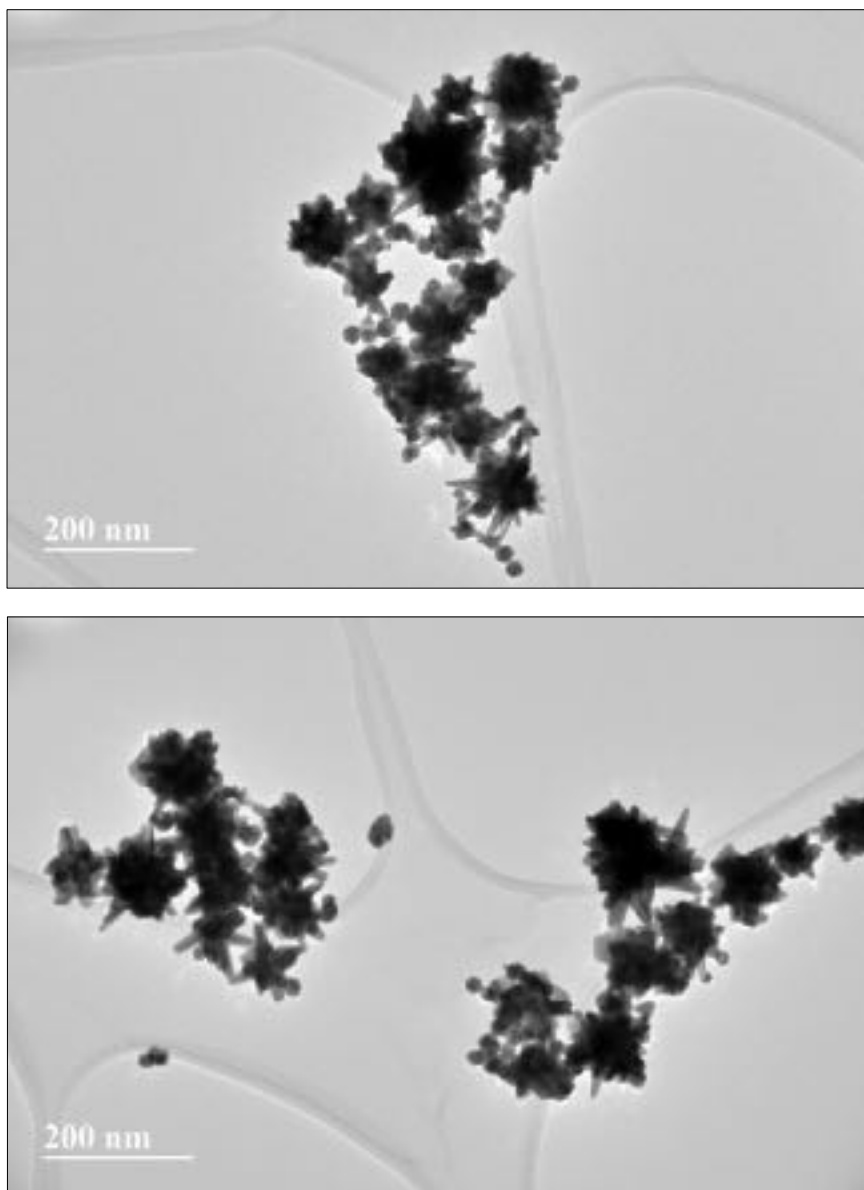


Figure B.1: TEM micrographs of the NS/Tt formulation.

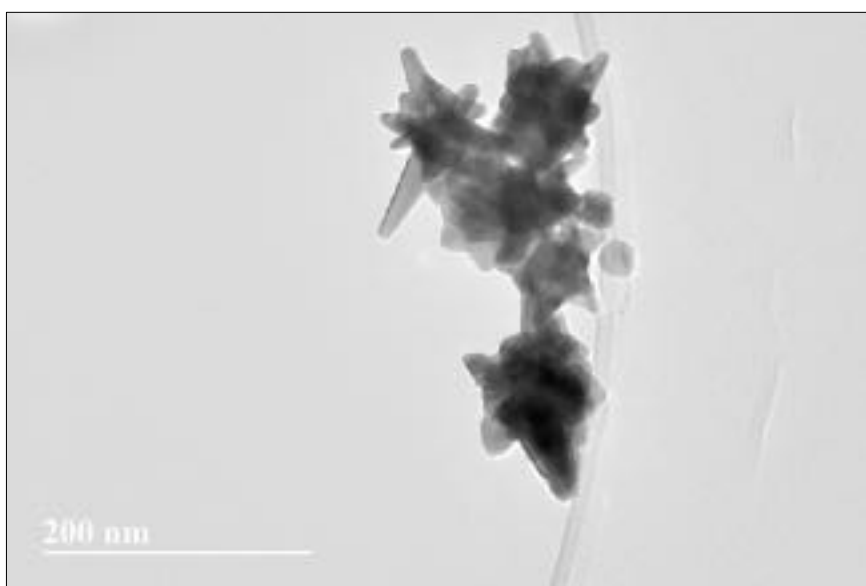
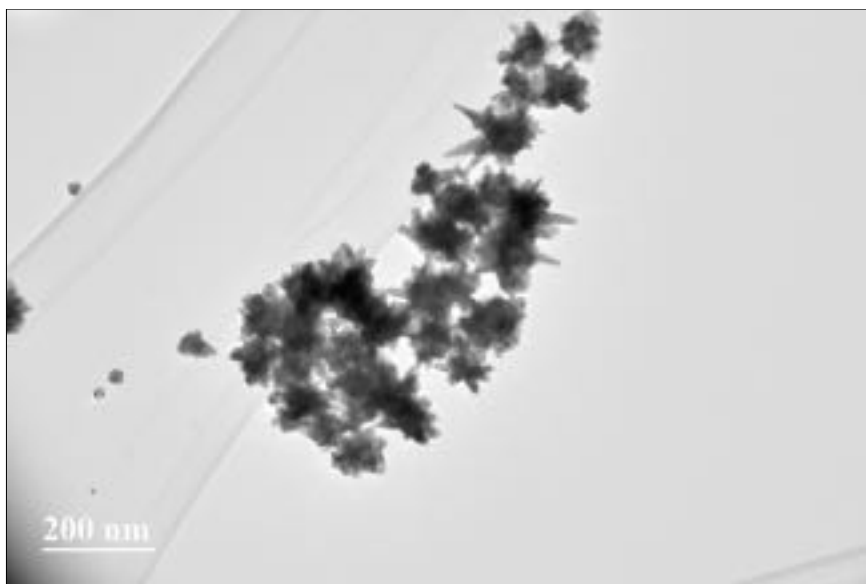


Figure B.2: TEM micrographs of the NS/Ac formulation.

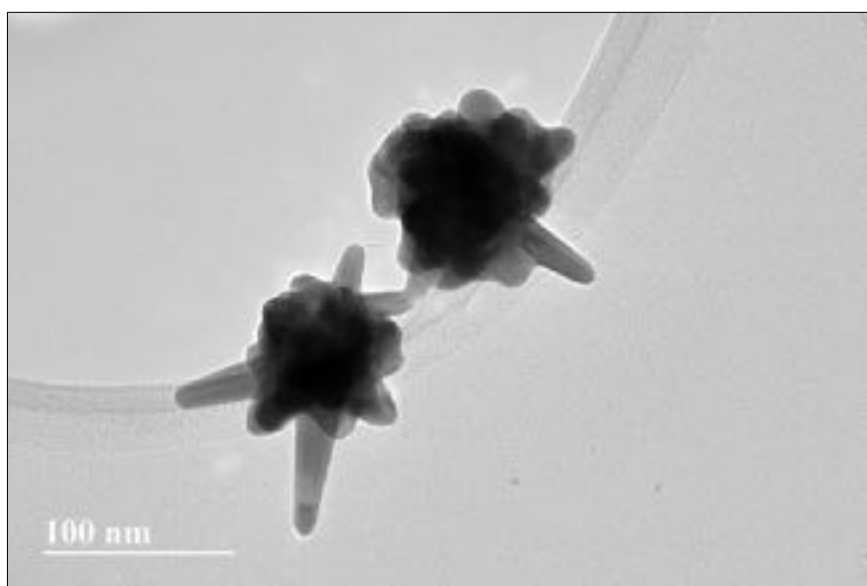
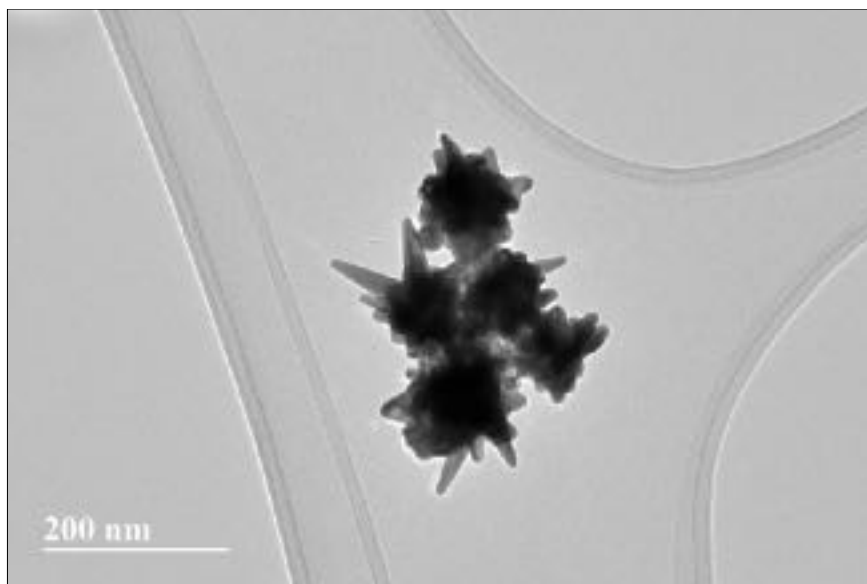


Figure B.3: TEM micrographs of the NS/CO₃²⁻(c) formulation.

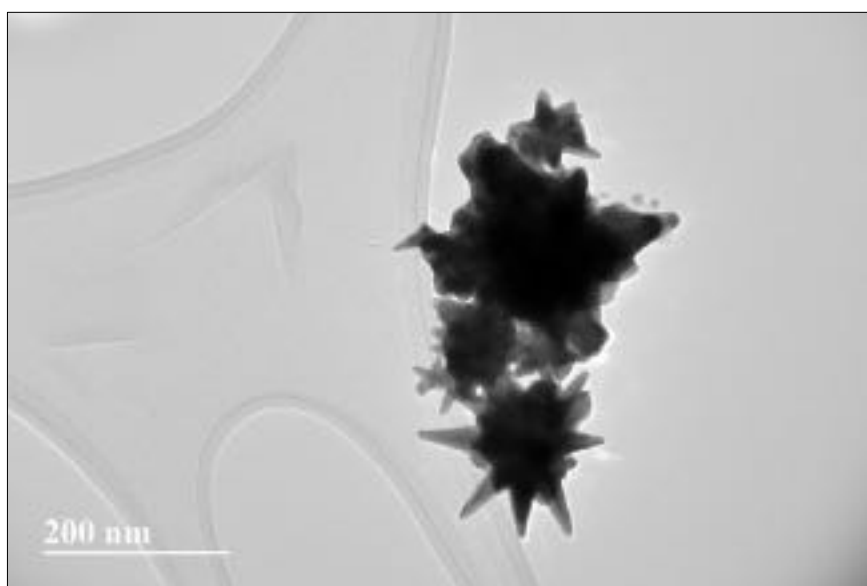
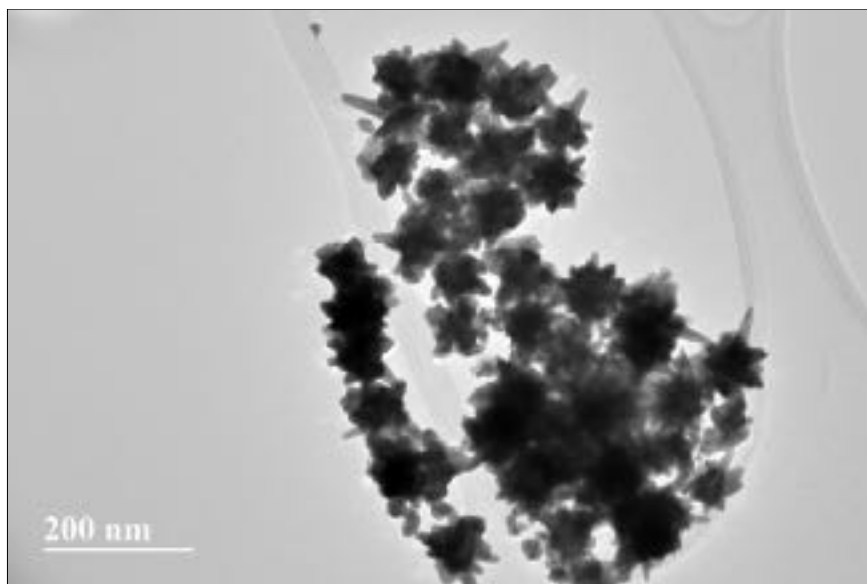


Figure B.4: TEM micrographs of the NS/CO₃²⁻(I) formulation.

APPENDIX C

ANOVA assumptions and other statistical tests

ANOVA F-test assumptions

An ANOVA F-test relies on the assumption that the data are: independent, linear, normal within groups, and homoskedastic. All assumptions were therefore tested ($\alpha = 0.05$), and the results are reported in the following subsections.

Summary of normality tests

Normality was tested via Anderson Darling (AD) test.

- H_0 : the data follow a normal distribution
- H_a : the data do not follow a normal distribution

At the tested significance level of 0.05, all data followed a normal distribution.

Table C.1: Summary of normality tests.

Figure	Table	Sample description	AD value	p-value
5.4	5.2	SERS intensities over time (all)	0.393	0.305
5.8	5.5	SERS intensities obtained with individual NS batches (all)	0.477	0.202
5.11	5.10	SERS intensities obtained with NS _{pooled} (all)	0.394	0.329
5.12	5.13	mock sensitivity test, [CV] = 10^{-7} M	0.361	0.411
5.12	5.13	mock sensitivity test, [CV] = 10^{-8} M	0.229	0.631
5.12	5.13	mock sensitivity test, [CV] = 5×10^{-9} M	0.136	0.935
5.20, 5.21	5.18, 5.21	AEF, NS/Ct	0.291	0.446
5.20, 5.21	5.18, 5.21	AEF, NS/Tt	0.414	0.194
5.20, 5.21	5.18, 5.21	AEF, NS/Ac	0.330	0.344
5.20, 5.21	5.18, 5.21	AEF, NS/CO ₃ ²⁻ (e)	0.245	0.573
5.20, 5.21	5.18, 5.21	AEF, NS/CO ₃ ²⁻ (l)	0.424	0.181
5.20	5.18	AEF, NS/CTAB	0.326	0.223
5.21	5.21	AEF, NS/OH	0.532	0.085

Summary of equal variances tests

Homoskedasticity was tested by either Levene's or Bartlett's test, depending on prior knowledge on normality.

- $H_0: \sigma_1 / \sigma_2 = 1$
- $H_a: \sigma_1 / \sigma_2 \neq 1$

Table C.2: Summary of homoskedasticity tests.

Figure	Table	Sample description	p-value (test)
5.8	5.5	SERS intensities obtained with individual NS batches (all)	0.737 (Levene's)
5.10		SERS, individual NS batches vs NS _{pooled}	0.005 (Levene's)
5.11	5.10	SERS intensities obtained with NS _{pooled} (all)	0.646 (Levene's)
5.12	5.13	mock sensitivity test	0.053 (Bartlett's)
5.20	5.18	AEF, new NS vs NS/CTAB	0.090 (Levene's)
5.21	5.21	AEF, new NS vs NS/OH	0.280 (Levene's)

Exploratory data analysis

Exploratory data analysis via box-and-whiskers plot identified one outlier in the SERS intensity data set obtained with the NS_{pooled} substrate preparation.

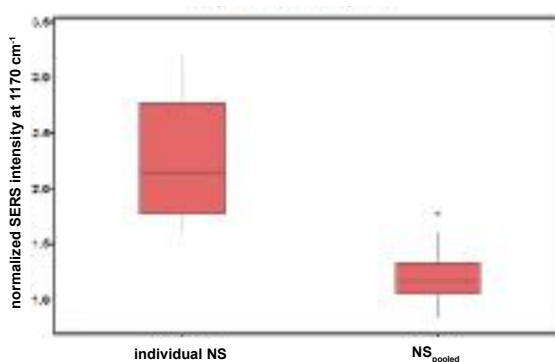


Figure C.1: Exploratory data analysis of the SERS intensities obtained with individual NS batches and NS_{pooled} substrates. One outlier is identified in the NS_{pooled} group.

ANOVA means

Table C.3: ANOVA means for the normalized SERS intensity of CV at 1170 cm^{-1} over time.

Level	N	Mean	Std Error	Below 95%	Above 95%
t_0	2	2.09	0.09	1.85	2.32
t_8	2	2.40	0.09	2.16	2.64
t_{16}	2	2.40	0.09	2.16	2.63
t_{26}	2	2.45	0.09	2.22	2.69
t_{35}	2	2.27	0.09	2.03	2.50

The standard error is calculated on the basis of the aggregated variance (N = 10).

Table C.4: ANOVA means for the normalized SERS intensity of CV at 1170 cm^{-1} for each of the five individual NS batches.

Level	N	Mean	Std Error	Below 95%	Above 95%
$\lambda_{LS\ PR}$ 676 nm (NS #5)	3	1.6	0.1	1.4	1.8
$\lambda_{LS\ PR}$ 691 nm (NS #2)	3	1.9	0.1	1.6	2.1
$\lambda_{LS\ PR}$ 710 nm (NS #3)	3	2.1	0.1	1.9	2.3
$\lambda_{LS\ PR}$ 728 nm (NS #4)	3	2.6	0.1	2.4	2.8
$\lambda_{LS\ PR}$ 742 nm (NS #1)	3	3.0	0.1	2.7	3.2

The standard error is calculated on the basis of the aggregated variance (N = 15).

Table C.5: ANOVA means for the normalized SERS intensity of CV at 1170 cm^{-1} for each of the five $\text{NS}_{\text{pooled}}$ samples.

Level	N	Mean	Std Error	Below 95%	Above 95%
$\text{NS}_{\text{pooled}}$ #5	3	1.16	0.05	1.05	1.28
$\text{NS}_{\text{pooled}}$ #2	3	0.94	0.05	0.83	1.06
$\text{NS}_{\text{pooled}}$ #1	2	1.56	0.05	1.42	1.70
$\text{NS}_{\text{pooled}}$ #3	3	1.28	0.05	1.17	1.40
$\text{NS}_{\text{pooled}}$ #4	3	1.07	0.05	0.96	1.19

The standard error is calculated on the basis of the aggregated variance (N = 14).

Table C.6: ANOVA means for the normalized SERS intensity of CV at 1170 cm^{-1} at different concentrations, and obtained with different $\text{NS}_{\text{pooled}}$ samples.

Level	N	Mean	Std Error	Below 95%	Above 95%
[CV] 5×10^{-9} M/ $\text{NS}_{\text{pooled}}$ #6	5	0.07	0.08	-0.09	0.23
[CV] 10^{-8} M/ $\text{NS}_{\text{pooled}}$ #7	5	0.41	0.08	0.24	0.57
[CV] 10^{-7} M/ $\text{NS}_{\text{pooled}}$ #1–5	14	1.18	0.08	1.08	1.27

The standard error is calculated on the basis of the aggregated variance (N = 24).

Table C.7: ANOVA means for the AEF values of the CV-NS systems under study.

Level	N	Mean	Std Error	Below 95%	Above 95%
CV + NS/Ct	5	1.58×10^5	0.08×10^5	1.42×10^5	1.74×10^5
CV + NS/Tt	5	1.41×10^5	0.08×10^5	1.25×10^5	1.56×10^5
CV + NS/Ac	5	1.50×10^5	0.08×10^5	1.34×10^5	1.65×10^5
CV + NS/ $\text{CO}_3^{2-}_{(c)}$	5	1.40×10^5	0.08×10^5	1.24×10^5	1.55×10^5
CV + NS/ $\text{CO}_3^{2-}_{(l)}$	5	0.89×10^5	0.08×10^5	0.74×10^5	1.05×10^5
CV + NS/CTAB	3	0.004×10^5	0.1×10^5	-0.2×10^5	0.2×10^5

The standard error is calculated on the basis of the aggregated variance (N = 28).

Table C.8: ANOVA means for the AEF values of the CV-NS systems under study, compared to CV-NS/OH.

Level	N	Mean	Std Error	Below 95%	Above 95%
CV + NS/Ct (pH 5.5)	5	1.58×10^5	0.08×10^5	1.42×10^5	1.74×10^5
CV + NS/Tt (pH 4.5)	5	1.41×10^5	0.08×10^5	1.25×10^5	1.56×10^5
CV + NS/Ac (pH 5.0)	5	1.50×10^5	0.08×10^5	1.34×10^5	1.65×10^5
CV + NS/ $\text{CO}_3^{2-}_{(c)}$ (pH 6.5)	5	1.40×10^5	0.08×10^5	1.24×10^5	1.55×10^5
CV + NS/ $\text{CO}_3^{2-}_{(l)}$ (pH 9.5)	5	0.89×10^5	0.08×10^5	0.74×10^5	1.05×10^5
CV + NS/OH (pH 9.5)	5	0.83×10^5	0.08×10^5	0.67×10^5	0.99×10^5

The standard error is calculated on the basis of the aggregated variance (N = 30).

Plot of residuals for the Hill fit

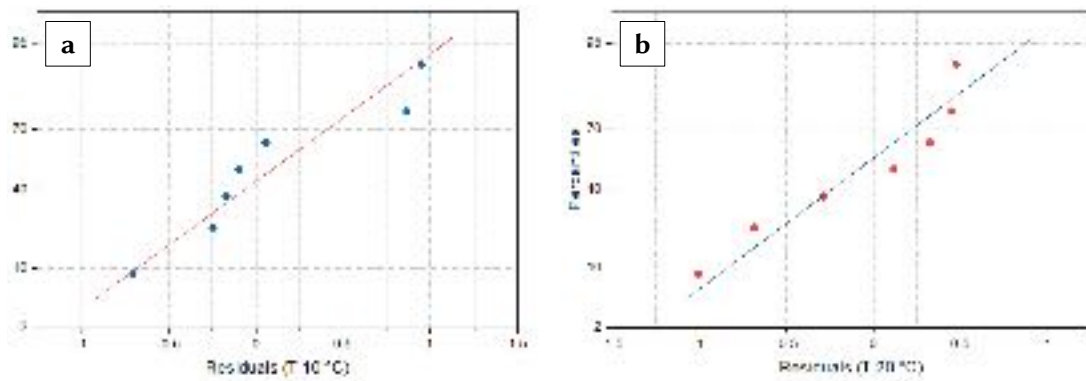


Figure C.2: Plot of residuals for the adsorption isotherm fitted by the Hill expansion of the Langmuir model presented in *Chapter 6*. (a) Data acquired at 10°C; (b) data acquired at 20°C. The residuals show a near normal behavior.

APPENDIX D

Background SERS spectra of the developed NS formulations

The background spectra of all of the developed nanostar formulations do not show any significant spectral features. This of course does not mean that no species is adsorbed on the surface; rather, this can be considered a proof that the adsorbed species have a very small SERS cross section, and thus, they are unlikely to interfere with the SERS measurement by producing bands that overlap with those of the target analyte.

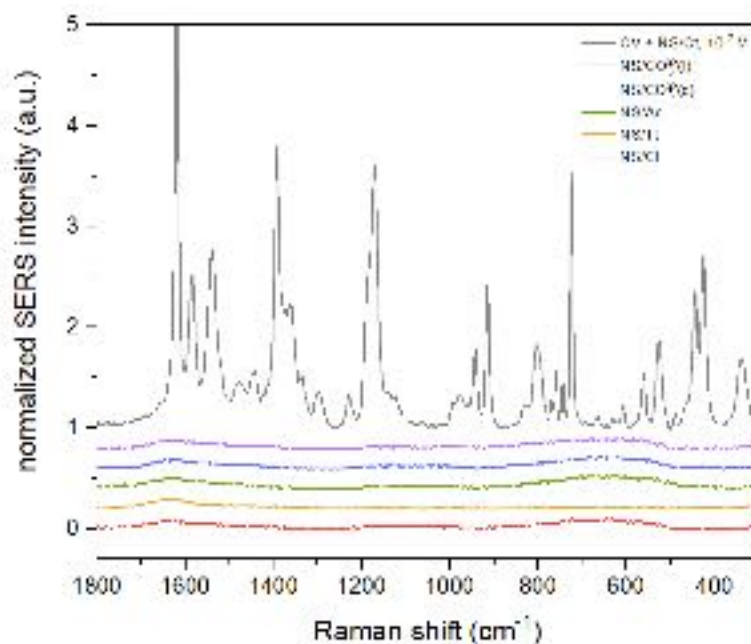


Figure D.1: Background spectra of all of the developed nanostars formulations. As a term of comparison for intensities, the spectrum of CV is reported (10^{-7} M, obtained with NS/Ct); no aggregating agent was utilized. All spectra have been normalized to the intensity of the band at 3200, attributed to $\nu(\text{OH})$ of water. All spectra are on the same scale and are stacked for ease of comparison.

APPENDIX E

Calculation of ζ potential from electrophoretic mobility

All electrophoretic mobility values ($N_{\text{tot}} = 72$; $N = 9$ for each titration point) were initially screened for outliers; Iglewicz and Hoaglin's modified Z-score was utilized for flagging potential outliers, and the generalized Extreme Studentized Deviate (ESD) many-outlier procedure was then utilized to detect and confirm the outliers.¹ *Tables E.1 and E.2* report the raw mobility data at the two temperatures; the outliers are shown in italics and were excluded from all subsequent calculations.

As explained in the *Methods* section, the ζ potential values utilized for the estimate of the adsorption constants were derived from the measured electrophoretic mobilities, according to the method published by Ohshima.² This method is valid for all particle geometries,² and was successfully utilized by Haes's group³ for quantitative studies on colloidal monometallic gold nanostars. The equation utilized to derive the ζ potential values combines *Equations 3.7 and 3.8* showed in the *Methods* section, as follows:

$$\mu = \frac{\varepsilon_r \varepsilon_0}{\eta} \zeta \left\{ \frac{2}{3} \left\{ 1 + \frac{1}{2 \left\{ 1 + \left[\frac{2.5}{\kappa a} \right] [1 + 2e(-\kappa a)] \right\}^3} \right\} \right\} \quad (9.1)$$

where ε_r and ε_0 are the dielectric permittivities of the dispersant and vacuum, respectively, η is the viscosity of the dispersant, a is the radius of curvature of the nanostructure, and κ is the Debye-Hückel parameter [m^{-1}], that is, the inverse of the Debye length (κ^{-1}). While ε_r , ε_0 , and η are constant at a given temperature and can be found in the literature, a is a substrate-specific parameter, and κ depends on the concentration of charged species (*Equation 3.9*). The average radius of curvature, a , of the NS/Ct was calculated from the TEM micrographs ($N = 150$), and was equal to 4.0 nm, with a standard error of ± 0.1

nm. The Debye-Hückel parameter, κ , was calculated by first determining the number concentration, n_{c_i} , of all charged species and at each titration point. Speciation of the charged forms of citrate was achieved by measuring the pH of the nanostars and utilizing the Henderson-Hasselbalch equation to calculate the concentrations. All calculated parameters are reported in *Tables E.3* and *E.4*.

Table E.1: Electrophoretic mobility. Raw data at $T = 10^\circ\text{C}$.

[Ct] (M)	electrophoretic mobility ($\mu\text{m}\cdot\text{cm}/\text{V}\cdot\text{s}$)		
	batch 1	batch 2	batch 3
1.91×10^{-4}	-1.524	-1.500	-1.581
	-1.540	-1.577	-1.614
	-1.537	-1.616	-1.594
2.87×10^{-4}	-1.713	-1.745	-1.701
	-1.903	-1.885	-1.871
	-1.653	-1.709	-1.787
3.83×10^{-4}	-1.813	-1.847	-1.853
	-1.888	-1.851	-1.895
	-1.893	-1.945	-1.953
4.78×10^{-4}	-2.046	-1.906	-1.956
	-2.119	-2.082	-2.044
	-2.026	-1.967	-1.993
5.74×10^{-4}	-2.160	-2.168	-2.088
	-2.195	-2.315	-2.232
	-2.245	-2.186	-2.254
7.66×10^{-4}	-2.254	-2.260	-2.270
	-2.367	-2.394	-2.355
	-2.311	-2.409	-2.390
9.57×10^{-4}	-2.460	-2.428	-2.489
	-2.448	-2.399	-2.402
	-2.373	-2.359	-2.436
1.15×10^{-3}	-2.568	-2.496	-2.499
	-2.455	-2.481	-2.464
	-2.118	-2.278	-2.220

Outliers are shown in italics.

Table E.2: Electrophoretic mobility. Raw data at $T = 20^\circ\text{C}$.

[Ct] (M)	electrophoretic mobility (mcm/Vs)		
	batch 1	batch 2	batch 3
1.91×10^{-4}	-1.751	-1.798	-1.833
	-1.769	-1.775	-1.841
	-1.839	-1.845	-1.904
2.87×10^{-4}	-2.091	-2.073	-2.141
	<i>-1.615</i>	-1.875	-2.040
	-1.961	-2.019	-2.098
3.83×10^{-4}	-2.157	-2.156	-2.210
	-2.111	-2.165	-2.116
	-2.241	-2.166	-2.269
4.78×10^{-4}	-2.218	-2.338	-2.362
	-2.274	-2.347	-2.463
	-2.457	-2.424	-2.529
5.74×10^{-4}	-2.434	-2.397	-2.482
	-2.618	-2.602	-2.639
	-2.501	-2.483	-2.589
7.66×10^{-4}	-2.681	-2.761	-2.780
	-2.556	-2.599	-2.653
	-2.560	-2.575	-2.522
9.57×10^{-4}	-2.717	-2.752	-2.758
	-2.682	-2.829	-2.781
	-2.575	-2.781	-2.787
1.15×10^{-3}	-2.666	-2.875	-2.765
	-2.767	-2.732	-2.828
	-2.533	-2.588	-2.637

Outliers are shown in italics.

Table E.3: T = 10°C.

[Ct] (M)	pH of NS/[Ct] _i	$\sum(n_{c_i} z_i)$	κ	κa	$f\kappa a$
1.91 x 10 ⁻⁴	4.0	-1.25 x 10 ²⁴	105171746	0.4207	0.666771
2.87 x 10 ⁻⁴	4.0	-1.42 x 10 ²⁴	112207640	0.4488	0.666797
3.83 x 10 ⁻⁴	4.0	-1.04 x 10 ²⁴	95774618	0.3831	0.666742
4.78 x 10 ⁻⁴	4.5	-1.44 x 10 ²⁴	112878314	0.4515	0.666800
5.74 x 10 ⁻⁴	4.5	-8.95 x 10 ²³	88974257	0.3559	0.666725
7.66 x 10 ⁻⁴	4.5	-5.06 x 10 ²³	66897882	0.2676	0.666689
9.57 x 10 ⁻⁴	5.0	-7.99 x 10 ²³	84061453	0.3362	0.666715
1.15 x 10 ⁻³	5.0	-7.46 x 10 ²³	81224076	0.3249	0.666710

Table E.4: T = 20°C.

[Ct] (M)	pH of NS/[Ct] _i	$\sum(n_{c_i} z_i)$	κ	κa	$f\kappa a$
1.91 x 10 ⁻⁴	4.0	-1.25 x 10 ²⁴	105741603	0.4230	0.666773
2.87 x 10 ⁻⁴	4.0	-1.42 x 10 ²⁴	112815621	0.4513	0.666799
3.83 x 10 ⁻⁴	4.0	-1.04 x 10 ²⁴	96293558	0.3852	0.666743
4.78 x 10 ⁻⁴	4.5	-1.44 x 10 ²⁴	113489929	0.4540	0.666802
5.74 x 10 ⁻⁴	4.5	-8.95 x 10 ²³	89456351	0.3578	0.666726
7.66 x 10 ⁻⁴	4.5	-5.06 x 10 ²³	67260359	0.2690	0.666689
9.57 x 10 ⁻⁴	5.0	-7.99 x 10 ²³	84516928	0.3381	0.666716
1.15 x 10 ⁻³	5.0	-7.46 x 10 ²³	81664177	0.3267	0.666710

REFERENCES

- [1] Iglewicz, B.; Hoaglin, D.C. How to Detect and Handle Outliers. In *The ASQC Basic References in Quality Control: Statistical Techniques; Volume 16*; Mykytka, E.F., Ed.; ASQC Quality Press: Milwaukee, 1993.
- [2] Ohshima, H. A Simple Expression for Henry's Function for the Retardation Effect in Electrophoresis of Spherical Colloidal Particles. *J. Colloid Interface Sci.*, **1994**, *168*(1), 269–271.
- [3] Xi, W.; Phan, H.T.; Haes, A.J. How to accurately predict solution-phase gold nanostar stability. *Anal. Bioanal. Chem.*, **2018**, *410*, 6113–6123.

APPENDIX F

Starting geometries and Cartesian coordinates of optimized structures

Starting geometries

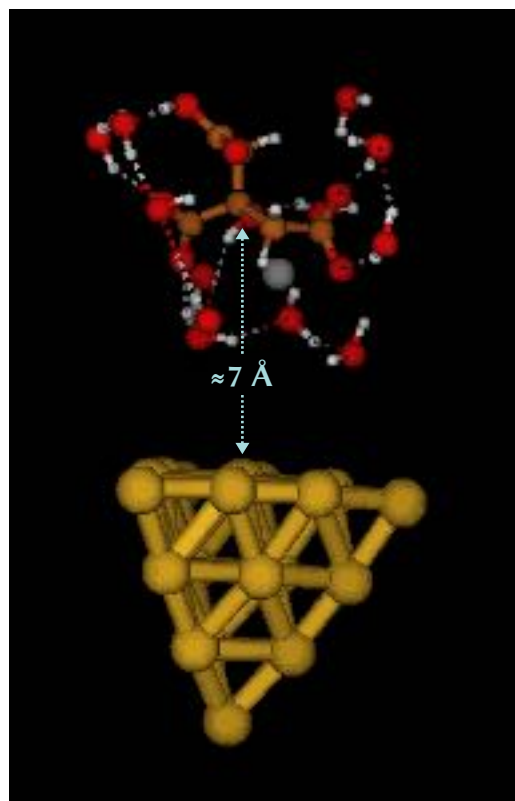


Figure F.1: Initial guess structure for the optimization of the citrate/Au₂₀ complex. The [HCitrate²⁻ + Na⁺ + 12 H₂O] supramolecular system, centered on the central C atom of citrate, was placed at $\approx 7 \text{ \AA}$ from the central surface atom of the cluster.

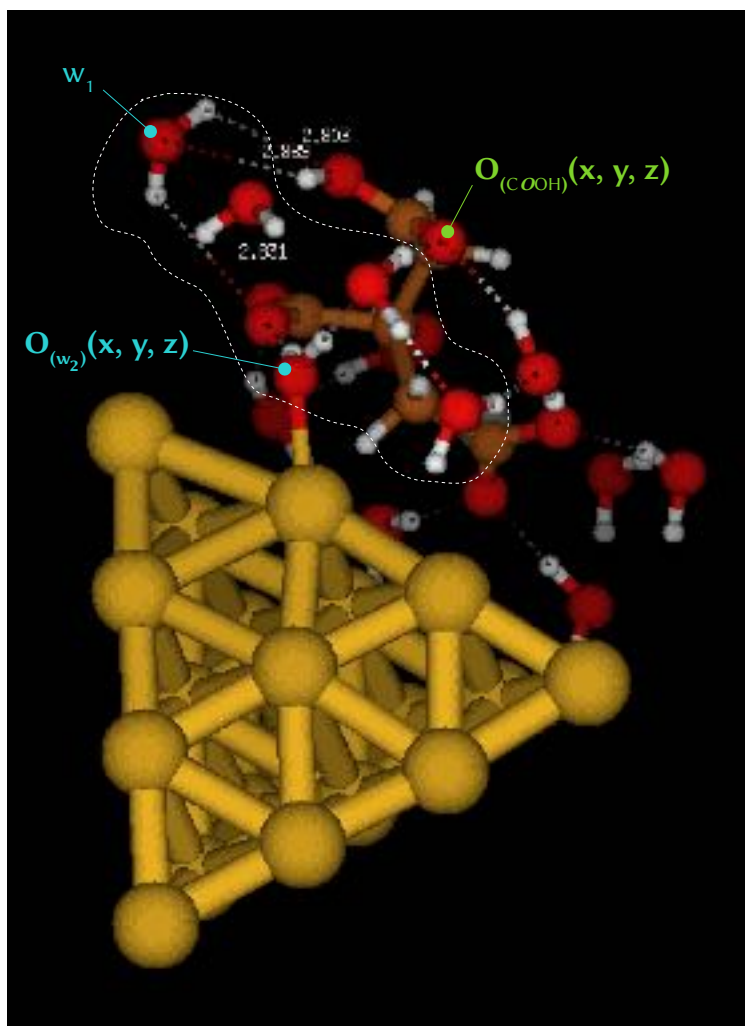


Figure F.2: Stable geometry of complex $S2$. Highlighted are the coordinates of the oxygen atoms that were utilized to calculate the translation vector for the obtainment of starting geometry for complex $S3$ optimization. The vector was applied to the 5 molecules of water circled in white. This group includes water molecules w_1 and w_2 .

Cartesian coordinates of optimized geometries

Au₂₀

(charge 0, multiplicity 1)

Au 3.1980844700 -6.5997512200 -4.9932655200
Au 5.6248089200 -7.9819727300 -4.8801839800
Au 8.0247061600 -9.2501752400 -4.5955870000
Au 8.9985268800 -10.0916731200 -1.8070692100
Au 10.3890429200 -7.7815997000 -3.2859226300
Au 7.8459531100 -6.4623430000 -3.7851893500
Au 6.3802531500 -8.8912632100 -2.2231548000
Au 7.4591932600 -9.5795992500 0.3865720500
Au 8.8699434800 -7.3496830300 -0.8412690100
Au 10.0825617900 -5.2166733700 -2.4035344700
Au 7.3762995300 -3.7966752200 -2.7205984400
Au 5.2786959100 -5.0956327200 -3.8868981500
Au 3.8879959300 -7.4038083300 -2.4052288800
Au 4.7508387600 -8.1547222500 0.0731410200
Au 6.0200105900 -5.8552461400 -1.1783095800
Au 7.1155027900 -6.6937981400 1.3844991200
Au 5.8280702100 -8.8853788700 2.5477057800
Au 8.3471808000 -4.6413746600 0.0733007900
Au 9.5770553400 -2.6404274400 -1.4419087300
Au 10.5094700000 -10.4432503500 -4.1320190200

[HCitrate²⁻ + Na⁺ + 12 H₂O]

(charge -1, multiplicity 1)

C -1.5285979600 1.5707921243 0.2323879918
C -0.4525739782 0.4771671486 -0.0450548290
C 0.9572112715 0.7370009166 0.6066504025
C 1.9950799789 1.2573129791 -0.3847142387
O 2.2705482853 2.5077416540 -0.4097792855
C -1.8475106358 1.9649848313 1.6669009268
O -3.0220707089 1.7015203381 2.1343158266
O -0.9395149510 2.6152373778 2.3231252618
C -0.9351130415 -0.9215695480 0.4092477736
O -1.0853836716 -1.1456194715 1.6583926044
O -0.3530194676 0.4698394490 -1.5029929948
O -1.1126789522 -1.7984360941 -0.5279442112
O 2.5458497294 0.3968182335 -1.1924756361
H -1.1609609122 2.4703310822 -0.2732305593
H -2.4489817645 1.2461778654 -0.2586787776
H 1.3347805429 -0.2020996748 1.0230654940
H 0.8348754076 1.4440239095 1.4285781717
H -3.8771585892 0.1491920750 2.6797616254
H -0.5762400852 -0.4319245955 -1.8371635657
Na 0.3413315547 1.9017206052 -3.2022879459
O -0.4797330551 0.5450118000 -4.8169416054
H -0.0551911950 0.4911953932 -5.6895834219
H -0.5047059710 -0.3724935297 -4.3866200995
O 0.6396254899 3.9059340163 -2.1315287379

H 0.2175271871 4.2544546599 -1.3010084870
H 1.5214719553 3.5905029479 -1.8216848065
O 2.6351021786 1.7290377638 -3.4490749975
H 3.2422129606 2.4890090315 -3.4568401587
H 2.8088600780 1.1720995329 -2.6219893670
O -0.3567535805 -1.7053424369 -3.5438154175
H 0.4875450822 -1.8589365232 -2.9793140993
H -1.1098404171 -2.1827474544 -3.1544276172
O 1.5292718787 -1.9785541265 -1.8169513937
H 0.9494910311 -2.2559334055 -1.0795580412
H 1.9880883493 -1.1103495632 -1.5726037152
O -3.8753724942 -0.6283961772 3.2892588882
H -3.8815506623 -1.5180724563 2.7894920134
H -2.6895949457 -0.5122667492 3.9247441299
O -1.6150161021 -0.3614066176 4.1627787915
H -1.1197045426 -0.5824457596 3.3312196091
H -1.3773403107 0.6060535048 4.5855329812
O -3.2555702394 -2.7830396788 2.0770581290
H -2.3282582066 -2.4398914953 2.0251805409
H -3.4525818934 -3.2164049994 1.2053366139
O -1.2049049150 1.9640038472 4.8921685972
H -0.9028414684 2.3580126001 4.0200767013
H -2.1100415216 2.3704730602 5.0529506644
O -2.9346839872 -3.7433970048 -0.4120202898
H -2.2301072198 -3.0327850170 -0.5009292681
H -2.5121604203 -4.6201546779 -0.3757132727

O -3.6011125744 2.9002109675 4.4511308604
H -3.7715610291 3.8511528136 4.3369681525
H -3.4868255496 2.4596932265 3.5491638161
O 0.4060763346 4.2921784598 0.5297133903
H -0.1345339709 3.8906401015 1.2526445858
H 1.2154727244 3.7295487201 0.4167273260

S1 Complex

(charge -1, multiplicity 1)

Au -1.10532206 -3.67334483 0.41697524
Au 0.87037214 -5.22835699 1.67460796
Au 2.73644856 -6.65730643 3.05571500
Au 2.07679164 -7.45419260 6.05463651
Au 4.19053735 -5.34276590 5.41636888
Au 2.46380090 -3.83066693 3.66346977
Au 0.19109660 -6.13382331 4.36264991
Au -0.39043114 -6.85900049 7.17199942
Au 1.66451272 -4.71842777 6.80889077
Au 3.80903667 -2.71354064 5.96299246
Au 1.68930628 -1.12006098 4.39494204
Au 0.32694529 -2.32057643 2.38476423
Au -1.78942610 -4.45196907 3.05150185
Au -2.29860649 -5.30020231 5.60020794
Au -0.34170500 -3.14789894 5.16362871

Au -0.64909037 -3.75567627 8.00278719
Au -2.81700990 -6.21422576 8.14749974
Au 1.25648346 -1.91459765 7.28529106
Au 3.13728047 -0.02207784 6.51468134
Au 4.54125197 -8.00419629 4.66008059
Na -4.39236508 0.59411704 3.59193573
O -3.18465199 2.41328084 2.97319175
O -3.32189716 -1.52949645 2.89785805
O -6.48072169 -0.21883797 3.18549166
H -2.77672071 2.88112618 3.76567413
H -2.40995117 2.11635423 2.44907179
H -2.76468703 -1.22240130 3.67950330
H -2.76372237 -1.83352813 2.15870050
H -7.31503169 0.06642910 2.78162202
H -6.33872458 -1.22963611 3.12303551
C -5.09046158 -0.11104264 8.04406892
C -4.83539443 -0.70952394 9.40326879
O -3.80572751 -0.42479259 10.07901432
C -4.57312165 -0.98318368 6.84350470
C -5.16743407 -2.41806452 6.88208604
O -6.10305431 -2.69758202 6.07828575
O -5.04617181 -0.33137062 5.63778845
C -3.02651815 -1.09956917 6.77709758
C -2.33205903 0.03485003 6.04408697
O -2.21276916 -0.09056983 4.75175121
O -5.75106373 -1.57904872 9.81320334

O -1.88935859 1.04129788 6.69739310
O -4.62157436 -3.22960306 7.73723199
H -4.59800354 0.86172675 7.97038217
H -6.16760055 0.01304686 7.90709397
H -5.89429895 -0.74628218 5.34969525
H -2.77443105 -2.02438793 6.25252515
H -2.62505521 -1.16499766 7.78793635
H -5.41538371 -2.32379212 10.48901311
O -0.04089928 -1.33783476 10.66917442
H 0.53206996 -1.93665853 10.15737820
H -0.39112155 -0.58747958 10.07518735
O -2.35608718 -2.22569386 11.50514276
H -2.91012239 -1.43338825 11.29308281
H -1.37838617 -1.96245810 11.43078736
O -5.71402490 -2.65597459 3.30315033
H -4.75028704 -2.44415282 3.16290951
H -5.87853686 -2.97432851 4.22026564
O -1.29210889 0.47093390 9.30242536
H -2.22032344 0.38734420 9.61925136
H -1.30886032 0.76687419 8.35670318
O -4.81325794 -3.51185676 11.11413279
H -3.93749679 -3.36214616 11.54018570
H -4.81364166 -4.30373993 10.51839529
O -2.45288263 -3.43167548 9.21881322
H -3.26048061 -3.21924533 8.67200738
H -2.40614394 -2.98116233 10.12394645

O -1.53533974 3.16859168 4.93365395
H -0.83483511 2.80233693 4.34561918
H -1.64266615 2.53594000 5.69105409
O -4.93432805 -5.37418925 8.98728401
H -4.98145038 -4.55503374 8.35150335
H -5.65915445 -6.00609626 8.83005097
O -0.58848993 1.27078324 3.15809492
H 0.17736241 0.76407142 2.83058447
H -1.12487506 0.71912782 3.80832978

S2 Complex

(charge -1, multiplicity 1)

Au 0.60167808 -1.17057242 -5.57996702
Au 2.62930040 -2.63289023 -4.29296693
Au 4.51861352 -3.97459907 -2.86045033
Au 3.82727415 -4.90990779 0.02311812
Au 5.78232753 -2.63573622 -0.36430384
Au 4.02522896 -1.20511496 -2.15113971
Au 1.86261791 -3.67304173 -1.69131939
Au 1.31088747 -4.56256188 1.02644800
Au 3.12138668 -2.23738563 0.90709983
Au 5.18237738 -0.07503695 0.26555568
Au 3.07726686 1.41815251 -1.39584857
Au 1.88066305 0.19273780 -3.50352421

Au -0.15436317 -2.05965223 -3.01203707
Au -0.73575565 -3.02006688 -0.52389668
Au 1.13087977 -0.77045545 -0.78342815
Au 0.66338119 -1.45303422 2.01025817
Au -1.19178823 -4.04813899 1.96263361
Au 2.50969330 0.50350525 1.44413085
Au 4.31014460 2.53988165 0.84328671
Au 6.35659018 -5.24521721 -1.20972520
Na -2.86621525 2.99638023 -2.46909115
O -1.58450736 4.78352917 -3.01442846
O -4.96304002 2.28346885 -2.91712363
C -3.33436346 2.54220551 1.99954890
C -3.10290845 1.97403505 3.37602113
O -1.95141770 2.00355941 3.91703283
C -3.00956662 1.54480319 0.83455768
C -3.76589965 0.19324093 0.99416287
O -4.73240122 -0.02442256 0.19877459
O -3.48465440 2.17090993 -0.38751669
C -1.49759085 1.24279824 0.69237579
C -0.71567215 2.32158587 -0.03611135
O -0.59159929 2.18606063 -1.32918679
O -4.14751810 1.42874731 3.95803890
O -0.21070070 3.29634744 0.61895572
O -3.33509259 -0.60963924 1.91303024
H -1.17069620 5.23590034 -2.21862574
H -0.81360697 4.48717694 -3.54506289

H -5.80223118 2.57630446 -3.30393220
H -4.87788952 1.26651332 -2.88281722
H -2.70339026 3.42307630 1.85217706
H -4.38523790 2.82222166 1.90234969
H -4.36139667 1.76971236 -0.60818674
H -1.37182955 0.30705752 0.14209364
H -1.07781029 1.10721674 1.68790685
H -3.92326859 0.67472111 4.74240605
O -1.87045508 0.81694808 -3.10984127
H -1.27563675 1.12856859 -2.35413859
H -1.34256132 0.50268085 -3.86637001
O 1.61838296 0.70817741 4.75724478
H 2.24356147 0.07152506 4.36818124
H 1.39987411 1.43791846 4.09278579
O -0.88249674 0.04680446 5.39524452
H -1.29447441 0.88724094 5.05467210
H 0.11401950 0.17907528 5.41266702
O -4.31909262 -0.17321071 -2.57874331
H -3.35010918 -0.03121421 -2.75479917
H -4.48739978 -0.40430554 -1.63534186
O 0.60943753 2.52719381 3.15154662
H -0.34073984 2.48585874 3.42947111
H 0.63023924 2.90144367 2.23939984
O -3.62721873 -0.44603814 5.43751103
H -2.70812904 -0.52727399 5.77653475
H -3.94665706 -1.24274534 4.89049330

O -1.17922709 -1.37365239 3.24820779
H -1.95650097 -1.03241175 2.71735211
H -1.07199039 -0.89848278 4.14282681
O 0.12389090 5.47992503 -1.06575808
H 0.78630980 5.10473363 -1.69118741
H 0.01964729 4.82446366 -0.32770560
O -4.44714318 -2.14261408 3.68648863
H -5.35932717 -2.46303664 3.59680241
H -4.13976258 -1.66016077 2.85519632
O 0.97252223 3.61070707 -2.91937247
H 1.75330134 3.14210793 -3.26710078
H 0.46327353 3.02222262 -2.27518856

S3 Complex

(charge -1, multiplicity 1)

Au 2.3407193718 -3.8729205836 -4.4954725799
Au 3.6430617174 -4.5047581558 -2.0860907206
Au 4.7599255421 -4.9883503207 0.3510399685
Au 2.8871903948 -4.9068502418 2.8893350241
Au 5.1488824531 -2.6693195601 2.2894621585
Au 4.1884987882 -2.2357207152 -0.3970400569
Au 1.8590914126 -4.6920072131 0.2683368700
Au 0.1375902489 -4.5414525692 2.6728397972
Au 2.3061468705 -2.1325508834 2.2809768765

Au 4.3069009931 -0.1540025843 1.6144962814
Au 2.8714440460 0.3340141755 -0.9910074041
Au 2.6002056235 -1.6664670908 -2.7983505799
Au 0.6522538236 -3.9570573835 -2.2592796444
Au -0.9243290418 -3.9686708774 -0.0373319228
Au 0.9005552379 -1.7192741054 -0.3880539513
Au -0.4519738512 -1.7420873166 2.1895267480
Au -2.4611388941 -3.6510358405 2.2798306222
Au 1.1376876133 0.4356601206 1.5809770366
Au 3.2111057886 2.3095901794 0.9140135119
Au 5.7483455130 -5.3099799741 2.9151803520
Na -3.5466785928 1.3722085153 -3.7653098838
O -2.5010143611 3.4643699718 -4.2308897350
O -4.6183496938 -0.6769960284 -3.2176722245
H -2.0436805362 3.8738955075 -3.4145447852
H -1.8825570647 2.9196085391 -4.7591314975
H -5.1314410224 -0.4088040407 -4.0280048461
H -4.1221273272 -1.5574712309 -3.2953895939
C -4.6338371106 0.5092706013 1.4478555504
C -3.9607967424 0.2339475990 2.7595639487
O -2.7385255406 0.3322603783 3.0040471419
C -4.1683671133 -0.3393895115 0.2431985401
C -4.2490928364 -1.8786521138 0.5223366943
O -4.1894204131 -2.6648222983 -0.4686203890
O -5.0659174881 0.0579817802 -0.8206627393
C -2.6693375466 -0.1445920714 -0.1501452082

C -2.2420936497 1.1389853093 -0.8245034158
O -1.6509104896 1.0256018283 -1.9798804636
O -4.8426223667 -0.0189618408 3.7698914898
O -2.4174984248 2.2788054106 -0.2463535585
O -4.2147201133 -2.2237358872 1.7819977767
H -4.4485818524 1.5601187047 1.1934354927
H -5.7067327380 0.3577110422 1.5622480051
H -4.9365617542 -0.4244943080 -1.7169737980
H -2.3961456452 -0.9695252103 -0.8067723339
H -2.0758896343 -0.2407686585 0.7649434810
H -4.3543930646 -0.2173624661 4.5992102403
O -0.9414397433 -0.9904914828 -3.4606205970
H -1.1510252037 -0.3109413908 -2.7373026428
H -0.0502128487 -1.3792263136 -3.3472738701
O -6.6327111754 2.6857047108 -5.7016996444
H -6.0477865654 3.3066659593 -5.1065362900
H -7.5836446938 2.8389457528 -5.5895714067
O -5.1016722790 3.8994579677 -4.1321327909
H -5.1768606346 3.5023222816 -3.2223887977
H -4.1295183148 3.9366976755 -4.3632746583
O -3.1017426379 -2.7429972884 -3.0339258448
H -2.2161502157 -2.3182838416 -3.1346538326
H -3.3298098146 -2.9418697770 -2.0932048005
O -0.6994668680 1.9785243040 1.9964808472
H -1.3555944251 1.4351696265 2.4964625621
H -1.1494969919 2.3249193945 1.1890098215

O -4.7533161913 2.4765387524 -1.8929781449
H -5.0821598026 1.6402490552 -1.4411256149
H -4.0624649266 2.8634156835 -1.3146774268
O -5.3136147486 0.5748281485 -5.3909203707
H -5.9586123711 1.3664080214 -5.5613302547
H -4.9630155139 0.2206537770 -6.2252210436
O -1.3575027627 4.2798935286 -2.0342581180
H -0.4253566580 3.9472512770 -2.1307301865
H -1.7720975782 3.7552792277 -1.3066556042
O -1.7690236627 0.8130195187 -5.2405479715
H -1.3332172385 0.0811826287 -4.7088396978
H -1.7504772848 0.6016022857 -6.1890265356
O 0.5822150068 2.5477015612 -2.3969186215
H 1.4241629888 2.1750737716 -2.0736653220
H -0.1655653743 1.9022426325 -2.2849724180

V1 Complex

(charge -1, multiplicity 1)

Au 0.29030014 -6.86650050 2.74359652
Au -1.03644524 -4.81671956 1.39247320
Au -2.38044885 -2.70781377 0.23474332
Au -5.60105837 -2.66929305 0.49241317
Au -4.68218375 -3.51710413 -2.10943954
Au -2.86115498 -5.32874026 -0.74683330

Au -3.87527399 -4.48110004 1.98943958
Au -6.74627878 -4.33295456 2.33059384
Au -6.01662992 -5.44706189 -0.29335681
Au -4.79354770 -6.20531538 -2.76090970
Au -3.15498147 -8.26030125 -1.33099698
Au -1.39846566 -7.66570893 0.63337760
Au -2.43084182 -6.64950868 3.37008422
Au -5.10508800 -6.44222121 3.79115307
Au -4.20710966 -7.66840889 1.29950066
Au -7.07692171 -7.34940526 1.62320287
Au -7.87589516 -6.25569294 4.06595923
Au -6.15891056 -8.30089275 -0.76854715
Au -5.06696792 -9.04223467 -3.20338323
Au -4.32573359 -0.97372474 -1.27912261
Na -3.44246866 6.85653156 -1.58500355
O -2.00497413 8.28845284 -0.64292981
O -5.28939201 6.64926044 -2.81801001
C -4.15458073 3.57709724 0.99373435
C -4.14820881 2.40295905 1.92419541
O -3.16612733 2.20459500 2.70349513
C -3.26674843 3.40291264 -0.28586071
C -3.74553813 2.18229541 -1.12353924
O -4.35339796 2.40096131 -2.21190520
O -3.51052420 4.58798520 -1.08828733
C -1.73250470 3.22929214 -0.03250212
C -0.93765598 4.52317425 0.05568993

O -0.60788610 5.09550653 -1.05049560
O -5.19302517 1.59450870 1.90282917
O -0.60065688 4.98017647 1.21505298
O -3.46089558 1.02159242 -0.61360961
H -1.75572177 8.15051519 0.30969394
H -1.18391465 8.23657412 -1.19675626
H -6.18258292 6.98712981 -2.97840952
H -5.06147170 5.84842564 -3.39523927
H -3.79732288 4.45461609 1.55324145
H -5.17415487 3.75937092 0.64785690
H -4.08588800 4.31038210 -1.84497884
H -1.31545279 2.65774669 -0.86642142
H -1.59035732 2.64661924 0.87760934
H -5.06979495 0.70791247 2.46129282
O -1.95044120 5.80227290 -3.20124450
H -1.54865081 5.27823697 -2.44682097
H -1.28475209 6.47231339 -3.45931255
O -0.13095522 1.22001538 4.40761332
H 0.80810211 1.08338718 4.60627079
H -0.32633399 2.16763059 4.12671845
O -2.12375135 -0.09212340 3.38733741
H -2.56485418 0.79258431 3.24093436
H -1.29228186 0.11462519 3.91689719
O -4.20095107 4.64991300 -4.00922573
H -3.26051015 4.97969843 -3.93021818
H -4.29401874 3.70919413 -3.74712482

O -1.01244938 3.57212165 3.50454206
H -1.88951818 3.17756987 3.25634802
H -0.67239837 4.05208047 2.70139234
O -4.72873483 -0.58690220 3.12487140
H -3.77768515 -0.69280611 3.40882894
H -5.09011229 -1.40748107 2.73450762
O -1.71788038 -0.59516282 0.83730894
H -2.22902598 0.09572891 0.34779373
H -1.79398850 -0.47652159 1.84119730
O -1.09691508 7.45154710 1.75619110
H -0.52496842 7.91377116 2.39250502
H -0.73528984 6.53347031 1.51189322
O -2.99444830 5.83401811 3.18530223
H -2.49100465 6.52543976 2.69661163
H -2.35156378 5.22305491 3.60434464
O 0.11466771 7.3772382 -2.04787209
H 1.04553603 7.63058384 -2.16535457
H 0.01782155 6.51936387 -1.52368708

Au₁₉Ag homotops

Au₁₉Ag “c”

(charge 0, multiplicity 1)

Au -3.64825091 -0.06042347 -3.77123423
Au -1.23139355 -1.44970602 -3.66806705

Au 1.17716846 -2.70808406 -3.37150649
Au 2.14643742 -3.54915014 -0.59343127
Au 3.53109923 -1.24527181 -2.06822052
Au 0.99070417 0.08143827 -2.56835124
Au -0.47713716 -2.35657449 -1.00563273
Au 0.60658351 -3.04811222 1.60759570
Au 2.01626337 -0.81104186 0.37737300
Au 3.23631427 1.32486605 -1.18821331
Au 0.52911068 2.73398153 -1.51077864
Au -1.56199504 1.43802125 -2.67403808
Au -2.95600257 -0.87567913 -1.19088603
Au -2.09463571 -1.62479477 1.27902188
Ag -0.81004269 0.66110883 0.02467478
Au 0.27624070 -0.16086729 2.59388725
Au -1.02366654 -2.34094952 3.75797627
Au 1.50490902 1.88518886 1.28638462
Au 2.72124093 3.89292960 -0.22507012
Au 3.65901241 -3.90364361 -2.91496678

Au₁₉Ag “v”

(charge 0, multiplicity 1)

Au 7.84164242 -6.47257914 -3.80866640
Au 5.99047048 -5.85869664 -1.16781374
Au 8.36415530 -4.62953360 0.01322566
Ag 9.61270790 -2.57061254 -1.43720331

Au 7.41987385 -3.81149567 -2.68129273
Au 5.29535234 -5.09213942 -3.87431930
Au 3.88961977 -7.42121290 -2.41546690
Au 4.75433608 -8.17402108 0.06783216
Au 5.83615956 -8.86661061 2.54499467
Au 7.12447715 -6.68117891 1.36753686
Au 8.87843050 -7.37698736 -0.82995120
Au 10.03735309 -5.18619992 -2.37617476
Au 10.38048934 -7.76457451 -3.27702235
Au 10.51289575 -10.42624904 -4.12816771
Au 8.98707925 -10.10267935 -1.81520106
Au 7.44301286 -9.58832304 0.38278523
Au 6.35242644 -8.95044064 -2.23143738
Au 8.02132145 -9.26110352 -4.58753745
Au 5.61311308 -7.99546507 -4.87240814
Au 3.20927139 -6.58494604 -4.98863014

Au₁₉Ag “e”

(charge 0, multiplicity 1)

Au 7.84527975 -6.46259688 -3.79188527
Au 6.04603982 -5.85342500 -1.14721612
Ag 8.38085768 -4.58901071 0.05064798
Au 9.60025916 -2.60997921 -1.50919966
Au 7.38751410 -3.79991314 -2.70532987
Au 5.27128608 -5.10893276 -3.83984120

Au 3.89657604 -7.41764219 -2.40944695
Au 4.74866941 -8.19343622 0.06487533
Au 5.81863393 -8.90043490 2.53578576
Au 7.12202847 -6.69088040 1.35461409
Au 8.84970201 -7.32681779 -0.81902845
Au 10.07058548 -5.20788775 -2.39104384
Au 10.37475751 -7.78928417 -3.23999520
Au 10.51553261 -10.42614223 -4.12709329
Au 8.98411821 -10.09372209 -1.81095141
Au 7.43006935 -9.60504005 0.37873942
Au 6.35943249 -8.93646017 -2.23420102
Au 8.03170012 -9.24232316 -4.60081957
Au 5.62454761 -7.97756926 -4.88570902
Au 3.20659816 -6.58355092 -4.98781971

APPENDIX G

Supporting Information, § 8.3.1

The following appendix is reprinted with minor modifications from the Supporting Information of Deriu, C.; Conticello, I.; Mebel, A. M.; McCord, B. *Micro Solid Phase Extraction Surface-Enhanced Raman Spectroscopy (μ -SPE/SERS) Screening Test for the Detection of the Synthetic Cannabinoid JWH-018 in Oral Fluid. Analytical Chemistry, 2019, 91(7), 4780–4789. Copyright (2019) American Chemical Society. This work was supported by Award #2015-IJ-CX-K006 of the National Institute of Justice, Office of Justice Programs, U.S. Department of Justice. Points of view in the document are those of the authors and do not necessarily represent the official view of the U.S. Department of Justice.*

Table G.1: Preparation of fortified oral fluid samples.

JWH-018 in FOF (ng/mL)	OF (μ L)	JWH-018 20,000 ng/mL in methanol (μ L)	methanol (μ L)	methanol (% v/v)
7500	500	300		37.5
3750	250	75.0	75.0	37.5
1875	250	37.5	112.50	37.5
937.5	250	18.75	131.25	37.5
468.7	250	9.38	140.62	37.5
225.0	250	4.50	145.50	37.5
180.0	250	3.60	146.40	37.5
150.0	250	3.00	147.00	37.5
112.5	250	2.25	147.75	37.5
90.00	250	1.80	148.20	37.5
75.00	250	1.50	148.50	37.5
37.50	250	0.75	149.25	37.5
25.00	250	0.50	149.50	37.5

FOF, fortified oral fluid; *OF*, oral fluid.

Table G.2: μ -SPE protocol.

step	solutions/solvents	procedure description
Wetting	100% Acetonitrile, UHPLC grade	Aspirate 10 μ L of wetting solvent, discard to waste, and repeat another time
Equilibration	1% formic acid in ultrapure water	Aspirate 10 μ L of equilibration solution, discard to waste, and repeat another time
Binding	1% formic acid in FOF supernatant recovered after protein crashing	Aspirate 10 μ L of acidified FOF supernatant, dispense through the same medium, and repeat this step for a total of 10 times.
Washing	1% formic acid in ultrapure water	Aspirate 10 μ L of washing solution, discard to waste and repeat another time
Elution	100% methanol, UPLC grade	Aspirate 4 μ L of elution solvent and expel into a new vial. Repeat this step for a total of 2 times.

FOF, fortified oral fluid.

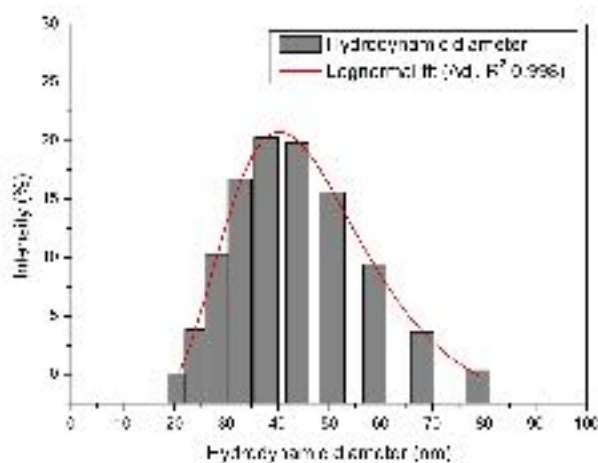


Figure G.1: Size distribution histogram of citrate-reduced gold nanoparticles. The data was obtained by dynamic light scattering (DLS) and follows a lognormal distribution (adjusted R^2 0.998), as expected for a colloidal sol. The resulting hydrodynamic diameter is 42 ± 11 nm.

Table G.3: Analysis time breakdown of μ -SPE/SERS method.

sample	average ζ potential (mV)	standard deviation
as-synthesized	-33	2
aggregated (MgCl_2 1.67×10^{-2} M)	-23	2

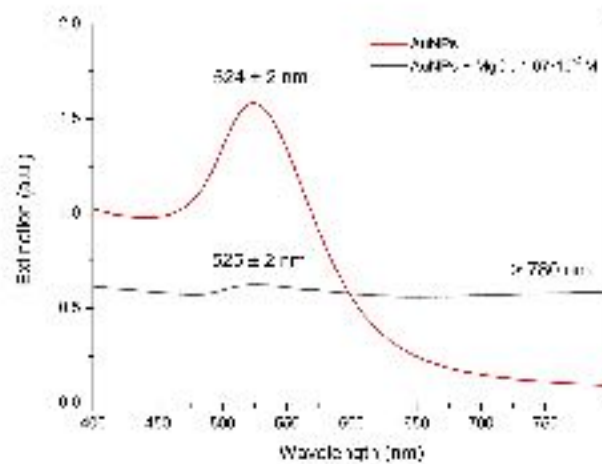


Figure G.2: Extinction spectra of the as synthesized (red) and salt-aggregated (dark grey) citrate-reduced gold nanoparticles. The average plasmon bands are marked on the graph. The one at >780 nm is assigned to the aggregated fraction of the nanoparticles population in the sample containing MgCl_2 .

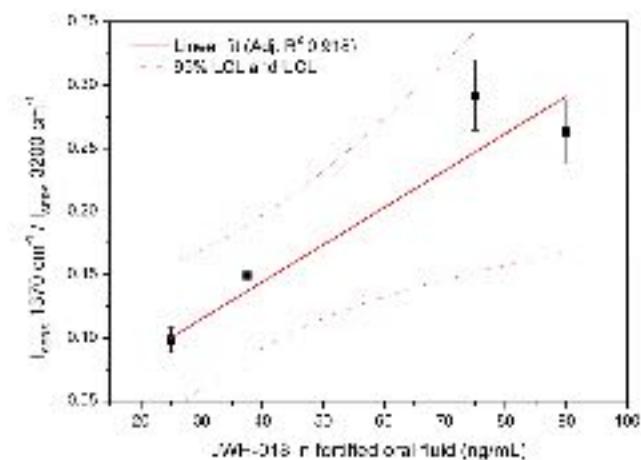


Figure G.3: Calibration curve for fortified oral fluid samples obtained by plotting the normalized intensity of the marker band versus the known concentration of JWH-018 in fortified oral fluid. The equation is $y = 0.0029 \pm 0.0005x + 0.03 \pm 0.02$ and the adjusted R^2 is 0.918. The dotted lines represent the upper and lower 95% confidence limit.

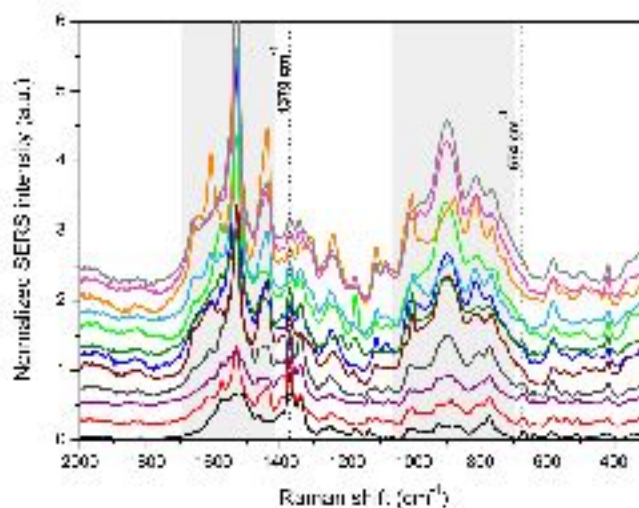


Figure G.4: SERS spectra obtained from fortified oral fluid extracts at different initial concentration of JWH-018 using portable instrumentation in auto-exposure and auto-accumulation operating mode. The vertical dashed line marks the drug’s characteristic bands at 1370 cm^{-1} assigned to the $\nu(\text{C}=\text{C})$ of the naphthalene moiety (used for normalization), and at 674 cm^{-1} assigned to the naphthalene ring deformation (used as marker band). The shadowed areas highlight the regions in which the spectral profile becomes affected by spurious bands as the concentration of the target drug decreases.

Table G.4: Analysis time breakdown of μ -SPE/SERS method.

step	time
Protein crashing	10 minutes
μ -SPE	4 minutes
SERS sample incubation	20 minutes
SERS acquisition	1 minute and 35 seconds

Cartesian coordinates of the optimized structure of JWH-018

(charge 0, multiplicity 1)

```
C 0 -6.74848 2.78644 0.312056
C 0 -6.70736 1.419054 0.205623
C 0 -5.47706 0.739926 0.004784
C 0 -4.26402 1.497704 -0.08793
C 0 -4.34483 2.911753 0.032005
C 0 -5.55407 3.535646 0.22445
C 0 -5.4289 -0.67457 -0.09812
C 0 -4.23754 -1.32319 -0.29889
C 0 -3.04266 -0.58183 -0.42305
C 0 -3.03464 0.79623 -0.32455
C 0 -1.71744 1.531426 -0.38649
C 0 -0.80166 1.230989 -1.48816
O 0 -1.43127 2.362725 0.467415
C 0 -1.07545 0.526551 -2.64817
N 0 0.007406 0.527549 -3.47967
C 0 1.03655 1.241389 -2.86957
C 0 0.557878 1.709317 -1.62165
C 0 2.327989 1.516394 -3.324
C 0 3.143532 2.282279 -2.50142
C 0 2.684675 2.75918 -1.26096
C 0 1.400854 2.483361 -0.81204
C 0 0.082248 -0.14721 -4.77073
C 0 0.748945 -1.52761 -4.7052
C 0 0.813257 -2.20805 -6.0764
```

C 0 1.478167 -3.58936 -6.03878
C 0 1.535301 -4.26731 -7.41023
H 0 -7.69392 3.294385 0.466316
H 0 -7.61845 0.833543 0.2735
H 0 -3.43503 3.493429 -0.00602
H 0 -5.59168 4.615434 0.315566
H 0 -6.35376 -1.23508 -0.00878
H 0 -4.20467 -2.40512 -0.36071
H 0 -2.10698 -1.10822 -0.56974
H 0 -1.99102 0.042532 -2.94966
H 0 2.687687 1.151712 -4.27894
H 0 4.151973 2.51648 -2.82307
H 0 3.348547 3.356629 -0.64646
H 0 1.036599 2.856388 0.135243
H 0 0.622016 0.504565 -5.46396
H 0 -0.93798 -0.23829 -5.15227
H 0 0.190851 -2.1557 -4.00192
H 0 1.757916 -1.42127 -4.29337
H 0 1.359747 -1.56525 -6.77866
H 0 -0.20166 -2.30794 -6.48297
H 0 0.934794 -4.23104 -5.33522
H 0 2.49332 -3.48906 -5.63708
H 0 2.015178 -5.2475 -7.34949
H 0 2.101586 -3.66439 -8.12685
H 0 0.531784 -4.41384 -7.82172

VITA

CHIARA DERIU

Born, Cagliari, Sardinia, Italy

- 2011 B.S., Technologies for the Conservation and Restoration of Cultural Heritage
focus in: Analytical Chemistry for Cultural Heritage
University of Bologna
Ravenna, Italy
- 2014 M.S., Science for the Conservation-Restoration of Cultural Heritage
focus in: Analysis of Organic Materials
University of Bologna
Ravenna, Italy
- 2018 M.S., Chemistry (*en route*)
Florida International University
Miami, Florida
- 2020 Dissertation Year Fellowship
PhD in Chemistry, exp. December 2020
Florida International University
Miami, Florida

PUBLICATIONS AND PRESENTATIONS

Deriu, C.; Conticello, I.; Mebel, A.M.; McCord, B. Micro Solid Phase Extraction Surface-Enhanced Raman Spectroscopy (μ -SPE/SERS) Screening Test for the Detection of the Synthetic Cannabinoid JWH-018 in Oral Fluid. *Anal. Chem.*, 2019, *91*(7), 4780–4789.

Wang, L.; Deriu, C.; Wu, W.; Mebel, A.M.; McCord, B. Surface-enhanced Raman spectroscopy, Raman, and density functional theoretical analyses of fentanyl and six analogs. *J. Raman Spectrosc.*, 2019, *50*, 1405–1415.

Deriu, C.; Paudyal, J.; Bhardwaj, V.; McCord, B. SERS for the Forensic Toxicological Screening of Drugs. In *Surface-Enhanced Raman Spectroscopy: Methods, Analysis and Research*; Bhardwaj, V., McGoron, A. J., Eds.; Nova Science Publishers: Hauppauge, NY., 2019.

Wang, L.; Vendrell-Dones, M.O.; Deriu, C.; Doğruer, S.; Harrington, P. de B.; McCord, B. Multivariate Analysis Assisted Surface Enhanced Raman Spectroscopy (MVA-SERS)

Determination of Fentanyl in Cocaine and Heroin Mixtures Using a Handheld Raman Spectrometer, *Appl. Spectrosc.*, *submitted*)

Deriu, C.; Bracho, A.; McCord, B. Tailored colloidal nanostars for SERS applications: optimization of formulation components and study of the stabilizer-nanoparticle interactions, *manuscript in preparation*. (Target journals: *J. Colloid Interface Sci.*, *Langmuir*)

Deriu, C.; Morozov, A.N.; Mebel, A.M.; McCord, B. Adsorption of citrate on mono- and bimetallic noble metal clusters, *manuscript in preparation*. (Target journals: *ACS Nano*, *Nanoscale*)

Deriu, C.; Prifti, M.; Harrington, P.; Mebel, A.M.; McCord, B. Towards an *in silico* Raman library for synthetic cannabinoids with matching algorithm, *manuscript in preparation*. (Target journals: *Talanta*, *Forensic Sci. Int.*)

Deriu, C.; Bracho, A.; Wang, L.; Morozov, A.N.; Mebel, A.M.; McCord, B. Optimization of the surface environment of SERS-active colloidal nanomaterials. NanoFlorida 2020, Miami, FL, September 2020. (*Virtual poster, 3rd place winner*)

Deriu, C.; Conticello, I.; Mebel, A.M.; McCord, B. SERS as an analytical tool for synthetic cannabinoids screening in oral fluid. SciX 2019, Palm Springs, CA, October 2019. (*Invited talk*)

Deriu, C.; Mebel, A. M.; McCord, B. The determination of synthetic cannabinoids in oral fluid using Surface-enhanced Raman spectroscopy (SERS). In *Novel Forensic Chemistry Research from Early-Career Scientists*, September 19, 2018; Forensic Technology Center of Excellence (FTCoE). (*Webinar*)

Deriu, C.; McCord, B. Insight on the surface chemistry of bimetallic nanostars: capping agents and stability. PITTCON 2018 Conference and Expo, Orlando, FL, February 2018 (*Oral presentation*)

Deriu, C.; McCord, B. Surfactant-free anisotropic nanoparticles: stabilization approaches and trends in capping efficacy. NanoFlorida, Miami, FL, September 2017 (*Oral presentation*)